

NR68H-434

VOLUME II

AD 723824

INTERNAL AERODYNAMICS MANUAL

June 1970

Prepared for

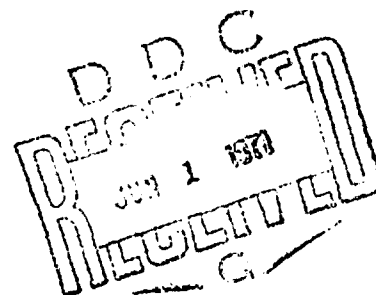
NAVAL AIR SYSTEMS COMMAND
WASHINGTON, D.C.

CONTRACT NO. 66-0460-d

APPROVED FOR PUBLIC RELEASE;
DISTRIBUTION UNLIMITED

Prepared by

COLUMBUS DIVISION
NORTH AMERICAN ROCKWELL CORPORATION
COLUMBUS, OHIO 43216



VOL I = AD 723823

Reproduced by
NATIONAL TECHNICAL
INFORMATION SERVICE
Springfield, Va. 22151

515

NR68H-434

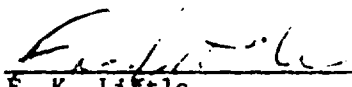
INTERNAL AERODYNAMICS MANUAL

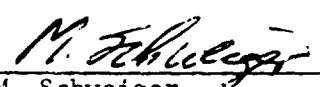
Prepared for
NAVAL AIR SYSTEMS COMMAND
WASHINGTON, D.C.

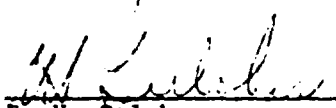
CONTRACT N0w66-0460-d

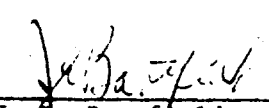
Prepared by
COLUMBUS DIVISION
NORTH AMERICAN ROCKWELL CORPORATION
COLUMBUS, OHIO 43216

APPROVED BY


F. K. Little
Manager
Thermodynamics & Propulsion


M. Schweiger
Manager
Aero-Thermo


R. H. Gulcher
Chief Engineer
Aircraft Research
and Engineering


J. B. Bartfield
Aircraft R&D

June 1970

REPRODUCTION QUALITY NOTICE

This document is the best quality available. The copy furnished to DTIC contained pages that may have the following quality problems:

- **Pages smaller or larger than normal.**
- **Pages with background color or light colored printing.**
- **Pages with small type or poor printing; and or**
- **Pages with continuous tone material or color photographs.**

Due to various output media available these conditions may or may not cause poor legibility in the microfiche or hardcopy output you receive.

☐ **If this block is checked, the copy furnished to DTIC contained pages with color printing, that when reproduced in Black and White, may change detail of the original copy.**

ABSTRACT

The Internal Aerodynamics Handbook has been developed in order to provide a convenient, accurate and reliable internal aerodynamics design manual which enables rapid determination of the internal airflow effects on airplane performance. It also enables the computation of internal airflow systems performance by developed theoretical and empirical methods. The scope of the design manual relates specifically to internal aerodynamics for the complete aircraft speed range up to and including Mach 3.5. In addition to the detailed data and methods presentation, an extensive bibliography is provided.

KEY WORDS

Additive Drag
Airflow
Control System
Cooling
Diffuser
Ejector
Exhaust Nozzle
High Bypass Ratio
Inlet
Instability
Installation Loss
Jet Effects
Thermodynamics
Thrust
Thrust Reverser

TABLE OF CONTENTS

<u>Section</u>	<u>Title</u>	<u>Page</u>
	List of Figures	xii
	Introduction	xxxii
1.0	Inlet Design Considerations	1-1
	1.1 Inlet Sizing	1-2
	1.2 Inlet Location	1-3
	1.3 Method of Pre-Compression	1-3
	1.4 Compression Surface Orientation	1-5
	1.5 Boundary Layer Removal Provisions	1-5
2.0	Air Induction System Loss Determination	2-1
	2.1 Inlet Lip Losses - Sharp Lips	2-1
	2.2 Inlet Lip Losses - Rounded Lips	2-2
	2.3 Low Speed Inlet Loss Calculation Method	2-3
	2.4 Inflow Losses at Subsonic Speeds; Mass-Flow-Ratio Less Than 1.0	2-5
	2.5 Shock Loss Determination	2-5
	2.5.1 Normal Shock Loss	2-5
	2.5.2 Two-Dimensional Oblique Shock Wave Analysis	2-6
	2.5.3 Axisymmetric or Three-Dimensional Oblique Shock Wave Analysis	2-8
	2.6 Internal Ducting Losses	2-10
	2.6.1 Principles of Ducting Loss Analysis	2-10
	2.6.1.1 Sources of Losses	2-10
	2.6.1.2 Correlation of Duct Component Pressure Loss Data	2-11
	2.6.1.3 Evaluation of Overall Inlet System Loss	2-13
	2.6.2 Subsonic Diffusion Losses	2-14
	2.6.2.1 General Considerations	2-14
	2.6.2.2 Conical Diffuser Losses	2-16
	2.6.2.3 Non-Conical Diffuser Losses	2-17
	2.6.2.4 Boundary Layer Control Provisions	2-17

<u>Section</u>	<u>Title</u>	<u>Page</u>
	2.6.3 Miscellaneous Losses	2-18
	2.6.3.1 Elbows	2-18
	2.6.3.2 Constant Area Ducts	2-19
	2.6.3.3 Screens	2-20
	2.6.4 Effects of Losses on Pressure Recovery	2-20
	2.6.5 Pressure Distortion Effects	2-21
	2.6.6 Subsonic Duct Loss Calculation Method	2-22
3.0	Boundary Layer Considerations	3-1
	3.1 Boundary Layer Thickness	3-1
	3.2 Boundary Layer Profiles	3-2
	3.3 Fuselage Boundary Layer Removal	3-3
	3.4 Compression Surface Boundary Layer Removal	3-4
4.0	Additive Drag	4-1
	4.1 Theoretical Additive Drag	4-1
	4.2 Subsonic Additive Drag	4-7
	4.3 Supersonic Additive Drag	4-7
	4.3.1 Two-Dimensional Inlets	4-11
	4.3.2 Three-Dimensional Inlets	4-12
	4.4 Terminal Shock Wave Position	4-14
	4.5 Additive Drag Correction	4-16
5.0	Inlet Instability and Unsteady Flow Phenomena	5-1
	5.1 Unsteady Flow at Static and Subsonic Flight Conditions	5-1
	5.2 Duct Humble and Twin Duct Instability	5-2
	5.3 Supersonic Unsteady Flow Phenomena	5-3
	5.3.1 Supersonic Normal Shock Oscillation	5-3
	5.3.2 Inlet Buzz	5-4
	5.4 Inlet/Engine Dynamic Interaction	5-5

<u>Section</u>	<u>Title</u>	<u>Page</u>
6.0	Inlet Control Considerations	6-1
6.1	Requirements for an Air Inlet Control System	6-2
6.1.1	Inlet Control System Performance	6-3
6.1.2	Inlet Off-Design Point Penalties	6-4
6.1.3	Inlet-Engine Airflow Matching	6-5
6.1.4	Inlet Transients, Buzz and Distortion Limits	6-5
6.2	Configuration of Variable Geometry Inlets	6-6
6.2.1	Two-Dimensional Inlets (2-D)	6-6
6.2.1.1	Ramps	6-6
6.2.1.1.1	Ramp Location	6-7
6.2.1.1.2	By-Pass Ring or Doors	6-7
6.2.1.1.2.1	By-Pass Ring	6-8
6.2.1.1.2.2	By-Pass Doors	6-8
6.2.2	Axially Symmetric (3-D) Inlets	6-8
6.2.2.1	Spike	6-9
6.2.2.1.1	Translating Spike	6-9
6.2.2.1.2	Collapsible Spikes	6-9
6.3	Comparison of 2-D and 3-D Inlet Control Systems	6-10
6.4	Inlet Control System	6-10
6.4.1	Closed vs Open Loop Systems	6-11
6.4.2	Considerations for Inlet Control System Selection	6-12
6.4.2.1	Signals	6-13
6.4.2.2	Manual Control	6-14
6.4.2.3	Flexibility	6-14
6.4.2.4	Complexity	6-14
6.4.2.5	Installation	6-15
6.4.2.6	Power Consumption	6-15
6.4.2.7	Weight	6-15
6.5	Sensors	6-15
6.5.1	Mechanical Sensors	6-16

<u>Section</u>	<u>Title</u>	<u>Page</u>
	6.5.1.1 Jet Pipe Concept	6-16
	6.5.1.2 Hydro-Mechanical Vector Sensor	6-16
	6.5.1.3 Force Balancing Beam Concept	6-17
	6.5.2 Electronic Sensors	6-17
	6.5.3 Pure Fluid Amplifiers	6-18
6.6	Servo Valve	6-19
	6.6.1 Output Power of Servo Valve	6-21
	6.6.1.1 Two-Stage Hydraulic Servo Valves	6-22
6.7	Actuators	6-23
	6.7.1 Design Considerations	6-24
	6.7.2 Weight Formulae and Curves	6-25
	6.7.3 Design Summary	6-26
6.8	Linkages	6-27
	6.8.1 Power Linkages	6-27
	6.8.2 Follow-up Linkages	6-27
6.9	Error Analysis	6-28
	6.9.1 Control System Errors	6-28
	6.9.1.1 Sensor Characteristics	6-28
	6.9.1.2 Computer Characteristics	6-29
	6.9.1.3 Feedback Characteristics	6-30
	6.9.2 Sample Error Analysis	6-30
	6.9.2.1 Local Mach Sensor Error	6-30
	6.9.2.2 Scheduling Cam Error	6-30
	6.9.2.3 Control Shifts	6-31
	6.9.2.4 Feedback Error	6-32
	6.9.3 Vehicle Impact	6-32
	6.9.4 Type III Characteristics (Mach 2.5 and Above)	6-33

<u>Section</u>	<u>Title</u>	<u>Page</u>
7.0	Secondary Airflow Systems Performance	7-1
7.1	Introduction	7-1
7.1.1	Definition of Secondary Airflow	7-1
7.1.2	Purposes	7-1
7.2	Engine Cooling	7-1
7.2.1	Cooling Configurations	7-1
7.2.2	Structural Temperatures	7-2
7.3	Inlet Matching	7-2
7.4	Nozzle Performance	7-3
7.4.1	Effects of Secondary Airflow	7-3
7.4.2	Engine Compartment Pressure	7-4
7.5	Estimating Secondary Airflow Quantities	7-6
7.5.1	Method of Calculation with Overboard Dump	7-6
7.5.2	Method of Calculation with Flow Through Compartment	7-10
7.5.3	Engine Compartment Bursting Loads	7-12
7.5.4	Overboard Exits	7-12
7.6	Secondary Airflow Losses	7-14
7.6.1	Inlets and Diffusers	7-14
7.6.1.1	Flush Inlet Losses	7-15
7.6.1.2	Flush Slots	7-17
7.6.1.3	Ram Scoops	7-18
7.7	Heat Exchanger Drag	7-19
7.7.1	Heat Exchanger Types	7-19
7.7.2	Heat Exchanger Drag Estimation	7-20
7.8	Auxiliary Cooling Drag	7-24
7.9	Boundary Layer Bleed Drag	7-24
7.10	Boundary Layer Diverter	7-27
7.10.1	Sizing Considerations	7-27
7.10.2	Drag Estimation	7-28
7.11	By-Pass Door Drag	7-29
7.12	Miscellaneous Drag	7-29

<u>Section</u>	<u>Title</u>	<u>Page</u>
	7.12.1 Screen Drag	7-29
	7.13 Internal Ducting Losses	7-30
8.0	Exhaust Nozzle Performance	8-1
	8.0.1 Introduction	8-1
	8.0.2 Thermodynamic Background	8-2
	8.1 Theoretical Performance	8-4
	8.1.1 Theoretical Thrust Types	8-4
	8.1.2 Convergent Nozzle Thrust Parameter Derivation	8-4
	8.1.2.1 Derivation for Un-Choked Nozzle	8-4
	8.1.2.2 Derivation for Choked Nozzle	8-6
	8.1.3 Optimum Thrust Parameter Derivations	8-7
	8.1.3.1 Derivation of $\frac{F_1}{W T_T}$	8-8
	8.1.3.2 Derivation of $\frac{F_1}{A^* P_T}$	8-10
	8.1.4 Area Ratio	8-15
	8.1.4.1 Optimum Thrust Area Ratio	8-15
	8.1.4.2 Non-Optimum Area Ratio	8-15
	8.2 Coefficients	8-18
	8.2.1 Basic Coefficients	8-18
	8.2.2 Nozzle Efficiency Terms	8-20
	8.3 Discussion and Experimental Performance of Various Nozzle Types	8-22
	8.3.1 Convergent Nozzles	8-22
	8.3.1.1 Simple Convergent	8-22
	8.3.1.2 Annular (For Fan Air)	8-22
	8.3.2 Performance Characteristics of Convergent-Divergent Nozzles	8-25

<u>Section</u>	<u>Title</u>	<u>Page</u>
8.3.3	Convergent Divergent Ejector Nozzles	8-31
8.3.3.1	Experimental Results	8-31
8.3.3.2	Exhaust Angularity	8-35
8.3.3.3	Pumping and Flow Characteristics	8-36
8.3.3.3.1	Nozzle Flow Characteristics	8-36
8.3.3.3.2	Nozzle Flow Instability	8-39
8.3.3.3.3	Nozzle Pumping	8-43
	Characteristic Estimation	
8.3.3.3.4	Ejector Gross Thrust Estimation	8-50
8.3.3.4	Nozzle Flow Separation	8-52
8.3.3.4.1	Base Nozzle Flow Consideration	8-52
8.3.3.4.2	Nozzle Static Thrust Performance	8-54
8.3.3.5	External Aerodynamic Effects on Nozzles	8-56
8.3.4	Plug Nozzles	8-60
8.3.4.1	Introduction	8-60
8.3.4.2	Quiescent Air Testing	8-60
8.3.4.3	Supersonic Expansion	8-60
8.3.4.3.1	Isentropic Plug	8-60
8.3.4.3.2	Conical Plug	8-65
8.3.4.3.3	Convergent-Divergent Plug Nozzle Configuration	8-65
8.3.4.4	Non-Supersonic Expansion	8-66
8.3.4.4.1	Aerodynamic Boattail Nozzle	8-66
8.3.4.4.2	Convergent Plug Nozzle	8-68
8.3.5	Blow-In-Door Ejector Nozzles	8-72
8.3.6	Expansion-Deflection Nozzle	8-75
8.4	Comparison of Nozzle Performance	8-77

<u>Section</u>	<u>Title</u>	<u>Page</u>
	8.4.1 Introduction	8-77
	8.4.2 Nozzle Types	8-78
	8.4.3 Integration and Evaluation	8-80
8.5	Thrust Reversers	8-82
	8.5.1 Aircraft Applications for Reverse Thrust	8-82
	8.5.2 Configurations of Thrust Reversers	8-83
	8.5.3 Performance of Thrust Reversers	8-85
	Symbols	8-89
	References	8-92
9.0	Afterbody and Exhaust System Drag	9-1
9.1	Afterbody Drag	9-4
9.1.1	Skin Friction Drag Component	9-4
	9.1.1.1 Two-Dimensional Bodies	9-7
	9.1.1.2 Three-Dimensional Bodies	9-8
	9.1.1.3 Effects of Wall Temperature	9-9
	9.1.1.4 Effects of Surface Roughness	9-11
9.1.2	Pressure Drag Component	9-18
	9.1.2.1 Subsonic-Transonic Speeds	9-18
	9.1.2.2 Supersonic Speeds	9-19
	9.1.2.2.1 Two-Dimensional Afterbodies	9-20
	9.1.2.2.2 Three-Dimensional Afterbodies	9-21
	9.1.2.3 Bodies of Arbitrary Cross-Section	9-23
9.2	Base Drag	9-24
9.2.1	Two-Dimensional Base Drag	9-24
	9.2.1.1 Base Flow Characteristics and Flow Analogy	9-24
	9.2.1.2 Effects of Afterbody Boattailing	9-27
	9.2.1.2.1 Subsonic Speeds	9-27
	9.2.1.2.2 Supersonic Speeds	9-28
	9.2.1.3 Effect of Angle of Attack	9-32

<u>Section</u>	<u>Title</u>	<u>Page</u>
9.2.2	Axisymmetric Base Drag	9-33
9.2.2.1	Three-Dimensional Wake Characteristics	9-33
9.2.2.2	Effects of Afterbody Boattailing	9-34
9.2.2.2.1	Subsonic-Transonic Speeds	9-34
9.2.2.2.2	Supersonic Speeds	9-36
9.2.2.3	Effect of Angle of Attack	9-38
9.3	Jet Interference Effects on Afterbody and Base Drag	9-39
9.3.1	Description of Jet Interference Flow Phenomena	9-40
9.3.1.1	Analytical Flow Model	9-40
9.3.1.2	Criterion for Incipient Separation	9-44
9.3.1.3	Pressure Rise Across Reattachment Region	9-47
9.3.2	Calculation Procedures	9-48
9.3.3	Test Results	9-54
9.3.3.1	Afterbody Shaping	9-54
9.3.3.2	Test Model Design	9-55
9.3.3.3	Analysis of Results	9-55
9.3.3.3.1	Consider Drag at Subsonic Mach Numbers for Configuration with Non-Augmented Nozzles	9-56
9.3.3.3.2	Consider Drag at Subsonic Mach Numbers for Configurations with Augmented Setting Nozzles	9-58
9.3.3.3.3	Consider Drag for Low Supersonic Mach Numbers and Configurations with Augmented Nozzles	9-59
9.3.3.4	Conclusions	
10.0	High Bypass Ratio Turbofan Installation	10-1
10.1	Introduction	10-1
10.2	High Bypass Ratio Turbofan Installation Considerations	10-5

<u>Section</u>	<u>Title</u>	<u>Page</u>
	10.2.1 Windmilling Performance	10-5
	10.2.2 Exhaust Path Design	10-5
	10.2.3 Cooling	10-7
	10.2.4 Miscellaneous	10-7
10.3	Installation Loss Breakdown	10-7
	10.3.1 External Losses	10-7
	10.3.1.1 Additive Drag	10-8
	10.3.1.2 Fan Cowl Friction	10-8
	10.3.1.3 Boattail Drag	10-8
	10.3.1.4 Scrubbing and Interference Drag	10-10
	10.3.1.5 Testing Methods	10-12
	10.3.2 Internal Losses	10-14
10.4	Performance Summary	10-15
10.5	Thrust Reverser Installation	10-17
Appendices		
	Appendix A. Basic Thermodynamic Relationships	A1
	Appendix B. Normal Shock Wave Parameters	B1
	Appendix C. Two-Dimensional Shock Wave Analysis	C1
	Appendix D. Three-Dimensional Shock Wave Analysis	D1
	Appendix E. Corrected Weight Flow Parameters	E1
	Appendix F. Parameters for Thrust Calculation	F1

LIST OF FIGURES

<u>Figure No.</u>	<u>Title</u>	<u>Page</u>
1-1	Typical Variation of Corrected Airflow.	1-8
1-2	Typical Pressure Recovery Schedule.	1-9
1-3	Typical Variation of Freestream Tube Area.	1-10
1-4	Example of Relationship of A_0 to A_c .	1-11
1-5	Local Flow Conditions on a Body.	1-12
1-6	Inlet Local Angle of Attack and Mach Number as Measured in Flight, Side Inlet Location.	1-3
2-1	Theoretical Sharp Lip Inlet Total Pressure Recovery.	2-26
2-2	Low Speed Lip Loss Correlation. $M_0 = 0.166$	2-27
2-3	Ratio of Experimental Lip Suction Coefficient to Coefficient Required to Make Lip Loss Vanish. $MFR = 1.0$ $M_0 = 0-0.4$	2-28
2-4	Lip Suction Coefficient, K , Required to Make Lip Loss Vanish. $M_0 = 0$	2-29
2-5	Lip Suction Coefficient, K , Required to Make Lip Loss Vanish.	2-30
2-6	Inlet Lip Loss Correlation.	2-31
2-7	Inlet Lip Loss Correlation. $M_0 = 0.237$	2-32
2-8	Inlet Lip Loss Correlation Elliptical Profiles. $M_0 = 0.237$	2-33
2-9	Examples of Normal Shocks.	2-34
2-10	Normal Shock Wave Parameter.	2-35
2-11	Oblique Shock Wave Velocity Relationships.	2-36
2-12	Optimum Pressure Recovery for 2, 3 And 4-Shock, 2-Dimensional Inlet.	2-37
2-13	Optimum Deflection Angles for 2-Shock, 2-Dimensional Inlet.	2-38
2-14	Optimum Deflection Angles for 3-Shock, 2-Dimensional Inlet.	2-39
2-15	Optimum Deflection Angles for 4-Shock, 2-Dimensional Inlets.	2-40
2-16	Shock Wave Angles Corresponding to Optimum Deflection Angles for 2-Shock, 2-Dimensional Inlet.	2-41
2-17	Shock Wave Angles Corresponding to Optimum Deflection Angles for 3-Shock, 2-Dimensional Inlet.	2-42
2-18	Shock Wave Angles Corresponding to Optimum Deflection Angles for 4-Shock, 2-Dimensional Inlet.	2-43

<u>Figure No.</u>	<u>Title</u>	<u>Page</u>
2-19	Downstream Mach Numbers Corresponding to Optimum Deflection Angles for 2-Shock, 2-Dimensional Inlet.	2-44
2-20	Downstream Mach Numbers Corresponding to Optimum Deflection Angles for 3-Shock, 2-Dimensional Inlet.	2-45
2-21	Downstream Mach Numbers Corresponding to Optimum Deflection Angles for 4-Shock, 2-Dimensional Inlet.	2-46
2-22	Deflection Angles for Shock Detachment and Sonic Flow, 2-Dimensional.	2-47
2-23	Double Cone in Supersonic Flow.	2-48
2-24	Optimum Deflection Angles for Axisymmetric 2 and 3-Shock Inlets.	2-49
2-24	Turbulent Boundary Layer Thickness and Friction Criteria. (References 10 and 11)	2-50
2-26	Compressibility Effects in Diffusers. (Reference 16)	2-51
2-27	Effect of Diffuser Divergence Angle on Length.	2-52
2-28	Diffuser Momentum and Turbulence Loss Criteria. (Reference 16)	2-53
2-29	Diffuser Friction Loss Criteria.	2-54
2-30	Typical Conical Diffuser Losses.	2-55
2-31	Typical Losses for Various Types of Diffusers. (Reference 16)	2-56
2-32	Typical Supersonic Shock Compression Boundary Layer Control.	2-57
2-33	Typical Boundary Layer Control Provisions for Annular Subsonic Diffusers.	2-58
2-34	Elbow Pressure Losses. (Reference 14)	2-59
2-35	Screen Pressure Losses. (Reference 20 and 24)	2-60
2-36	Effect of Subsonic Losses on Inlet Pressure Recovery.	2-61
2-37	Inlet Flow Mach Number Parameters.	2-62
3-1	Variation of Reynolds Number with Mach Number at Various Altitudes, Standard Atmosphere.	3-6
3-2	Boundary Layer Thickness Data, Fuselage Station 221, Lower Surface.	3-7
3-3	Boundary Layer Thickness Data, Fuselage Station 274, Altitude 40,000 Ft.	3-8
3-4	Boundary Layer Thickness Data, Fuselage Station 258, Altitude 40,000 Ft.	3-9
3-5	Theoretical Performance of Inlets in the Presence of a Boundary Layer Without Precompression.	3-10
3-6	Theoretical Performance of Inlets in the Presence of a Boundary Layer Without Compression.	3-11
3-7	Theoretical Performance of Inlets in the Presence of a Boundary Layer Without Compression.	3-12
3-8	Theoretical Performance of Inlets in the Presence of a Boundary Layer Without Compression.	3-13

<u>Figure No.</u>	<u>Title</u>	<u>Page</u>
3-9	Theoretical Performance of Inlets in the Presence of a Boundary Layer Without Compression.	3-14
3-10	Theoretical Performance of Inlets in the Presence of a Boundary Layer Without Compression.	3-15
3-11	Theoretical Performance of Inlets in the Presence of a Boundary Layer Without Compression.	3-16
3-12	Theoretical Performance of Inlets in the Presence of a Boundary Layer Without Compression.	3-17
3-13	Theoretical Performance of Inlets in the Presence of a Boundary Layer Without Compression.	3-18
3-14	Theoretical Performance of Inlets in the Presence of a Boundary Layer Without Compression.	3-19
3-15	Theoretical Performance of Inlets in the Presence of a Boundary Layer Without Compression.	3-20
3-16	Theoretical Performance of Inlets in the Presence of a Boundary Layer Without Compression.	3-21
3-17	Typical Boundary Layer Diverter on a Two-Dimensional Horizontal Ramp Inlet.	3-22
3-18	Typical Boundary Layer Diverter on a Two-Dimensional Vertical Ramp Inlet.	3-23
3-19	Diverter Static Pressure Distribution - $M_0 = 0.9$.	3-24
3-20	Diverter Static Pressure Distribution - $M_0 = 1.57$.	3-25
3-21	Diverter Static Pressure Distribution - $M_0 = 1.97$.	3-26
3-22	Compression Surface Boundary Layer Control.	3-27
3-23	Effect of Compression Surface Bleed on Inlet Performance and Distortion - $M_0 = 2.05$.	3-28
3-24	Summary of Bleed Effectiveness - $M_0 = 2.05$.	3-29
3-25	Effect of Mach Number on Bleed Flow.	3-30
4-1	Illustration of Meaning of Additive Drag.	4-19
4-2	Schematic Representation of Forces Acting on a Typical Propulsion System - Using Stations 1 and e.	4-20
4-3	Schematic Representation of Forces Acting on a Typical Propulsion System - Using Stations 0 and e.	4-21
4-4	Illustration of Inlet Spillage.	4-22
4-5	Illustration of a Control Volume Used to Calculate Additive Drag.	4-23
4-6	Example for Theoretical Additive Drag Calculation.	4-24
4-7	Open Nose Inlet at Mass Flow Ratio Less Than 1.0.	4-25
4-8	Theoretical Additive Drag Coefficient - Open Nose Inlet.	4-26
4-9	Illustration of Stagnation Point Movement With Mass Flow Variation for a Blunt-Lipped Inlet. (a) Stagnation Stream-Tube Area Variation (b) Mathematical Approximation	4-27

<u>Figure No.</u>	<u>Title</u>	<u>Page</u>
4-10	Example of Inlet Surface Velocity Distribution and Stagnation Point Movement for an Axisymmetric Inlet_Potential Flow Simulation.	4-28
4-11	Flow Patterns for Sharp-Lip Inlet.	4-29
4-12.	Theoretical Additive Drag for a Sharp Lip (Supersonic) Operating at Subsonic Speeds.	4-30
4-13	Illustration of Terminal Shock Wave Position and Approximation Used in Theoretical Additive Drag Calculations.	4-31
4-14	Theoretical Additive Drag Coefficient for 2-Shock, All-External Inlet or Mixed Compression Inlet with Single External Shock.	4-32
4-15	Theoretical Additive Drag Coefficient for 2-Shock, All-External Inlet or Mixed Compression Inlet with Single External Shock.	4-33
4-16	Theoretical Additive Drag Coefficient for 2-Shock, All-External Inlet or Mixed Compression Inlet with Single External Shock.	4-34
4-17	Theoretical Additive Drag Coefficient for 2-Shock, All-External Inlet or Mixed Compression Inlet with Single External Shock.	4-35
4-18	Theoretical Additive Drag Coefficient for 2-Shock, All-External Inlet or Mixed Compression Inlet with Single External Shock.	4-36
4-19	Theoretical Additive Drag Coefficient for 2-Shock, All-External Inlet or Mixed Compression Inlet with Single External Shock.	4-37
4-20	Theoretical Additive Drag Coefficient for 2-Shock, All-External Inlet or Mixed Compression Inlet with Single External Shock.	4-38
4-21	Theoretical Additive Drag Coefficient for 2-Shock, All-External Inlet or Mixed Compression Inlet with Single External Shock.	4-39
4-22	Illustration of 3-Shock Geometric Relationships.	4-40
4-23	Theoretical Additive Drag Coefficient for 3-Shock, All-External Inlet or Mixed Compression Inlet with Two-External Shocks.	4-41
4-24	Theoretical Additive Drag Coefficient for 3-Shock, All-External Inlet or Mixed Compression Inlet with Two-External Shocks.	4-42
4-25	Theoretical Additive Drag Coefficient for 3-Shock, All-External Inlet or Mixed Compression Inlet with Two-External Shocks.	4-43
4-26	Theoretical Additive Drag Coefficient for 3-Shock, All-External Inlet or Mixed Compression Inlet with Two-External Shocks.	4-44

<u>Figure No.</u>	<u>Title</u>	<u>Page</u>
4-27	Theoretical Additive Drag Coefficient for 3-Shock, All-External Inlet or Mixed Compression Inlet with Two-External Shocks.	4-45
4-28	Theoretical Additive Drag Coefficient for 3-Shock, All-External Inlet or Mixed Compression Inlet with Two-External Shocks.	4-46
4-29	Theoretical Additive Drag Coefficient for 3-Shock, All-External Inlet or Mixed Compression Inlet with Two-External Shocks.	4-47
4-30	Theoretical Additive Drag Coefficient for 3-Shock, All-External Inlet or Mixed Compression Inlet with Two-External Shocks.	4-48
4-31	Illustration of Additive Drag Calculation Path for an Axisymmetric Inlet.	4-49
4-32	Diagram Showing Conical Flow Field Streamline Construction.	4-50
4-33	Theoretical Additive Drag Design Charts for Axisymmetric (Single Cone) Inlets. Cone Semi-Vertex Angle $\theta_{r1} = 5^\circ$	4-51
4-34	Theoretical Additive Drag Design Charts for Axisymmetric (Single Cone) Inlets. Cone Semi-Vertex Angle $\theta_{r1} = 6^\circ$	4-52
4-35	Theoretical Additive Drag Design Charts for Axisymmetric (Single Cone) Inlets. Cone Semi-Vertex Angle $\theta_{r1} = 7^\circ$	4-53
4-36	Theoretical Additive Drag Design Charts for Axisymmetric (Single Cone) Inlets. Cone Semi-Vertex Angle $\theta_{r1} = 8^\circ$	4-54
4-37	Theoretical Additive Drag Design Charts for Axisymmetric (Single Cone) Inlets. Cone Semi-Vertex Angle $\theta_{r1} = 10^\circ$	4-55
4-38	Theoretical Additive Drag Design Charts for Axisymmetric (Single Cone) Inlets. Cone Semi-Vertex Angle $\theta_{r1} = 12.5^\circ$	4-56
4-39	Theoretical Additive Drag Design Charts for Axisymmetric (Single Cone) Inlets. Cone Semi-Vertex Angle $\theta_{r1} = 15^\circ$	4-57
4-40	Theoretical Additive Drag Design Charts for Axisymmetric (Single Cone) Inlets. Cone Semi-Vertex Angle $\theta_{r1} = 17.5^\circ$	4-58
4-41	Theoretical Additive Drag Design Charts for Axisymmetric (Single Cone) Inlets. Cone Semi-Vertex Angle $\theta_{r1} = 20^\circ$	4-59

<u>Figure No.</u>	<u>Title</u>	<u>Page</u>
4-42	Theoretical Additive Drag Design Charts for Axisymmetric (Single Cone) Inlets. Cone Semi-Vertex Angle $\theta_{r1} = 25^\circ$	4-60
4-43	Theoretical Additive Drag Design Charts for Axisymmetric (Single Cone) Inlets. Cone Semi-Vertex Angle $\theta_{r1} = 30^\circ$	4-61
4-44	Theoretical Additive Drag Design Charts for Axisymmetric (Single Cone) Inlets. Cone Semi-Vertex Angle $\theta_{r1} = 35^\circ$	4-62
4-45	Illustration of Double-Cone Inlet Flow Field.	4-63
4-46	Illustration of Two-Dimensional Detached Shock Wave Geometry.	4-64
4-47	Compilation and General Correlation of Data on Detachment Distance for Two-Dimensional and Axisymmetric Nose Shapes. (Reference 7)	4-65
4-48	Illustration of Theoretical CD_a Variation Resulting From "Attached" Terminal Shock Position Assumption. Mach 2.4 Design Isentropic Ramp at Mach 2.4.	4-66
4-49	Illustration of Method Employed to Obtain Corrected Additive Drag.	4-67
4-50	Drag Variation With Mass Flow Ratio.	4-68
4-51	Drag Variation With Mass Flow Ratio.	4-69
4-52	Drag Variation With Mass Flow Ratio.	4-70
4-53	Variation of Corrected to Theoretical Additive Drag Ratio. θ_{r1} = Initial Ramp Angle - θ_{r2} = Second Ramp Angle (Reference 11)	4-71
5-1	Theoretical Diffuser Static Pressure Rise as a Function of Initial Mach Number - $\theta/2 = 2^\circ$.	5-7
5-2	Theoretical Diffuser Static Pressure Rise as a Function of Initial Mach Number - $\theta/2 = 4^\circ$.	5-8
5-3	Theoretical Diffuser Static Pressure Rise as a Function of Initial Mach Number - $\theta/2 = 6^\circ$.	5-9
5-4	Sketch of Test Model.	5-10
5-5	Static Pressure Fluctuation Characteristics of Straight Diffuser Models.	5-11
5-6	Diffuser Exit Static Pressure Fluctuation Data	5-12
5-7	Representation of the Nature of Diffuser Total Pressure Fluctuations.	5-13
5-8	Amplitude and Frequency of Diffuser Exit Total Pressure of Sharp Lipped Inlet.	5-14
5-9	Amplitude and Frequency of Diffuser Exit Total Pressure of Round Lipped Inlet.	5-15

<u>Figure No.</u>	<u>Title</u>	<u>Page</u>
5-10	Theoretical Variation of Compressor Face Mach Number with Inlet Mach Number.	5-16
5-11	Streamtube at Low Inlet Mass-Flow-Ratios	5-17
5-12	Twin Duct Instability.	5-18
5-13	Typical Supersonic Inlet Performance Curve with Regions of Instability.	5-19
5-14	Schematics of Buzz Triggering Theories.	5-20
5-15	Effect of Inlet Pressure Fluctuation on Stall.	5-21
6-1	Inlet Compression.	6-35
6-2	Typical Inlet Performance Characteristics.	6-36
6-3	Engine Airflow Matching.	6-37
6-4	Off-Design Inlet Performance.	6-38
6-5	Off-Design Engine Performance.	6-39
6-6	Buzz and Distortion Regions with Varying Engine Airflow.	6-40
6-7	Typical Two-Dimensional Inlet Control System.	6-41
6-8	By-Pass Door Configuration.	6-42
6-9	Illustration of a Conical Spike Inlet Control System.	6-43
6-10	Inlet Control Concepts.	6-44
6-11	Signal With Ideal Control Characteristics.	6-45
6-12	Signal With Poor Control Characteristics.	6-46
6-13	Jet Pipe Pressure Ratio Sensor.	6-47
6-14	Force Vector - Pressure Ratio Sensor.	6-48
6-15	Pressure Ratio Sensor Block Diagram. Compliments of AiResearch Mfg. Div.	6-49
6-16	Stretched Diaphragm Pressure Sensor.	6-50
6-17	Variable Capacitance Concentric Cylinder Pressure Sensor.	6-51
6-18	Pure Fluid Amplifiers.	6-52
6-19	Pressure Ratio Sensor.	6-53
6-20	General Configuration of Valve Ports Showing Control Dimensions.	6-54
6-21	Omitted	6-55
6-22	Omitted	6-56
6-23	Omitted	6-57
6-24	Illustration of Jet Pipe Valve Characteristics.	6-58
6-25	Idealized Characteristics of a Hydraulic Servo Valve.	6-59
6-26	Two-Stage Electrohydraulic Servo Valve. The First Stage is a Four-Way Flapper Valve With a Calibrated Pressure Output, Driving a Second Stage Spring-Loaded Four-Way Spool Valve.	6-60
6-27	Two-Stage Valve With Mechanical Feedback. The First Stage is a Three-Way Valve. The Second Stage is a Four-Way Spool Valve.	6-61
6-28	Two-Stage Valve With Mechanical Feedback. The First Stage is a Four-Way Flapper Valve. The Second Stage is a Four-Way Spool Valve. The extension of the Flapper into a Leaf Spring Acts as the Feedback Element.	6-62

<u>Figure No.</u>	<u>Title</u>	<u>Page</u>
6-29	Two-Stage Servo Valve With a Jet-Pipe First Stage and Mechanical Feedback. The Second Stage is a Four-Way Spool Valve Attached to the First-Stage Nozzle by a Special Feedback Spring.	6-63
6-30	Actuation Geometry and Legend.	6-64
6-31	Actuator Bore Vs Force Gradient - M/L.	6-65
6-32	Actuator Bore Vs Force Gradient - M/L.	6-66
6-33	Actuator Bore.	6-67
6-34	Actuator Stroke Vs Lever Arm and Deflection.	6-68
6-35	Weights of Plain, Single Rod End Actuator Assemblies.	6-69
6-36	Weights of Tandem or Parallel Actuators and Valves Assemblies.	6-70
6-37	Signal Variations	6-71
6-38	Local Mach Sensor - Pressure Ratio Error Vs M_∞	6-72
6-39	Performance of Pressure Ratio Sensor	6-73
6-40	Bypass Door Control Loop Pressure Recovery Vs Signal Pressure Ratio	6-74
6-41	Bypass Door Control Loop - Typical Sensor Accuracy Requirements	6-75
6-42	Centerbody Control Loop - Sensor Accuracy Requirements	6-76
7-1	Typical Engine Compartment Cooling Configuration.	7-33
7-2	Estimated T2B Forward Engine Compartment Secondary Airflow.	7-34
7-3	Structural Temperature Variation With Secondary Airflow.	7-35
7-4	Inlet Optimization.	7-36
7-5	Typical Plot of Nozzle Gross Thrust Coefficient.	7-37
7-6	Sketch of Ejector Configurations.	7-38
7-7	Effect of Secondary Airflow on Ejector Performance - $M_o = 0.9$, 35000 Ft.	7-39
7-8	Effect of Secondary Airflow on Ejector Performance - $M_o = 1.6$, 35000 Ft.	7-40
7-9	Effect of Secondary Airflow on Ejector Performance - $M_o = 2.0$, 35000 Ft.	7-41
7-10	Comparison of Nozzle Gross Thrust Coefficients.	7-42
7-11	Nozzle Pumping Characteristics.	7-43
7-12	Engine Compartment Pressure at Mach No. = 2.0.	7-44
7-13	Engine Compartment Bursting Pressure Versus Power Setting.	7-45
7-14	Sketch of Cooling Configuration.	7-46
7-15	Secondary Airflow Matching.	7-47
7-16	Secondary Airflow Versus Gap Area.	7-48
7-17	Sketch of RA-5C Ground Cooling Configuration.	7-49
7-18	Ground Cooling Airflow Matching.	7-50
7-19	Engine Compartment Bursting Pressures.	7-51

<u>Figure No.</u>	<u>Title</u>	<u>Page</u>
7-20	Sketch of Interaction Between Exit Flow and Free Stream Flow.	7-52
7-21	Performance of the 15-Deg Oblique Exhaust Nozzle with External Flow.	7-53
7-22	Performance of the 30-Deg Oblique Exhaust Nozzle with External Flow.	7-54
7-23	Performance of the 45-Deg Oblique Exhaust Nozzle with External Flow.	7-55
7-24	Performance of the 60-Deg Oblique Exhaust Nozzle with External Flow.	7-56
7-25	Sketch of Flush and Shielded Exits.	7-57
7-26	Performance Comparison of Flush and Shielded Exits.	7-58
7-27	Sketch of RA-5C Engine Compartment Pressure Relief Door.	7-59
7-28	Flow Coefficients for RA-5C Engine Compartment Pressure Relief Door.	7-60
7-29	Correlated Characteristics of Drilled Materials in Normal Flow: $q/P_0 \geq .64$.	7-61
7-30	$q(\sqrt{E_0})$ and $f(\sigma_0)$ for Drilled Materials in Parallel Flow from Equation 1.	7-62
7-31	Nomenclature.	7-63
7-32	Sample Determination of σ_0 as a Function of \overline{AP}/P_0 for the Case of: $\frac{\sqrt{V-T_0}}{\delta_0 A_0} = .010$; $\overline{H}_0 = 1.20$; $l/D_H = 1.00$	7-64
7-33	Recovery Characteristics of a Flush Rectangular Inlet. Reference: (NASA MEMO 12-21-58L).	7-65
7-34	Drag Characteristic of a Flush Rectangular Inlet. Reference: (NASA MEMO 12-21-58L).	7-66
7-35	Recovery Characteristic of a Flush Rectangular Inlet. Reference: (NASA MEMO 12-21-58L).	7-67
7-36	Drag Characteristic of a Flush Rectangular Inlet. Reference: (NASA MEMO 12-21-58L).	7-68
7-37	Recovery Characteristic of a Flush Rectangular Inlet. Reference: (NASA MEMO 12-21-58L).	7-69
7-38	Drag Characteristic of a Flush Rectangular Inlet. Reference: (NASA MEMO 12-21-58L).	7-70
7-39	Recovery Characteristic of a Flush Rectangular Inlet. Reference: (NASA MEMO 12-21-58L).	7-71
7-40	Drag Characteristic of a Flush Rectangular Inlet. Reference: (NASA MEMO 12-21-58L).	7-72
7-41	Recovery Characteristic of a Flush Rectangular Inlet. Reference: (NASA MEMO 12-21-58L).	7-73
7-42	Drag Characteristic of a Flush Rectangular Inlet. Reference: (NASA MEMO 12-21-58L).	7-74

<u>Figure No.</u>	<u>Title</u>	<u>Page</u>
7-44	Pressure Recovery Characteristic of Flush Rectangular Inlet Using a 7° Approach Ramp with Diverging Walls. (NACA Submerged Inlet.) Reference: (NASA MEMO 12-21-58L).	7-75
7-45	Drag Characteristics of a Flush Rectangular Inlet Using a 7° Approach Ramp with Diverging Walls. (NACA Submerged Inlet.) Reference: (NASA MEMO 12-21-58L).	7-76
4-46	Variation of Required Inlet Area with Mach Number for Operation at Equal Mass Flows and Minimum Drag for Each Flush Rectangular Inlet.	7-77
7-47	Mass Flow Ratio for Various Fractions of Boundary Layer Velocity Profile Parameter $M = 7$. Reference: NACA TN 3533.	7-78
7-48	Total Momentum Ratio for Various Fractions of Boundary Layer Velocity Profile Parameter $M = 7$. Reference: NACA TN 3533.	7-79
7-49	Momentum Ratio for Various Fractions of Boundary Layer Velocity Profile Parameter $M = 7$. Reference: NACA TN 3533.	7-80
7-50	Total Pressure Recovery of Attached Rectangular Boundary Layer Inlets for Various Inlet Heights. Velocity Profile Parameter $M = 7$. Reference: NACA TN 3533.	7-81
7-51	Test of Submerged and Scoop Inlet. Reference: NACA RM E53L22c.	7-82
7-52	Total Pressure Recovery of Submerged and Scoop Inlets. Reference: NACA RM E53L23b.	7-83
7-53	Mass Flow Characteristics of a Scoop Inlet.	7-84
7-54	Estimated Actual to Theoretical Mass Flow and Recovery Characteristics of a Scoop Inlet.	7-85
7-55	Typical Heat Exchanger Effectiveness Curves.	7-86
7-56	Typical Heat Exchanger Pressure Drops.	7-87
7-57	Pressure Loss Through Heat Exchanger used in Example.	7-88
7-58	Effect of Ramp Bleed on Inlet Duct Performance.	7-89
7-59	Ramp Bleed Flow Rates.	7-90
7-60	Boundary Layer Diverter Geometry.	7-91
7-61	Turbulent Boundary Layer Profile Characteristics.	7-92
7-62	Turbulent Boundary Layer Profile Characteristics.	7-93
7-63	Mach Number Function For Turbulent Boundary Layer.	7-94
7-64	Free-Stream Reynolds Number Per Unit Length.	7-95
7-65	Equivalent Flat Plate Distance For Turbulent Boundary Layers.	7-96
7-66	Wedge Diverter Pressure Drag Coefficient.	7-97
7-67	Wedge Diverter Pressure Drag Coefficient.	7-98
7-68	Wedge Diverter Pressure Drag Coefficient.	7-99
7-69	Wedge Diverter Skin-Friction Coefficient (Turbulent Flow)	7-100
7-70	Wedge Diverter Skin-Friction Multiplication Factor.	7-101
7-71	Comparison of Results to Experimental Data.	7-102

<u>Figure No.</u>	<u>Title</u>	<u>Page</u>
7-72	Total-Pressure-Loss Coefficient Design Chart for Screens for Values of Loss Coefficient from 0 to 1.0.	7-103
8-1	Turbojet Engine Cycle and Nozzle Process.	8-108
8-2	Isentropic Nozzle Expansion.	8-109
8-3	Real Nozzle Process.	8-110
8-4	Unchoked Convergent Nozzle.	8-111
8-5	Choked Convergent Nozzle.	8-112
8-6	Theoretical Convergent Nozzle Gross Thrust Parameter.	8-113
8-7	Theoretical Convergent Nozzle Gross Thrust Parameter.	8-114
8-8	Theoretical Convergent Nozzle Gross Thrust Parameter.	8-115
8-9	Optimum or Theoretical Maximum Gross Thrust Parameter.	8-116
8-10	Optimum or Theoretical Maximum Gross Thrust Parameter.	8-117
8-11	Optimum or Theoretical Maximum Gross Thrust Parameter.	8-118
8-12	Optimum or Theoretical Maximum Gross Thrust Parameter.	8-119
8-13	Converging Conical Nozzle, Gross Thrust.	8-120
8-14	Converging Conical Nozzle Gross Thrust.	8-121
8-15	Converging Conical Nozzle Gross Thrust.	8-122
8-16	Convergent Divergent Nozzle Terminology.	8-123
8-17	Optimum Nozzle Area Ratio.	8-124
8-18	Variable C-D Nozzle Thrust Coefficients.	8-125
8-19	Variable C-D Nozzle Discharge Coefficients.	8-126
8-20	Theoretical Thrust Variation from Optimum for Various Fixed Area Ratio Nozzles.	8-127
8-21	Theoretical Thrust Types.	8-128
8-22	Theoretical C-D Thrust Variation with Area Ratio and Pressure Ratio, $\gamma = 1.2$.	8-129
8-23	Theoretical C-D Thrust Variation with Area Ratio and Pressure Ratio, $\gamma = 1.25$.	8-130
8-24	Theoretical C-D Thrust Variation with Area Ratio and Pressure Ratio, $\gamma = 1.3$.	8-131
8-25	Theoretical C-D Thrust Variation with Area Ratio and Pressure Ratio, $\gamma = 1.30$.	8-132
8-26	Theoretical C-D Thrust Variation with Area Ratio and Pressure Ratio, $\gamma = 1.35$.	8-133
8-27	Convergent Nozzle Thrust Coefficient.	8-134
8-28	Variable Convergent Nozzle Thrust Coefficient.	8-135
8-29	Estimated Performance of Convergent Nozzle with Blunt Base.	8-136
8-30	Effect of Lip Angle Variation on Gross Thrust Coefficient and Flow Coefficient of a Convergent Nozzle.	8-137
8-31	Effect of Lip Angle Variation at Two Inlet-to-Outlet Diameter Ratios on the Flow Coefficient.	8-138

<u>Figure No.</u>	<u>Title</u>	<u>Page</u>
8-32	Effect of Inlet-to Outlet Diameter Ratio on the Flow Coefficient at Various Lip Angles and at Two Jet Total Pressure Ratios.	8-139
8-33	Annular Nozzle Configurations.	8-140
8-34	Fan Air Exhaust Nozzle on Fan Engine.	8-141
8-35	Schematic Diagram of Jet-Exit Model Installed in 3- by 6-Foot Supersonic Wind Tunnel.	8-142
8-36	Installation of Nozzle in Test Chamber.	8-143
8-37	Thrust Coefficient Characteristics for Conical Nozzle.	8-144
8-38	Thrust Coefficients of Convergent-Divergent Conical Nozzles for Expansion Ratio of 2.65 and Divergent Angles of $7^{\circ}10'$, $11^{\circ}50'$, 24° and 50° .	8-145
8-39	Schematic Diagrams of Convergent-Divergent Conical Nozzles.	8-146
8-40	Nozzles Designed Conical and by Characteristics (All dimensions in inches).	8-147
8-41	Nozzles of Various Throat and Diffuser Geometry, Dimensions in Inches.	8-148
8-42	Variation of Thrust Coefficient with Various Contours.	8-149
8-43	Variation in Thrust Coefficient at a Nozzle Pressure Ratio of 2.0 with Divergence Angle for Nozzles of Various Design Pressure Ratios.	8-150
8-44	Generalized Pressure Distributions Along Divergent Walls of Several Convergent-Divergent Conical Nozzles Having Various Divergence Angles at a Nozzle Pressure Ratio of Approximately 4.	8-151
8-45	Variation of Thrust Coefficient for a Nozzle Designed by Characteristic Theory.	8-152
8-46	Thrust Coefficients for Two C-D Nozzles Having Different Throat Contours Downstream of Throat; Expansion Ratio, 1.8.	8-153
8-47	Thrust Coefficients for Nozzles Having Various Wall Angles; Expansion Ratio = 1.55; $q_d/P_t = .44$	8-154
8-48	Nozzle Thrust Coefficient Characteristics for a Range of Freestream Mach Numbers; Expansion Ratio = 1.39; Nozzle is Conical.	8-155
8-49	Nozzle Thrust Coefficient Characteristics for a Range of Freestream Mach Numbers; Expansion Ratio = 9.0; Nozzle is Conical.	8-156
8-50	Friction Effects on a Convergent-Divergent Conical Nozzle; Expansion Ratio, 1.39; Divergence Angle, $7^{\circ}10'$.	8-157
8-51	Variation in Thrust Coefficient and Nozzle-Exit Area Resulting from Decreases in Divergent Angle.	8-158
8-52	Comparison of Theoretical and Experimental Thrust Variation.	8-159

<u>Figure No.</u>	<u>Title</u>	<u>Page</u>
8-53	Ejector Configurations of NACA RM E55G21a.	8-160
8-54	Test Results of Ejector 1 of NACA RM E55G21a.	8-161
8-55	Test Results of Ejector 2 of NACA RM E55G21a.	8-162
8-56	Test Results of Ejector 3 of NACA RM E55G21a.	8-163
8-57	Test Results of Ejector 4 of NACA RM E55G21a.	8-164
8-58	Test Results of Ejector 5 of NACA RM E55G21a.	8-165
8-59	Test Results of Ejector 6 of NACA RM E55G21a.	8-166
8-60	Test Results of Ejector 11 of NACA RM E55G21a.	8-167
8-61	Test Results of Ejector 12 of NACA RM E55G21a.	8-168
8-62	Ejector Geometry of NASA TN D-763.	8-169
8-63	Performance of Ejector 1 of NASA TN D-763.	8-170
8-64	Pumping Performance of Ejector 1 of NASA TN D-763.	8-171
8-65	Performance of Ejector 2 of NASA TN D-763.	8-172
8-66	Pumping Performance of Ejector 2 of NASA TN D-763.	8-173
8-67	Corrected Ejector Temperature Ratios For Typical Conditions.	8-174
8-68	Ejector Configurations, NACA RM E57F13.	8-175
8-69	Effect of Flow Divergence Angle on Thrust Coefficient at Design Pressure Ratio.	8-176
8-70	Performance of Ejector 1. Exit Diameter Ratio, 1.24; Throat Diameter Ratio, 1.08; Spacing Ratio, 0.38; Flow Divergence Angle, 13°; Shroud Divergence Angle, 15°.	8-177
8-71	Performance of Ejector 2. Exit Diameter Ratio, 1.24; Throat Diameter Ratio, 1.08; Spacing Ratio, 0.28; Flow Divergence Angle, 23°; Shroud Divergence Angle, 20°.	8-178
8-72	Performance of Ejector 3. Exit Diameter Ratio, 1.24; Throat Diameter Ratio, 1.08; Spacing Ratio, 0.22; Flow Divergence Angle, 28°; Shroud Divergence Angle, 25°.	8-179
8-73	Performance of Ejector 4. Exit Diameter Ratio, 1.46; Throat Diameter Ratio, 1.10; Spacing Ratio, 0.69; Flow Divergence Angle, 19°; Shroud Divergence Angle, 15°.	8-180
8-74	Performance of Ejector 5. Exit Diameter Ratio, 1.46; Throat Diameter Ratio, 1.10; Spacing Ratio, 0.51; Flow Divergence Angle, 25°; Shroud Divergence Angle, 20°.	8-181
8-75	Performance of Ejector 6. Exit Diameter Ratio, 1.46; Throat Diameter Ratio, 1.10; Spacing Ratio, 0.40; Flow Divergence Angle, 30°; Shroud Divergence Angle, 25°.	8-182
8-76	Comparison of Nozzle Performance for Two Nozzles with Different Shroud Divergence Angles.	8-183

<u>Figure No.</u>	<u>Title</u>	<u>Page</u>
8-77	Ejector Configuration.	8-184
8-78	Performance of Ejector at Weight-Flow Ratio of About .032. Exit Diameter Ratio, 1.8; Throat Diameter Ratio, 1.0.	8-185
8-79	Shroud Static Pressure Distribution for Various Primary Nozzle Pressure Ratios. Shroud Divergence = 15°. Corrected Weight Flow Ratio, = .032	8-186
8-80	Effect of Secondary Airflow on Nozzle Performance.	8-187
8-81	Shroud Static Pressure Distribution at Several Corrected Weight Flows.	8-188
8-82	Low Base Drag Nozzle Configuration.	8-189
8-83	Low Base Drag Nozzle Pressure Distributions.	8-190
8-84	Converging-Diverging Nozzle with Supersonic Convergence.	8-191
8-85	Typical Diverging Wall Pressures. Nozzle Pressure Ratio $\Delta = 2.336$ $0 = 2.323$	8-192
8-86	Effect of Nozzle Misalignment on Nozzle Performance.	8-193
8-87	Axially Symmetric Compressible Nozzle Flow.	8-194
8-88	Compound-Compressible Flow in a Nozzle of Fixed Geometry.	8-195
8-89	Evolution of a One-Dimensional Compound-Wave.	8-196
8-90	Relationship of Flow Parameters in a Convergent-Divergent Nozzle.	8-197
8-91	Relationship of Flow Parameters During Choked Flow.	8-198
8-92	Stream Mach Numbers at the Nozzle Throat During Choked Flow.	8-199
8-93	Comparison of Compound Compressible Flow Theory with Experimental Results.	8-200
8-94	Schematic of Analytical Model Used in Computations.	8-201
8-95	Choked Pumping Characteristics - Two Flow Ejector $\gamma_1 = 1.3$ $\gamma_2 = 1.4$.	8-202
8-96	Two-Flow Nozzle Pumping Characteristics.	8-203
8-97	Two-Flow Nozzle Pumping Characteristics. $\gamma_1 = 1.3$ $\gamma_2 = 1.4$ $A^*_1/A_{EXIT} = 0.2$	8-204
8-98	Two-Flow Nozzle Pumping Characteristics. $\gamma_1 = 1.3$ $\gamma_2 = 1.4$ $A^*_1/A_{EXIT} = 0.3$	8-205
8-99	Two-Flow Nozzle Pumping Characteristics. $\gamma_1 = 1.3$ $\gamma_2 = 1.4$ $A^*_1/A_{EXIT} = 0.4$	8-206
8-100	Two-Flow Nozzle Pumping Characteristics. $\gamma_1 = 1.3$ $\gamma_2 = 1.4$ $A^*_1/A_{EXIT} = 0.5$	8-207
8-101	Two-Flow Nozzle Pumping Characteristics. $\gamma_1 = 1.3$ $\gamma_2 = 1.4$ $A^*_1/A_{EXIT} = 0.6$	8-208

<u>Figure No.</u>	<u>Title</u>	<u>Page</u>
8-102	Two-Flow Nozzle Pumping Characteristics. $\gamma_1 = 1.3 \quad \gamma_2 = 1.4 \quad A^*_{11}/A_{EXIT} = 0.7$	8-209
8-103	Two-Flow Nozzle Pumping Characteristics. $\gamma_1 = 1.3 \quad \gamma_2 = 1.4 \quad A^*_{11}/A_{EXIT} = 0.8$	8-210
8-104	Two-Flow Nozzle Pumping Characteristics. $\gamma_1 = 1.3 \quad \gamma_2 = 1.4 \quad A^*_{11}/A_{EXIT}$	8-211
8-105	Variation in P_{t2}/P_{t1} with Primary Nozzle Pressure Ratio.	8-212
8-106	Comparison of Theoretical and Experimental Static Thrust Characteristics for One Ejector Operating Point.	8-213
8-107	Optimum Area Ratio and Thrust Trends for Converging-Diverging Nozzles (Reference 1).	8-214
8-108	Typical Operating Regimes for Conical Converging-Diverging Nozzles (References 2 and 3).	8-215
8-109	Convergent-Divergent Ejector Nozzle Flow Fields.	8-216
8-110	Effect of Exit-to-Primary Area Ratio on Divergent Shroud Nozzle Thrust (Reference 10).	8-217
8-111	Effect of Nozzle and Shroud Exit Spacing on Divergent Shroud Ejector Nozzle Thrust.	8-218
8-112	Effect of Secondary Flow on Divergent Shroud Ejector Nozzle Thrust.	8-219
8-113	External Aerodynamic Flow Effects on Nozzle Thrust. (Reference 9)	8-220
8-114	Isentropic Plug Flow and Design Characteristics.	8-221
8-115	Comparison of Nozzle Performance.	8-222
8-116	Two Nozzle Configuration with a Design Pressure Ratio of 16.5.	8-223
8-117	Variation of Gross Thrust-Minus-Drag Coefficient with Jet Total Pressure Ratio.	8-224
8-118	Variation of Gross Thrust Coefficient with Jet Total-Pressure Ratio.	8-225
8-119	Gross Thrust-Minus-Drag and Gross Thrust Coefficients v_{x2} , Mach Number for Jet Total-Pressure Ratio Schedule.	8-226
8-120	Effect of Design Pressure Ratio on Gross Thrust Coefficient.	8-227
8-121	Afterbody Configurations.	8-228
8-122	Comparison of Conical Plug Performance to Isentropic Plug Performance.	8-229
8-123	Other Types of Plug Nozzles.	8-230
8-124	Aerodynamic Boattail Nozzle Configuration and Flow Pattern.	8-231
8-125	Effect of Jet Total-Pressure Ratio and Mach Number on Gross Thrust Coefficient.	8-232

<u>Figure No.</u>	<u>Title</u>	<u>Page</u>
8-126	Effect of Jet Total-Pressure Ratio and Mach Number on Gross Thrust-Minus-Drag Coefficient.	8-233
8-127	Effect of Truncation on Gross Thrust-Minus-Drag and Gross Thrust Coefficients vs. Mach Number at a Jet Total-Pressure Ratio Schedule.	8-234
8-128	Configuration of Convergent Plug Nozzle.	8-235
8-129	Blow-In-Door Ejector.	8-236
8-130	Effect of Mach Number on Ejector Performance.	8-237
8-131	Effect of Blow-In-Door Area on Ejector Performance.	8-238
8-132	Effect of Gross Section Geometry on Ejector Performance.	8-239
8-133	Variation of Gross Thrust Minus Boattail and Shroud Drag Performance with Primary Total-Pressure Ratio for Constant Corrected Weight-Flow Ratios and Mach Numbers.	8-240
134	Variation of Ejector Performance and External Drag Characteristics with Mach Number for a Scheduled Primary Total-Pressure Ratio and Corrected Weight-Flow Ratio.	8-241
8-135	Variation of Nozzle Performance and External Drag Characteristics as a Function of Nozzle Pressure Ratio.	8-242
8-136	Variation of Nozzle Performance and External Drag Characteristics with Mach Number for a Jet Total-Pressure Ratio Schedule.	8-243
8-137	Variation of Average Nozzle Performance Coefficient with Primary Total-Pressure Ratio, Mach No., $M = 0.70$, $\alpha = 5.5^\circ$ (angle of attack).	8-244
8-138	Variation of Average Nozzle Performance Coefficient with Primary Total-Pressure Ratio; Mach No., 1.2; $\alpha, 2^\circ$.	8-245
8-139	Propulsion System Weight.	8-246
8-140	Propulsion System Weight.	8-247
8-141	Nozzle Performance Comparison.	8-248
8-142	Nozzle and Afterbody Analysis Area.	8-249
8-143	Nozzle Types and Relationship.	8-250
8-144	Nozzle Variations.	8-251
8-145	Convergent Nozzles.	8-252
8-146	J79-10, 17 Convergent Divergent Nozzle, Guided Expansion.	8-253
8-147	J79-8, 15 Aerodynamic Vector Nozzle.	8-254
8-148	Flow Diagrams for J79 Exhaust Nozzles.	8-255
8-149	Blow-In-Door Ejector.	8-256
8-150	Blow-In-Door Ejector Flow Diagram.	8-257
8-151	Isentropic Plug Nozzle.	8-258

<u>Figure No.</u>	<u>Title</u>	<u>Page</u>
8-152	Aerodynamic Boattail Nozzle.	8-259
8-153	Aerodynamic Boattail Nozzle with Aft Flap.	8-260
8-154	Performance of Convergent-Divergent Ejector Nozzles.	8-261
8-155	Blow-In-Door Ejector Nozzle.	8-262
8-156	Long-Cone Plug Nozzle, (ABH).	8-263
8-157	Fixed Ejector Exit Configuration.	8-264
8-158	Clustered Jet Exits.	8-265
8-159	Engine Interfairing Pressure Distributions, $M = 1.2$.	8-266
8-160	Performance of Basic-and Extended-Interfairing Configurations, $M = 1.2$.	8-267
8-161	Effect of Nozzle Efficiency on Sea Level Dash Fuel Requirements, $M = 0.85$ Sea Level.	8-268
8-162	Ratio of Gross to Net Thrust with Bypass Ratio.	8-269
8-163	Comparative Effectiveness of Thrust Reversers and Drag Parachutes for Ground Roll Distance Reduction.	8-270
8-164	Comparative Effectiveness of Thrust Reverser Speed Brakes for In-Flight Aircraft Deceleration.	8-271
8-165	Typical Types of Common Reversers.	8-272
8-166	Typical Thrust Reverser Static Performance.	8-273
8-167	Conical Clamshell Target Reverser Performance Trends.	8-274
8-168	Coannular E-D Nozzle.	8-275
8-169	E-D Nozzle Performance.	8-276
8-170	Sting in Base.	8-277
8-171	Base Vent Through Sting.	8-278
8-172	Base Bleed Through Sting.	8-279
8-173	Radial Base Bleed.	8-280
8-174	Axial Base Bleed.	8-281
8-175	Effectiveness of Sting Concepts in Increasing Base Thrust.	8-282
9-1	Transverse Curvature Effects of Turbulent Boundary Layer. (Reference 1)	9-64
9-2	Effect of Compressibility on Skin Friction to Smooth and "Completely Rough" Surfaces.	9-65
9-3	Increase of Skin Friction Due to Surface Roughness.	9-66
9-4	Superposition of Pressure Distribution. (Reference 8)	9-67
9-5	Subsonic Wave Drag of Conical Afterbodies.	9-68
9-6	Subsonic-Transonic Wave Drag of Circular Arc Afterbodies.	9-69
9-7	Conical Boattail Analogy. (Reference 8)	9-70
9-8	Supersonic Wave Drag of Wedge Afterbodies. (Reference 11)	9-71
9-9	Supersonic Wave Drag of Conical Afterbodies. (Reference 11)	9-72
9-10	Supersonic Wave Drag of Parabolic Afterbodies. (Reference 11)	9-73
9-11	Pressure Coefficients on Conical Afterbodies at Supersonic Speeds. (Reference 11)	9-74
9-12	Pressure Coefficients on Cylinder Behind Cone. (Reference 11)	9-75

<u>Figure No.</u>	<u>Title</u>	<u>Page</u>
9-13	Subsonic and Transonic Flow Past a Blunt-Trailing-Edge Section. (Reference 19)	9-76
9-14	Supersonic Flow Analogy.	9-77
9-15	Critical Pressure-Rise Coefficient for Turbulent Boundary Layer on Two-Dimensional Afterbodies.	9-78
9-16	Two-Dimensional Base Pressures ($\alpha = \beta = 0^\circ$, No Jet)	9-79
9-17	Two-Dimensional Wake Turning Angle.	9-80
9-18	Mach Number Notation.	9-81
9-19	Two-Dimensional Boattail Flow Conditions.	9-82
9-20	Two-Dimensional Boattail Separation Angle.	9-83
9-21	Two-Dimensional Afterbody at Angle of Attack.	9-84
9-22	Base Pressure Coefficient for Cylindrical Afterbodies.	9-85
9-23	Axisymmetric Wake Turning Angle. (Reference 8)	9-86
9-24	Subsonic-Transonic Base Pressures on Axisymmetric Boattails.	9-87
9-25	Axisymmetric Boattail Angle at Separation.	9-88
9-26	Axisymmetric Boattail Flow Conditions.	9-89
9-27	Pressure Rise Required for Separation of a Turbulent Boundary Layer on Afterbodies of Revolution. (Reference 6)	9-90
9-28	Supersonic Base Drag Coefficients on Axisymmetric Boattails. (Reference 6)	9-91
9-29a	Supersonic Base Drag Coefficients on Axisymmetric Boattails. (Reference 6)	9-92
9-29b	Supersonic Base Drag Coefficients on Axisymmetric Boattails. (Reference 6)	9-93
9-29c	Supersonic Base Drag Coefficients on Axisymmetric Boattails (Continued). (Reference 6)	9-94
9-29d	Supersonic Base Drag Coefficients on Axisymmetric Boattails (Continued). (Reference 6)	9-95
9-29e	Supersonic Base Drag Coefficients on Axisymmetric Boattails (Concluded). (Reference 6)	9-96
9-30	Schematic Diagram of Attached External Flow.	9-97
9-31	Schematic Diagram of Separated External Flow.	9-98
9-32a	Sequence of Events Denoting Jet Interference Effects on Afterbody (Reference 25)	9-99
9-32b	Sequence of Events Denoting Jet Interference Effects on Afterbody (Concluded) (Reference 25)	9-100
9-33	Plateau Pressure Rise Coefficient in Turbulent Separated Flow. (Reference 42)	9-101
9-34	Turning Angle Required to Compress Flow to Plateau Pressure Level. (Reference 25)	9-102
9-35	Height of Mach 1.4 Line in Turbulent Boundary Layer.	9-103
9-36	Effect of Pressure Feed-Back on Incipient Separation of Turbulent Boundary Layer. (Reference 32)	9-104
9-37	Flow Schematic of Jet Interference Problem with Attached Boundary Layer.	9-105

<u>Figure No.</u>	<u>Title</u>	<u>Page</u>
9-38	Calculated Requirements for Incipient Separation	9-106
9-39a	Effect of Jet Temperature Ratio on Wake-Pressure Ratio - Continued. (Reference 25)	9-107
9-39b	Effect of Jet Temperature Ratio on Wake-Pressure Ratio - Continued. (Reference 25)	9-108
9-39c	Effect of Jet Temperature Ratio on Wake-Pressure Ratio - Concluded. (Reference 25)	9-109
9-40	Effect of Mixing Length Ratio on Wake-Pressure Ratio. (Reference 25)	9-110
9-41	Effect of Internal Specific Heat Ratio on Wake-Pressure Ratio.	9-111
9-42	Extent of Separation Upstream of Disturbance for Turbulent Flow.	9-112
10-1	Turbofan Gas Flow Paths.	10-20
10-2	Propulsive Efficiency.	10-21
10-3	Specific Fuel Consumption.	10-22
10-4	Specific Thrust.	10-23
10-5	Thrust Lapse With Speed.	10-24
10-6	Cruise to Static Thrust Ratio.	10-25
10-7	JT9D-1 Cutaway.	10-26
10-8	RB.203 Trent Cutaway.	10-27
10-9	Estimated Windmilling Drag.	10-28
10-10	Typical Fan Exit Static Pressure Distortion.	10-29
10-11	Fan Cowl Comparison	10-30
10-12	Cowl Length Comparison	10-31
10-13	Typical Compartment Temperature Zones.	10-32
10-14	Typical High Bypass Turbofan Inlet Velocity Profile.	10-33
10-15	External Drag Breakdown.	10-34
10-16	Afterbody Boattail Drag Test Results.	10-35
10-17	Front Fan Nacelle.	10-36
10-18	Skin Friction Drag Coefficient Based on Surface Wetted Area	10-37
10-19	Reynolds Number	10-38
10-20	Effect of Mach Number on the Skin-Friction Coefficient.	10-39
10-21	Skin Friction Drag Coefficient.	10-40
10-22	Total Nacelle Scrubbing Drag.	10-41
10-23	Scrubbing Drag.	10-42
10-24	Change in Airplane Drag with Nacelle Position.	10-43
10-25	Nacelle Pressure Coefficients, Effect of Fuselage and Wing Proximity.	10-44
10-26	Flow-Through Nacelles.	10-45
10-27	Incremental Nacelle Drag Comparison.	10-46
10-28	Blowing Nacelle.	10-47
10-29	Afterbody Drag vs. Fan Gross Thrust.	10-48
10-30	Powered Fan Simulation.	10-49
10-31	Powered Fan Simulation Calibration.	10-50
10-32	Powered Fan Simulation Calibration Facility.	10-51

<u>Figure No.</u>	<u>Title</u>	<u>Page</u>
10-33	Powered Fan Simulator Performance.	10-52
10-34	Auxiliary Inlets.	10-53
10-35	Auxiliary Inlet Performance	10-54
10-36	Offset Fan Nozzle Velocity Coefficients.	10-55
10-37	Typical Nacelle Drag Breakdown.	10-56
10-38	Effect of Installation on Cruise SFC.	10-57
10-39	Total Installation Loss.	10-58
10-40	Typical Reverser Effectiveness.	10-59
10-41	Thrust Reverser Comparison.	10-60
10-42	Attached Flow Reingestion.	10-61
10-43	Inlet Pressure Recovery.	10-62
10-44	Inlet Distortion.	10-63
10-45	Average Inlet Air Temperature Rise.	10-64
10-46	Effect of Reingestion on Reverser Thrust.	10-65

INTRODUCTION

Airbreathing vehicles have been developed for much of the flight spectrum applicable to their operation. In the twenty year history of turbojet operation, flight speeds have advanced from moderate subsonic to Mach 3 and beyond. Recently, new innovations have appeared such as high by-pass ratio turbofans with high air handling capacities which make induction system losses and associated drag more critical performance items than with conventional turbojets. Variable 3-dimensional inlets, translating spikes, and translating cowls are fairly recent innovations aimed at propulsion system optimization. New exhaust system techniques such as variable guided expansion ejector nozzles, blow-in-door nozzles and IP suppression plug nozzles are appearing on the scene to broaden the spectrum of performance trade-off to be accomplished.

A large quantity of data has been gathered on airbreathing propulsion system performance. Some of these data reside with this contractor in its several divisions, in publications of several governmental agencies and of other contractors. In the field of propulsion, inlet and exhaust flows and their effects on vehicle performance characteristics, there has existed a definite need to bring isolated, though related, items of data together to be correlated and interpreted in the light of known theory. The effort presented herein was developed as a tool by which future design evaluations can be made on the basis of a much more complete and comprehensive correlation of the large quantity of existing data than has been available in the past.

8.0 Exhaust Nozzle Performance

8.0.1 Introduction

Considerable interest exists in nozzle design, largely because some advanced nozzle designs are sensitive to the airframe nozzle installation. Adverse installations may reduce nozzle thrust, or nozzle drag and fuselage afterbody drag may be increased. Thus, the interest in nozzle design and afterbody configuration stems from the impact on installed propulsion system performance.

The total engine weight may vary about 25 percent and the supersonic thrust about 20 percent depending on nozzle selection: convergent, convergent divergent (C-D), Blow-in-door, or plug nozzle. Installed S.F.C. for subsonic cruise may vary 10 percent with the nozzle selection. Weight, supersonic thrust, cruise SFC are items requiring an assessment for nozzle selection.

At both supersonic speeds and subsonic cruise, 1 percent in nozzle efficiency is worth about 1.7 percent in net thrust. The large range in nozzle pressure ratio and exit area presents difficulty in maintaining high internal thrust efficiency and low external base or boattail drag. For fighter aircraft, nozzle pressure ratio may vary from about 3 for subsonic cruise up to 15 or 20 for high supersonic speeds. For a variable geometry C-D nozzle, the nozzle exit area may vary by a factor of about 4 between subsonic cruise and high supersonic. This area variation of course presents the potential for large nozzle base or boattail drag for non-afterburning subsonic operation.

For the above reasons, nozzle selection is complicated for multi-mission aircraft. Nozzle selection or design is less difficult for an aircraft emphasizing Mach 3 operation, or for an aircraft designed only for subsonic attack. Nozzle selection and performance estimation is further complicated by interaction between the jet and the afterbody external flow. The jet may reduce nozzle or afterbody drag and the external flow can also effect internal thrust performance. Internal thrust may be severely affected for off design point operation.

Many of the nozzle types have particular advantages or are better suited for certain aircraft speeds than others. For insight into nozzle performance, the fundamental internal and external aerodynamic relationships involved must be well understood; therefore, the important flow relationships derived from basic energy, momentum, and continuity laws, and several performance coefficients utilizing these relationships are formulated. These performance coefficients compare the maximum possible value of the performance parameter to that obtained by experimental results. The various types examined are the convergent, fixed convergent-divergent, fixed ejector, variable geometry ejector, plug, blow-in-door, and

inverted. The examination emphasis is placed upon a general operating knowledge of the nozzle, geometric effects upon performance, and the operating range of the nozzle. The external aerodynamic effects are also given an extensive examination. Throughout the examination of nozzle performance, significant data are presented to clarify and illustrate various nozzle characteristics.

8.0.2 Thermodynamic Background

A bewildering array of parameters and coefficients exist for description of nozzle performance, therefore review of the fundamentals is required to avoid misuse of some of those terms. Since the basic thrust relationship comes directly from the general energy equation, we will start with this fundamental but important equation.

The general energy equation as applied to the turbojet engine for the inflight case is a good review method for the equation. The turbojet cycle is illustrated on a $h - s$ diagram in Figure 3-1. The equation is

$$h_c + \frac{V_o^2}{2gJ} + W_{\text{comp}} + \frac{Q}{\text{lb. } W_a} = W_{\text{turb}} + h_8 + \frac{V_8^2}{2gJ} \quad (8.1)$$

↑
heat supplied per lb. of air by combustion

Equation 8.1 reduces to:

$$h_o + \frac{V_o^2}{2gJ} + \frac{Q}{\text{lb. } W_a} = h_8 + \frac{V_8^2}{2gJ} \quad (8.2)$$

$$\text{Recalling that } h = c_p T \quad (8.3)$$

$$h_T = h + \frac{V^2}{2gJ} \quad (8.4)$$

$$c_p T_T = c_p T + \frac{V^2}{2gJ} \quad (8.5)$$

Also the relationship for isentropic expansion or compression:

$$\frac{T_1}{T_2} = \left(\frac{P_1}{P_2} \right)^{\frac{\gamma-1}{\gamma}} \text{ and for a flow process:} \quad (8.6)$$

$$\frac{T_T}{T} = \left(\frac{P_T}{P} \right)^{\frac{\gamma-1}{\gamma}} \quad (8.7)$$

Figure 8-2 illustrates the nozzle expansion process where potential energy (at a high pressure) is converted into kinetic energy. The general energy equation for this flow process

$$h_T = h_T + h_{\text{exit}} + \frac{v_{\text{exit}}^2}{2gJ} \quad (8.8)$$

turbine
nozzle

discharge
entrance

(excluding tail-

pipe losses)

$$c_p T_{Tjet} = c_p T_{jet} + \frac{v_{jet}^2}{2gJ} \quad (8.9)$$

\uparrow
static temp

From the isentropic relationships, using T_{Tjet} and P_{Tj}/P_{amb} , T_{static} can be calculated

from $\frac{T_T}{T} = \left(\frac{P_T}{P}\right)^{\frac{\gamma-1}{\gamma}}$, and theoretical thrust can be evaluated:

$$F_{gross} = \frac{W_{gas} V_j}{g} + (P_{exit} - P_{amb}) A_{exit} \quad (3.10)$$

\nwarrow
static pressure

This equation is derived thoroughly in Pages 13 through 18 of "Aircraft Jet Powerplants" by F. P. Durham, published by Prentice-Hall.

Maximum isentropic gross thrust (ideal C-D nozzle) is obtained when P_{exit} equals P_{amb} .

For a convergent nozzle, we quickly reach a case where $P_{exit} = P_{amb}$ complicating the following ideal (theoretical) convergent nozzle thrust parameter derivation:

$$\frac{F_g}{P_{amb} A_j} = f \left(\frac{P_{Tj}}{P_{amb}} \right) \quad (8.11)$$

8.1 Theoretical Performance

8.1.1 Theoretical Thrust Types

Before starting the convergent nozzle thrust derivation, we should note we will be looking at three major theoretical thrust derivations.

- (a) Ideal convergent nozzle thrust
- (b) Optimum thrust (complete expansion)
- (c) Theoretical C-D nozzle thrust

(Exit area of C-D nozzle not optimum)

8.1.2 Convergent Nozzle Thrust Parameter Derivation

8.1.2.1 Derivation of convergent nozzle thrust for pressure ratios below choking:

$$M_j < 1$$

A convergent nozzle provides a maximum nozzle exit Mach number of 1. From the flow equation relating pressure ratio and Mach number

$$\frac{P_T}{P_{\text{static}}} = \left[1 + \frac{\gamma-1}{2} M_{\text{exit}}^2 \right] \frac{\gamma}{\gamma-1} \quad (8.12)$$

For $\gamma = \frac{c_p}{c_v} = 1.4$ for air at normal temperatures, $M_{\text{exit}} = 1$

$$\frac{P_T}{P_e} = \left(1 + \frac{1.4-1}{2} \right) \frac{1.4}{1} = (1.2)^{3.5} = 1.89, P_e = P_{\text{exit}} \quad (8.13)$$

For a convergent nozzle, recognizing that exit Mach is limited to 1, therefore

$$\frac{P_e}{P_T} = \frac{1}{1.89} = .529, M_j = 1 \quad (8.14)$$

If P_T supplied to the nozzle increases (once a pressure ratio of 1.89 is reached), then P_e must increase correspondingly.

Below a pressure ratio of 1.89 ($\gamma = 1.4$), $P_{\text{exit}} = P_{\text{amb}}$, $M_j < 1$
 then equation 8.11 becomes

$$F_g = \frac{W_{\text{gas}}}{g} V_{\text{jet}} + (P_e - P_{\text{amb}}) A_{\text{jet}} = \frac{W_g}{g} V_{\text{jet}} \quad \text{for } \frac{P_T}{P_{\text{amb}}} < 1.89$$

$$F_g = \frac{\rho A V}{g} (V_{\text{jet}}) \quad (8.15)$$

For convenience, gas flow will be defined at the nozzle throat, which is also the exit for a convergent nozzle.

$$F_g = \frac{(\rho A V)_{\text{exit}}}{g} (V_{\text{jet}}) = \frac{\rho_e A_e V_j^2}{g} \quad \text{See Figure 8-4} \quad (8.16)$$

Substituting for density ρ by.

$$p v = RT \quad \text{or} \quad \frac{p}{\rho} = RT \quad (8.17)$$

$$F_g = \frac{p}{RT} \frac{A}{g} V_j^2 = \frac{p}{RT} \frac{A}{g} M^2 a^2 \quad (8.18)$$

$$= \frac{p}{RT} \frac{A M^2}{g} \left(\sqrt{\gamma g RT} \right)^2 = \frac{p}{RT} \frac{A M^2}{g} \gamma g RT$$

$$= P_e A_e M_j^2 \gamma \quad (8.19)$$

To put in terms of pressure ratio from

$$\frac{P_T}{P} = \left[1 + \frac{\gamma-1}{2} M^2 \right]^{\frac{\gamma}{\gamma-1}}$$

$$\left(\frac{P_T}{P} \right)^{\frac{\gamma-1}{\gamma}} = 1 + \frac{\gamma-1}{2} M^2$$

$$\frac{2}{\gamma-1} \left[\frac{P_T}{P}^{\frac{\gamma-1}{\gamma}} - 1 \right] = M^2$$

Substituting for M^2 in equation 8.19

$$F_g = \gamma P A \left(\frac{2}{\gamma-1} \right) \left[\left(\frac{P_T}{P} \right)^{\frac{\gamma-1}{\gamma}} - 1 \right] , P_e = P_{\text{amb}} \quad (8.20)$$

Putting equation 8.20 in terms of a gross thrust parameter

$$\frac{F_g}{P_{amb} A_{jet}} = \frac{2\gamma}{\gamma-1} \left[\left(\frac{P_T}{P_{amb}} \right)^{\frac{\gamma-1}{\gamma}} - 1 \right] \quad (8.21)$$

This completes the convergent nozzle gross thrust parameter derivation, for the case where the nozzle is not choked.

We are now ready to examine the other half of the convergent nozzle thrust parameter derivation; the case where we have a pressure ratio higher than that required for choked flow. Mach number of the jet is limited to 1, but P_{exit} may become greater than P_{amb} .

8.1.2.2 Derivation of convergent nozzle thrust parameter for pressure ratios at or above choking ($M_{jet} = 1$).

The significance of this case is that the nozzle exit pressure area term must be included as illustrated in Figure 8-5.

$$F_{gross} = \frac{W_{gas}}{g} V_j + (P_e - P_{amb}) A_{jet}, \text{ substituting Equation 8.19 into 8.10}$$

$$F_{gross} = \gamma P_e A_e M_j^2 + (P_e - P_{amb}) A_{jet} \quad (8.22)$$

For Mach 1 at the convergent nozzle exit, P_{exit} is dependent on the P_{Tjet} level.

$$\begin{aligned} \frac{P_{Tjet}}{P_e} &= \left[1 + \frac{\gamma-1}{2} M^2 \right]^{\frac{\gamma}{\gamma-1}} \\ &= \left[1 + \frac{\gamma-1}{2} (1) \right]^{\frac{\gamma}{\gamma-1}} \\ &= 1.89 \text{ for } \gamma = 1.4 \end{aligned}$$

$$\text{then } P_e = \frac{P_{Tj}}{P_{Tj}/P_e} = \frac{P_{Tj}}{1.89}, \text{ Substituting Equation 8.23 into 8.22} \quad (8.23)$$

$$\begin{aligned} F_g &= \gamma \frac{P_{Tj}}{1.89} A (1)^2 + (P_e - P_{amb}) A_{jet} \\ &= \gamma \frac{P_{Tj}}{1.89} A_j + \left(\frac{P_{Tj}}{1.89} - P_{amb} \right) A_j \end{aligned}$$

To obtain the thrust parameter form:

$$\begin{aligned} \frac{F_g}{P_{amb} A_j} &= \frac{\gamma}{1.89} \frac{P_{Tj}}{P_{amb}} A_j + \frac{1}{1.89} \frac{P_{Tj}}{P_{amb}} - 1 \\ &= \frac{\gamma+1}{1.89} \frac{P_{Tj}}{P_{amb}} - 1 \end{aligned} \quad (8.25)$$

By substituting the general relationship for the choking pressure ratio:

$$\begin{aligned} \frac{P_{Tj}}{P_e} &= \left[1 + \frac{\gamma-1}{2} M^2 \right]^{-\frac{\gamma}{\gamma-1}} = \left[\frac{\gamma+1}{2} \right]^{-\frac{\gamma}{\gamma-1}}, M=1 \\ \frac{F_g}{P_{amb} A_j} &= \left(\frac{\gamma+1}{\left(\frac{\gamma+1}{2} \right)^{\frac{\gamma}{\gamma-1}}} \right) \frac{P_{Tj}}{P_{amb}} - 1 \\ \text{for } \frac{P_{Tj}}{P_{amb}} &= 4 \text{ and } \gamma = 1.4, \frac{F_{gi}}{P_{amb} A_j} = 4.08 \end{aligned} \quad (8.26)$$

Figure 8-6 through 8-8 are plots of the theoretical convergent nozzle thrust parameter.

While the theoretical convergent nozzle thrust value has of course been used as an efficiency base for years for subsonic aircraft with fixed convergent nozzles, optimum thrust (for an isentropic expansion) is now being used more commonly as the base. The thrust parameter $F_g/P_{amb} A_j$ for optimum thrust or in other words for a complete isentropic expansion (theoretical ideal convergent-divergent expansion), is shown in Figures 8-9 through 8-12. The thrust parameter $F_g/(w_g \sqrt{T_T})$ for a convergent nozzle is presented in Figures 8-13 through 8-15.

8.1.3 Optimum Thrust Parameter Derivations

Two optimum thrust parameters are often used; one parameter involving flow rate and temperature and the other parameter using total pressure and nozzle throat area. Figure 8-16 illustrates the terms utilized in these thrust derivations.

8.1.3.1 Derivation of Optimum Thrust Parameter $\frac{F_1}{W/T}$

$\frac{F_1}{W/T}$ relates: 1) Maximum ideal gross thrust
2) Nozzle total gas flow, lb/sec
3) Nozzle total temperature, °R
4) Nozzle pressure ratio

for the optimum nozzle area ratio equation:

$$\frac{F_1}{W/T} = \sqrt{\frac{2\gamma R}{(\gamma-1)g}} \left[1 - \left(\frac{P_T}{P_{amb}} \right)^{\frac{1-\gamma}{\gamma}} \right] \quad (8.27)$$

Derivation:

$$F_1 = F_{gopt} = \frac{W}{g} V_e + (P_e - P_{amb}) A_e$$

For the optimum nozzle area ratio $\frac{A_e}{A^*}$

$$P_e = P_{amb}, \quad (P_e = \text{static pressure})$$

$$F_g = \frac{W}{g} V_e \quad (8.28)$$

$$V_e = M_e a_e = M_e \sqrt{\gamma g R T_e} \quad (8.29)$$

$$\frac{P_T}{P_{amb}} = \left[1 + \frac{\gamma-1}{2} M_e^2 \right]^{\frac{\gamma}{\gamma-1}}$$

$$M_e = \sqrt{\frac{2}{\gamma-1} \left[\left(\frac{P_T}{P_{amb}} \right)^{\frac{\gamma-1}{\gamma}} - 1 \right]} \quad (8.30)$$

Substituting equation 8.30 into 8.29, then substituting the result into 8.28

$$F_g = \frac{W}{g} \sqrt{\frac{2}{\gamma-1} \left[\left(\frac{P_T}{P_{amb}} \right)^{\frac{\gamma-1}{\gamma}} - 1 \right]} \sqrt{\gamma g R T_e}$$

$$F_g = W \sqrt{\frac{2}{\gamma-1} \frac{\gamma R}{g^2} \left[\left(\frac{P_T}{P_{amb}} \right)^{\frac{\gamma-1}{\gamma}} - 1 \right]} \sqrt{T_a} \quad (8.31)$$

$$\frac{T_T}{T} = \left(\frac{P_T}{P} \right)^{\frac{\gamma-1}{\gamma}}, \quad T_e = \frac{T_T}{\left(\frac{P_T}{P_e} \right)^{\frac{\gamma-1}{\gamma}}}$$

$$\sqrt{\left[\left(\frac{P_T}{P_{amb}} \right)^{\frac{\gamma-1}{\gamma}} - 1 \right]} \sqrt{T_e} = \sqrt{\left[\left(\frac{P_T}{P_{amb}} \right)^{\frac{\gamma-1}{\gamma}} - 1 \right]} \frac{T_T}{\left(\frac{P_T}{P_{amb}} \right)^{\frac{\gamma-1}{\gamma}}}$$

$$\sqrt{\left[1 - \left(\frac{P_T}{P_{amb}} \right)^{\frac{\gamma-1}{\gamma}} \right]} T_T = \sqrt{\left[1 - \left(\frac{P_T}{P_{amb}} \right)^{\frac{1-\gamma}{\gamma}} \right]} T_T$$

then:

$$F_g = W \sqrt{\frac{2}{\gamma-1} \frac{\gamma R}{g} \left[\left(\frac{P_T}{P_{amb}} \right)^{\frac{\gamma-1}{\gamma}} - 1 \right]} T_e$$

$$= W \sqrt{\frac{2}{(\gamma-1)} \frac{\gamma R}{g} \left[1 - \left(\frac{P_T}{P_{amb}} \right)^{\frac{1-\gamma}{\gamma}} \right]} T_T$$

$$\frac{F_1}{W \sqrt{T_T}} = \sqrt{\frac{2\gamma R}{(\gamma-1)g} \left[1 - \left(\frac{P_{Tjet}}{P_{amb}} \right)^{\frac{1-\gamma}{\gamma}} \right]} \quad (\text{Ref. 8.27})$$

for optimum A_e/A^*

This parameter is presented in Appendix F

8.1.3.2 Derivation of Optimum Thrust Parameter

$$\frac{F_1}{A^* p_T}$$

- $\frac{F_1}{A^* p_T}$ relates:
- 1) Maximum ideal gross thrust
 - 2) Nozzle throat or minimum area, in.²
 - 3) Nozzle total pressure, psia
 - 4) Nozzle pressure ratio

for optimum nozzle area ratio

Equation:

$$\frac{F_1}{A^* p_T} = \sqrt{\frac{2\gamma^2}{\gamma-1} \left(\frac{2}{\gamma+1}\right)^{\frac{\gamma+1}{\gamma-1}} \left[1 - \left(\frac{p_{amb}}{p_T}\right)^{\frac{\gamma-1}{\gamma}}\right]} \quad (8.32)$$

Derivation:

$$F_1 = F_{gopt} = \frac{W}{g} V_e + (p_e - p_{amb}) A_e$$

For the optimum nozzle area ratio $\left(\frac{A_e}{A^*}\right)$

$$p_e = p_{amb} \quad (p_e = \text{static pressure})$$

$$F_g = \frac{W}{g} V_e = \frac{\rho A V}{g} V_e = \frac{\rho^* A^* V^*}{g} V_e \quad (8.33)$$

$$= \frac{A^* V^*}{V^* g} V_e \quad (\text{defining } W \text{ by conditions at the throat})$$

Define V_e as the velocity at the exit; then for a flow process

$$h_T = h_1 + \frac{V_1^2}{2gJ} = h_2 + \frac{V_2^2}{2gJ} \quad ; \quad Q = 0 \quad (8.34)$$

$$W = 0$$

$$h_{Te} = h_e + \frac{v_e^2}{2gJ}$$

$$c_p (T_T - T_{exit}) = \frac{1}{2gJ} (v_e^2), \quad T_{exit} \text{ is a static temperature}$$

$$c_p - c_v = R/J \quad (8.35)$$

$$c_p = \frac{\gamma R}{(\gamma-1)J} \quad (8.36)$$

$$\frac{\gamma R}{(\gamma-1)J} (T_T - T_e) = \frac{1}{2gJ} v_e^2 \quad (8.37)$$

$$\frac{2g \gamma R}{\gamma-1} (T_T - T_e) = v_e^2$$

$$\frac{2g \gamma R}{\gamma-1} T_T \left(1 - \frac{T_e}{T_T} \right) = v_e^2 \quad (8.38)$$

$$\frac{T_T}{T} = \left(\frac{P_T}{P} \right)^{\frac{\gamma-1}{\gamma}}$$

$$\frac{T}{T_T} = \left(\frac{P}{P_T} \right)^{\frac{\gamma-1}{\gamma}}, \quad P_e = P_{amb}$$

$$v_e = \sqrt{\frac{2g \gamma R}{\gamma-1} T_T \left[1 - \left(\frac{P_{amb}}{P_T} \right)^{\frac{\gamma-1}{\gamma}} \right]} \quad (8.39)$$

Determine V^* now:

$$V = Ma \quad M = 1 \text{ at throat}$$

$$V^* = \sqrt{\gamma g R T^*}, \quad T^* \text{ is a static temperature}$$

$$\frac{T_T}{T} = 1 + \frac{\gamma-1}{2} M^2, \text{ for } M = 1 \text{ at the throat} \quad (8.40)$$

$$\frac{T_T}{T} = 1 + \frac{\gamma-1}{2} = \frac{\gamma+1}{2} \quad (8.41)$$

$$h_T = h^* + \frac{V^{*2}}{2gJ}$$

$$c_p (T_T - T^*) = \frac{1}{2gJ} (V^*)^2$$

$$c_p = \frac{\gamma R}{(\gamma-1)J}$$

$$\frac{\gamma R}{(\gamma-1)J} (T_T - T^*) = \frac{1}{2gJ} (V^*)^2$$

$$\frac{2g\gamma R}{\gamma-1} T_T \left(1 - \frac{T^*}{T_T} \right) = (V^*)^2 \quad (8.42)$$

$$\text{at } A^*; \frac{T_T}{T^*} = \frac{\gamma+1}{2} \quad (8.43)$$

Substituting equation 8.43 into 8.42

$$\frac{2g\gamma R}{\gamma-1} T_T \left(1 - \frac{2}{\gamma+1} \right) = \frac{2g\gamma R}{\gamma-1} T_T \left(\frac{\gamma+1-2}{\gamma+1} \right) = (V^*)^2$$

$$\frac{2g\gamma R}{\gamma-1} T_T \left(\frac{\gamma-1}{\gamma+1} \right) = \frac{2g\gamma R}{\gamma+1} T_T = (V^*)^2$$

$$V^* = \sqrt{\frac{2g\gamma R}{\gamma+1} T_T} \quad (8.44)$$

Determine v^* , $p_T = RT$

$$\frac{T_T}{T} = \left(\frac{p_T}{p} \right)^{\frac{\gamma-1}{\gamma}} = \left(\frac{v}{v_T} \right)^{\gamma-1}$$

$$\frac{T_T}{T} = 1 + \frac{\gamma-1}{2} M^2, \quad \text{for } M = 1$$

$$\frac{T_T}{T^*} = 1 + \frac{\gamma-1}{2}(1) = \frac{2+\gamma-1}{2} = \frac{\gamma+1}{2}$$

$$\frac{T_T}{T^*} = \left(\frac{v^*}{v_T} \right)^{\gamma-1} = \frac{\gamma+1}{2} \quad (8.45)$$

$$\left(\frac{v^*}{v_T} \right) = \left(\frac{\gamma+1}{2} \right)^{\frac{1}{\gamma-1}}, \quad v^* = v_T \left(\frac{\gamma+1}{2} \right)^{\frac{1}{\gamma-1}}$$

$$v^* = \frac{RT_T}{p_T} \left(\frac{\gamma+1}{2} \right)^{\frac{1}{\gamma-1}} = \frac{ft^3}{lb} \quad (8.46)$$

$$F_g = \frac{W}{g} v = \frac{\rho AV}{g} v_e = \frac{A^* v^*}{v^* g} v_e \quad (8.47)$$

Now substituting equations 8.39, 8.44, 8.46 into 8.47

$$F_g = \frac{A^* \sqrt{\frac{2g \gamma R}{\gamma+1}} T_T \sqrt{\frac{2g \gamma R}{\gamma-1}} T_T \left[1 - \left(\frac{p_{amb}}{p_T} \right)^{\frac{\gamma-1}{\gamma}} \right]}{\left[\frac{RT_T}{p_T} \left(\frac{\gamma+1}{2} \right)^{\frac{1}{\gamma-1}} \right] g} \quad (8.48)$$

$$F_E = \frac{A^* \sqrt{\frac{E^2 \gamma R^2}{gR}} \sqrt{\frac{T_T^2}{T_T}} \sqrt{\frac{2\gamma^2}{\gamma-1}} \sqrt{\frac{2}{\gamma+1}} \left[1 - \left(\frac{P_{amb}}{P_T} \right)^{\frac{\gamma-1}{\gamma}} \right]}{\left[\frac{1}{P_T} \left(\frac{\gamma+1}{2} \right)^{\frac{1}{\gamma-1}} \right]} \quad (8.49)$$

Notes:

$$\begin{aligned} \frac{\sqrt{\frac{2}{\gamma+1}}}{\left(\frac{\gamma+1}{2} \right)^{\frac{1}{\gamma-1}}} &= \frac{\sqrt{\frac{2}{\gamma+1}}}{\left(\frac{\gamma+1}{2} \right)^{\frac{2}{\gamma-1}}} \\ &= \sqrt{\frac{\left(\frac{2}{\gamma+1} \right)}{\left(\frac{2}{\gamma+1} \right)^{\frac{-2}{\gamma-1}}}} = \sqrt{\left(\frac{2}{\gamma+1} \right)^{1 + \frac{2}{\gamma-1}}} = \sqrt{\left(\frac{2}{\gamma+1} \right)^{\frac{\gamma+1}{\gamma-1}}} \end{aligned}$$

Substituting into equation 8.49

$$F_E = A^* P_T \sqrt{\frac{2\gamma^2}{\gamma-1}} \sqrt{\left(\frac{2}{\gamma+1} \right)^{\frac{\gamma+1}{\gamma-1}}} \sqrt{1 - \left(\frac{P_{amb}}{P_T} \right)^{\frac{\gamma-1}{\gamma}}}$$

$$\frac{F_E}{A^* P_T} = \sqrt{\frac{2\gamma^2}{\gamma-1} \left(\frac{2}{\gamma+1} \right)^{\frac{\gamma+1}{\gamma-1}} \left[1 - \left(\frac{P_{amb}}{P_T} \right)^{\frac{\gamma-1}{\gamma}} \right]} \quad (\text{Ref. 8.32})$$

for non viscous flow optimum area ratio nozzle

Tabulated values of this parameter are presented in Appendix F

8.1.4 Area Ratio

8.1.4.1 Optimum Thrust Area Ratio

For optimum thrust, the foregoing derivations were based on expansion in the nozzle down to ambient pressure. In other words, the nozzle area variation provided an exit pressure equal to ambient or the pressure level the gas is being discharged to. Figure 8-17 illustrates the nozzle exit to throat area ratio required for a given specific heat ratio. Area ratio can be calculated from equation 8.50.

$$\frac{A_2}{A_1} = \frac{M_1}{M_2} \left[\frac{1 + \frac{\gamma-1}{2} M_2^2}{1 + \frac{\gamma-1}{2} M_1^2} \right]^{\frac{\gamma+1}{2(\gamma-1)}} \quad (8.50)$$

Where A_1 can be taken as the nozzle throat with $M_1 = 1$.

M_2 or M_{exit} can be calculated from equation 8.51.

$$\frac{P_T}{P} = \frac{P_T}{P_{\text{amb}}} = \left[1 + \frac{\gamma-1}{2} M_{\text{exit}}^2 \right]^{\frac{\gamma}{\gamma-1}} \quad (8.51)$$

Figures 8-18 and 8-19 show estimated actual (not theoretical) nozzle performance for a high supersonic aircraft where C-D nozzle area ratio is held close to optimum as the flight speed and pressure ratio varies.

8.1.4.2 Non-Optimum Area Ratio

Because of the weight, complexity, and control system needed for optimum area ratio (variable), most operational C-D nozzles use fixed exits, or exits that are slaved to the primary nozzle (throat) such as the J79 nozzles. Exits that are slaved to the primary provide essentially 2 position exits, or 2 exit to throat area ratios. For non-afterburning, a diameter ratio (about 1.1) providing good subsonic cruise is obtained from the nozzle kinematics when the primary is in the dry position. When the primary nozzle opens up (50 to 100 percent area increase) for afterburning, the nozzle linkage provides a diameter ratio (1.2 to 1.3) which is a good compromise ratio for afterburning operation over the supersonic flight speed range.

Theoretical variations in gross thrust, at given fixed area ratios, are illustrated in Figure 8-20. For a fixed area ratio nozzle designed for optimum thrust at high pressure ratios, very large thrust losses are indicated at low pressure ratios.

We have examined 2 theoretical nozzle cases previously; convergent and optimum nozzles. To complete our theoretical thrust variations, we will now look at the third case of convergent divergent nozzles at non-optimum area ratios. These 3 cases are illustrated in Figure 8-21. The difference between optimum thrust and C-D nozzle thrust, at a particular area ratio, is often a source of confusion.

To calculate theoretical C-D nozzle thrust for any area ratio, we must add the pressure area term to our thrust equation.

$$F_g = \frac{W_{gas} V_j}{g} + (P_{exit} - P_{amb}) A_{exit}$$

We can put this in a familiar optimum thrust parameter form by substituting $\frac{P_{Tj}}{P_{exit}}$ for $\frac{P_{Tj}}{P_{amb}}$

$$\frac{F_g}{A^* P_{Tj}} = \sqrt{\frac{2\gamma^2}{\gamma-1} \left(\frac{2}{\gamma+1}\right)^{\frac{\gamma+1}{\gamma-1}} \left[1 - \left(\frac{P_{exit}}{P_{Tj}}\right)^{\frac{\gamma-1}{\gamma}}\right]} + \frac{(P_{exit} - P_{amb}) A_{exit}}{A^* P_{Tj}} \quad (8.52)$$

The easiest way to calculate non-optimum area ratio thrust is:

- (a) Select a pressure ratio
- (b) Select an exit Mach number
- (c) Calculate exit static pressure from the Mach number at the exit.
- (d) Calculate the area ratio required for the exit Mach number

Selecting an exit Mach number, for Step (c), P_{exit} can be calculated from equation 8.53.

$$\frac{P_{Tj}}{P_{exit}} = \left[1 + \frac{\gamma-1}{2} M_{exit}^2\right]^{\frac{\gamma}{\gamma-1}} \quad (8.53)$$

For step (d), the area ratio can be calculated from equation 8.54.

$$\frac{A_{\text{exit}}}{A_{\text{throat}}} = \frac{M_{\text{throat}}}{M_{\text{exit}}} \left[\frac{1 + \frac{\gamma-1}{2} M_{\text{exit}}^2}{1 + \frac{\gamma-1}{2} M_{\text{throat}}^2} \right]^{\frac{\gamma+1}{2(\gamma-1)}}$$

or

$$\frac{A_{\text{exit}}}{A_{\text{throat}}} = \frac{1}{M_{\text{exit}}} \left[\frac{1 + \frac{\gamma-1}{2} M_{\text{exit}}^2}{1 + \frac{\gamma-1}{2} M_{\text{throat}}^2} \right]^{\frac{\gamma+1}{2(\gamma-1)}} \quad (8.54)$$

Now we have an exit pressure and $\frac{A_{\text{exit}}}{A^*}$ to plug into the equation for $\frac{F_g}{A^* P_{Tj}}$.

Figures 8-22 through 8-26 present curves relating thrust, area ratio, and pressure ratio for a theoretical C-D nozzle. Since optimum thrust is available from many tables or plots, Figures 8-22 through 8-26 present the variation in thrust from optimum for any area ratio. This presentation is useful in that the allowable area deviation (from optimum) to maintain thrust at a given percentage (compared to optimum) can be quickly determined from these plots. The plots are for different specific heat ratios, Figure 8-25 presents theoretical thrust variation, at a specific heat ratio of 1.3, out to a pressure ratio of 48.

These theoretical trends for thrust variation with area ratio and pressure ratio are representative of actual C-D nozzles for under-expanded flow (A_{exit} too small). For overexpanded flow, fortunately the theoretical trend is conservative compared to actual test results due to flow separation or detachment from the divergent walls. This is a separate subject and experimental results will be presented later.

8.2 Coefficients

8.2.1 Basic Coefficients

Two basic factors are important in the design of a nozzle. One is the flow capacity; the other is the nozzle's effectiveness in converting pressure energy into kinetic energy (velocity). These two factors are evaluated by means of two coefficients which are defined as follows:

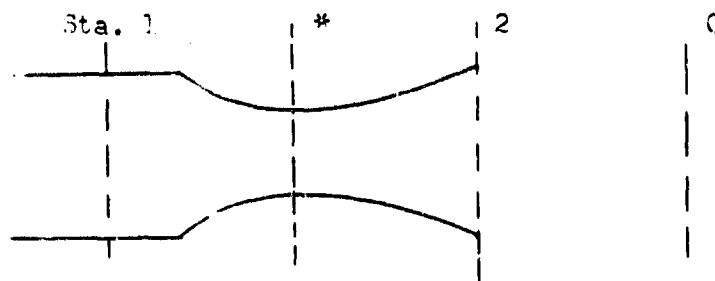
$$C_d = \frac{W_M}{W_t} \quad \text{flow coefficient}$$

$$= \frac{\text{Actual Mass Rate of flow}}{\text{Mass rate of flow with isentropic flow}}$$

$$C_{vel} = \frac{V_M}{V_t} \quad \text{velocity coefficient}$$

$$= \frac{\text{Actual velocity at nozzle exit}}{\text{Velocity at nozzle exit with isentropic flow and same exit pressure}}$$

For clarity the following nozzle will be used as a reference:



The actual jet thrust then is

$$F_j \text{ actual} = M \frac{d V_M}{dT} \quad (8.55)$$

If the fluid is assumed to start from rest (stagnation condition) equation (8.55) can be written as:

$$F_j \text{ actual} = \frac{W_M}{g} V_M = \frac{W_M}{W_t} \frac{W_t}{g} \frac{W_M}{V_t} V_t \quad (8.56)$$

Then substituting the two coefficients into 8.56,

$$F_j \text{ actual} = \frac{C_d W_t}{g} C_{vel} V_t \quad (8.57)$$

For equation 8-57 to be useful both coefficients must be known. If the gas flow rate is known then only the velocity coefficient is required.

$$F_j \text{ actual} = \frac{WM}{g} C_{vel} V_t$$

To compute the actual thrust from Equation 8-57, the theoretical weight flow rate (W_t) and the theoretical velocity (V_t) must be known.

As already shown in Section 8.0, theoretical values are based on an isentropic expansion of the jet to ambient pressure. Since the nozzle unchoked, ambient pressure (P_{amb}) will occur at the exit. Equation 8.37 of Section 8.3.1.2 is derived based on a complete isentropic to ambient at the exit, but in an unchoked condition the ambient pressure occurs at the exit. Therefore:

$$V_t = V_e = \sqrt{\frac{2g \gamma R}{\gamma - 1} T_T \left[1 - \left(\frac{P_{amb}}{P_T} \right)^{\frac{\gamma - 1}{\gamma}} \right]} \quad (8.58)$$

Defining the flow at the exit, then

$$W_t = \rho_e A_e V_e = \rho_e A_e V_t \quad (8.59)$$

$$\rho_e = \frac{P_e}{RT_e} \text{ and } T_e = T_T \left(\frac{P_e}{P_T} \right)^{\frac{\gamma - 1}{\gamma}}$$

but $P_e = P_{amb}$

Therefore,

$$\rho_e = \frac{P_{amb}}{RT_e} \text{ and } T_e = T_T \left(\frac{P_{amb}}{P_T} \right)^{\frac{\gamma - 1}{\gamma}}$$

Substituting into equation 8.59

$$W_t = \frac{P_{amb} A_e V_t}{RT_T \left(\frac{P_{amb}}{P_T} \right)^{\frac{\gamma - 1}{\gamma}}} \quad (8.60)$$

$$W_t = \frac{A_e P_{amb}}{RT_T} \left(\frac{P_{amb}}{P_T} \right)^{\frac{\gamma - 1}{\gamma}} V_t$$

$$\text{or } W_t = A_e \frac{P_{amb}}{RT_T} \left(\frac{P_T}{P_{amb}} \right)^{\frac{\gamma - 1}{\gamma}} V_t \quad (8.61)$$

At a choked condition ($M = 1.0$ at the throat and $P_{amb} \neq P_e$) the following equations apply at the nozzle throat.

$$V_t = V^* = \sqrt{\frac{2g \gamma R}{\gamma+1} T_T}$$

Again, defining W_t at the throat

$$W_t = \rho^* A^* V^* = \frac{A^* V^*}{v^*}$$

Substituting equations 8.46 and 8.44

$$W_t = \frac{A^*}{\frac{RT_T}{P_T} \left(\frac{\gamma+1}{2}\right)^{\frac{1}{\gamma-1}}} \sqrt{\frac{2g \gamma RT_T}{\gamma+1}}$$

$$W_t = P_T A^* \sqrt{\frac{g \gamma RT_T}{R^2 T_T^2} \left(\frac{\frac{2}{\gamma+1}}{\left(\frac{\gamma+1}{2}\right)^{\frac{2}{\gamma-1}}}\right)}$$

$$W_t = P_T A^* \left(\frac{2}{\gamma+1}\right)^{\frac{\gamma+1}{\gamma-1}} \sqrt{\frac{\gamma g}{RT_T}} \quad (8.62)$$

8.2.2 Nozzle Efficiency Terms

A myriad of variations in nozzle efficiency terms exist. We will encounter different efficiency terms as we examine individual experimental efforts in this field. These variations of course make comparisons of data difficult. Confusion over just what is included in nozzle efficiency or thrust coefficient can lead to invalid results or comparisons.

Some of the more important thrust coefficients are listed below. The biggest problem probably lies in variations in nomenclature.

Nomenclature

Thrust Coefficient

C_{f_g}

Nozzle gross thrust

Ideal primary thrust (isentropic)

C_v

Nozzle gross thrust

Ideal primary thrust (isentropic)

NomenclatureThrust Coefficient

$$\frac{F_{ej}}{F_{1p}}$$

Gross thrust of primary and secondary
Ideal primary thrust

$$\frac{F_g}{F_p}$$

Gross thrust of nozzle
Actual convergent nozzle thrust
of the primary

$$C_{fg \text{ eq}}$$

Gross thrust minus secondary ram drag
Ideal primary thrust (isentropic)

$$C_F$$

Gross thrust minus external nozzle drag
Ideal primary thrust (isentropic)

$$C_{ej}$$

$$\frac{C_{fg}}{.98} \quad \text{or} \quad \frac{C_F}{.98}$$

Since engine specifications are generally presented in terms of .98 or .985 of isentropic thrust, a C_{ej} coefficient is just a means of applying an actual thrust coefficient to specification thrust as shown below.

$$F_{g \text{ actual nozzle}} = C_{ej} (F_{g \text{ spec}}) = \frac{C_{fg}}{.98} (.98 F_{g \text{ ideal}})$$

8.3 Discussion and Experimental Performance of Various Nozzle Types

8.3.1 Convergent Nozzles

8.3.1.1 Simple Convergent

The simple convergent nozzle operation has been briefly discussed in Section 8.1.1. Theoretical performance methods are derived and some plots presented. In this section, actual performance is the main concern.

Thrust and Flow coefficient. Figures 8-27 and 8-28 show the typical performance of a convergent nozzle. The thrust of the convergent nozzle is very good at the low pressure ratio but suffers as the pressure ratio increases. This is why the convergent nozzle is good for subsonic operations, as can be seen from the estimated performance curve, Figure 8-29.

There are two main variables with this nozzle, the lip angle and the outlet/inlet diameter ratio. Figure 8-30 shows the effect of angle variation on the flow coefficient and thrust coefficient over a wide range of pressure ratios. The flow coefficient decreases and the lip angle increases; and at a constant lip angle, the flow coefficient increases up to a certain pressure ratio and then becomes constant. Figure 8-31 shows the effect of the lip angle at low pressure ratios more clearly, and over a wider range of angles.

Figure 8-32 shows that at the lower lip angles the best flow coefficients occur at about a diameter ratio of .75 at the low pressure ratios. At the higher pressure ratio the coefficient decreases with an increasing lip angle.

The thrust coefficient is little affected by the lip angle and diameter ratio. Figure 8-30 shows some experimental results. The pressure ratio is the main variable to effect the thrust coefficient. Below the critical pressure ratio, the overall performance is rather good, but above the critical pressure ratio the thrust coefficient begins to rapidly decline.

8.3.1.2 Annular (For Fan Air)

The annular nozzle is special type of convergent nozzle. Figure 8-33 illustrates some different configurations of an annular nozzle. As can be easily seen from the figure, these configurations are a plug-type nozzle. For this reason then, some of these configurations are discussed under the plug nozzles. Section 8.3.4.

The main interest, here, is the application of the annular nozzle to the high bypass fan engine. Figure 8-34 shows the main components of the high bypass fan engine. If the after-body cowl is thought of as a plug, then, the nozzle for the fan air is basically an annular nozzle.

The fan nozzle is just one aspect of the total performance of the fan engine exhaust system's performance. Many other things have to be considered to estimate the overall thrust-minus-drag performance.

Since the fan nozzle's performance is only a small part of the overall performance, the discussion here will be brief, only mentioning some general observations. For more information refer to reference 4.

For a typical fan engine the gross thrust is about $2\frac{1}{2}$ times the engine's net thrust. The primary gross thrust is about $\frac{3}{4}$ of the net thrust. Because of this relationship, the SFC is affected much more by the fan nozzle C_v losses than by the primary C_v losses.

The thrust loss of a fan nozzle is a result of three effects; friction turning (secondary flow and turbulence), and local separation. Since it is very hard to analytically predict the behavior of these variables, a good estimation of a fan nozzle's performance can only be developed from experimental testing. It is important to note that careful consideration must be given to the internal design of the nozzle. Poor internal design can result in local separation which can cause substantial C_v losses.

References: Convergent Nozzles

1. Grey, R. E., and Wilsted, H. D.; Performance of Conical Jet Nozzles in Terms of Flow and Velocity Coefficients: Lewis Flight Propulsion Laboratory, Cleveland, Ohio. NACA TN No. 1751, November 1948
2. Baker, Von D.; Johnson, Richard A.; Allison Division, General Motors Corporation, Indianapolis, Indiana and Brasket, Richard G.; Lamb, Owen P.; Fluidyne Engineering Corporation, Minneapolis, Minnesota; AIAA Paper No. 65-574, 1965. (Presented at AIAA Propulsion Joint Specialist Conference June 14-18, 1965).
3. Holdhusen, James S.; and Lamb, Owen P.; Scale Model Studies of Exhaust Nozzle Performance. Fluidyne Engineering Corporation Minneapolis, Minnesota; AIAA Paper No. 66-641, 1966
4. Frazier, G. T.; Aerodynamic Considerations for Engine Exhaust Design for Subsonic High-Bypass Fan Engines. Presented at the "Aeronautic and Space Engineering and Manufacturing Meeting, Los Angeles, Calif. October 3-7, 1966.

8.3.2 Performance Characteristic of Convergent-Divergent Nozzles

The non-ejector convergent divergent nozzle is examined so that its performance characteristics can be determined to aid in understanding the more complex nozzles. Although the convergent divergent nozzle designed for aircraft use ordinarily incorporates a variable geometry ejector nozzle using secondary airflow, this section considers a nozzle with fixed geometry and no secondary airflow. The convergent-divergent nozzle is examined in its simplest form so that the basic characteristics of the nozzle are easily studied, and with this basic data the operation of a nozzle with variable geometry and secondary flow can be better understood.

The performance efficiency is examined as a function of nozzle pressure ratio, nozzle shape and free stream Mach number. Emphasis is placed on nozzle operation at off design pressure ratios, the effects of large divergence angles of the divergent area of the nozzle, and the effects of free stream Mach number on over-expanded flow in the nozzle.

Several experimental studies have been accomplished utilizing wind tunnels, Figure 8-35 and static testing facilities, Figure 8-36 to obtain performance data.

The fixed geometry convergent-divergent nozzle is of course designed for a certain nozzle pressure ratio. When the nozzle is operated at other than design pressure ratio, thrust losses occur due to under or over-expansion of the flow at the nozzle exit. Figure 8-37 shows the thrust coefficient variation for a convergent-divergent conical nozzle calculated for one-dimensional isentropic flow and also experimental data obtained for the nozzle. The design pressure ratio of the nozzle is 5.3. The performance characteristics of the convergent-divergent nozzle compare well between the theoretical results and the experimental data. For higher than design pressure ratios the nozzle is under-expanded and the thrust losses incurred are not prohibitive of the nozzle's use; however, the thrust losses for the nozzle operating at lower than design pressure ratio are very large. Figure 8-38 shows data for several conical nozzles and Figure 8-39 shows the geometry of the nozzles.

Several experimental investigations have been made to study design and off-design operation of convergent-divergent nozzles having various geometric configurations. Three geometrical configurations for the divergent section are considered; the first nozzle class considered have conical convergent-divergent sections, the second nozzle class have the divergent section designed by characteristic

theory for uniform flow at the nozzle exit for design pressure ratio, and the third class consists of several convex and concave shapes. Figures 8-40 & 8-41 show nozzles representative of each class.

The nozzle operation at design pressure ratio is considered first. It is shown in Figure 8-42 where design point coefficient of thrust versus diffuser divergence angle is given that for conical nozzles the thrust coefficient decreases with diffuser angle, the thrust coefficient does not significantly increase with nozzles designed to have parallel flow at the nozzle exit, and performance of the class three nozzles was not as good as the conical nozzle.

For operation of all nozzle types at pressure ratios, well below design point the thrust losses are very high. The experimental studies show that for nozzles with large diffuser divergence angles the flow in the nozzle will separate and the thrust loss is not as large. Figure 8-43 illustrates the improvement of thrust coefficient with diffuser divergence angle for conical nozzles, and Figure 8-44 shows data of wall pressure variation with flow area ratio. The data in Figure 8-44 shows that for below design point thrust coefficient improvement is directly related to the point of separation in that the sooner the flow separates the higher the C_T is. Also for nozzle operation at below design point pressure ratios, the thrust coefficient increases with divergence angle (Figure 8-43).

The off-design point pressure ratio operation for a nozzle designed utilizing characteristics theory is shown in Figure 8-45 , thrust coefficient data are presented as a function of nozzle pressure ratio. Upon examination of the data, it is found that the separation effects, present for conical nozzles, are less favorable for nozzles designed by characteristics theory.

The design of the nozzle throat is an important consideration. Data for a nozzle with several different throat geometries are presented in Figure 8-46 . The data show that decreasing the divergent section length by decreasing the divergent section throat radius does not affect the thrust coefficient. However, data also show (Figure 8-47) that by inserting a step in the nozzle throat the throat coefficient is significantly reduced, and that the thrust coefficient is essentially unaffected by the cone angle after the step at the nozzle throat. The reason for the loss in thrust when the step is present is the uncontrolled three-dimensional expansion that takes place after the step, and the shock waves necessary to turn the flow back to the angle of the diffuser cone.

The data that have been presented are for static conditions only. Data are presented in Figures 8-48, -49 for conical nozzles that show free stream Mach number effects on the thrust coefficient. Upon examination of Figures 8-48, -49, the thrust coefficient at below design pressure ratios is found to be adversely affected by increasing external flow. The reason for this effect is that as Mach number increases nozzle base pressure decreases so that the nozzle exit

pressure decreases, and the flow separation that normally takes place is delayed so that the flow in the nozzle follows the thrust coefficient curve for one-dimensional isentropic flow. For the nozzle tested, the phenomenon of flow separation does not occur for Mach numbers above 2.0. The data that are presented in Figures 8-48, 8-49 does not include friction effects so that this data are not compatible with other data in the section.

The thrust coefficient is computed with nozzle shroud pressures utilizing the following method because the experimental study did not include any force measurement.

Actual Thrust:

$$F = m V_T + (P_T - P_o) A_T + \int_{A_T}^{A_e} (P - P_o) dA \quad (8.63)$$

where

V = velocity
 m = mass flow
 P = static pressure on shroud
 A = cross-sectional area
 F = thrust

subscripts:

T = nozzle throat
 e = nozzle exit
 o = free stream
 i = ideal conditions

Ideal Thrust

$$F_i = m V_e$$

Thrust Coefficient:

$$C_v = F/F_i$$

The internal skin friction of a convergent-divergent nozzle can be computed once the velocity and pressure distribution on the nozzle surface are known. The velocity and pressure inside the nozzle can be obtained experimentally or one-dimensional flow theory can be utilized since previous experimental studies indicate that the actual flow in the nozzle is approximated by one-dimensional flow. The basic equation is:

$$D = (C_F) (R_C) \left[\frac{C_F}{C_F(M=0)} \right] \frac{\gamma}{2} (P) (M^2) A_W \quad (8.64)$$

Where:

D = Drag due to skin friction

C_F = Skin friction coefficient for incompressible flow

R_C = Surface roughness correction factor (choose for surface used - 1.05 nominal value)

$\frac{C_F}{C_F(M=0)}$ = Compressibility correction factor on skin friction coefficient

M = Mach number

P = Ambient pressure

A_W = Wetted area

The formulation for the skin friction factor and compressibility correction factor is as follows:

From the Prandtl-Schlichting equation:

$$C_F = 0.455 \left[\log_{10} RN \right]^{-2.58}$$

where

RN = Reynolds Number

$$RN = \frac{VL\rho}{u}$$

V = Velocity (ft/sec)

L = Characteristic length (ft)

ρ = Density (slug/ft³)

u = Viscosity $\left(\frac{\text{lb-sec}}{\text{ft}^2} \right)$

The compressibility factor is:

$$\frac{C_F}{C_F(M=0)} = \left[1 + \left(\frac{\gamma-1}{2} \right) M^2 \right]^{-.467}$$

γ = ratio of specific heats (1.4 for air)

The skin friction drag may now be computed using equation (8.64) in the following manner:

- (1) The velocity and pressure distribution, are found from one-dimensional isentropic flow theory (or experimental).
- (2) The nozzle is broken up into discrete areas.
- (3) The values of the variable are set to the average of the discrete area.
- (4) Equation (8.64) is then utilized to discretely integrate skin friction over the surface of the nozzle.

Data are presented in Figure 8-50 comparing one-dimensional flow in a nozzle with experimental data obtained with and without the effects of skin friction.

It has been shown that a short nozzle is used in preference to a long nozzle. For a certain pressure ratio, a nozzle of a specific length has an optimum diffuser divergence angle. The reason for the trade-off in thrust is that by decreasing shroud divergence angle the thrust is increased until under-expansion losses are greater than thrust increases due to decrease in divergence angle. Figure 8-51 illustrates this divergence angle versus under-expansion trade-off.

The data indicate that for fixed single flow C-D nozzles a rapidly divergent conical nozzle has an advantage over any other type of fixed geometry convergent-divergent nozzle because the efficient operating range is larger, Mach number affects are favorable, separation effects are favorable and the nozzle weight and friction loss penalties are less than for uniform exit and conical nozzles with low divergence angles.

References: Convergent-Divergent Nozzles

1. Musial, Norman T.; Ward, James J.; Over Expanded Performance of Conical Nozzles with Area Ratios of 6 and 9 with and Without Supersonic External Flow; Lewis Research Center, Cleveland, Ohio. NASA TM-X-83, September 1959
2. Krull, H. George and Steffen, Fred W.; Performance Characteristics of One Convergent and Three Convergent-Divergent Nozzles; Lewis Research Center, Cleveland, Ohio. NACA RME52H12
3. Fradenburgh, Evan A.; Gorton, Gerald C.; and Beke, Andrew; Thrust Characteristics of Series of Convergent-Divergent Exhaust Nozzles at Subsonic and Supersonic Flight Speeds; Lewis Flight Propulsion Laboratory, Cleveland, Ohio. NACA E53L23.
4. Steffen, Fred W. and Krull, George H. and Schmiedlin, Ralph F.; Effect of Divergence Angle on the Internal Performance Characteristics of Several Conical Convergent-Divergent Nozzles. Lewis Flight Propulsion Laboratory, Cleveland, Ohio; NACA RM E54H25.
5. Krull, George H. and Beale, William T.; Internal Performance Characteristics of Short Convergent-Divergent Exhaust Nozzles Designed by the Method of Characteristics. Lewis Flight Propulsion Laboratory, Cleveland, Ohio. NACA RM E56D27a.
6. Steffen, Fred W.; Krull, George H. and Schmiedlin, Ralph F. Effects of Several Geometric Variables on Internal Performance of Short Convergent-Divergent Exhaust Nozzles. Lewis Flight Laboratory, Cleveland, Ohio. NACA RM E54L09.

8.3.3 Convergent-Divergent Ejector Nozzles

8.3.3.1 Experimental Results

Ejector nozzles provide a common exit for two gas streams, normally the primary (engine exhaust) stream and the secondary (engine compartment cooling airflow) stream. For subsonic turbojet aircraft, the ejector nozzle is usually a convergent nozzle with a short cylindrical shroud to accomplish cooling air pumping. For aircraft employing a variable convergent divergent nozzle (usually a variable primary to allow afterburning with a C-D exit linked to the primary or convergent nozzle throat), ejector capability is also included in the nozzle design. The ejector capability is useful for a number of purposes:

- 1) Cooling divergent nozzle flaps.
- 2) Pumping of engine compartment air.
- 3) Reduction of over-expansion losses.
- 4) Thrust augmentation in flight by pressurizing secondary flow.

The J79 nozzle is a common example of an ejector C-D nozzle. For ejector nozzles, the throat geometry of the nozzle varies greatly depending on whether the C-D exit is variable and whether a divergent wall or flaps are employed. Variation in ejector throat to primary throat diameter ratio greatly affects pumping with generally only a small effect on the total gross thrust of the ejector nozzle.

Ejector nozzle performance of course basically follows the theoretical trend as illustrated in Figure 8-52. Performance at low, off design, pressure ratios is aided by secondary flow which changes the effective area ratio, and aids beneficial primary flow separation to avoid over-expansion. Nozzle flow separation characteristics are covered in a later section.

A considerable amount of static test experimental data has been obtained on exhaust nozzle models, principally by NASA and the engine manufacturers. Currently, test emphasis is on external flow tests of nozzles, (wind tunnel tests) because of drag considerations and also the influence of base pressures on the nozzle internal flow.

For an introduction to experimental test results, several excerpts from NASA reports, dealing with practical C-D nozzle configurations with area ratios of interest in air breathing

propulsion, are presented in Figures 53 through 66. With each group of test data, a sketch illustrating nozzle arrangement, terminology, and test variations is included. These test results also introduce us to the effect of corrected secondary flow.

$$\text{Corrected secondary flow} = \frac{W_s}{W_p} \sqrt{\frac{T_s}{T_p}}$$

where

W_s = Secondary (Cooling) flow, lb/sec.

W_p = Engine gas flow, lb/sec.

T_s = Temperature of entering secondary flow, $^{\circ}R$

T_p = Nozzle discharge total temperature, $^{\circ}R$

For use in determining actual secondary airflow rates, some typical square root temperature ratios are:

- (a) $\sqrt{\frac{T_s}{T_p}}$ of .71 for low bypass ratio fan engine at subsonic cruise
- (b) $\sqrt{\frac{T_s}{T_p}}$ of .55 for a turbojet engine at subsonic cruise
- (c) $\sqrt{\frac{T_s}{T_p}}$ of .4 for maximum afterburning at Mach 1.2

Figure 8-67 presents a more complete table showing particular temperatures used.

For a particular engine, where the relationship of ram drag to gross thrust is known, it is convenient to evaluate nozzles using secondary flow in terms of an equivalent thrust coefficient, C_{fg} eq.

Equivalent gross thrust coefficient presents total ejector gross thrust minus ram drag of the secondary flow, the remainder being ratioed to ideal thrust of the primary. This coefficient therefore allows the resulting thrust minus drag effect of the secondary flow to be clearly seen. Some data for Ejector 1, Figure 8-54, has been put in the C_{fg} eq form in the following example:

1. With engine specification values at some flight condition, for instance:

Mach	1.2
Altitude	36,089
T_{T2} °R	502 °R
F_n Spec.	8780
Ram Drag ($\frac{W_a V_o}{g}$)	3530
F_g Spec.	12310
C_v Spec.	.985
F_{gi}	12500
P_{Tj}/P_o	4.95
T_{Tj} °R	3660 °R

2. From Ejector 1 data, Figure 8-54

$\frac{W_s}{W_p} \sqrt{\frac{T_s}{T_p}}$.058	.086
F_{ej}/F_{ip}	.995	1.023

3. Calculating corrected temperature ratio:

T_{T2} °R	502 °R
T_{Tj}	552 °R
T_{Ti}	3660 °R
$\frac{T_{Ts}}{T_{Tj}}$.388

4. Calculating actual secondary flow ratios:

$\frac{W_s}{W_p} \sqrt{\frac{T_s}{T_p}}$.058	.086
$\frac{W_s}{W_p}$.1495	.222

5. Calculating total thrust minus secondary drag values:

$\frac{W_s}{W_p} \sqrt{\frac{T_s}{T_p}}$.1495	.222
$\frac{F_{ej}}{F_{ip}}$.995	1.023
F_{ip}	12500	12500
F_{ej}	12440	12800
$\frac{W_a V_v}{g}$	3530	3530
$\frac{W_{sec} V_v}{g}$	527	784
$F_{ej} - \frac{W_{sec} V_v}{g}$	11913	12016
$C_{f_{g eq}}$.953	.961

Quite often ejector nozzle performance, in terms of equivalent thrust coefficients, $C_{f_{g eq}}$, is plotted against flight Mach number to provide a fair comparison with nozzle types not using secondary flow, such as a convergent nozzle or a plug nozzle. In other words, both the thrust and drag of all gas streams must be charged to provide a realistic evaluation of nozzle performance. More inclusive yet is the thrust minus external nozzle drag coefficient C_f where boattail, or blunt base drag of the nozzle is included. Some nozzle performance in these terms is presented in the nozzle comparison section.

The experimental ejector nozzle performance presented is from model tests. Losses for aircraft variable nozzles are higher than model tests because of airflow leakage between flaps and the increased friction of the flap edges. This leakage plus added friction effect generally accounts for an additional .5 percent thrust loss.

8.3.3.2

Exhaust Angularity

The flow divergence angle is an important variable in the operation of a convergent-divergent ejector nozzle. It is defined in Figure 8-68 as α . It is always slightly higher than the shroud divergence angle. Its main value lies in its use for a theoretical prediction of the change in thrust due to a change in the flow divergence angle at the design pressure ratio. It was found in Reference 1 that the following equation predicted the change in thrust to an acceptable degree:

$$\frac{\Delta F}{F_{P1}} = \frac{1}{2} (1 + \cos \alpha) \quad (8.65)$$

Figure 8-69 shows how well the experimental results agreed with the theoretical prediction. It must be remembered that this is only applicable when the nozzle is operating at the design pressure ratio. Figure 8-69 also shows that as the angle increases, the thrust coefficient decreases. But as the angle increases the length of the shroud becomes shorter, resulting in reduced weight and a smaller amount of surface area which requires cooling. Also when the nozzle is in the cruise position (the shroud divergence angle equals zero), the thrust coefficient is increased over the afterburning condition. But in the cruise position the boattail angle is rather large with the high divergent angle nozzle. Therefore there will be an increase in the boattail drag which will tend to offset the gain made by using a high flow divergence angle.

Figure 8-70 through 8-75 show the experimental results of Reference 1. To fully understand these figures it is necessary to understand the flow characteristics of the nozzle. This is extensively covered in Section 8.3.3.3.

Figure 8-76 shows the comparison of the thrust coefficients for two flow divergence angles. At the low pressure ratios, the higher flow divergence angle gives a better performance. As discussed in the aforementioned section, the C-D ejector acts as a convergent nozzle until the pressure ratio is high enough to force the flow to become attached to the shroud. It could be expected, then, that at the higher divergence angle, a higher pressure ratio is required for the flow to become attached to the shroud. Therefore, the nozzle with the higher divergence angle tends to act like a convergent nozzle for a longer time resulting in a better performance at the low pressure ratios. At the higher pressure ratios

the thrust coefficient is lower at the higher flow divergence angles.

8.3.3.3 Pumping and Flow Characteristics

8.3.3.3.1 Nozzle Flow Characteristics

The flow in a convergent-divergent ejector nozzle is similar to that encountered in single flow nozzles used on rocket applications. An understanding of the flow within the nozzle will allow a theoretical approach to determine the pumping characteristics. Figure 8-77 shows a typical convergent divergent nozzle with the various items of importance defined.

Figure 8-78 shows the important parameters associated with ejector nozzle performance, the gross thrust coefficient and the pumping characteristics. The corrected weight flow ratio for the nozzle shown is about .032. The exit diameter ratio (D_e/D_p) is approximately 1.8 and the throat diameter ratio (D_s/D_p) is 1.1. The shape of the thrust curve is typical of both C-D ejector and C-D nozzles. The shape of the curve can be explained by examining the flow as it passes through the divergent shroud. The static pressure profile along the shroud provides a means of understanding the flow. Figure 8-79 shows the static pressure distribution along the shroud for the ejector nozzle performance shown in Figure 8-78. The ambient static level is shown along the right side of Figure 8-79. The distribution is similar to that found on ordinary C-D nozzles. Any change in the thrust of a C-D ejector nozzle, when the throat is choked, is brought about by static pressure changes along the divergent shroud. At Point A on the thrust coefficient curve of Figure 8-78, the primary jet issues from the choked primary nozzle near ambient pressure and the performance is essentially that of a convergent nozzle. The pressure distribution for this condition is shown as the upper curve of Figure 8-79 with ($P_{tp}/P = 2.56$) and the ambient pressure is represented by the dashed line for ($P_0/P_{tp} = .391$). The flow is subsonic through the secondary annular exit and through the shroud. This is shown by the fact that ambient pressure changes affect the secondary total pressure in the vicinity of Point A in the lower curve of Figure 8-78. The primary flow is detached from or at least not influenced by the shroud in this region of operation.

As the primary ratio is increased from Point A to B, the primary jet expands as it leaves the primary nozzle and aspirates the region between the primary jet and the shroud. This reduces the wall pressures to below ambient along the shroud, especially in the vicinity of the primary nozzle exit ($A/A_p = 1.21$). This lower than ambient pressure on the divergent shroud area creates a force term in an axial direction which nullifies a portion of the available jet thrust and lowers the thrust coefficient.

At Point B, the primary jet expands until the flow in the shroud chokes, and the complete cross-sectional area of the divergent shroud is filled with supersonic flow to some plane downstream of the primary nozzle exit. Now, changes in the ambient pressure no longer affect the secondary passage pressure ratio as the primary nozzle pressure ratio is changed (by decreasing ambient). The primary flow is essentially attached to the shroud for a short distance downstream of the primary nozzle exit as evidenced by the static pressure profile. This is shown on Figure 8-79 as the curve with a $P_{TP}/P = 4.58$. The static pressure ratio for the first portion of the shroud becomes a fixed minimum value and no longer changes as the primary nozzle pressure ratio increases. This indicates supersonic flow along this portion of the shroud. At about an area ratio of 1.75, a shock occurs and the pressure gradually rises toward ambient as the flow progresses along the shroud. All the area of the shroud is below ambient pressure (see Figure 8-79) which reduces the thrust coefficient to a minimum. As the primary pressure ratio is increased beyond Point B (Figure 8-78), the flow expands supersonically farther and farther beyond the primary nozzle exit until it reaches Point C. Here the entire shroud is filled with supersonic flow and most of the shroud wall pressures are above ambient (Figure 8-79). The flow has not completely expanded to ambient and thus is not at its design point. The thrust coefficient shows a rise as primary nozzle pressure ratio increases from B to C because the overexpansion losses are being reduced as the positive pressure area increases.

At Point D, the static pressure at the end of the shroud is equal to the ambient pressure and the ejector is operating at the design pressure ratio. All the shroud area is above ambient pressure and the thrust coefficient is at its maximum. As the primary nozzle pressure ratio is increased beyond Point D, the thrust coefficient decreases because of underexpansion. The static pressure at shroud exit is higher than ambient and, if the shroud were extended, would provide an additional thrust force that is now lost.

If the shroud divergence angle is increased, the shape of the curve is the same, but the locations of various points change. A higher shroud angle allows ambient pressure to feed back to the low pressure area at the nozzle exit and pressurize the area. Thus, the nozzle thrust coefficient will increase. Also, the higher angled shroud requires a higher nozzle pressure ratio before it attaches to the shroud. Thus, Point B

will shift to the right with larger shroud angles. The maximum thrust coefficient for a high angle shroud will be less than that shown in Figure 8-78 because the non-axial component of the velocity at the shroud exit increases as the shroud angle increases. The thrust ratio may be approximated by a factor of $1/2 (1 + \cos \alpha)$, where α is the flow divergence angle shown in Figure 8-77.

Figure 8-80 shows the effect of secondary flow on C-D ejector nozzle performance. The principle area of influence is in the region of overexpansion of the primary flow. Static pressure profiles are shown in Figure 8-81. For very low primary nozzle pressure ratios (Points A, A', A", Figure 8-80), the primary flow is detached from the shroud as is shown from the static pressure distribution on Figure 8-81. The static pressures are not as low as the bottom curve at these pressure ratios indicating ambient pressure was affecting the pressure; hence, the primary stream was detached. For zero and low secondary flows, the shroud pressures are nearly ambient all along the shroud and the thrust coefficient high. For the high corrected flow, the secondary pressure is nearly the same as primary pressure and the ejector acts as a conventional C-D nozzle with the throat diameter equal to D_g . The shroud pressures near the primary exit are very low. This indicates relatively high velocities due to overexpansion of the flow in this region and is responsible for the relatively poor thrust coefficient at A".

As the primary pressure ratio increases to Point B, with zero secondary airflow, the thrust coefficient falls off because of the effect of expanding primary jet on the shroud pressures. At Point C, the supersonic jet suddenly attaches itself to the shroud walls near the primary nozzle exit and shroud pressures are markedly reduced (Figure 8-80, curve $P_{tp}/P_0 = 4.09$). In this region, the ejector performance with zero airflow is discontinuous and no stable operation is possible between Points B and C on Figure 8-80.

If a small amount of secondary air is introduced in the area of primary jet overexpansion, it acts as a cushion and decreases the sudden expansion losses as the jet leaves the primary nozzle. It essentially increases the boundary layer thickness allowing pressure equalization and feed back to occur. The pressures on the nozzle shroud are increased and the nozzle thrust coefficient increases over that with zero flow. The pressure ratio at which the supersonic flow first attaches to the shroud is increased to about 4.58 from 3.5 for zero flow. With low secondary flow, a shock forms in the shroud at a point nearer the primary nozzle exit for a given value of primary pressure ratio, decreasing the overexpansion losses at C' and increasing the thrust coefficient in this region (Figure 8-81)

For the high corrected weight flow ratio, the secondary flow expands along with the primary jet and helps fill the shroud. The amount of overexpansion of the primary jet is reduced and the thrust coefficient, over the no flow case, is increased in the region of pressure ratio from point C' to C". However, because of the high energy level of the secondary air, the combined streams tend to remain overexpanded at a much lower pressure ratio than with lower secondary flows.

The peak thrust coefficients with secondary flow (Points D', D", Figure 8-80) occur at lower primary nozzle pressure ratios than for zero secondary airflow (Point D), because the increased mass flow passing through the fixed shroud area reaches ambient static at the end of the shroud at a lower primary nozzle pressure ratio than when the primary jet has the area for itself. Increasing secondary airflow has the effect of decreasing the exit diameter ratio (D_e/D_p) and shifts the thrust coefficient curves laterally toward lower primary nozzle pressure ratios. The peak thrust coefficient at Point D is slightly lower than Point D' because of expansion losses associated with the higher flow angularity at the primary nozzle exit and the lower shroud wall pressures when no secondary is present. Figure 8-81 shows an area of reduced pressure just downstream of the primary nozzle exit on the nozzle with zero airflow compared with one where some flow is used. For most nozzles, the peak thrust coefficient does not change when secondary airflow is varied. Corrected secondary airflows of the order of 3 percent will reduce the loss in thrust coefficient due to overexpansion (primary nozzle pressure ratios less than design) by as much as 75 percent when compared to nozzles with zero secondary.

One form of nozzle instability has been encountered in this explanation of the nozzle flow. When no secondary airflow is supplied the nozzle, an unstable condition exists near the point of primary jet attachment to the shroud. The instability is alleviated by the introduction of secondary air. The instability is probably caused by the secondary volume being evacuated and subsequently refilled by the only source of mass in the vicinity, the primary jet.

8.3.3.3.2 Nozzle Flow Instability

Several types of nozzle flow instability have been encountered in the flight testing of C-D ejector nozzles. Mentioned in the last section was the instability of the overexpanded flow at the point of supersonic attachment to the divergent shroud. The solution to this type of instability was the introduction of a small amount of secondary airflow to allow pressure equalization through an increased boundary layer.

A second type of instability was encountered on the J79-GE-5 low base drag nozzle used on the B-58. It was called high area ratio separation buffeting (Reference 2). Figure 8-82 shows the two positions to which the nozzle was scheduled, the open position for afterburning and the closed for dry subsonic cruise. The nozzle has a converging nozzle and a divergent nozzle. Each consists of flaps hinged at the forward end and supported and positioned by an actuation ring. There are seals between each of the flaps and they ride on the flaps. The converging nozzle is fully variable, but the divergent has only the two positions shown in Figure 8-82.

The high area ratio separation buffeting was encountered when the nozzle was in the open position at low flight speeds. Here the nozzle pressure ratio was not sufficient to expand the gases to fill completely the nozzle exit area. As shown previously, the gas flow separates from the divergent shroud with attendant shock waves. Figure 8-83 shows the static pressure distribution along the divergent shroud surface for several operating conditions. The lowest curve shows the fully expanded case; the other two show operation at lower nozzle pressure ratio. The flow overexpands and the shroud pressures are considerably below ambient. The flow then separates and shocks back to ambient. This action coupled with the elastic properties of the long nozzle flaps created an aeroelastic instability. The buffeting occurred at nozzle pressure ratios of from 2.5 to 3.8. The nozzle flaps made double amplitude excursions of about 1 inch at the tips at about 9 to 12 cps. The diverging flap exit assumed an elliptical shape that rotated about the engine longitudinal axis. This instability occurred at the condition where the static non-elastic scale models exhibited dual valued expansion characteristics with the thrust and pressure distribution dependent upon the direction from which the test point was approached. This instability was encountered with some secondary airflows. From the previous data, it was seen that the phenomenon occurred on NACA test models only with zero secondary airflow. The energy storage capability of the flaps apparently allowed this to occur with some secondary airflow.

The solution to the problem involved providing four axial slots in the divergent shroud that opened to the cavity between the diverging wall and the outer or boattail wall. This cavity is an extension of the secondary airflow passage which supplies cooling air to the nozzle. The total slot area was 12.6 percent of the primary nozzle area when it was in the maximum afterburning position (full open). In dry operation, the slots are completely closed.

The slots stabilized the flow by minimizing the circumferential pressure gradient by venting to a common plenum chamber. The slots allowed pressure feed back from the high static pressure region aft of the shock to the low pressure region before the shock. This allowed the flow to separate or the shock position to remain stable in an axial location.

Another type of nozzle instability encountered is termed low area ratio vibration. This phenomenon occurs when the nozzle is shaped such that there is an area between the nozzle throat and the exit that is greater than the exit area. Such a geometry is shown in Figure 8-84. Several modes of operation are possible depending upon the nozzle pressure ratio.

At low subcritical nozzle pressure ratios, region 1 is a subsonic acceleration to $M \leq 1$, region 2 is a subsonic deceleration, and region 3 is a subsonic acceleration such that the exit static pressure equals ambient pressure. At higher nozzle pressure ratios, region 1 is subsonic acceleration to Mach 1, region 2 is supersonic acceleration, normal shock, and subsonic deceleration, region 3 is a subsonic acceleration to ambient pressure. At high nozzle pressure ratios, region 1 is a subsonic acceleration to Mach 1.0, region 2 is a supersonic acceleration, and region 3 is a supersonic deceleration to an exit Mach number greater than 1.0.

In operating the nozzle, as the nozzle pressure is increased, there is a smooth transition from the first to the second type of flow. However, the transition from the second to the third type flow was unstable, resulting in changes in nozzle loading and coupled with the elasticity of the nozzle led to an aeroelastic dynamic instability. Figure 8-85 shows the pressure distribution. The phenomenon that occurs is that a normal shock forms inside the nozzle when operating in the second type of flow. Increasing the pressure ratio slightly, moved the shock out of the nozzle and resulted in the third type of flow. The rapid shock motion caused aeroelastic nozzle instability. The difference between this instability and the last was that the flow remained attached during the normal shock transient.

The solution to this problem took several paths. One was to increase the area ratio, eliminating the supersonic deceleration region in the aft part of the nozzle. Another was to spring load the nozzle flaps and seals so as to change the damping characteristics. A third means of stabilizing the flow was to provide a slot in the divergent shroud. An axial slot was tried and did not prove effective. However,

a series of circumferential slots or holes placed in the divergent shroud in the proper axial location produced damping sufficient to produce stability. Scale model tests of this nozzle showed a high frequency vibration and a rapid transition from the normal to oblique shock during the instability. The ventilation of the shroud and nozzle contour changes eliminated the instability on the model tests also.

The third type of instability encountered was called subsonic jet acoustic oscillation. This is a low frequency oscillation generated during operation with subsonic nozzle pressure ratio with an overexpanded area ratio. These are pure tone vibrations coming from the coupled system of tailpipe and jet nozzle. The source of the instability appears to be the jet nozzle, but the frequency is set by acoustic resonance in the tailpipe. It is somewhat similar to an organ pipe. It was noted on one engine/tailpipe combination with a nozzle area ratio of about 1.35 that at a nozzle pressure ratio of between 1.08 and 1.6 the oscillations began. When the nozzle area was scheduled to its normal value, (1.38 to 1.55) the oscillations were mild. At an area ratio of greater than 1.55, the intensity increased and sound pressure levels were 30 db higher than normal. The frequencies varied from 90 to 150 CPS and from 200 to 290 CPS. In the lower range, frequency was found to be a function of nozzle pressure ratio and increased from 90 CPS at 1.1 nozzle pressure ratio of 150 CPS at 1.6. The same correlation did not hold for the higher frequency range and the frequencies were not harmonics of one another.

Prior to the oscillation, the static pressures along the secondary nozzle inner walls indicated a minimum. The nozzle area ratio was found to be critical as far as generation of oscillation was concerned. The greatest oscillations occurred when the divergent shroud area was greater than normally scheduled. Venting the nozzle helped somewhat, but proper selection and position of the exit area appeared to be the best solution.

Still another type of nozzle ejector instability has been encountered on the F-106B aircraft. An engine nozzle that was misaligned with respect to airframe mounted exhaust ejector shroud caused flow attachment to the ejector shroud. Aircraft stability was affected by a tendency to yaw inadvertently. The tendency for the flow to attach or to change the pressure distribution on one side of an ejector nozzle shroud has been investigated by NACA (Reference 3). The results of the investigation indicate that misalignment does

change the pressure distribution and induces a non-axial force of sufficient magnitude that aircraft stability could be affected. Figure 8-86 shows the misalignment of the nozzle used in the test and the shroud pressure distribution measured on the top and bottom centerline. The problem can be alleviated by mounting the ejector with the engine; however, weight penalty results using this configuration. A means must be provided to keep the primary nozzle centered to prevent jet attachment if airframe mounted ejectors are to be used.

3.3.3.3 Ejector Pumping Characteristic Estimation

Ejector pumping characteristics can be estimated utilizing a recent technique developed and given in a recent paper (Reference 4). The theory developed follows one developed by Shapiro for single stream flow (Reference 5). The important consideration in the theory is that the fluid static pressure may vary along the nozzle but not across the nozzle as all the other fluid properties do. Any number of streams may be considered. The basic flow scheme is shown in Figure 8-87. At any position in the nozzle

$$A = \sum_{i=1}^n A_i ; \frac{dA}{dx} = \sum_{i=1}^n \frac{dA_i}{dx} \quad (8.65)$$

where A is the total flow area, A_i is the flow area of the (i)th stream, and X is the axial nozzle position coordinate. The transverse pressure gradients caused by streamline curvature are neglected and this leads to the condition of static pressure being a function of axial position only. Assume the flow is steady, adiabatic, isentropic and no stream mixing occurs. Figure 8-88 shows the model that was used to derive the equations. Each stream may be taken as a one dimensional single stream. From Table 8.2 of Reference 5, one obtains the relationship of static pressure and simple area variation.

$$\frac{dp}{p} = \frac{\gamma M^2}{1-M^2} \frac{dA}{A}$$

or

$$\frac{d}{dx} (\ln p) \frac{A_i}{\gamma_i} \left(\frac{1}{M_i^2} - 1 \right) = \frac{dA_i}{dx} \quad (8.66)$$

where γ_i is ratio of specific heats, M_i is the (i)th stream Mach number, and p is the static pressure.

Equations (8.65) and (8.66) are combined to yield:

$$\frac{d}{dx} (\ln p) = \frac{dA/dx}{\sum_{i=1}^n \frac{A_i}{\gamma_i} \left(\frac{1}{M_i^2} - 1 \right)} = \frac{1}{\beta} \frac{dA}{dx} \quad (8.67)$$

where:

$$\beta = \sum_{i=1}^n \frac{A_i}{\gamma_i} \left(\frac{1}{M_i^2} - 1 \right) \quad (8.68)$$

The term β is called the compound flow indicator and determines whether the flow is subsonic or supersonic. If the inlet conditions such as stagnation pressure (P_{T1}), and gas properties are known and constant, then the corrected weight flow parameter can be found from the total to static pressure ratio or Mach number.

$$\frac{W_1 \sqrt{\theta_T}}{\delta T_1 A_1} = f_1 (M_1) = f (P_{T1}/P_1)$$

Thus for any given value of p at the inlet plane, where the A_i are known, the airflows (W_i) can be found. With the airflow fixed by the inlet pressures, it can be shown that the local areas (A_i) are functions only of the local pressure (p) and the known quantities in the remainder of the nozzle. Since the local mach number (M_i) is a function of pressure ratio and γ_i , it follows that the local value of β (Equation (8.67)) is a function of inlet pressure, local static pressure, and known quantities. Therefore, Equation (8.68) can be integrated from inlet to exit for any value of inlet pressure.

Referring to Figure 8-88 one may assess the effect of varying inlet pressure on the other fluid properties in the stream. If inlet static pressure (p) is high enough, the total to static pressure ratio yields a very small Mach number (M_1). This will produce a β greater than zero all along the nozzle and the static pressure will change in the same direction as A does (Equation (8-67)). Both p and A will have their smallest value at the geometric throat where A reaches its minimum. This distribution is represented on Figure 8-88 as curves a and b. Note that this integration shows what the back pressures must be to maintain these flows.

Differentiation of β with respect to p yields:

$$\frac{d\beta}{dp} = \sum_{i=1}^n \frac{A_i}{p \gamma_i^2 M_i^4} \left\{ (1-M_i^2)^2 + 2 \left(1 + \frac{\gamma_i+1}{2} M_i^2 \right) \right\} > 0 \quad (8.69)$$

which shows that β always changes in the same direction as p . " β " also changes in the same direction as A and reaches its minimum at the throat as shown by curves a and b. As the inlet static pressure is decreased the value of β at the throat will decrease also. If the static pressure is decreased even further, β finally reaches a value of zero and equation 8.67 becomes indeterminate. Application of L'Hospital's rule to Equation (8-67) yields

$$\frac{d(\ln p)}{dx} = \pm \sqrt{\frac{\frac{d^2 A}{dx^2}}{\sum_{i=1}^n \frac{A_i}{\gamma_i^2 M_i^4} (1-M_i^2)^2 + 2 \left(1 + \frac{\gamma_i+1}{2} M_i^2 \right)}}$$

The geometry of the throat is such that $\frac{d^2 A}{dx^2}$ is always greater than zero. Therefore $d(\ln p)/dx$ is a positive or negative root of a real number. Curve c of Figure 8-88 shows the pressure distribution when the positive root is chosen and d is in a divergent nozzle section. Any solution between the two can not be reached by an isentropic process. Intermediate points must be reached by a shock process as shown by curve e. The flow along curve c follows the same pattern as along a and b. Note that part c is chosen only when the exit pressure corresponds to that required by c. Similarly so for curve d.

The back pressure p_∞ influences the flow and inlet pressure if it is greater than that at c. If it is less than c, there is no effect at the inlet and the nozzle is choked. The value of the compound flow indicator β will determine flow through the nozzle.

If there is a pressure disturbance being transmitted upstream, it must travel as a plane wave. The disturbance cannot propagate at different velocities without violating the selected condition of constant static pressure across a section. Although the wave may not be plane, the pressure rise across it cannot vary from stream to stream.

In Figure 8-89, the absolute upstream velocity of the pressure wave is indicated by α . If α is positive, the flow is subsonic, if α is zero, the flow is sonic and if α is negative, the flow is supersonic. An expression for the wave velocity, α , can be derived by treating each stream separately as a flexible tube and conserving mass, momentum and entropy across the wave in the frame of reference of the wave. Therefore,

$$\frac{\Delta A_1}{A_1} = \frac{\Delta P_1}{\gamma_1 P_1} \left\{ \frac{1}{\left(\frac{\alpha}{\sqrt{\gamma_1 R_1 T_1}} + M_1 \right)^2} - 1 \right\} \quad (8.70)$$

where Δ is a change across the wave.

Since the flow area is constant at the section

$$\sum_{i=1}^n \Delta A_i = \Delta A = 0 \quad (8.71)$$

across the wave. Since $P_1 = p$ and $\Delta P_1 = p$, Equations (8.70) and (8.71) can be combined to give the relation for the wave velocity, α . Thus

$$\sum_{i=1}^n \frac{A_i}{\gamma_i} \left\{ \frac{1}{\left(\frac{\alpha}{\sqrt{\gamma_i R_i T_i}} + M_i \right)^2} - 1 \right\} = 0 \quad (8.72)$$

Equations (8.68) and (8.72) may be combined to give:

$$\sum_{i=1}^n \left[\frac{A_i}{\gamma_i} \left\{ \frac{1}{M_i^2} - \frac{1}{\left(\frac{\alpha}{\sqrt{\gamma_i R_i T_i}} + M_i \right)^2} \right\} \right] = \beta$$

From this equation, one can see that β and α must have the same sign. If the wave velocity (α) is positive, the flow indicator is positive and the flow is subsonic. If the wave velocity is zero, then β is zero and the flow is sonic. Note that waves cannot move upstream in the supersonic region. Therefore, shocks will arise in the supersonic region and cause the flow to be non-isentropic.

Several interesting items can be noted here, (1) choking flow does not necessarily occur at Mach one. When compound flow is choked, the individual stream Mach numbers will not be equal to 1 except for the case of all stream pressures equal and all stream Mach numbers equal to 1. Compound flow choking is determined by β and can occur only when $\beta = 0$ at the minimum nozzle flow area. Not every stream need have a Mach number less than 1 in order that the flow be subsonic. Not every stream need have a Mach number greater than 1 in order for the flow to be supersonic. In fact, Equation (8.68) shows that the various streams influence β in proportion to their flow areas. Note also that single stream results may be obtained when $n = 1$ in the foregoing equations.

The use of the equations will be illustrated next. To limit the computations, a C-D ejector nozzle with secondary flow will be used. The corrected flow parameter can be combined with Equation (8-65) to give:

$$\sum_{i=1}^n \frac{W_i \sqrt{T_{T1}}}{P_{T1}} \left(\frac{P_{T1}}{P} \right)^{\frac{1}{\gamma_1}} \left\{ \frac{2}{R_i} \frac{\gamma_1}{\gamma_1 - 1} \left[1 - \left(\frac{P}{P_{T1}} \right)^{\frac{\gamma_1 - 1}{\gamma_1}} \right] \right\}^{-1/2} = \sum_{i=1}^n A_i = A \quad (8.73)$$

Using Equation (8.73), a corrected airflow ratio can be determined at any point in the nozzle.

$$\frac{W_2 \sqrt{T_{T2}}}{W_1 \sqrt{T_{T1}}} = \left\{ \frac{A}{A_1} * \left[\left(\frac{2}{\gamma_1 - 1} \right) \left(\frac{\gamma_1 + 1}{2} \right)^{\frac{\gamma_1 + 1}{\gamma_1 - 1}} \right]^{1/2} - \left(\frac{P_{T1}}{P} \right)^{1/\gamma_1} \left[1 - \left(\frac{P}{P_{T1}} \right)^{\frac{\gamma_1 - 1}{\gamma_1}} \right]^{1/2} \right\} \left\{ \frac{R_1 \gamma_2}{R_2 \gamma_1} \left(\frac{\gamma_1 - 1}{\gamma_2 - 1} \right) \left[1 - \left(\frac{P}{P_{T2}} \right)^{\frac{\gamma_2 - 1}{\gamma_2}} \right]^{1/2} \right\} \left(\frac{P_{T2}}{P_{T1}} \right) \left(\frac{P}{P_{T2}} \right)^{1/\gamma_2} \quad (8.74)$$

Where

$$A_1 * = \frac{W_1 \sqrt{T_{T1}}}{P_{T1}} \sqrt{\frac{R_1}{\gamma_1} \left(\frac{\gamma_1 + 1}{2} \right)^{\frac{\gamma_1 + 1}{\gamma_1 - 1}}} \quad (8.75)$$

These are the equations for solving the two stream compound flow problems. When the flow is unchoked, the exit pressure is equal to the free stream pressure. Equation (8.74) can be applied to the exit station under these conditions. Solution of Equation (8.74) for unchoked flow is shown in Figure 8-90 for different A_1^*/A_e . Although these curves are generated for specific flow ratio and fluid properties, other values may be used and similar curves generated. Under choked conditions, it has been shown that the flow behavior is determined by the nozzle geometric throat where δ is zero. Equation (8.65) and the Mach number/pressure ratio equation are combined to give the following equation for choked flow:

$$\frac{W_2}{W_1} \frac{\sqrt{T_{T2}}}{\sqrt{T_{T1}}} = \left(\frac{\gamma_2}{\gamma_1} \frac{P_{T2}}{P_{T1}} \right) \left\{ \frac{\gamma_1 - 1}{2} \left[\left(\frac{P}{P_{T1}} \right)^{\frac{1 - \gamma_1}{\gamma_1}} - 1 \right]^{-1} - 1 \right\} \left\{ \left(\frac{P}{P_{T2}} \right)^{\frac{1}{\gamma_2}} \sqrt{\frac{2}{R_2} \left(\frac{\gamma_2}{\gamma_2 - 1} \right) \left[1 - \left(\frac{P}{P_{T2}} \right)^{\frac{\gamma_2 - 1}{\gamma_2}} \right]} \right\} / \left\{ 1 - \frac{\gamma_2 - 1}{2} \left[\left(\frac{P}{P_{T2}} \right)^{\frac{1 - \gamma_2}{\gamma_2}} - 1 \right]^{-1} \right\} \left\{ \left(\frac{P}{P_{T1}} \right)^{\frac{1}{\gamma_1}} \sqrt{\frac{2}{R_1} \left(\frac{\gamma_1}{\gamma_1 - 1} \right) \left[1 - \left(\frac{P}{P_{T1}} \right)^{\frac{\gamma_1 - 1}{\gamma_1}} \right]} \right\} \quad (8.76)$$

Equation (8.76) is solved by a trial and error method to determine the relationship between P_{T2}/P_{T1} , $W_2/\sqrt{T_{T2}}/W_1/\sqrt{T_{T1}}$, A_1^*/A_{throat} and P_{throat}/P_{T1} at choking. The relationships are shown plotted in Figure 8-91. From Figure 8-91, one can see that for a given corrected secondary air-flow ratio, there is a unique total pressure ratio (P_{T2}/P_{T1}) for each area ratio (A_1^*/A_{throat}). These values appear as the straight lines in Figure 8-90 because the back pressure does not affect the flow under choked conditions. From Figure 8-90, one can see that at the intersection point between the two flows the nozzle throat is choked. To the left, the flow is unchoked; to the right choked. The entire flow in the nozzle can be described by a single line. The dashed line shown on Figure 8-90 describes a nozzle with $A_1^*/A_{throat} = 0.431$ and $A_1^*/A_{exit} = 0.225$.

Figure 8-92 shows the Mach number of the two streams with various amounts of secondary flow with the throat at choked conditions. Note that neither flow is sonic at the nozzle throat. It is important to note also that the solutions are independent of the inlet areas, indicating that once the inlet pressures are known that the nozzle performance can be determined. The nozzle exit area or throat area really controls the flow behavior.

Experimental verification of the theory is shown in Figure 8-93. A convergent divergent nozzle was used of $A_1^*/A_{throat} = 0.431$ and $A_1^*/A_{exit} = 0.226$. Various secondary airflows and nozzle pressure ratios were used. The theory is in excellent agreement with the experimental results.

To facilitate prediction of ejector pumping characteristics over a large range of ejector geometries, a number of parametric curves are presented for a two flow nozzle. Figure 8-94 shows the basic nomenclature used for the curves.

During choked flow, the ejector pumping characteristics are determined exclusively by the A_1^*/A_{min} ratio and the temperature corrected mass flow ratio $W_2 \sqrt{T_{t2}}/W_1 \sqrt{T_{t1}}$. The choked flow pumping characteristic curve is shown in Figure 8-95. In using this curve, the pumping characteristic (P_{t2}/P_{t1}) is determined from the intersection of a given mass flow and given nozzle geometry. For example, if mass flow ratio is 1.2 and A_1^*/A_{min} is 0.3, then the pumping characteristic (P_{t2}/P_{t1}) is 0.538, (Figure 8-95).

During unchoked flow, the nozzle pressure ratio (P_{t1}/P_{∞}) has an effect upon pumping characteristics. The other two parameters needed to determine pumping characteristics are the area ratio (A_1^*/A_{exit}) and the mass flow ratio ($W_2 \sqrt{T_{t2}}/W_1 \sqrt{T_{t1}}$). Figures 8-96 through 8-104 yield the pumping characteristic for the unchoked nozzle conditions. If A_1^*/A_{exit} is 0.1, mass flow ratio is 1.2, and the primary pressure ratio is 4, then the pumping characteristic is 0.268 (Figure 8-96).

It is essential to determine whether the flow is choked or unchoked under a given set of conditions. To determine this, both pumping characteristics must be found. The solution giving the higher pumping characteristics (P_{t2}/P_{t1}) determines the flow regime. The curves of Figures 8-95 through 8-104 may be used to determine the nozzle pumping as a function of primary nozzle pressure ratio. Figure 8-105 shows the plotted characteristic utilizing curves from Figures 8-95 and 8-96.

8.3.3.3.4 Ejector Gross Thrust Estimation

In Reference 6, a method is developed for theoretically determining the gross thrust of an installed air-augmented nozzle. The method consists of three parts: (1) determining the thrust contribution of the primary nozzle by integrating exit pressure area and momentum terms, (2) determining the thrust contribution of the secondary airflow by integrating secondary exit pressure area and momentum terms and (3) determining the thrust contribution of the internal shroud by considering the effect of hydrostatic pressures on the surface and the effect of wall friction on the momentum thickness at the nozzle exit.

Figure 8-106 shows a comparison at one operating condition of calculated and experimental gross thrust coefficient. The agreement between the two is good. The results indicate that the calculated gross thrust coefficient might be conservative. A computer program is available for estimating the thrust coefficient from inlet conditions and nozzle geometry.

References: Convergent-Divergent Ejector Nozzles

1. Trout, Papell, and Povolny, "Internal Performance of Several Divergent Shroud Ejector Nozzles with High Divergence Angles", NACA RME57F13.
2. Alford and Taylor, "Aerodynamic Stability Considerations of High Pressure Ratio, Variable Geometry Jet Nozzles", AIAA Paper 64-247.
3. Stofan, A. J., "Effects of Nozzle Shroud Misalignment on Performance of a Fixed-Shroud Divergent Ejector", NASA TM X-97, March 1960.
4. Bernstein, Heiser, and Hevenor, "Compound-Compressible Nozzle Flow", ASME Paper No. 67-APM-L.
5. Shapiro, A. H., "The Dynamics and Thermodynamics of Compressible Fluid Flow", Ronald Press Co., New York, 1953.
6. Korst, Addy, and Chow, "Installed Performance of an Air Augmented Nozzle Based on Analytical Determination of Internal Ejector Characteristics", AIAA Paper No. 65-596.

8.3.3.4 Nozzle Flow Separation

8.3.3.4.1 Basic Nozzle Flow Considerations

Maximum thrust is obtained from a nozzle when it is designed for expansion of the propulsion gas flow to obtain an exit (static) pressure equal to the vehicle base pressure at the nozzle exit (Reference 1). If the nozzle pressure ratio is less than approximately two, the optimum expansion can be obtained with a converging nozzle (producing subsonic or sonic nozzle exit velocity). If the available inlet-to-base pressure ratio is greater than required for sonic nozzle exit velocity, the optimum expansion can be obtained only with a converging-diverging nozzle (producing supersonic nozzle exit velocity). The optimum exit-to-throat area ratio for a converging-diverging nozzle is a function of the available nozzle pressure ratio and the gas specific heat ratio (Figure 8-10). The thrust increases attainable with converging-diverging nozzles are increasingly important at higher pressure ratios.

When a converging-diverging nozzle is operated at design optimum pressure ratio, it produces a propulsion gas plume that is basically parallel to the nozzle axis over the entire nozzle exit plane. The flow field and thrust can be greatly altered at off-design pressure ratios (Figure 8-108). Pressure ratios higher than optimum (producing under expanded flow) cause relatively small thrust penalties and a propulsion gas plume that expands (through isentropic expansion waves) to a larger area than the nozzle exit plane. Pressure ratios lower than optimum (producing over expanded flow) can cause large thrust penalties and a propulsion gas plume that contracts (through non-isentropic shock waves) to a smaller area than the nozzle exit plane. Pressure ratios greatly lower than optimum (producing separated flow) usually cause moderate thrust penalties and a propulsion gas plume that is separated (at internal non-isentropic shock waves) to fill a smaller area than the nozzle exit plane. The flow field of the propulsion gas plume (unseparated or separated) affects base drag and base pressure (thereby also affecting in-flight nozzle pressure ratio). Nozzle flight flow regimes (in terms of ambient free stream pressure) are therefore dependent on vehicle base aerodynamic flow considerations.

The propulsion nozzle operating regime of lowest pressure ratio is commonly designated as separated flow, but several other types of flow can be obtained at low pressure ratios.

The boundary layers of converging-diverging nozzles are relatively thin, and flow separation does not necessarily occur when there are shocks within these nozzles (Reference 2). At very low pressure ratios (less than approximately 1.2), the nozzle flow would be subsonic (with or without flow separation). A more exact definition of all possible operating conditions would be (in order of increasing pressure ratio), subsonic, supersonic attached non-isentropic, supersonic separated non-isentropic, supersonic isentropic over expanded, design optimum, and supersonic isentropic under expanded. Subsonic operation is seldom of interest in propulsion applications. Supersonic non-isentropic attached operation is sometimes encountered in propulsion nozzles, but the overall effects of this operating condition are similar to separated non-isentropic operation. The upper pressure threshold for separated flow is a particularly important off-design nozzle performance parameter because it determines the limit of over-expanded flow thrust penalties (Figure 8-108).

For single stream nozzles at high pressure ratios, the separation pressure is primarily a function of nozzle pressure ratio, and the effects of specific heat ratio, divergence angle, and other factors are small (Figure 8-108). However, there is considerable scatter in the separation data (particularly at lower pressure ratios), and no definitive separation data are available for single stream convergent-divergent nozzles operated at pressure ratios less than ten (References 3 and 4). Dual gas stream (ejector) nozzles are usually employed for air breathing power plants. The secondary flow rate and various geometric factors must be considered in ejector nozzle operation criteria (References 5 and 6).

Convergent-divergent ejector nozzles can be classified as convergent, cylindrical or divergent shroud types (Figure 8-109). The most important geometric factor for these nozzles is the exit-to-primary area ratio or diameter ratio (D_e/D_p) because this (when corrected for secondary flow effects) determines the optimum (design point) pressure ratio. The nozzle spacing ratio (L/D_p) can be an important geometric factor because separation can be affected by the primary exhaust plume expansion angle producing impingement upstream of the shroud exit. The (exact) exit-to-primary diameter ratio (D_e/D_s) and divergent shroud half angle (β) could be geometric factors affecting the separation threshold, but have not been observed to be significant for normal nozzle application ranges. The secondary flow rate is an important factor in both the design and off-design ejector nozzle performance. Since the primary gas stream is usually at higher

temperature than the secondary air stream, a corrected secondary flow ratio ($W_s \sqrt{T_s} / W_p \sqrt{T_p}$) is used to identify relative magnitudes of secondary and primary gas flows. This ratio provides a theoretically sound correlation of ejector nozzle pumping and thrust with unseparated flow, but it is not known to accurately correlate flow separation effects. Ejector nozzle thrust performance is best defined in terms of ratio of actual thrust (F) and the sum of primary and secondary ideal thrust ($F_{ip} + F_{is}$). Ideal thrust is the thrust which could be obtained from the primary or secondary gas stream with an isentropic nozzle of optimum area ratio. Some early test data were reported as the ratio of actual total and ideal primary thrust (F / F_{ip}). This type of data can be confusing, particularly relative masking of the separation threshold.

Extensive nozzle flow and pressure survey data has been applied to postulate that ejector nozzle flow separation is produced by shocks in the secondary air stream (Figure 8-108). Ejector nozzle separation has been observed to occur at local nozzle pressures approximately 0.57 ± 0.1 times the nozzle base pressure for a wide range of nozzle geometric variations (References 7 and 8). However, separation has also been observed to occur at much lower pressures with similar ejector nozzles (References 9, 10 and 11). The flow fields are greatly different for single stream and ejector nozzles (Figures 8-108 and 8-109). Ejector nozzle separation would not be expected to conform with the trends for single stream nozzles (Figure 8-108). Single stream nozzle separation is not a simple function of pressure ratio at pressure ratio magnitudes less than ten. Ejector nozzle separation involves secondary flow as an additional variable, and simple definition of separation would not be expected at the relatively low pressure ratios of interest for air breathing propulsion.

8.3.3.4.2 Nozzle Static Thrust Performance

The trends in off-design thrust for divergent shroud ejector nozzles are fairly well known, but no general correlation of off-design performance has been achieved. The available data can be applied to estimate the approximate operational ranges in which separated flow is possible or probable, but the ejector nozzle flow separation mechanism is not consistent enough to allow prediction of exact separation thresholds at the low pressure ratios (two to ten) of interest for air breathing propulsion. Nozzles are usually designed to avoid the operation ranges which might involve large thrust performance penalties with unseparated over expanded flow.

The low pressure ratio thrust penalties increase with exit-to-primary diameter ratio (Figure 8-110). This reflects the trend of increase in optimum nozzle pressure ratio with area ratio. The theoretical design optimum pressure ratios are approximately 5, 17 and 32 for the 1.16, 1.54 and 1.97 diameter ratio test nozzles (neglecting secondary flow effects). The over-expanded flow (unseparated) thrust test data (Figure 8-110) are therefore in fairly good agreement with the theoretical trends for nozzles with these design pressure ratios. The separation thresholds implied by the data (for the two larger area ratios) vary from approximately 1/8 to 1/4 of the optimum pressure ratios.

The low pressure ratio thrust penalties increase with nozzle spacing ratio when there is secondary flow (Figure 8-111). Since a larger nozzle spacing ratio implies a smaller primary gas stream expansion angle for impingement on the shroud, separated flow would be expected at higher pressure ratios (as indicated by the data observed with secondary flow). However, the data for no secondary flow indicates different trends, including hysteretic flow surges between two levels of thrust performance (one stable for increasing and the other for decreasing primary pressure ratio). This type of instability may have existed without being observed during other nozzle tests, especially when few low pressure data points are taken (such as shown in Figure 8-110). The instabilities appear to be suppressed by very small (0.025) secondary-to-primary flow ratios (Figure 8-111, probably because the flow of low velocity secondary air along nozzle walls causes early separation (outside the pressure ranges of potential instability). The design optimum pressure ratio of these test nozzles is approximately 25 (for 1.83 diameter ratio with secondary flow effects neglected). The separation pressures implied by the data (with secondary flow) vary from approximately 1/5 and 1/3 of the design optimum ratios for the long and short nozzle spacings, respectively.

Low pressure ratio thrust penalties tend to decrease with increasing secondary flow (Figures 8-110, 8-111 and 8-112). However, the observed trends differ for nearly identical nozzles (Figure 8-112). With no secondary flow, three nozzles having nearly the same diameter and spacing ratios had different variations of thrust with pressure ratio. Only one of the three produced unstable flow surges, and detection of flow surges was likely with the techniques employed for these specific tests (Reference 5). At an intermediate secondary flow ratio (0.15), data for one

nozzle disagreed with that for two nearly identical ones, but this may have been due to secondary flow passage choking (Figure 8-112). One nozzle (of slightly lower exit-to-primary area ratio) exhibited a separation pressure approximately double that of the other nozzles. The actual implied separation pressures were about $1/4$ and $1/2$ of ambient pressure for the larger and smaller area ratios, respectively.

The above test data indicate that divergent shroud ejector nozzle flow separation thresholds vary due to unknown factors which do not appear consistently repeatable (a characteristic of many other types of flow separation). However, an envelope of overall observed data trends can be used to define possible ranges of separation (Reference 5 to 8). With no secondary flow, the separation threshold is likely to occur between 0.1 and 0.3 of the nozzle optimum pressure ratio, and unstable flow surges are unlikely. The above trends for ejector nozzles at low pressure ratios are substantially different than the trends for single stream nozzles at high pressure ratios (Figure 8-108).

The scope of test data available for cylindrical and convergent shroud nozzles is less complete than that for divergent shroud nozzles (References 5, 7, 8, 9, 10 and 12). However, separation effects appear to be similar for all types of shrouds, especially at the higher secondary flow ratios of most interest in propulsion applications. The similarity of data for divergent shroud nozzles of various secondary-to-primary area ratios and divergence angles tends to support the conclusion that separation effects are similar for cylindrical (and possibly convergent) nozzles.

8.3.3.5

External Aerodynamic Effects on Nozzles

Nozzle thrust performance as a function of the ratio of nozzle primary pressure to ambient free stream pressure is desirable so that thrust can be evaluated in terms of known air vehicle parameters. Static tests define nozzle thrust performance in terms of the ambient quiescent air pressure or the in-flight base pressure at the nozzle exit. If vehicle base pressures were known, nozzle static test data could be used to compute thrust performance in terms of ambient in-flight free stream pressures. The computations should include internal base drag as well as thrust increments due to differences between the base and ambient pressures. Internal base

drag is generally accounted for as a negative thrust acting on the internal nozzle walls to avoid possible confusion with external base drag. In-flight nozzle thrust performance can be greatly different from static performance. Specific test data indicated in-flight thrusts ranging from 0.6 to 1.3 times static thrusts for Mach numbers from 0 to 2 (References 9 and 12).

Exact external aerodynamic effects on nozzles are a complex function of many factors relating to the specific air vehicle. General trends in these effects can be evaluated for a simple case of a divergent shroud ejector nozzle in a conical boat-tail afterbody. The specific selected configuration has a nozzle with 1.81 diameter ratio and 1.90 spacing ratio mounted in an afterbody with a 12.5 degree boattail angle (Reference 9). This nozzle had relatively moderate off-design static thrust penalties (Figure 8-112).

External aerodynamic effects on thrust were significant at pressure ratios less than 5 for Mach numbers of 1.8 and 2.0 but not for Mach numbers of 0.7 and 1.5 (Figure 8-113). The Mach 1.8 and 2.0 separation threshold (P_p/P_o) of 3.5 at a base pressure ratio (P_b/P_o) of 0.7 indicates a separation threshold (P_p/P_b) of 5.0, and this agrees well with the observed quiescent separation threshold (P_p/P_o). The external flows at the higher Mach numbers suppressed internal nozzle flow separation in the 3.5 to 5.0 pressure range (P_p/P_o), and the resultant thrust penalties were as large as 25 percent.

For increasing nozzle primary pressure ratios at supersonic Mach numbers, the base pressures decreased greatly near the nozzle flow separation thresholds and then increased slightly (Figure 8-113). The large decrease of base pressure near the nozzle flow attachment threshold would be expected because the effective nozzle area ratio is larger with attached than with separated flow (Figure 8-108). The small increases of base pressure with further increases of nozzle pressure ratio would be expected because the exhaust plume (although remaining attached and over expanded) would have an increasingly favorable shape for producing higher base pressures.

The nozzle flow separation thresholds (and therefore the base pressures) were somewhat different for Mach 1.5 as compared with Mach 1.8 and 2.0. This was attributed to flow separation at Mach 1.5 (but not at Mach 1.8 or 2.0) on the external surface of the 12.5 degree boattail (Reference 19). Nozzles in a boattail likely to have external flow separation at all

Mach numbers produced monotonous small increments of thrust and base pressure for the same three supersonic Mach numbers (Reference 12). Actual nozzle installations in air vehicles usually involve more complex nearby external surface contours than simple boattails. Research is currently in progress to develop improved methods of predicting internal and external nozzle base drag computation methods (References 4, 7 and 8).

References: Nozzle Flow Separation

1. Sutton, George P., "Rocket Propulsion Elements", John Wiley and Sons, 1949.
2. Shapiro, Ascher H., "The Dynamics and Thermodynamics of Compressible Fluid Flow", The Ronald Press Company, 1953.
3. Anon, "Handbook of Supersonic Aerodynamics (Section 17); Ducts, Nozzles and Diffusers", NAVWEPS Report 1488 (Volume 6), January 1964.
4. Anon, "Exploratory Research Program for Turbo-Propulsion Exhaust Systems", Phase I Final Report on Contract No. AF33(615)-3128, Pratt and Whitney Aircraft Report No. PWA-2888, 31 July 1966.
5. Greathouse, William K. and Beale, William T., "Performance Characteristics of Several Divergent-Shroud Aircraft Ejectors", NACA RM E55G21a, September 8, 1955.
6. Hessman, F. W., "Drag Analysis For Boattailed Afterbodies in the Mach Number Range 0.6 to 2.5 with Emphasis Placed on Boundary Layer Separation", North American Aviation, Inc. Report No. NA64H-891, 30 October 1964.
7. Anon, "Exploratory Research Program for Turbo-Propulsion Exhaust Systems", Quarterly Progress Report on Contract No. AF33(615)-3129, Pratt and Whitney Aircraft Report No. PWA-3029, 31 January 1967.
8. Anon, "Exploratory Research Program for Turbo-Propulsion Exhaust Systems", Quarterly Progress Report on Contract No. AF33(615)-3128, Pratt and Whitney Aircraft Report No. PWA-3088, 28 April, 1967.
9. Klann, John L. and Huff, Ronald G., "Characteristics of Five Ejector Configurations at Free-Stream Mach Numbers from 0 to 2.0", NASA TM X-23, August 1959.
10. Stofan, Andrew J. and Mihalow, James R., "Performance of Variable Divergent-Shroud Ejector Nozzle Designed for Flight Mach Numbers Up to 3.0", NASA TM X-255, January 1961.
11. Mihalow, James R., "Internal-Performance Evaluation of Two Fixed-Divergent-Shroud Ejectors", NASA TN D-763, January 1961.
12. Valerino, Alfred S. and Yeager, Richard A., "External-Stream Effects on Gross Thrust and Pumping Characteristics of Ejectors Operating at Off-Design Mach Numbers", NACA RM E56C14, June 26, 1956.

8.3.4 Plug Nozzles

8.3.4.1 Introduction

The plug nozzle has many different shapes, each with its advantages and disadvantages. The plugs are discussed in two groups, one group having supersonic expansion and the other having non-supersonic expansion. Both groups have a nozzle design which seems to be the most promising, the isentropic plug of the first group and the aerodynamic boattail nozzle (ARN) of the second. Both of these designs are discussed rather extensively. Other types are more briefly explained.

8.3.4.2 Quiescent Air Testing

Since a nozzle will mostly operate in a free stream, quiescent testing results are relatively unimportant. Therefore, quiescent testing results are not discussed, except where necessary for clarity. If information is needed on quiescent testing, References 1, 2 and 3 may be useful.

8.3.4.3 Supersonic Expansion

8.3.4.3.1 Isentropic Plug

The isentropic plug is one of the more important types of plug nozzles. Its performance shows good thrust characteristics over a wide range of pressure ratio but it suffers from low boattail and base pressures. Methods to increase the boattail and base pressures are discussed later.

Figure 8-114d shows the isentropic plug and some of the design variables. The design of a cylindrical shroud, larger boat-tail angle and small base will be used as the basic configuration.

The isentropic plug is designed such that at the design pressure ratio the flow will be discharged axially (Figure 8-114a). This occurs because at the design pressure ratio the strength of the expansion wave is strong enough to turn the flow parallel to the plug axis.

The main advantage of the isentropic plug is its performance at pressure ratio below the design point. The main reason is that the plug pressure remains relatively high. Figure 8-114b shows that in quiescent air the jet can expand to ambient pressures. The plug pressure decrease to ambient to about Point A, but because of the curvature of the plug, the plug pressure downstream of A increases slightly above ambient. With this recompression, large over-expansion losses are not encountered, resulting in high thrust performance in quiescent air at low pressure ratios.

The external stream has a considerable effect on the performance of the nozzle, this performance being very dependent on the outer shroud. The discussion at this point will deal with one basic configuration.

Figure 8-114c shows the effect of the external stream. The jet now expands to the base pressure. The base pressures are lower than ambient a ratio of the total pressure P_T to the ambient P_0 would be smaller than the ratio of P_T to base pressure P_b . The ratio of P_T/P_b is called the "effective pressure" ratio. Say for a nozzle with a design pressure ratio of fifteen at a pressure ratio of five, the jet may already be over-expanded because P_T/P_b may have already exceeded the design pressure ratio of fifteen. In a test (reference 7) it was found that a nozzle with a design pressure ratio of twenty-five had an over-expanded flow at a pressure ratio as low as five.

Plug Pressures

When the nozzle is choked, the only effects the external stream can have are downstream effects and on boattail and base pressures. One of the downstream effects concerned the plug pressures.

The base pressure is the most influential factor in varying the plug pressure at low pressure ratios. As shown in Figure 8-114c the plug pressure recedes to about ambient at A, the same as in quiescent air. But since the base pressure is present the plug pressure is further reduced until at B the plug pressure is about equal to P_b . Then a shock is formed and pressure for the rest of the plug is relatively high. But these high pressures are over such a small area that it cannot compensate for the low pressure that is over most of the plug.

Then as the pressure ratio approaches the design pressure ratio the effect of the external stream and base pressure become increasingly less important until at the design pressure ratio the effect on plug pressure is negligible.

Thrust

The main asset of the isentropic plug is its good internal performance over a wide range of pressure ratios. Figure 8-115 shows this and compares the isentropic plug to the convergent and C-D nozzles.

The conventional equation for thrust is

$$F = \phi P_o A_c$$

Where ϕ is equal to the exit momentum in parametric form

$$\frac{F}{P_T A^*} = \frac{\phi}{P_T A^*} - \frac{P_o A_c}{P_T A^*}$$

The last term is clearly dependent on the total pressure ratio, but the first term depends on the "effective pressure ratio", P_T/P_b . Since P_b , in general equals P_o but varies with Mach number, thrust can also vary with Mach number at a constant total pressure ratio.

Figures 8-117 through 8-119 are experimental results of a isentropic plug nozzle designed for a pressure ratio of 16.5. The two configurations are shown in Figure 8-116. Configuration two is near our basic configuration and the results are typical of an isentropic plug performance. Both the thrust ratio and thrust minus drag ratio increase with an increasing Mach number and then these coefficients decrease as Mach number increases. This same trend is also noted at higher supersonic Mach number (Reference 7).

Figure 8-119 shows the thrust ratio and thrust versus drag coefficients for a typical total-pressure ratio schedule. The performance at subsonic speed is fairly good but thrust suffers in the transonic region. This poor transonic performance is typical for high design pressure ratio. A lower design pressure ratio would give better transonic performance but would have a much lower supersonic performance. Application of some of the afterbodies which are discussed later can increase the transonic performance.

Since the plug nozzle will have its peak thrust coefficient near its design pressure ratio, the performance of the nozzle in Figure 8-119 is very good in the supersonic range.

Design Pressure Ratio

At low pressure ratio, the effect of the design pressure ratio is especially noticeable, the higher the design pressure ratio the greater the thrust loss. Figure 8-120 shows this effect. This result would be expected from the variation of the plug pressures. It was shown that as the operating pressure ratio approached the design pressure ratio the effect of the external stream on plug pressure became less important. Therefore, if operating at a pressure ratio of 3, the external stream would have more effect on a nozzle with a design pressure ratio of twenty-five than on a nozzle design for a pressure ratio of ten, because the pressure ratio of three is proportionately closer to twenty-five than to ten.

Afterbody

The main deficiency of the isentropic plug nozzle of our basic configuration is the low base pressure that is encountered. There have been several investigations (Reference 5) of ways to reduce the low base pressure and several configurations have been found to be the most favorable. These are the boattail, extended bumps and rings (plain and contoured). These configurations are illustrated in Figure 8-121.

The boattail, both conical and circular, is rather successful in increasing the base pressures, plus it increases the thrust performance. But with the boattail the added drag reduces these gains. In a test at Mach 0.9 (Reference 6) the thrust minus drag performance was lower than the basic configuration; but in another report (Reference 7) substantial gains occurred at the supersonic flight speeds.

Another means of boattailing has been a reduction of the boattail angle, thereby increasing the base area. This reduction in boattail angle lessens the boattail drag. But for this to be effective this reduction of boattail drag must more than offset the increase in base drag due to the increased area.

The bump can have many configurations. Of these the extended bump is the most effective in reducing base pressures. But the bump increases the frontal area thereby increasing the drag. Also, since the aft section of the extender bump is just a circular boattail, a boattail drag would be present though it may be different from a pure circular boattail because of different flow field. The thrust improvements are about the same as the boattail. So, again, the trade-off of increased thrust and base pressure for increased drag is present.

Of all the configurations tested the ring, both plain and contoured seem to be the most promising. Although the plain ring does not reduce the base pressure as much as the boattail the plain ring does not suffer from the boattail drag. Also the ring increases the thrust performance. Therefore, the thrust-drag performance of the plain ring is substantially increased over the basic configuration. There has been very little investigation of the contoured ring and then only at high Mach number, (Reference 7) but the trends seem to indicate that it is a very effective method of increasing performance. It has much higher base pressures when compared to the plain ring, but it suffers from boattail drag. Thrust performance is increased about the same amount as the plain ring. It looks like a promising method to use but more testing is necessary before a general conclusion can be reached.

Variable Area Throat

Two principal requirements are necessary to avoid large thrust losses with a variable area system. The throat should remain at a constant axial position on the plug, and large boattail angles should be avoided. Testing has shown that a shifting of the axial position of the throat can vary the thrust performance by several percent, while only small losses are incurred when the position is kept constant. (Reference 10)

From the discussion on afterbodies it is evident why high boattail angles should be avoided.

A system which conforms to the above conditions is rather complex and weight has to be considered. But the increase in performance can offset this increase in weight.

8.3.4.3.2 Conical Plug

There are methods all of which try to approximate the performance of the isentropic plug. The cone is one of these methods. Its main asset is its easy construction when compared to the construction of the isentropic plug.

As can be expected, the overall performance of the cone is below that of the isentropic plug. As shown in Figure 8-122 the cone's performance is only slightly below that of the isentropic plug, but at the design pressure ratio and at pressure ratios above it, there is a significant loss in performance. A trade-off might be considered between easy construction and reduced thrust but, so far, it has been found to be unjustifiable.

8.3.4.3.3 Convergent-Divergent Plug Nozzle Configuration

The plug type nozzle shown in Figure 8-123 is simulating a C-D nozzle. Its performance was found to be compatible with that of a simple C-D nozzle (Reference 4).

Plug Pressures

The plug pressure for the configuration depends mostly on internal performance. The plug pressures show that the flows expanded supersonically and the flow agrees rather well with one dimensional isentropic flow theory. Only when the flow is highly over-expanded does a shock enter the nozzle.

Thrust

The thrust for this configuration is little affected by the external stream. Thrust characteristics of these nozzles with an external stream are in excellent agreement with results of testing in quiescent air. The overall thrust drag performance was comparable to that of a conventional C-D nozzle with the same design point.

Afterbody Pressures

The boattail pressures are little affected by the nozzle pressure ratio even at pressure ratio above the design pressure ratio. On comparison to a conventional C-D nozzle a difference in trend of the boattail pressure is noted at pressure ratios above the design pressure ratio. The conventional C-D boattail pressures decrease at pressure ratios above the design pressure ratio. But the boattail pressure of the plug nozzle is not affected by pressure ratios above the design point. The reason for this condition cannot be explained but is thought to be a result of difference in flow angles (both internal and external) in the plane in which the boattail terminates.

The trend for the base pressures is the same as for a conventional C-D nozzle but the effect of the jet is not the same. At comparable pressure ratios the plug nozzle does not increase the base pressure as much as the conventional C-D nozzle. This again may be connected with the difference in flow angle as mentioned above.

Concave Central Base Plug

The nozzle shown in Figure 8-123 is another type of the plug nozzle. Static tests (Reference 2) have shown that the concave base is more efficient in increasing the base pressure. This nozzle creates a ring vortex flow which is more efficient than a turbulent wake in transmitting pressure from the jet flow to the base.

Little testing of the nozzle has been done with an external flow. Only Reference (12) has results of a wind tunnel test, and then only at transonic speed. Therefore no general discussion will be attempted.

8.3.4.4 Non-Supersonic Expansion

8.3.4.4.1 Aerodynamic Boattail Nozzle

The aerodynamic boattail nozzle (ABN) seems to be the most promising of the plug nozzles. Figure 8-124 shows that it is composed of a long shallow plug on a nacelle with a low boattail angle.

This design utilizes the dividing streamline between the internal and external flow as a continuation of the low boattail shroud; and also causes a gradual recompression along the dividing streamline which is reflected on the plug giving a high installed thrust performance. Because of the low boattail angle and increased fineness ratio the thrust minus drag performance is optimized. The design also allows a small maximum outer diameter by putting the mechanism for aero variations (if used) inside the plug.

Plug Pressures

To understand the effect of the external stream it is necessary to look at some static results. The curvature just before the exit can cause a pressure below ambient at the throat at an unchoked condition or slightly above choked. The remaining plug pressures are at ambient pressure for an unchoked condition. At slightly above choked a weak shock forms just downstream of the exit, but its effect is negligible because the rest of the plug is still near ambient. As the pressure ratio increases, the shock, following the initial over-expansion, initiates a train of alternate compression and expansion waves until the train of waves continues to the end of the plug. (Reference 13)

The external stream does not seem to affect the plug pressure at low subsonic flight speed. From $M = 0$ to $M = .6$ no effect on plug pressure is observed. From $M = .6$ to $M = .9$ the external stream causes a change in the initial expansion curve, and causes the train of reflected waves to damp out at about half the plug length. At $M = .9$ the plug pressure results in a thrust force at low pressure ratios but becomes a drag force at the higher pressure ratios. At $M = .95$ a drag force results at all pressure ratios. At supersonic speed the exit shock causes a pressure rise along the jet boundary. The pressure difference across the jet boundary is equalized by a shock in the jet which emanates from the jet boundary and ends on the plug.

Thrust

The maximum thrust performance at subsonic speed is relatively high, but at supersonic speeds the maximum performance steadily decreases as shown in Figure 8-125. The same trend is seen in the thrust-minus-drag ratio in Figure 8-126. As seen from the figures mentioned above, both quantities generally increase with an increasing pressure ratio.

At a typical turbojet total-pressure ratio schedule, the thrust minus drag performance remains relatively high at subsonic speed. Increasing the speed to supersonic, the thrust-minus-drag performance steadily will decrease as shown in Figure 8-127.

Truncations

Since weight is a main disadvantage of the ABN, methods to reduce the weight have been investigated, truncation being one of these methods. One test (Reference 13) found the following result:

Truncation has little effect on the remaining plug pressures. The cone was cutoff to $1/2$ and $1/3$ of its original length and the remaining plug pressures were not affected.

Truncation, though, does have an effect on the thrust minus drag performance. At $1/2$ of its original length, losses from 1% at subsonic to 3 to 5 percent at supersonic were incurred. At $1/3$ of its original length, sizeable losses occurred, from 6 to 7 percent at subsonic speed to 14 percent at supersonic speeds. These effects are noted in Figure 8-127.

Cone Angle Variations

The cone half angle of 10° is considered a near optimum angle. An increase in the cone angle causes a decrease in performance. A 10° half-cone angle is the lowest cone angle that has been tested but a decrease in the angle adds to the length and weight. If any gain in performance did occur it would probably be very small and not worth the increase in weight and length.

8.3.4.4.2 Convergent Plug Nozzle

The plug is placed in such a position that the resultant is a convergent nozzle except for the protruding plug as shown in Figure 8-128. The plug is the same as the plug was in the C-D position which has been discussed earlier (Reference 4). This position represented the other extreme position of a variable-throat-area nozzle.

Plug Pressures

The plug pressure distribution shows that the flow expands very rapidly, and some plug pressure may go below ambient. This especially occurs in the low pressure ratio range with the plug

contributing a drag force. Though rapid expansion still occurs at the high pressure ratio range, the plug is more likely to exhibit a thrust force. Generally, the flow characteristics were similar to the flow of a diverging nozzle.

Thrust

In general the thrust ratio was low at the basic pressure ratios. This is primarily because of drag force exhibited by the plug. But in contrast to the conventional convergent nozzle there was a smaller decrease after a pressure ratio of 4. This is a result of the force that the plug exhibited as noted before.

The free stream Mach number and angle of attack have little effect on the jet thrust. A comparison to quiescent air testing showed rather good agreement between the thrust ratio in both cases. Though the thrust ratio is generally lower than the thrust ratio for a conventional convergent, the thrust-minus-drag performance compares favorably with a conventional convergent nozzle. This indicates that the thrust loss due to the drag force of the plug is more than compensated for by the low boattail drag.

Afterbody

The effect of the jet of this plug nozzle on boattail and base pressure is similar to a conventional convergent nozzle. Since the base pressures are affected in a manner very similar to a conventional convergent nozzle, boattail pressure variation will be primarily discussed.

The boattail pressure drag is reduced at pressure ratios above 5 at supersonic external flow and at all subsonic speeds. This effect is similar to a conventional convergent nozzle, so there is no gain over the conventional convergent nozzle. The main reduction of boattail pressure drag is a result of the reduced projected afterbody area of the plug nozzle configuration. This occurs because of the area occupied by the plug. Therefore, the value of the boattail pressure drag is substantially lower for the plug type convergent nozzle.

References: Plug Nozzles

1. Krull, H. George, and Beale, William T.; Effect of Plug Design on Performance Characteristics of Convergent - Plug Exhaust Nozzles, Lewis Flight Propulsion Laboratory, Cleveland, Ohio; NACA RM E54H05 Oct. 25, 1954.
2. Corson, Blake W. Jr.; and Mercer, Charles E., Static Thrust of an Annular Nozzle With Concave Central Base; Langley Research Center, Langley Field, Va.; NASA TN-418.
3. Jones, J. H.; Thrust Characteristics of Several Variable Geometry Exit Nozzles; Arnold Engineering Development Center; (AEDC-TN-60-65) AD316466-L.
4. Hearsh, Donald P.; and Gorton, Gerald C.; Investigation of Thrust and Drag Characteristics; of a Plug-Type Exhaust Nozzle, Lewis Flight Propulsion Laboratory, Cleveland, Ohio; NACA RM E53L16, Feb. 19, 1954.
5. Salmi, R. J., and Cortright, E. M. Jr.; Effects of External Stream Flow and Afterbody Variations on the Performance of a Plug Nozzle at High Subsonic Speeds, Lewis Flight Propulsion Laboratory, Cleveland, Ohio, NACA E56F11a.
6. Salmi, R. J.; Preliminary Investigation of Methods to Increase Base Pressure of Plug Nozzles at Mach 0.9 Lewis Flight Propulsion Laboratory, Cleveland, Ohio; Dec. 19, 1956.
7. Valerino, Alfred S.; Zappa, Robert F., and Abdalla, Kalleel L.; Effects of External Stream on the Performance of Isentropic Plug-Type Nozzles at Mach Numbers of 2.0, 1.8 and 1.5, Lewis Research Center, Cleveland, Ohio; NASA MEMO 2-17-59E, March 1959.
8. Norton, Harry T. Jr., and Swinhart, John M.; Effect of Terminal Fairings on the Performance of a Plug-Type Nozzle in Quiescent and at Mach Numbers of 1.62, 1.93, 2.55 and 3.05; Langley Research Center, Langley Field, Va.; NASA TM X-463, March 1961.
9. MF 295A Advanced Turbofan, Exhaust Nozzle Selection, Flight Propulsion Division, General Electric, Cincinnati, Ohio; August 18, 1961.
10. JT 11 Turbojet Engine Exhaust System; Pratt & Whitney Aircraft Division of United Aircraft Corporation, Florida Research and Development Center; FWA FR-265, Oct. 10, 1961.

- 11) Willis, Conrad M., and Norton, Harry T. Jr.; Effect of Afterbody Terminal Fairings on The Performance of Plug-Type Exhaust Nozzles at Transonic Speeds; Langley Research Center, Langley Station, Hampton, Va; NASA TMX-762, March 1963
- 12) Mercer, Charles E., and Salters, Leland B. Jr.; Performance of a Plug Nozzle Having a Concave Central Base With and Without Terminal Fairings at Transonic Speeds; Langley Research Center, Langley Station, Hampton, Va., NASA TN D-1804, May 1963
- 13) Schmeer, James W.; Kirkham, Frank S., and Salters, Leland B. Jr.; Performance Characteristics of a 10° Conical Plug Nozzle at Mach Numbers up to 1.29, Langley Research Center, Langley Station, Hampton, Va.; NASA TMX-913, March 1964
- 14) Berrier, Bobby L., and Mercer, Charles E.; Off-Design Performance for a Pressure Ratio of 16.5, Langley Research Center, Langley Station, Hampton, Va.; NASA TN D-3852, March 1967.

8.3.5 Blow-In-Door Ejector Nozzles

The blow-in-door ejector nozzle illustrated in Figure 8-129 is a fairly recent nozzle innovation, presenting good performance with minimum complexity, but requiring careful incorporation into the aircraft. Because of the mechanical complexity and weight of variable convergent divergent nozzles, and because of the subsonic flight off-design performance penalties of fixed exit ejectors - variable primary nozzles with a fixed divergent shroud designed for the high pressure ratios of supersonic flight, the blow-in-door ejector (BIDE) has seen extensive development effort.

The blow-in-door ejector (BIDE) utilizes a fixed divergent shroud built into the airframe or cantilevered aft of the engine primary nozzle. At supersonic speeds, the BIDE functions as a convergent divergent nozzle. Air loaded trailing edge flaps, limited by mechanical steps, are sometimes attached to the aft portion of the divergent shroud to provide more optimum nozzle flow exit to area ratios. Trailing edge flaps improve the thrust coefficient about 1 percent over the flight Mach number range, but these flaps are not a fundamental part of BIDE nozzles.

At subsonic speeds, blow-in-doors admit tertiary airflow (external to the aircraft) and introduce this airflow around the primary nozzle at the entrance to the fixed divergent shroud. This extra airflow (tertiary flow) fills the excess divergent shroud area and reduces over-expansion of the primary jet. In other words, at subsonic speeds and especially for non-afterburning operation, the blow-in-door air effectively modifies the nozzle area ratio. At subsonic speeds, this effective area ratio modification prevents large over-expansion losses of the primary flow or engine exhaust flow. For cases where the primary jet would not over-expand, or would not attach to the divergent shroud and flow full, the blow-in-door air avoids an effective high drag blunt base annulus condition around the primary jet.

It is obvious that the blow-in-door airflow capacity is affected by the nozzle installation in the aircraft. Therefore this nozzle type, like the plug nozzle, is especially sensitive to airframe nozzle integration. This is not necessarily a decisive disadvantage, since any nozzle including the variable C-D nozzle requires careful shaping of the aircraft afterbody to provide low drag of the nozzle external boattail surface.

Major source of BIDE design information and experimental results is of course Pratt & Whitney aircraft. A very good discussion of BIDE design philosophy and performance trends is contained in Reference (1). Some of the Reference (1) P&W Report are presented in Figures 8-130

through 8-132 . Typical variation in velocity coefficient and thrust minus drag coefficient for a Mach 3 nozzle design is illustrated in Figure 8-130.

An item of major interest is the blow-in-door area needed. The area requirements, measured normal to the flow direction into the ejector, are indicated in Figure 8-131 for Military and maximum afterburning power. An area of general nozzle interest is presented in Figure 8-132 showing the effect of nozzle cross sectional shape (circular versus rectangular) on nozzle performance.

In addition to Pratt and Whitney material, BIDE experimental results from external flow wind tunnel tests have been reported extensively by the NASA Langley Research Center. Besides isolated nozzle tests, thorough tests of BIDE nozzles in a twin jet model have been conducted. These classified reports are listed as References (2) through (4).

Figures 8-133 and 8-134 show BIDE performance as affected by secondary (engine compartment) airflow. Performance levels from these confidential NASA reports are not revealed in the figures to avoid classifying them. The trends and incremental changes can be noted from Figures 8-133 and 8-134 however.

An earlier test conducted at Langley explored basic BIDE performance characteristics without any secondary flow simulated, Reference (3). Performance results are illustrated in Figures 8-135 and 8-136 showing performance at given Mach numbers as affected by pressure ratio and then basic performance variation with Mach number.

Wind tunnel test results of BIDE nozzles installed in a particular twin jet aircraft model are presented in Reference (4). Reference (2) and (3), discussed above dealt with an isolated nacelle test environment. Performance results for a twin jet installation are presented in Figures 8-137 and 8-138 along with comparisons of isolated nacelle performance. As far as comparing isolated to twin jet configuration results , it must be kept in mind that the results are for a specific aircraft configuration.

Installed performance of BIDE nozzles with emphasis on afterbody drag for a specific aircraft configuration mode, is presented in Reference (5). Results on this development model are contrasted with a research model also indicating the variations in total afterbody and nozzle drag that may be obtained depending on how fuselage afterbody closure between the nozzles is achieved.

Since the experimental results available are limited to confidential reports, the above discussion is intended to briefly indicate the scope of these references.

References: Blow-In-Door Ejector Nozzles

1. JT 11 Turbojet Engine Exhaust Systems; Pratt and Whitney Aircraft, Division of United Aircraft Corporation; PWA FR-265; 10 Oct. 1961
2. Schmeer, James W.; Mercer, Charles E.; and Kirkham, Frank S.; Effect of Bypass Air on the Performance of a Blow-In-Door Ejector Nozzle at Transonic Speeds; Langley Research Center, Langley Station, Hampton, Va.; NASA TMX-896.
3. Kirkham, Frank S. and Schmeer, James W.; Performance Characteristics at Mach Numbers Up to 1.29 of a Blow-In-Door Ejector Nozzle with Doors Fixed in Full-Open Position; Langley Research Center, Langley Station, Hampton, Va., NASA TMX-830.
4. Schmeer, James W.; Lauer, Rodney F., Jr.; and Berrier, Bobby L.; Performance of Blow-In-Door Ejector Nozzles Installed on a Twin-Jet Variable-Wing-Sweep Fighter Airplane Model; Langley Research Center, Langley Station, Hampton, Va. NASA TMX-1383.
5. Runckel, Jack F.; Jet-Exit and Airframe Interference Studies on Twin-Engine-Fuselage Aircraft Installations; Langley Research Center Langley Station, Hampton, Va., NASA TMX-1274.

8.3.6 Expansion - Deflection Nozzle

The expansion-deflection nozzle (inverted nozzle) is a direct variation of the plug nozzle. The expansion-deflection (E-D) nozzle has good performance for high nozzle pressure ratio i.e., 100 through 300 where the nozzle compares favorably with the plug nozzle. The utilization of the E-D nozzle should be considered for hypersonic speed and above. The E-D nozzle could be of use in space flight due to its performance at very high pressure ratios.

Figure 8-168 illustrates the E-D nozzle's basic configuration. The nozzle's basic component is a flat base plug; the engine flow expands around the plug, and the flow expansion in the nozzle is then controlled by the nozzle plug base pressure and by the shape of the outer wall. From Figure 8-168, the nozzle is seen to be very short so that the nozzle is the lightest of the basic nozzle types. Due to the small nozzle length, the nozzle emits a small infrared signature. Also the nozzle has very little boattail (drag) surface.

The operation of the nozzle is easily explained. The exhaust gasses issue forth from a short combustion chamber then turned outward from the engine centerline and compressed by the action of the plug. As the exhaust gasses flow out of the nozzle throat, the gasses expand about the plug where the expansion is controlled by the plug base pressure, and then the outer nozzle shroud controls the outward expansion of the exhaust gas and turns the exhaust gasses so that the gasses are discharged axially.

The basic E-D nozzle has two inherent difficulties: (1) the base pressure levels are low on the nozzle plug, and (2) the nozzle has limited aerodynamic adjustment when operating over-expanded. Figure 8-169 illustrates typical E-D nozzle performance, the high pressure ratio operating range is quite evident from the figure so that the nozzle is seen to operate best in the hypersonic speed regime and above. The base pressures of the E-D nozzle can be improved utilizing several base bleed techniques as illustrated in Figures 8-170 through 8-174. The performance of these E-D nozzles are illustrated in Figure 8-175. Again note the good performance at very high pressure ratios. The base bleed E-D nozzles have comparable performance characteristics to any of the other basic nozzle types, so that the E-D nozzle should be considered for use at high pressure ratios.

References: Expansion-Deflection Nozzles

1. Rao, G.V.R., "Recent Developments in Rocket Nozzle Configurations:", ARS Journal, Vol. 31, November 1961, pages 1488-4.
2. Pratt & Whitney Aircraft, Division of United Aircraft Corp., "Exploratory Research Program for Turbo-Propulsion Exhaust Systems (U)" Phase I, Final Report, 31 July 1966 PWA-2888.

8.4 COMPARISON OF NOZZLE PERFORMANCE

8.4.1 Introduction

Nozzle selection and afterbody design can have a large impact on aircraft performance and cost. Nozzle selection is not as straightforward as examining thrust to weight ratio for different nozzle types at important flight conditions. Figure 8-139 illustrates thrust to weight variation at a supersonic condition showing the effect of a convergent divergent nozzle compared to a convergent nozzle. Effect of inlet weight and engine bypass ratio is also presented. Figure 8-140 presents the same comparison for sea level static conditions to emphasize the importance of flight conditions.

Nozzle performance for the various candidate nozzles must be examined upon a mission impact basis. Therefore, we have to examine the efficiency variation of the nozzles in terms of the primary variable, jet nozzle pressure ratio. Figure 8-141 shows a typical comparison of internal nozzle performance.

In Figure 8-141, we see that a penalty to subsonic and transonic performance for maximum afterburning may be involved with selection of a C-D nozzle. Also we need to know the secondary airflow required for the internal thrust coefficients. The C-D nozzle requires a corrected secondary flow of 2 percent or an actual secondary flow of 5 percent at transonic speeds. This secondary flow ram drag is worth about 2 percent reduction in net thrust at Mach 1.2, maximum afterburning. At this flight condition, the ratio of ram drag to net thrust is about .4.

Although at high supersonic speeds, the C-D nozzle provides about 15 percent more net thrust, a weight penalty is incurred which must be carried throughout the subsonic cruise. A C-D nozzle will run 400 to 600 pounds heavier than a simple variable convergent nozzle. For the subsonic cruise, however, drag is much less for a boattailed C-D nozzle than for a convergent nozzle (hinged flaps) forming a blunt base.

Figure 8-142 illustrates the scope of the problem, now that we have progressed from a brief discussion of internal thrust coefficients and nozzle weight, to nozzle drag. Areas of performance impact noted in Figure 8-142 are:

- (a) Nozzle type, weight, internal performance
- (b) Nozzle drag

- (c) Effect of afterbody shape on nozzle drag
- (d) Interaction between nozzle, fuselage centerbody, and external flow

The engine cycle or bypass ratio selection will effect the importance of such items as nozzle drag by varying the nozzle drag area (projected area) at a given thrust level.

For interaction regions between the nozzles and airframe afterbody, model test is generally required for assessment. Even with model tests, the degree of simulation must be questioned since the point of external flow separation on the nozzles and afterbody will greatly influence thrust minus drag performance.

The foregoing considerations will influence nozzle type selection. A discussion of nozzle types is presented next.

8.4.2

Nozzle Types

The exhaust nozzle types of most interest on FX and VFAX are:

- (a) Convergent
- (b) Convergent divergent (C-D)
- (c) Blow-in-door ejector
- (d) Plug

Of course the major functional division of nozzles is between convergent nozzles and convergent divergent nozzles. The fixed ejector nozzle, designed to pump cooling air or to increase the efficiency of nozzle supersonic flow expansion, is a variation of both the convergent and convergent divergent nozzle types. A fixed ejector nozzle utilizing secondary air can provide very high design point performance, but since the ejector exit or nozzle exit is fixed, performance can suffer greatly at off design condition; especially if the nozzle throat varies to allow after-burning. The blow-in-door ejector (BIDE) is designed to overcome this off design problem by use of large quantities of tertiary or external fuselage surface air.

Although markedly different in constructions and appearance, members of the convergent divergent nozzle family are the:

(a) Blow-in-door ejector

(b) Plug nozzle (isentropic plug)

These nozzles are designed to provide the area ratio for supersonic flow expansion. A plug nozzle not designed for supersonic expansion is more correctly referred to as an aerodynamic boattail nozzle (ABN). The purpose of the ABN, actually a convergent nozzle, is to reduce the external flow boattail angle.

In discussing the four major nozzle types considered for FX and VFAX, there is considerable overlap between them in principle of operation. This overlap is illustrated in block diagram form in Figure 8-143.

Additional variations from the basic nozzle types are listed in Figure 8-144. Many mechanical or aerodynamic approaches to a basic nozzle type occur.

Approaches to convergent nozzle design are presented in Figure 8-145. Different C-D nozzle designs are presented in Figures 8-146, 8-147 and 8-148. These two C-D nozzle designs are J79 engine nozzle versions. The J93 nozzle is similar but more complex than the J79-10, -17 nozzle. The J93 nozzle incorporates individual actuation of both the primary nozzle throat and the divergent nozzle exit. This allows varying area ratio with jet pressure ratio in order to achieve near optimum thrust over the flight Mach number range.

Blow-in-door nozzle sketches are presented in Figure 8-149. Flow paths are illustrated in Figure 8-150. Floating trailing edge flaps are an option with the BIDE providing better performance at a nozzle weight penalty.

A plug nozzle of the C-D family (an isentropic plug configuration) is sketched in Figure 8-151. The isentropic configuration shown suffers from low boattail pressures and therefore has not seen any turbojet or turbofan engine application. The aerodynamic boattail nozzle (ABN) is receiving study and development for a strategic aircraft application. IR considerations are a major factor for this configuration. Performance of the ABN is very good, but weight is a major problem with this nozzle type. An ABN nozzle is shown in Figure 8-152. The basic ABN, it should be kept in mind, is a convergent nozzle.

Figure 8-153 shows an ABN nozzle with a shroud or flaps (floating or actuated versions of flaps are being considered) to provide the internal area ratio for supersonic flow expansion. The ABN modifications place these nozzles in the C-D nozzle branch.

Typical performance, in terms of thrust minus drag, is shown in Figures 8-154 through 8-157 for the major nozzle types. This performance is based on isolated nacelle conditions (podded). Performance efficiency bands are shown versus Mach number since the thrust minus drag coefficient depends on engine cycle and power setting.

Figures 8-157 illustrates a fixed ejector sized for high supersonic application. Performance of this nozzle is similar to a C-D nozzle, except very poor off design point performance can be sustained due to the fixed exit area. Plots of internal performance data obtained by NASA have been presented in Section 8.3.3.1. Figures 8-68 through 8-75 present additional performance data obtained in an investigation of the effect of low divergence angle from the primary nozzle throat to the ejector exit.

External flow can exert a strong influence on the internal performance of fixed ejectors operating off design. This influence on internal performance is achieved by modification of the degree of overexpansion obtained in the nozzle. External flow and low base pressures retards flow separation from the divergent nozzle or ejector nozzle walls thereby promoting very large overexpansion thrust losses. This subject is covered in Section 8.3.3.4 and 8.3.3.5.

8.4.3 Integration and Evaluation

For optimum nozzle selection, the installed thrust minus drag performance must be assessed. Figure 8-158 illustrates the variation in nozzle thrust minus drag values between isolated nacelle (pod) conditions and a 4-engine clustered jet configuration.

Figures 8-159 and 8-160 show fuselage afterbody pressures and performance effects for different fuselage fairings or fuselage extensions between a twin exhaust nozzle configuration. Of course external pressures on the aft fuselage extension, depend on the nozzle and afterbody combination. Close cooperation between the airframe contractor aerodynamic personnel and the airframe manufacturer propulsion system personnel is required in this area. Close cooperation is needed to achieve:

- (a) High performance nozzle installation (or a good nozzle and afterbody combination)
- (b) Accurate bookkeeping on thrust and drag

This contractor recommends for most fighter and attack aircraft configurations, with fuselage installed engines, that airframe

afterbody drag and nozzle external drag be charged against installed thrust. In other words, at the fuselage station where the nozzles start, all external drag aft of this station should be charged against installed thrust. In this region, nozzle thrust is the dominant term; therefore, smaller terms (drag) should be charged against the nozzle.

Even with this definition of responsibility, airframe contractor propulsion personnel must work closely with aerodynamics personnel to obtain satisfactory fuselage shaping to accommodate the desired nozzle external flow field.

To further define responsibility, it is recommended that the airframe contractor be responsible for the thrust minus drag performance of the nozzle. Since thrust of some modern nozzle designs (plug nozzle for instance) depends heavily on the airframe afterbody flow field, nozzle performance should be assigned to the party responsible for the flow field, the airframe contractor.

Besides installed nozzle thrust minus drag and fuselage afterbody drag, nozzle weight has become of major interest. Performance must be weighed against nozzle weight in terms of mission effect. Figure 8-161 presents an analysis comparing two nozzle types. For the mission used, which included 400 nautical miles dash at Mach .85, sea level, the ABN nozzle reduced fuel load requirements by about 10 percent. This fuel saving reduces the gross weight 3 to 5 per cent. However, the weight increment of the ABN over a convergent nozzle of 400 to 600 pounds negates the major part of the fuel saving. Final result is a reduction of T.O.G.W. of 1 to 2 percent.

The impact of engine bypass ratio on the nozzle analysis is also shown in Figure 8-161; internal fuel load versus nozzle thrust minus drag coefficient. High nozzle efficiency is more important with high engine fan bypass ratios. High bypass ratio engine performance sensitivity to nozzle efficiency results from the relationship of gross thrust to net thrust. Figure 8-162 presents a plot of gross to net thrust ratio against bypass ratio, for the Mach .85, sea level condition.

8.5 Thrust Reversers

8.5.1 Aircraft Applications for Reverse Thrust

The most important application for reverse thrust has been reduction of landing and take-off refusal ground roll distances with large multi-engine commercial and military transports. There has also been some use of reverse thrust to achieve more rapid controlled descent for landing with transports. Application of reverse thrust to military combat aircraft could be beneficial for several other in-flight purposes (not important with transports). Maneuverability could be improved by the use of reverse thrust for steeper controlled dives and more rapid decelerations (especially prior to turns). Rapid reverser actuation (with high engine speeds) could improve rates of change of thrust magnitude and direction. There are various other methods of achieving ground roll and in-flight maneuvering effects similar to that produced by thrust reversers.

Arrester gears provide the most flexible aircraft landing deceleration attainable. They are in universal use on naval aircraft carriers, and they have had limited application to short portable military air strips. Arrester gear installations require relatively precise landing approaches, and rapid thrust control response (attainable with a reverser) could be beneficial during such approaches. The rapid recovery of full forward thrust (attainable with a reverser) could also provide improved performance after landing refusal (wave-off) at an arrester gear installation. Because of various physical usage considerations, arrester gears have not been extensively applied to air fields except for runway emergency overrun protection. Other methods of landing roll deceleration are therefore important for most of the air fields.

Considering wheel brake effectiveness, an absolute aircraft braking deceleration limit is imposed by the coefficient of friction between the tires and runway. Drag parachutes and thrust reversers are primarily important for additional deceleration on wet or icy runways (Figure 8-463). Thrust reversers are most effective on aircraft with high thrust-to-weight ratios, but can also significantly reduce ground roll distances with low thrust-to-weight ratios (especially on slippery runways). Drag parachutes require higher maximum decelerations to obtain landing roll reductions comparable with thrust reversers because the parachute drag decreases rapidly with aircraft velocity during ground roll deceleration. With the

indicated 160 knot touchdown velocity ground rolls (Figure 8-163), maximum deceleration "g" forces would be 0.55 to 0.85 for thrust reversers and 1.55 to 1.85 for drag parachutes. The required repacking after each use and periodic replacement are additional disadvantages of drag parachutes not encountered with thrust reversers. Both reversers and parachutes can be beneficial relative to improving brake and tire service life as well as reducing ground roll distances.

Most high performance military aircraft have speed brakes (retractable aerodynamic drag flaps) to limit air speeds during steep dives and to provide rapid in-flight decelerations. However, the effectiveness of a speed brake decreases rapidly with flight velocity, and a thrust reverser might provide better maneuverability than a speed brake (Figure 8-164). The deceleration attainable with a reverser is (approximately) a function of thrust-to-weight ratio and the magnitude of incremental base drag produced by the reverser action. A reverser would usually have significant aircraft deceleration performance at lower velocities than speed brakes of practical size. A reverser could also apply the deceleration (and acceleration) force more rapidly than a speed brake because engine rotational speed changes are not required for thrust reversal. Actuators (for reversers or speed brakes) can usually be operated in less than one second (between full forward and full reverse thrust), but turbine driven engines require approximately three to fifteen seconds for thrust changes (between idle and full thrust). The value of speed brakes and thrust reversers for in-flight maneuvering will vary greatly with the specific aircraft mission and the type of engine.

Substitution of a turbojet engine thrust reverser for a drag parachute and/or speed brake may produce improved landing and in-flight maneuvering performance without a major difference of aircraft system installed weight. On some aircraft it may be desirable to use a drag parachute and/or speed brake to supplement the performance of a thrust reverser.

8.5.2 Configurations of Thrust Reversers

Aircraft with variable pitch propellers nearly always incorporate reverse thrust because of the simplicity of achieving it by rotational actuation of propeller blades to a suitable reverse thrust position. More complex reverse thrust provisions are required for turbojet and turbofan engines because the compressor and fan blades are fixed, and the gas stream flowing to the rear for forward

propulsion must be diverted through an angle greater than 90 degrees to achieve reverse thrust. There are many possible basic approaches to turbojet and turbofan thrust reversers. Early development work indicated that mechanical devices (utilizing solid walls) were more practical and effective than aerodynamic devices (utilizing auxiliary gas jets) for reversing propulsive gas streams (References 1 and 2). Turbojet and turbofan reversers can be used at relatively low velocities (generally less than 30 knots), but the minimum reversed thrust velocity is usually limited by exhaust reingestion, entrained debris ingestion, structural heating (by exhaust gases), or other factors.

On a high bypass ratio turbofan engine (without afterburning), effective reverse thrust may be obtained by diverting the entire exhaust stream of the unheated bypass air only. On a turbojet engine (without afterburning), heated (turbine outlet) gas must be diverted, and the exposed reverser components have to be fabricated from high temperature materials. On an afterburning engine, cooling would probably be required to avoid overheating of exposed reverser components unless the afterburner was shut down during periods of reverse thrust (with some consequent performance penalty). Heating of low temperature aircraft structure by the forward diversion of exhaust gas can be an important design consideration (particularly for turbojet engines). The reverser structural heating and installation considerations are substantially different for submerged and podded engines. Special provisions are sometimes necessary to avoid interference of a thrust reverser with engine secondary cooling air (Reference 3). Noise mufflers are frequently integral with thrust reversers.

Turbojet and turbofan reversers can be classified as the following types:

- (a) Target
- (b) Blockage Diversion

The target type is a device which is deployed behind the engine nozzle exit to direct impinging engine propulsion gases forward. The blockage diversion type is a device which blocks the engine (forward thrust) nozzle and opens diversion nozzles discharging propulsion gases forward. There are many specific mechanical concepts for reversers, but few basic concepts are practical relative to deployment for reverse thrust and storage for forward thrust. The conical clamshell target type and cascade blockage diversion type have had greatest usage (Figure 8-165). The conical clamshell is adaptable

to stowage outside an engine nozzle in two or more segments (Reference 3). The cascade reversing passages can be incorporated in an engine exhaust pipe, and blockage devices (flaps, petals, duct bills, etc.) can be stowed within engine exhaust pipes in a manner shutting off cascade flow (Reference 4). Reversers are usually designed to assume the stowed position in the event of reverser control failure (for safety).

A clamshell target reverser produces two or more discrete gas streams (depending on the number of segments) flowing forward to give reverse thrust. The cascade reverser has greater flexibility relative to location of reversed flow passages, but it usually extends around the entire engine periphery. Both types of reversers could be considered for podded engines, but annular cascades (handling fan air only) have certain usage advantages for high bypass ratio engines (Reference 5). Two or three segment clamshell reversers can be favorable for avoiding hot air impingement on empennage surfaces with submerged engines (Reference 3).

8.5.3 Performance of Thrust Reversers

Reverser effectiveness is most commonly defined as the ratio of reverse thrust (with reverser deployed) and forward thrust (with reverser stowed). Static reverser effectiveness (with zero aircraft velocity) is dependent on how efficiently and how close to 180 degrees the propulsion stream is turned. The reverse thrust effectiveness of a cascade reverser is typically high (approximately 75 to 90 percent) because the flexibility of reverse nozzle arrangement allows design optimization (Figure 8-166). The reverse thrust effectiveness of a conical (two segment) clamshell target reverser is relatively lower (approximately 55 to 60 percent). This is attributed to the inefficiencies of turning the engine gas jet into two strong discrete reverse jets rather than a basic limitation of target type reversers. Hemispherical target reversers have attained efficiencies as high as 80 percent (References 6 and 7), but their configuration makes stowage outside a round nozzle difficult to achieve without excessive space requirements (which may violate desired external aircraft contours). Multiple segment target reversers have practical usage aspects for the annular fan stream of high bypass ratio turbofan engines (Reference 5).

Static reverse thrust effectiveness and aircraft thrust-to-weight ratio are the important factors in the landing and take-off refusal ground roll distance reductions obtained with reversers (Figure 8-168). Except with very large frontal areas (such as drag parachutes), the

aircraft aerodynamic drag forces at ground roll velocities are small compared with static reverse thrust forces. However, dynamic pressure increases rapidly with flight velocity, and the in-flight aircraft drag can become much larger than the static reverse thrust (Reference 5). When a thrust reverser is deployed, it directs a propulsive gas stream forward and outward around the nacelle of a podded engine or the fuselage of a submerged engine type of aircraft. This alters the external aerodynamic flow field in a manner tending to produce a region of very high base drag behind the reverser (not present with the stowed reverser for forward thrust operating condition). A thrust reverser therefore produces an in-flight incremental drag force (similar to that of a speed brake) in addition to the reversed engine thrust itself (Figure 8-164).

A cascade reverser is usually designed to extend completely around the engine. This tends to produce lower base pressures than a clamshell reverser because the clamshell usually has two discrete reversed jets not completely covering the engine periphery. However, the projected (base) area of a deployed clamshell is usually larger than the projected area of the region behind a cascade reverser nozzle. Relatively high base drags can be obtained with both types of reversers (Reference 3 and 5), but exact attainable base drag is dependent on many specific reverser and aircraft configuration factors. The beneficial deceleration effects of reverser base drag are slightly reduced by reverser operational effects on engine inlet additive drag. The additive drag is lower on an aircraft with a thrust reverser (at maximum reverse thrust engine operation) than on a similar aircraft without a thrust reverser (at flight idle engine operation).

In-flight thrust reversers impose important performance considerations additional to the magnitude of incremental aircraft deceleration force attainable. The reversed propulsion gas jets can alter the aircraft stability and control characteristics, particularly if the reversed jets are near aerodynamic control surfaces (such as the empennage components of a submerged engine aircraft). Aircraft buffet characteristics are likely to be altered by reverser operation, and thrust instabilities are frequently encountered at partially deployed reverser settings of interest for in-flight maneuvering. Wind tunnel model tests are desirable to develop in-flight thrust reversers suitable for specific aircraft.

Thrust reverser installations can impose penalties on aircraft performance (such as speed, range, take-off distance, etc.) when the reverser is stowed. Reverser installed weight (including

necessary structural reinforcements) is usually significant (approximately 0.03 to 0.05 pounds weight per pound of engine forward thrust), but overall aircraft weight may not increase significantly if addition of a reverser eliminates need for a drag parachute and/or speed brake (References 1, 2 and 3). The blockage diversion type reversers stow as part of the engine tailpipe and there can be flight performance losses due to duct leakage, internal duct friction, and/or external aerodynamic drag. The target type diffusers usually stow outside the engine duct and there can be a flight performance loss from stowed reverser aerodynamic drag. Stowed reverser performance penalties are usually a primary evaluation factor relative to combat military aircraft.

Certain basic factors must be considered in the design of turbojet and turbofan reversers. It is usually desirable to divert the propulsion gas stream forward for reverse thrust without significantly altering the engine operating conditions. With a target type reverser, this can be achieved easily by designing for sufficient distance between the engine nozzle and deployed target to preclude adverse engine back pressure. With a blockage diversion type reverser, the reverse flow nozzles can be designed for the same engine back pressure as the forward thrust nozzle, but it is usually impractical to design for constant back pressure at all reverser positions (from fully stowed to fully deployed). An in-flight reverser may be required to actuate with high engine and flight speeds, and the reverser design is then dependent on the engine characteristics and desired aircraft mission performance.

Blade design considerations for cascade blockage diversion reversers are similar to those for turning vanes (References 4 and 5). General design data are not available for target reversers, but the performance trends are known, particularly for the common conical (two segment) clamshell type reverser (Figure 8-167). Door sweep angles between 10 and 15 degrees produce relatively high reverse thrust performance without thrust instability. Door wrap angles between 120 and 180 degrees produce relatively high reverse thrust, and these angles are usually practical for compact stowage around engine nozzles. Target-to-nozzle area ratios of 3 to 4 produce relatively high reverse thrust, but area ratios greater than 4 are useful only for increasing base drag with in-flight reversers (static reverse thrust remaining constant at area ratios greater than 4). Ratios of end plate height and nozzle diameter between 0.10 and 0.15 have been commonly used for high reverse thrust performance (Figure 8-167). However, higher end plates probably yield slightly higher reverse thrust when choking is not encountered in the external reversed gas jets (Reference 3). Choking is not usually encountered when a clamshell reverser is deployed approximately one nozzle diameter behind the nozzle exit plane.

References: Thrust Reversers

1. Hawk, G. Wayne, "Summary of Development of Mechanical Type Thrust Reversers", WADC Report TR 57-17, May 1957.
2. McDermott, J. F., Jr., "Summary of Development of Aerodynamic Type Thrust Reversers", WADC Report TR 57-18, May 1957.
3. Hilbig, J. H., "In Flight Reversers for Tactical Fighter Applications", Air Force Systems Command Report AFAPL-TR-66-118, January 1967.
4. Henzel, James G., Jr. and McArdle, Jack G., "Preliminary Performance Data of Several Tail-Pipe-Cascade-Type Model Thrust Reversers", NACA Report RM E55F09, August 29, 1955.
5. Poland, Dyckman T., "The Aerodynamics of Thrust Reversers for High By-Pass Turbofans", AIAA 3rd Propulsion Joint Specialist Conference, July 1967.
6. Steffen, Fred W., McArdle, Jack G., and Coats, James W., "Performance Characteristics of Hemispherical Target-Type Thrust Reversers", NACA Report RM E55E18, September 27, 1955.
7. Povolny, John H., Steffen, Fred W., and McArdle, Jack G., "Summary of Scale Model Thrust-Reverser Investigation", NACA Report 1314, 1957.

Symbol Key

A	Area
a	Speed of Sound
Cd	Flow Coefficient
C_{ej}	$\frac{C_{fg}}{.98}$ or $\frac{C_F}{.98}$
C_F	$\frac{\text{Gross Thrust Minus External Nozzle Drag}}{\text{Ideal Primary Thrust (Isentropic)}}$
C_{Fg}	$\frac{\text{Nozzle Gross Thrust}}{\text{Ideal Primary Thrust (Isentropic)}}$
$C_{fg, eq.}$	$\frac{\text{Gross Thrust Minus Secondary Ram Drag}}{\text{Ideal Primary Thrust (Isentropic)}}$
C_p	Specific Heat at Constant Pressure
C_v	$\frac{\text{Nozzle Gross Thrust}}{\text{Ideal Primary Thrust (Isentropic)}}$
C_{vel}	Velocity Coefficient
F	Thrust
F_g	Gross Thrust
$\frac{F_{ej}}{F_{ip}}$	$\frac{\text{Gross Thrust of Primary and Secondary}}{\text{Ideal Primary Thrust}}$
$\frac{F_g}{F_p}$	$\frac{\text{Gross Thrust of Nozzle}}{\text{Actual Convergent Nozzle Thrust of the Primary}}$
g	Acceleration of Gravity
h	Enthalpy
j	Mechanical Equivalent of Heat (778 Ft-Lb/BTU)
m	Mass
M	Mach No.

Symbol Key

P	Pressure
Q	Heat Energy
R	Universal Gas Constant
s	Enthropy
SFC	Specific Fuel Consumption
T	Temperature
V	Velocity
v	Specific Volume
W, W _a	Weight Flow
W _{comp}	Work Done by the Compressor
W _{turb}	Work Done by the Turbine
α	Flow Divergence Angle
ρ	Density
θ_T	Temperature Ratio $\frac{T_T}{T \text{ Std. Day}}$
δ_T	Pressure Ratio $P_T/P \text{ Std. Day}$
\emptyset	Exit Momentum
γ	Ratio of Specific Heats

Subscripts

T,o	Stagnation Conditions
exit, 8,e	Exit Conditions
amb,	Free stream conditions
j	Jet conditions
i	Ideal conditions
t	Throat Conditions
s	Secondary
p	Primary
i	Ideal Conditions

Superscripts

*	Nozzle Throat Conditions
---	--------------------------

References

Source: Ames Aeronautical Laboratory, Moffett Field, California

1. Havill, C. Dewey and Wingrove, Rodney C., Flight Investigations of a Full-Scale Aircraft Ejector With Various Spacing Ratios and Correlation With Small-Scale Tests (U), NACA RM A58 D21, August 26, 1958

References

Source: Arnold Engineering Development Center.

1. Warwick, William R. and Smith, Robert E., Performance and Leakage Investigation of the J93-GE-3 Ejector Nozzle (U), AD 317 944-L, July 1960
2. Piasecki, R. F., An Investigation of Supersonic Turbojet Propulsion Nozzles in The Transonic Range (U), AD 307 326-L, May 1959
3. Jones, J. H., Thrust Characteristics of Several Variable Geometry Exit Nozzles, (U), AD 316 466-L, April 1960

References

Source: General Electric Company, Cincinnati, Ohio

1. Kutney, John T., Propulsion System Development for V/STOL Transports. AIAA, Paper No. 64-606, 1964
2. Alford, J. S. and Taylor, R. P., Aerodynamic Stability Considerations of High Pressure Ratio, Variable Geometry Jet Nozzles, AIAA Paper No. 64-247, 1964
3. Flight Propulsion Division, Large Jet Engine Department, Exhaust Nozzle Selections, (U), MF295A Advanced Turbofan, August 18, 1961
4. Armer, R. C., Subsonic Cruise Performance Evaluation of a Three Finger Nozzle Compared to the J79-2 Ejector Nozzle (U), R61 FPD 48 March 15, 1961

References

Source: Langley Research Center, Langley Station, Hampton, Virginia

1. Schmeer, James W., Berrier, Bobby L. and Lauer, Rodney F. Jr., Performance of Blow-In-Door Ejector Nozzles Installed on A Twin-Jet Variable-Wing-Sweep Fighter Airplane Model, NASA TM X-1383, June 1967
2. Re, Richard J., Runckel, Jack F. and Wilmoth, Richard G., Investigation of Effects of Afterbody Closure and Jet Interference on the Drag of a Twin-Engine Tactical Fighter, NASA TM X-1382, June 1967
3. NASA Conference on Aircraft Aerodynamics, May 23-25, 1966, SP-124
4. Runckel, Jack F.; Jet-Exit and Airframe Interference Studies on Twin-Engine-Fuselage Aircraft Installations; Langley Research Center, Langley Station, Hampton, Va.; NASA TM X-1274
5. Kirkham, Frank S., Lauer, Rodney P. Jr. and Lee, Edwin E. Jr., Afterbody Drag of Several Clustered Jet Configurations at Transonic Speeds, NASA TM X-1216, March 1966
6. Mercer, Charles E. and Schmeer, James W., Transonic Performance of Ejector Nozzles Having Zero Boattail Angle and an Internal Base (U), NASA TM X-1104, June 1965
7. Norton, Harry T., Jr. and Pendergraft, Odis C. Jr., Transonic Performance of a Convergent-Divergent Ejector Nozzle Designed for a Corrected Secondary-Weight-Flow Ratio of 0.07 (U), NASA TM X-974, June 1964
8. Schmeer, James W., Kirkham, Frank S. and Salters, Leland B. Jr., Performance Characteristics of a 10° Conical Plug Nozzle at Mach Numbers Up to 1.29 (U), NASA TM X-913, March 1964
9. Norton, Harry T. Jr., Runckel, Jack F. and Pendergraft, Odis C. Jr., Transonic Performance of Two Convergent-Divergent Ejector Nozzles Designed for Corrected Secondary Flows of 3 and 9.4 Percent, NASA TM X-909, February 1964
10. Proceedings of NASA Conference on Supersonic-Transport Feasibility Studies and Supporting Research (U), NASA TM X-905, September 17-19, 1963
11. Schmeer, James W.; Mercer, Charles E. and Kirkham, Frank S.; Effect of Bypass Air on the Performance of a Blow-In-Door Ejector Nozzle at Transonic Speeds; Langley Research Center, Langley Station, Hampton, Va., NASA TM X-896.

12. McEwan, Frank S. and Schaefer, James W. Performance Characteristics at High Numbers Up to 1.2 of a Blow-In-Door Ejector Nozzle with Doors Fixed in Full-Open Position; Langley Research Center, Langley Station, Hampton, Va., NACA TM X-830.
13. Mercer, Charles E. and Salters, Leland B. Jr., Performance of a Plug Nozzle Having a Concave Central Base With and Without Terminal Fairings at Transonic Speeds, NASA TN D-1604, May 1953
14. Stocomb, Travis, H. Jr. and Andrews, Earl H. Jr., The Effect on Thrust Minus Base Drag of Exchanging Base Area for Nozzle Expansion in Supersonic Nozzles at Transonic Mach Numbers, NASA TN D-754, April 1961
15. Corson, Blake W., Jr. and Mercer, Charles E., Static Thrust of an Annular Nozzle With a Concave Central Base, NASA TN D-418, Sept. 1960
16. Flange, Ralph A. and Judd, Joseph H., Low-Lift Flight Tests of Four-Engine Delta-Wing Configurations to Obtain Wing Pressure and Aerodynamic Coefficients Including Some Jet Effects from Mach Number 0.5 to 1.5 (U), NASA TM X-292, May 1960
17. Horton, Harry T. Jr., Cassett, Marlowe D. and Mercer, Charles E., Transonic Off-Design Performance of a Fixed Divergent Ejector Design for a Mach Number of 2.0 (U), NASA TM X-165, December 1959
18. Cabbage, James M., Jr., Effect of Multiple-Jet Exit on the Base Pressure of a Simple Wing-Body Combination at Mach Number of 0.6 to 1.27, NASA TM X-25, August 1959
19. Lee, Edwin E. Jr., Salters, Leland B. Jr., Effects of Afterbody Shape and Hot Jet Exhaust on Pressures, Temperatures, and Drag of Twin-Engine Fighter Airplane Model Having an Overhanging Fuselage (U), NASA MEMO 12-29-58L, January 1959
20. Cabbage, James M. Jr., Effect of Convergent Ejector Nozzles on the Boattail Drag of a 16' Conical Afterbody at Mach Numbers of 0.6 to 1.26(U) NACA RM L58 G25, September 17, 1958
21. Nelson, William J., Scott, William R., Jet Effects on the base Drag of a Cylindrical Afterbody with Extended Nozzles (U) NACA RM L58A27, April 15, 1958
22. Norton, Harry T. Jr., Swihart, John M. Effect of a Hot-Jet Exhaust on Pressure Distribution and External Drag of Several Afterbodies on A Single-Engine Airplane Model at Transonic Speeds (U), NACA RM L57 J04 March 4, 1958
23. Stoney, William E. Jr., Collection of Zero-Lift Drag Data on Bodies of Revolution from Free-Flight Investigations, NACA TN 4201, January 1958

24. Hunkel, Jack F. and Delhart, John W., A Hydrogen Peroxide Turbojet Engine Simulator for Wind-Tunnel Powered Model Investigations (U), NACA RM L57 H15, November 4, 1957
25. Cabbage, James M. Jr., Jet Effects on the Drag of Conical Afterbodies for Mach Numbers of 0.6 to 1.28, NACA RM L57E21, April 12, 1957
26. Mitcham, Grady I., A Summary of the Longitudinal and Lateral Stability and Control Characteristics Obtained from Rocket-Model Test of Swept-Wing Fighter-Type Aircraft at Mach Numbers from 0.5 to 1.9 (U), NACA RM L56 K19, February 27, 1957
27. Silhan, Frank V. and Cabbage, James M. Jr., Drag of Conical and Circular-Arc Boattail Afterbodies at Mach Numbers from 0.6 to 1.3 (U), NACA RM L56K22, January 22, 1957
28. Henry, Beverly Z. Jr. and Chan, Maurice S., Additional Results of an Investigation at Transonic Speeds to Determine the Effects of a Heated Propulsive Jet on the Drag Characteristics of a Series of Related Afterbodies (U), NACA RM L56G12, September 24, 1956
29. Cornette, Eldew S. and Ward, Donald H. Transonic Wind-Tunnel Investigation of the Effects of a Heated Propulsive Jet on the Pressure Distribution Along A Fuselage Overhang (U), NACA RM L56A27, April 4, 1956
30. Cabbage, James M. Jr. Jet Effects on Base and Afterbody Pressures of a Cylindrical Afterbody at Transonic Speeds (U), NACA RM L56 G21, March 6, 1956
31. Love, Eugene S. and Grigsby, Carl E., Some Studies of Axisymmetric Free Jets Exhausting from Sonic and Supersonic Nozzles Into Still Air and Into Supersonic Streams, NACA L54L31, May 10, 1955
32. O'Donnel, Robert M. and McDearmon, Russell W., Experimental Investigation of Effects of Primary Jet Flow and Secondary Flow Through A Zero-Length Ejector on Base and Boattail Pressures of a Body of Revolution at Free Stream Mach Numbers of 1.62, 1.93 and 2.41, NACA RM L54I22, December 6, 1954

References

Source: Lewis Research Center, Cleveland, Ohio

1. Mihalocw, James R., Internal Performance Evaluation of Two Fixed Divergent Shroud Ejectors, NASA TN D-763, January 1961
2. Stofan, Andrew J. and Mihalocw, James R., Performance of a Variable Divergent Shroud Ejector Nozzle Designed for Flight Mach Numbers Up to 30, NASA TM X-255, January 1961
3. Stofan, Andrew J., Effects of Nozzle-Shroud Misalignment on Performance of a Fixed Shroud Divergent Ejector (U), NASA TN X-97, March 1960
4. Mucial, Norman T.; Ward, James J.; Over-Expanded Performance of Conical Nozzles with Area Ratios of 6 and 9 With and Without Supersonic External Flow; Lewis Research Center, Cleveland, Ohio, NASA TM X-83, September 1959
5. Grey, R. E., and Wilsted H. D.; Performance of Conical Jet Nozzles in Terms of Flow and Velocity Coefficients; Lewis Flight Propulsion Laboratory, Cleveland, Ohio; NACA TN No. 1757, November 1948
6. Klann, John L. and Huff, Ronald G., Characteristics of Five Ejector Configurations at Free Stream Mach Numbers from 0 to 2.0, NASA TM X-23, August 1959
7. Valerino, Alfred S., Zappa, Robert F., Abdalla, Kaseel L., Effects of External Stream on the Performance of Isentropic Plug-Type Nozzles at Mach Numbers of 2.0, 1.8 and 1.5 (U), NASA MEMO 2-17-59E, March 1959
8. Behnke, Milton A., Off-Design Performance of Divergent Ejectors, NACA RM E56H10a, September 30, 1958
9. Trout, Arthur M., Papell, S. Stephen and Povolny, John H., Internal Performance of Several Divergent Shroud Ejector Nozzles with High Divergence Angles, NACA RM E57F13, October 2, 1957.
10. Baughman, L. Eugene and Kochendorfer, Fred D., Jet Effects on Base Pressure of Conical Afterbodies at Mach 1.91 and 3.12, NACA RM E57E06, August 12, 1957
11. Beale, William T. and Povolny, John H., Internal Performance of Two-Dimensional Wedge Exhaust Nozzles (U), NACA RM E56K29b, February 28, 1957
12. Salari, Reino J., Preliminary Investigation of Methods to Increase Base Pressure of Plug Nozzles at Mach 0.9 (U), NACA RM E56J05, Dec. 19, 1956

13. Salmi, R. J., Courtright, E. M. Jr., Effects on External Stream Flow and Afterbody Variations on the Performance of a Plug Nozzle at High Subsonic Speeds (U), NACA E56 F11a, October 2, 1956
14. Krull, H. George and Beale, William T., Internal Performance Characteristics of Short Convergent-Divergent Exhaust Nozzles Designed by Method of Characteristics (U), NACA RM E56D 27A, July 24, 1956
15. Valerino, Alfred S. and Yeager, Richard A., External Stream Effects on Gross Thrust and Pumping Characteristics of Ejectors Operating at Off-Design Mach Numbers, NACA RM E56 C14, June 26, 1956
16. Greathouse, William K. and Beale, William T., Performance Characteristics of Several Divergent Shroud Aircraft Ejectors, NACA RM E56G21a, Sept. 8, 1956
17. Salmi, Reino J. and Klann, John L., Investigation of Boattail and Base Pressures of Twin-Jet Afterbodies at Mach Number 1.91 (U), NACA E55C01, April 21, 1955
18. Effect of Free-Stream Mach Number on Gross-Force and Pumping Characteristics of Several Ejectors (U), NACA RM E54E23a, March 15, 1955
19. Steffen, Fred W.; Krull, H. George; and Schmiedlin, Ralph F.; Effects of Sever Geometric Variables on Internal Performance of Short Convergent-Divergent Exhaust Nozzles; Lewis Flight Laboratory, Cleveland, Ohio; NACA RM E54E09
20. Steffen, Fred W., Krull, H. George and Schmiedlin, Ralph F., Effect of Divergent Angle on the Internal Performance Characteristics of Several Conical Nozzles (U), NACA RM E54E25, November 29, 1954
21. Salmi, Reino J., Experimental Investigation of Drag of Afterbodies With Existing Jet at High Subsonic Mach Numbers, NACA RM E54I13, Nov. 29, 1954
22. Hearsh, Donald P. and Valerino, Alfred S., Thrust and Pumping Characteristics of a Series of Ejector-Type Exhaust Nozzle at Subsonic and Supersonic Flight Speeds (U), NACA RM E54H19, November 17, 1954
23. Krull, H. George and Beale, William T., Effects of Plug Design on Performance Characteristics of Convergent-Plug Exhaust Nozzles (U), NACA RM E54H05
24. Ciepluch, C. C. and Ferni, D. B. Experimental Data for Four Full-Scale Conical Cooling-Air Ejectors (U), NACA RM E54F02, November 1, 1954
25. Allen, John, Pumping Characteristics for Several Simulated Variable Geometry Ejectors with Hot and Cold Primary Flow (U), NACA RM E54G15, September 8, 1954
26. Kochendorfer, Fred D., Note on Performance of Aircraft Ejector Nozzles at High Secondary Flows (U), NACA RM E54F17a, August 24, 1954

27. International, William A., Performance Characteristics of Several Full-Scale Cooling-Air Ejector Configurations Over a Range of Primary Gas Temperatures (U), NACA RM E54D07, August 19, 1954
28. Gorton, Gerald G., Pumping and Drag Characteristics of an Aircraft Ejector at Subsonic and Supersonic Speeds (U), NACA RM E54D06, June 5, 1954
29. Greathouse, W. K., Preliminary Investigation of Pumping and Thrust Characteristics of Full-Size Cooling Air Ejectors at Several Exhaust-Gas Temperatures, NACA RM E54A18, April 9, 1954
30. Pennington, Donald P. and Simon, Paul C., Internal Performance at Mach Numbers to 2.0 of Two Auxiliary Inlets Immersed in Fuselage Boundary Layer (U), NACA RM E53L28b, March 10, 1954
31. Frojenbaugh, Evan A., Gorton, Gerald C. and Beke, Andrew, Thrust Characteristics of a Series of Convergent-Divergent Exhaust Nozzles, at Subsonic and Supersonic Flight Speeds (U), NACA RM E53L23, March 12, 1954
32. Hearsh, Donald P. and Norton, Gerald C., Investigation of Thrust and Drag Characteristics of a Plug-Type Exhaust Nozzle (U), NACA RM E53L16, February 19, 1954
33. Huntley, S. C. and Yanowitz, Herbert, Pumping and Thrust Characteristics of Several Different Cooling Air Ejectors and Comparison of Performance With Conical and Cylindrical Ejectors (U), NACA RM E53J13, January 20, 1954
34. Greathouse, W. K. and Hollister, D. P., Air-Flow and Thrust Characteristics of Several Cylindrical Cooling-Air Ejectors with a Primary to Secondary Temperature Ratio of 1.0 (U), NACA RM E52L24, March 6, 1953
35. Jack, John R., Theoretical Pressure Distributions and Wave Drag For Conical Boattail, NACA TN 2972, July 1953
36. Krull, H. George, Steffen, Fred W., Performance Characteristics of One Convergent and Three Convergent-Divergent Nozzles, NACA RM E52H12, September 29, 1952
37. Hollister, D. P. and Greathouse, W. K., Preliminary Air-Flow and Thrust Calculations of Several Conical Cooling Air Ejectors with a Primary to Secondary Temperature Ratio of 1.0, II - Diameter Ratios of 1.05 and 1.40 (U), NACA RM E52F26, August 12, 1952
38. Wallner, Lewis E. and Janson, Emmert T., Full-Scale Investigation of Cooling Shroud and Ejector Nozzle for a Turbojet Engine-Afterburner Installation (U), NACA RM E51J04, December 17, 1951
39. Wallner, Lewis E. and Wintler, John T., Experimental Investigation of Typical Constant and Variable-Area Exhaust Nozzles and Effects on Axial-Flow Turbojet-Engine Performance (U), NACA RM E51D19, July 9, 1951

40. Kochendorfer, Fred D. and Rousse, Morris D., Performance Characteristics of Aircraft Cooling Ejectors Having Short Cylindrical Shrouds, NACA RM E51E01, May 22, 1951
41. Grey, R. E. and Wilsted, H. D., Performance of Conical Jet Nozzles In Terms of Flow and Velocity Coefficients, NACA TN No. 1757, November 1948

References

Source: North American Rockwell Corporation

1. Nixon, J. A., Wind Tunnel Testing Techniques for Integrated Airframe-Exhaust Nozzle Systems, Second R&D Interim Technical (Quarterly) Report, Los Angeles Division, NA57-1448-7, October 2, 1967
2. A Proposal for a Study of Wind Tunnel Testing Techniques for Integrated Airframe-Exhaust Nozzle Systems, Los Angeles Division NA-66-1317, December 12, 1966
3. Mount, Joe, Material for Pratt & Whitney Exhaust Nozzles Studies, Los Angeles Division, TFD-65-722, October 15, 1965
4. Hope, Jack I., Barto, Roger and Rundell, Dan J., Variable Cycle Engines for Application to Multi-Mission Aircraft, Los Angeles Division, NA-65-560, 1965
5. Hessman, F. W., Drag Analysis for Boattailed Afterbodies in the Mach Number Range 0.6 to 2.5 With Emphasis Placed on Boundary Layer Separation(U), Columbus Division, NA64H-801, March 3, 1965
6. Hessman, F. W., Method for Predicting the Occurrence and Extent of Boundary Layer Separation Induced by a Jet Exhaust Plume (Supersonic Flow), Columbus Division, NA63H-1071, January 22, 1964
7. Hessman, F. W., Nozzle-Afterbody Interactions and Associated Flow Phenomena, Columbus Division, FSTN 6303, May 28, 1963
8. Mykityn, E., Static Test of Ejectors With Circular, Square, Circular-To-Square and Axisymmetric Mixing Sections, Los Angeles Division, NA-62-681, 1962
9. By Aero Lab, Test of 0.222 Scale A3J-1 Conical-Divergent Shroud Engine Ejector Nozzles in Quiescent Air to Determine the Effects of Changes in Nozzle Geometry on Nozzle Thrust (U), NA61H-28, January 17, 1961, Columbus Division
10. By Thermo Lab, A3J-1 Divergent-Shroud Ejector Nozzle Pretest Report, NA60H-678, November 17, 1959, Columbus Division
11. Kemp, R. H., Multi-Jet Effects on Afterbody and Base Pressures at Supersonic Speeds (U), Los Angeles Division, NA58-1040, September 1958
12. Engine Exhaust Nozzle Flow Interference Study (U), Space and Information Division, Prepared by Thermodynamics Engineering Department, Contract No. AF33(600)-36040

References

Source: Pratt & Whitney, East Hartford, Conn.

1. Exploratory Research Program for Turbo-Propulsion Exhaust Systems (U), Quarterly Progress Report, FWA-3000, April 28, 1967
2. Exploratory Research Program for Turbo-Propulsion Exhaust Systems (U), Quarterly Progress Report, FWA 3029, January 31, 1967
3. Exploratory Research Program for Turbo-Propulsion Exhaust Systems (U), Phase I Final Report, FWA-2303, July 31, 1966
4. Two Flow Ejector Pumping Characteristics Parametric Curves, January 1966
5. External Pressure Drag Coefficients for Axisymmetric Conical Surfaces, October 1965
6. Target Performance Goals for Turbo-Propulsion Exhaust Nozzles, Oct. 1965
7. Bernstein, Arthur; Heiser, William and Hovenor, Charles, Compound-Compressible Nozzle Flow (Abstract)
8. Morgan, J. J., An Aerodynamically Actuated Exhaust System for Supersonic Transport Aircraft (U), PWA Inst. 581, December 3, 1964
9. Inlet and Exhaust Nozzle Work at Pratt & Whitney Aircraft (U), TBM-1767, March 20, 1962
10. JT11 Turbojet Engine Exhaust Systems, PWA FR-265, October 11, 1961
11. Morgan, J. J., Installed Performance of PWA Exhaust Nozzles (U), TBM-1600, August 26, 1960
12. Migdal, D. and Valenti, J., Use of Secondary Flow for Ejector Nozzles (U), TBM-1606, July 1960
13. Hoff, R. H., Fixed Exhaust Nozzle Ejectors for Application to the JT4A-24 and JT4B-21 and Advanced JT4 Powerplants (U), PWA INST. MR. 175, May 3 1961
14. JT11 Turbojet Engine Exhaust Systems; Pratt & Whitney Aircraft, Division of United Aircraft Corporation; PWA FR-265, 10 October 1961

References

Source: United Aircraft Corporation, East Hartford, Conn.

1. Kraig, A. H., Motycka, D. L. and Stewart, D. J., Experimental Optimization of Subsonic Inlet Design Parameters, AIAA Paper No. 60-690
2. Jensen, R., Base Bleed Ejector Exhaust Nozzle Test In The 17-Inch Transonic Wind Tunnel, UAR-0713, September 2, 1960
3. Konarski, M., 17-Inch TWT Shakedown Test of the 4.0 Inch Diameter Modified Exhaust Balance, UAR-0712, August 25, 1960
4. Rustemeyer, A. H. and Twomey, E. J., Thrust and Drag Characteristics of Several Turbojet Exhaust Models at Supersonic and High-Subsonic Mach Numbers, R-0922-16, June 1957
5. Grossen, J. W., Studies of Boundary Layer Removal Sloops for High-Performance Supersonic Inlets (U), R-0955-21, October 1957
6. Pol, C. and Rustemeyer, A., Investigation of Turbojet Exhaust Interference Drag, R-0601-12, November 1955

References

Source: U.S. Naval Air Turbine Test Station, Trenton, New Jersey

1. Bednaski, Joseph R., Evaluation of the Guaranteed Performance of the Pratt & Whitney Aircraft J60-P-3A Turbojet Engine, NATTS-ATL-106, January 1966
2. Brunda, Donald F., Evaluation and Comparison of the Advanced Aerodynamic Nozzles and Standard Ejector Nozzle (U), NATTS-ATL-57, October 1951

Supplemental References

1. Nichols, Mark R., Aerodynamics Of Airframe-Engine Integration Of Supersonic Aircraft, Langley Research Center, Langley Station, Hampton, Virginia, NASA TN D-3390, August 1966
2. Korst, Helmut H., Addy, Alva L. and Chow, Wen L., Installed Performance Of Air-Augmented Nozzles Based On Analytical Determination Of Internal Ejector Characteristics, Journal of Aircraft, Vol. 3, No. 6, November - December 1966
3. Holdhusen, James S. and Lamb, Owen P., Scale Model Studies of Exhaust Nozzle Performance, AIAA Paper No. 66-641, 1966
4. Storkebaum, C., The Application Of An Ejector To VTOL Aircraft And Their Construction, (Translation), Foreign Technology Division, Air Force System Command, Wright Patterson Air Force Base, Ohio, FTD-TT-65-305, July 6, 1965
5. McDonald, H. and Hughes, P. F., Correlation of High Subsonic Afterbody Drag In The Presence Of A Propulsive Jet Or Support String, (British Aircraft Corp., Preston, Lancashire, England), Journal of Aircraft, Vol. 2, No. 3, May - June 1965
6. Mehus, T., An Experimental Investigation Into The Shape Of Thrust Augmenting Surfaces In Conjunction With Coanda-Deflected Jet Sheets (Part II) (U), U.S. Army TRECOM, UTIAS Technical Note No. 79, January 1965
7. Migdal, David and Morgan, John J., Thrust Nozzles For Supersonic Transport Aircraft, Journal of Engineering For Power, April 1964
8. Migdal, David and Morgan, John J., Thrust Nozzles For Supersonic Transport Aircraft, ASME Publications, American Society of Mechanical Engineers, 63-ANGT-73, January 22, 1963
9. Beheim, Milton A., Klann, John L. and Yeager, Richard A., Jet Effects On Annular Base Pressure and Temperature In A Supersonic Stream, Lewis Research Center, Cleveland, Ohio, NASA TR R-125, 1962
10. Beheim, Milton A., Flow In The Base Region Of Axisymmetric And Two Dimensional Configurations, Lewis Research Center, Cleveland, Ohio, NASA TR R-77, 1961
11. Creed, Richard L. and Wood, James W., F-106B Category II Performance, Stability and Control Tests (U), AD-317633, June 1960
12. Bottorff, Marion R., Wind Tunnel Tests At Mach Numbers From .82 to 2.05 Of A 4.2% Scale A3J-1 Base Drag Model Using Hydrogen-Air Combustors For Jet Simulation, University of Southern California Engineering Center, Aerodynamics Test Divisions, USCEC Report 65-7, November 2, 1959

13. Botterff, Marion R., Wind Tunnel Test At Mach Numbers From .9 To 2.05 Of A 4.2 Scale A3J-1 Base Drag Model Using Cold Air For Jet Simulation (U), University of Southern California Engineering Center, Aerodynamics Test Divisions, USCETC Report 65-5, January 29, 1959
14. Schweiger, M. and Olson, R., Determination Of The Thrust And Drag Characteristics Of Nozzle-Afterbody Combinations By Unique Force Balance Techniques (U), United Aircraft Corporation, Research Department, East Hartford, Conn., M-2000-69, October 8, 1958
15. Rowe, P. N., Tables Of Thrust Functions For The Design Of Supersonic Nozzles, Imperial College Report JRL No. 35, January 1958
16. Co. Wright, Edgar M., Jr., Some Aerodynamics Considerations Of Nozzle-Afterbody Combinations, Aeronautical Engineering Review, September 1956, (Presented As IAS Paper, January 23 - 26, 1956, Preprint No. 614)
17. Baker, Von D.; Johnson, Richard A.; Allison Division, General Motors Corporation, Indianapolis, Indiana and Braker, Richard G.; Lamb, Owen P.; Fluidyne Engineering Corporation, Minneapolis, Minnesota; AIAA Paper No. 65-374, 1965. (Presented At AIAA Propulsion Joint Specialist Conference, June 18-19, 1965).
18. Haldhusen, James S.; and Lamb, Owen P.; Scale Model Studies Of Exhaust Nozzle Performance, Fluidyne Engineering Corporation, Minneapolis, Minnesota, AIAA Paper No. 66-641, 1966
19. Frazier, G. T., Aerodynamic Considerations For Engine Exhaust Design For Subsonic High-Bypass Fan Engines. Presented At The Aerodynamic And Space Engineering And Manufacturing Meeting, Los Angeles, Calif. October 3 - 7, 1966

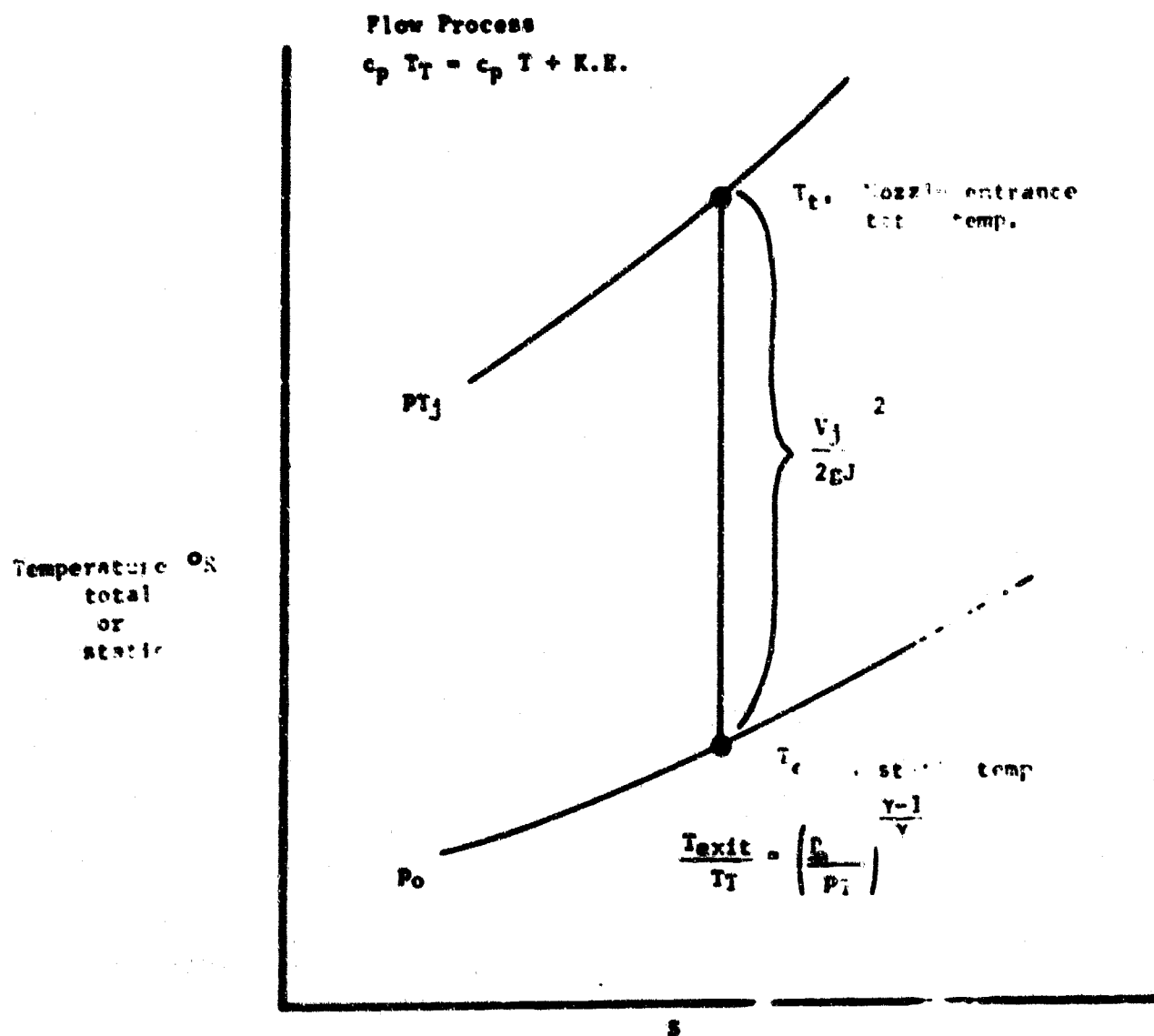


FIGURE 8-2 Isentropic Nozzle Expansion

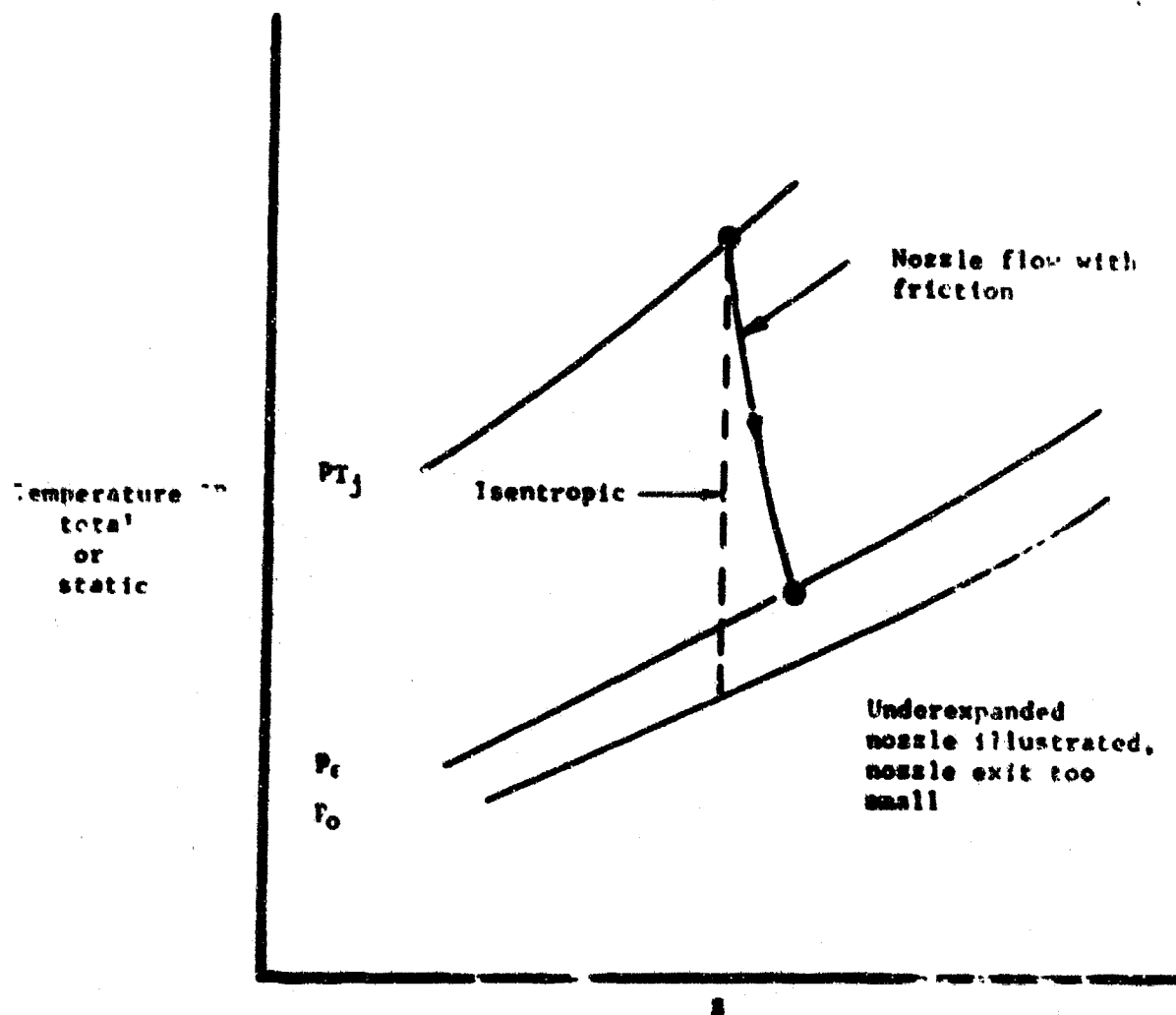


FIGURE 8-3. Real Nozzle Process

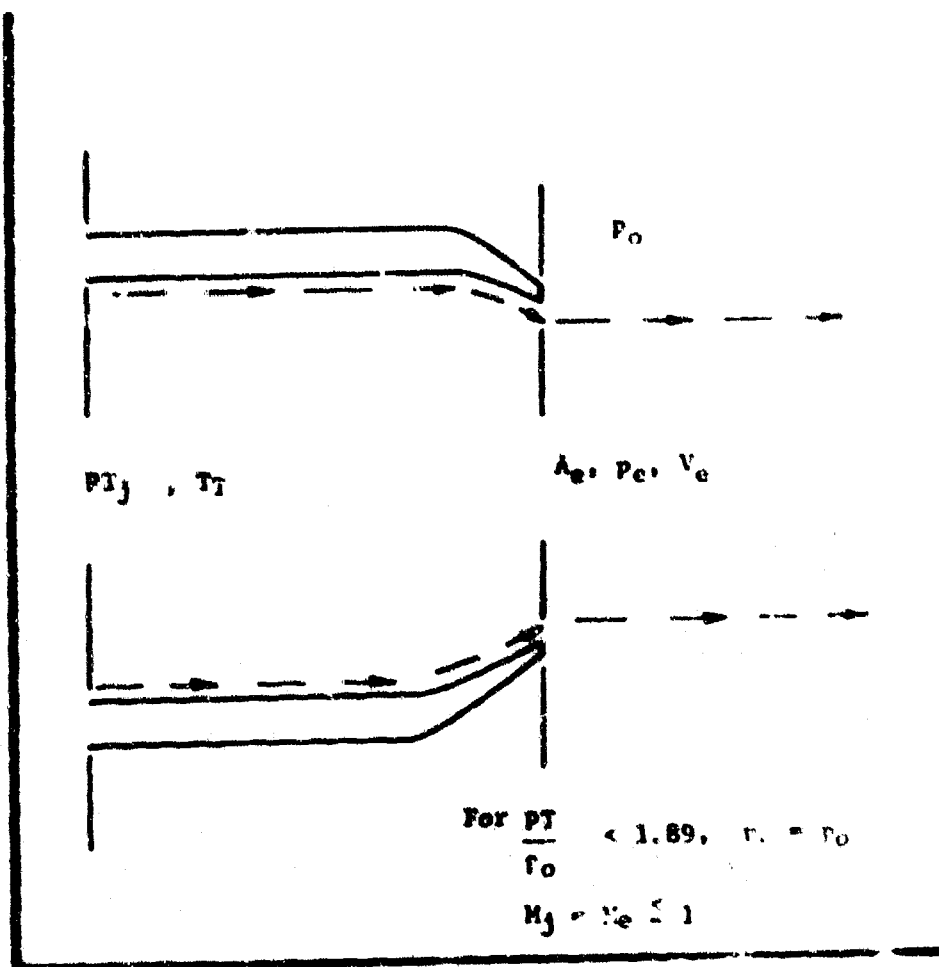


FIGURE 8-4 Unchoked Convergent Nozzle

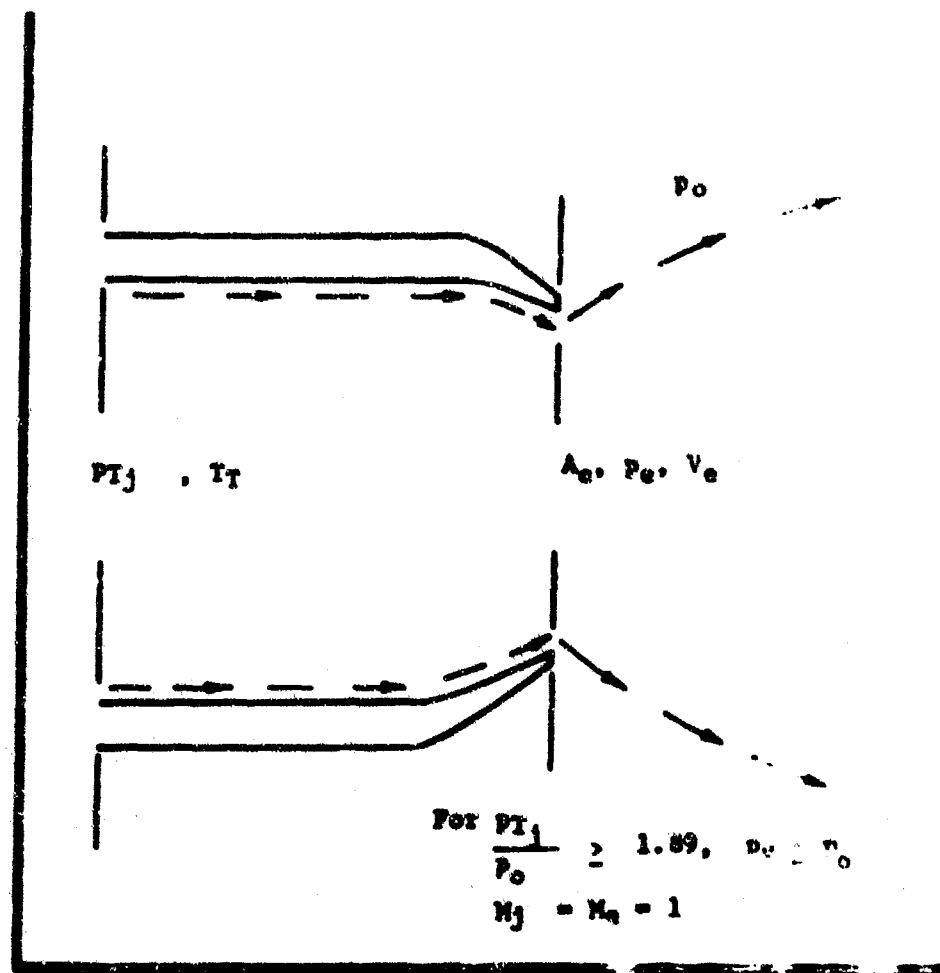


FIGURE 8-5 Choked Convergent Nozzle

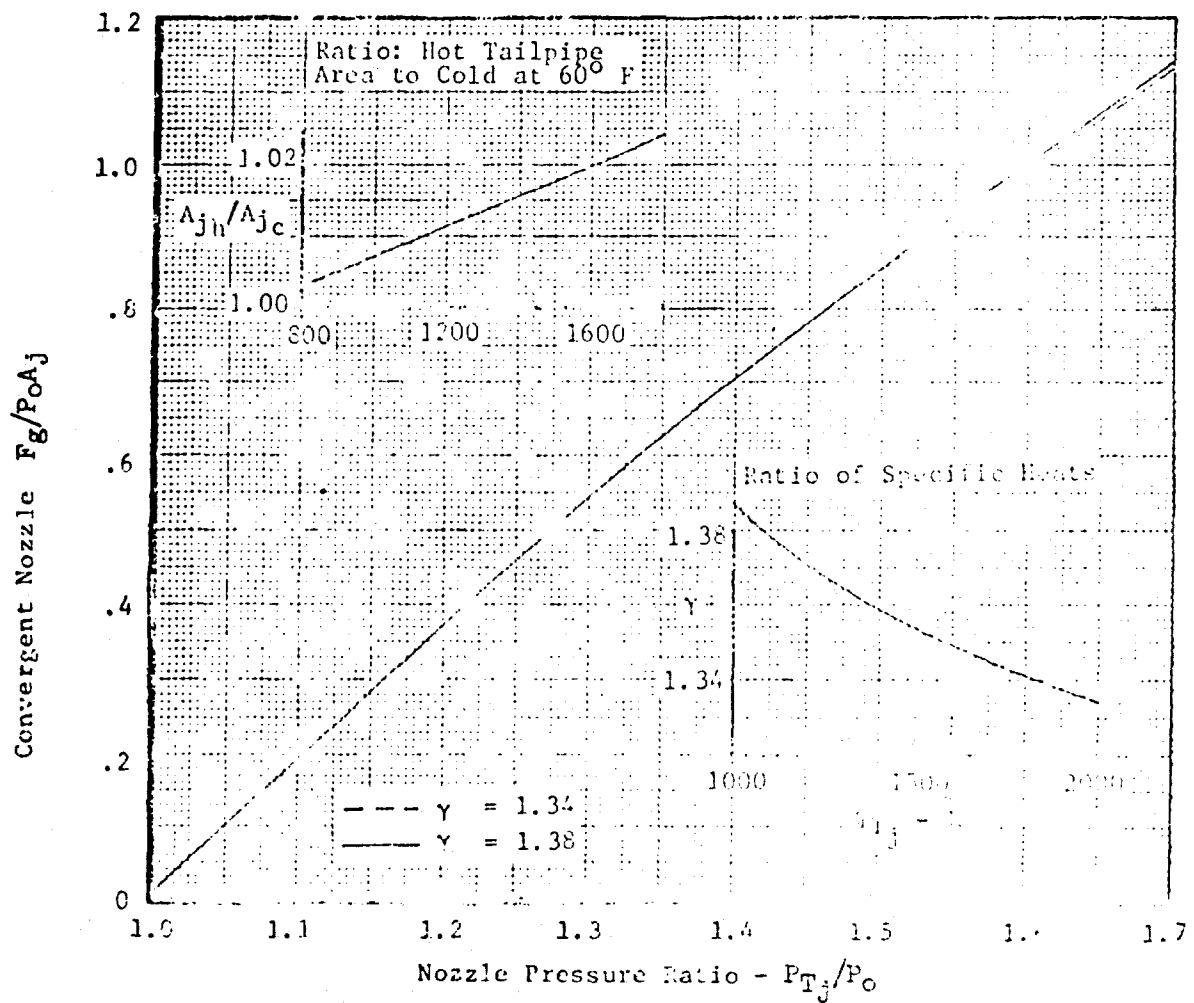


FIGURE 8-6. Theoretical Convergent Nozzle Cross Section Parameter

NOT REPRODUCIBLE

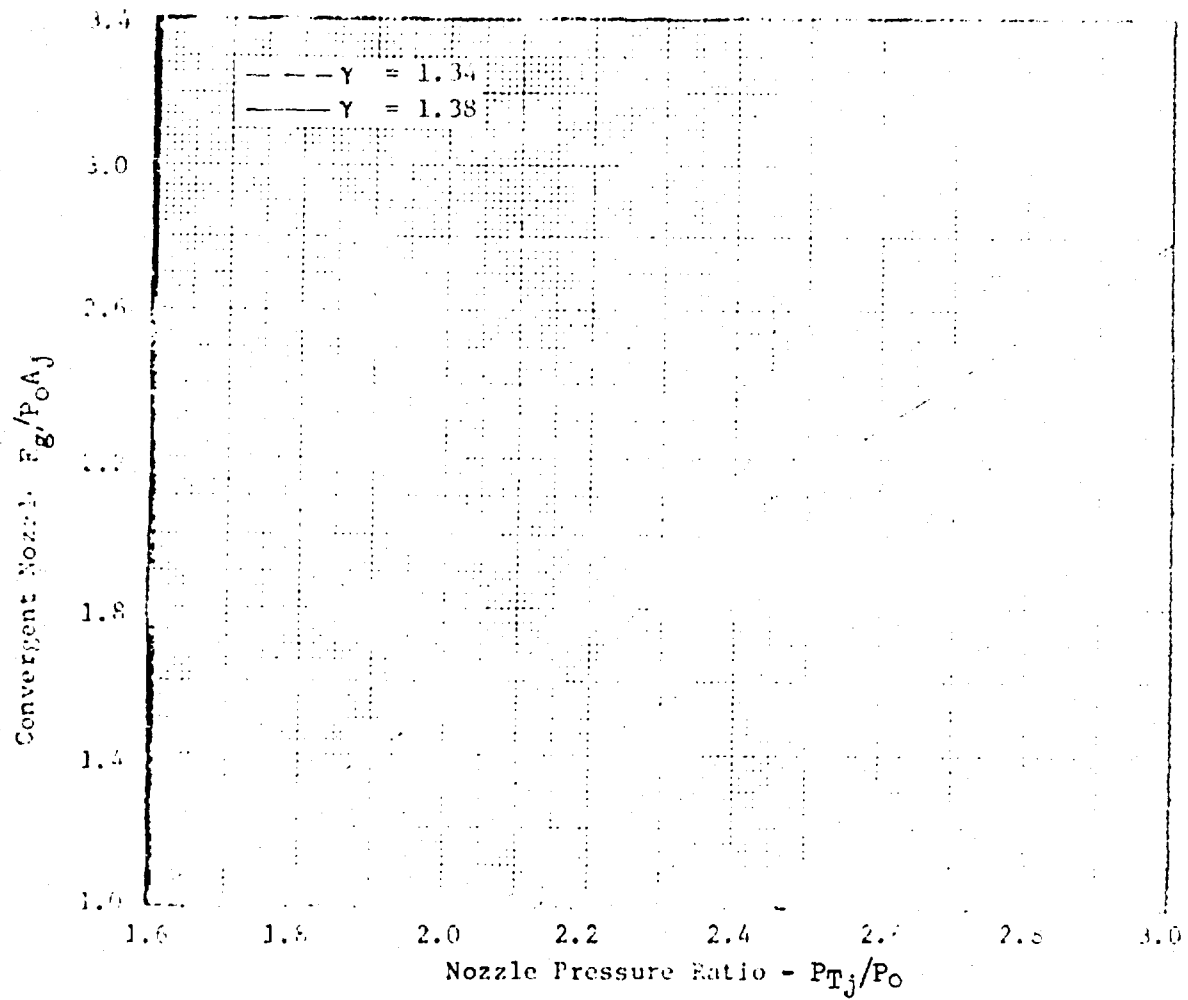


FIGURE 8-7. Theoretical Convergent Nozzle Gross Thrust Parameter

NOT REPRODUCIBLE

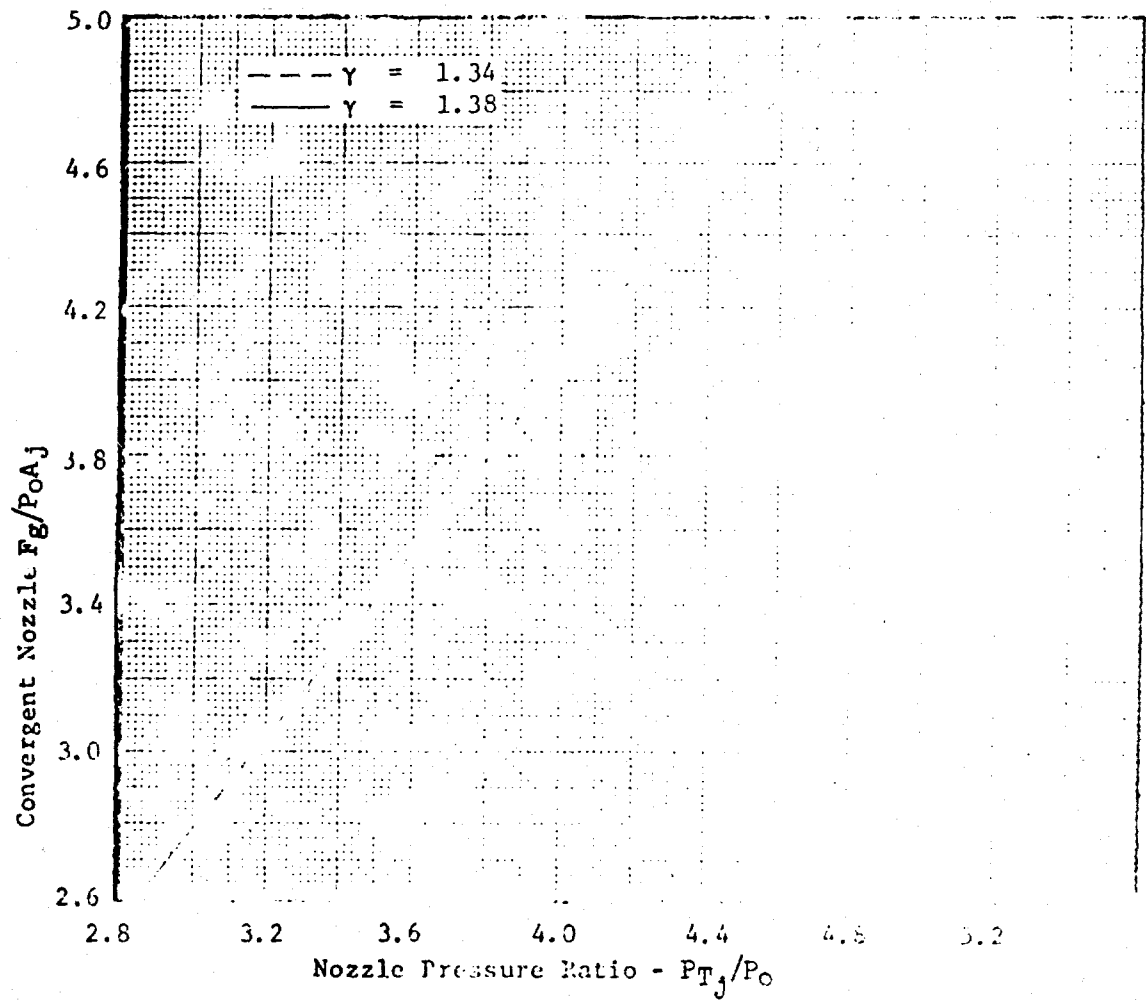


FIGURE 8-8. Theoretical Convergent Nozzle Gross Thrust Parameter

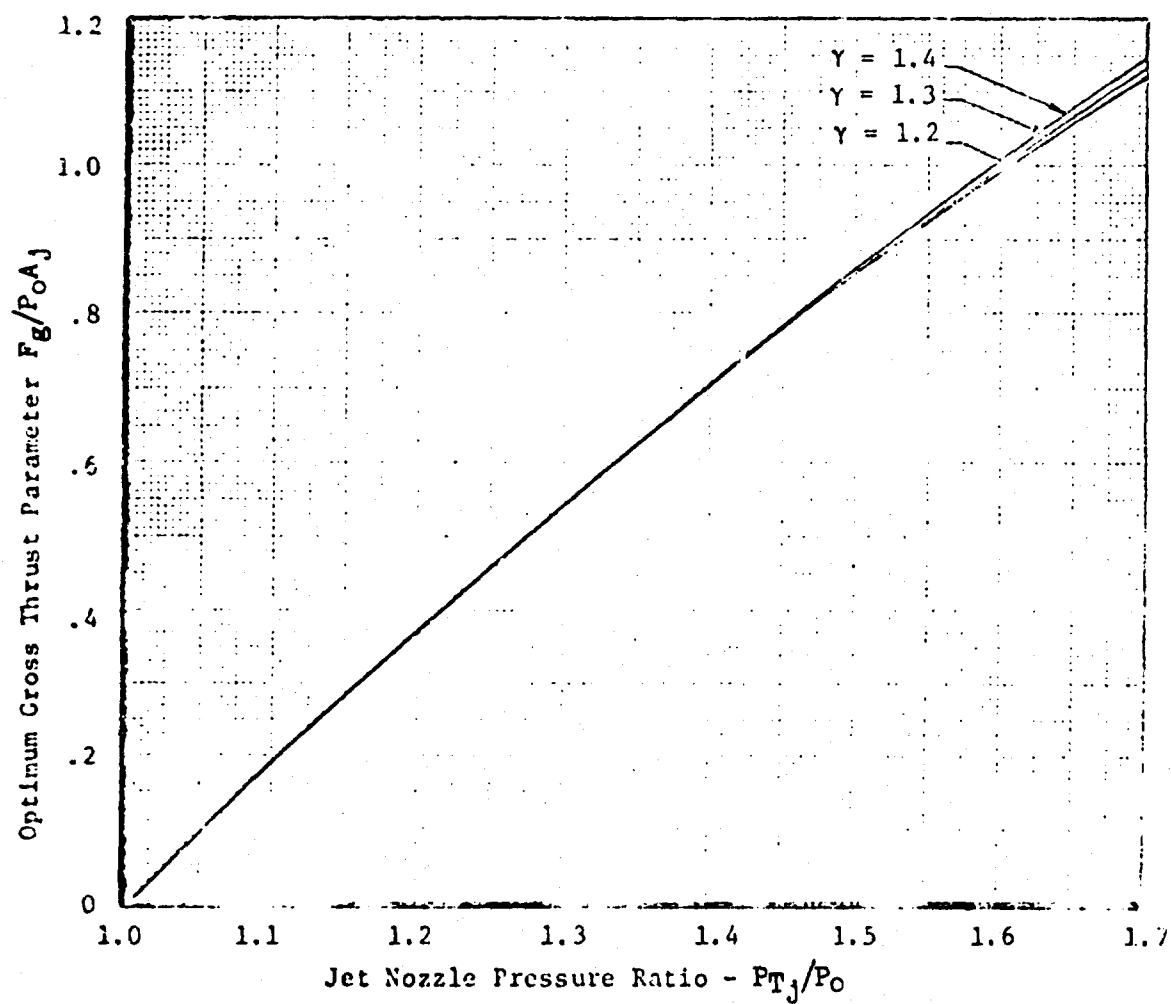


FIGURE 8-9. Optimum or Theoretical Maximum Gross Thrust Parameter

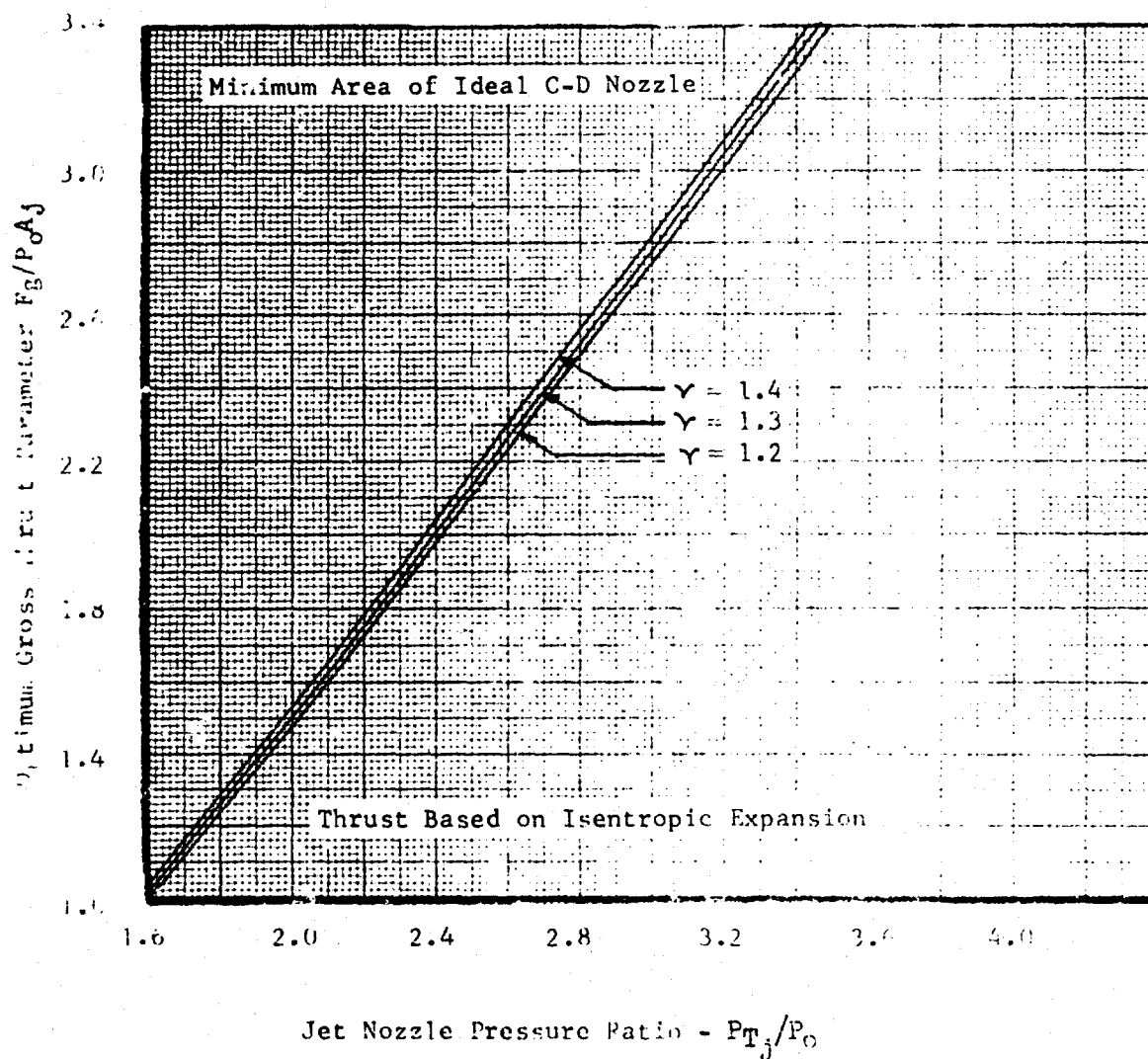


FIGURE 8-10. Optimum or Theoretical Maximum Gross Thrust Parameter

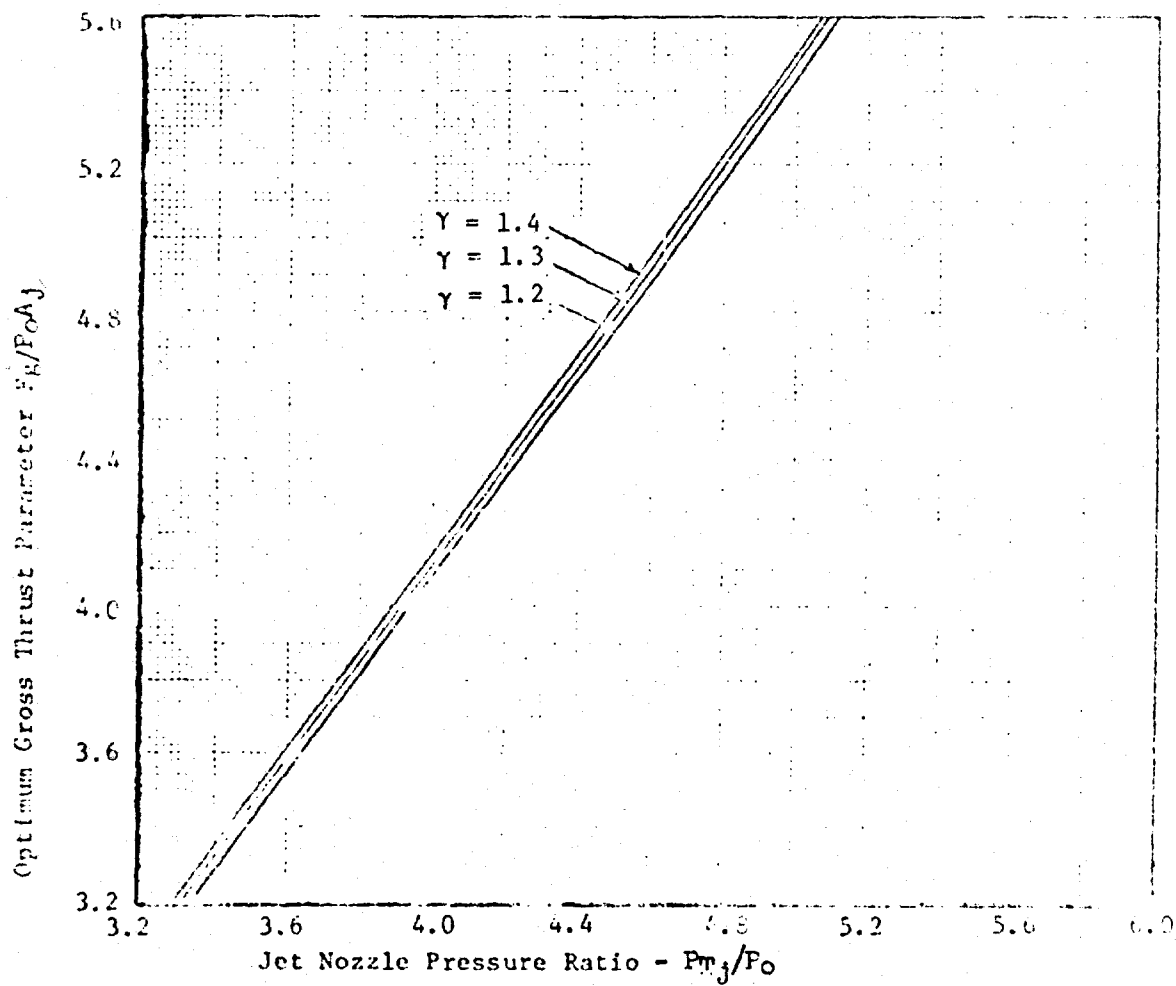


FIGURE 8-11. Optimum or Theoretical Maximum Gross Throat Parameter

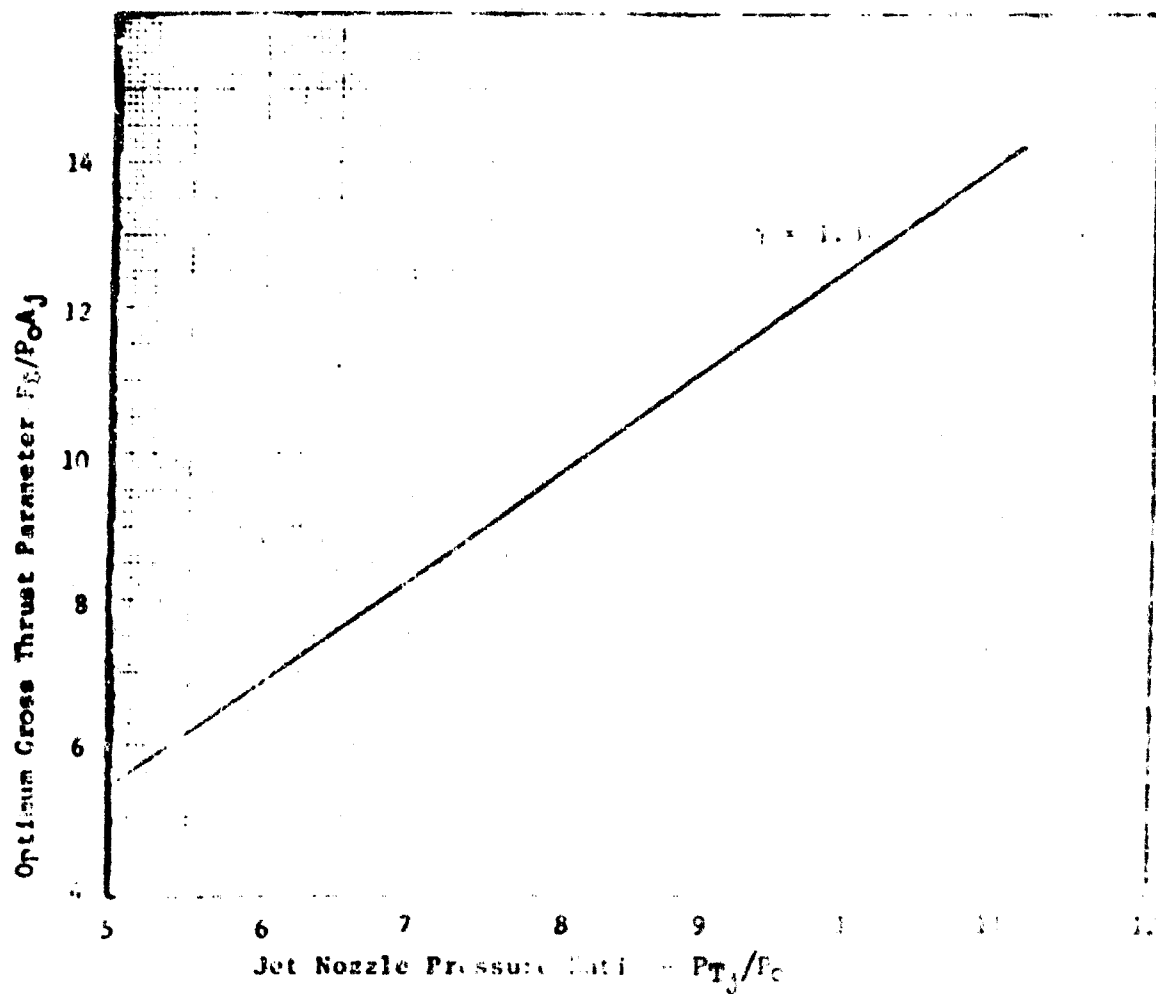


FIGURE 8-12 Optimum or The Critical Condition for $\gamma = 1.0$

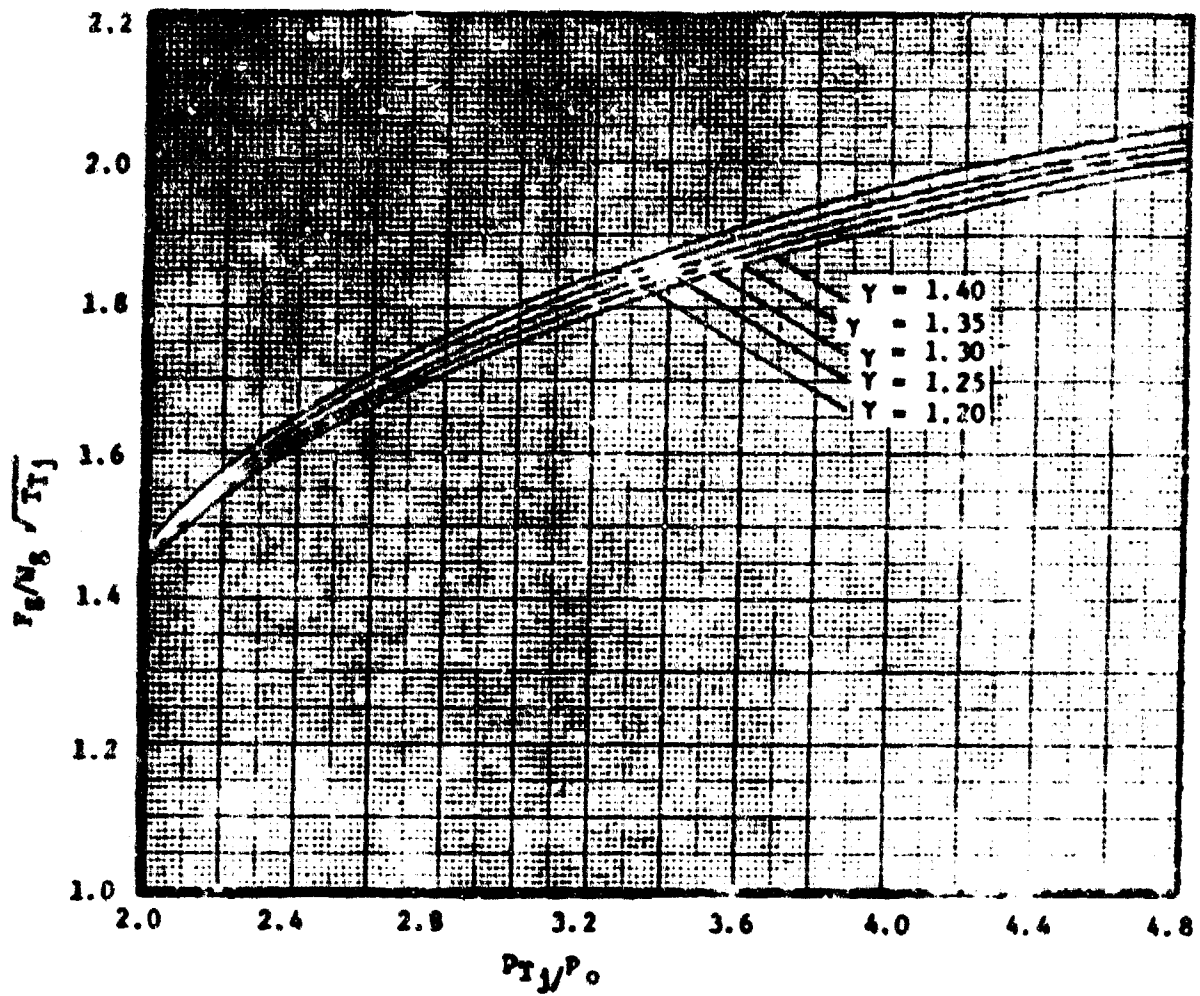


FIGURE 8-13 Converging Conical Nozzle, Gross Thrust

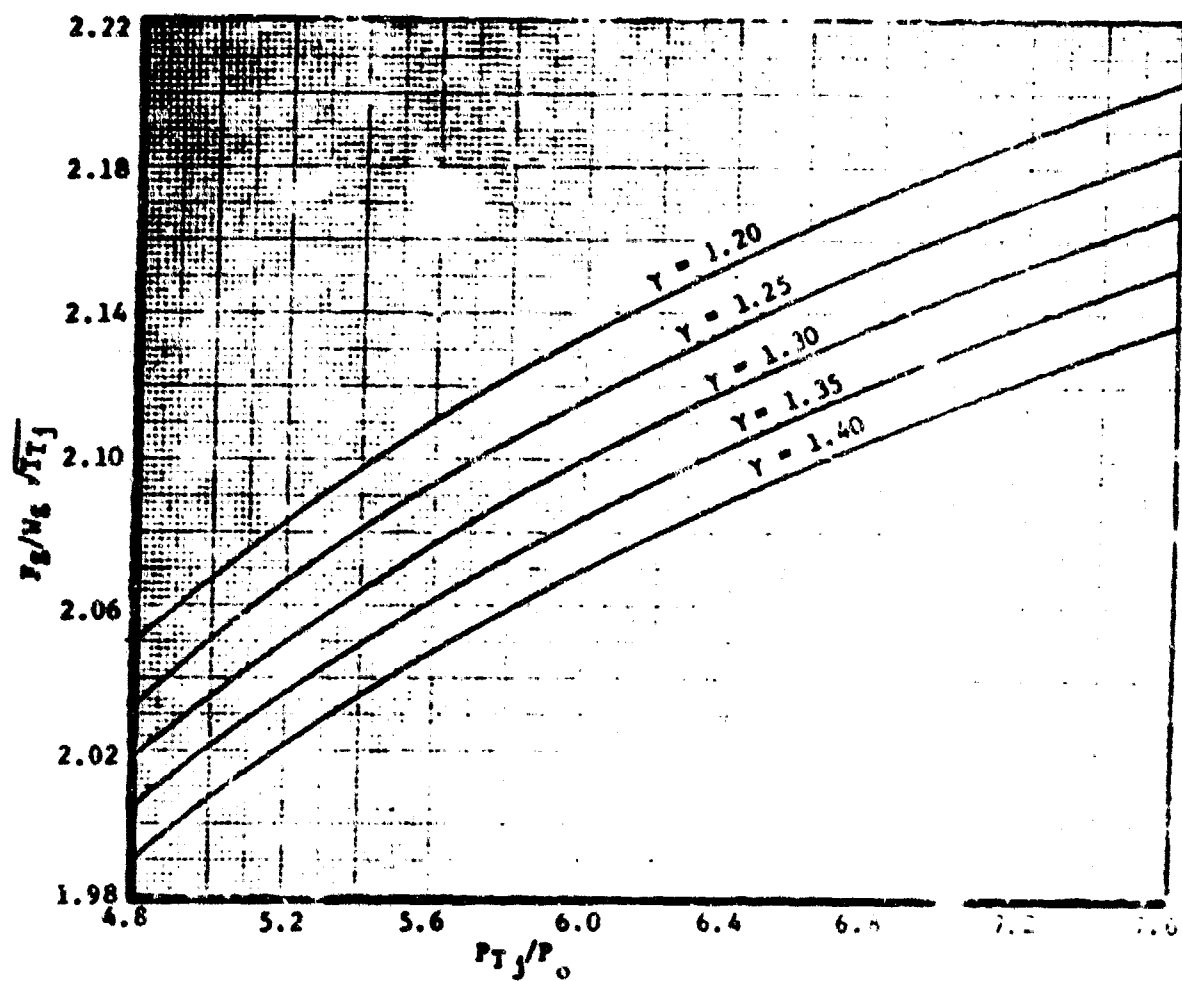


FIGURE 8-14 Converging Conical Nozzle Gross Thrust

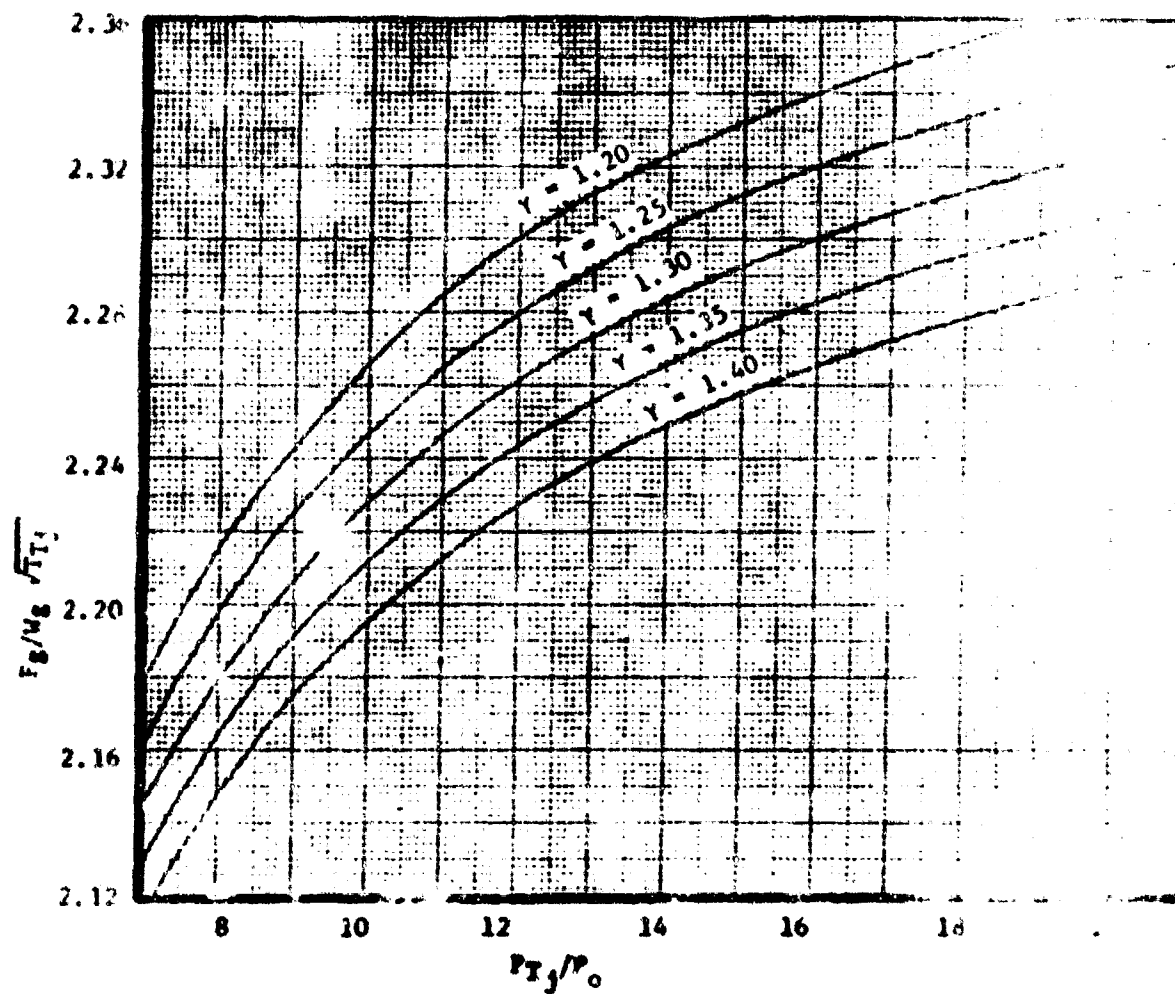


FIGURE 8-15 Converging Conical Nozzle Gross Thrust

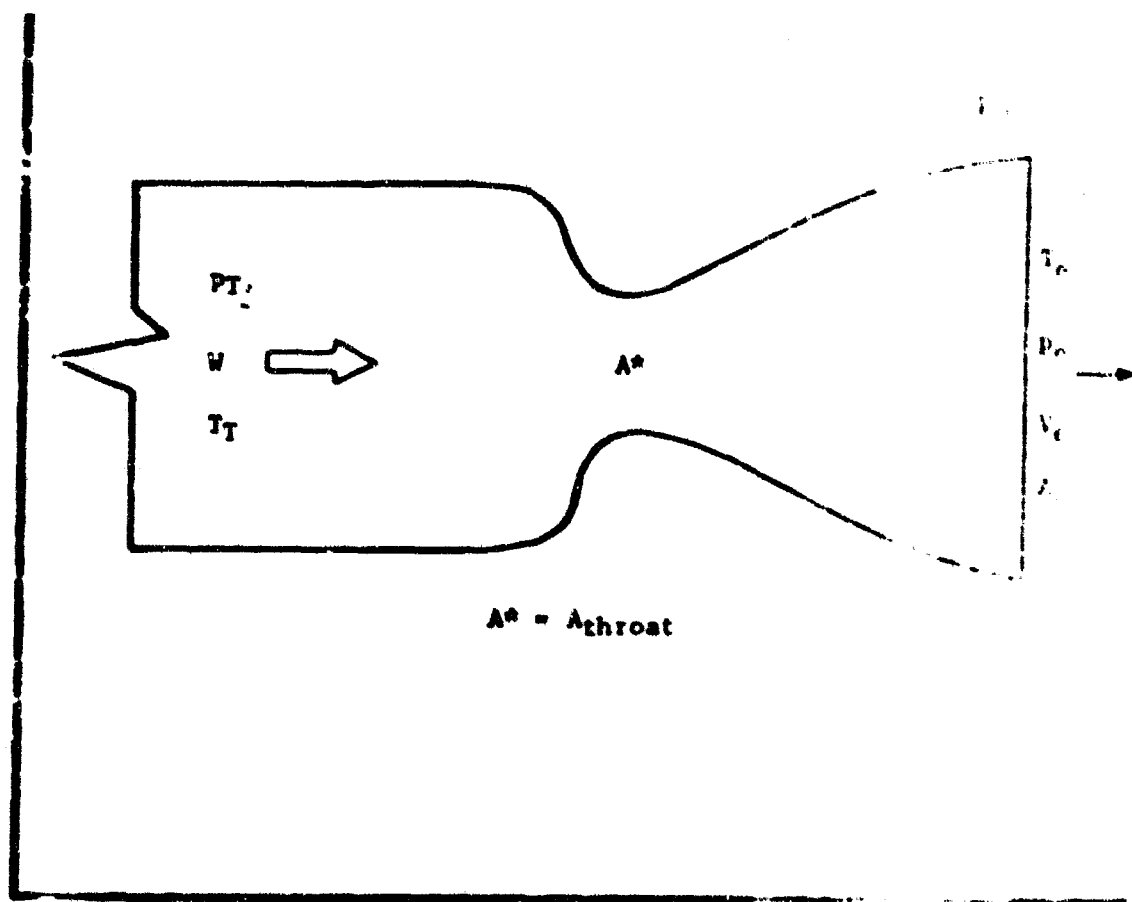


FIGURE 3-16 Convergent Divergent Nozzle Test

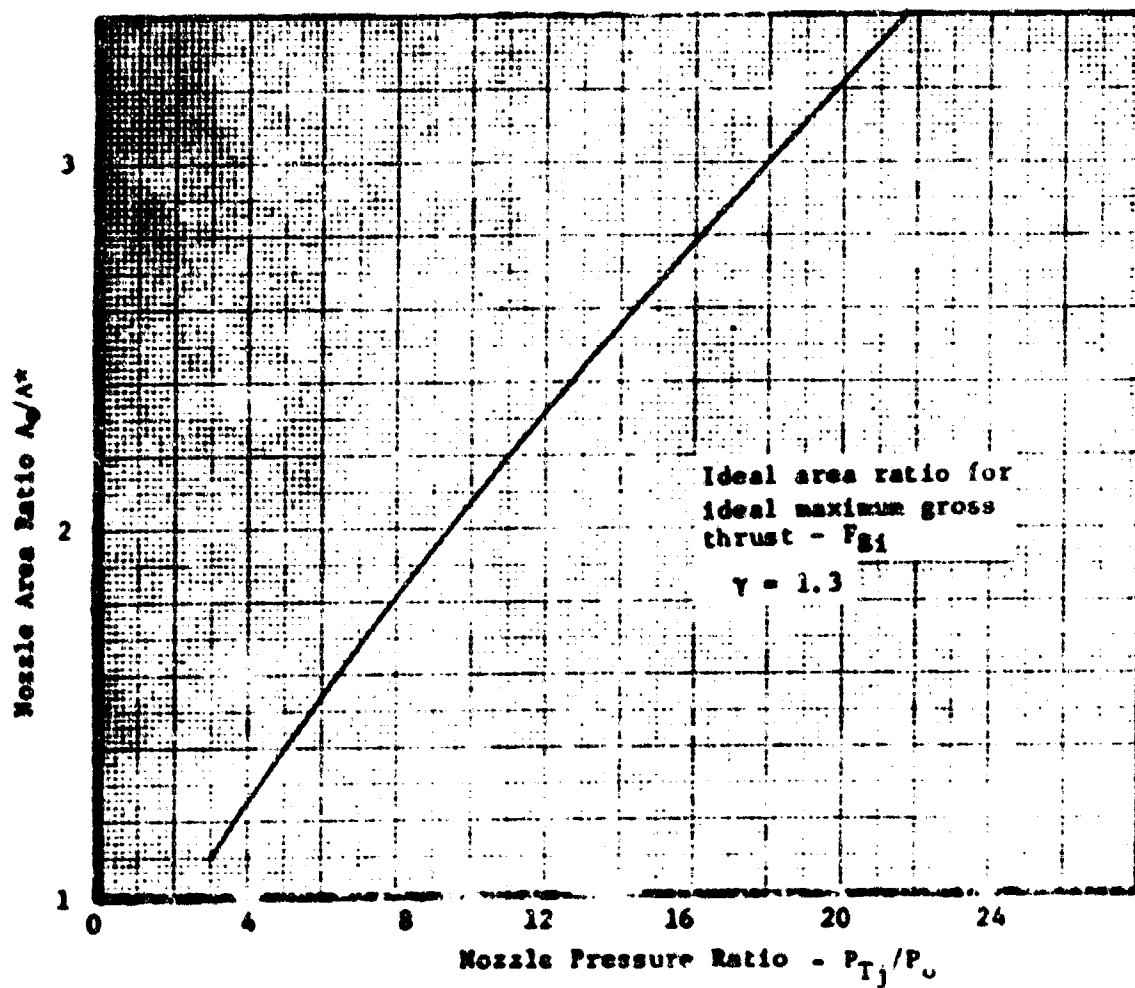


FIGURE 8-17 Optimum Nozzle Area Ratio

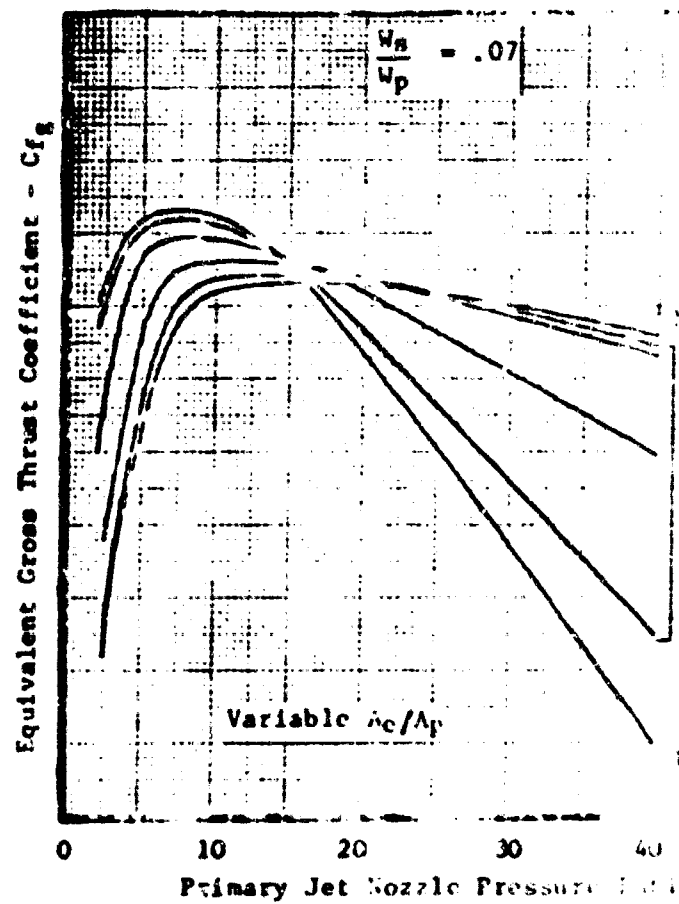


FIGURE 8-18 Variable C-D Nozzle Thrust Co.

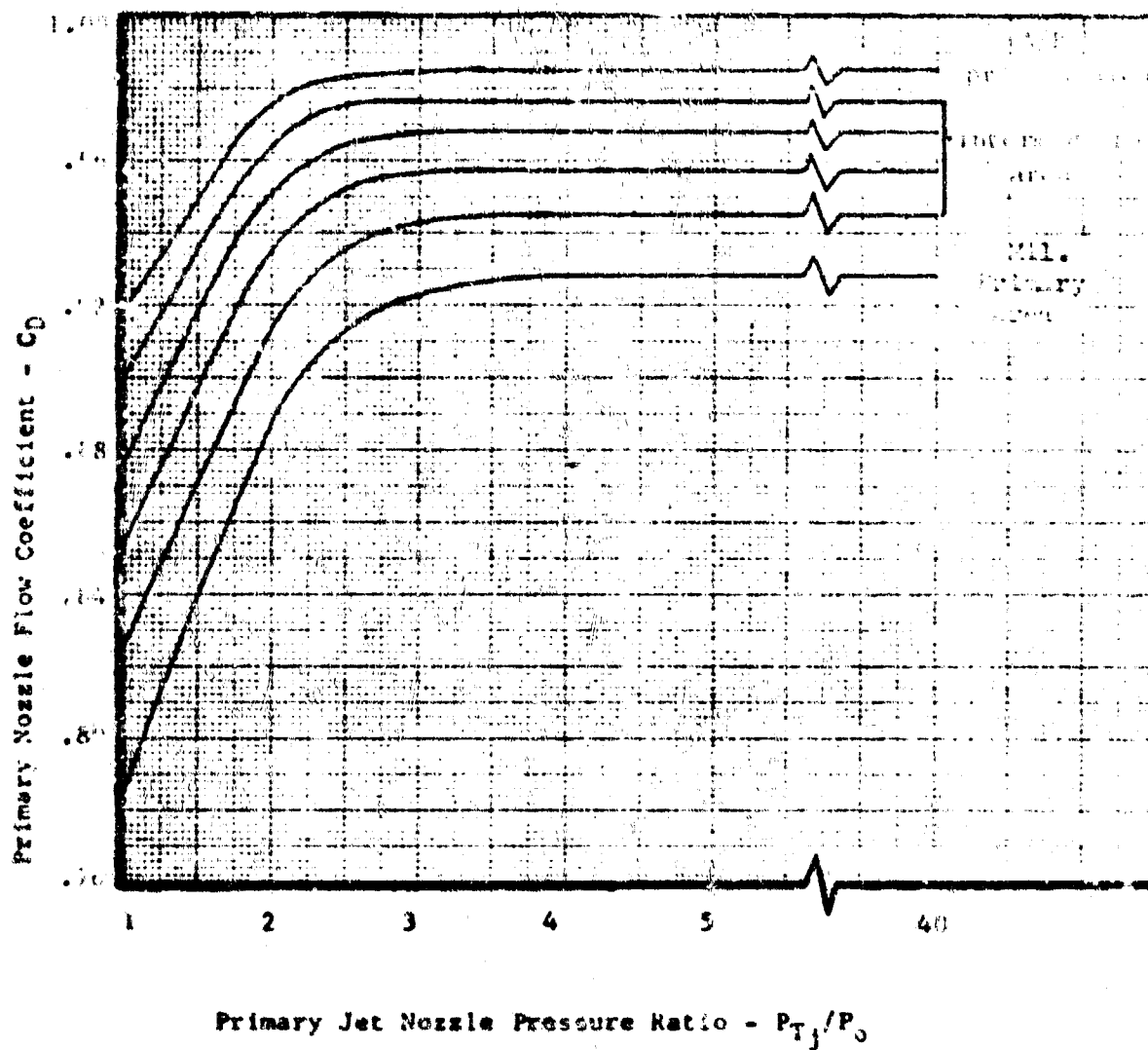


FIGURE 8-19. Variable C-D Nozzle Discharge Coefficients

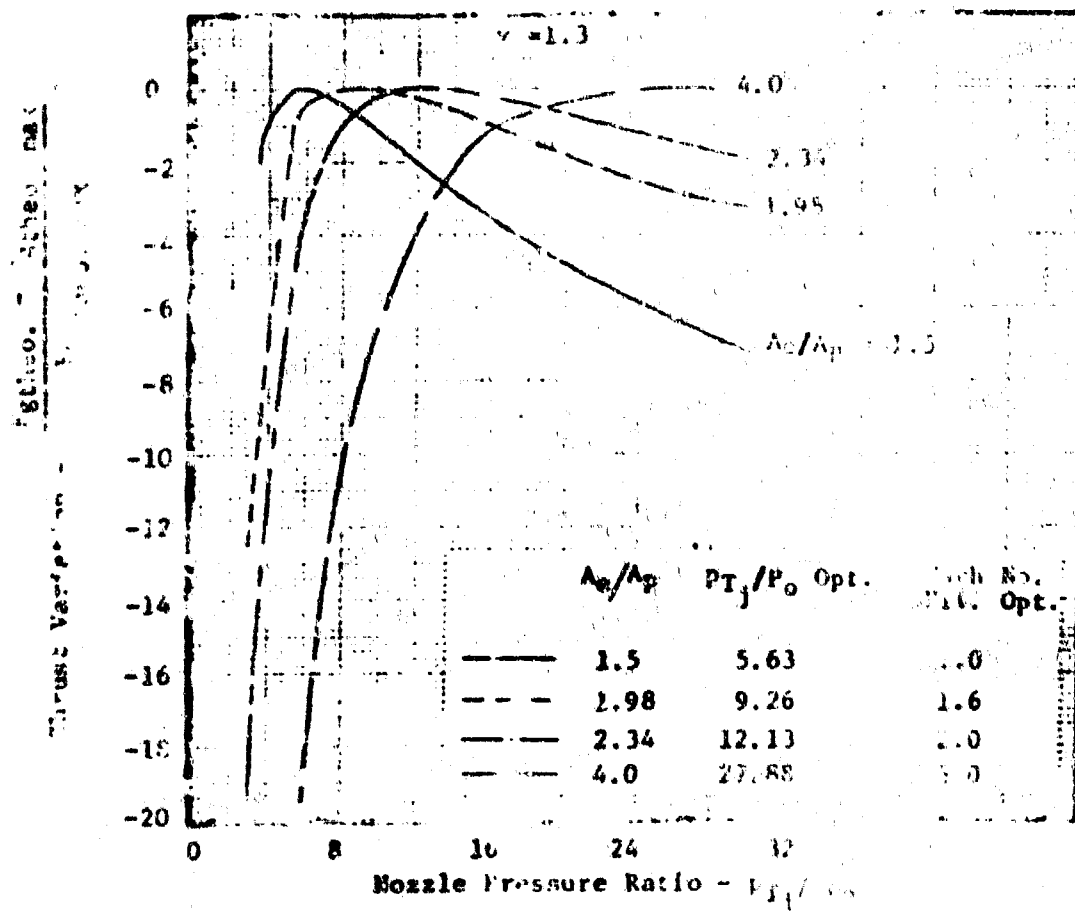


FIGURE 8-20 Theoretical Thrust Variation for Various Fixed Area Ratio Nozzles

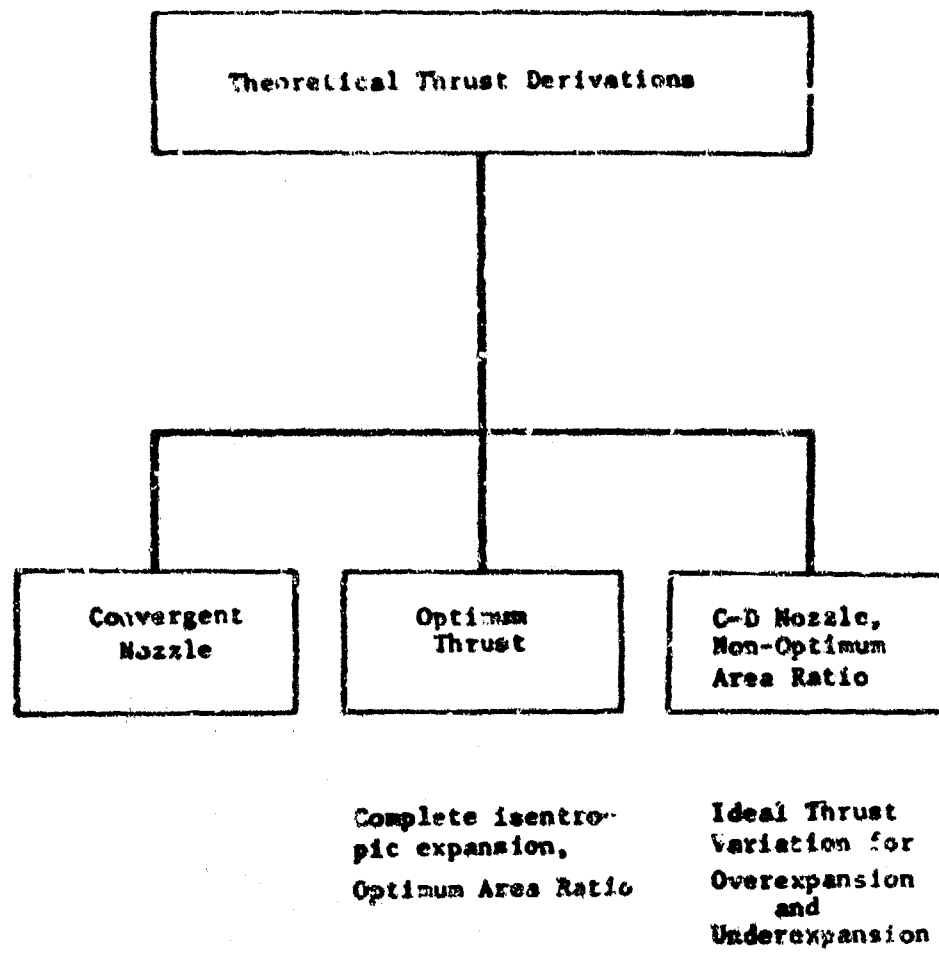


FIGURE 8-21 Theoretical Thrust Types

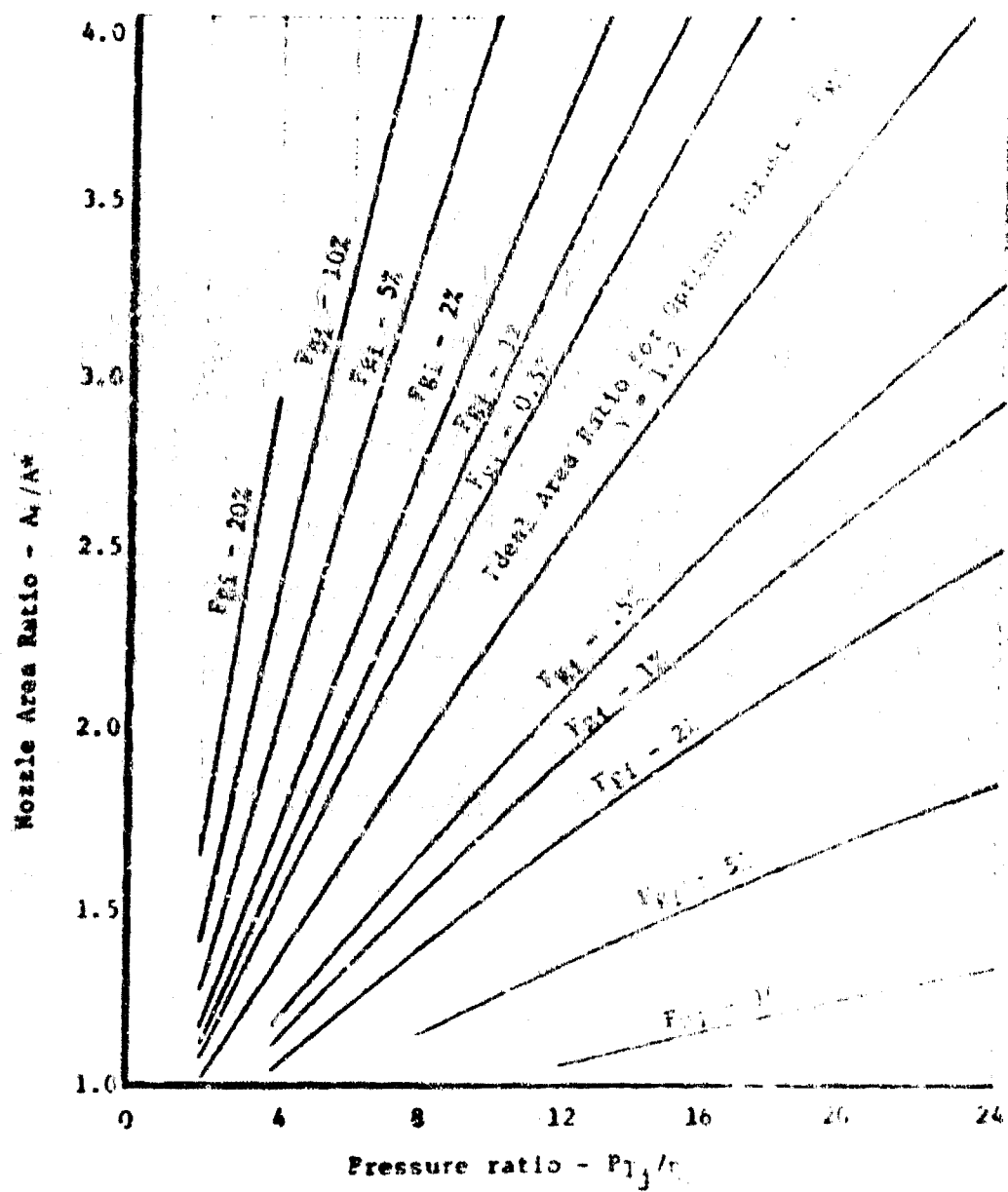


FIGURE 8-22 Theoretical C-D Thrust Variation with Area Ratio and Pressure Ratio, $\gamma = 1.7$

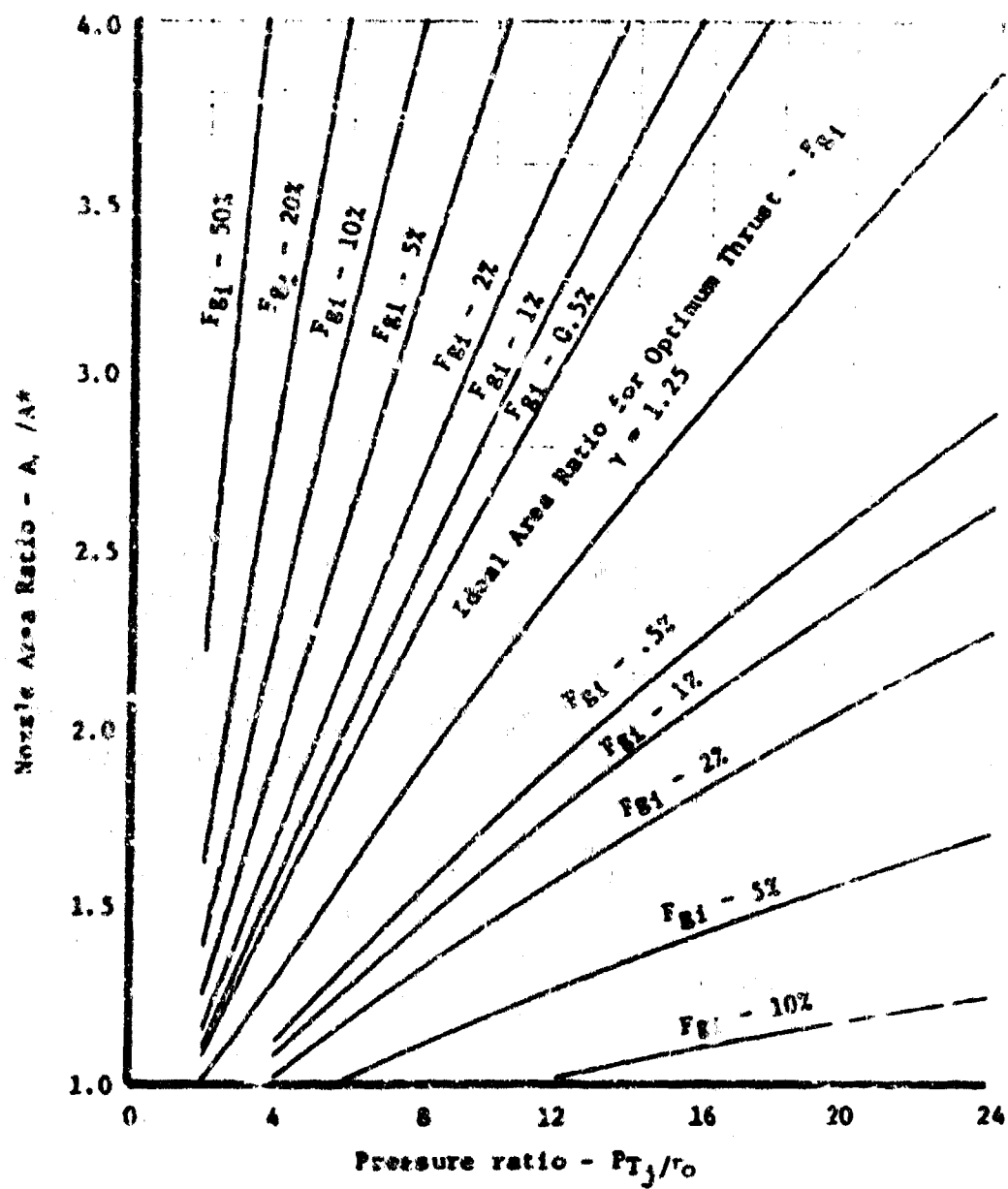


FIGURE A-23 Theoretical C-D Thrust Variation with Area Ratio and Pressure Ratio, $\gamma = 1.25$

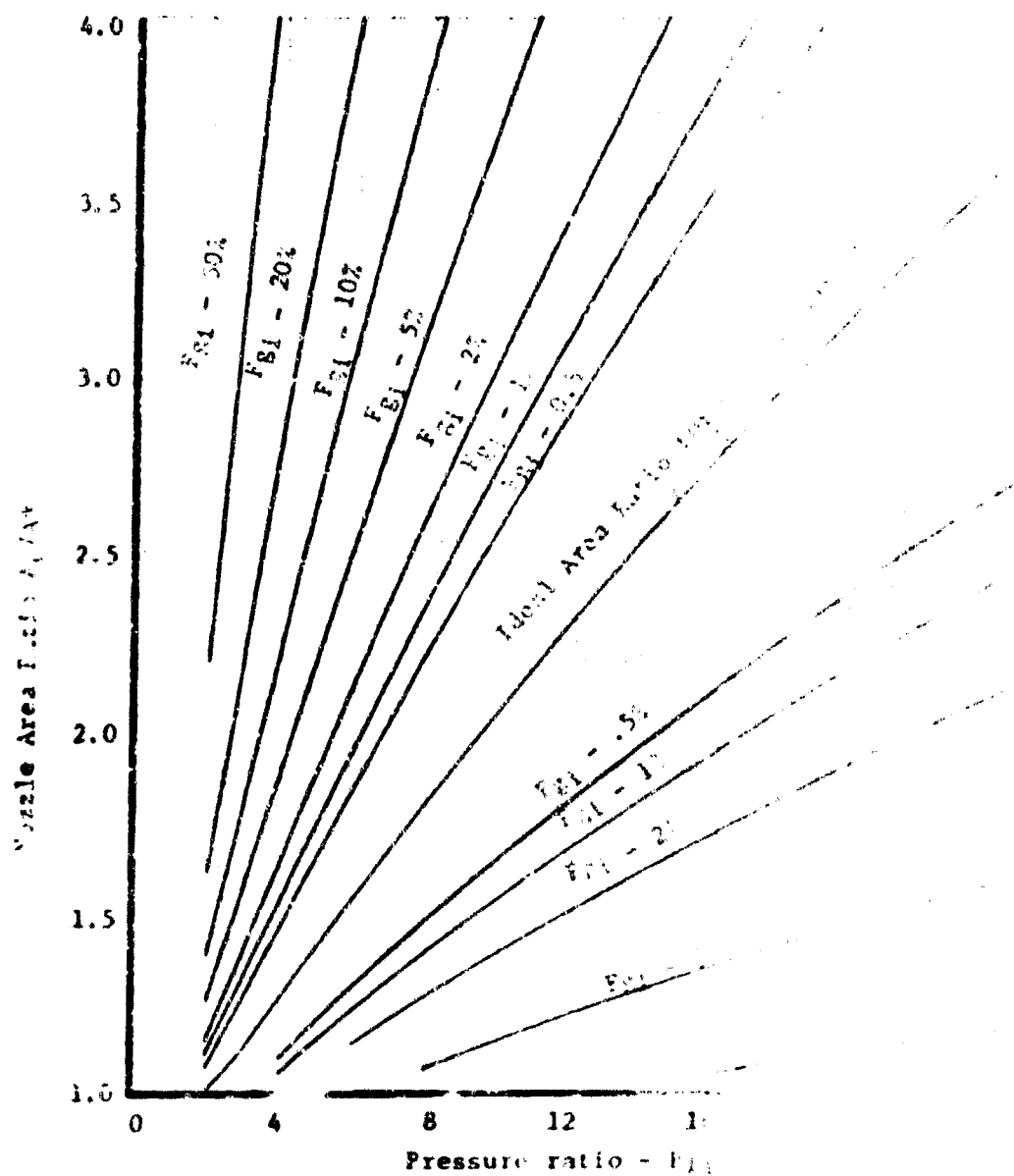


FIGURE 8-24 Theoretical C-D Thrust Coefficient
Ratio and Pressure Ratio

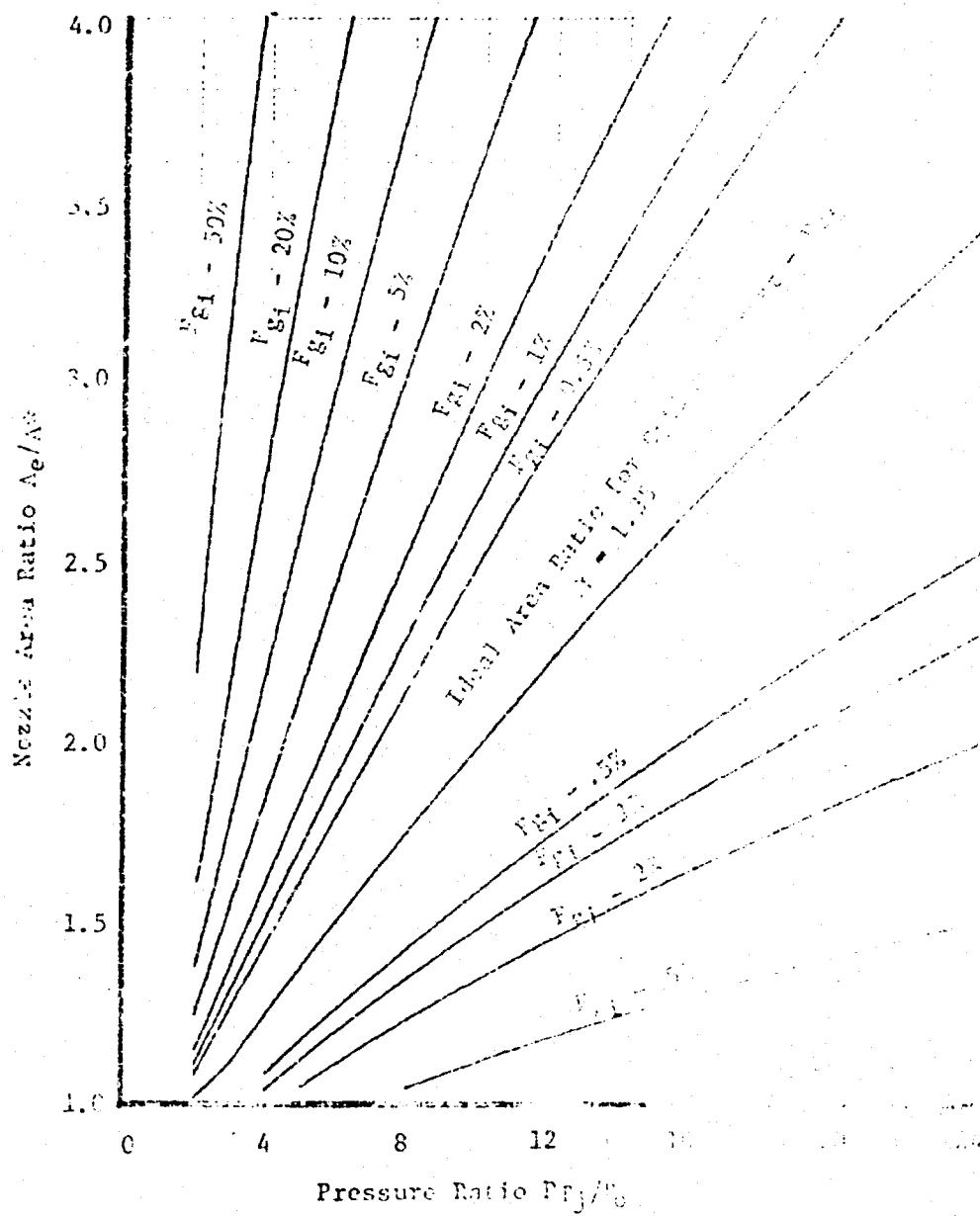


FIGURE 8-26 Theoretical C-D Thrust Variation with Area Ratio and Pressure Ratio, $\gamma = 1.4$

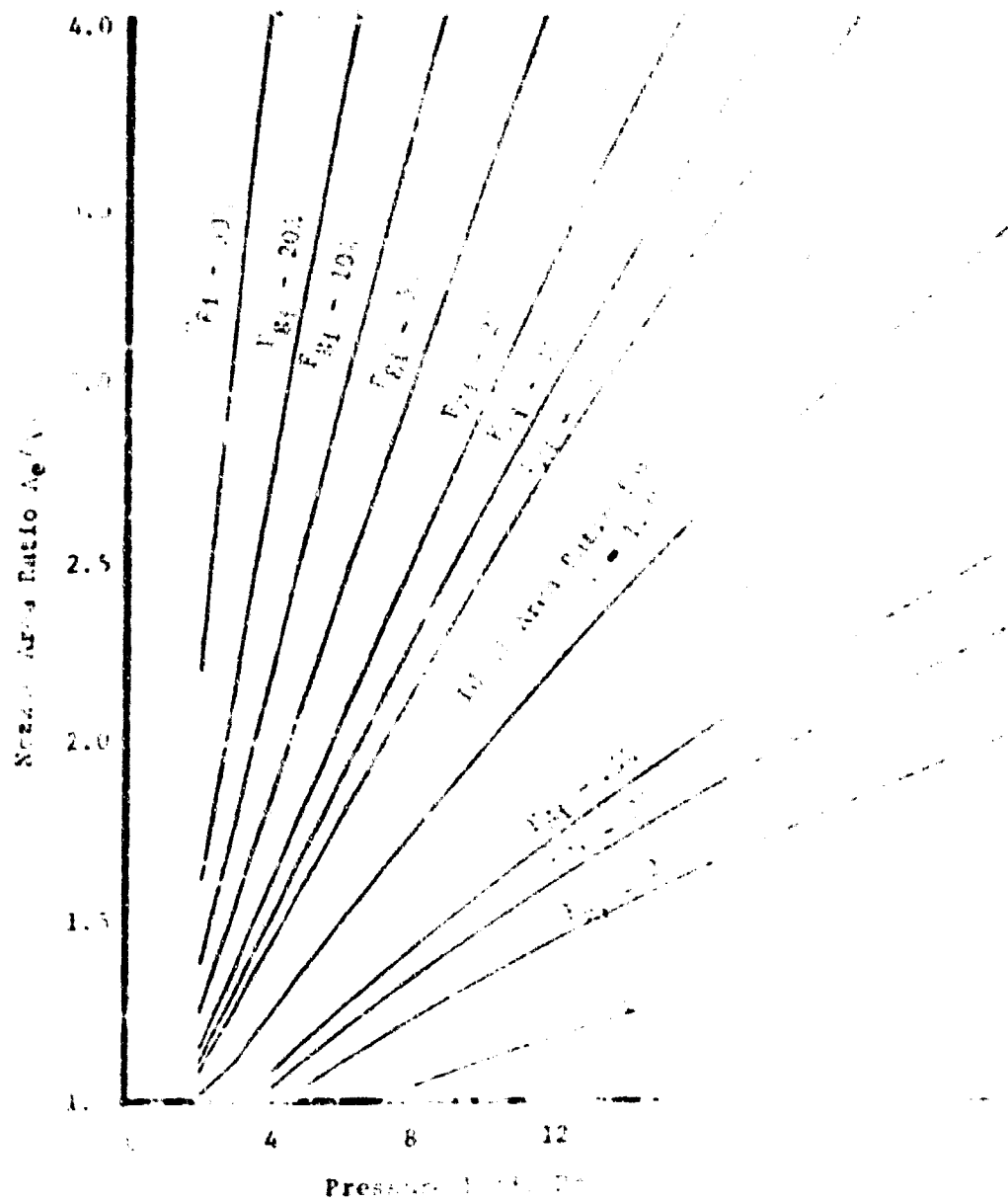


Fig. 8-26 Theoretical isentropic flow: Area ratio and pressure ratio.

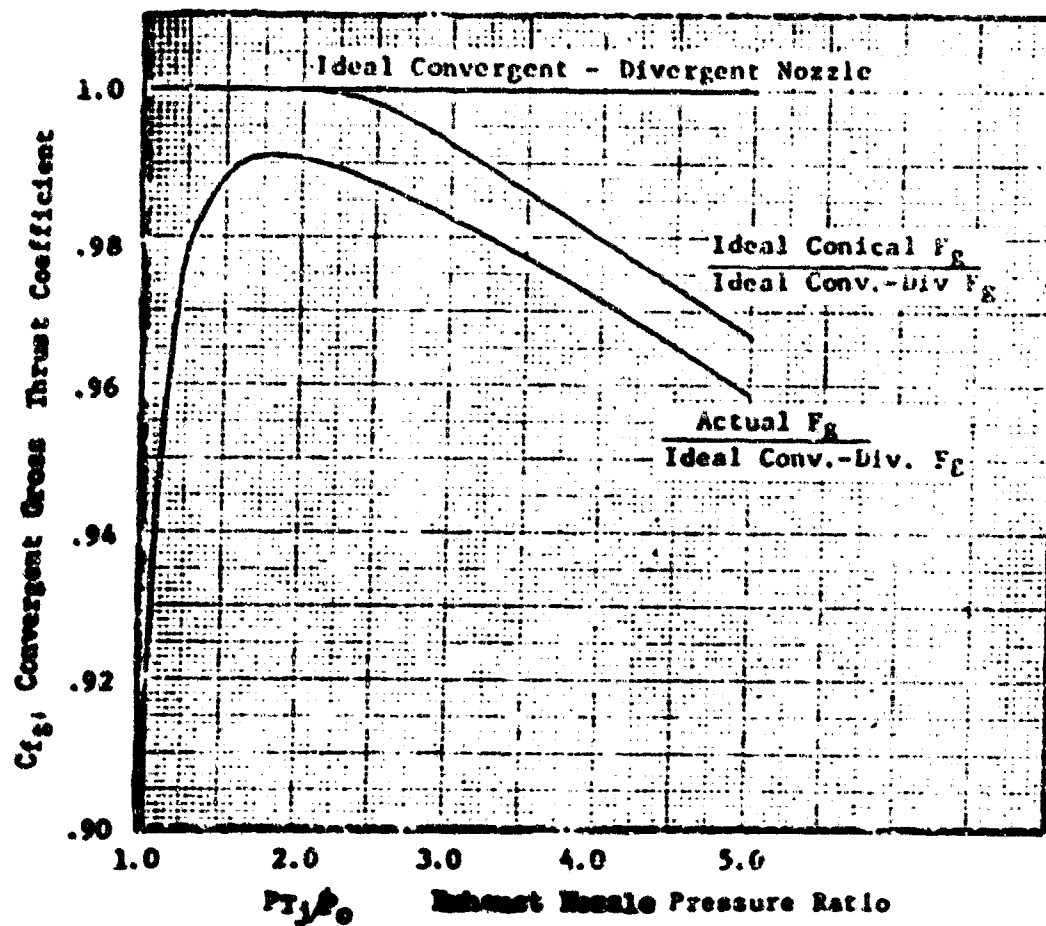


FIGURE 8-27 Convergent Nozzle Thrust Coefficient

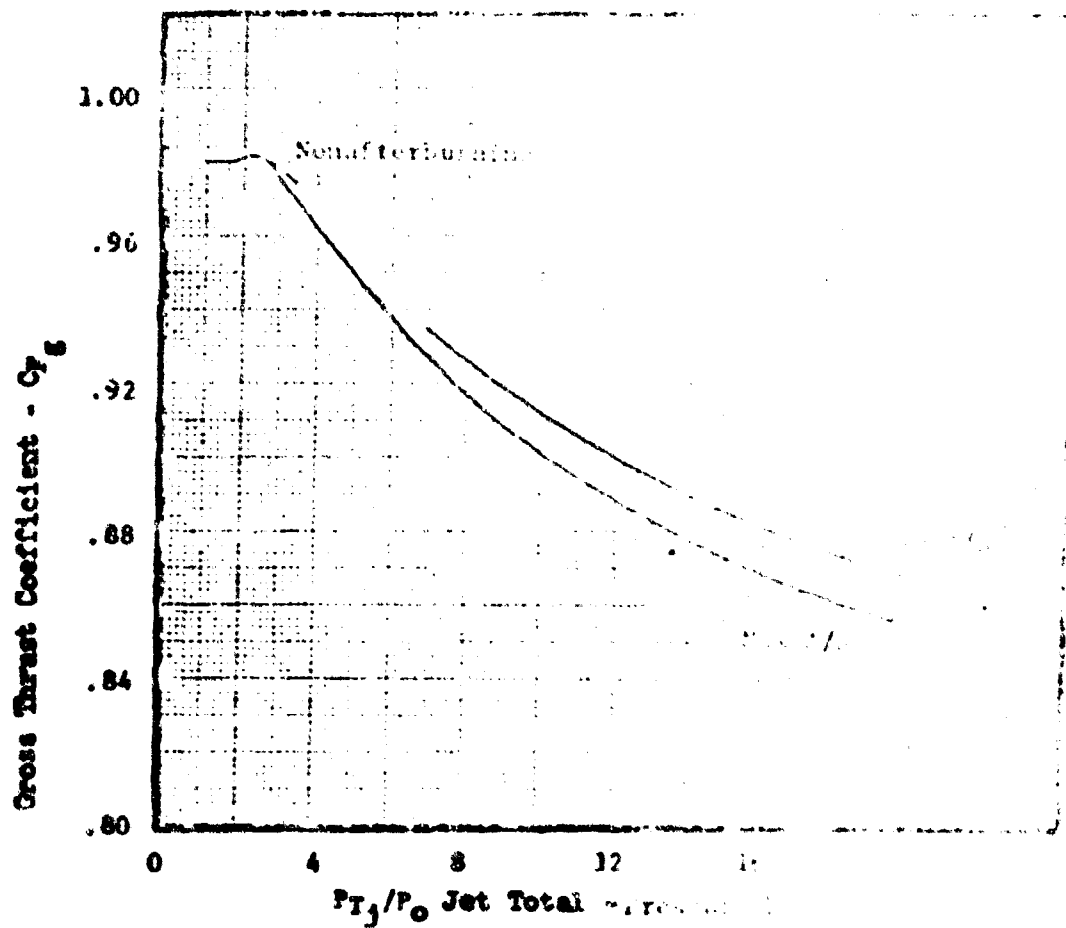


FIGURE 8-28 Variable Convergent Nozzle

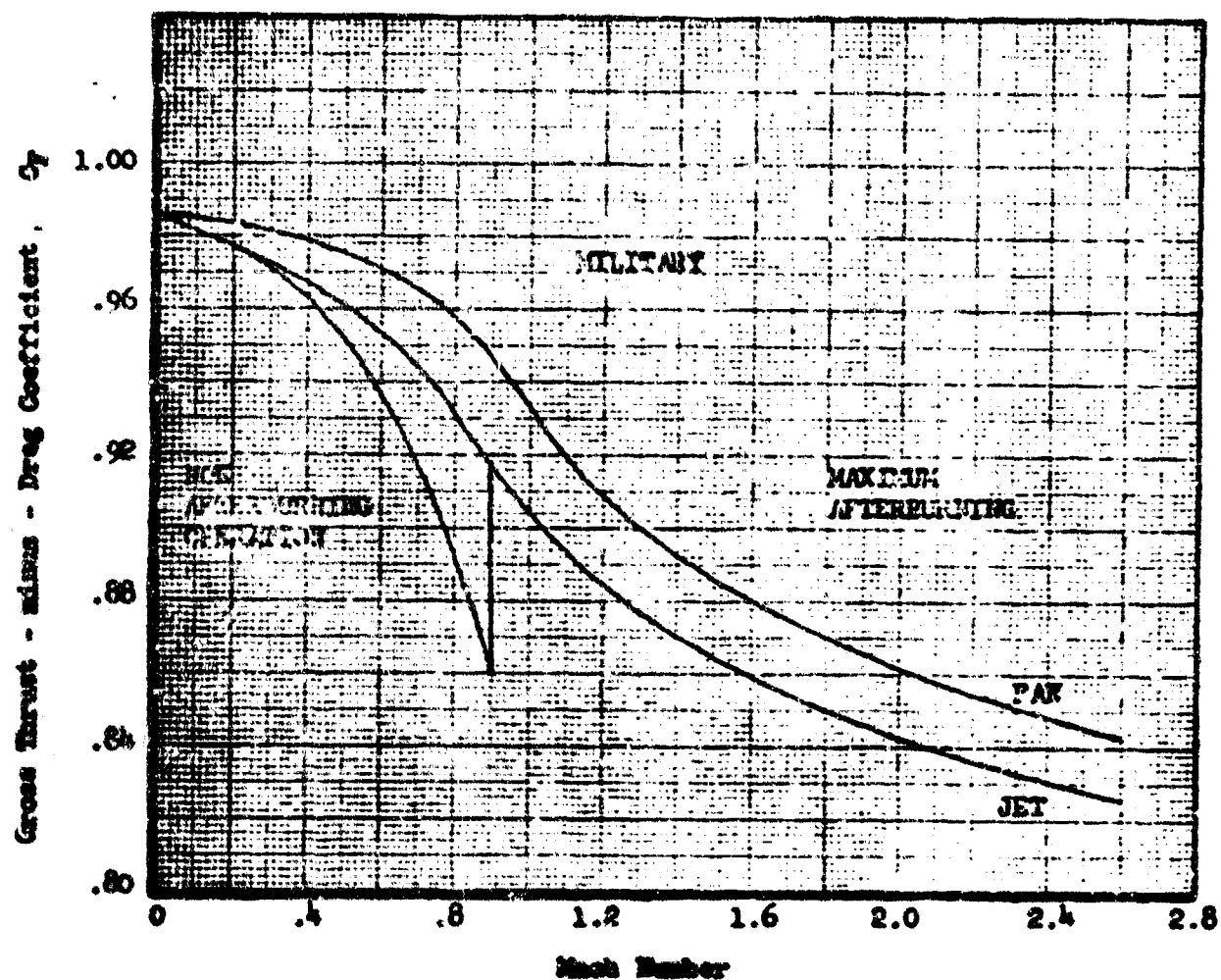


FIGURE 8-29 Estimated Performance of Convergent Nozzle with Runt Base

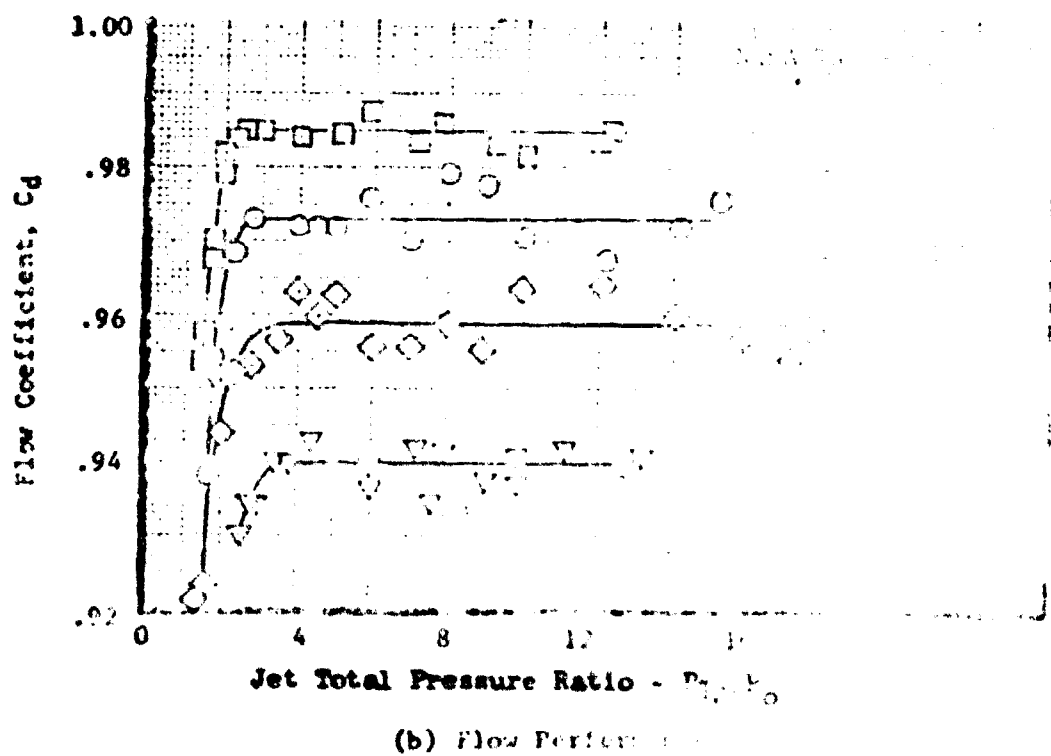
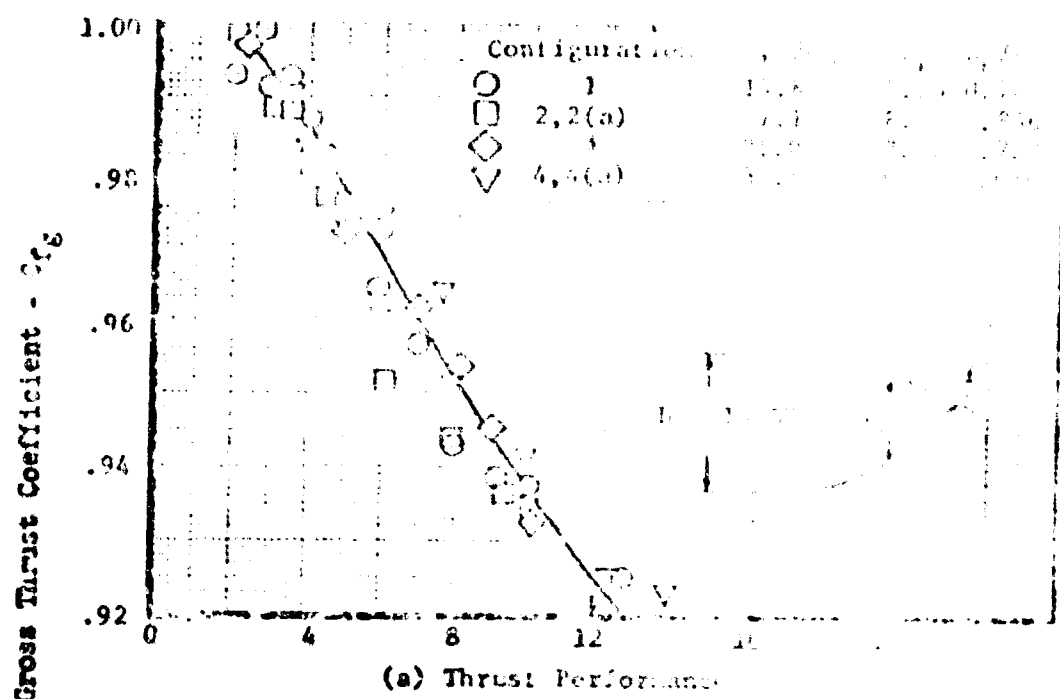


FIGURE 8-30 Effect of Lip Angle Variation on Thrust Coefficient and Flow Coefficient of a Convergent Nozzle

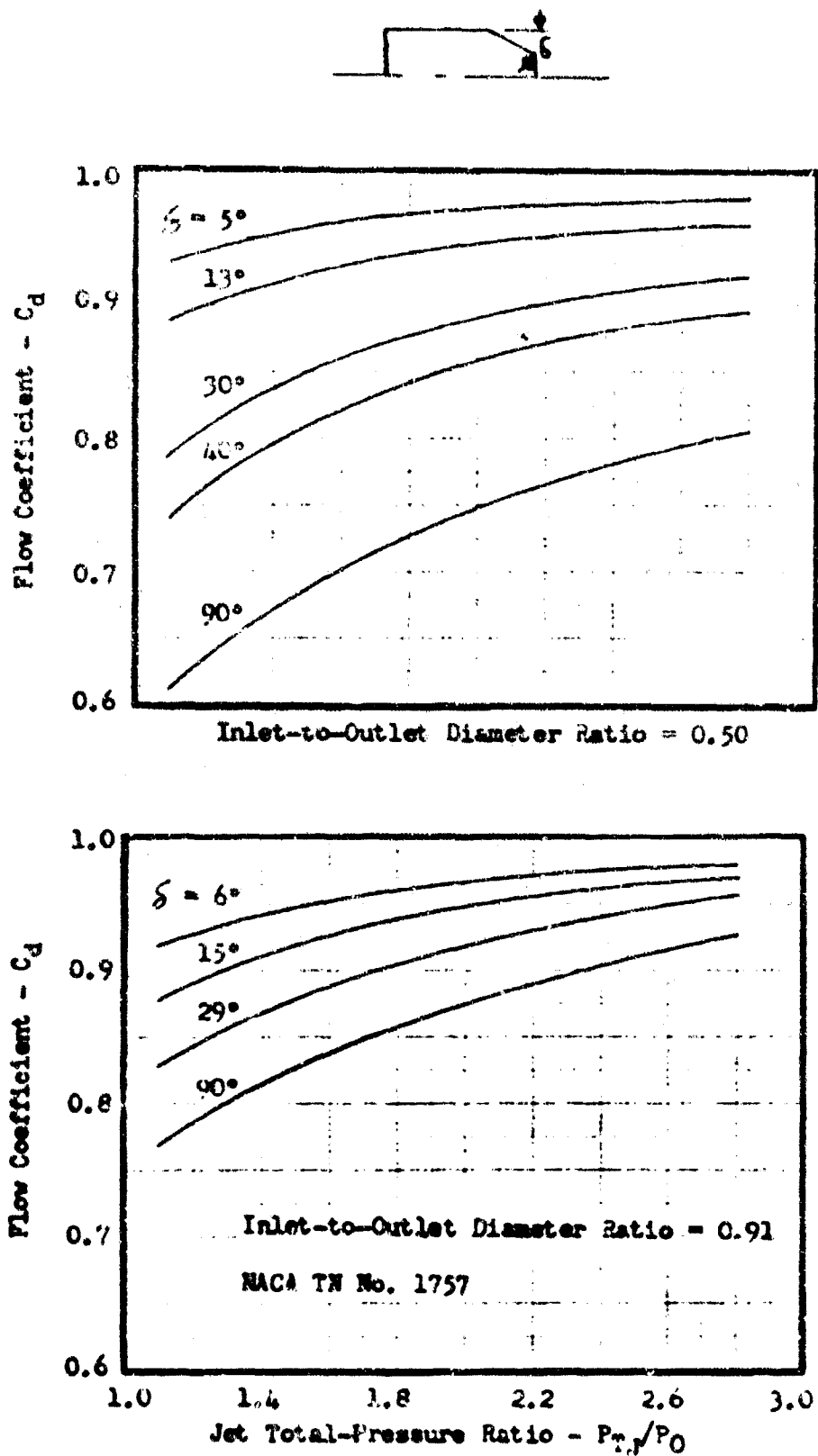


FIGURE 8-31. Effect of Lip Angle Variation at Two Inlet-to-Outlet Diameter Ratios on the Flow Coefficient

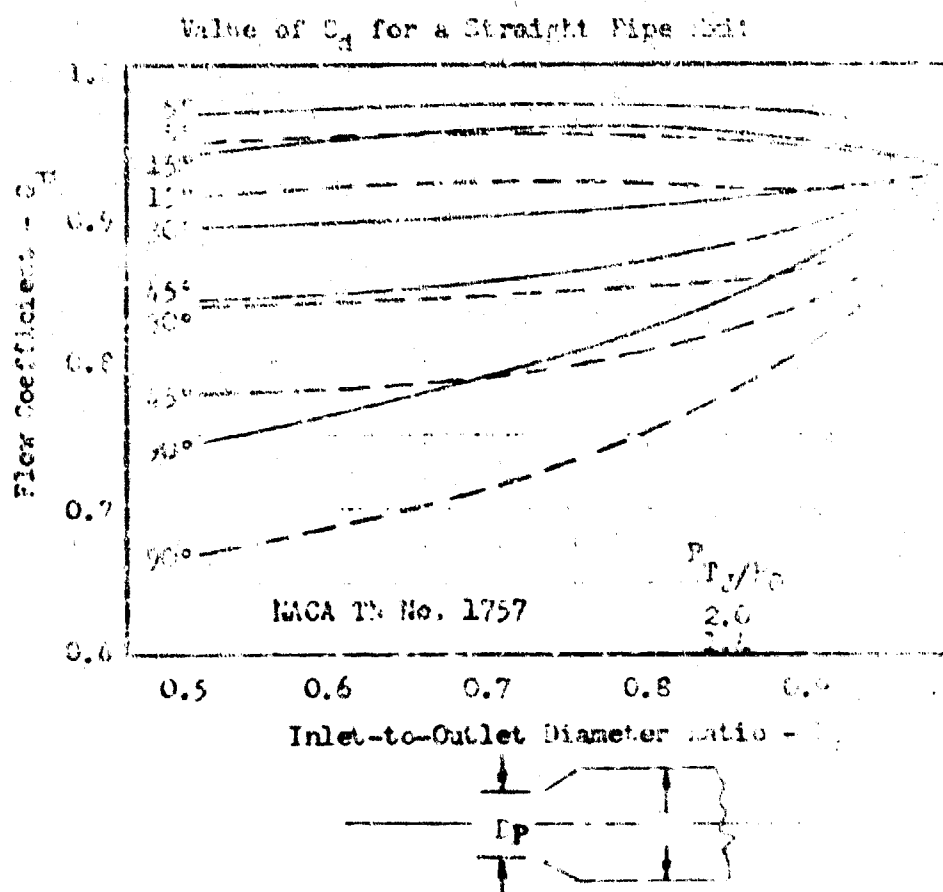


FIGURE 8-32. Effect of Inlet-to-Outlet Diameter Ratio on the Flow Coefficient at Various Angles and at Two Jet Formation Ratios

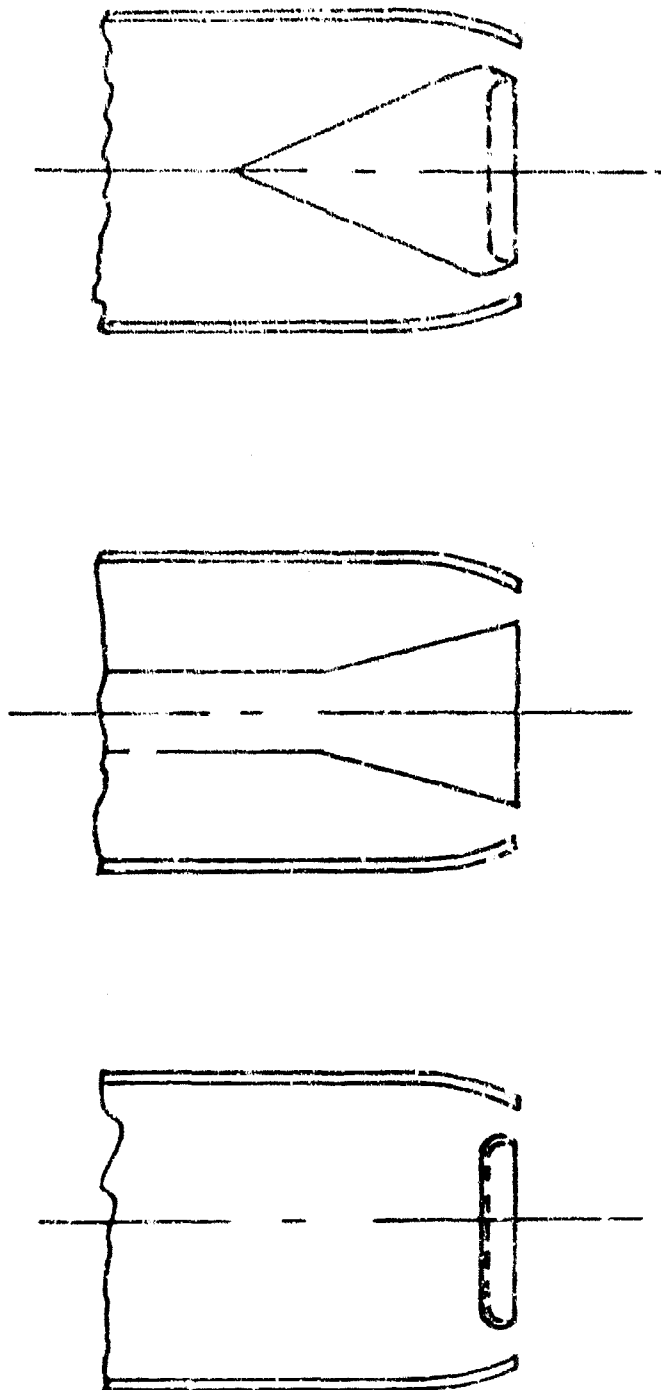
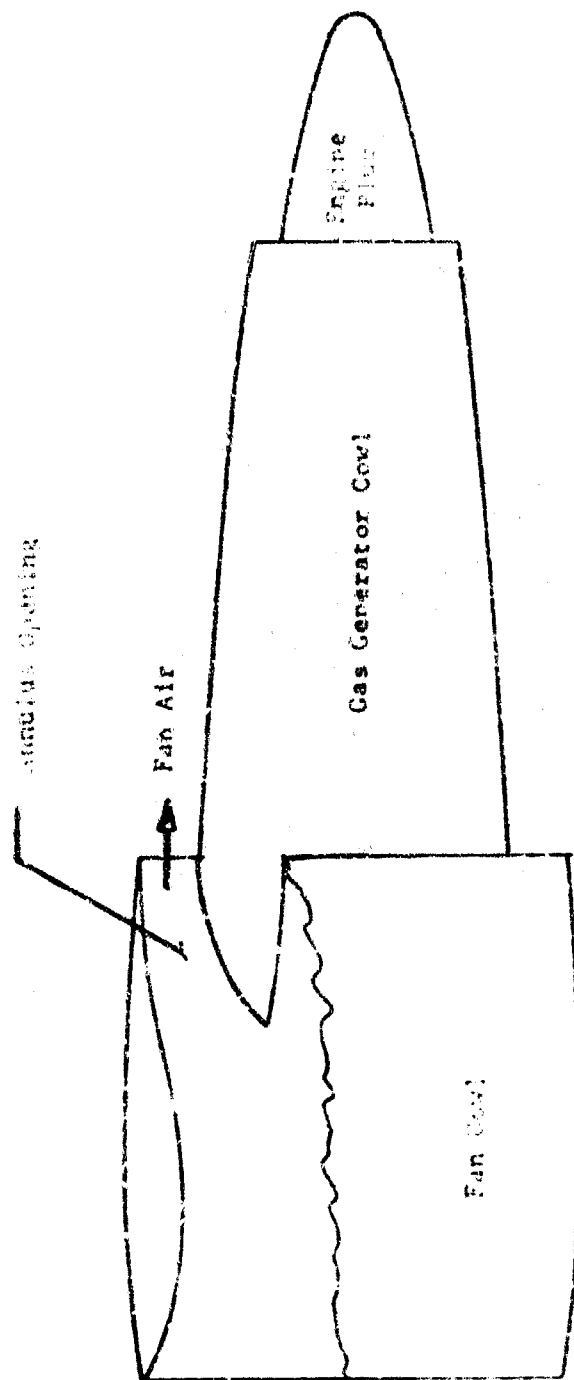


FIGURE 8-33. Annular Nozzle Configurations.



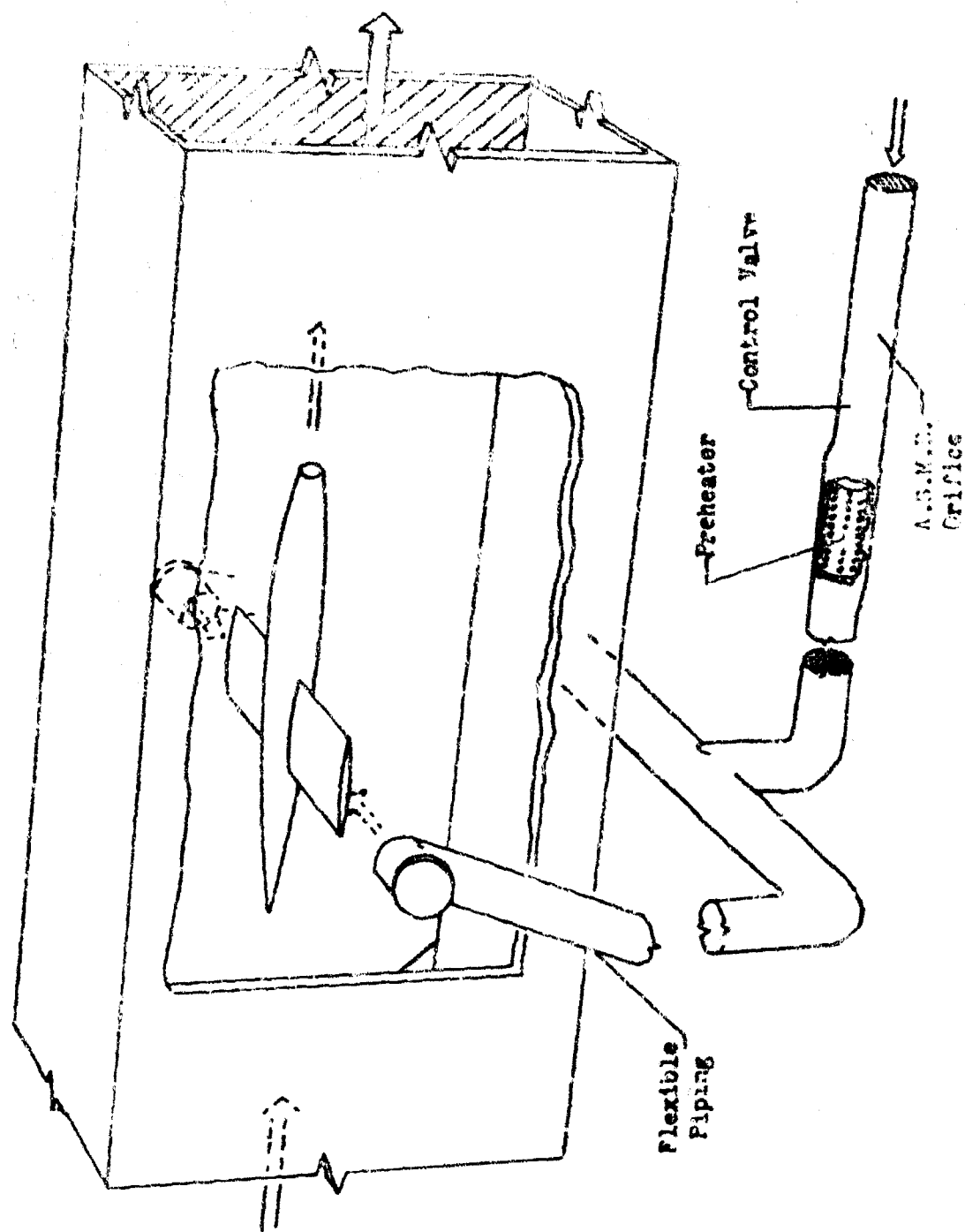
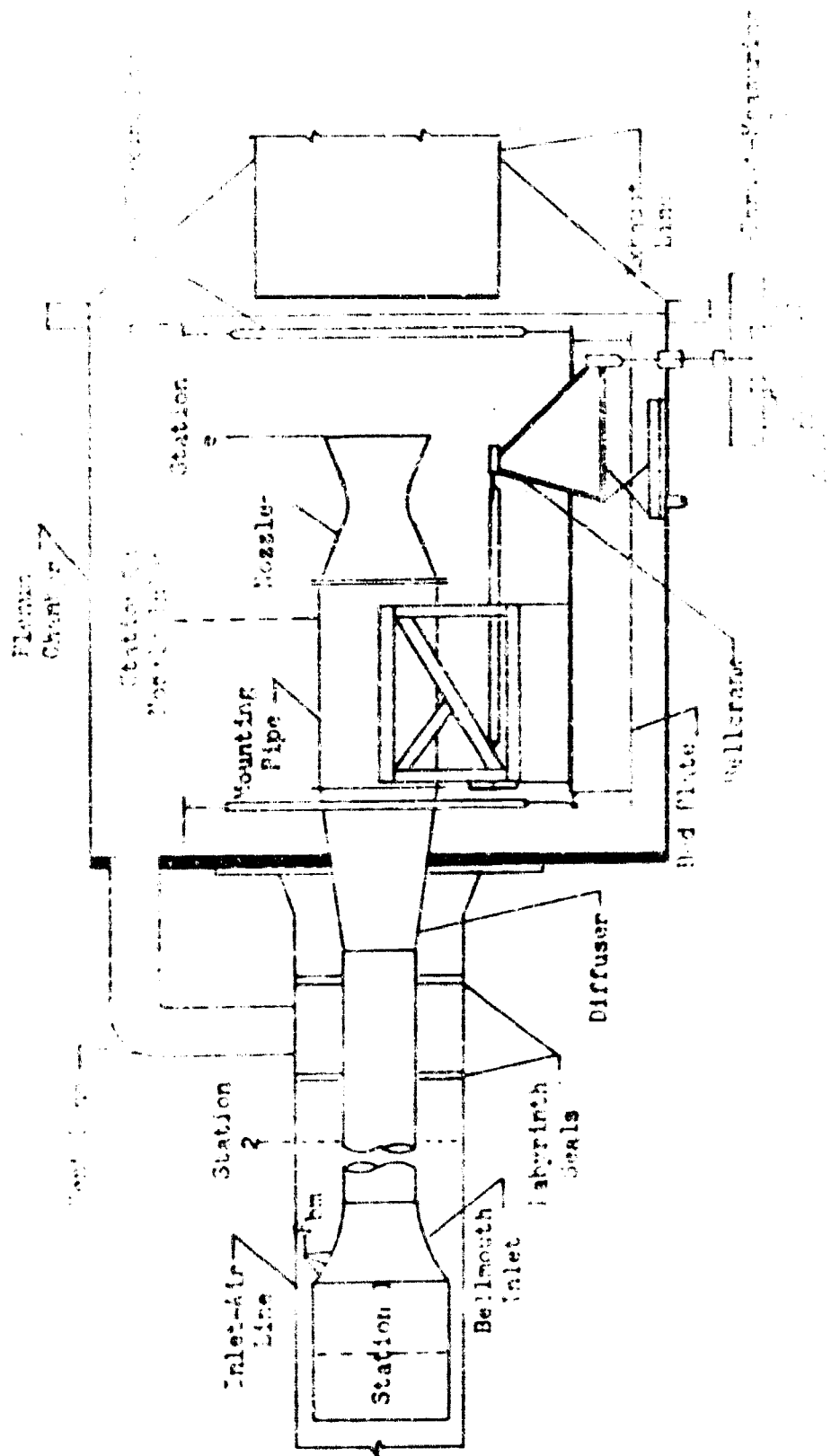


FIGURE 8 -35. Schematic Diagram of Jet-Ex Model Installed in 8- by 6-Foot Supersonic Wind Tunnel.



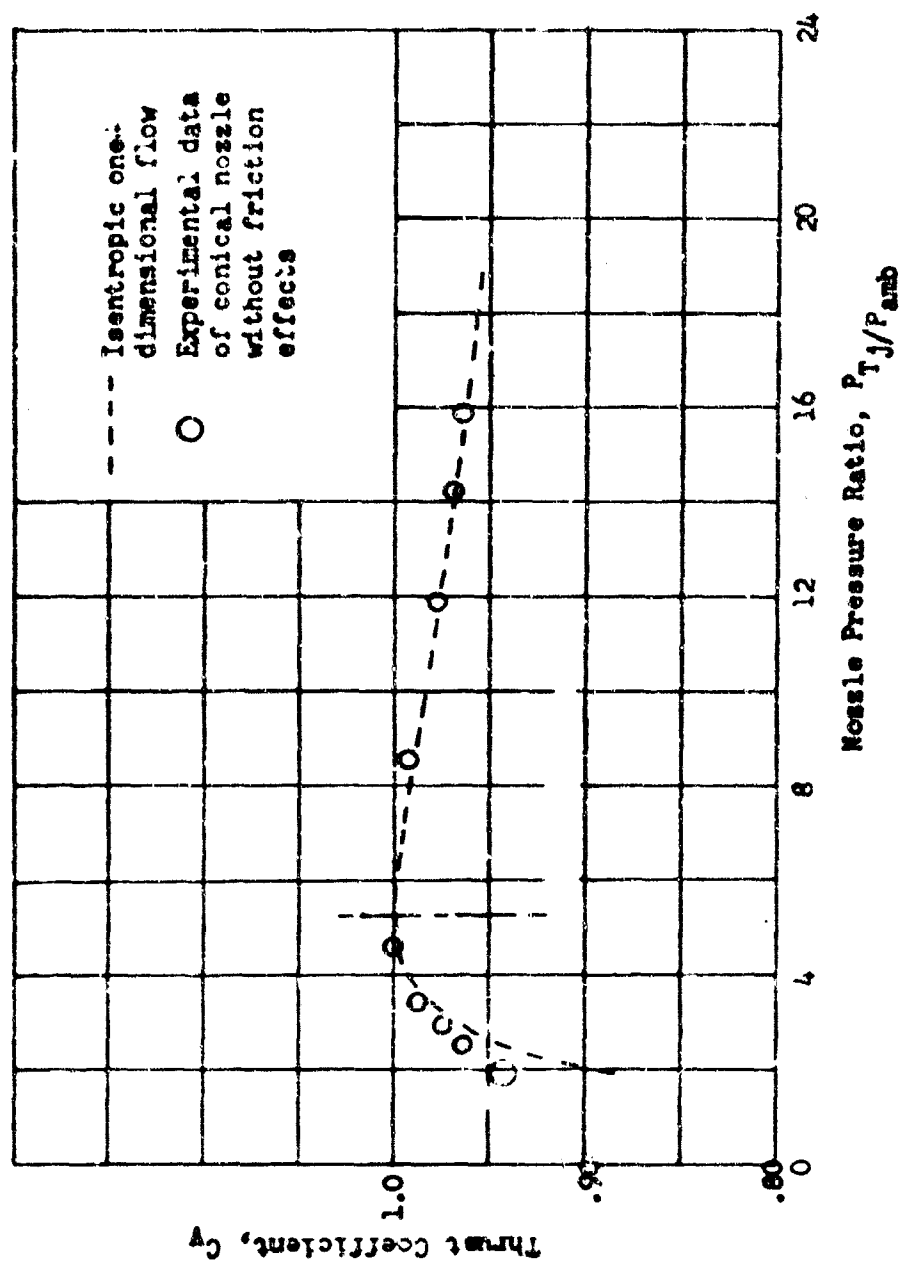
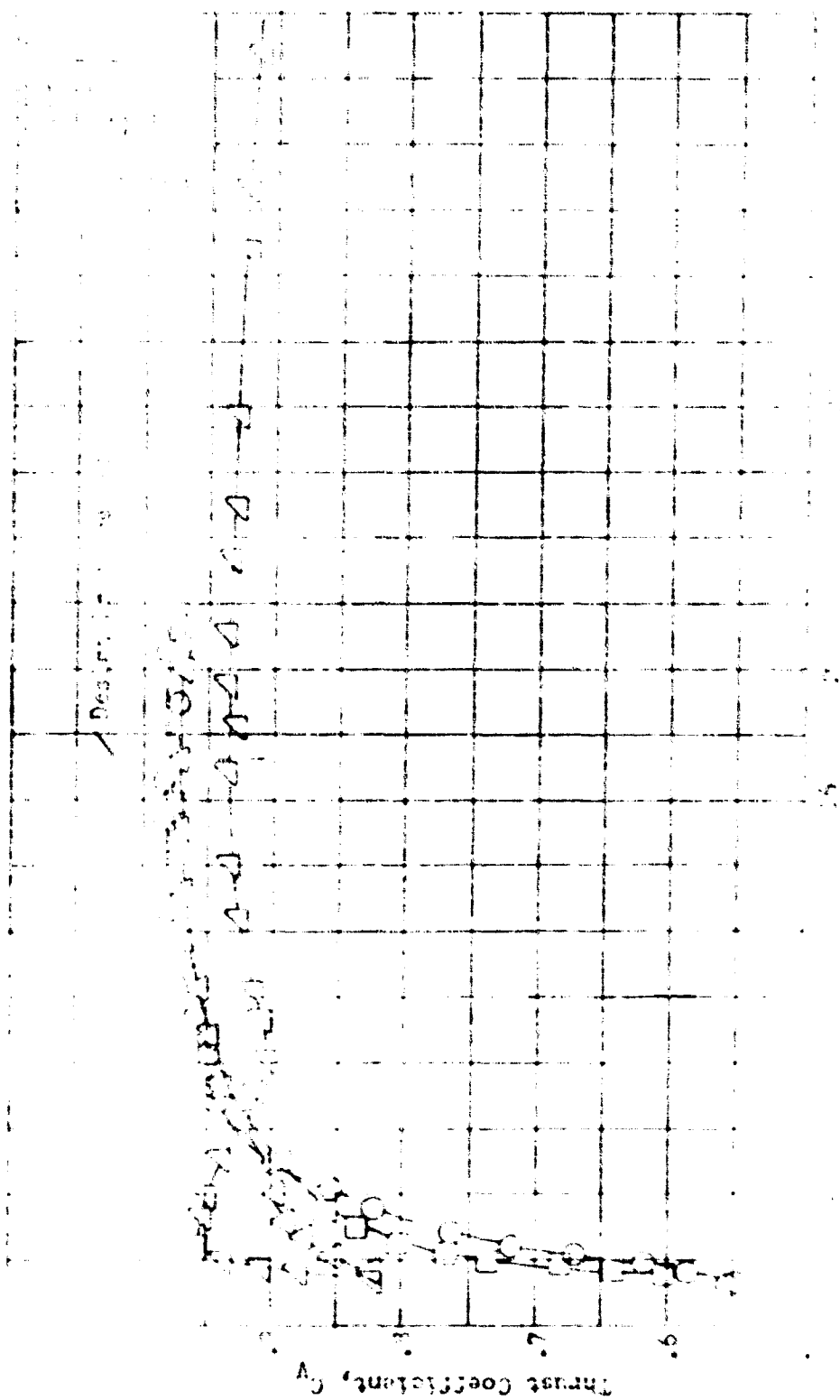


FIGURE 8 - 37. Thrust Coefficient Characteristics for Conical Nozzle.



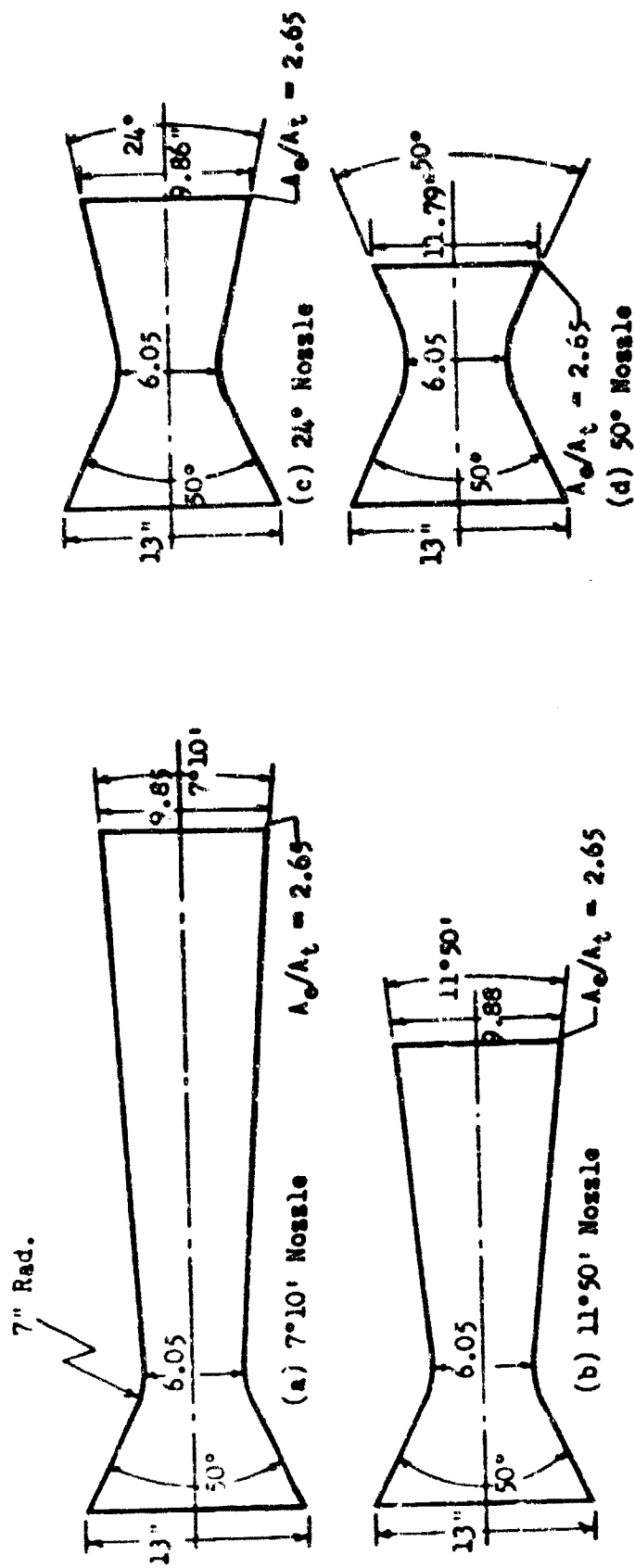
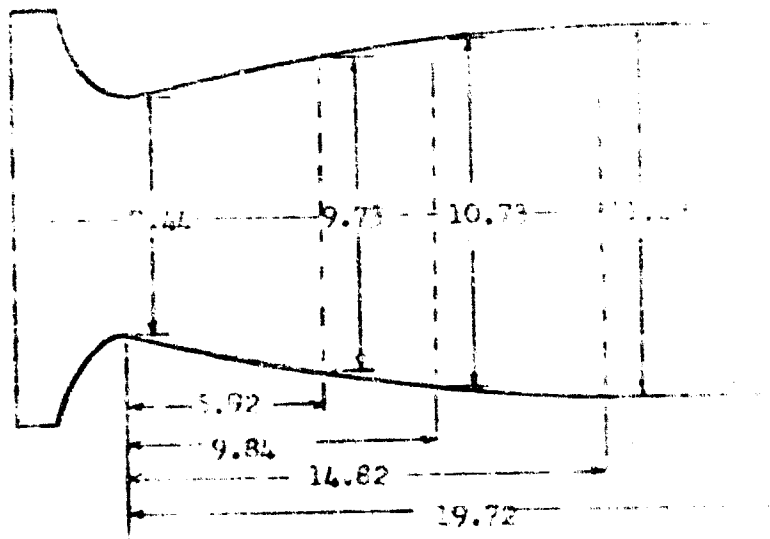
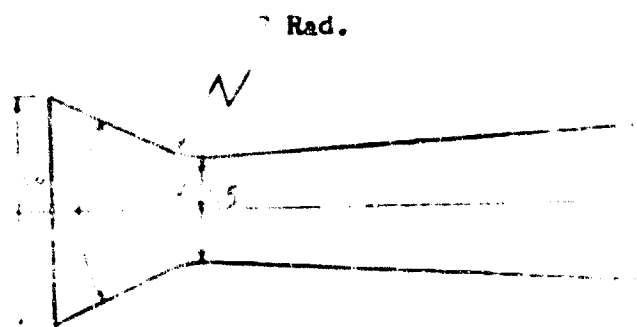


FIGURE 8 -39. Schematic Diagrams of Convergent-Divergent Conical Nozzles

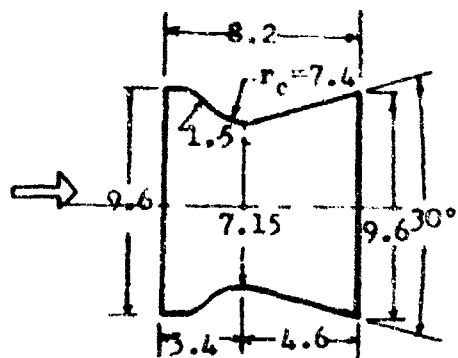


Nozzle Designed by Characteristic Method

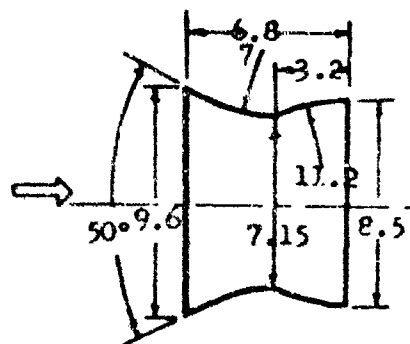


7°10' Conical Nozzle

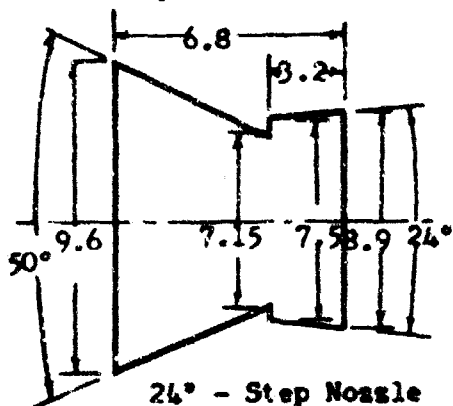
FIGURE 2-40 Nozzles Designed by Method
(All dimensions in inches)



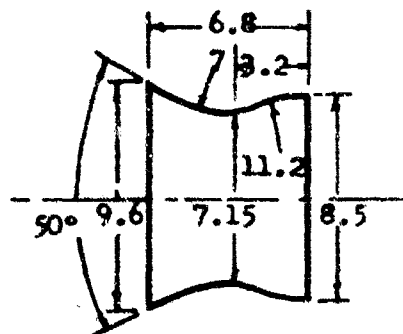
Throat Contour Radius
Ratio .34



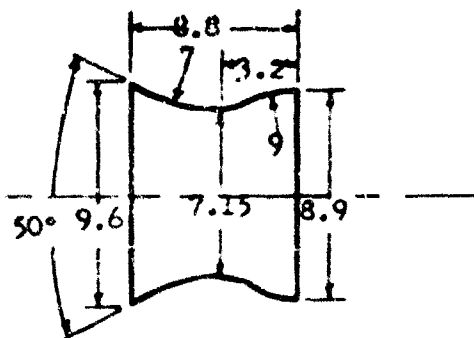
Concave - Contour Nozzle



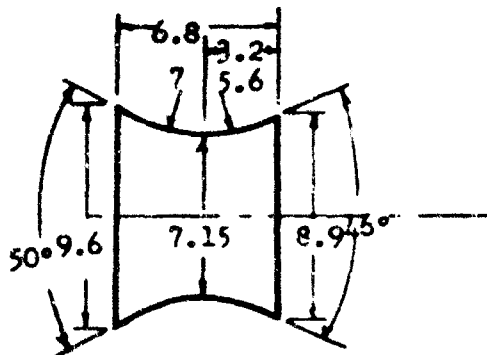
24° - Step Nozzle



Concave Nozzle



Ogee Nozzle



Convex Nozzle

FIGURE 8 - 41 Nozzles of Various Throat and Diffuser
Geometry, Dimensions in Inches.

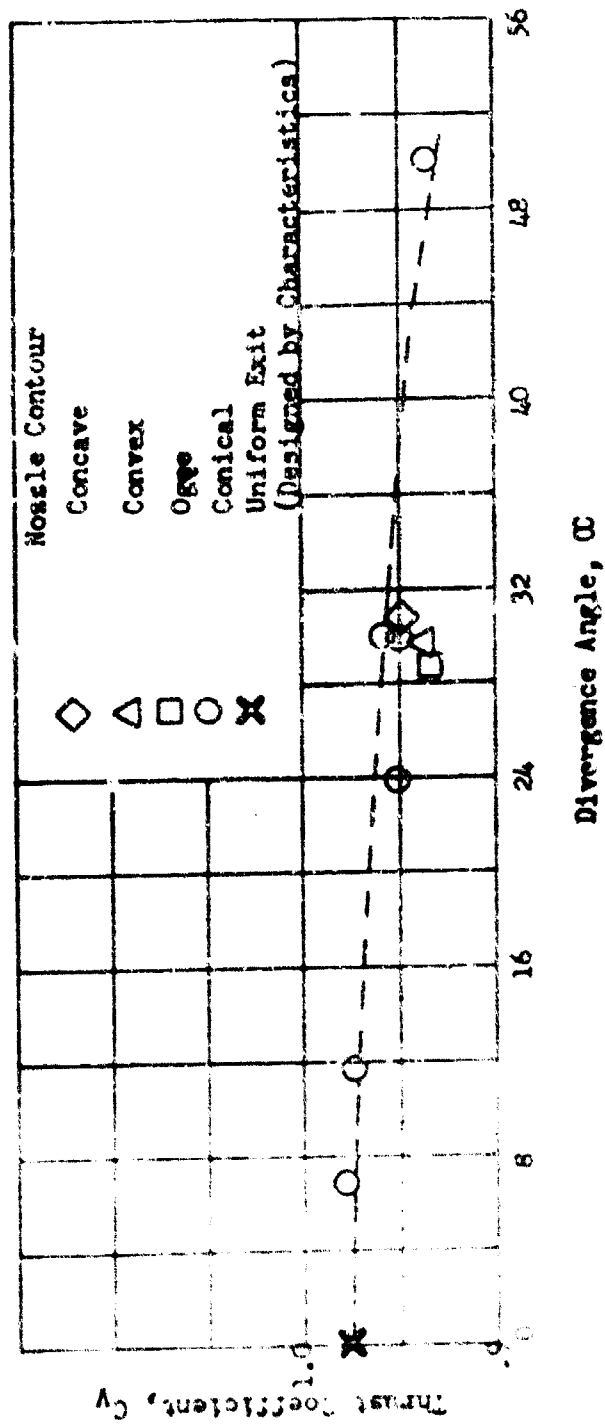


FIGURE 2-12 Variation of Thrust Coefficient with Various Nozzle Contours

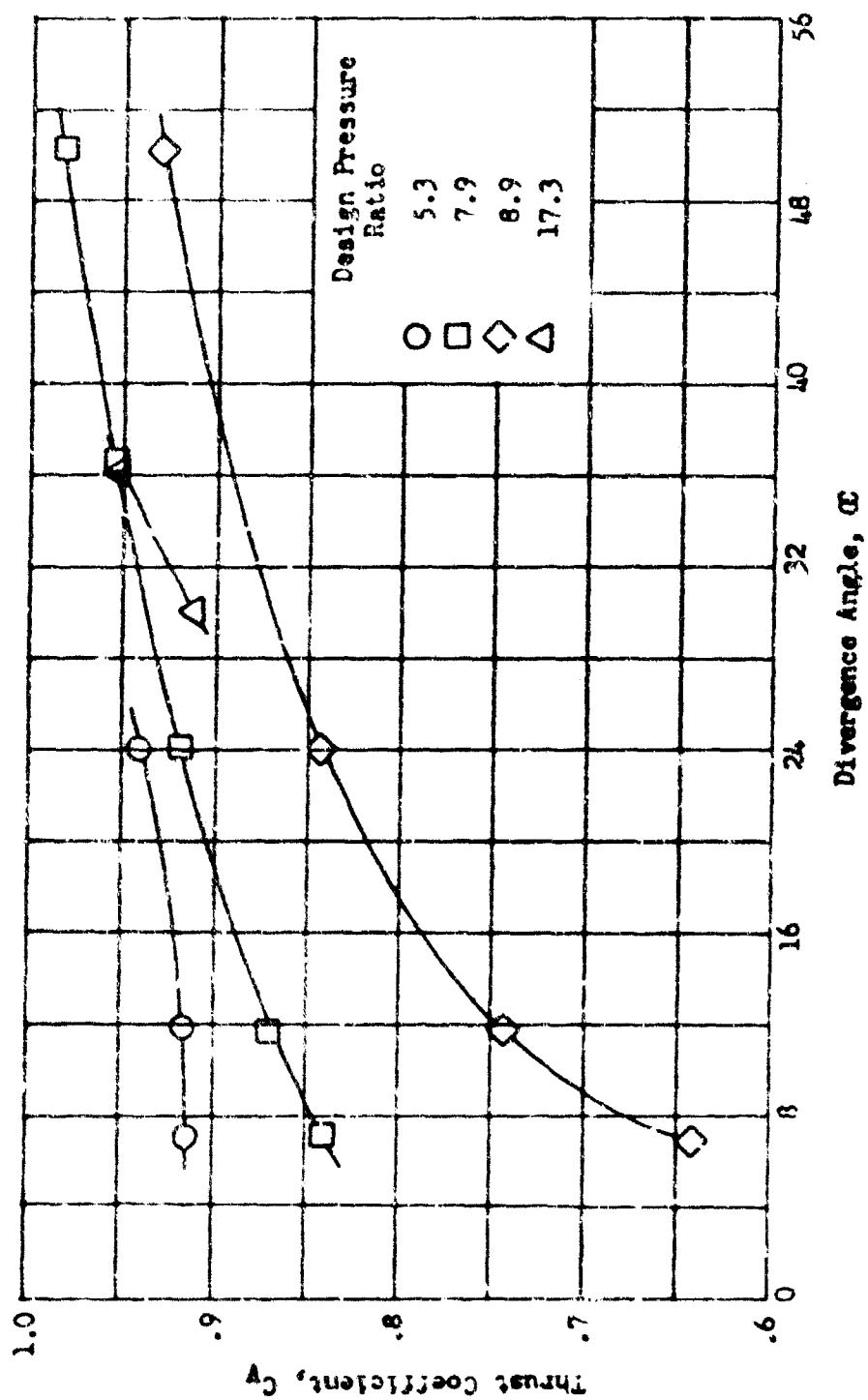
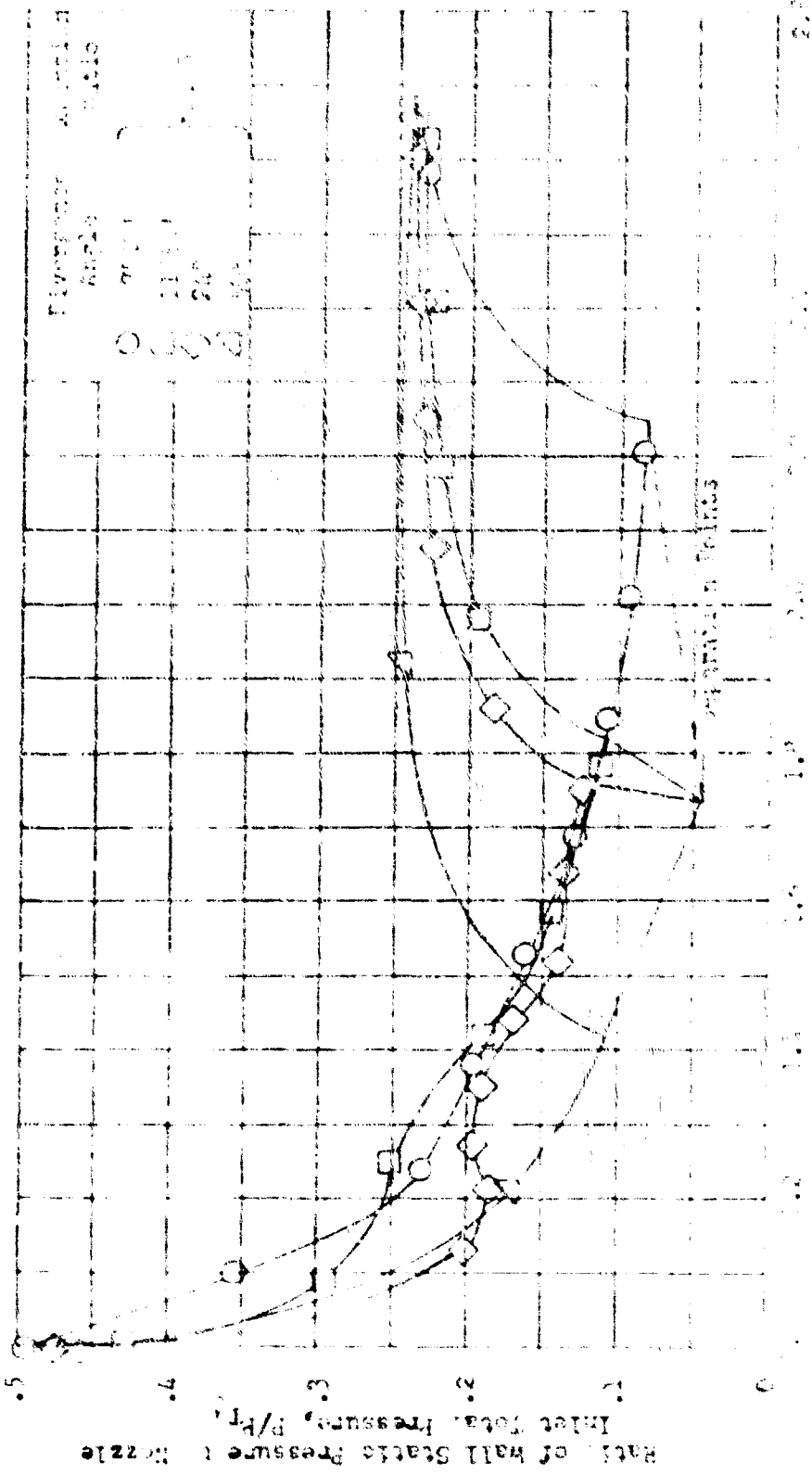


FIGURE 8 - 43. Variation in Thrust Coefficient at a Nozzle Pressure Ratio of 2.0 with Divergence Angle for Nozzles of Various Design Pressure Ratios.



151-8

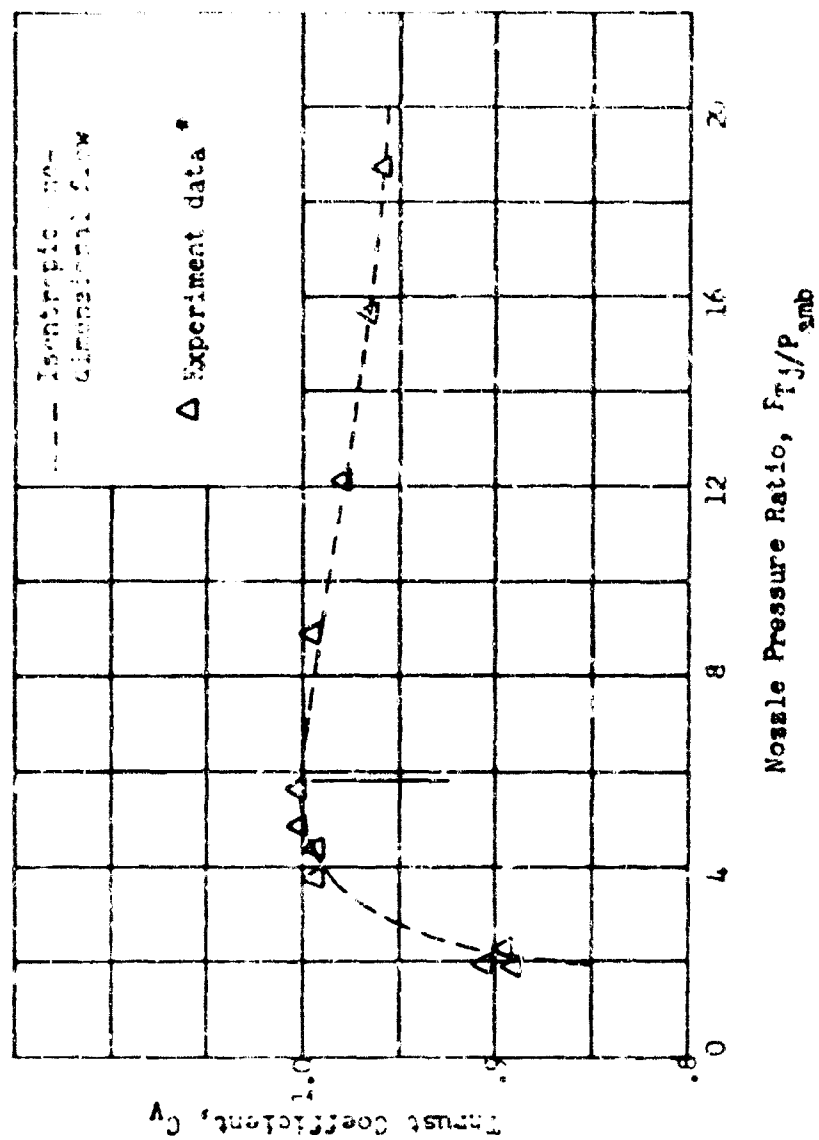


FIGURE 8 - 45. Variation of Thrust Coefficient for a Nozzle Designed by Characteristic Theory

* Note that friction effects are not measured to obtain data.

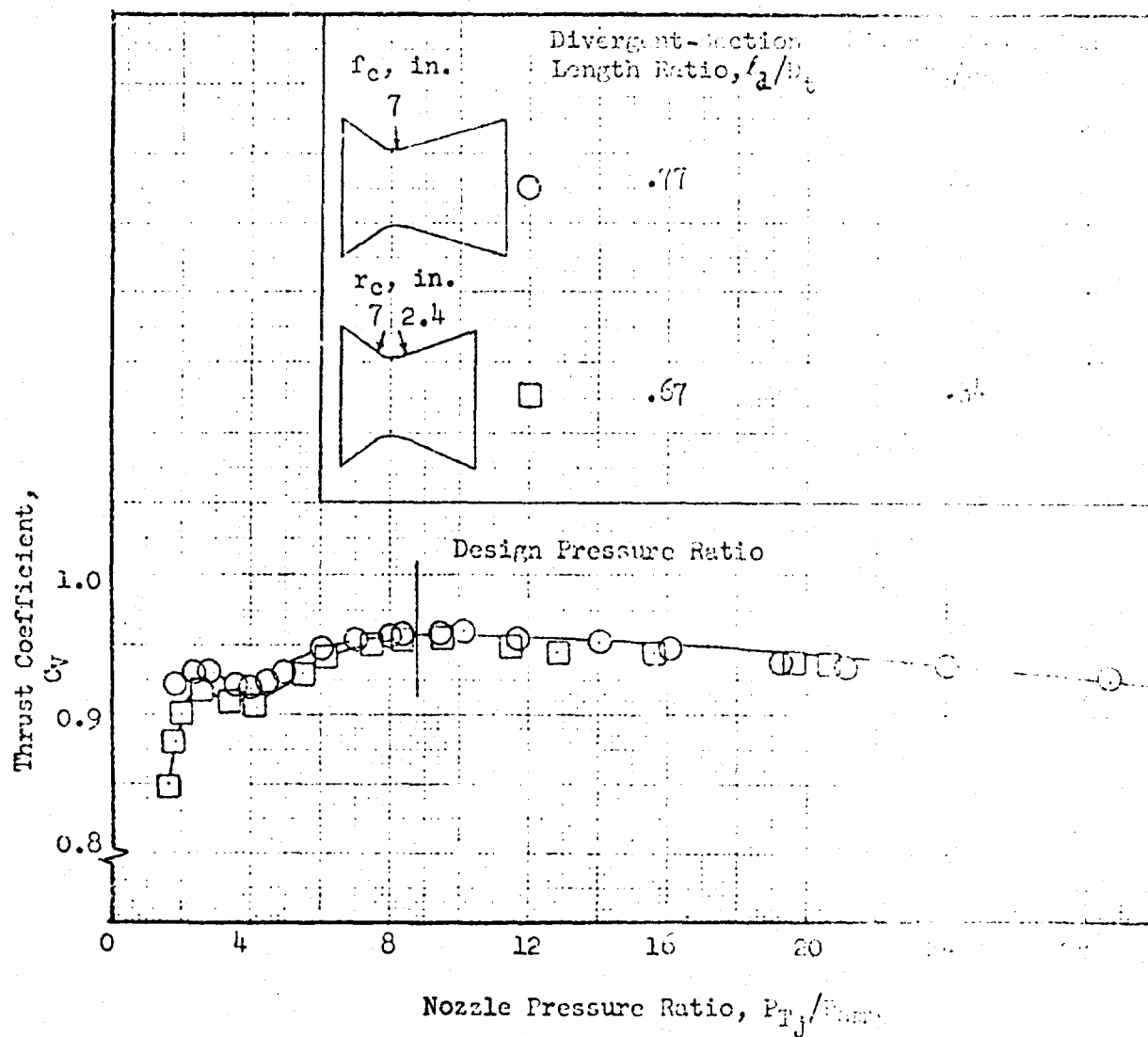


Figure 8 - 46. Thrust Coefficients for Two Nozzles having Different Throat Contours and Same Area of Throat; Expansion Ratio, 1.2

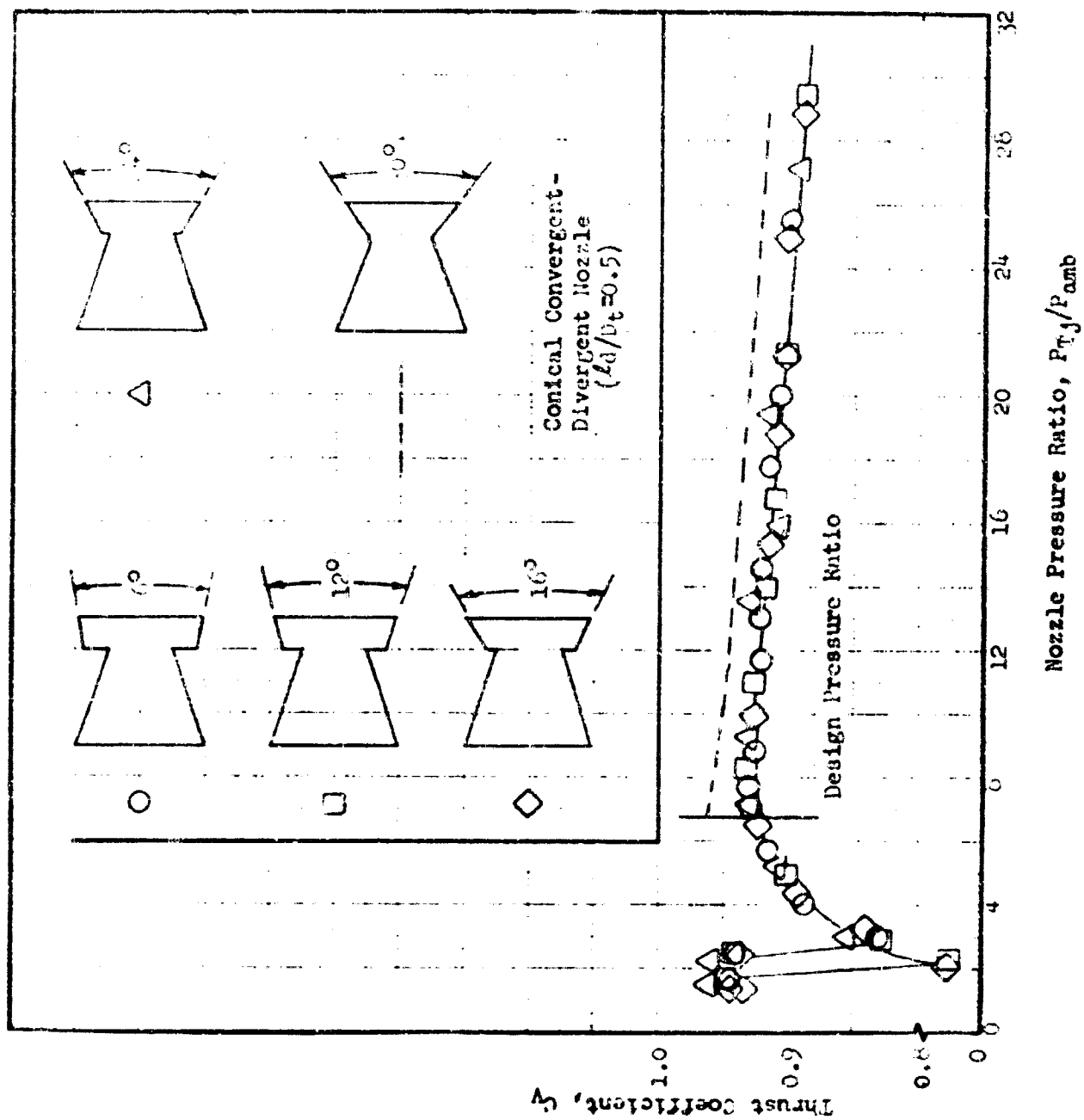
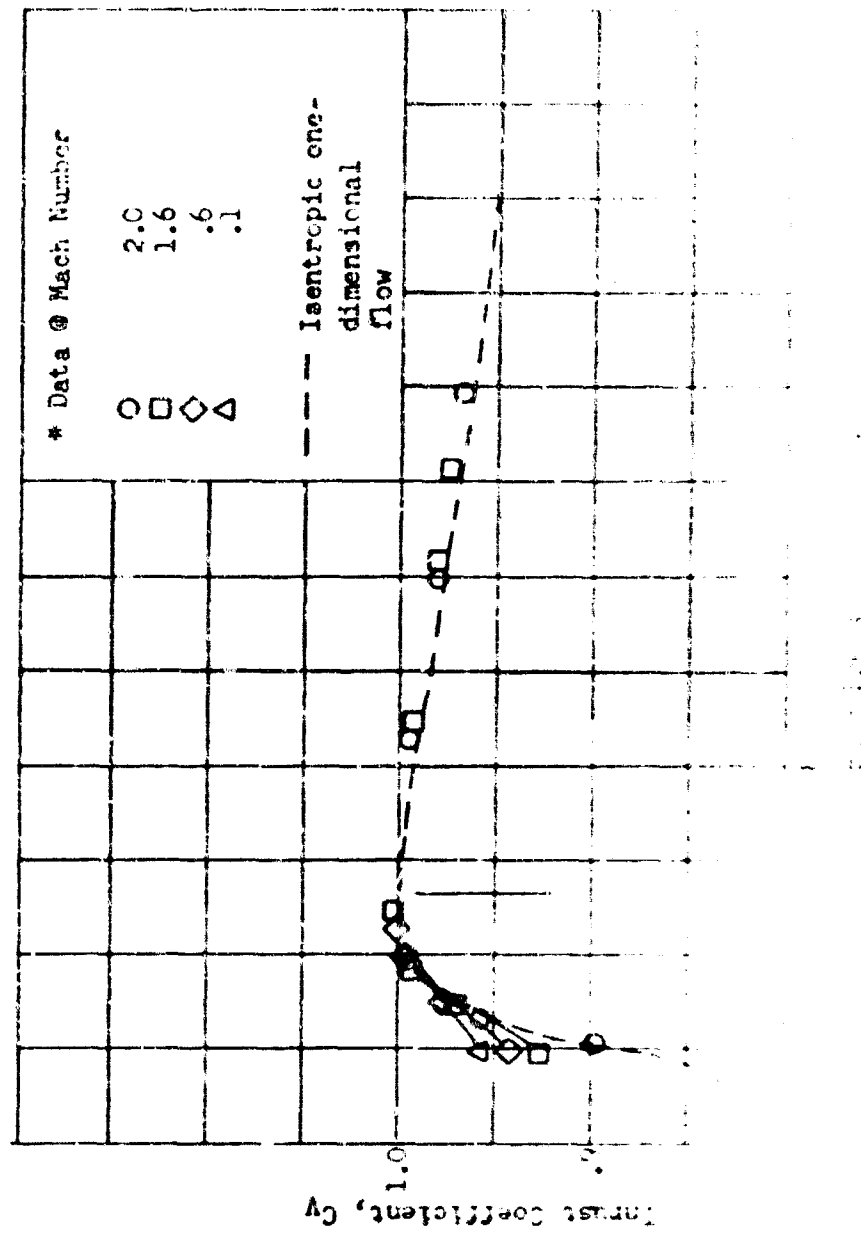


Figure 8 - 47. Thrust Coefficients for Nozzles having Various Wall Angles; Expansion Ratio = 1.55; $L_d/D_t = 0.5$



U.S. GOVERNMENT PRINTING OFFICE: 1964 O 345-155

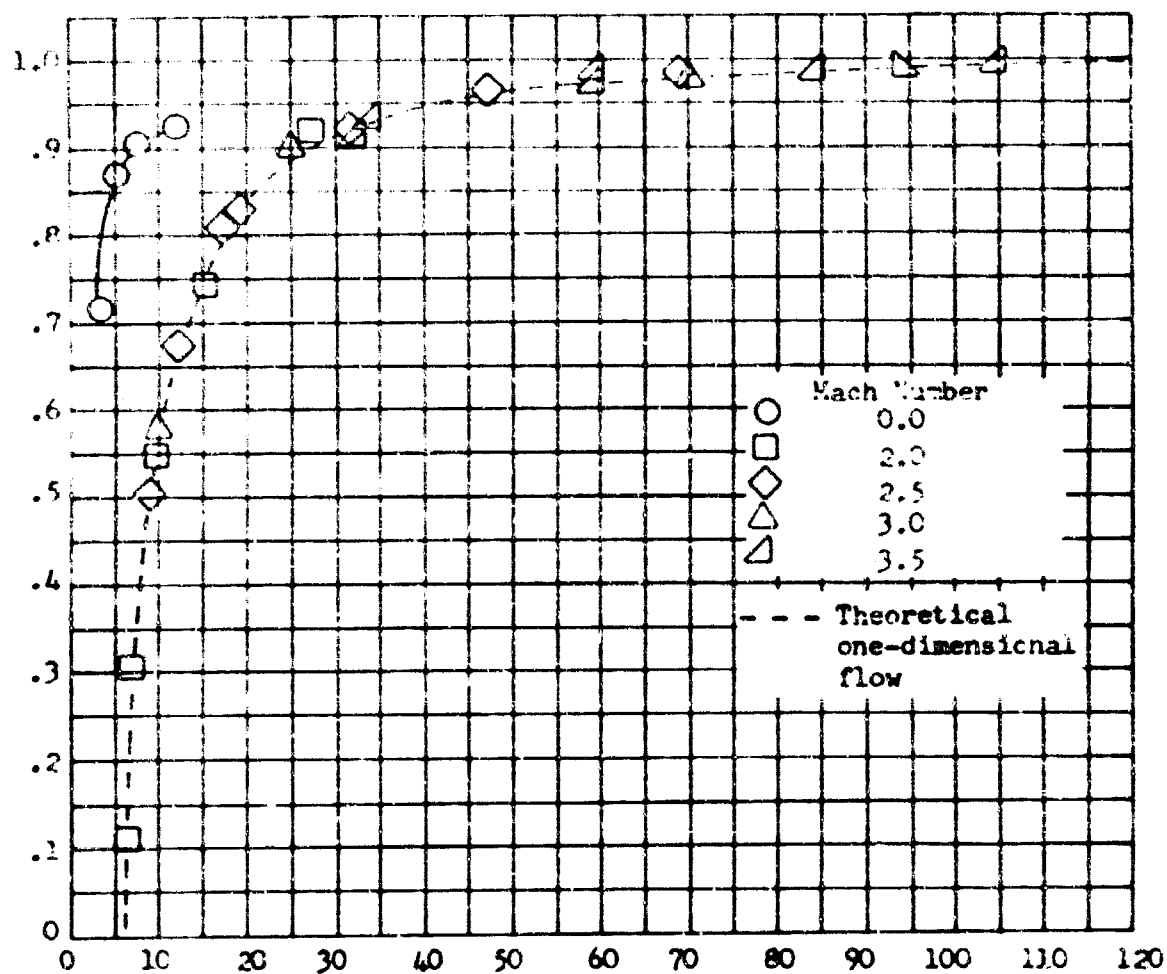


FIGURE 8 - 49. Nozzle Thrust Coefficient Characteristics for a Range of Freestream Mach Numbers; Expansion Rate = 9.0; Nozzle is Conical.

* Note that data do not include friction effects.

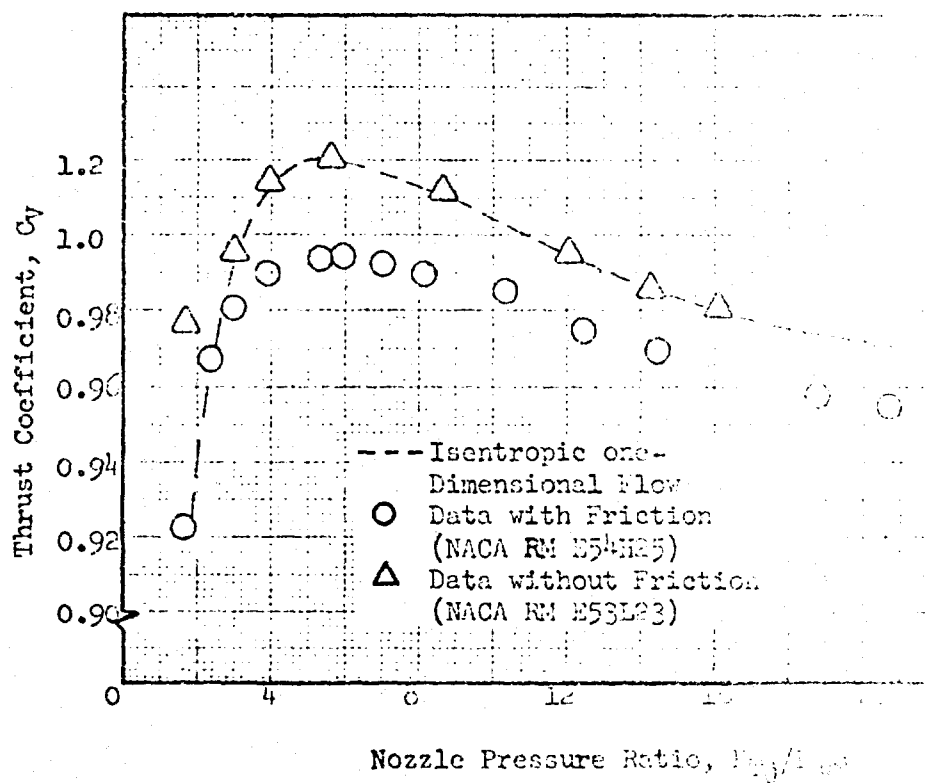


Figure 8 - 50. Friction Effects on a Convergent-Divergent Conical Nozzle; Nozzle Pressure Ratio, 1.39; Divergence Angle, 10° .

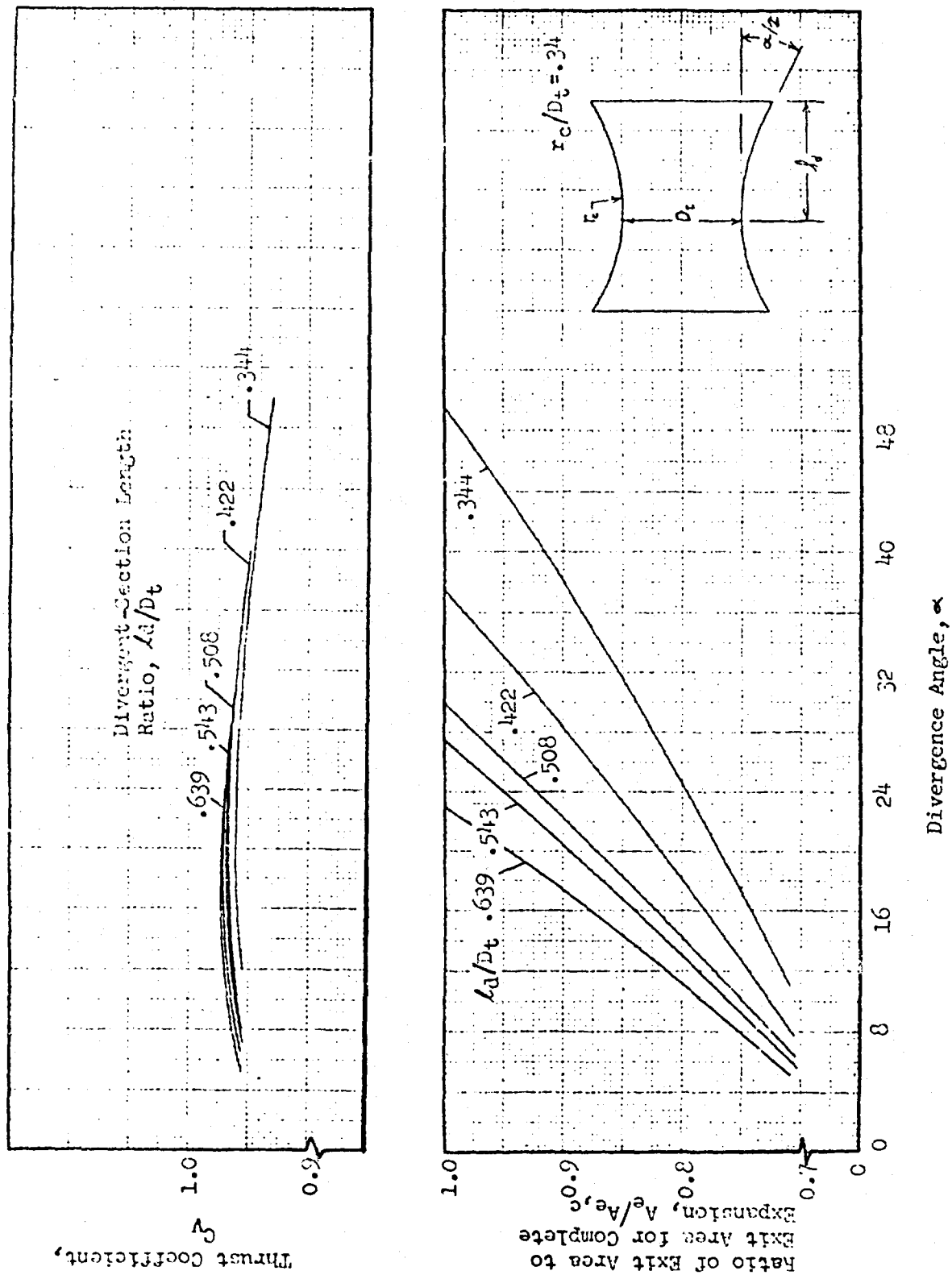


Figure 8 - 51. Variation in Thrust Coefficient and Nozzle-Exit Area Resulting from Decreases in Divergent Angle.

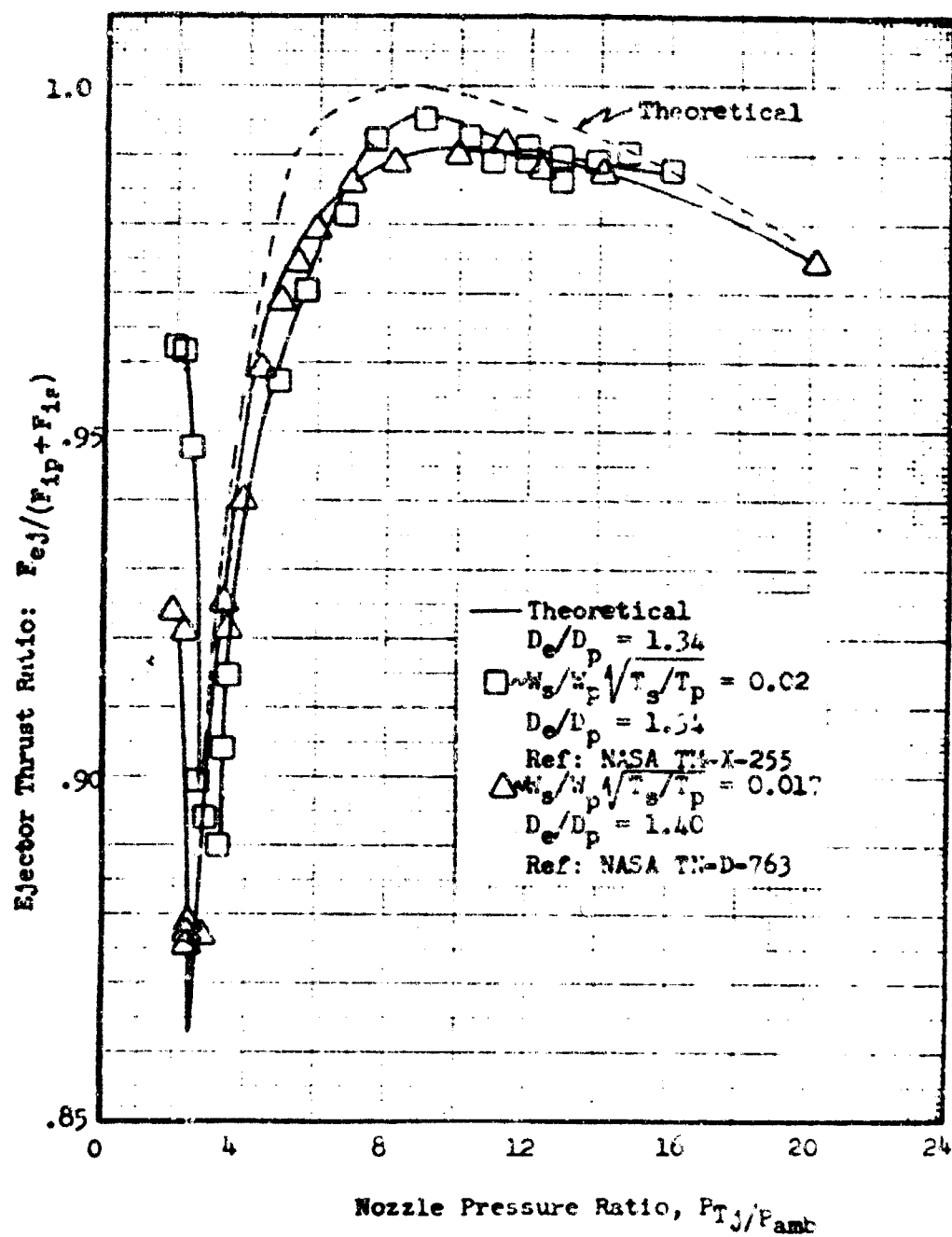
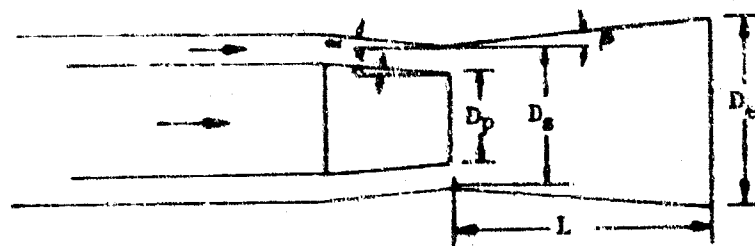


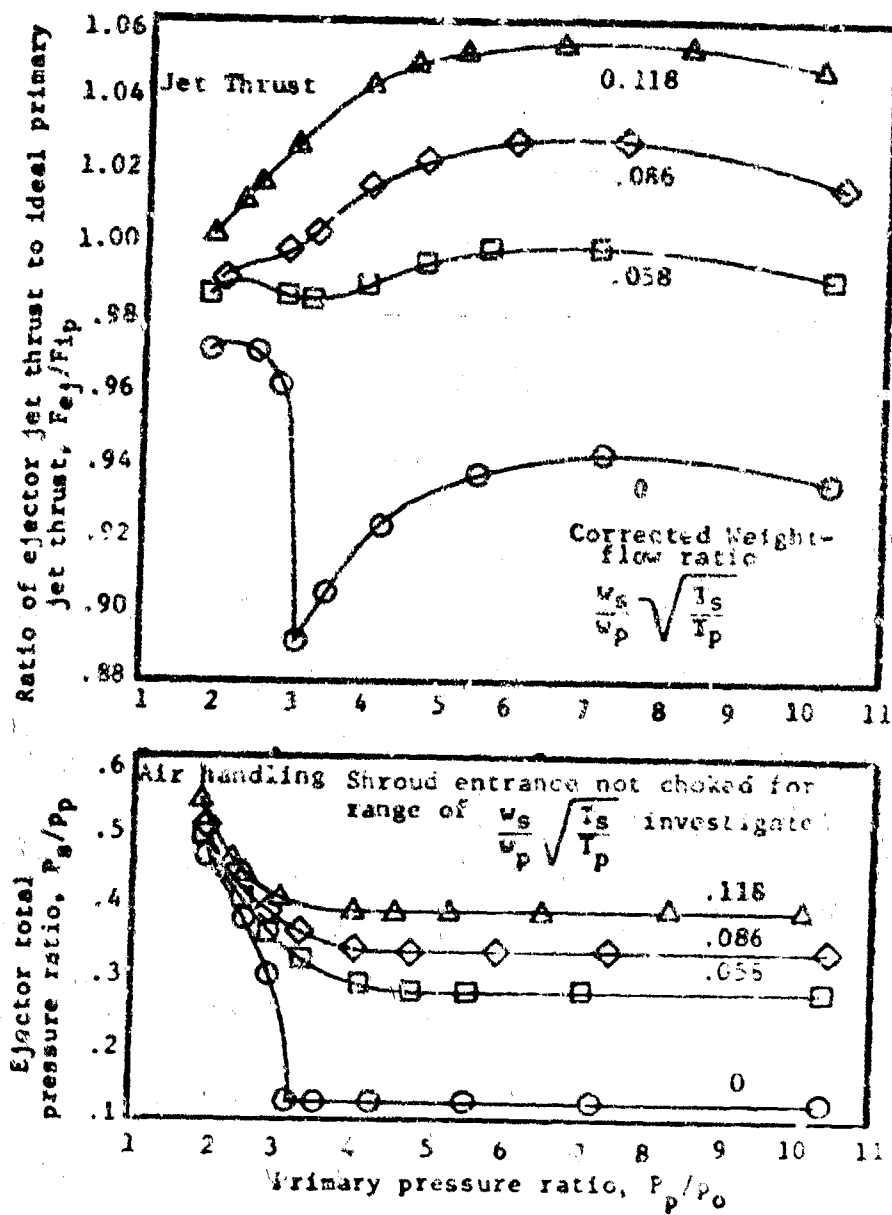
Figure 8-52 . Comparison of Theoretical and Experimental Thrust Variation.



$D_p = 0.01$ in. inside
 $= 6.15$ in. outside

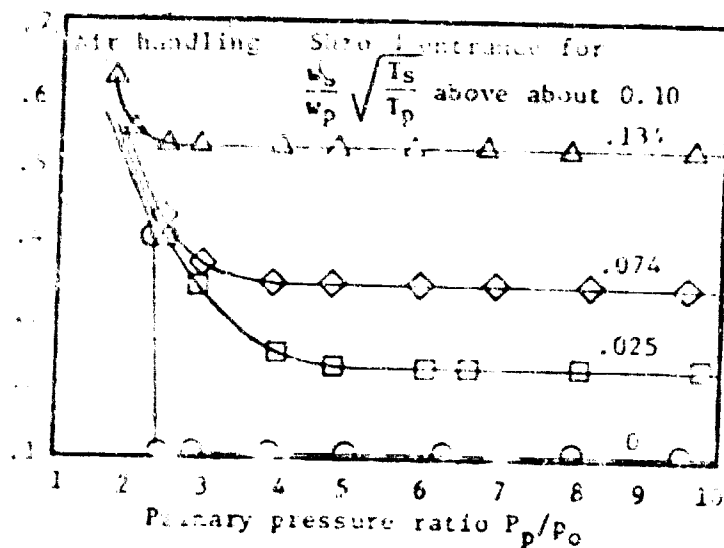
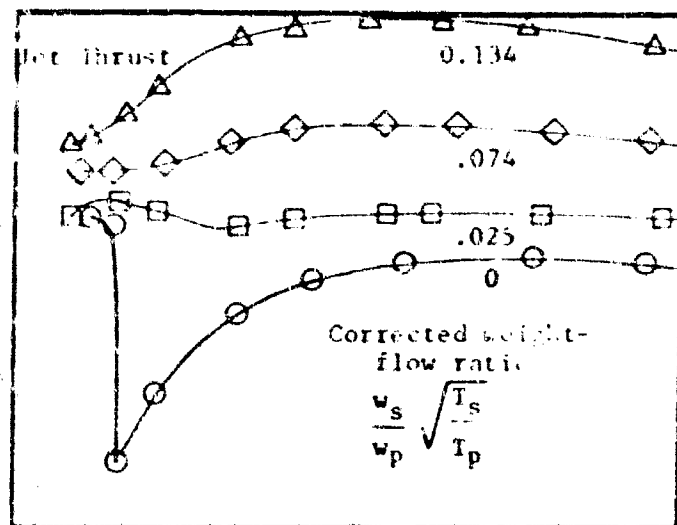
Series	Ejector	Exit diameter ratio D_e/D_p	Inlet diameter ratio D_s/D_p	Spacing ratio, L/D_p	Divergence angle, β	Approach angle α	Data in figure
VII-1	1	1.24	1.20	0.45	$2^\circ 51'$	$15^\circ 36.6'$	3(a)
	2	1.23	1.15	.47	$5^\circ 38'$	$17^\circ 24.5'$	(c)
	3	1.23	1.04	.47	$11^\circ 31'$	$20^\circ 9.45'$	(c)
	4	1.44	1.21	1.06	$6^\circ 22'$	$16^\circ 1.01'$	(d)
	5	1.45	1.09	1.06	$9^\circ 25'$	$19^\circ 7.12'$	(e)
	6	1.46	1.09	1.07	$9^\circ 39'$	90°	(f)
	7	1.70	1.34	1.07	$9^\circ 23'$	$11^\circ 54.9'$	(g)
	8	1.82	1.26	1.91	$8^\circ 20'$	$13^\circ 53.88'$	(h)
	9	1.81	1.21	1.91	$8^\circ 58'$	$15^\circ 28.47'$	(i)
	10	1.82	1.10	1.90	$13^\circ 34'$	$19^\circ 4.07'$	(i)
VIII-1	11	1.10	1.13	0.80	0°	90°	4(a)
	12	1.46	1.46	2.12	0°	90°	(b)

51 -53 Ejector Configurations of NACA RM E55C21a



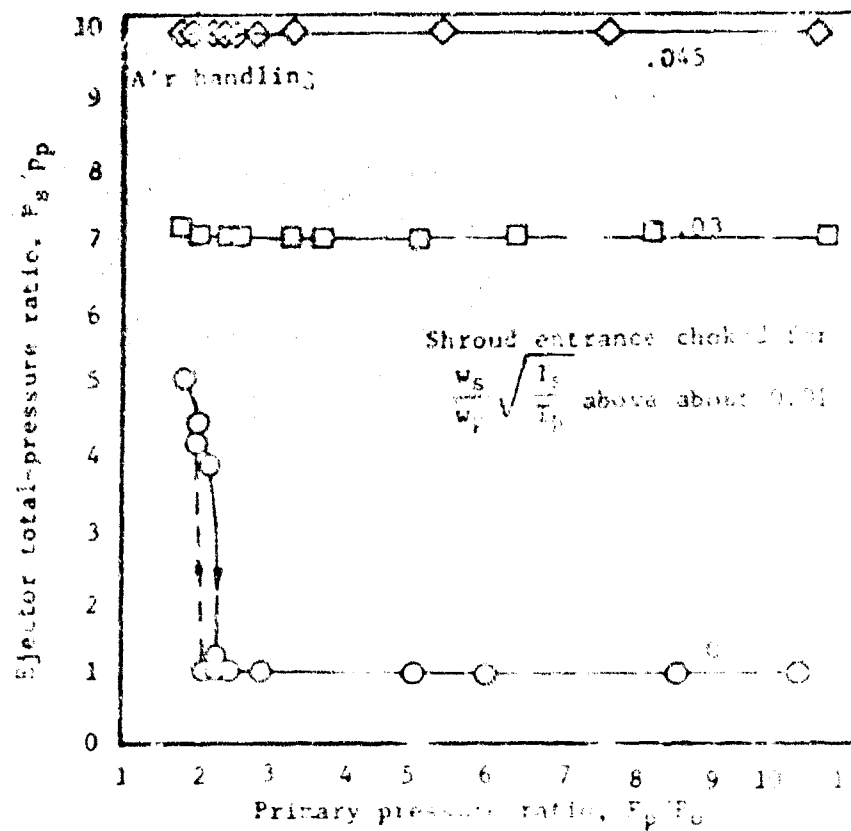
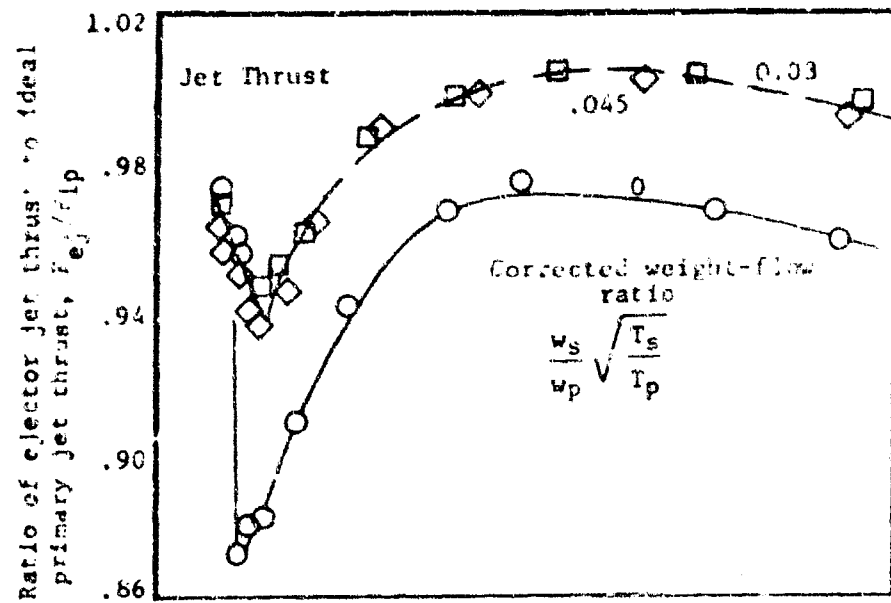
(a) Ejector 1.

FIGURE 8-54 Test Results of Ejector 1 of NACA FM E55621a



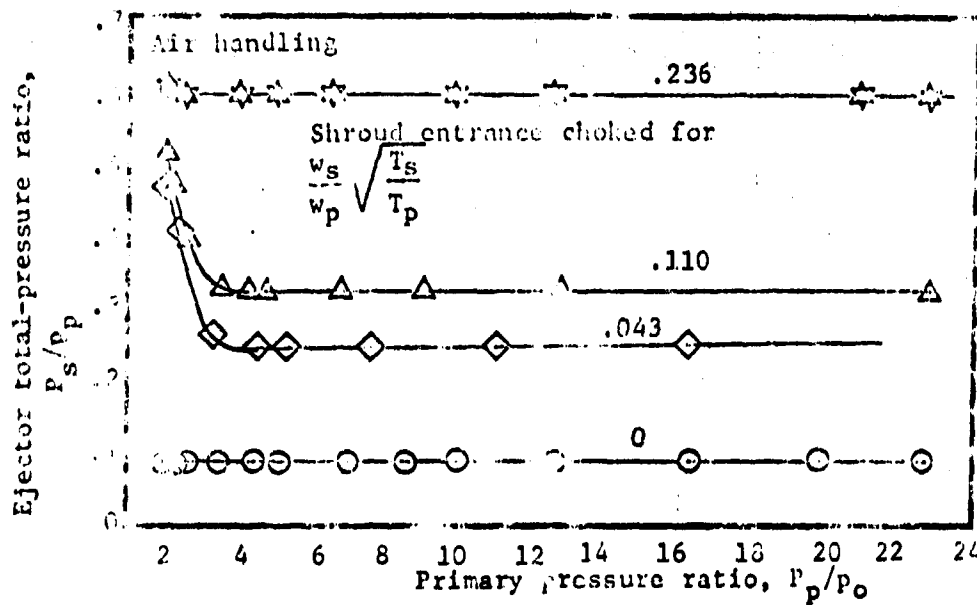
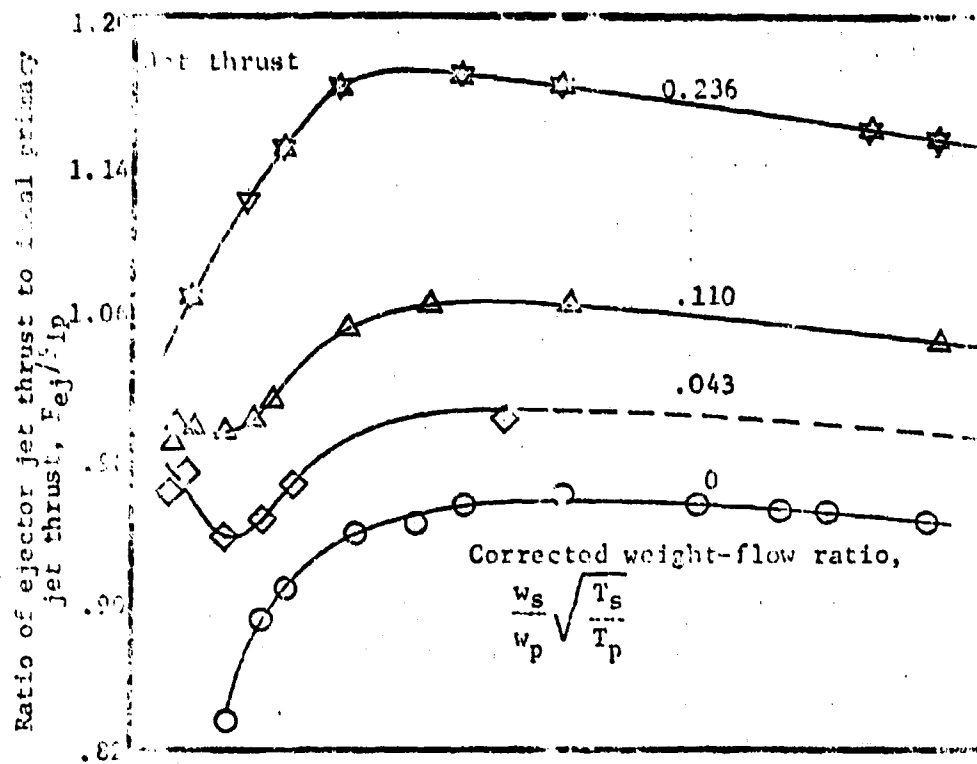
(b) Ejector 2

Fig. 15 -55 Test Results of Ejector 2 of NACA Report 1131



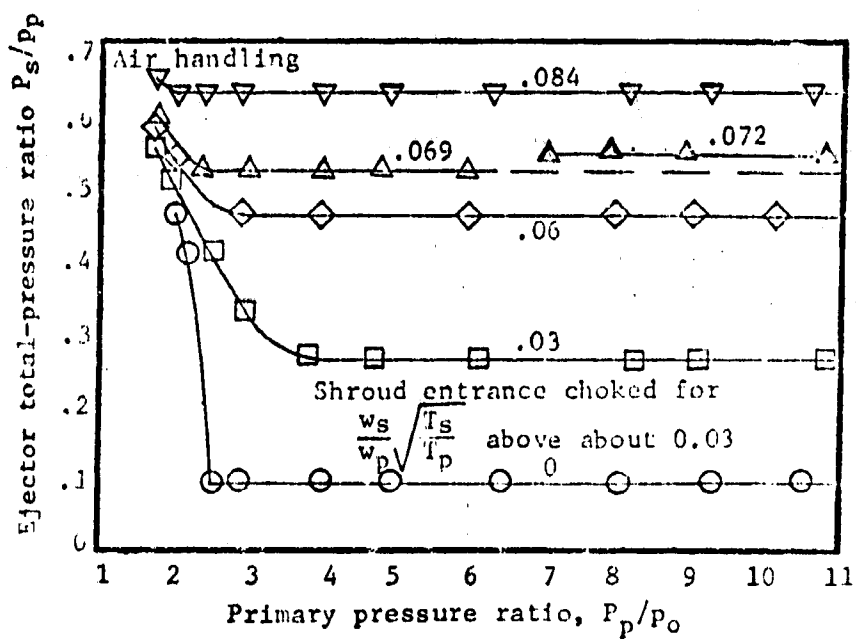
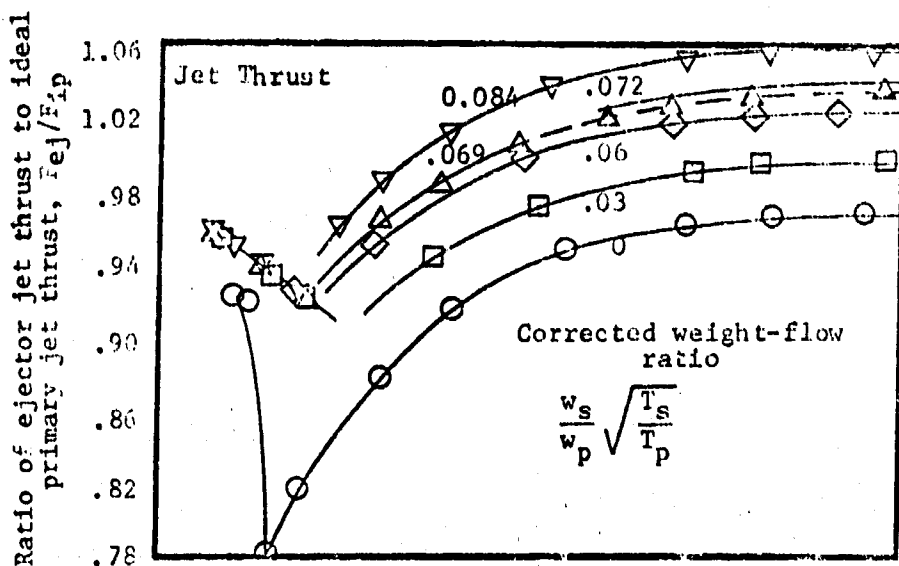
(c) Ejector 3

FIGURE 8-56 Test Results of Ejector 3 of NACA E-100-1



(d) Ejector 4

FIGURE 8-57 Test Results of Ejector 4 of NACA RM E55621a



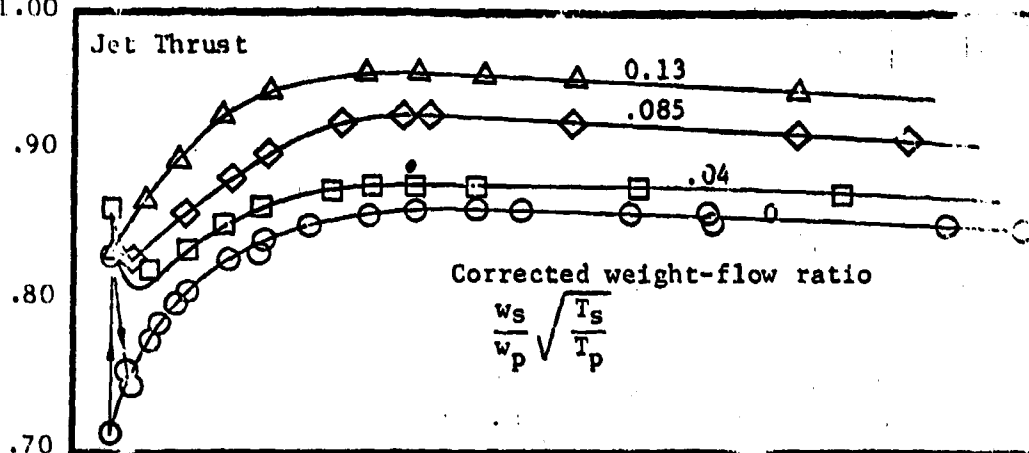
(e) Ejector 5

FIGURE 8-58 Test Results of Ejector 5 of NACA RM E55-121a

Ratio of ejector jet thrust to ideal
primary jet thrust, F_{ej}/F_{ip}

1.10

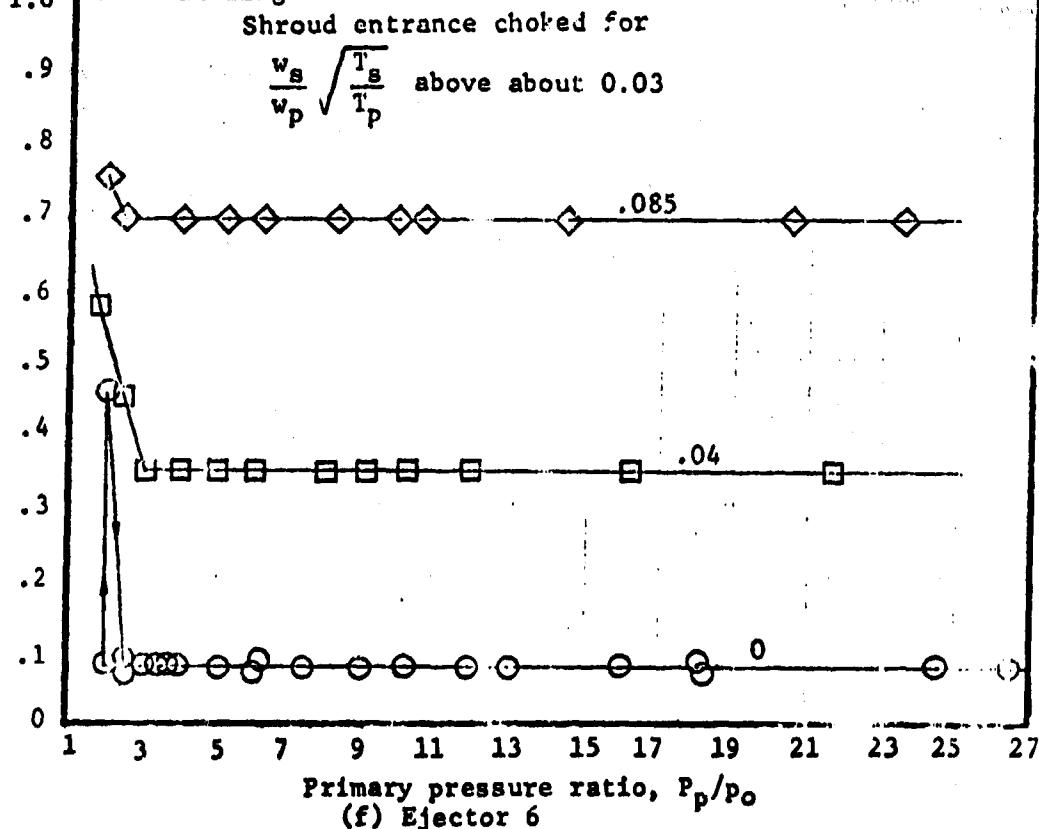
1.00



Ejector total-pressure ratio, P_s/P_p

1.1

1.0



(f) Ejector 6

FIGURE 8-59 Test Results of Ejector 6 of NACA RM E55G21a

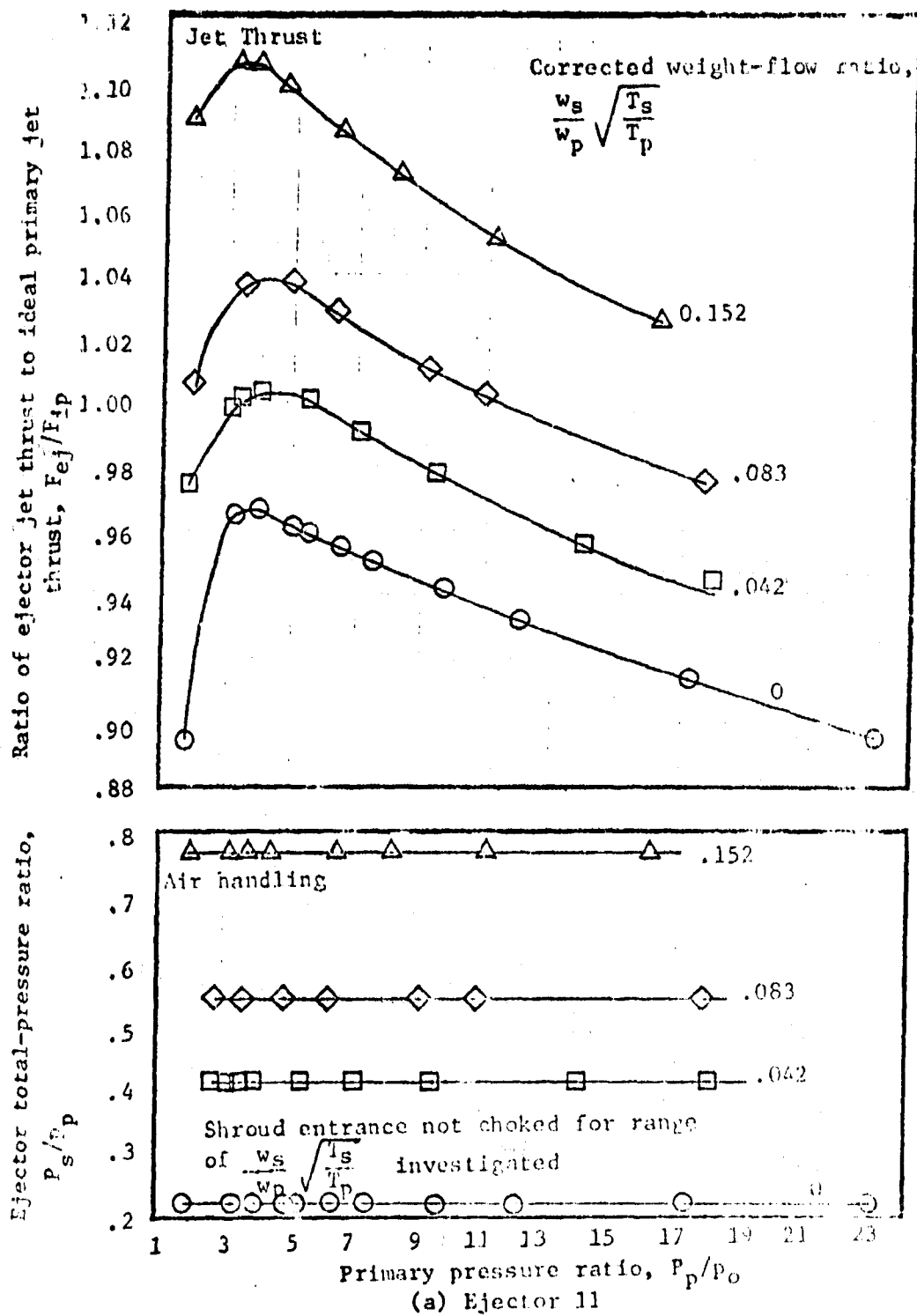


FIGURE 8.60 Test Results of Ejector 11 of NACA RM 54-621a

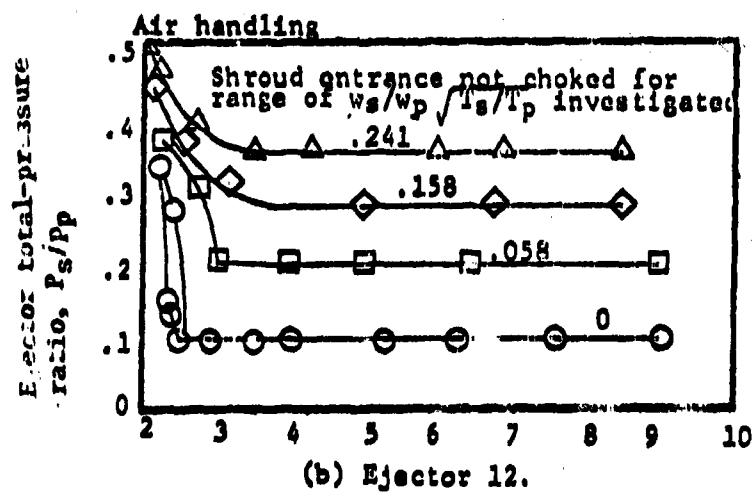
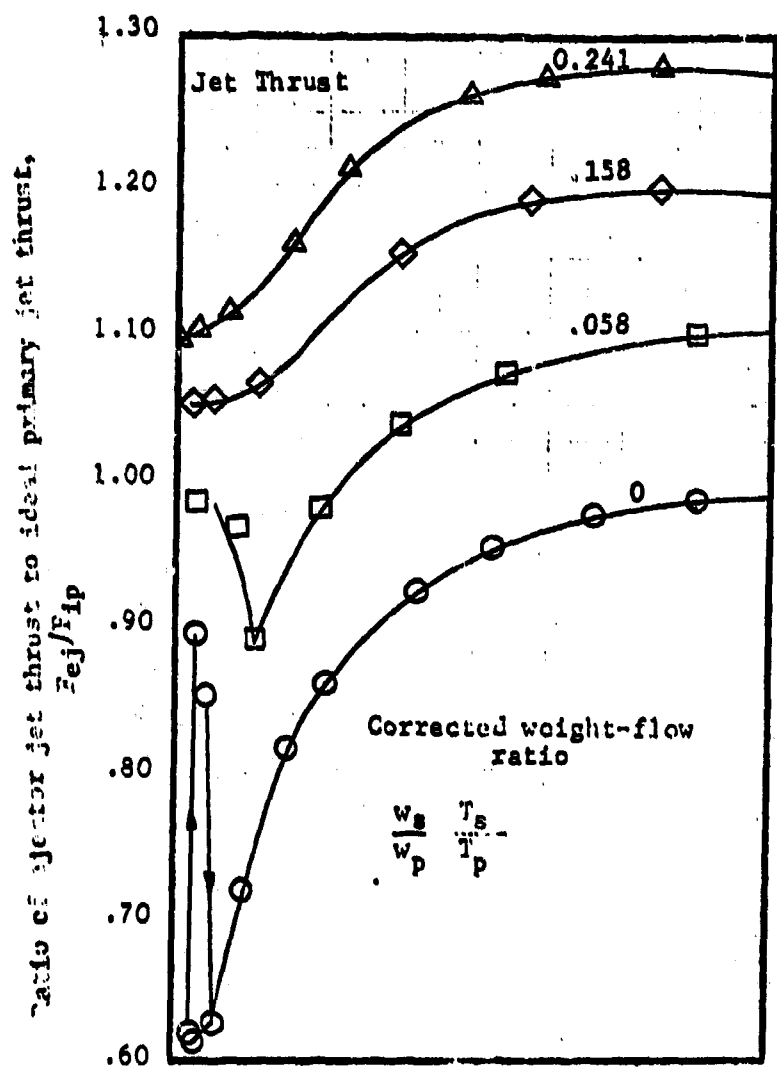
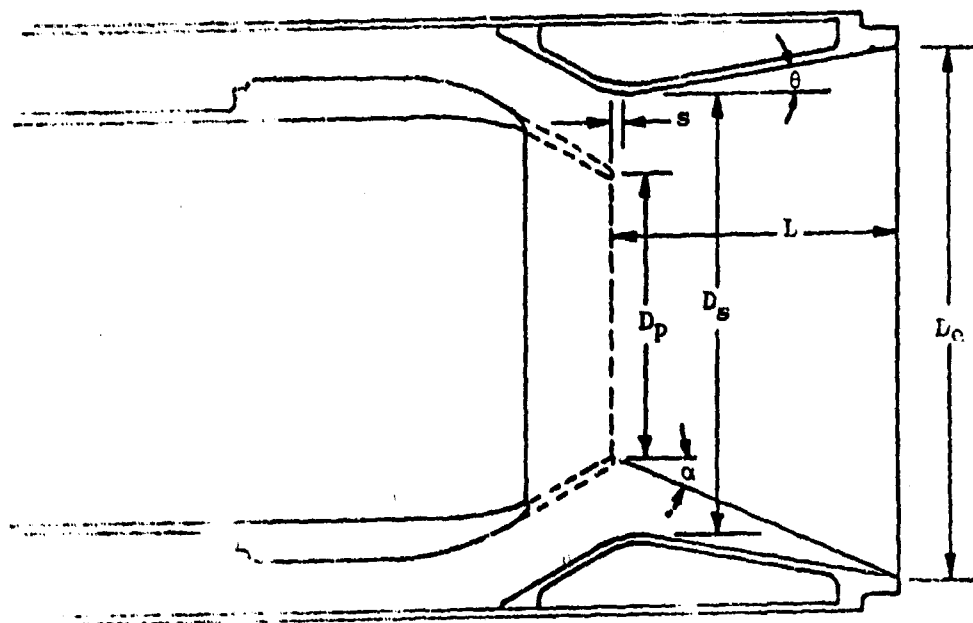
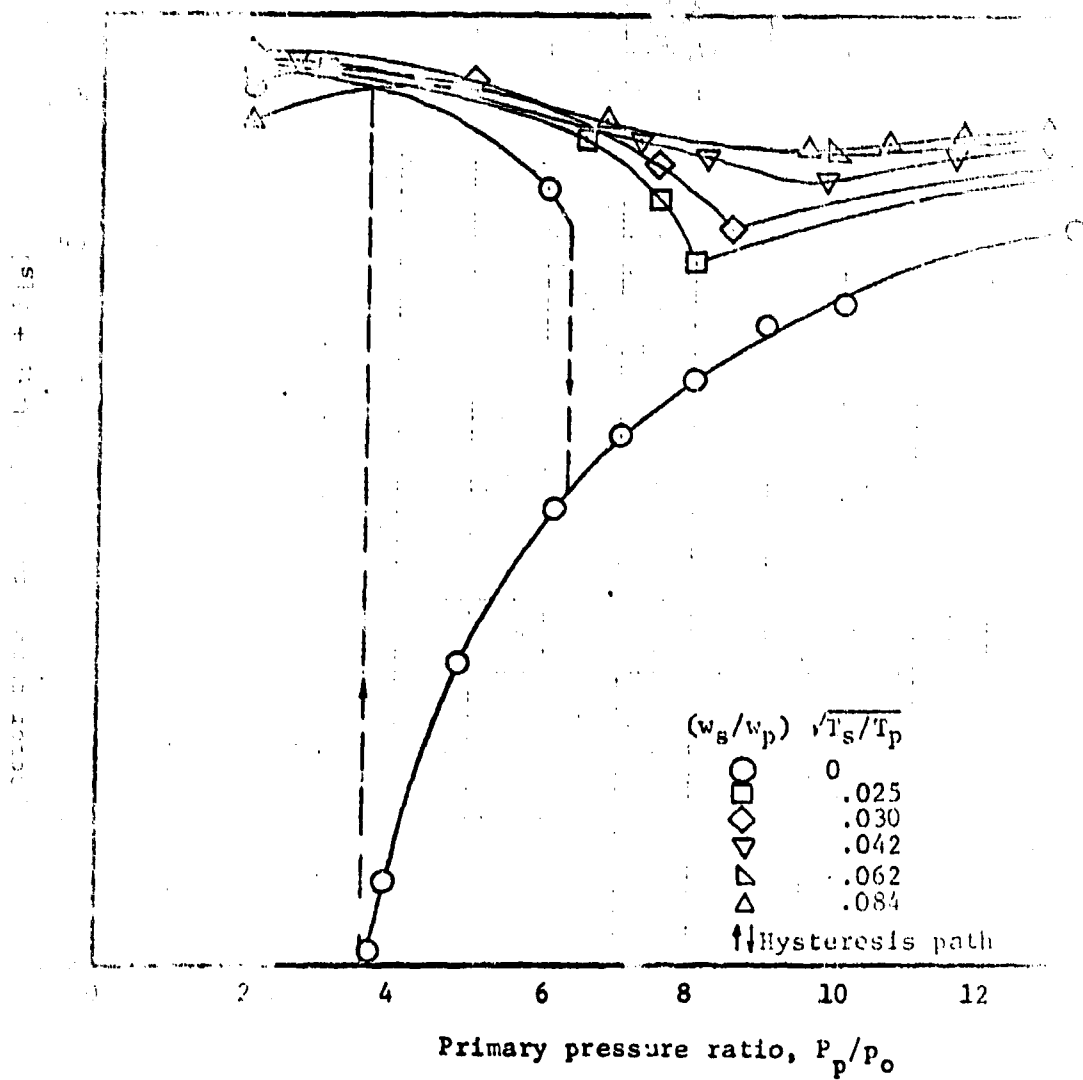


FIGURE 8-61 Test Results of Ejector 12 of NACA RM E59G21a



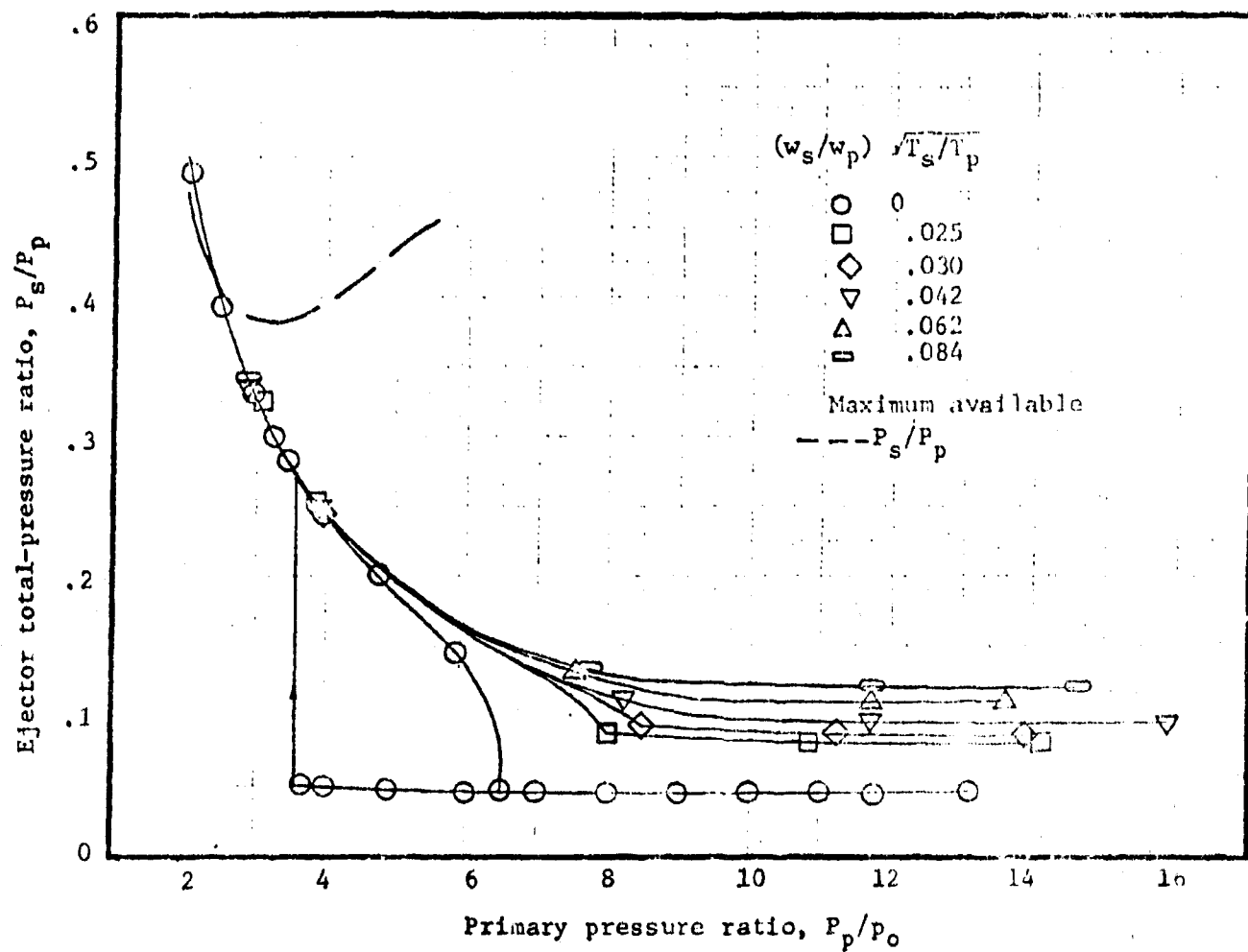
Ejector	Configuration	D_p in.	$\frac{D_e}{D_p}$	$\frac{D_s}{D_p}$	$\frac{L}{D_p}$	$\frac{s}{D_p}$	θ , deg	α , deg	D_e	D_s	s
1	Nonafterburning	7.31	1.84	1.52	1.05	0.096	10	21.8	13.45	11.1	.702
2	Nonafterburning modified	7.31	1.84	1.52	1.24	.284	10	18.7	13.45	11.1	2.977
3	Afterburning	9.59	1.40	1.16	1.01	.28	10	11.2	13.45	11.1	2.685
4	Afterburning modified	9.59	1.40	1.16	1.15	.42	10	9.9	13.45	11.1	4.05

FIGURE 8-62 Ejector Geometry of NASA TN D-763



(a) Nonafterburning; L/D_p , 1.05

FIGURE 8-63 Performance of Ejector 1 of NASA TN D-763



(a) Nonafterburning; L/D_p , 1.05

FIGURE 8-64 Pumping Performance of Ejector 1 of NASA TN D-763

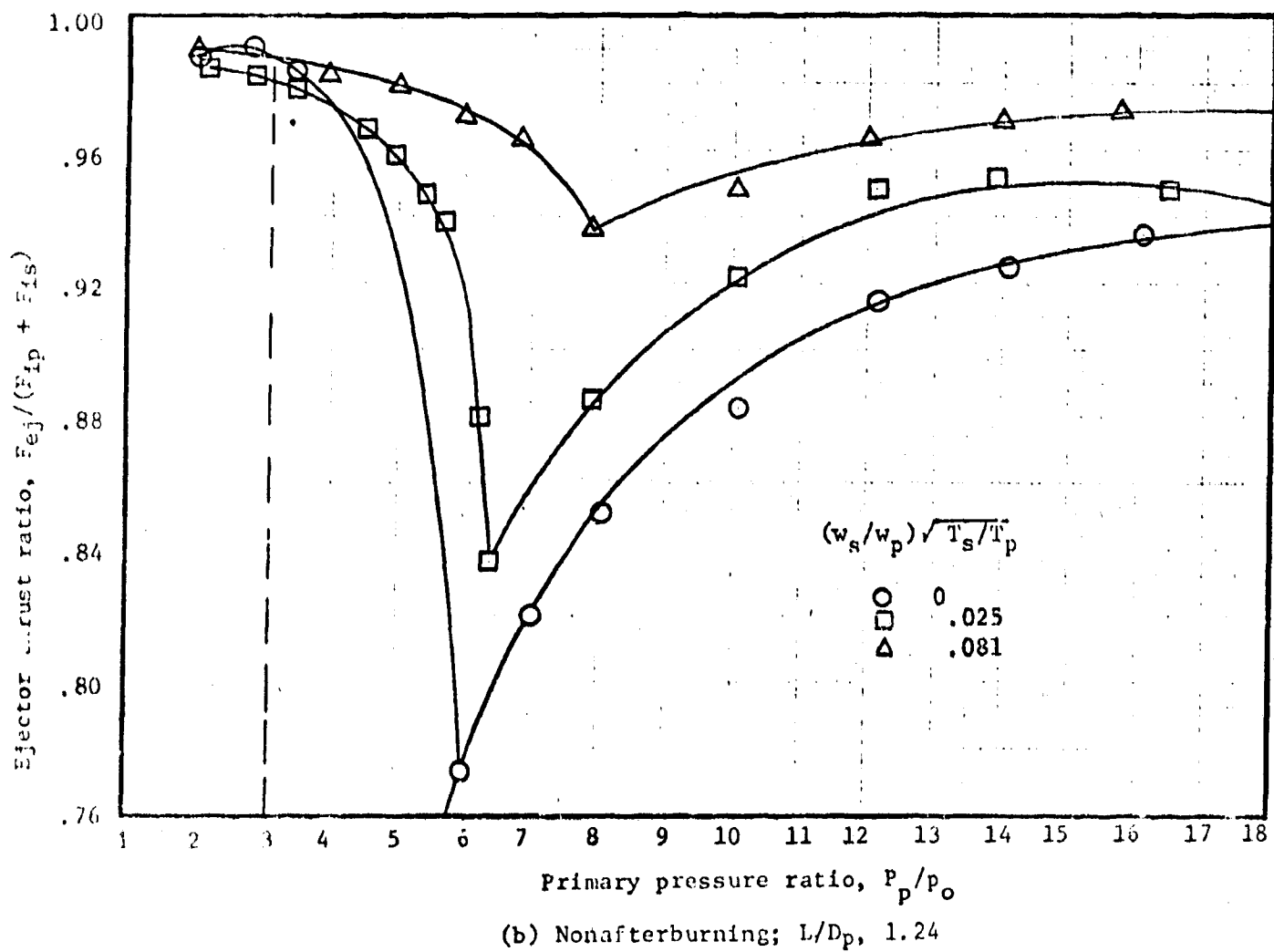
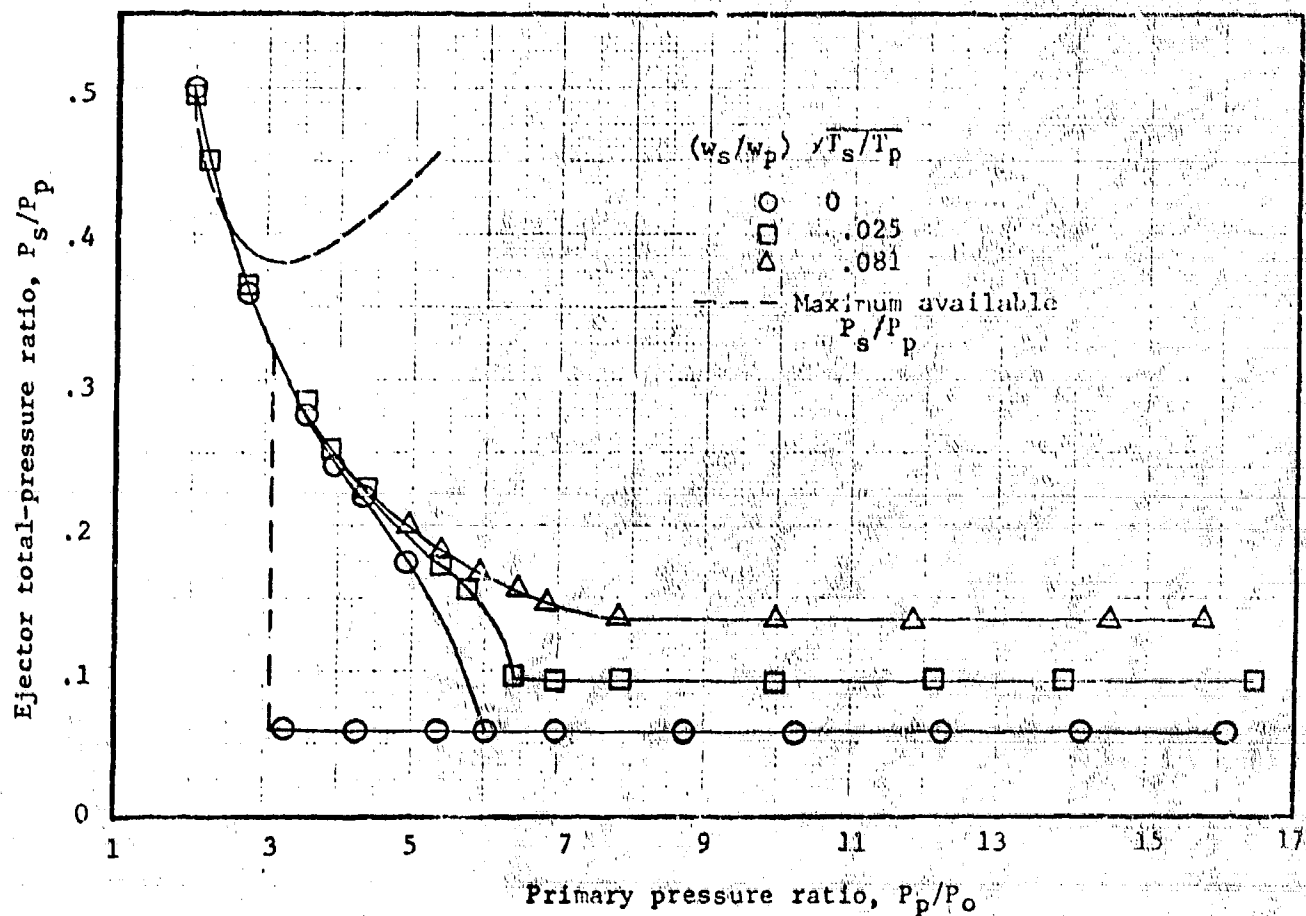


FIGURE 8-65 Performance of Ejector 2 of NASA TN D-763



(B) Nonafterburning; L/D_p , 1.24

FIGURE 8-66 Pumping Performance of Ejector 2 of NASA TN D-763

Engine	Power	Alt.	Mo	T_{T2}	T_{Tsec}	T_{Tjet}	$\frac{T_{Tsec}}{T_{Tj}}$	$\frac{T_{Ts}}{T_{Tj}}$
Fan	Dry	36089	.8	440	490	970	.505	.713
Jet	Dry	36089	.8	440	490	1605	.306	.554
Fan/Jet	A/B	36089	2	702	752	3500	.215	.463
Fan/Jet	A/B	36089	1.2	502	552	3500	.158	.398
Fan/Jet	A/B	36089	.8	440	490	3500	.14	.374
Fan/Jet	A/B	36089	2	702	752	3660	.2055	.453

Free stream total temperature is increased usually 50 to 100°F to account for engine compartment heating.

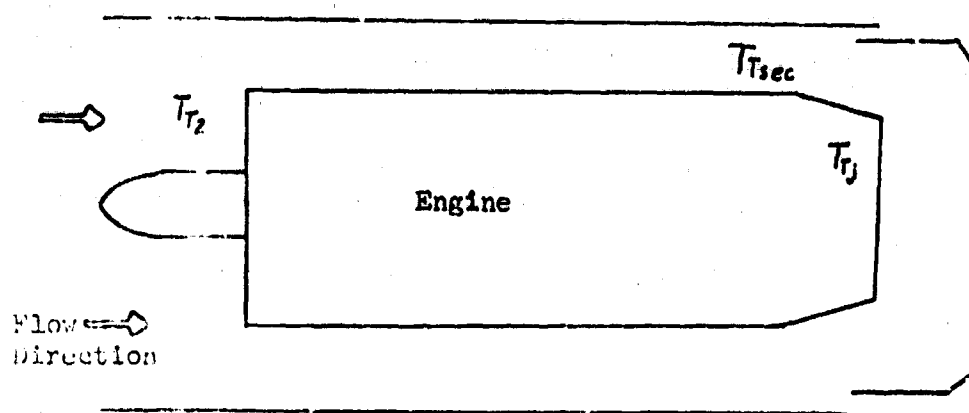
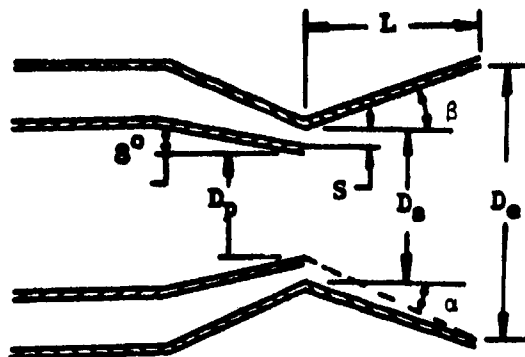


FIGURE 8- 67 Corrected Ejector Temperature Ratios For Typical Conditions



Config- uration	Exit diameter ratio, D_e/D_p	Throat diameter ratio, D_s/D_p	Annulus ratio, S/D_p	Shroud divergence angle, β deg.	Flow divergence angle, α deg.	Spacing ratio, L/D_p
1	1.24	1.08	0.024	15	18	0.38
2	1.24	1.08	.024	20	23	.28
3	1.24	1.08	.024	25	28	.22
4	1.46	1.10	.036	15	19	.69
5	1.46	1.10	.036	20	25	.51
6	1.46	1.10	.036	25	30	.40
7	1.82	1.10	.038	15	17	1.31
8	1.81	1.10	.038	20	23	.98
9	1.81	1.10	.038	25	29	.76

FIGURE 8 -68 Ejector Configurations
NACA RM E57F13

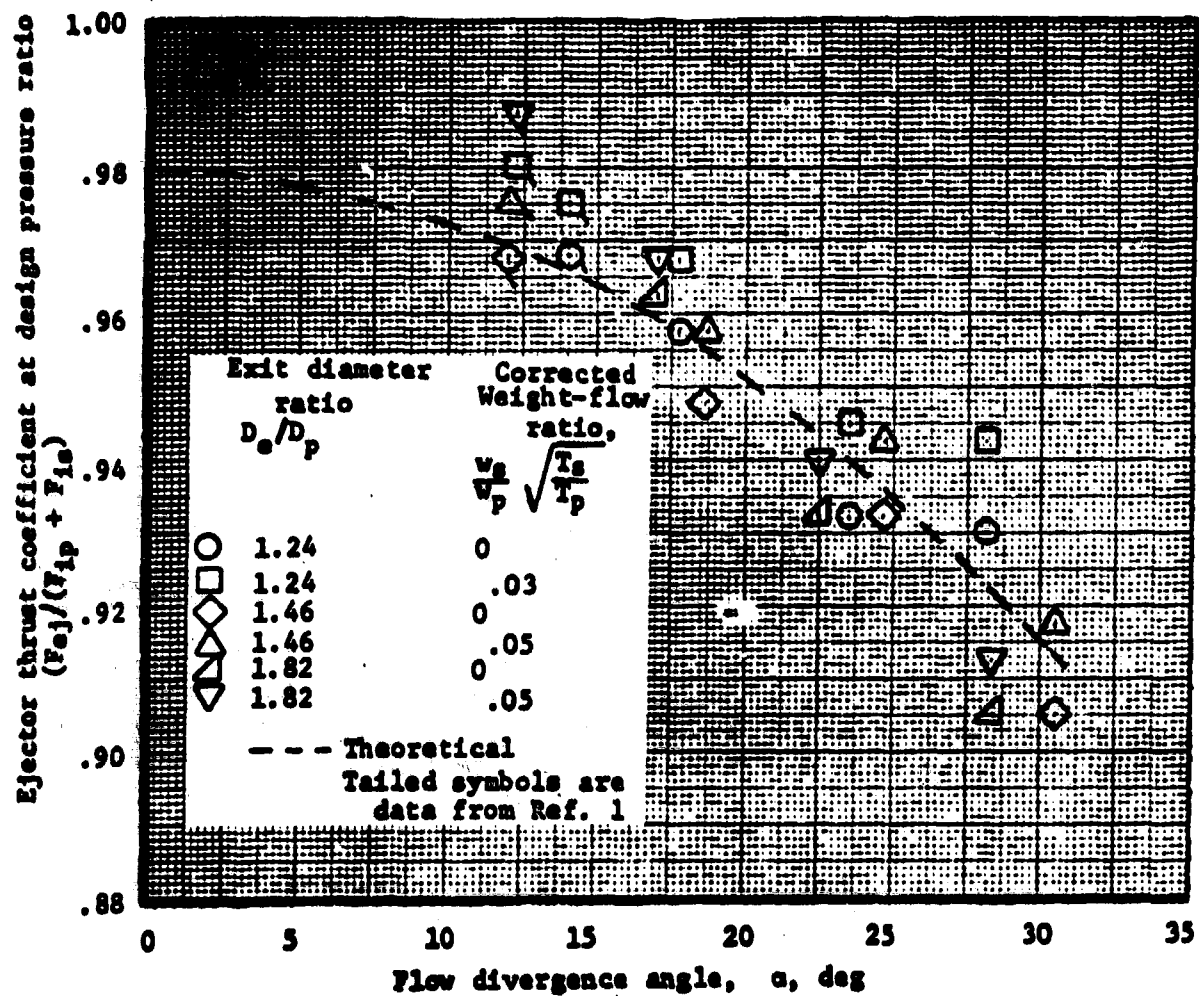
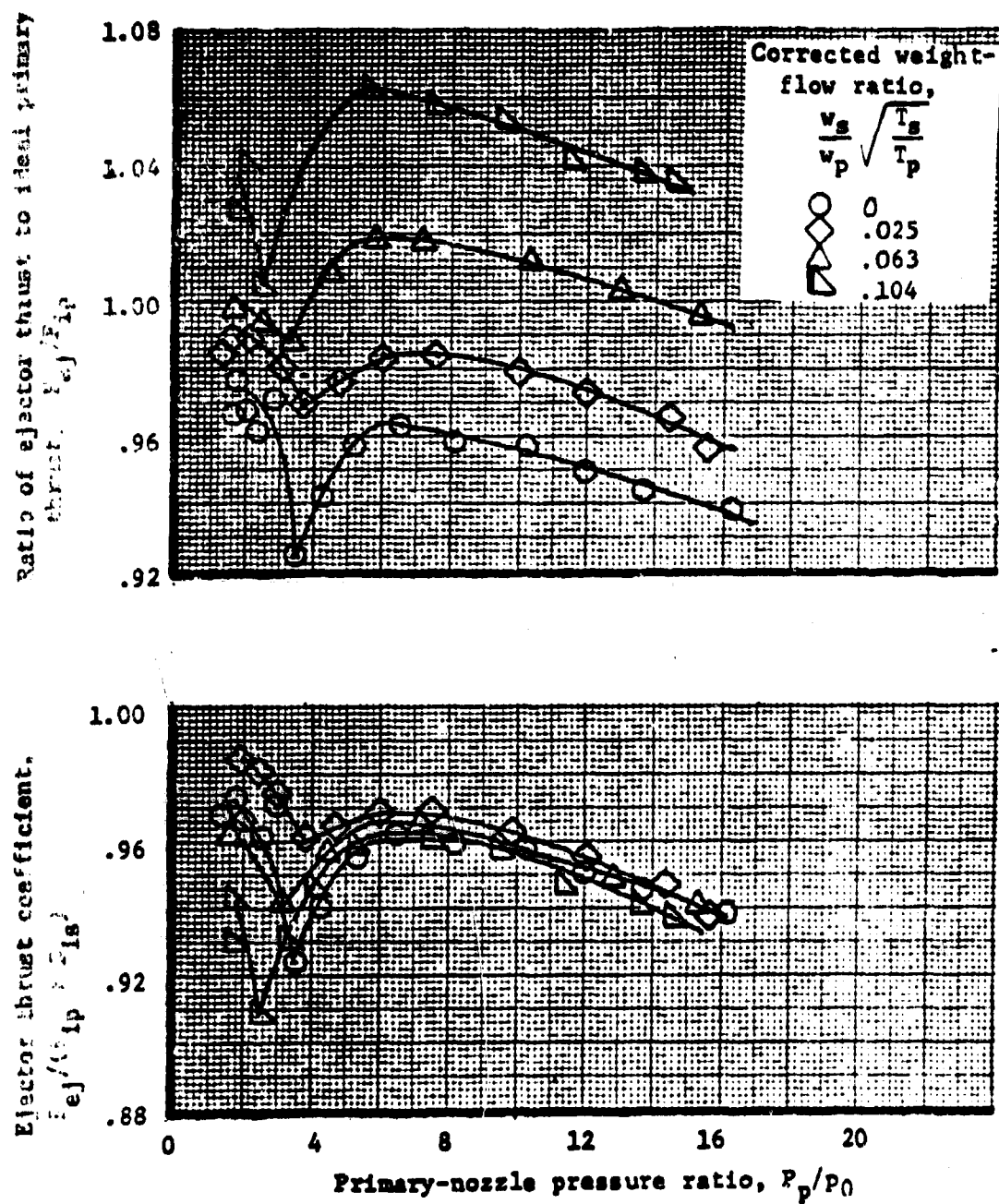
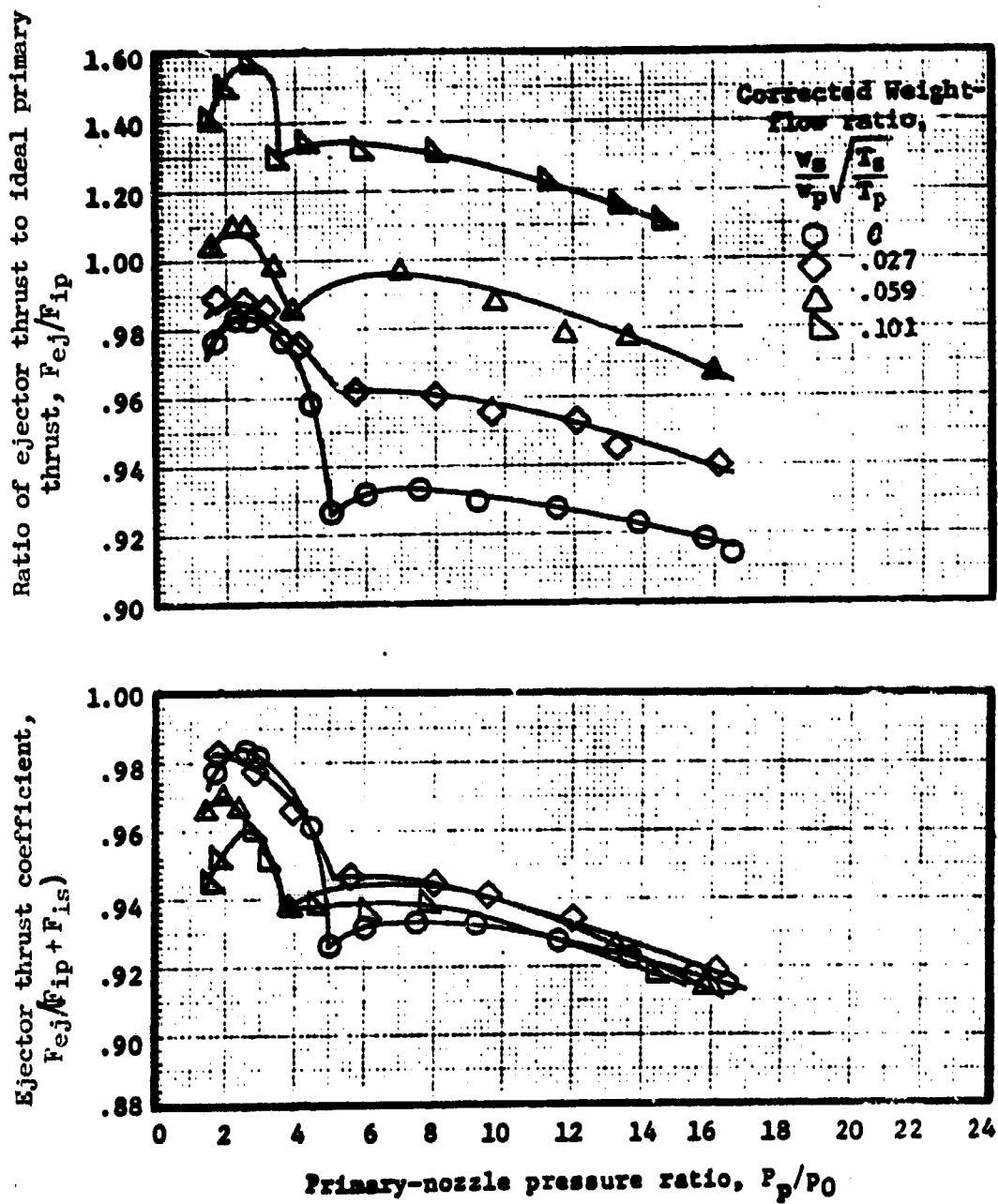


FIGURE 8.-69 Effect of flow divergence angle on thrust coefficient at design pressure ratio



(a) Thrust characteristics

FIGURE 8-70 Performance of ejector 1. Exit diameter ratio, 1.24; throat diameter ratio, 1.08; spacing ratio, 0.38; flow divergence angle, 18° ; shroud divergence angle, 15° .



(a) Thrust characteristics

FIGURE 8-71 Performance of Ejector 2. Exit diameter ratio, 1.24; throat diameter ratio, 1.08; spacing ratio, 0.28; flow divergence angle, 23° ; shroud divergence angle, 20° .

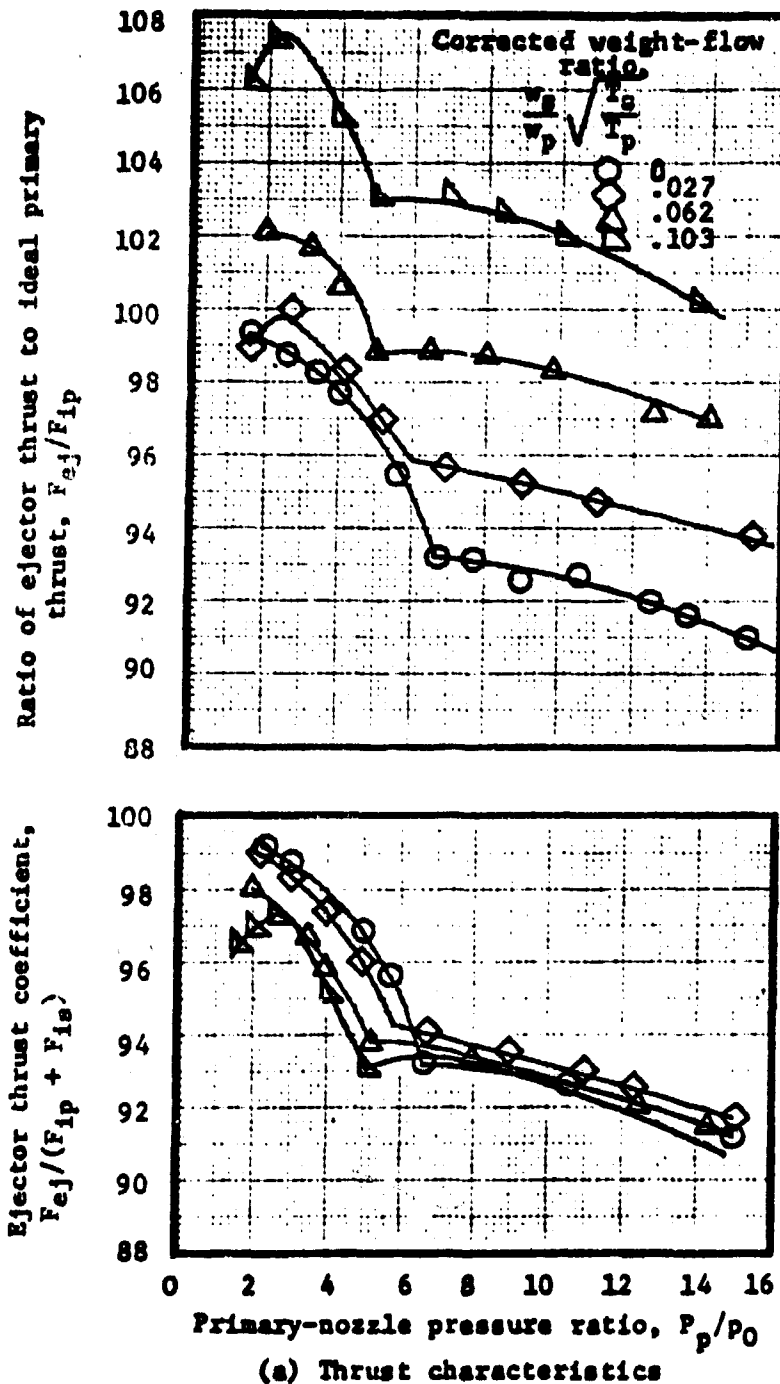


FIGURE 8-72 Performance of ejector 3. Exit diameter ratio, 1.24; throat diameter ratio, 1.08; spacing ratio, 0.22; flow divergence angle, 28° ; shroud divergence angle, 25°

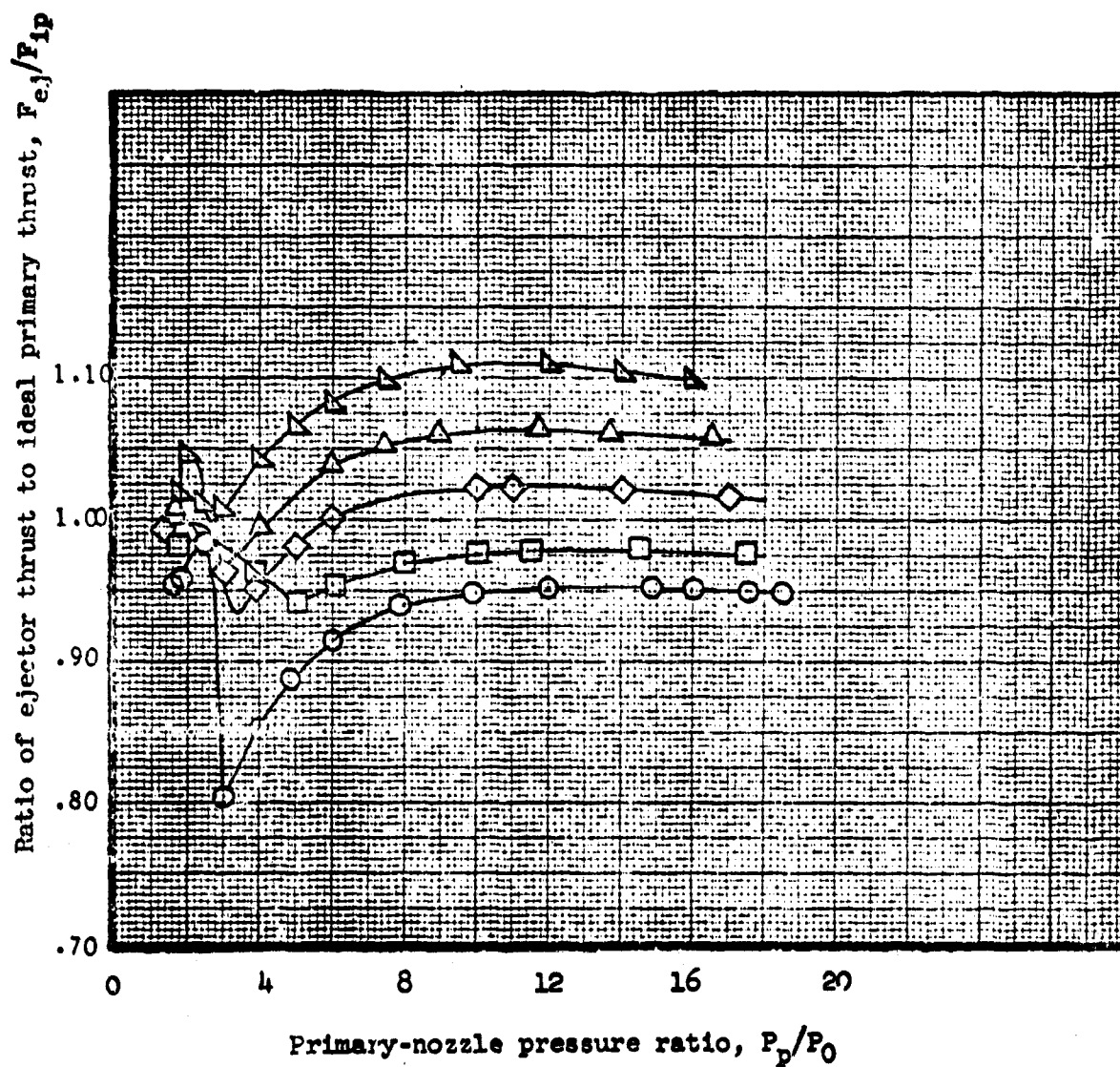
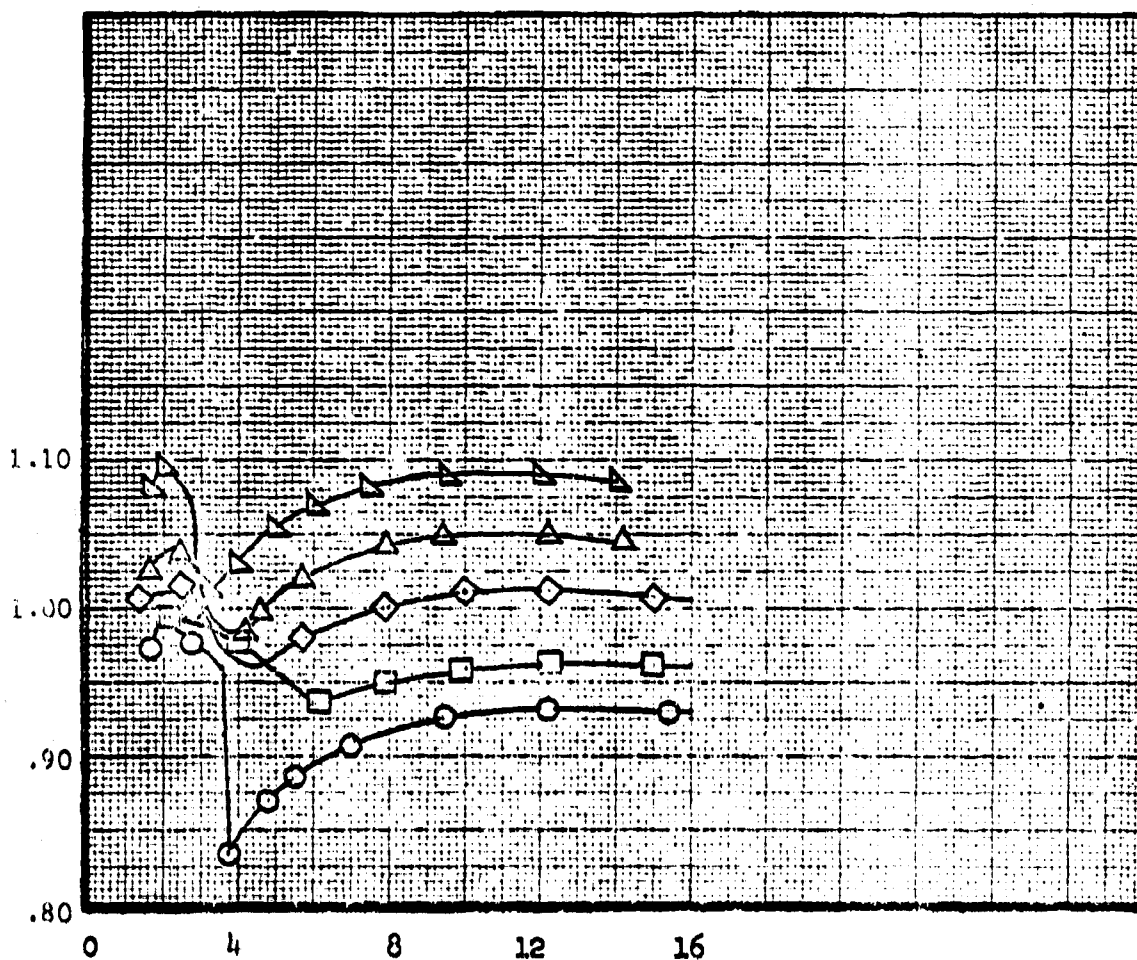


Figure 8-73 Performance of ejector 4. Exit diameter ratio, 1.46; throat diameter ratio, 1.10; spacing ratio, 0.69; flow divergence angle, 19° ; shroud divergence angle, 15° .

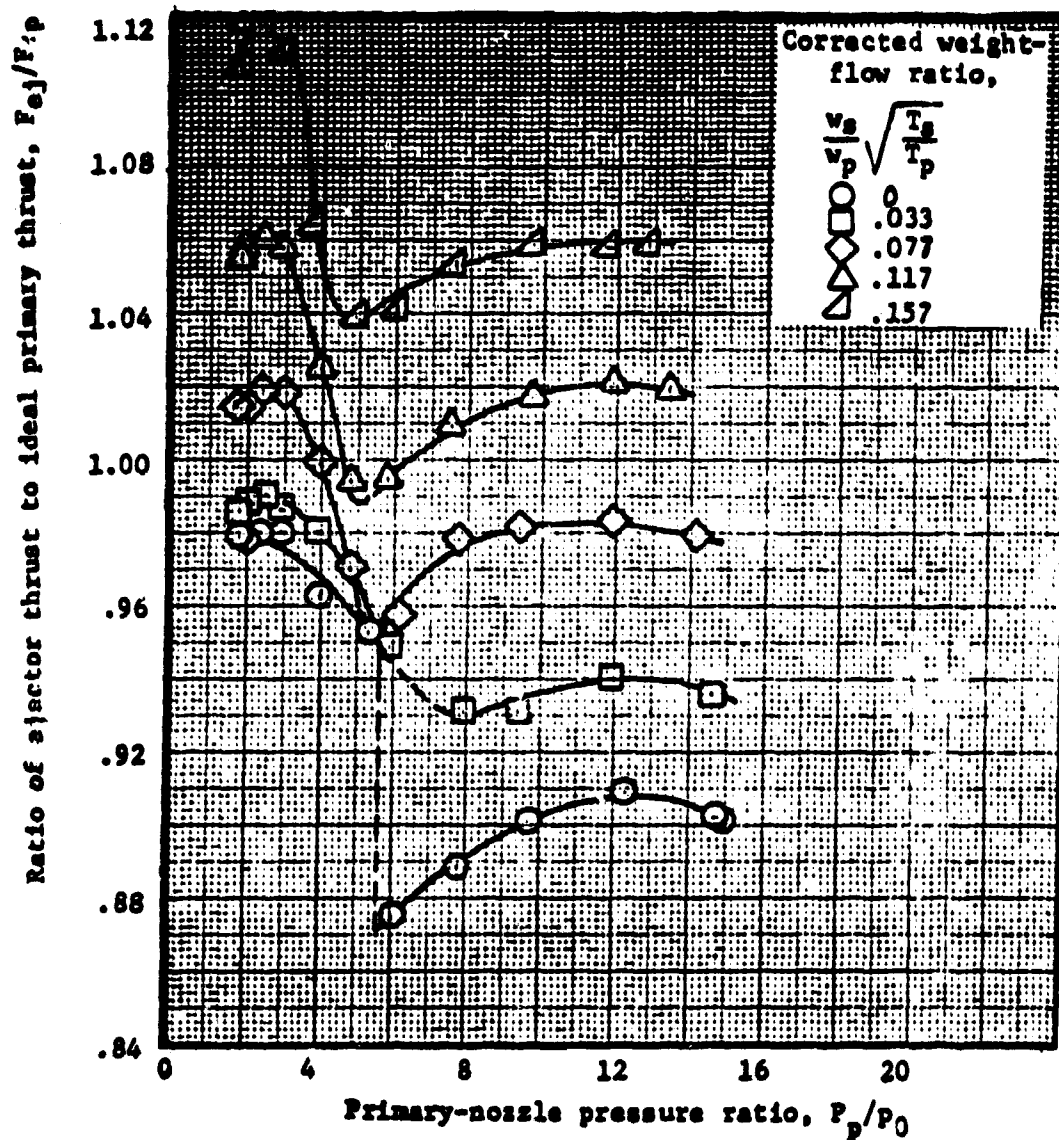
Ratio of ejector thrust to ideal primary thrust, F_{ej}/F_{ip}



Primary-nozzle pressure ratio, P_p/P_0

(a) Thrust characteristics

FIGURE 8-74 Performance of ejector 5. Exit diameter ratio, 1.46; throat diameter ratio, 1.10; spacing ratio, 0.51; flow divergence angle, 25° ; shroud divergence angle, 20°



(a) Thrust characteristics

FIGURE 8-75 Performance of ejector 6. Exit diameter ratio, 1.46; throat diameter ratio, 1.10; spacing ratio, 0.40; flow divergence angle, 30° ; shroud divergence angle, 25°

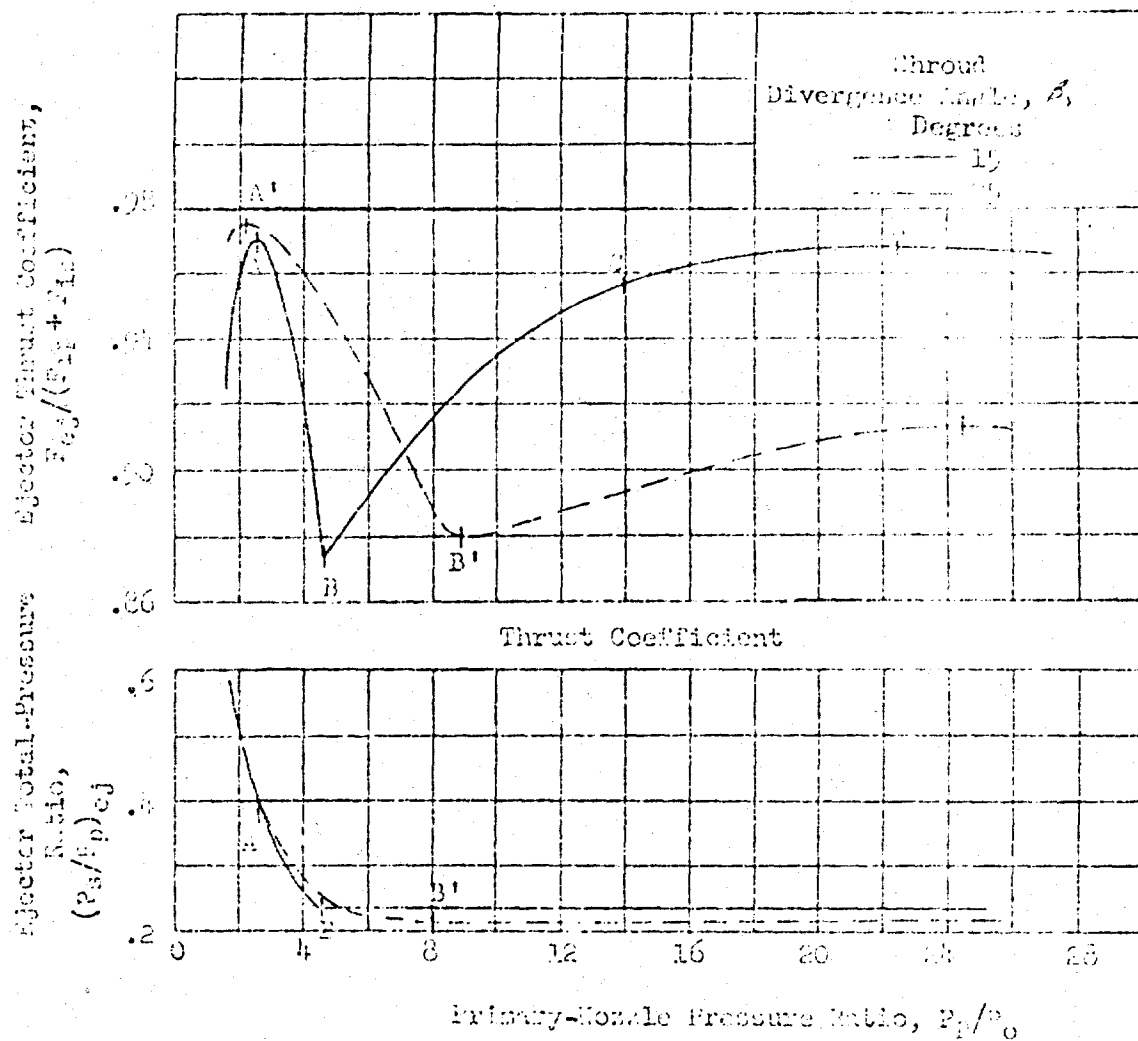


FIGURE 4-70. Characteristics of Nozzle Performance for Ejectors with Different Shroud Divergence Angles.

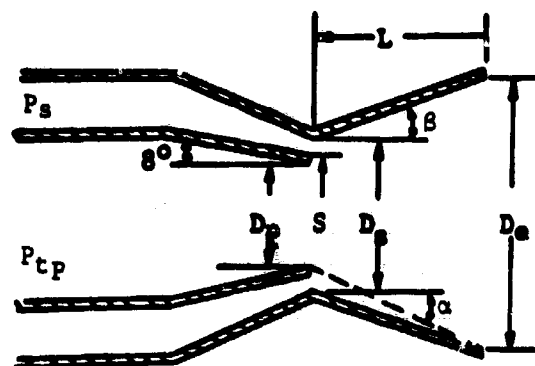
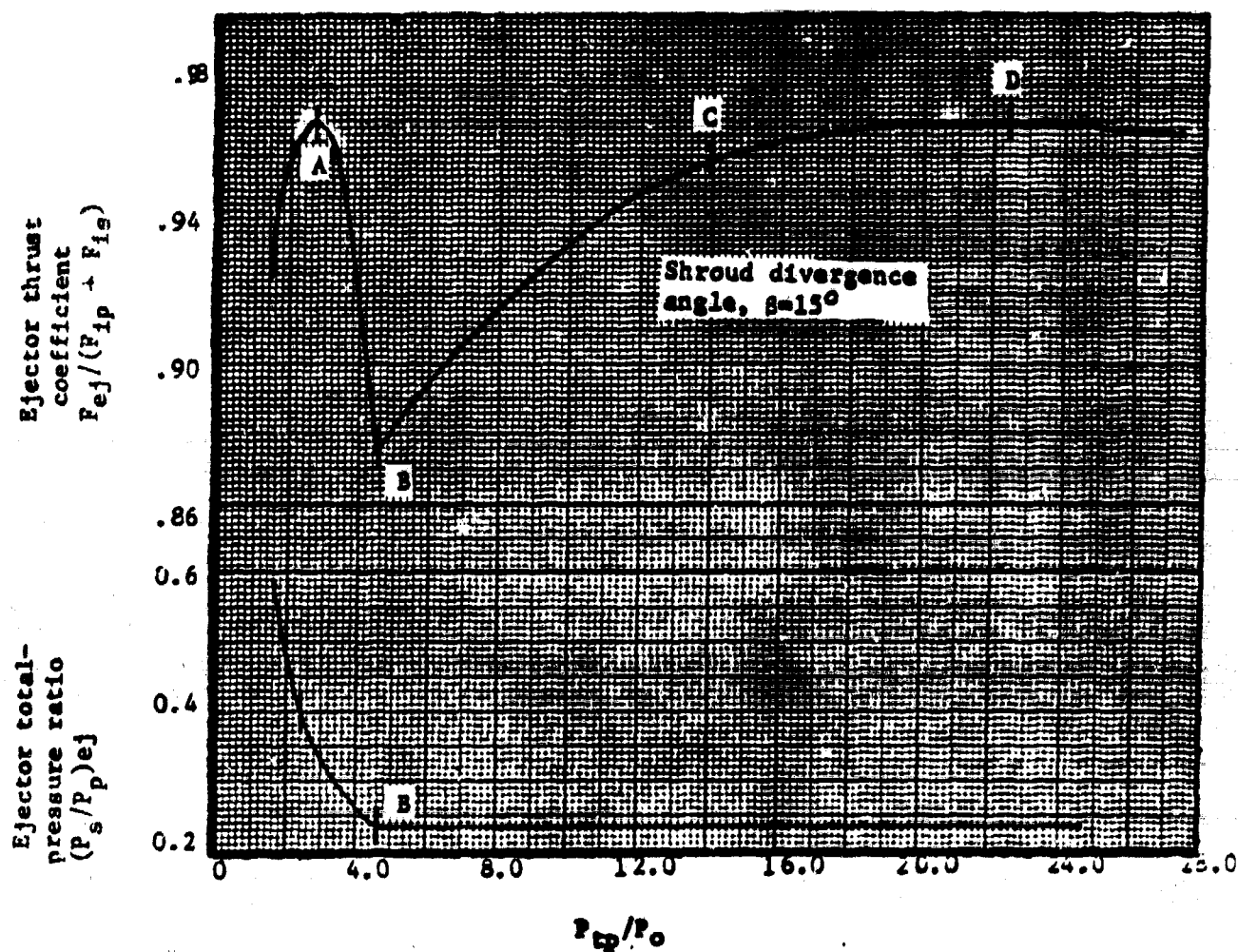


FIGURE 8-77 Ejector Configuration



Primary Nozzle Pressure Ratio

FIGURE 8-78 Performance of ejector at weight-flow ratio of about .032. Exit diameter ratio, 1.8; throat diameter ratio, 1.10.

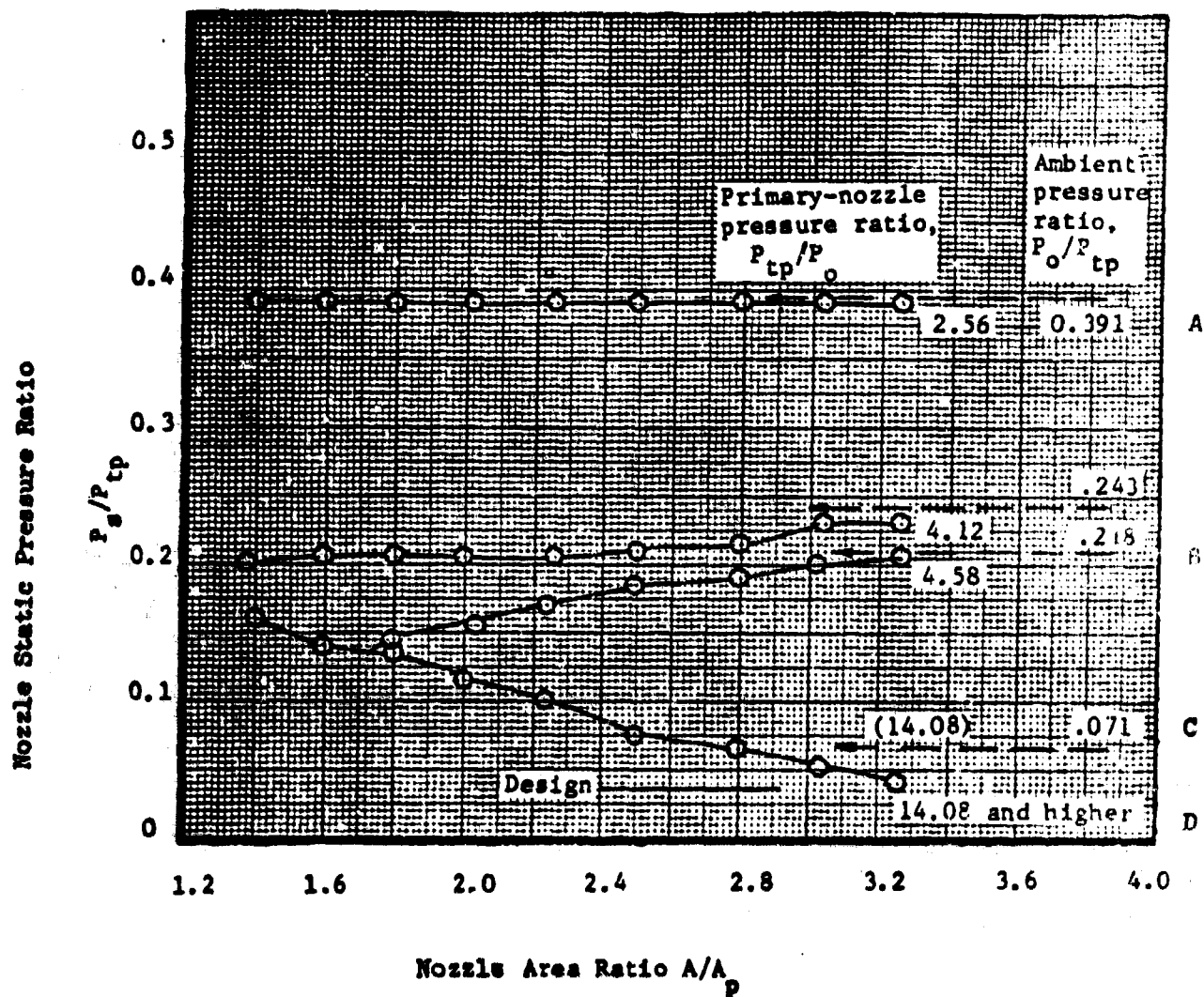
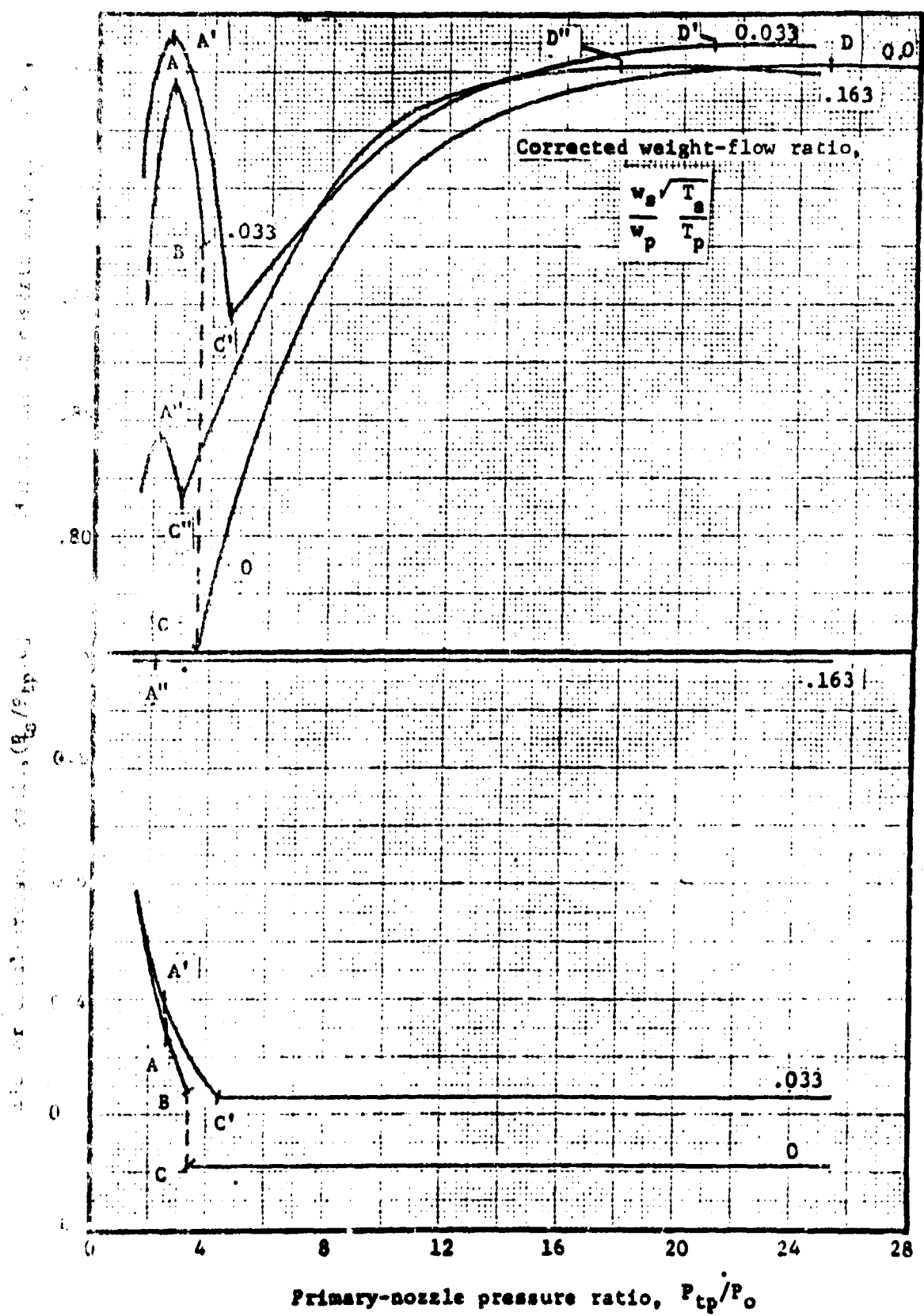


FIGURE 8-79 Shroud static pressure distribution for various primary nozzle pressure ratios.
Shroud divergence = 15°
Corrected weight flow ratio, $= .032$



8-80

Effect of Secondary Airflow on Nozzle Performance.

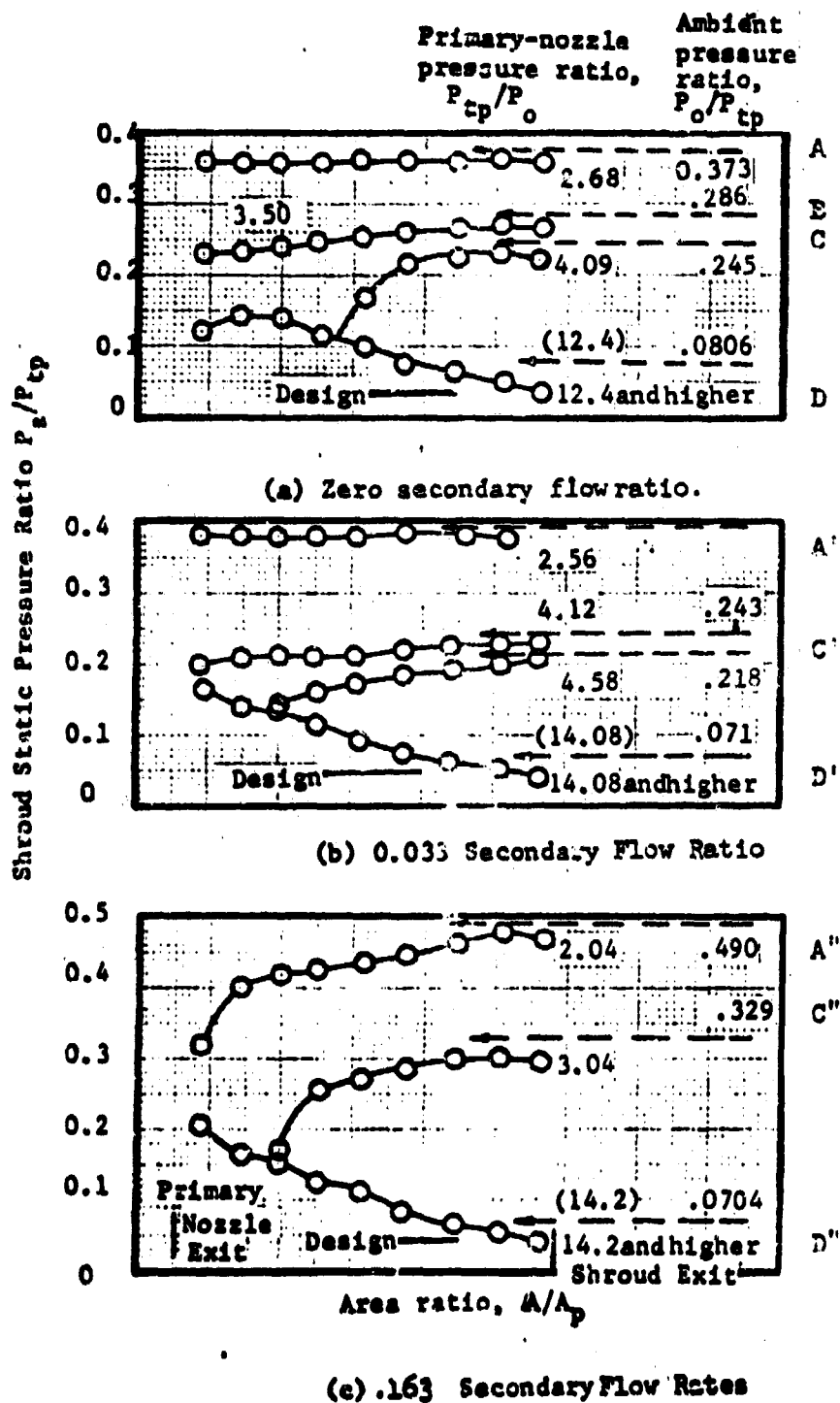


FIGURE 8-81 . Shroud Static pressure distribution at several corrected weight flows.

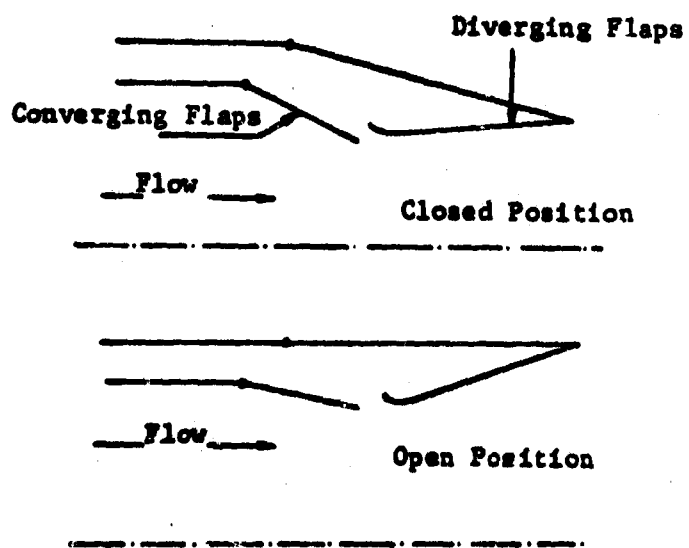


FIGURE 8-82 Low Base Drag Nozzle Configuration.

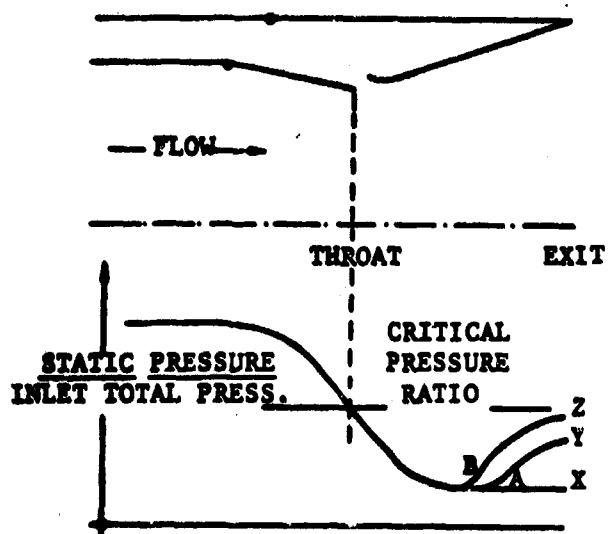


FIGURE 8-83 Low Base Drag Nozzle Pressure Distributions.

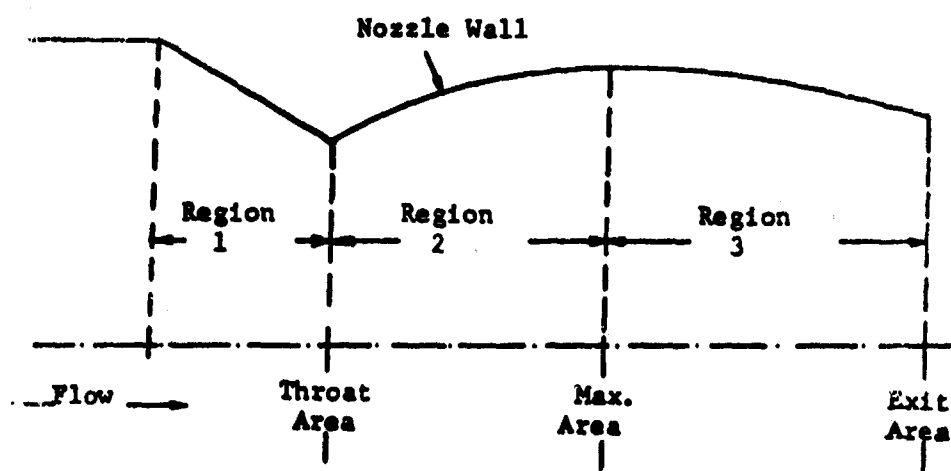


FIGURE 8-84 Converging-Diverging Nozzle with Supersonic Convergence.

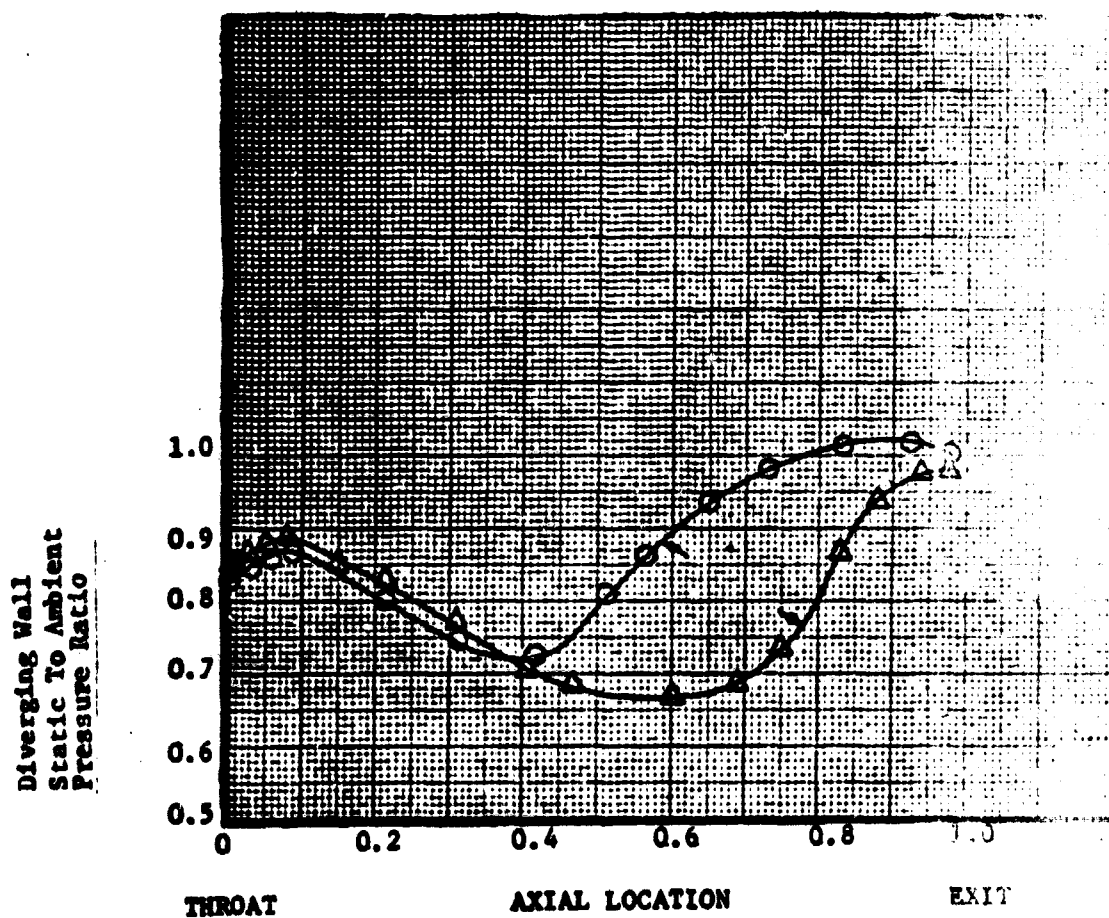


FIGURE 8-85 Typical Diverging Wall Pressures.
 Nozzle pressure ratio
 Δ = 2.336
 \circ = 2.323

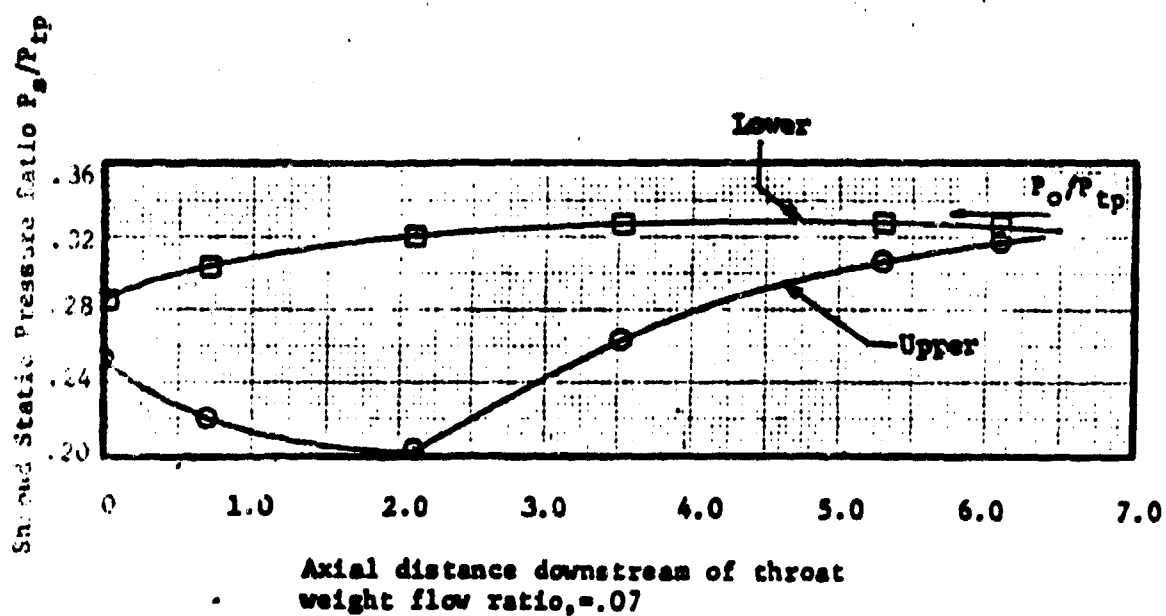
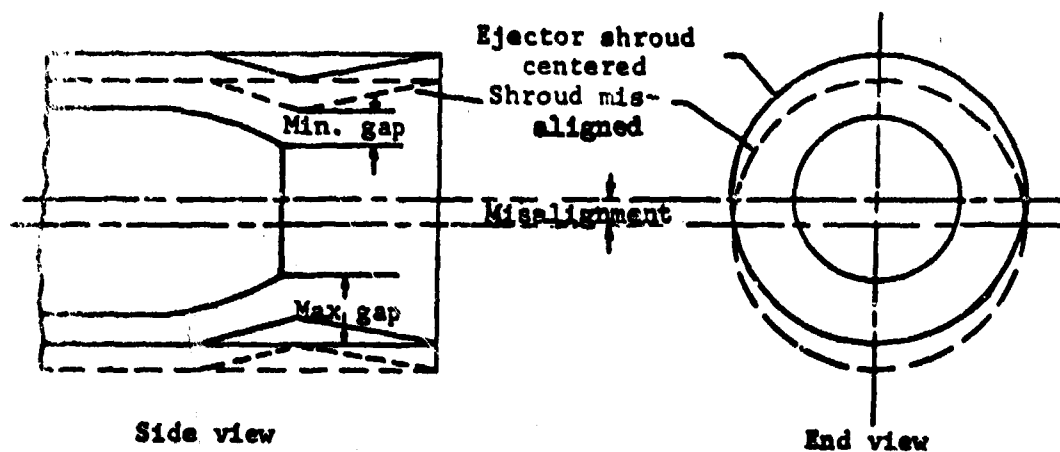


FIGURE 8-86 Effect of nozzle misalignment on nozzle performance.

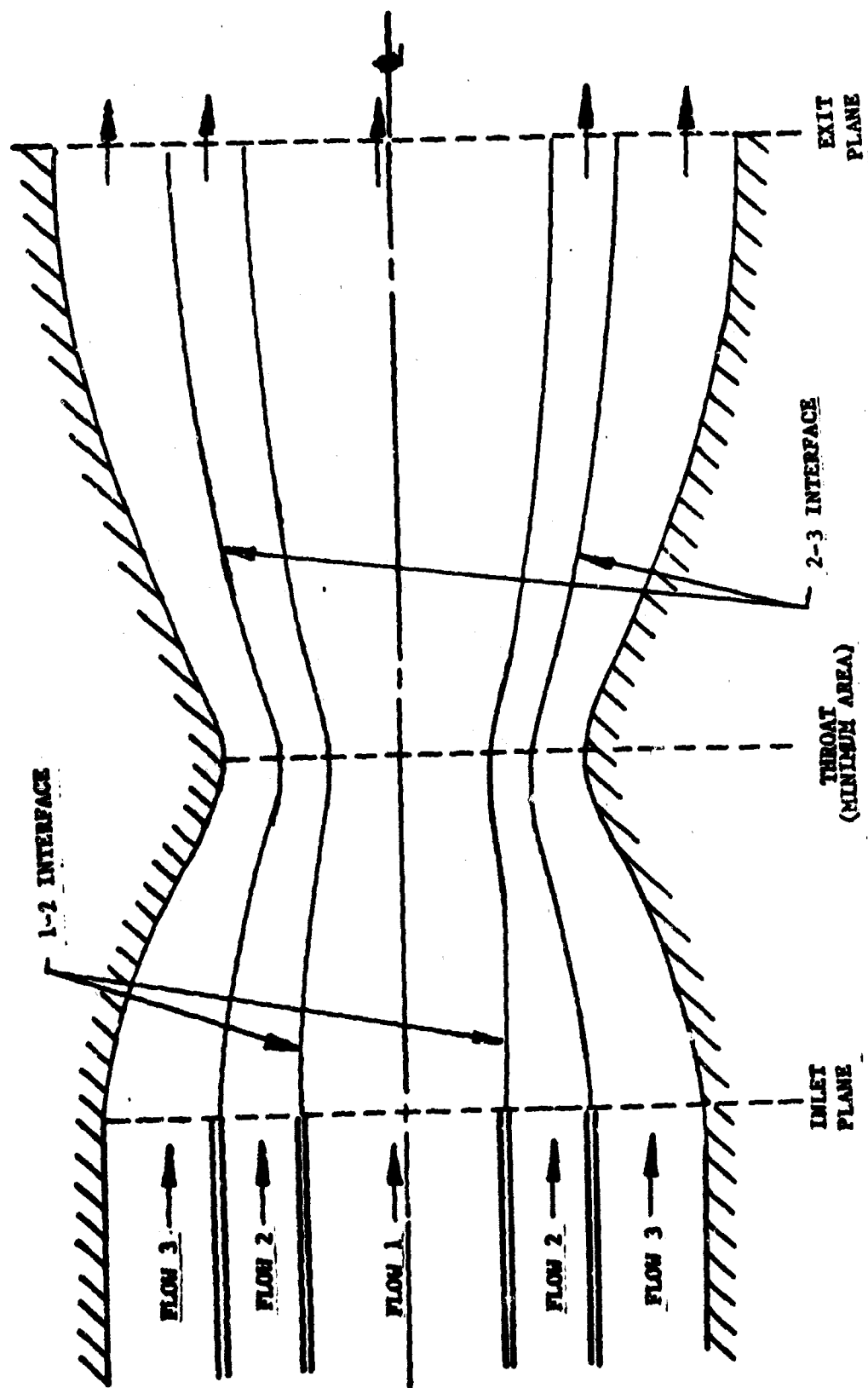


FIGURE 8-87 Axially Symmetric Compressible Nozzle Flow.

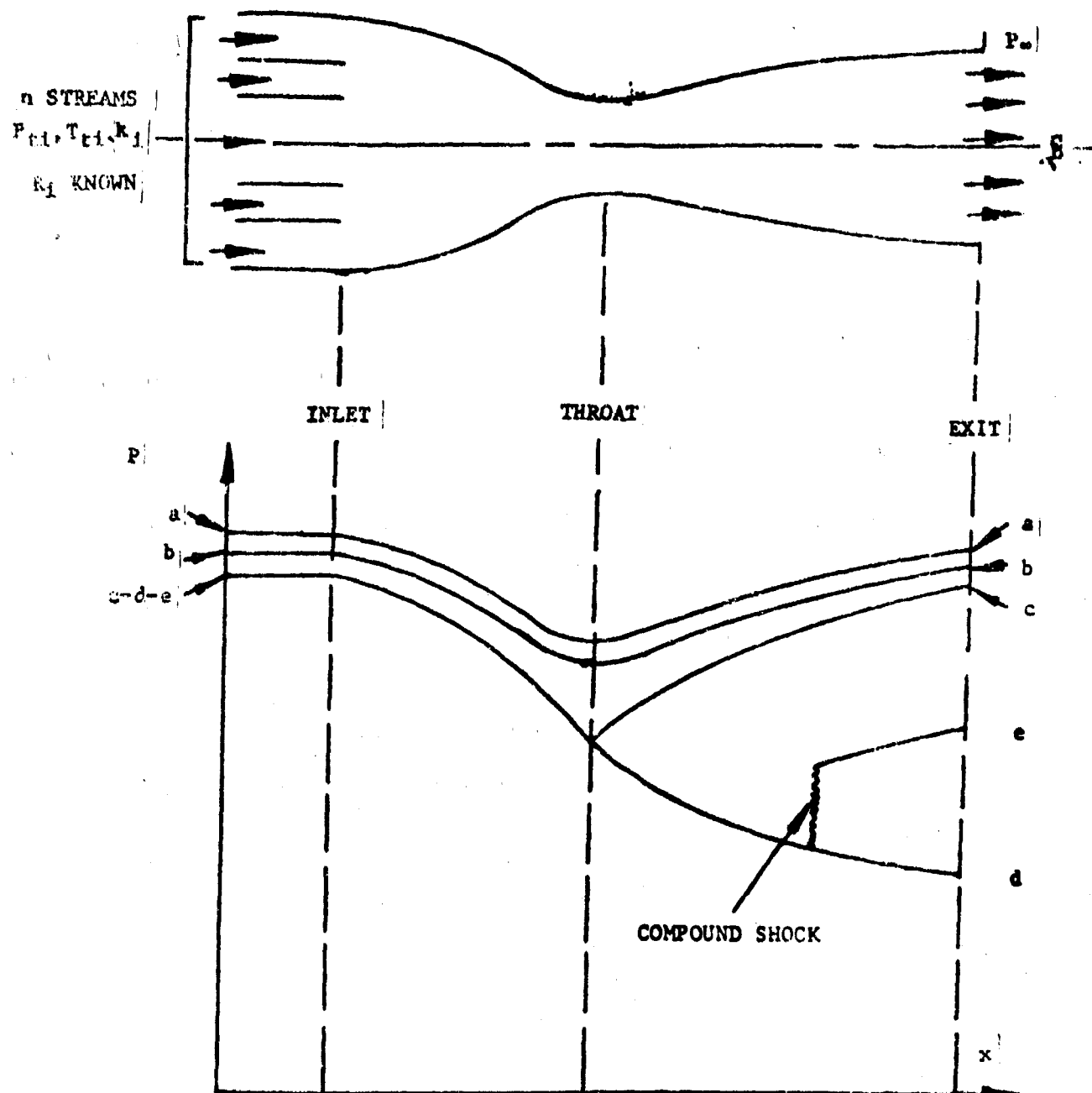


FIGURE 8-88 Compound-Compressible Flow in a Nozzle of Fixed Geometry.

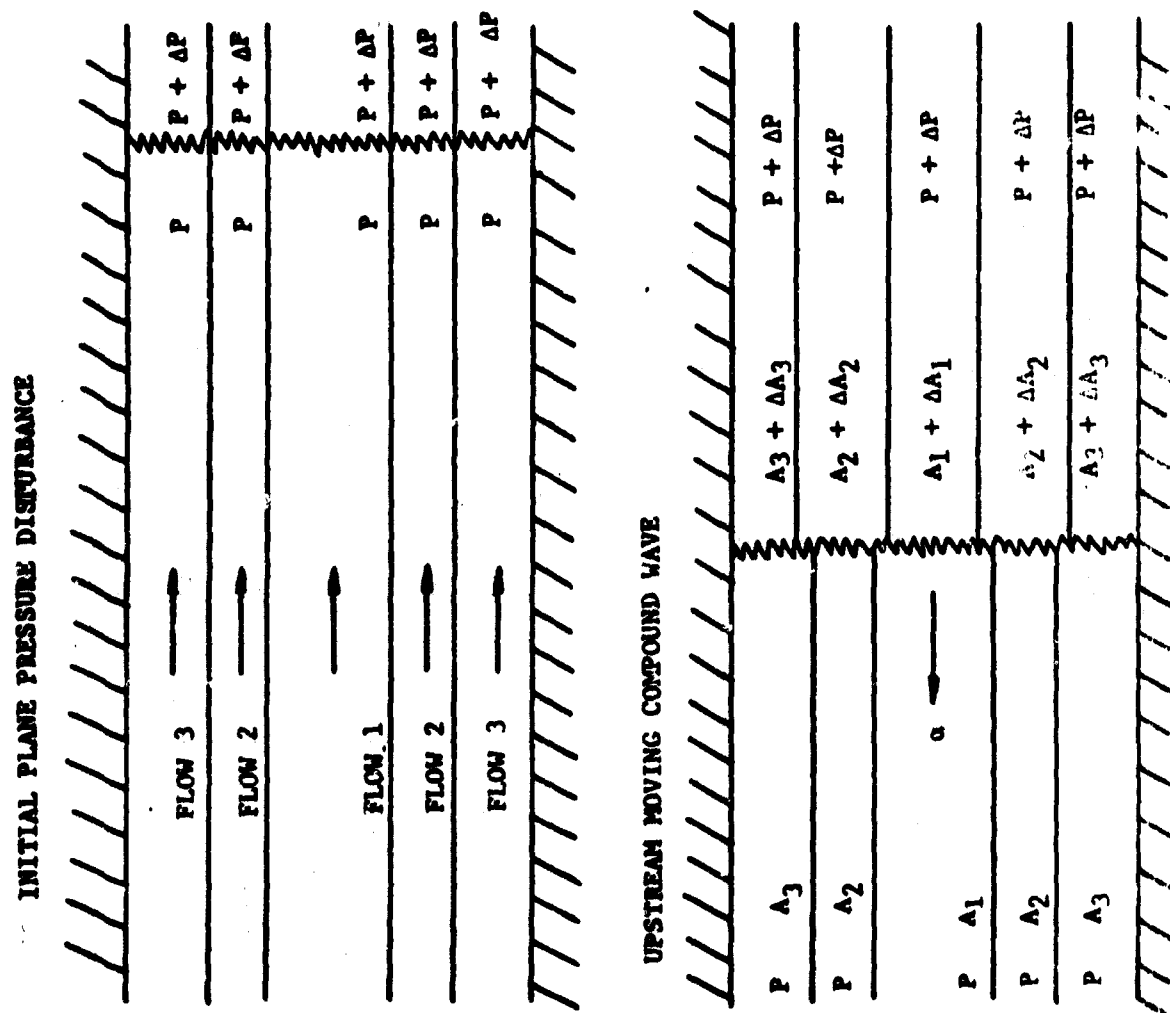


FIGURE 8-89 Evolution of a One-Dimensional Compound-Wave.

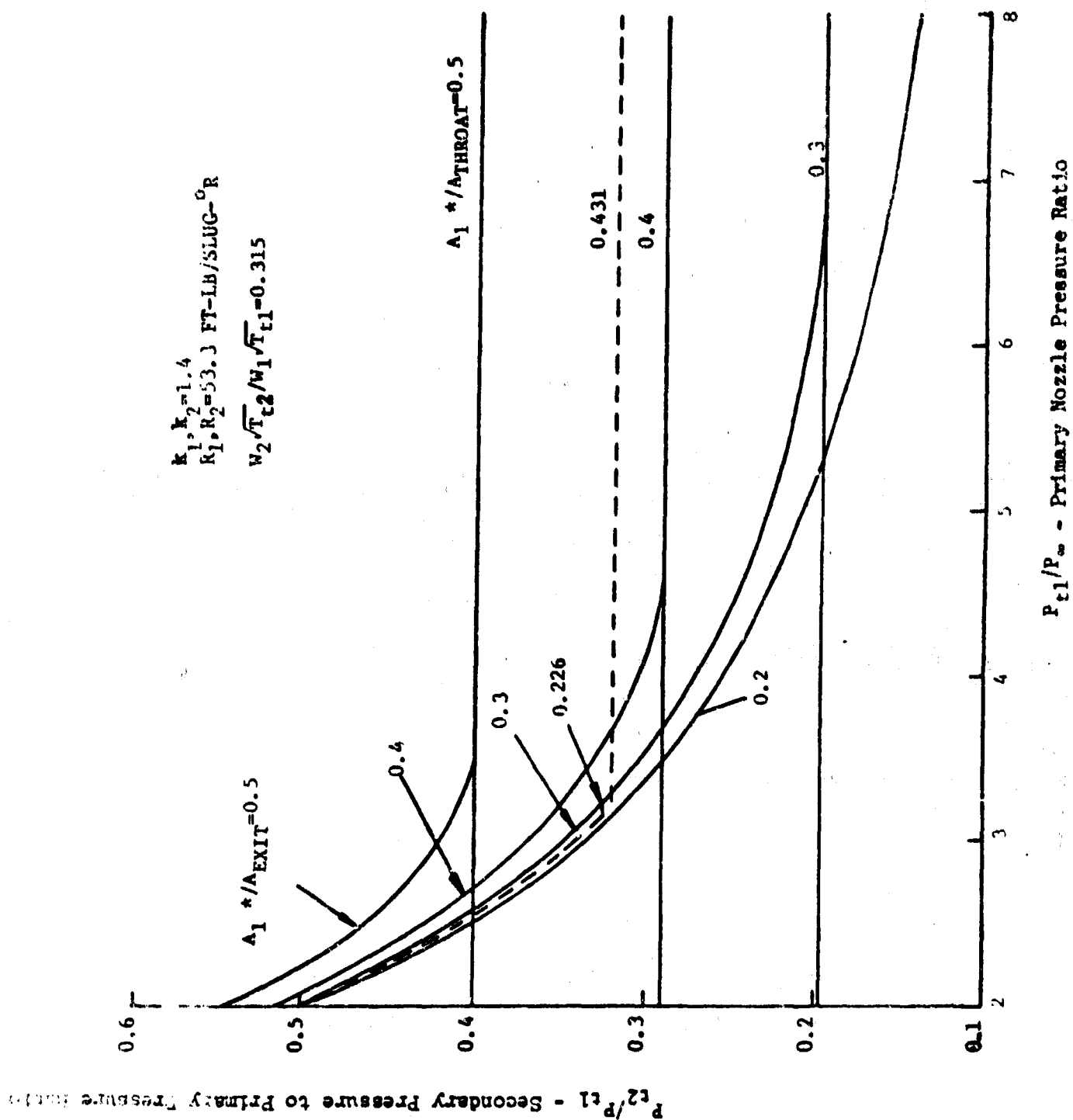


FIGURE 8-90 Relationship of Flow Parameters in a Convergent-Divergent Nozzle.

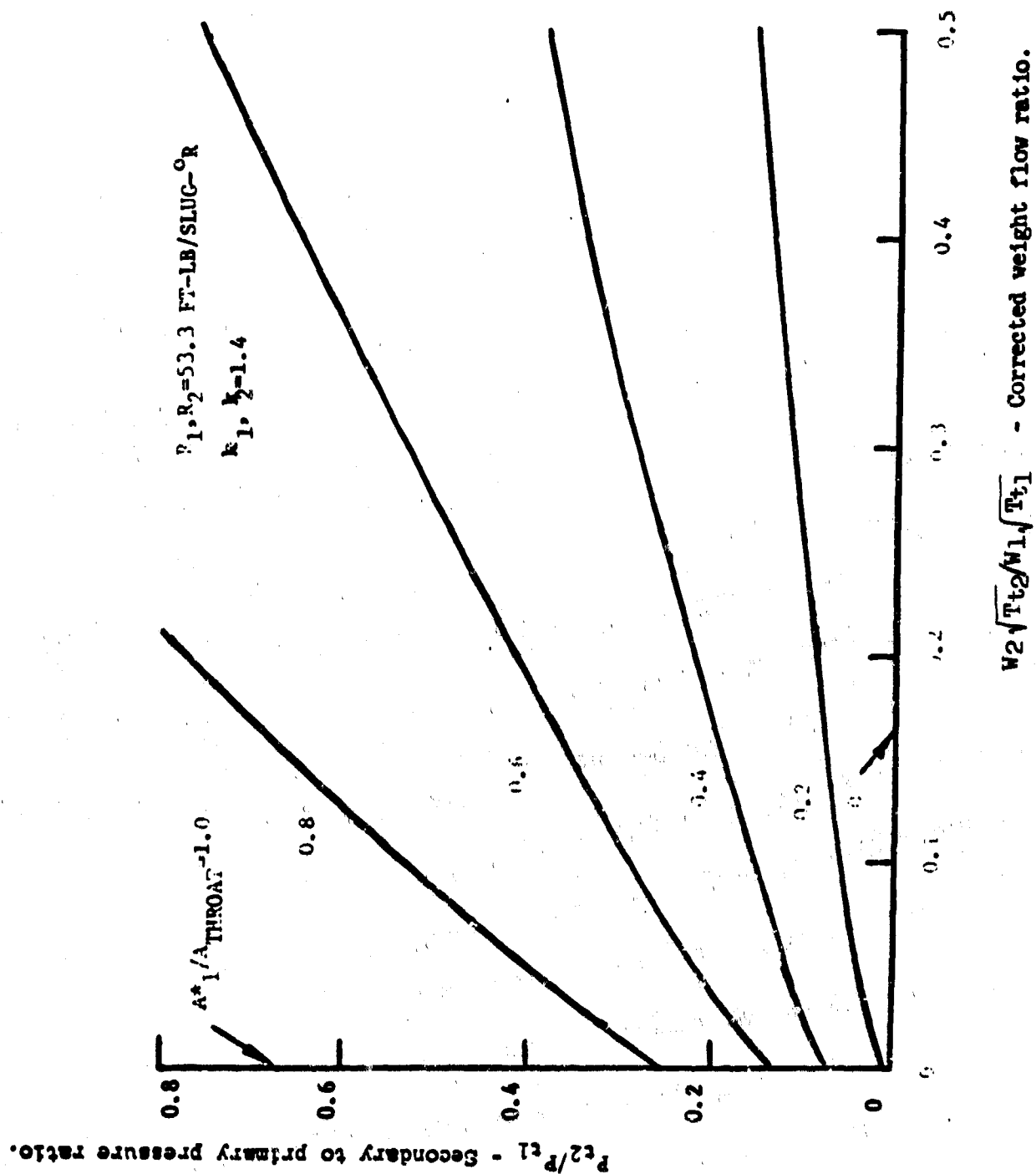


FIGURE 8-91 Relationship of Flow Parameters During Choked Flow

8-198

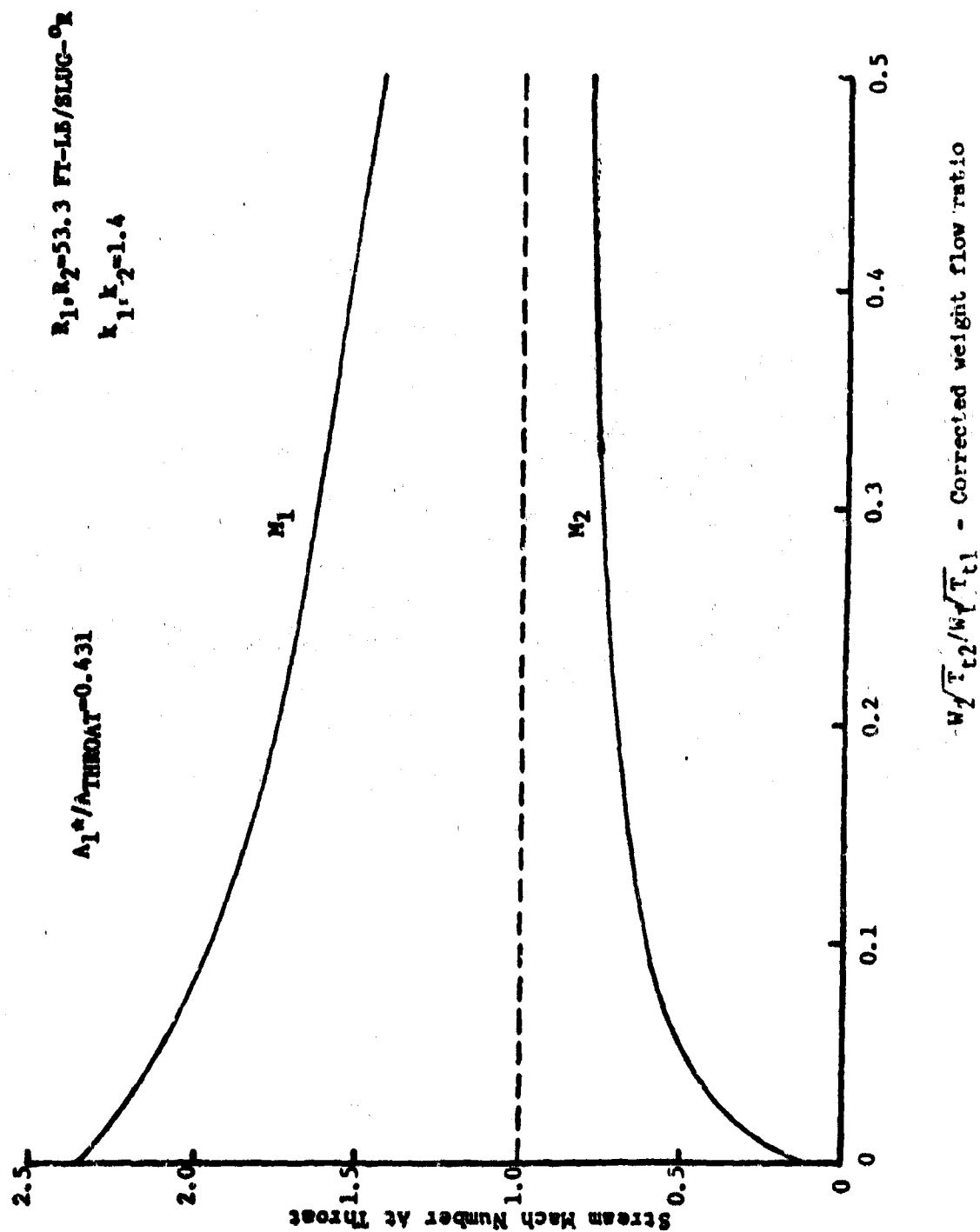


FIGURE 8-92 Stream Mach Numbers at the Nozzle Throat During Choked Flow.

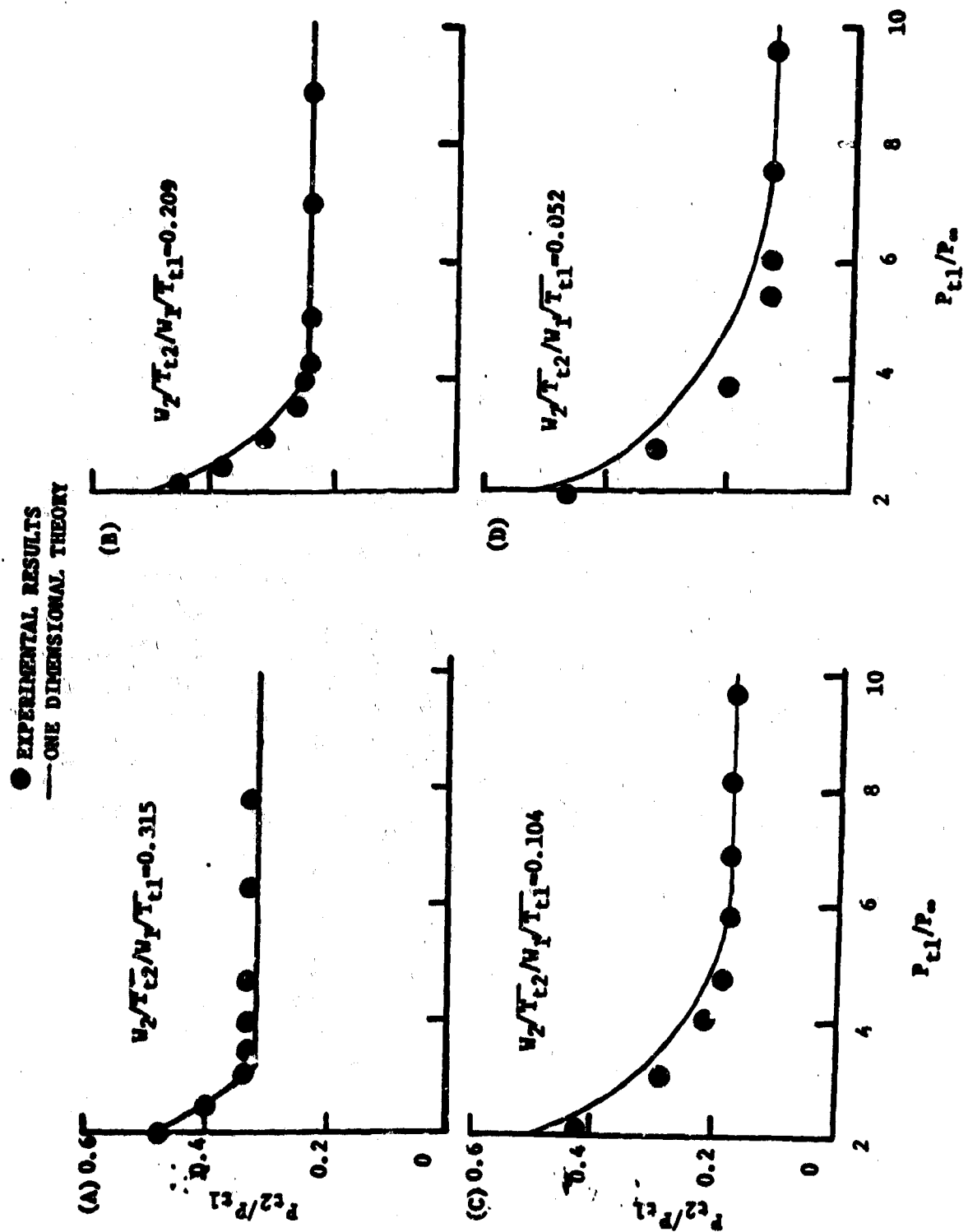


FIGURE 8-93 Comparison of Compound Compressible Flow Theory with Experimental Results.

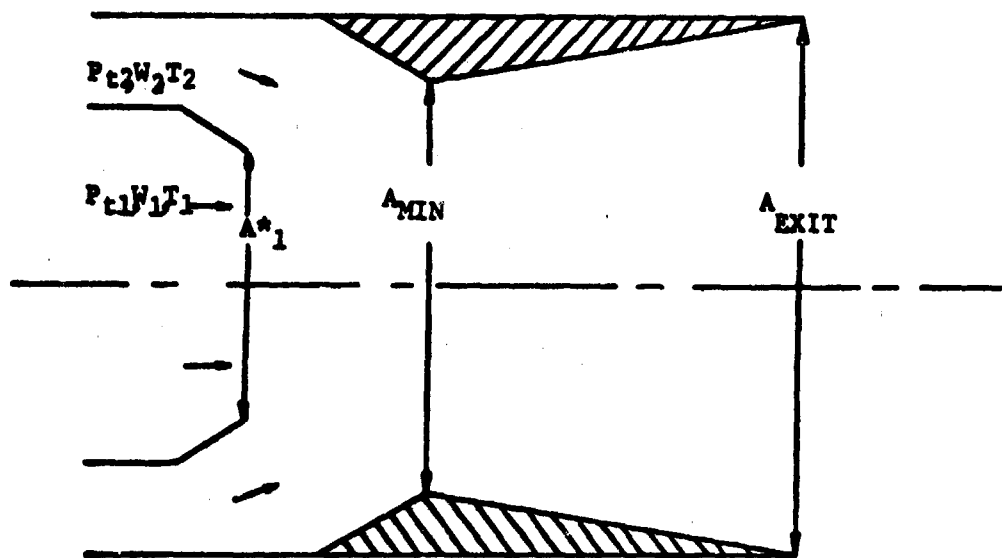


FIGURE 8-94 Schematic of Analytical Model Used in Computations.

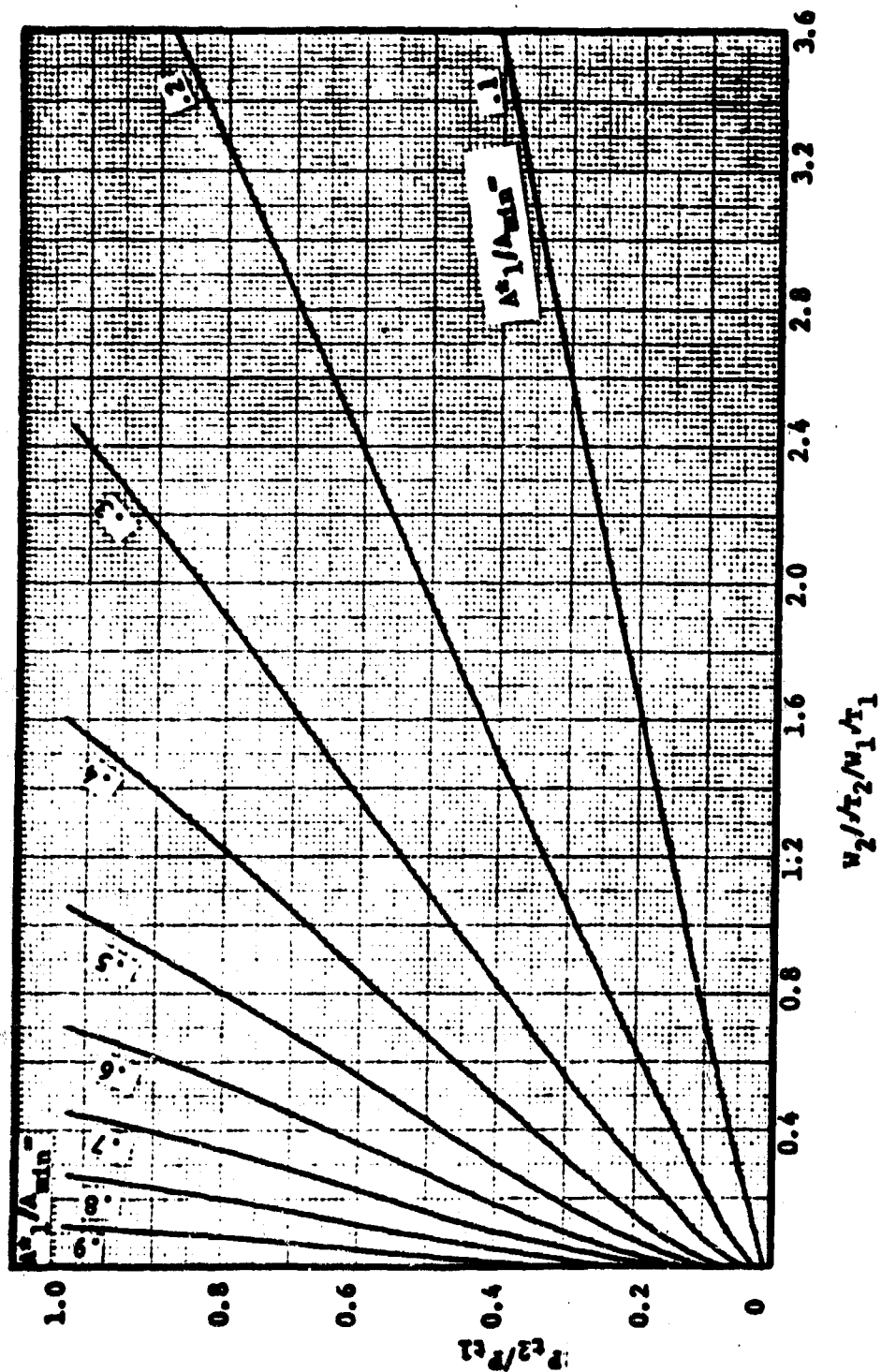


FIGURE 8-95 Choked Pumping Characteristics- Two Flow Ejector $\zeta_1=1.3$ $\zeta_2=1.4$

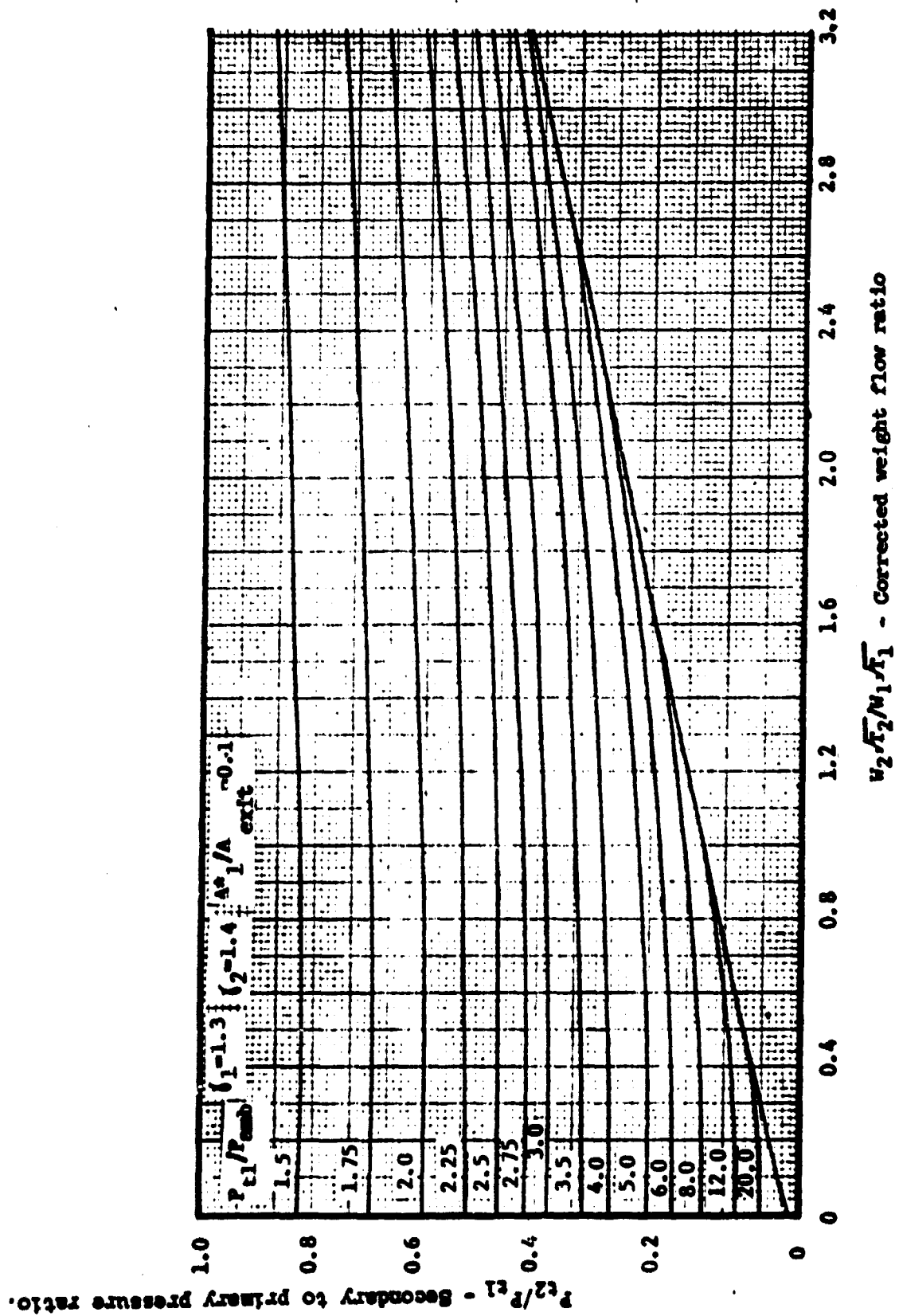


FIGURE 8-96 Two-Flow Nozzle Pumping Characteristics.

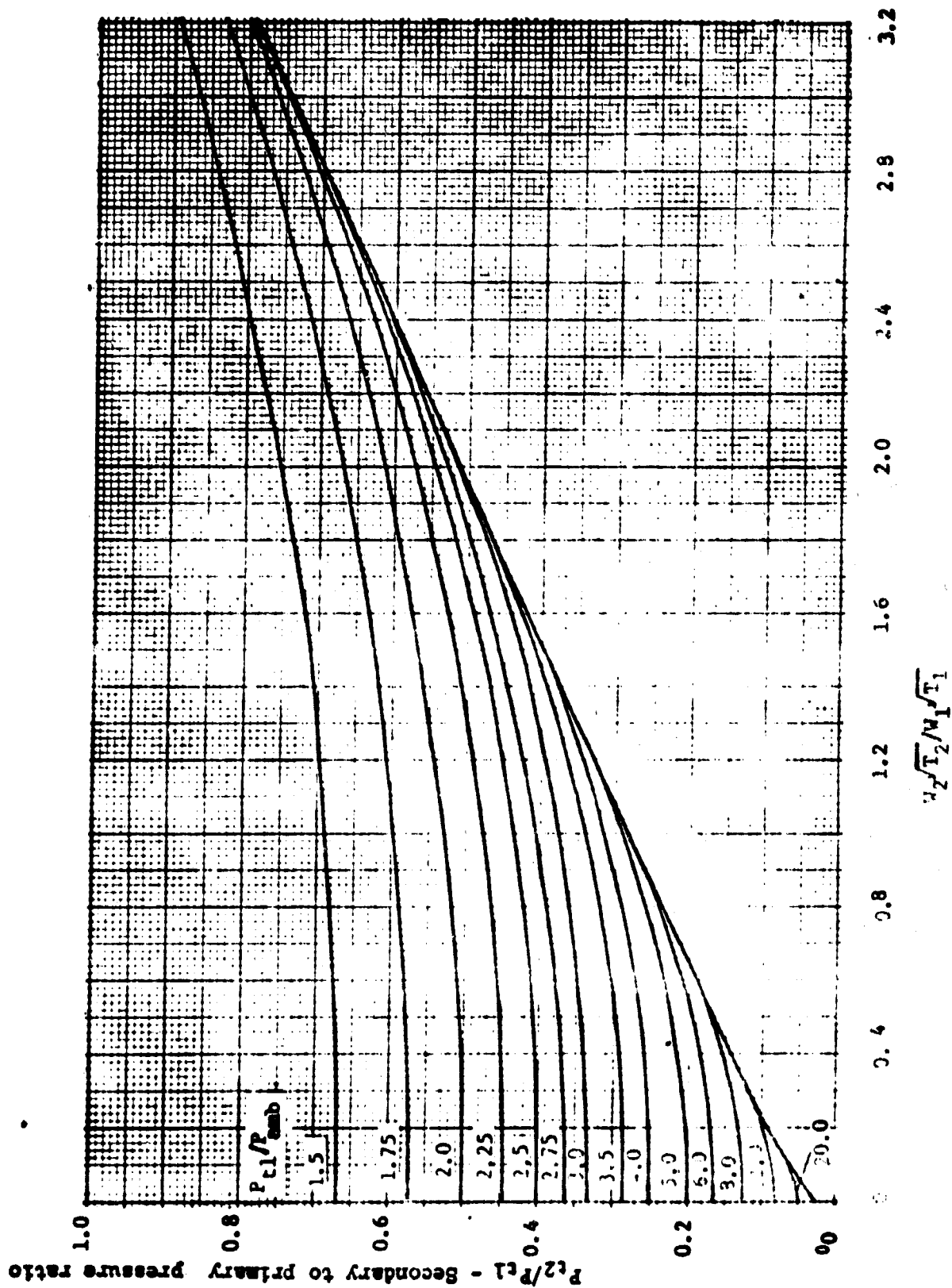


FIGURE 8-97 Two-Flow Nozzle Pumping Characteristics.
 $\gamma_1=1.3$ $\gamma_2=1.4$ $A^*_{t1}/A_{EXIT}=0.2$

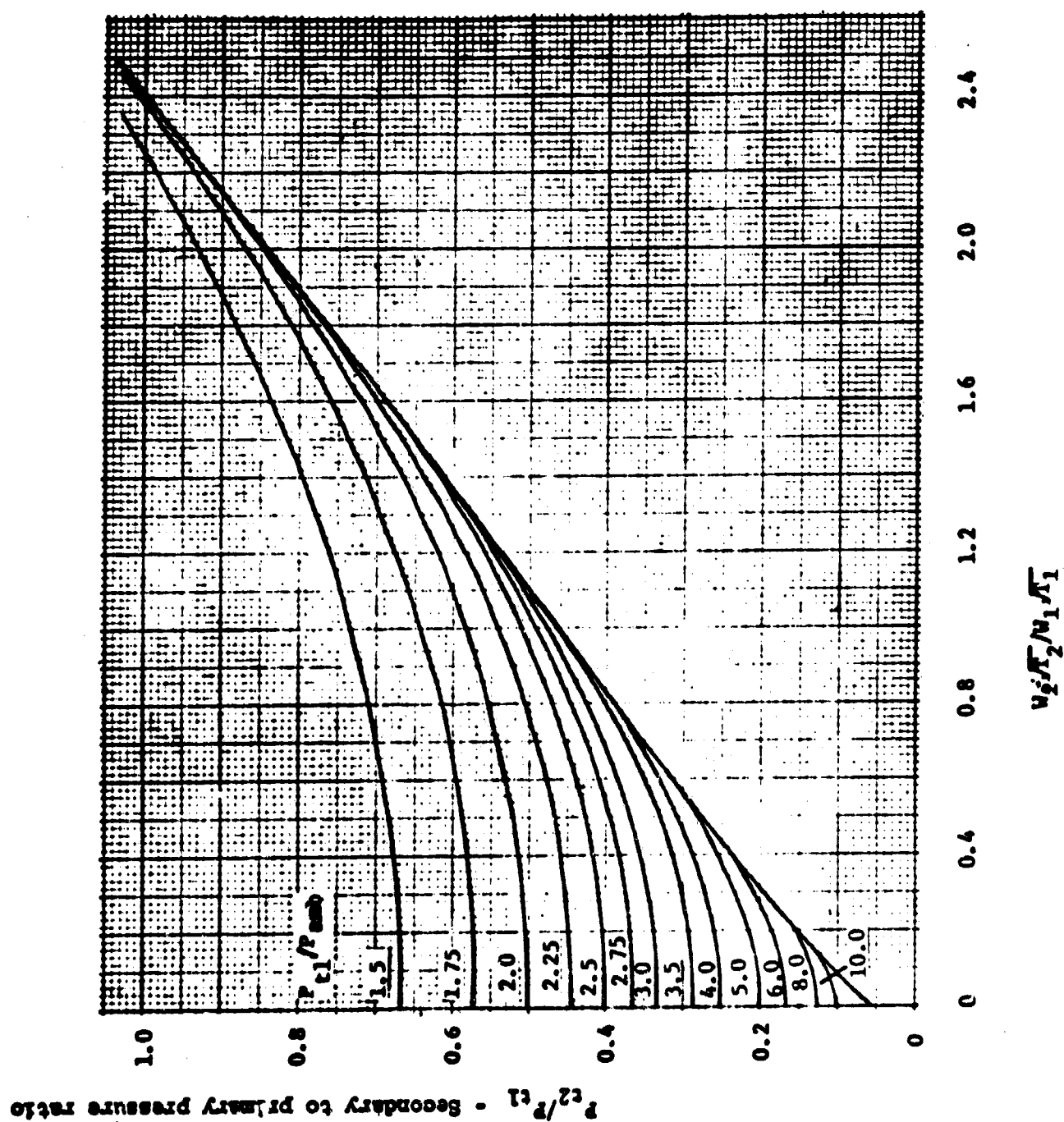


FIGURE 8-98 Two-Flow Nozzle Pumping Characteristics.
 $\gamma_1=1.3$ $\gamma_2=1.4$ $A^*_1/A_{EXIT}=0.3$

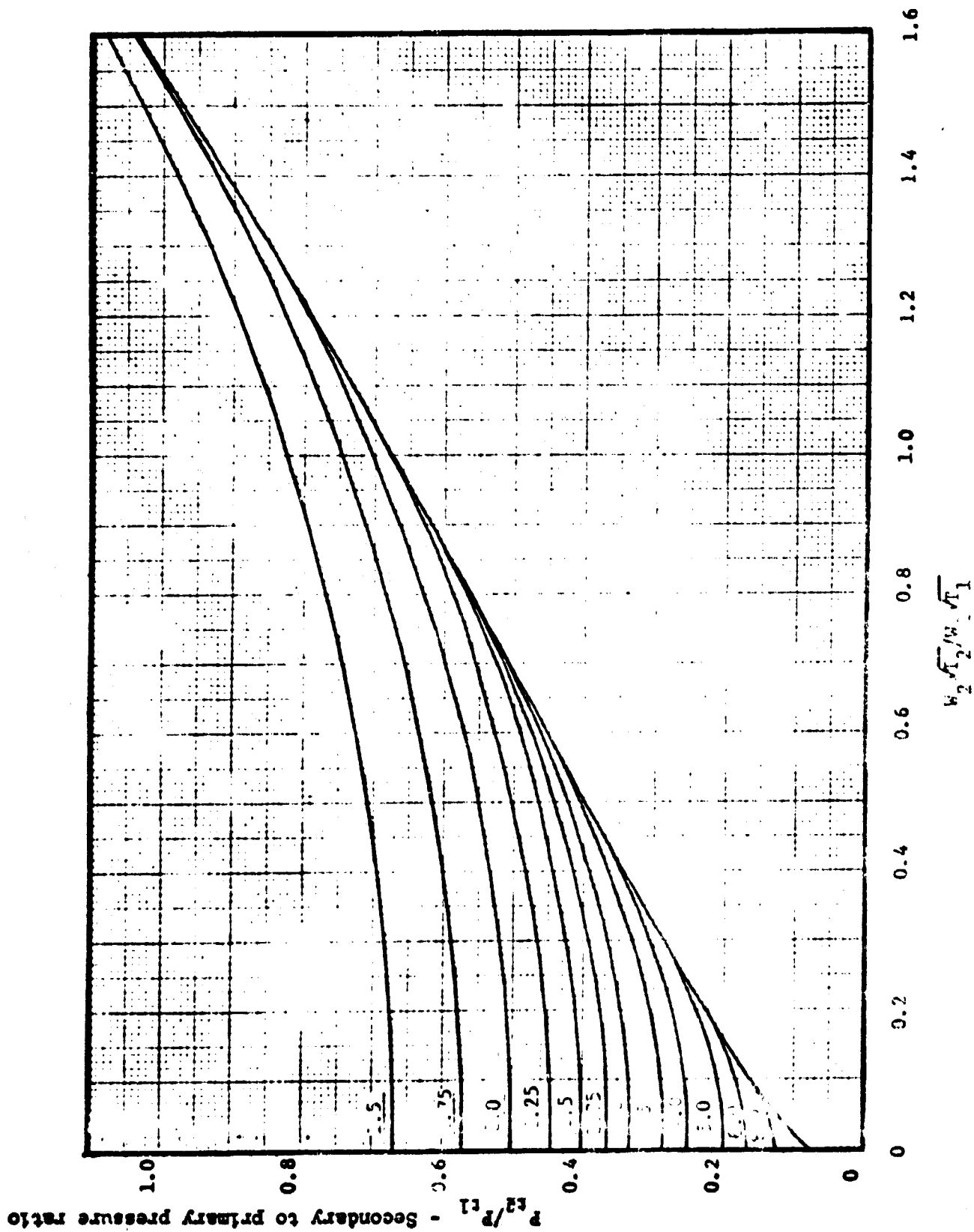


FIGURE 8-99 Two-Flow Nozzle Pumping Characteristics.
 $\gamma_1=1.3$ $\gamma_2=1.4$ $\lambda^*_1/\lambda_{EXIT}=0.4$

P-506

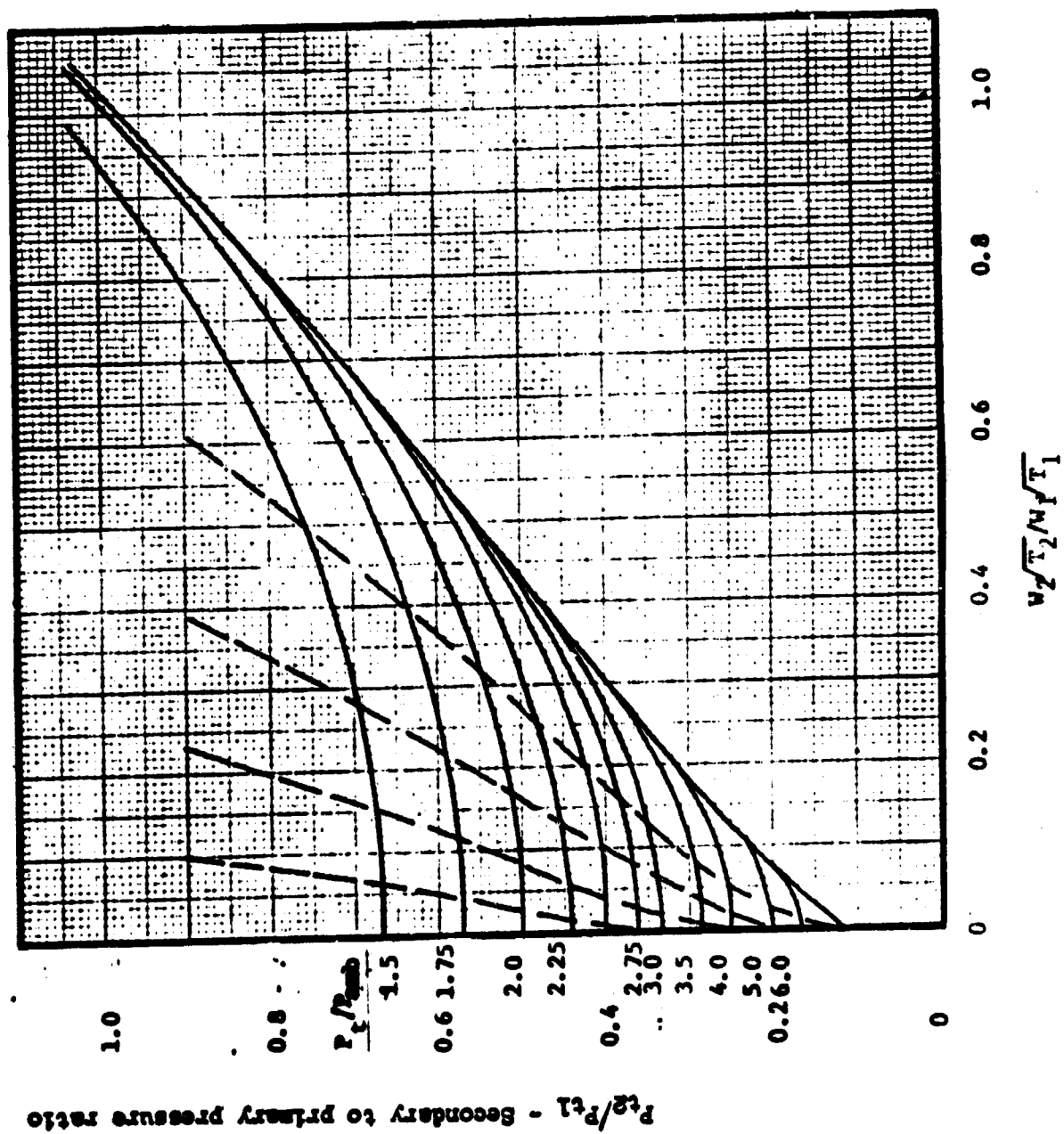


FIGURE 8-100 Two-Flow Nozzle Pumping Characteristics.
 $\gamma_1=1.3$ $\gamma_2=1.4$ $A^*_1/A_{EXIT}=0.5$

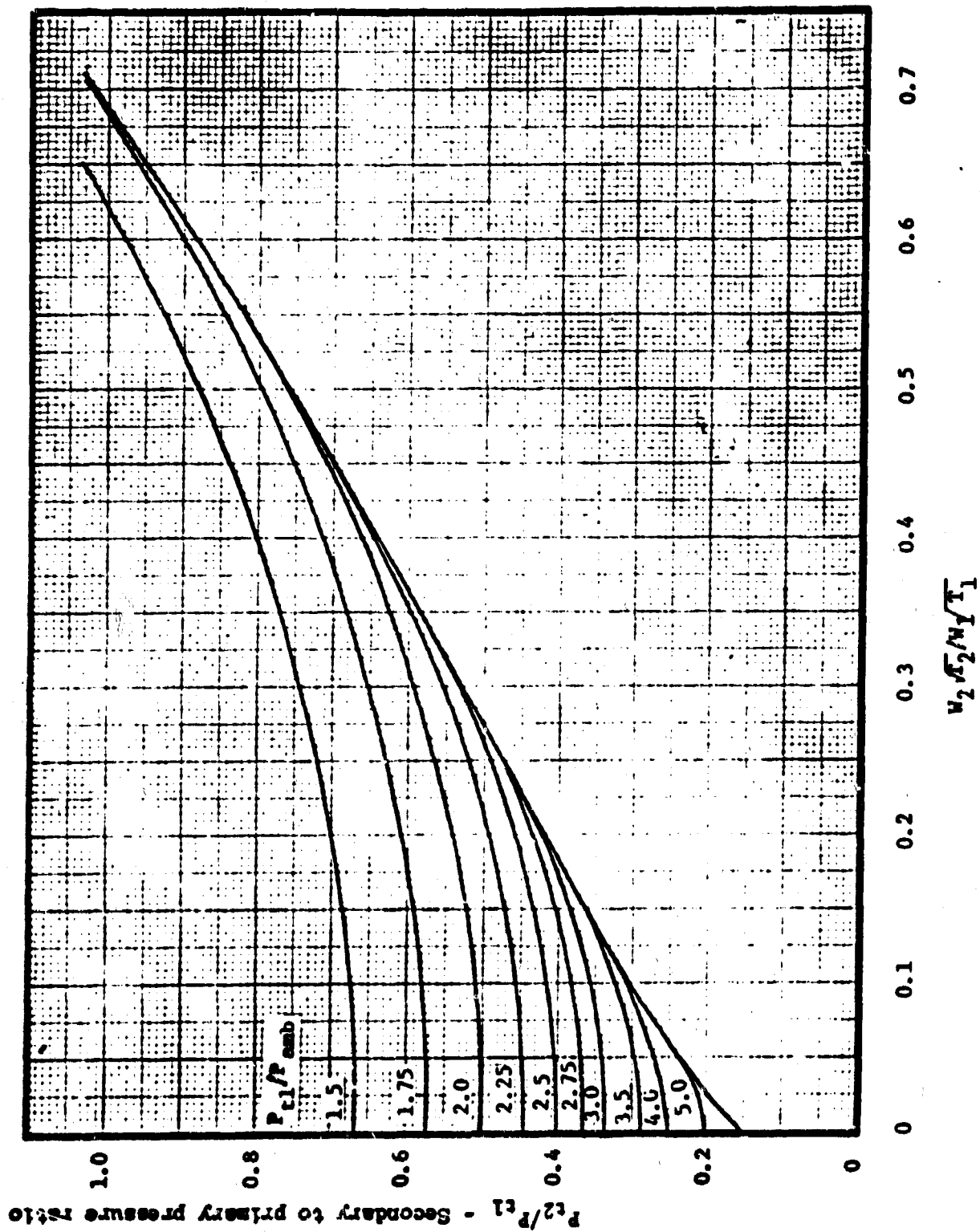


FIGURE 8-101 Two-flow Nozzle Pumping Characteristics.
 $\gamma_1=1.3$ $\gamma_2=1.4$ $A^*_{t1}/A_{EXIT}=0.6$

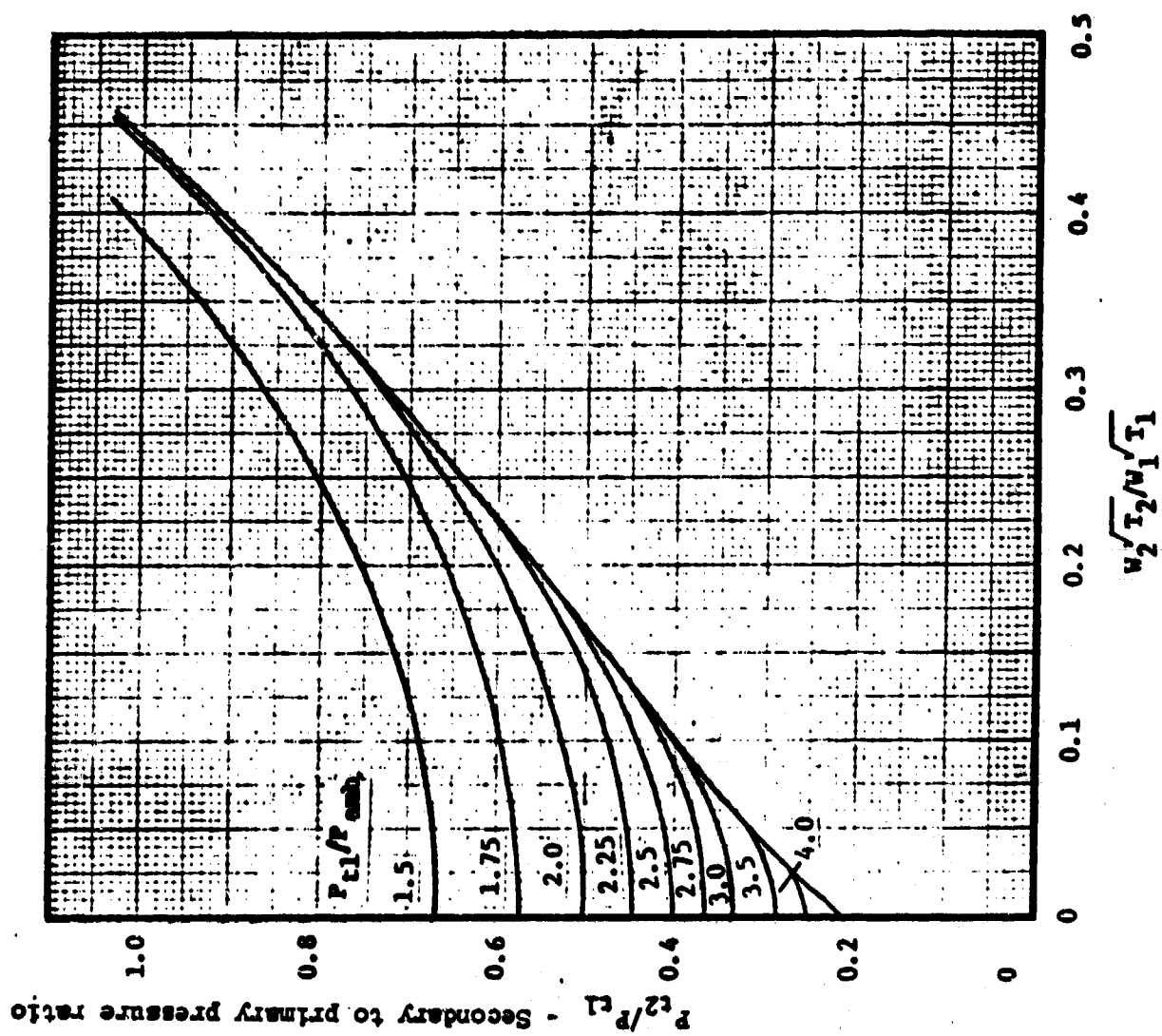


FIGURE 8-102 Two-flow Nozzle Pumping Characteristics.
 $\gamma_1=1.3$ $\gamma_2=1.4$ $A^*_1/A_{EXIT}=0.7$

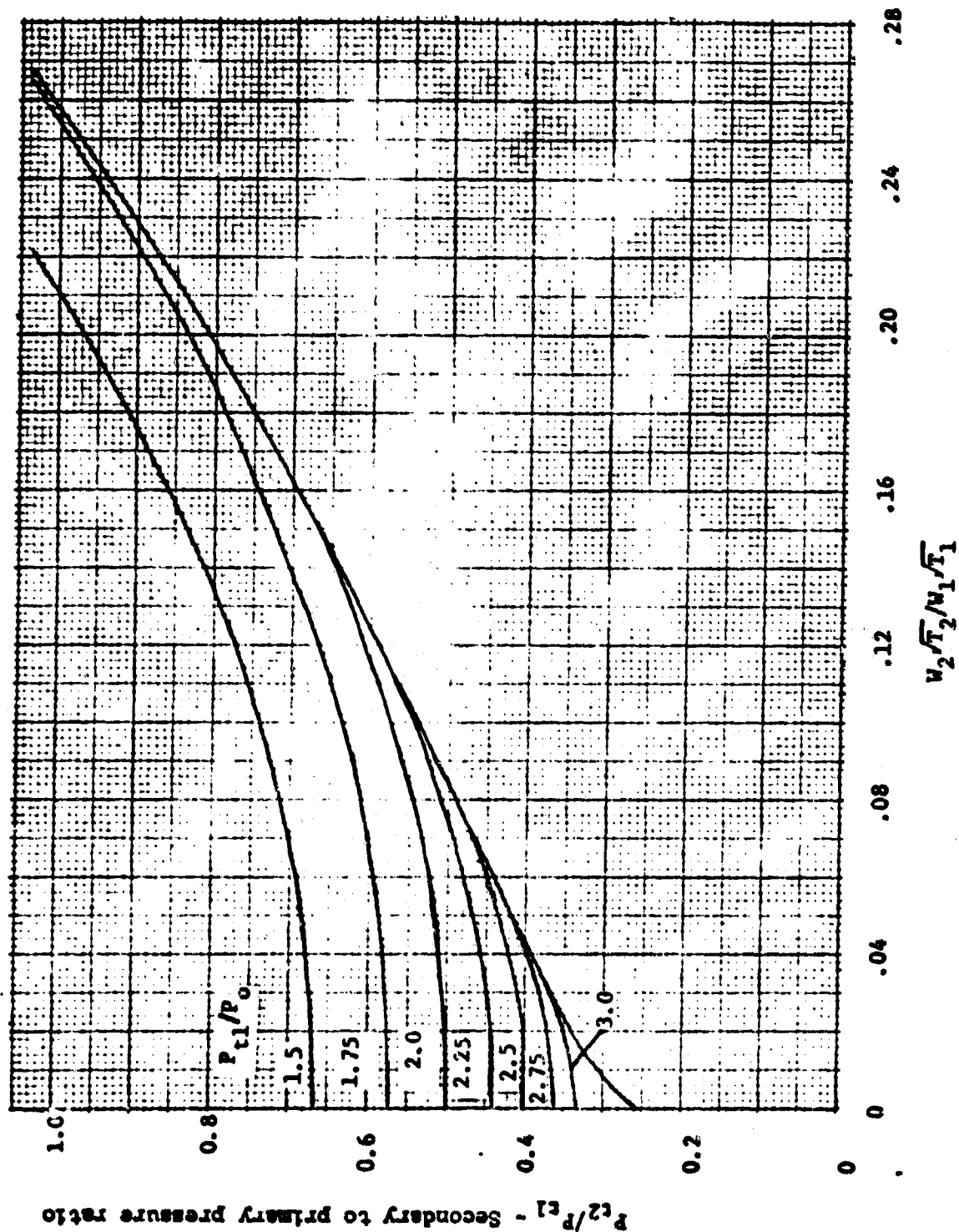


FIGURE 8-103 Two-Flow Nozzle Pumping Characteristics.
 $\gamma_1=1.3$ $\gamma_2=1.4$ $A^*/A_{EXIT}=0.8$

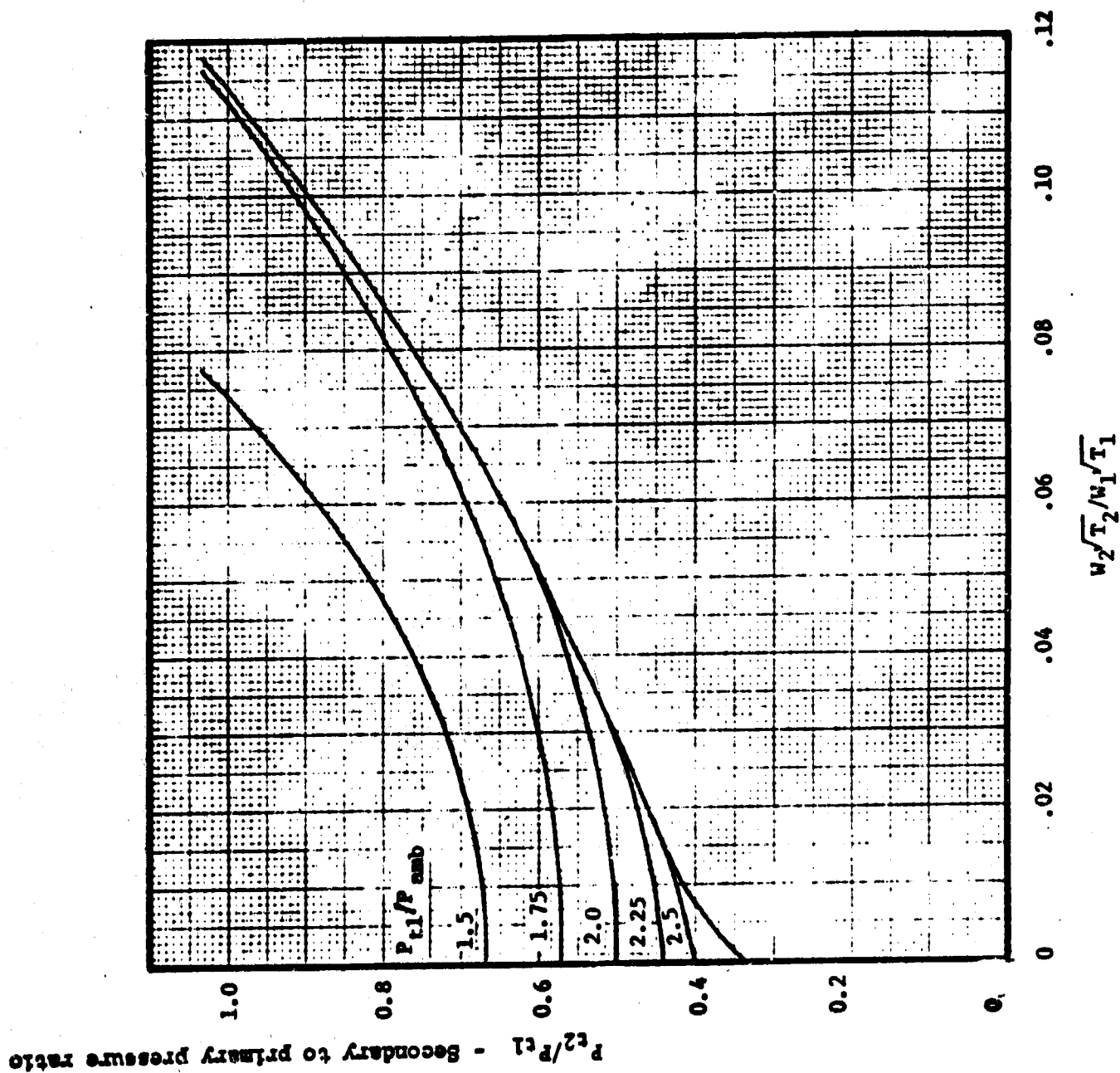


FIGURE 8-104 Two-flow Nozzle Pumping Characteristics.
 $\gamma_1=1.3$ $\gamma_2=1.4$ $A^*_{t1}/A_{EXIT}=0.9$

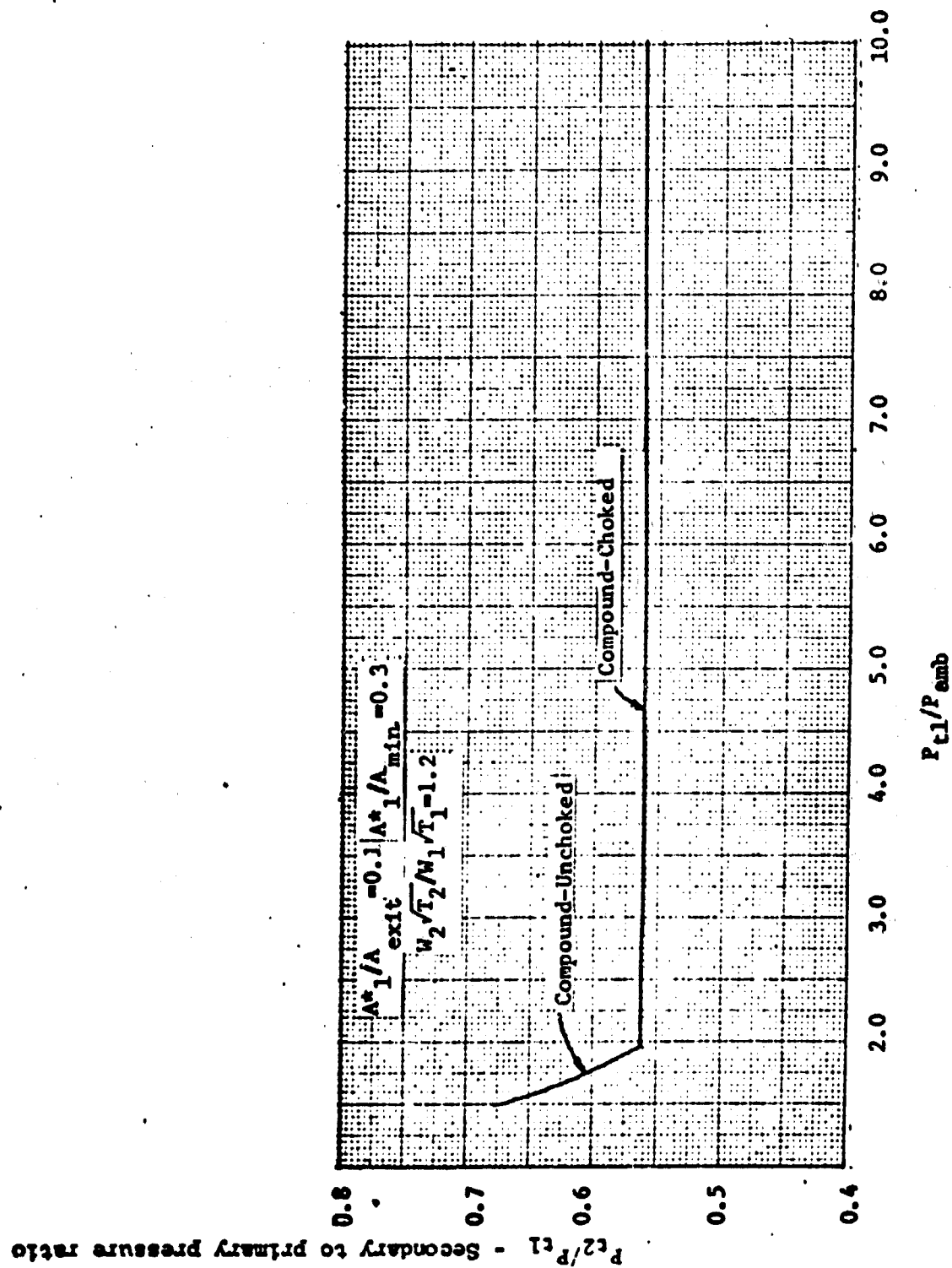


FIGURE 8-105 Variation in P_{t2}/P_{t1} with Primary Nozzle Pressure Ratio.

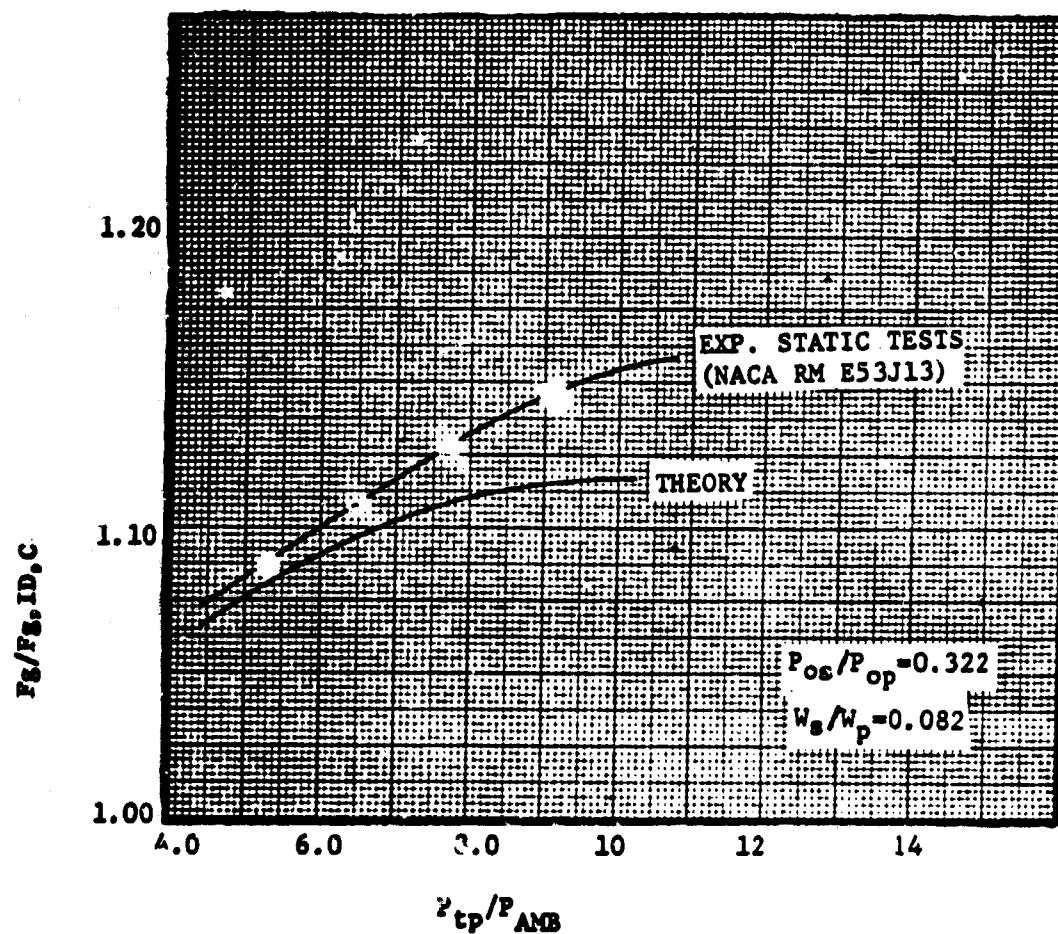


FIGURE 8-106 Comparison of Theoretical and Experimental Static Thrust Characteristics for One Ejector Operating Point.

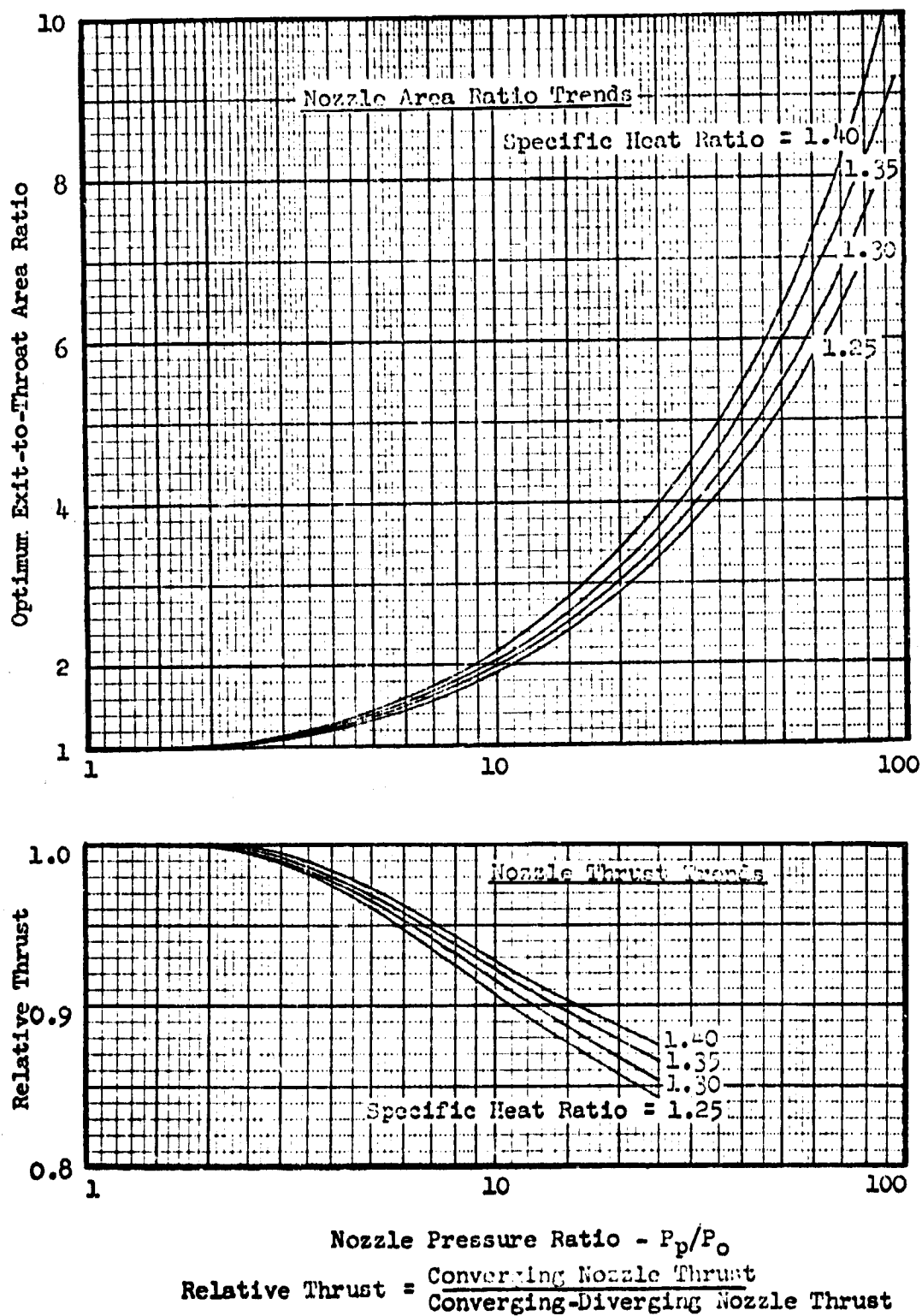


Figure 8 - 107. Optimum Area Ratio and Thrust Trends for Converging-Diverging Nozzles (Reference 1).

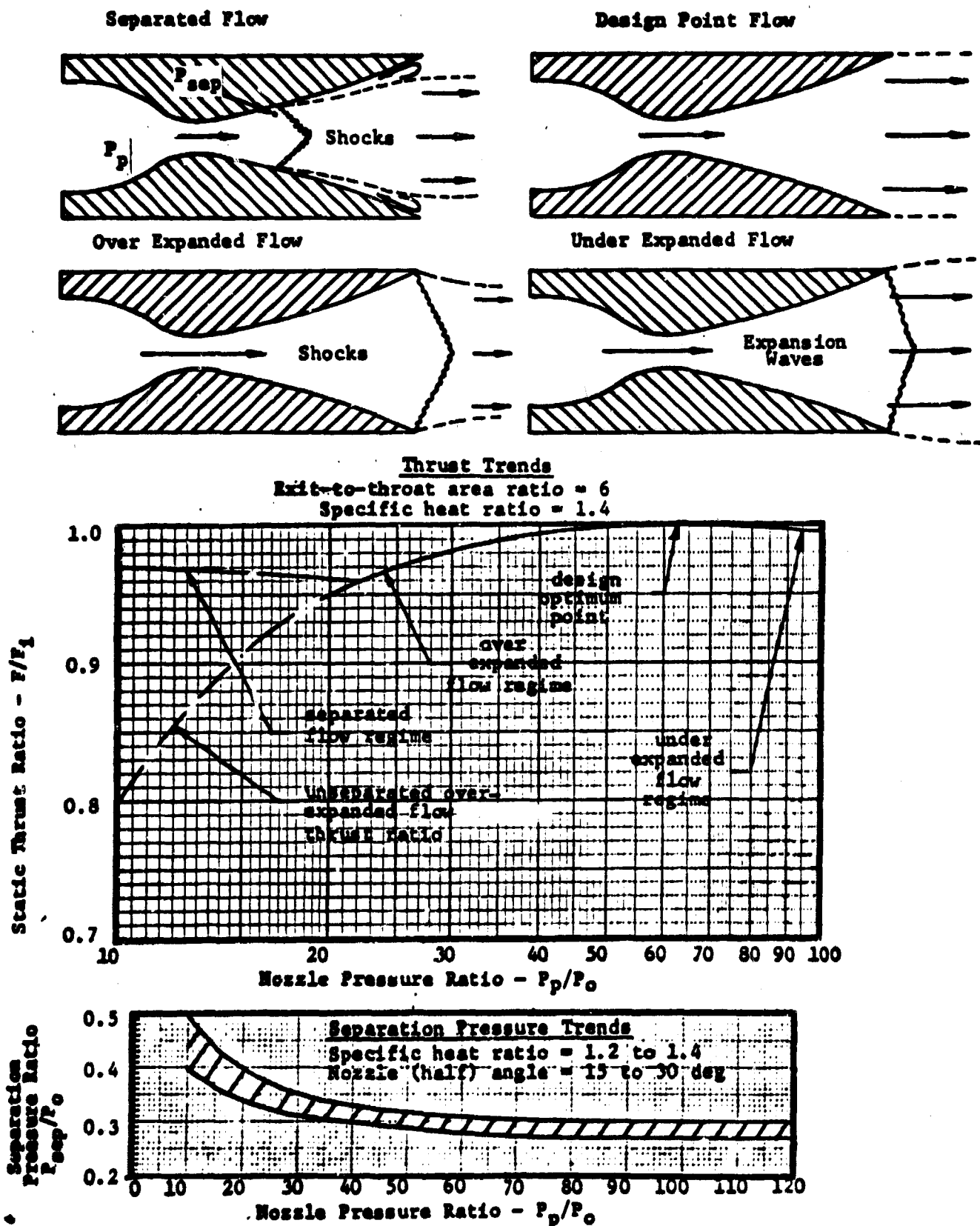


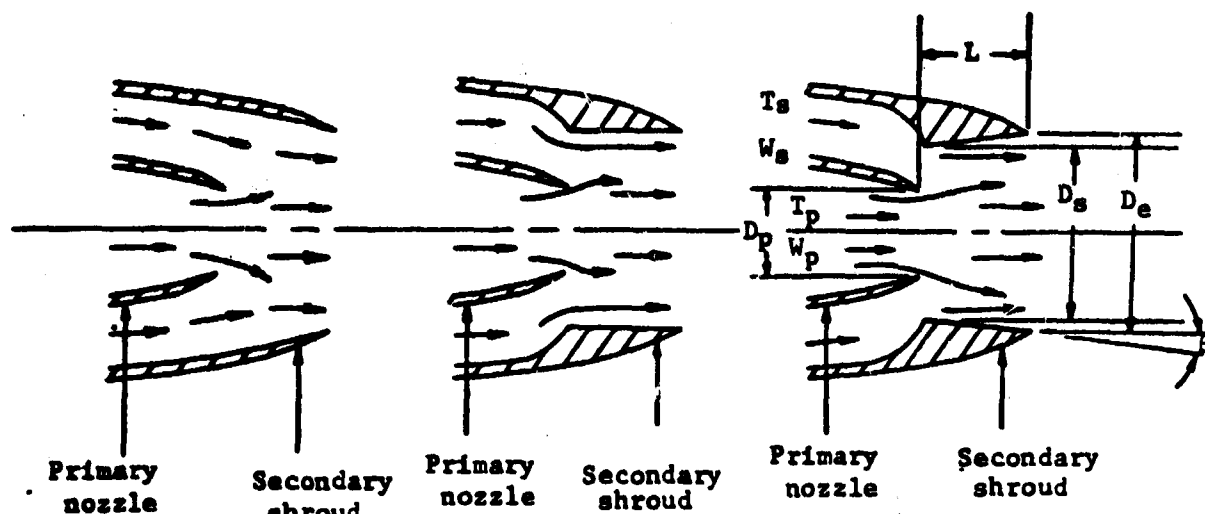
FIGURE 8-108 Typical Operating Regimes for Conical Converging-Diverging Nozzles (References 2 and 3)

Design Flow Fields of Ejector Nozzles

Convergent Shroud

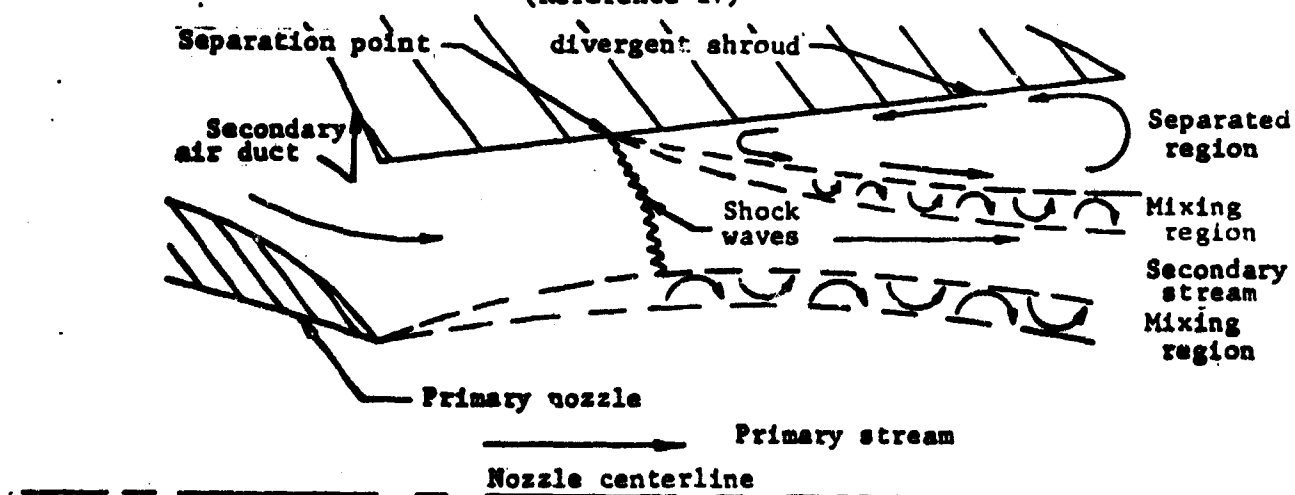
Cylindrical Shroud

Divergent Shroud



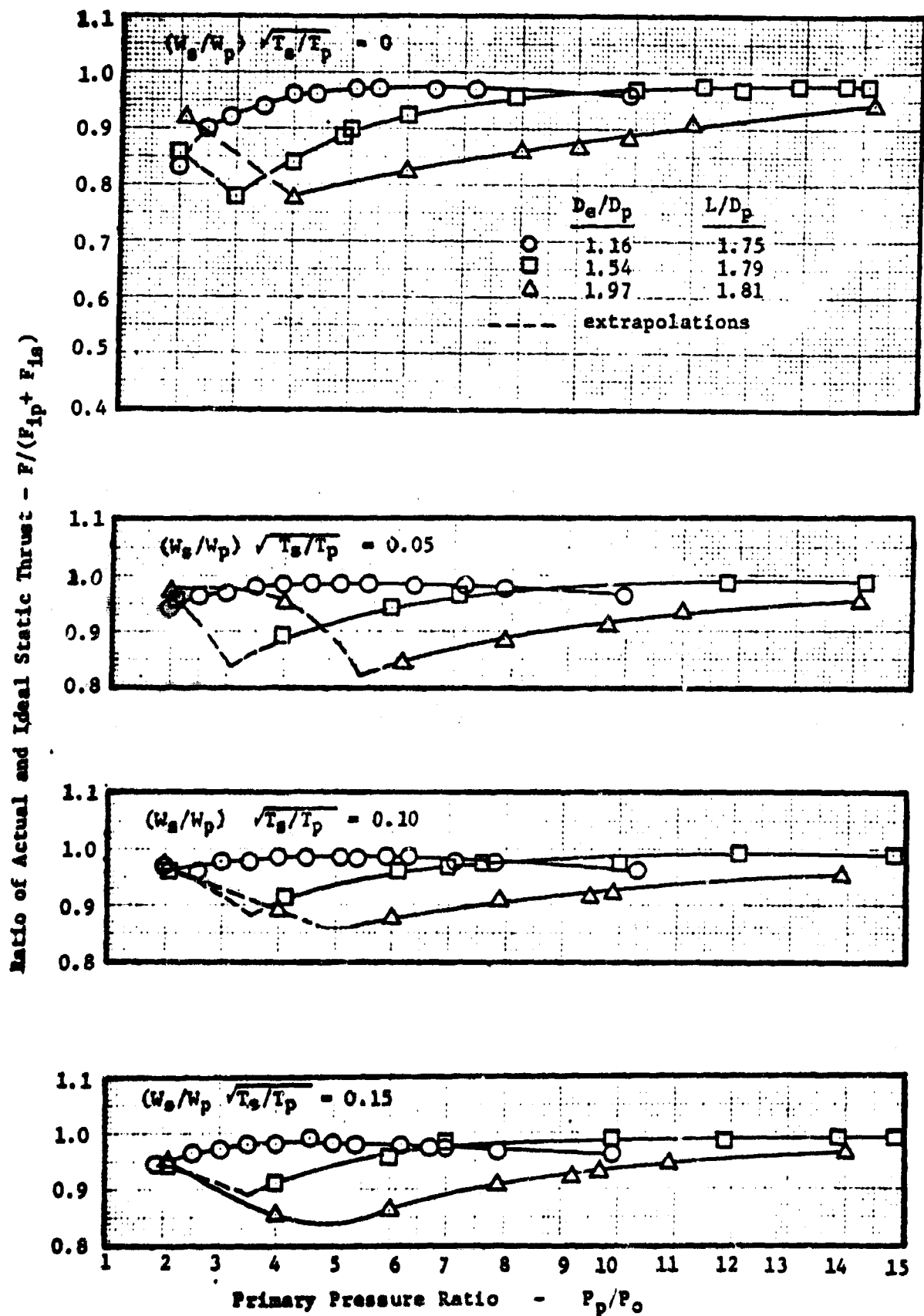
Divergent Shroud Nozzle Separated Flow Fields

(Reference 17)



- D_p = primary nozzle symbols
- D_e = divergent shroud exit diameter
- D_s = divergent shroud throat diameter
- L = spacing between nozzle and shroud exits
- W_p = primary (nozzle) gas flow rate
- W_s = secondary air flow rate
- T_p = primary (nozzle) gas total (absolute) temperature
- T_s = secondary air total (absolute) temperature

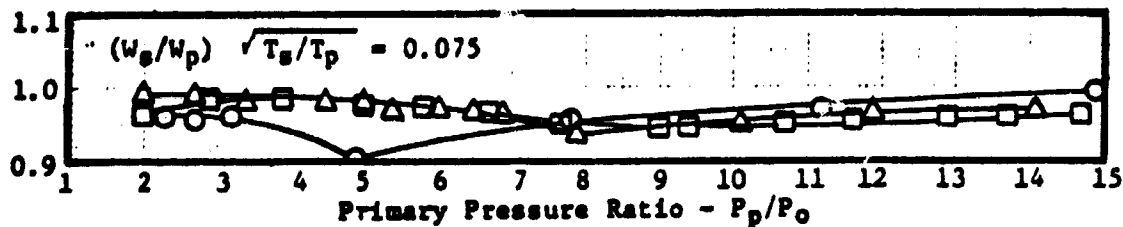
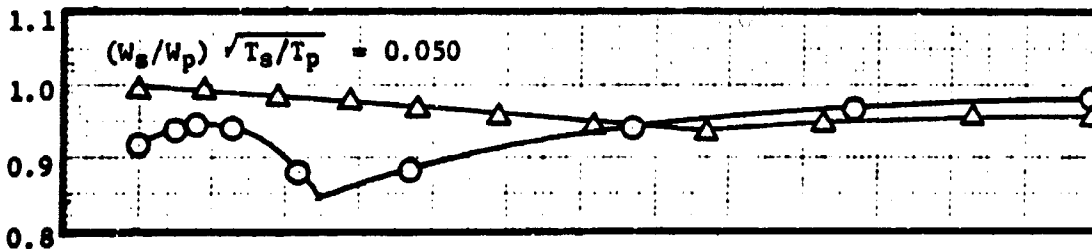
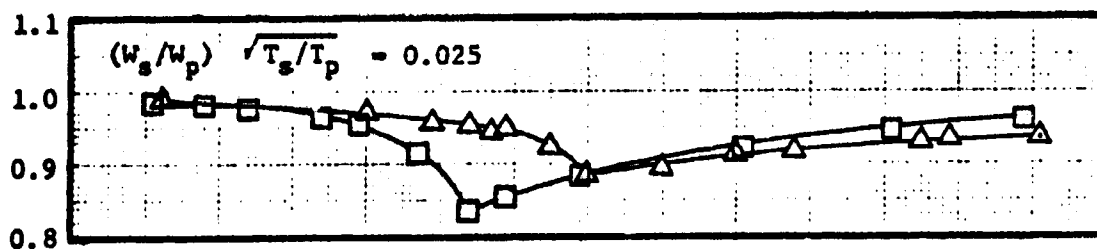
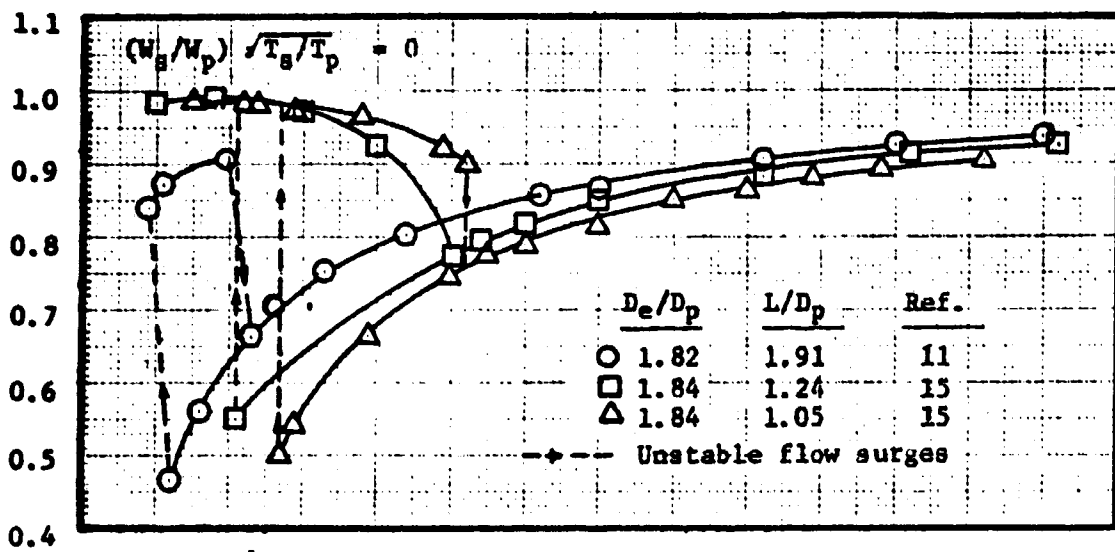
FIGURE 8-109 Convergent-Divergent Ejector Nozzle Flow Fields



Note: See Figure 8-109 for symbol identification

FIGURE 8-110 Effect of Exit-to-Primary Area Ratio on Divergent Shroud Nozzle Thrust (Reference 1)

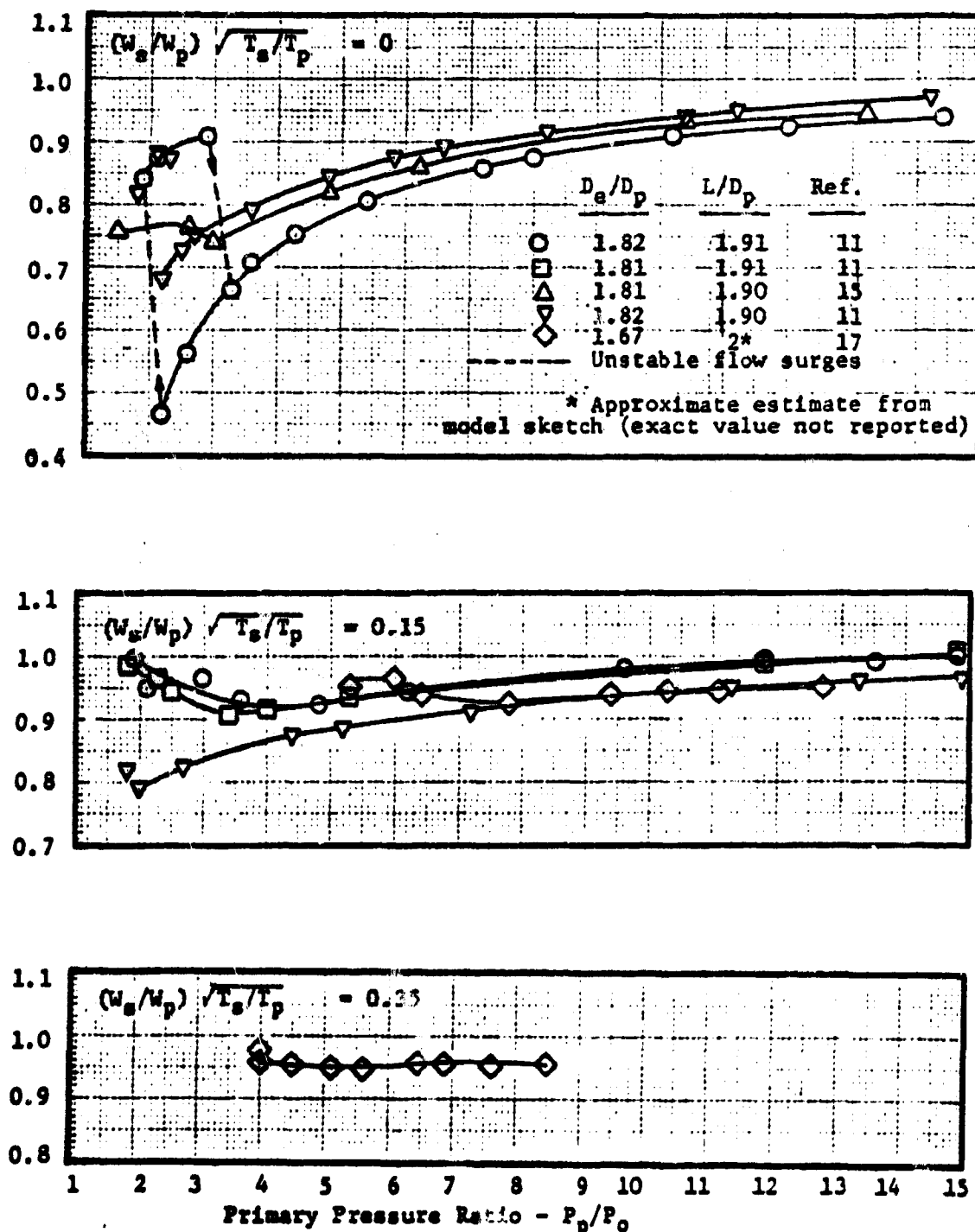
Ratio of Actual and Ideal Static Thrust - $F/(F_{ip} + F_{is})$



Note: See Figure 8-109 for symbol identification

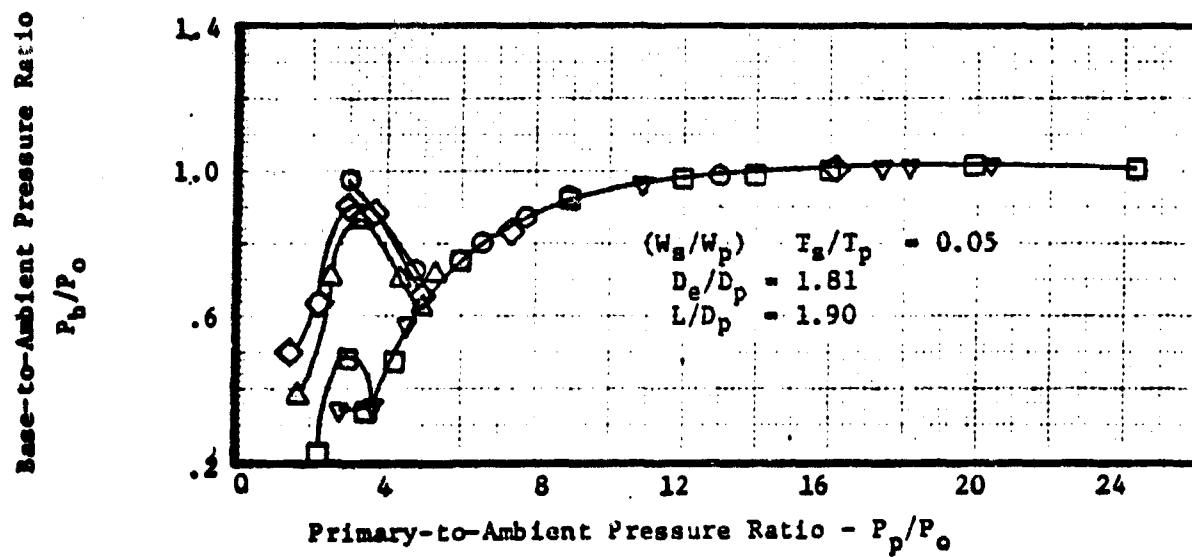
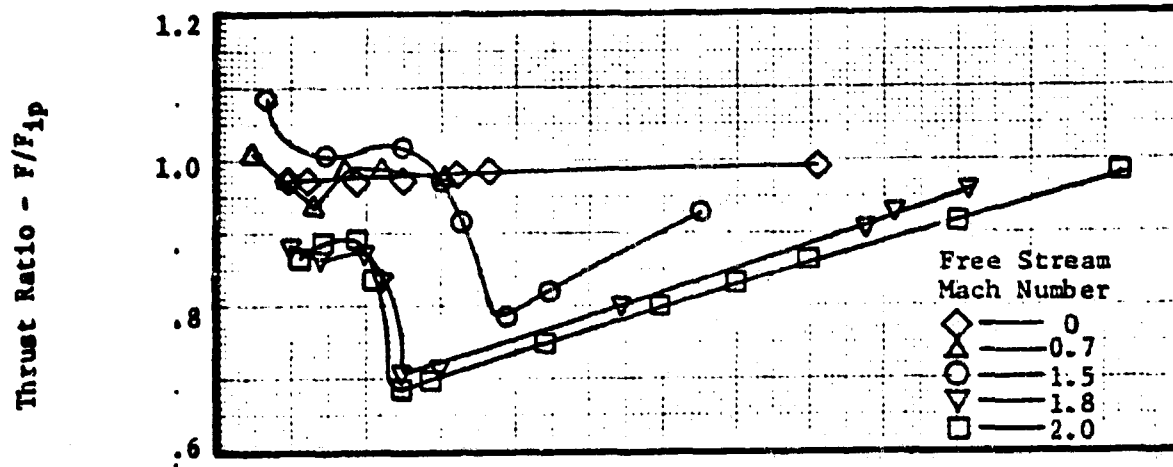
FIGURE 8-111 Effect of Nozzle and Shroud Exit Spacing on Divergent Shroud Ejector Nozzle Thrust

Ratio of Actual and Ideal Static Thrust - $F/(F_{ip}+F_{is})$



Note: See Figure 8-109 for symbol identification

FIGURE 8-112. Effect of Secondary Flow on Divergent Shroud Ejector Nozzle Thrust



NOTE: See Figure 8-109 for symbol identification

FIGURE 8-113. External Aerodynamic Flow Effects on Nozzle Thrust (Reference 9)

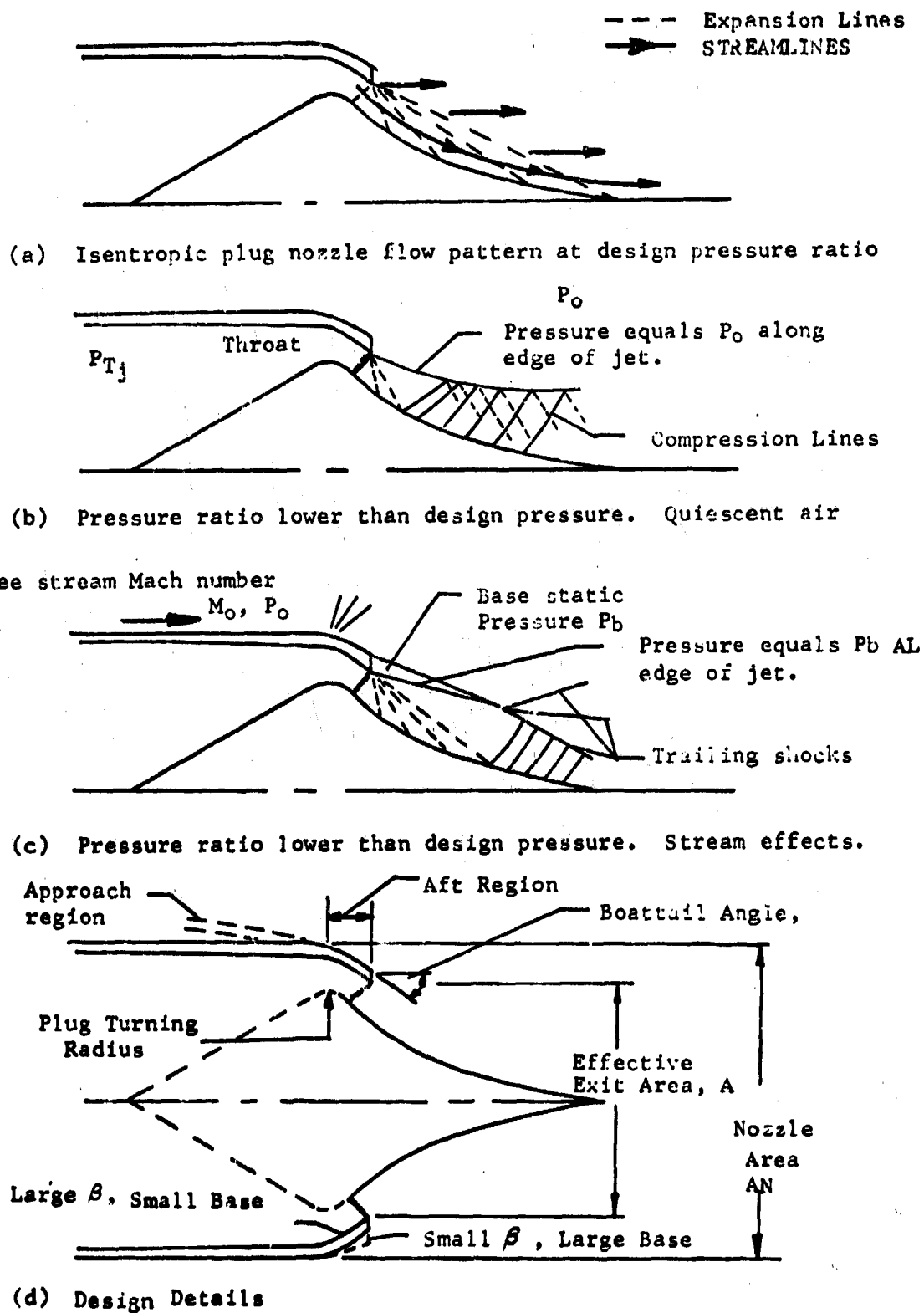


FIGURE 8-114. Isentropic Plug Flow and Design Characteristics

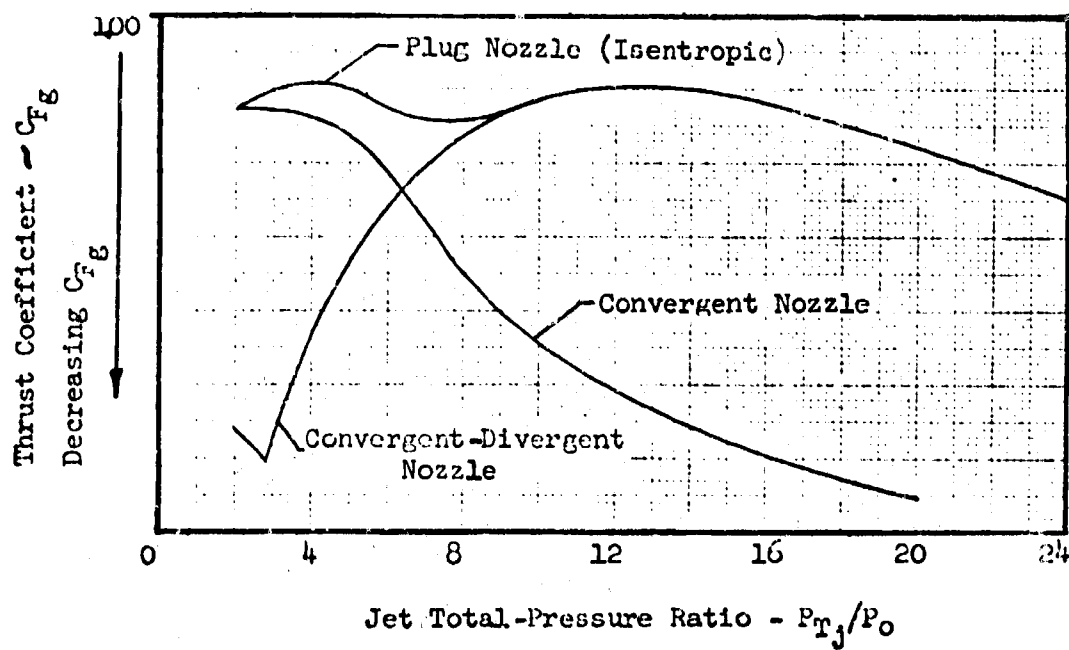


Figure 8 - 115 Comparison of Nozzle Performance.

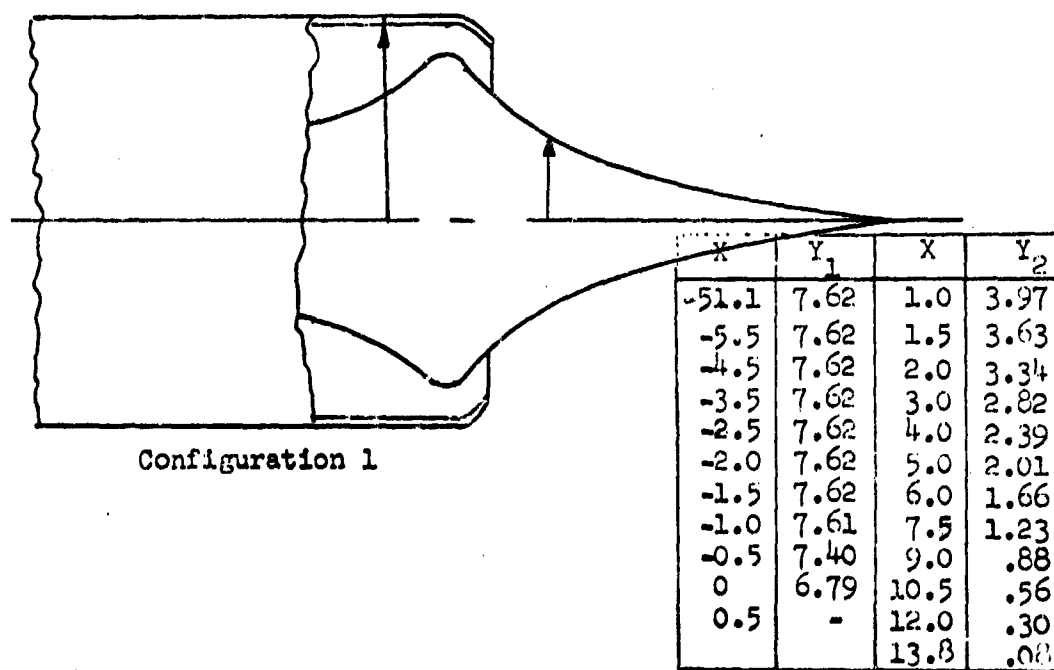
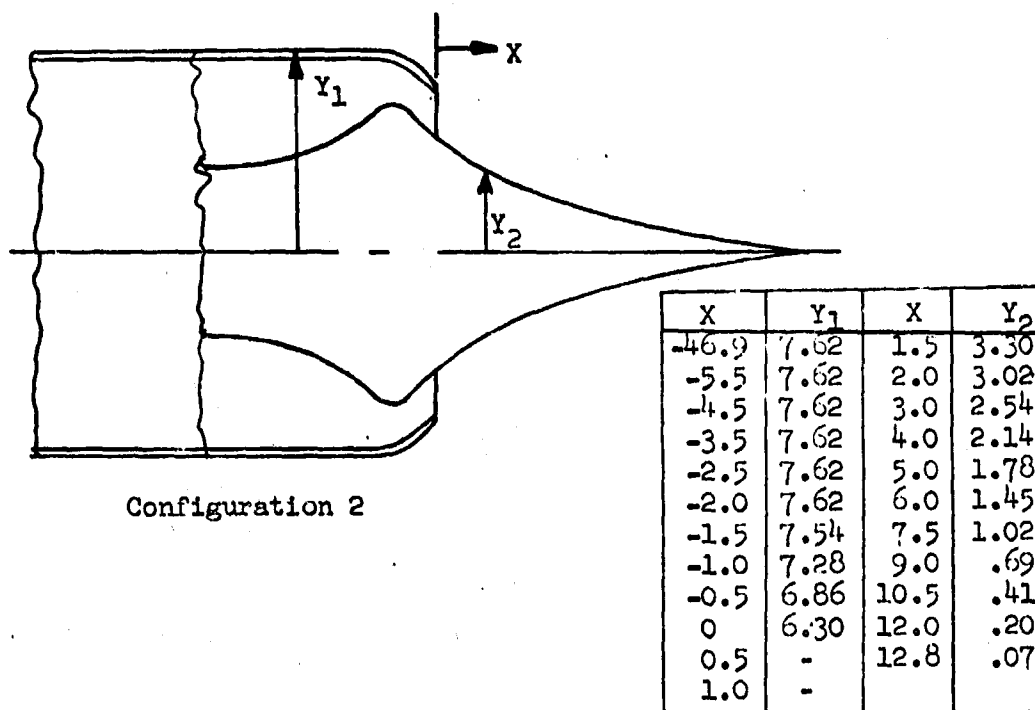


Figure 8 -116. Two Nozzle Configurations with a Design Pressure Ratio of 16.5.

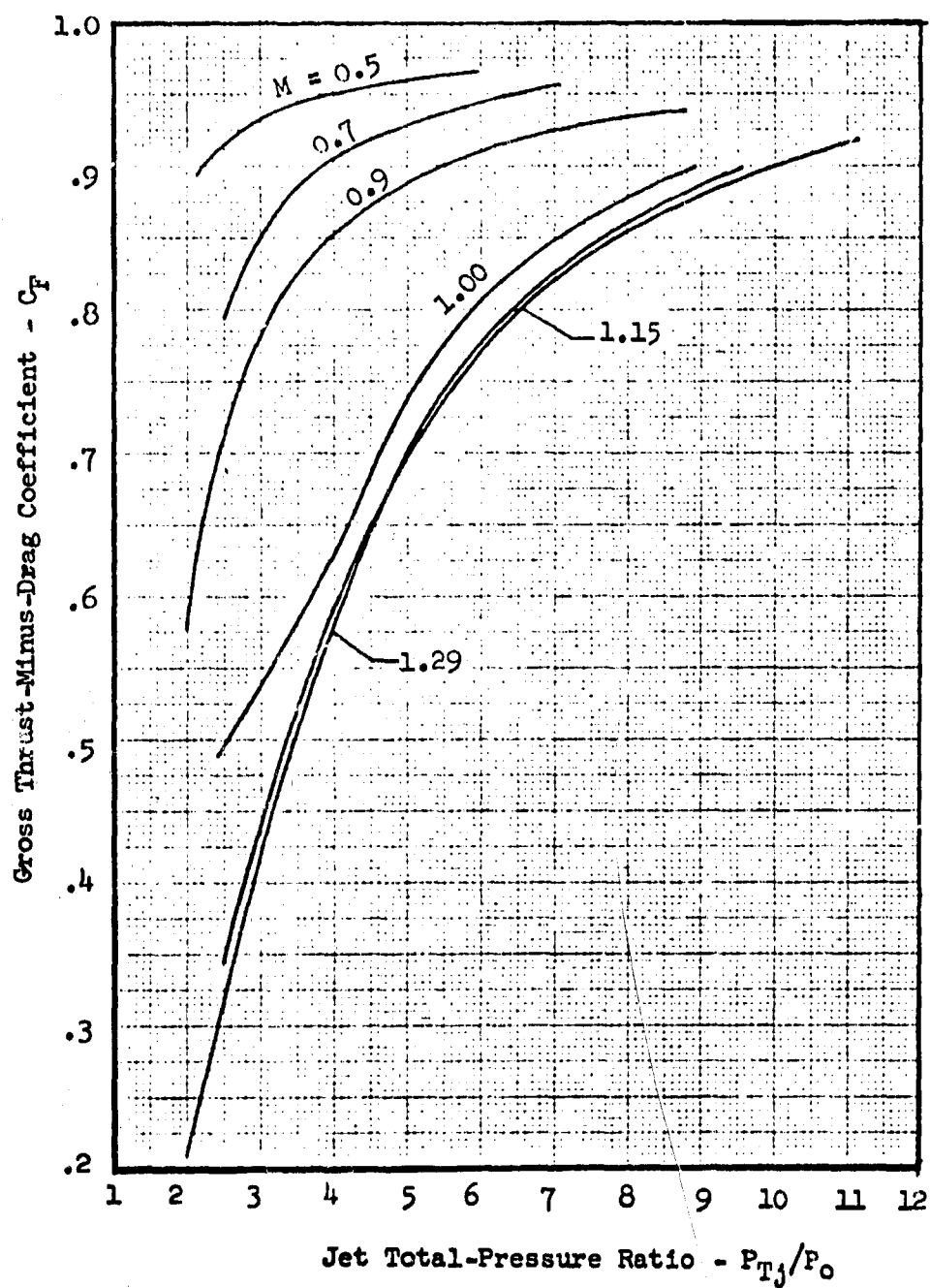


Figure 8 -117. Variation of Gross Thrust-Minus-Drag Coefficient with Jet Total Pressure Ratio.

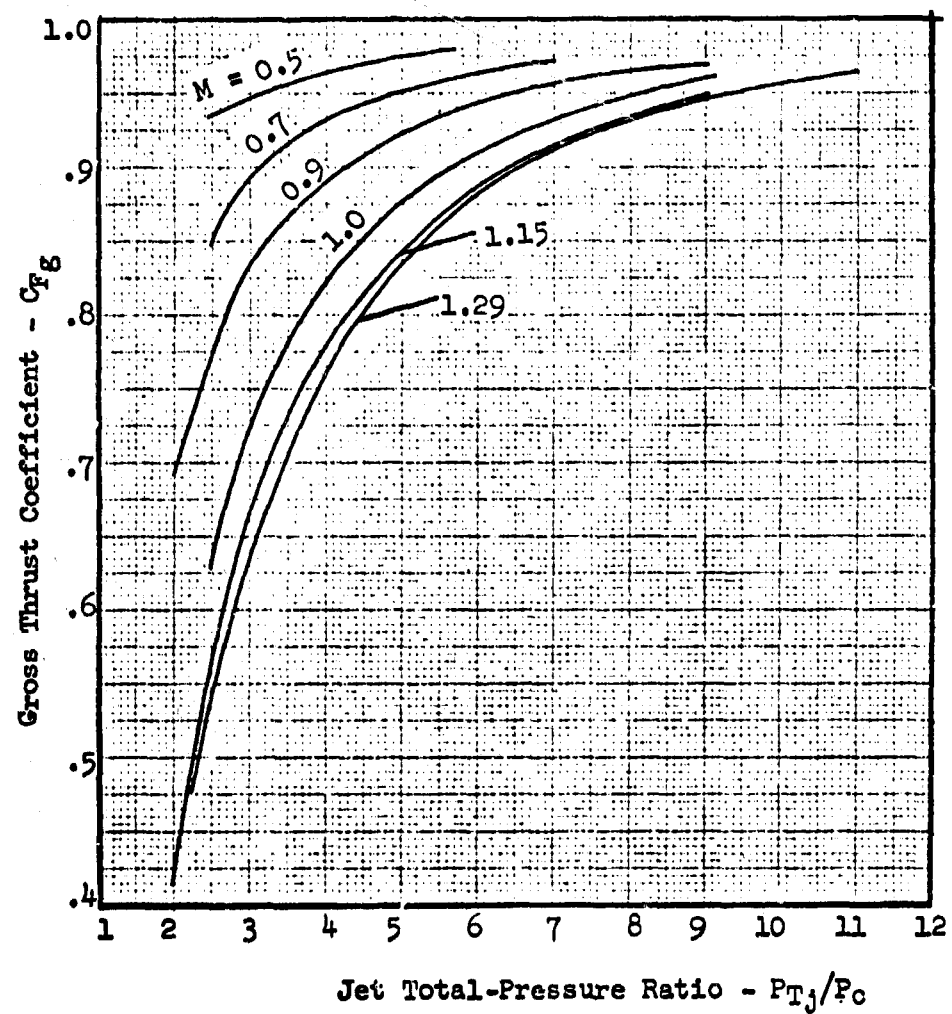


Figure 8 -118. Variation of Gross Thrust Coefficient with Jet Total-Pressure Ratio.

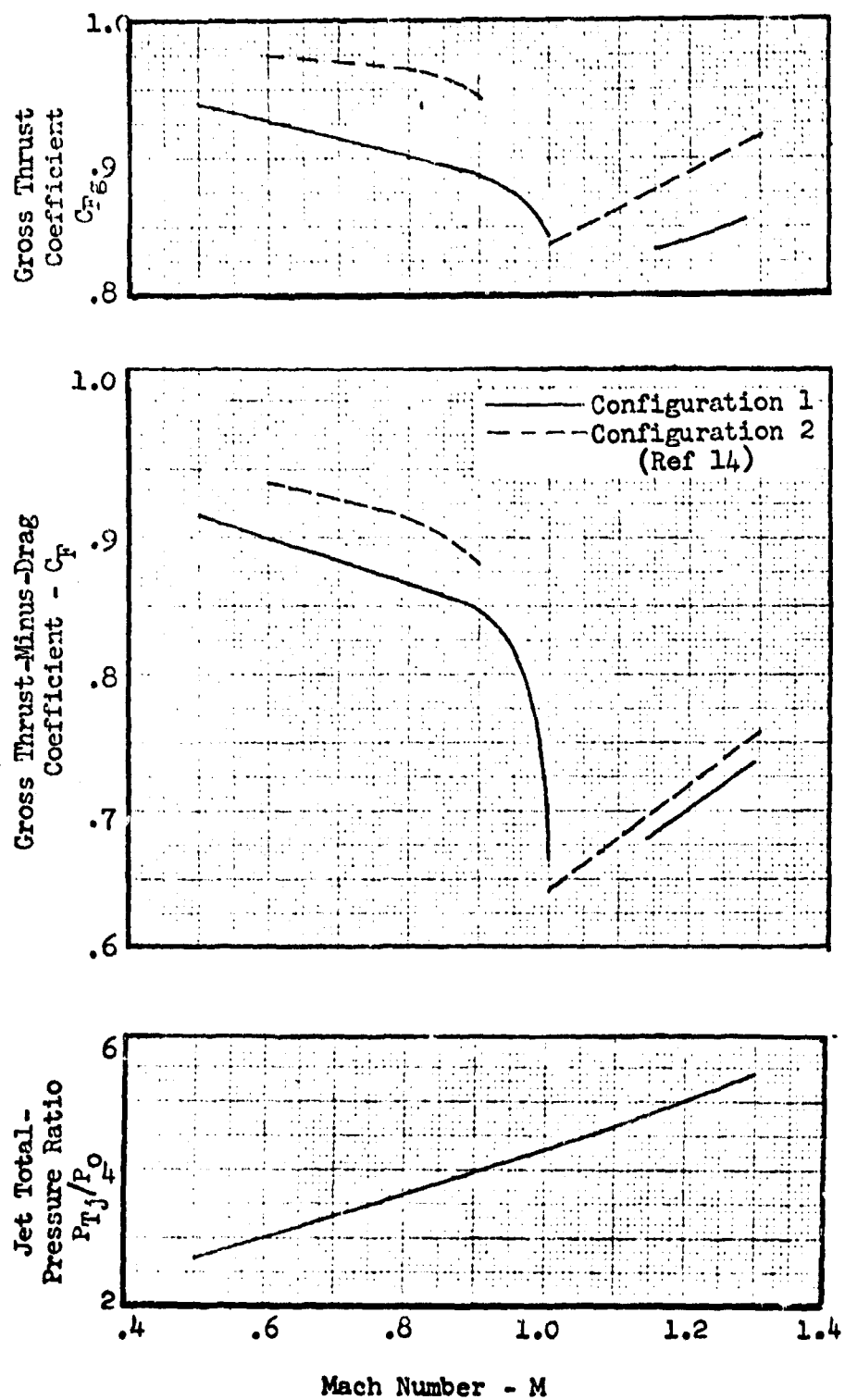


Figure 8 -119. Gross Thrust-Minus-Drag and Gross Thrust Coefficients vs. Mach Number for Jet Total-Pressure Ratio Schedule.

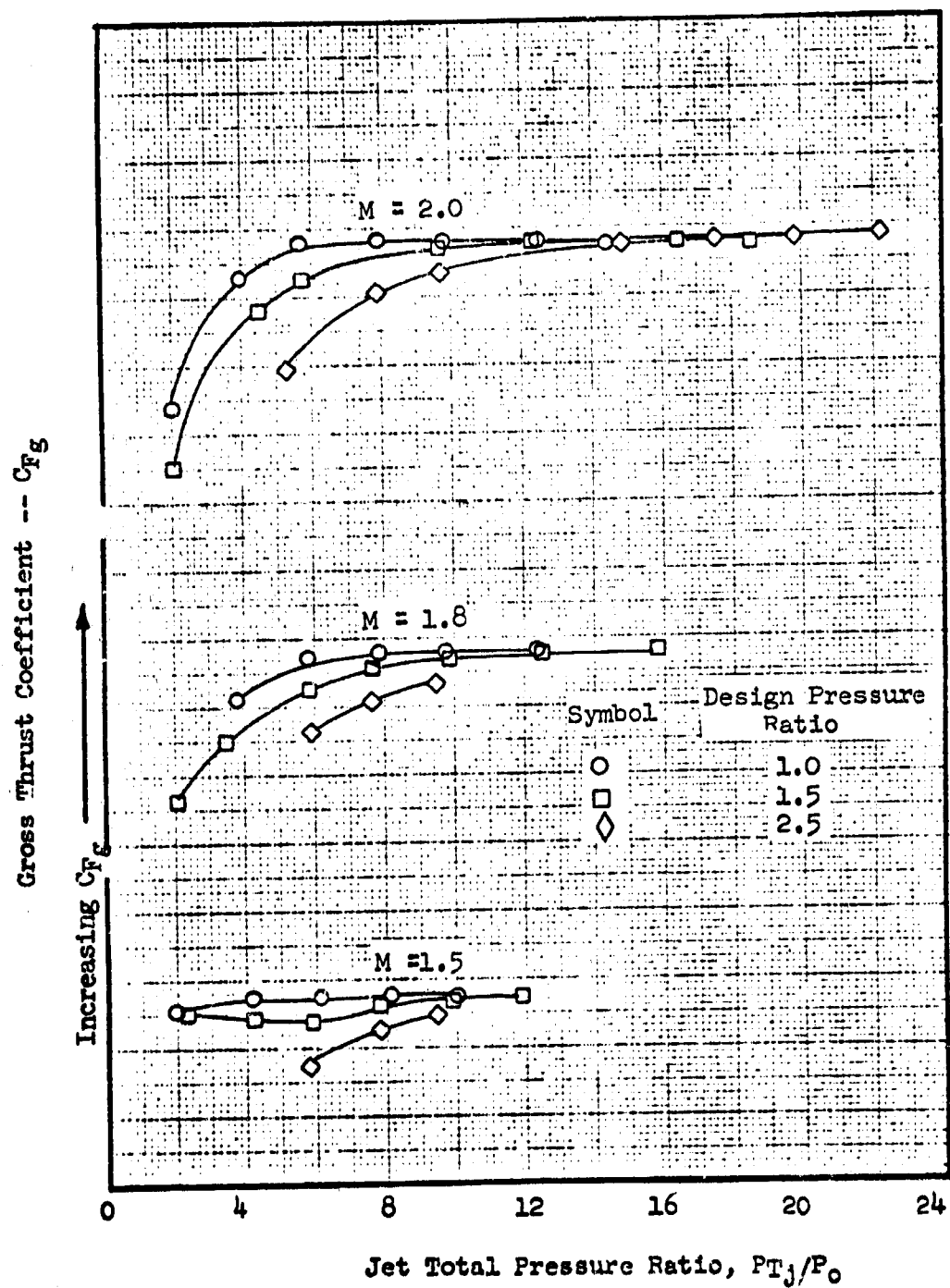
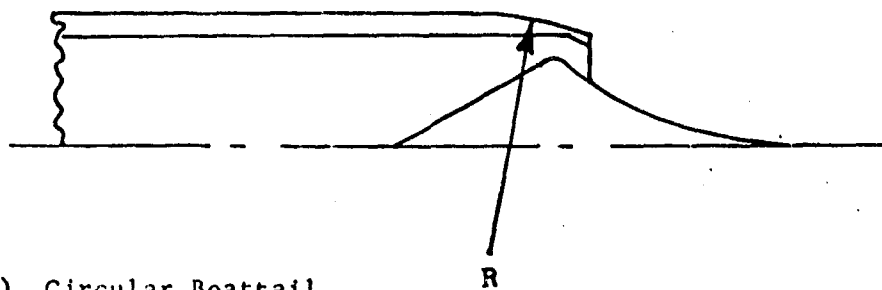


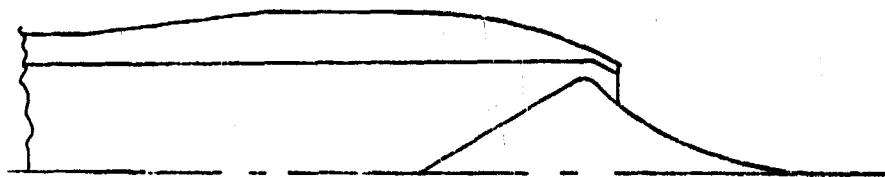
Figure 8 -120. Effect of Design Pressure Ratio on Gross Thrust Coefficient.



(a) Circular Boattail



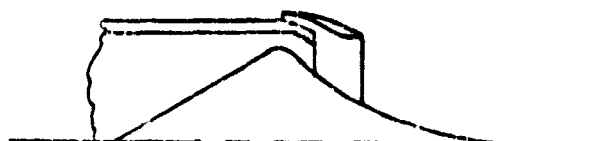
(b) Conical Boattail



(c) Extended Dump



Plain



Contoured

(d) Rings

FIGURE 8.121 Afterbody Configurations

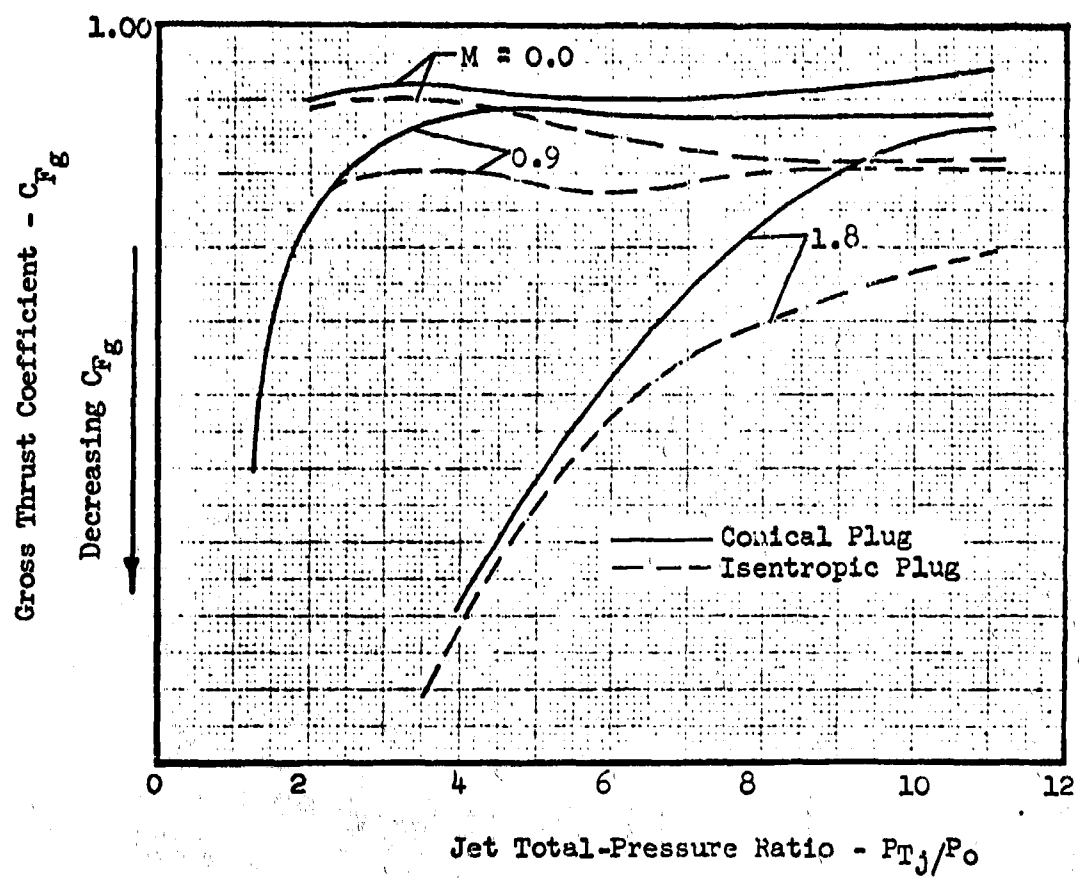
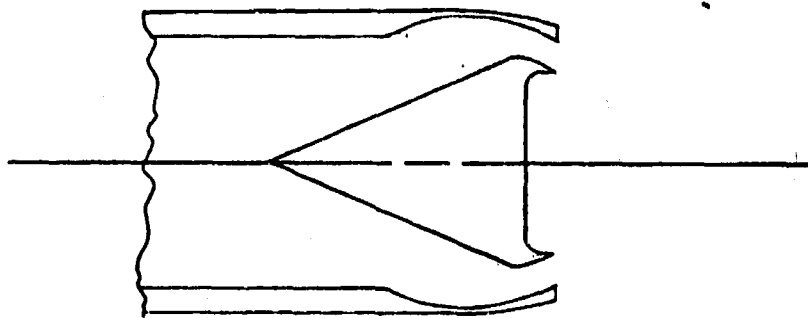
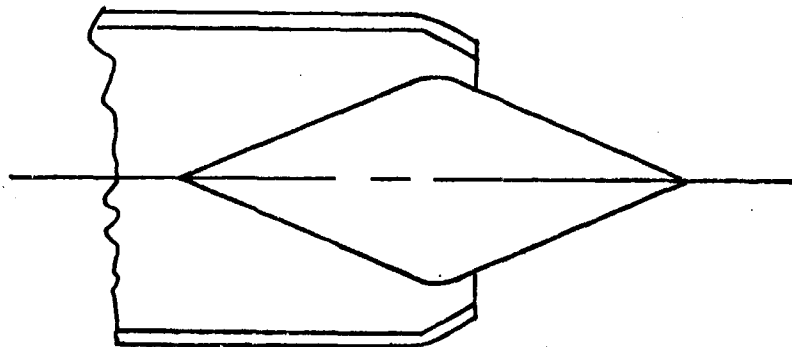


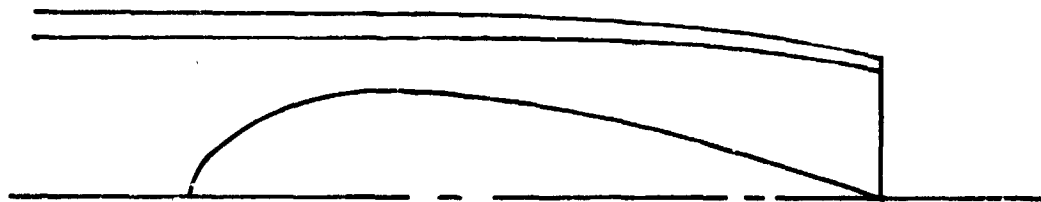
Figure 8 -122. Comparison of Conical Plug Performance to Isentropic Plug Performance.



(a) Plug With Concave Central Base



(b) Conical Plug



(c) Convergent-Divergent Plug Configuration

FIGURE 8-12, Other Types of Plug Nozzles

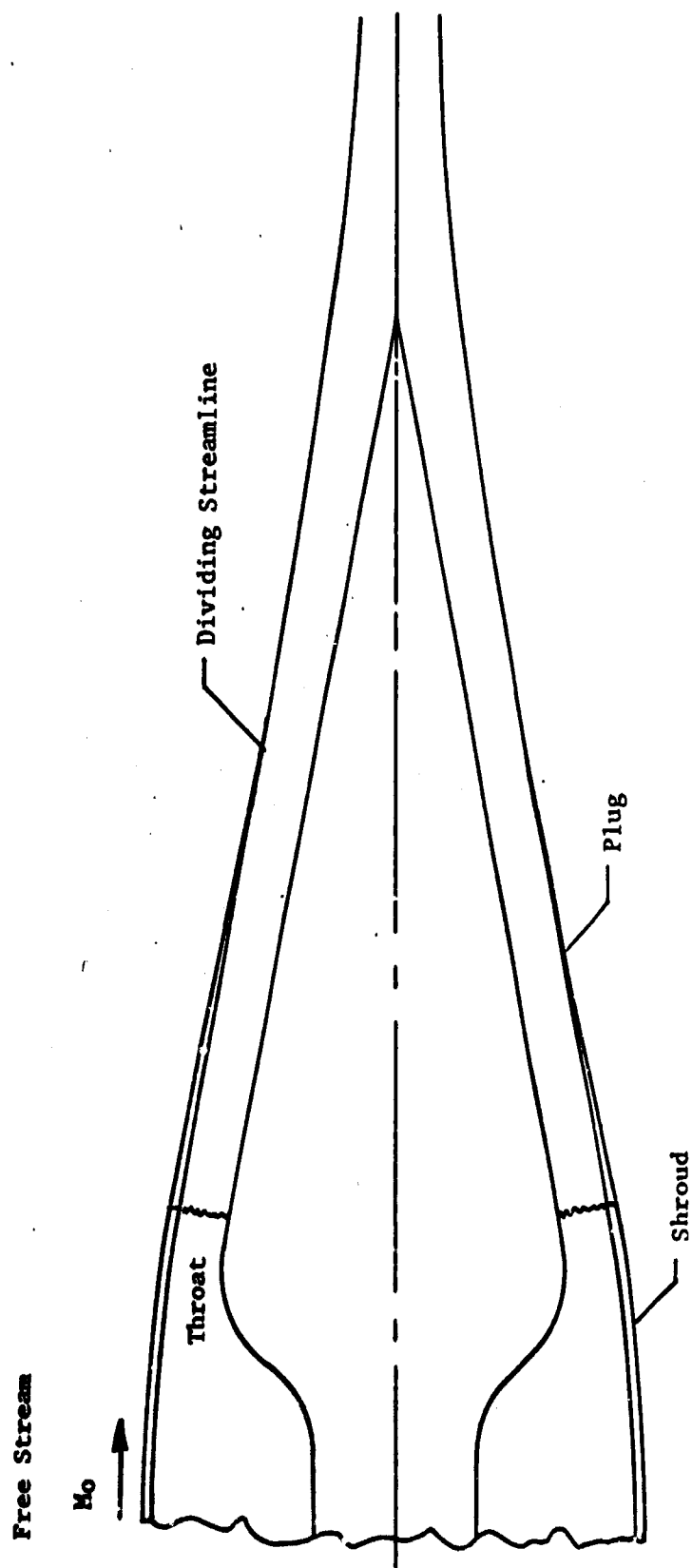


FIGURE 8-124 Aerodynamic Boattail Nozzle Configuration and Flow Pattern.

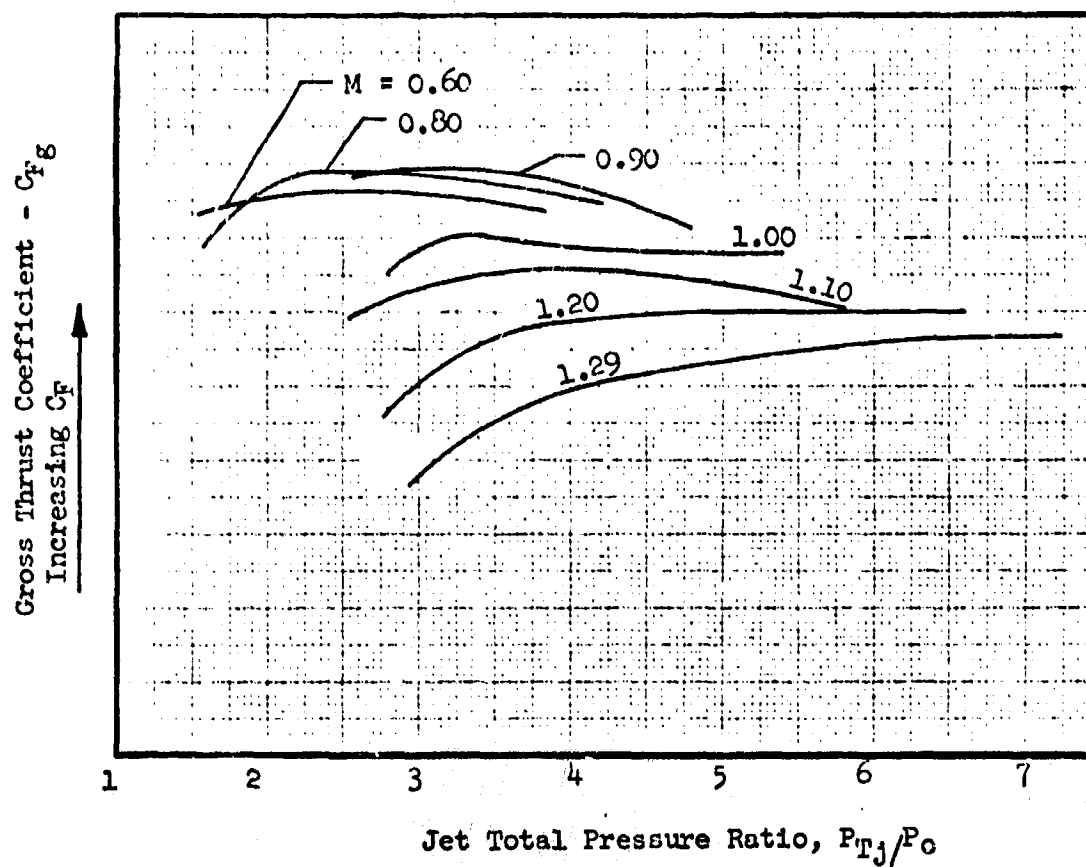


Figure 8 - 125 Effect of Jet Total-Pressure Ratio and Mach Number on Gross Thrust Coefficient.

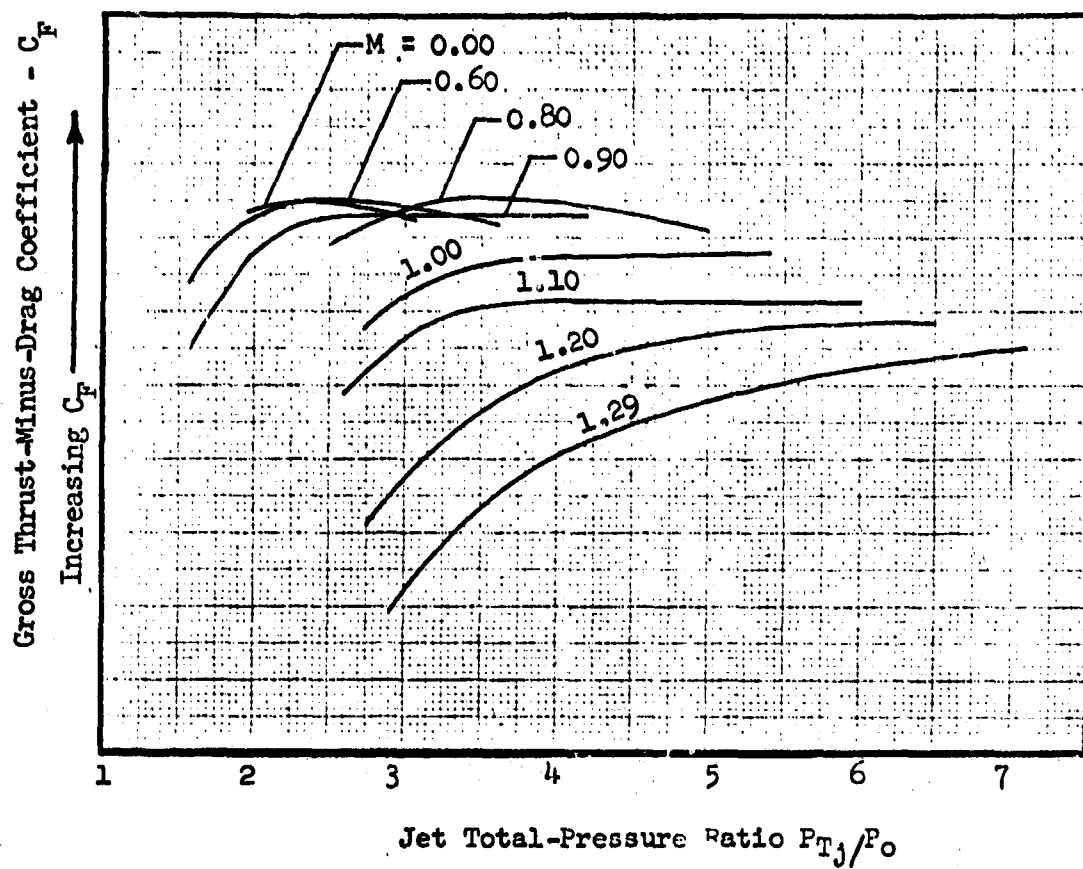


Figure 8 -126. Effect of Jet Total-Pressure Ratio and Mach Number on Gross Thrust-Minus-Drag Coefficient.

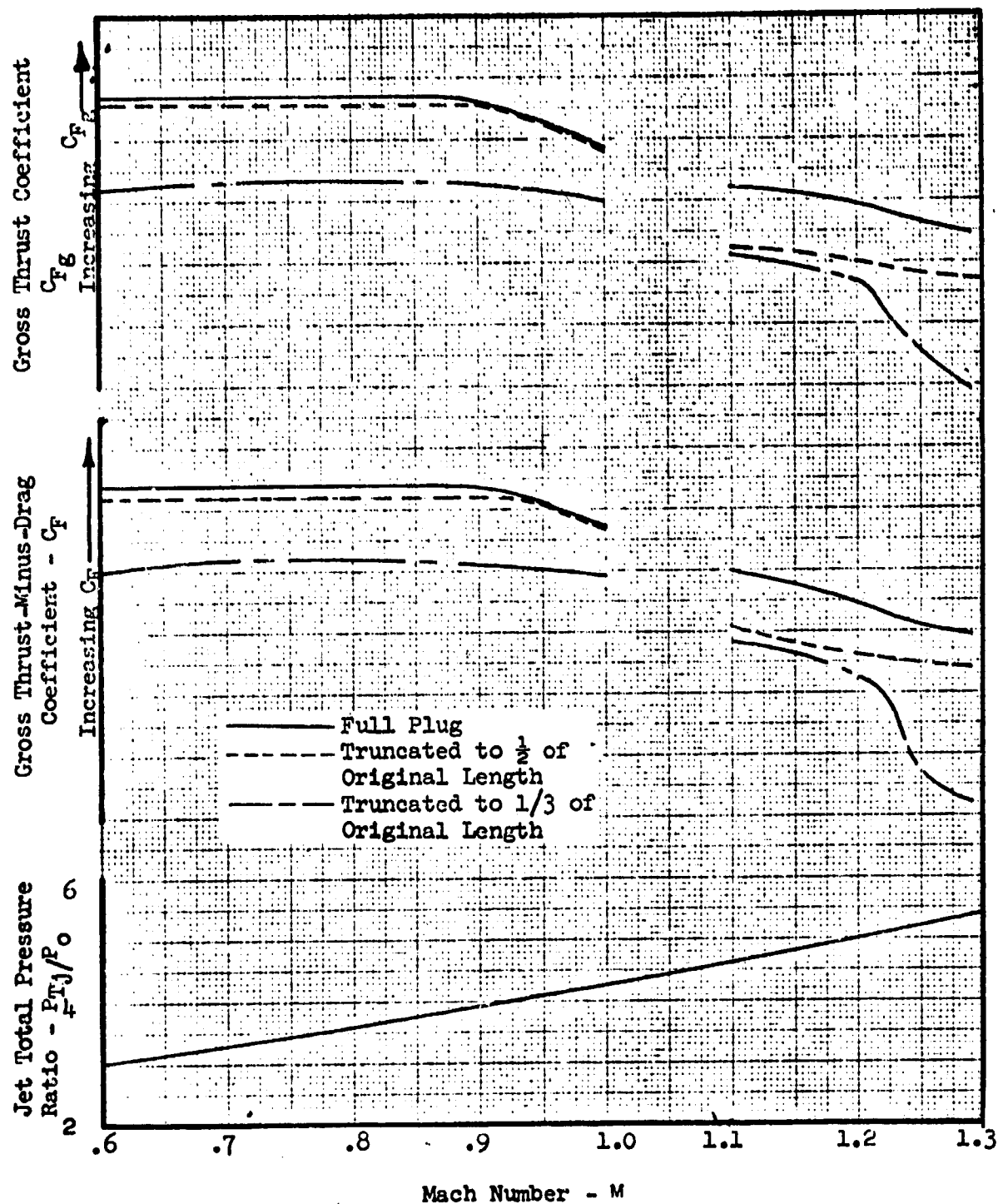


Figure 8 -127. Effect of Truncation on Gross Thrust-Minus-Drag and Gross Thrust Coefficients vs. Mach Number at a Jet Total-Pressure Ratio Schedule.

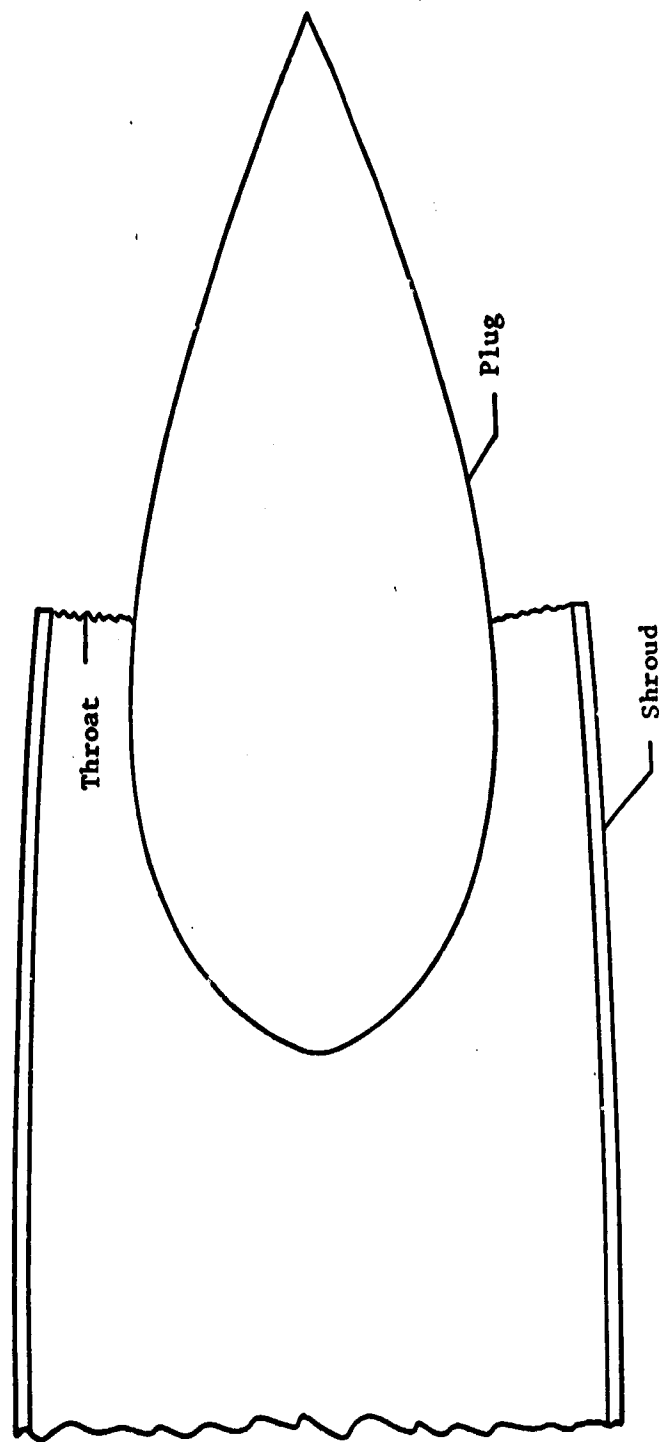
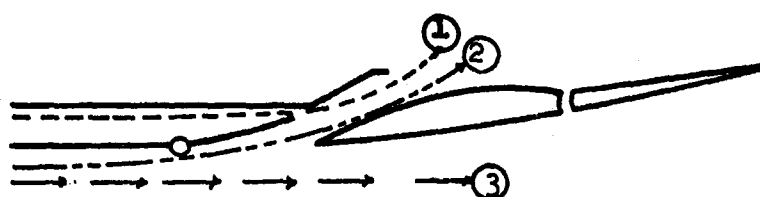


FIGURE 8-126 Configuration of Convergent Plug Nozzle

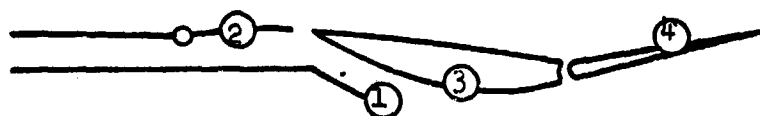


Primary
Airflow →

1. Secondary Flow
2. Tertiary Flow
3. External Flow

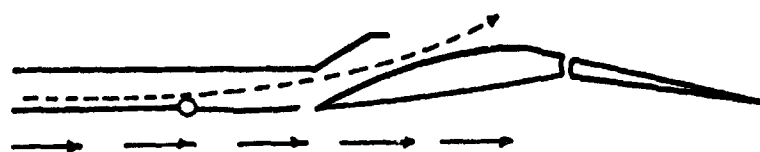


(a) Blow-In-Doors Open



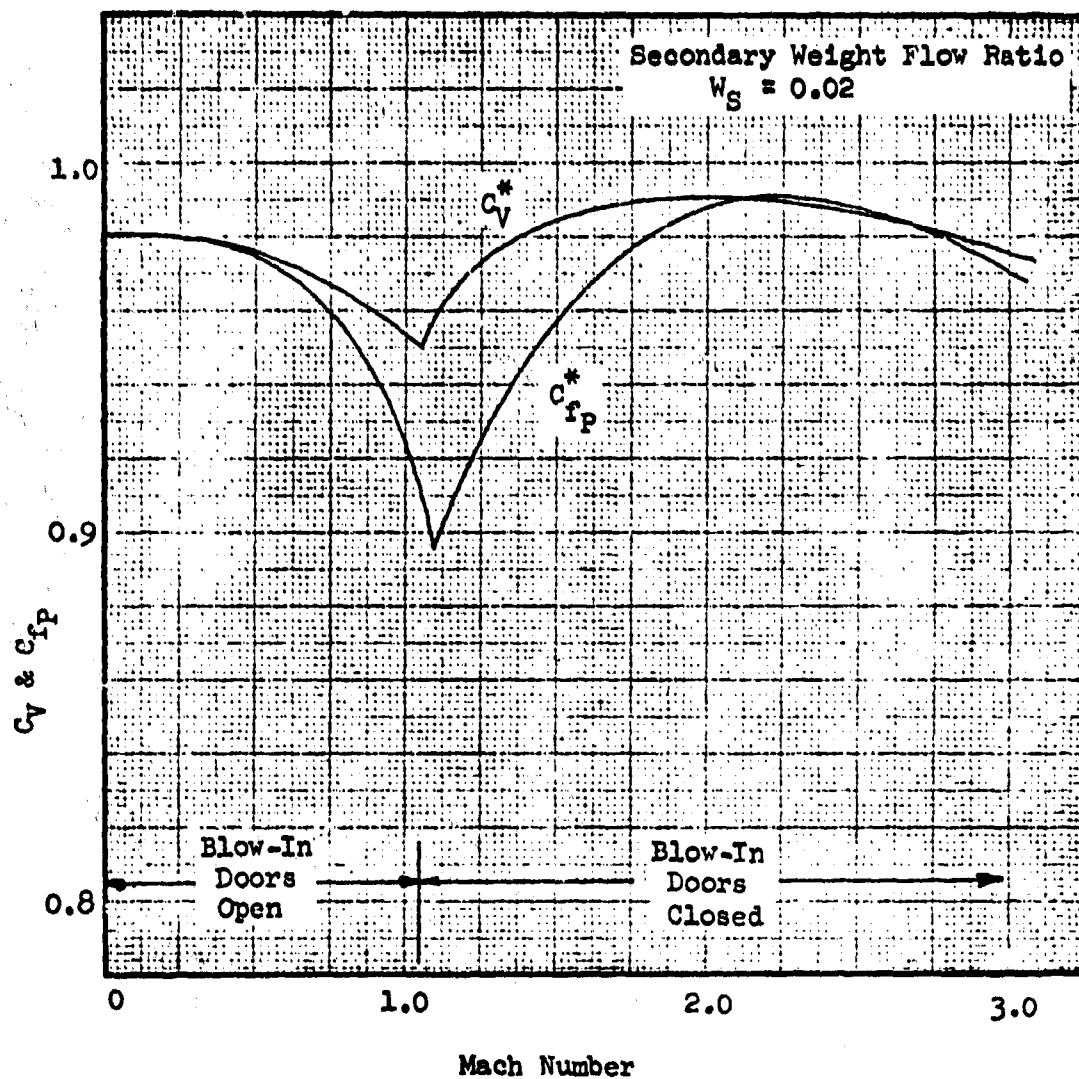
Primary
Airflow →

1. Primary Nozzle
2. Blow-In-Door
3. Fixed Shroud
4. Trailing Edge Flaps



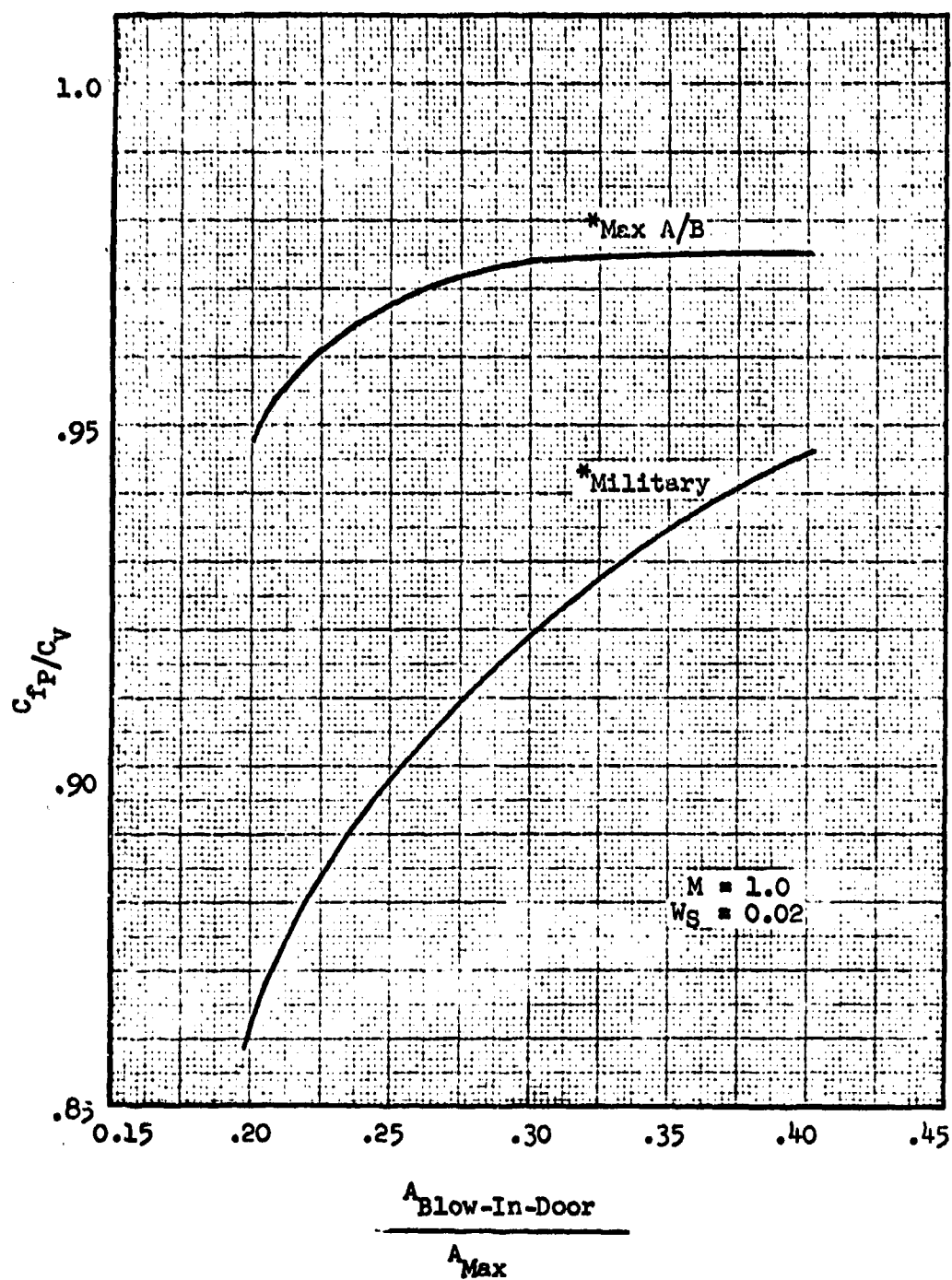
(b) Blow-In-Doors Closed

Figure 8-129. Blow-In-Door Ejector



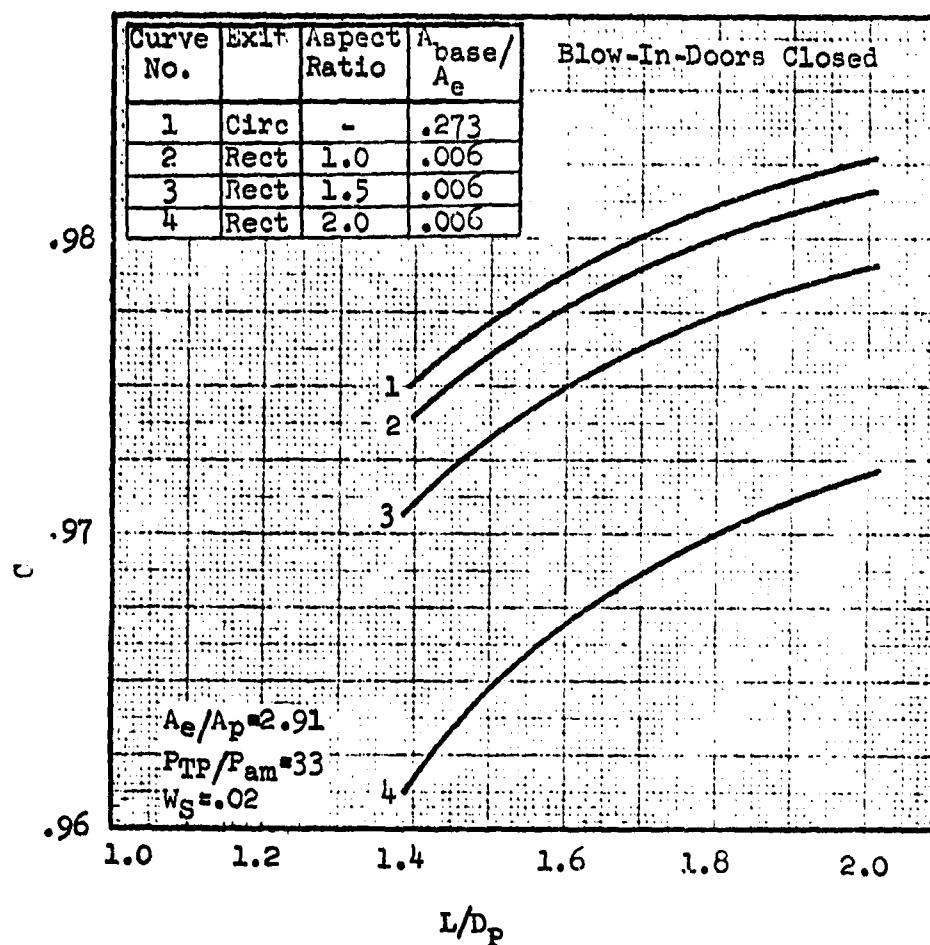
*Note: The values shown are given only to show ejector operating characteristic and should not be used for performance estimates.

Figure 8-130. Effect of Mach Number on Ejector Performance



*Note: The values shown are given only to show ejector operating characteristics and should not be used in performance estimates.

Figure 8-131. Effect of Blow-In-Door Area on Ejector Performance.



Note: The values are given only to show ejector operating characteristics and should not be used in performance estimates.

Figure 8-132. Effect of Cross Section Geometry on Ejector Performance.

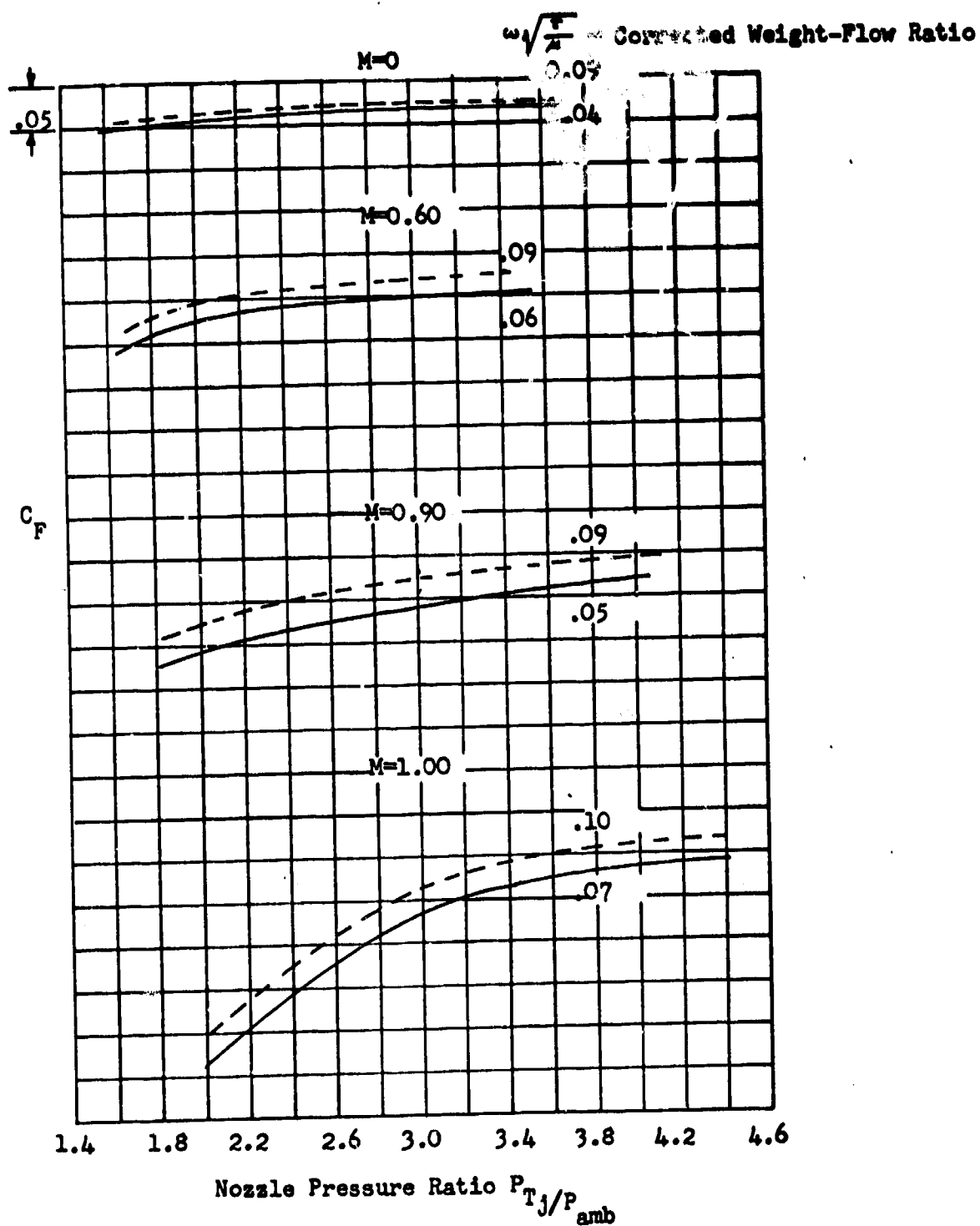


FIGURE 8-133. Variation of Gross Thrust Minus Boattail and Shroud Drag Performance with Primary Total-Pressure Ratio for Constant Corrected Weight-Flow Ratios and Mach Numbers.

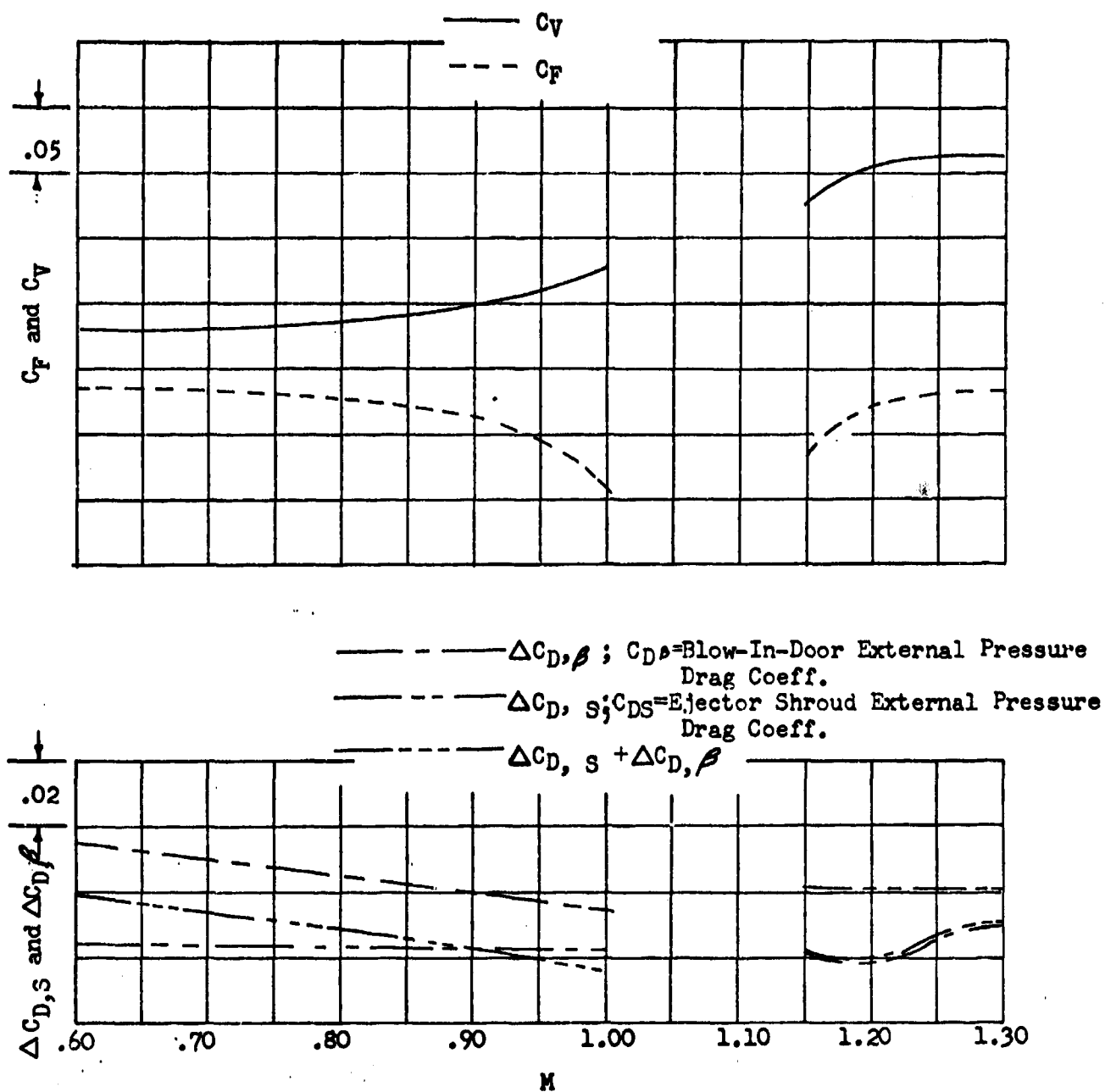


FIGURE 8-134. Variation of Ejector Performance and External Drag Characteristics with Mach Number for a Scheduled Primary Total-Pressure Ratio and Corrected Weight-Flow Ratio.

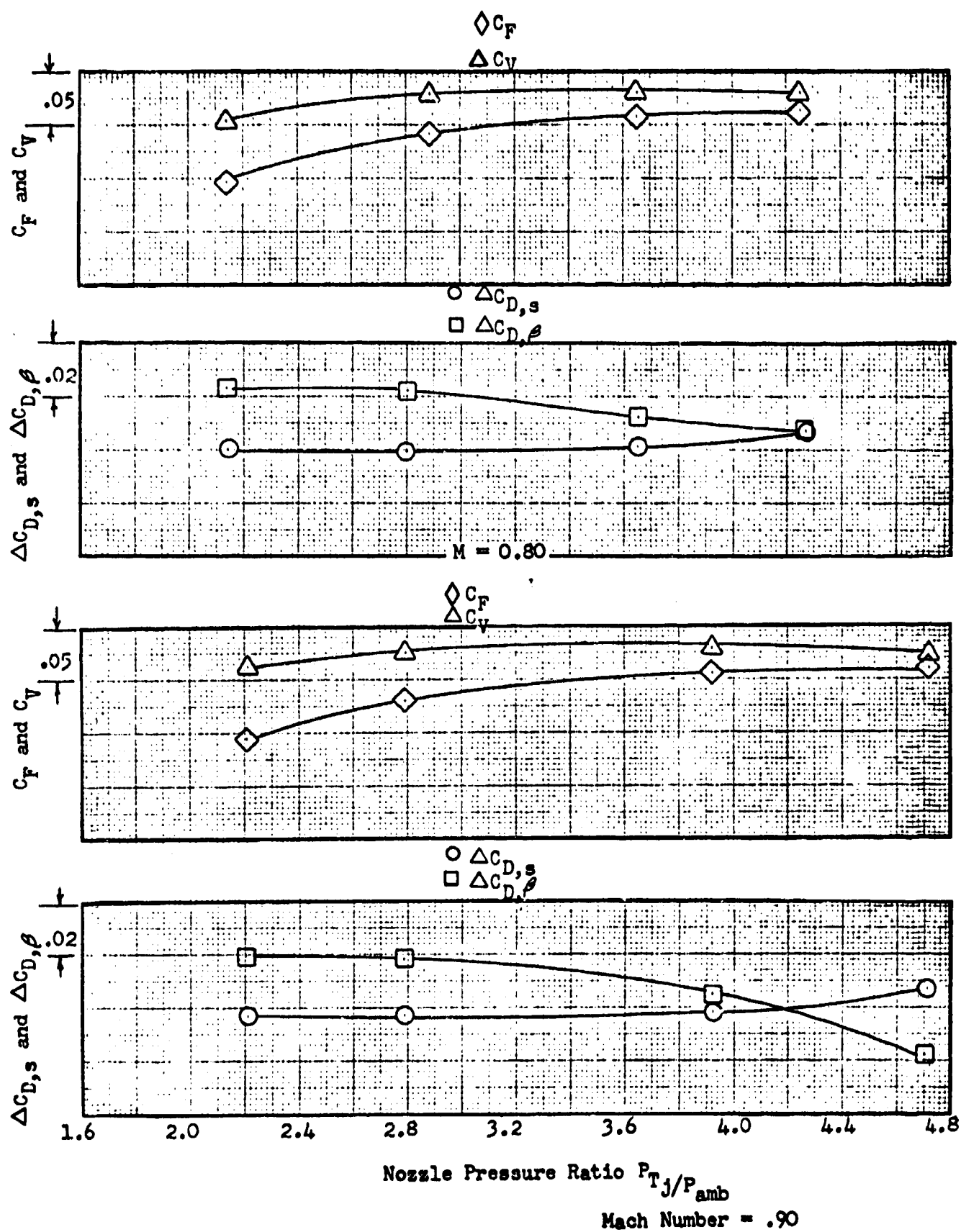


FIGURE 8-135. Variation of Nozzle Performance and External Drag Characteristics as a Function of Nozzle Pressure Ratio.

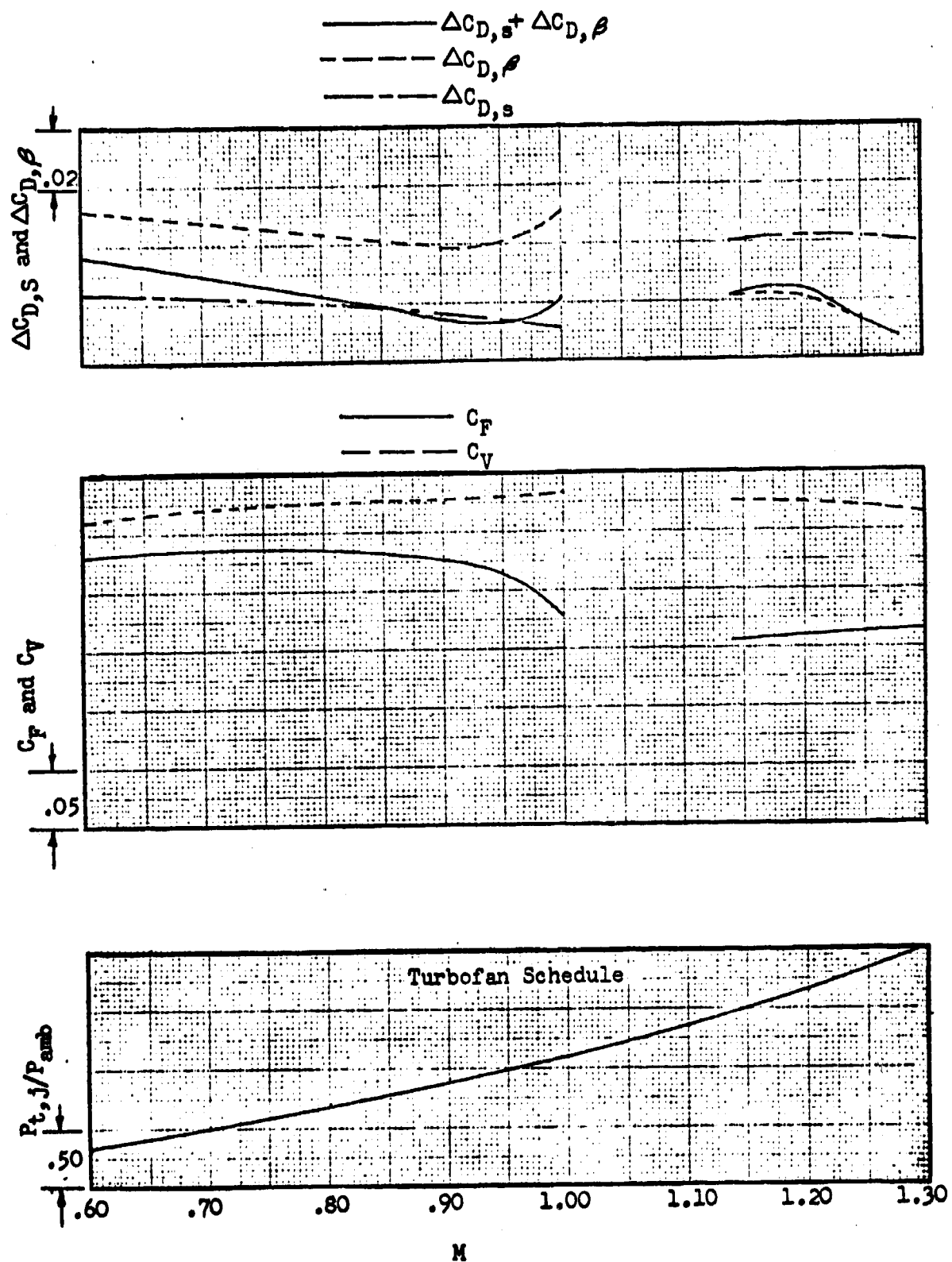
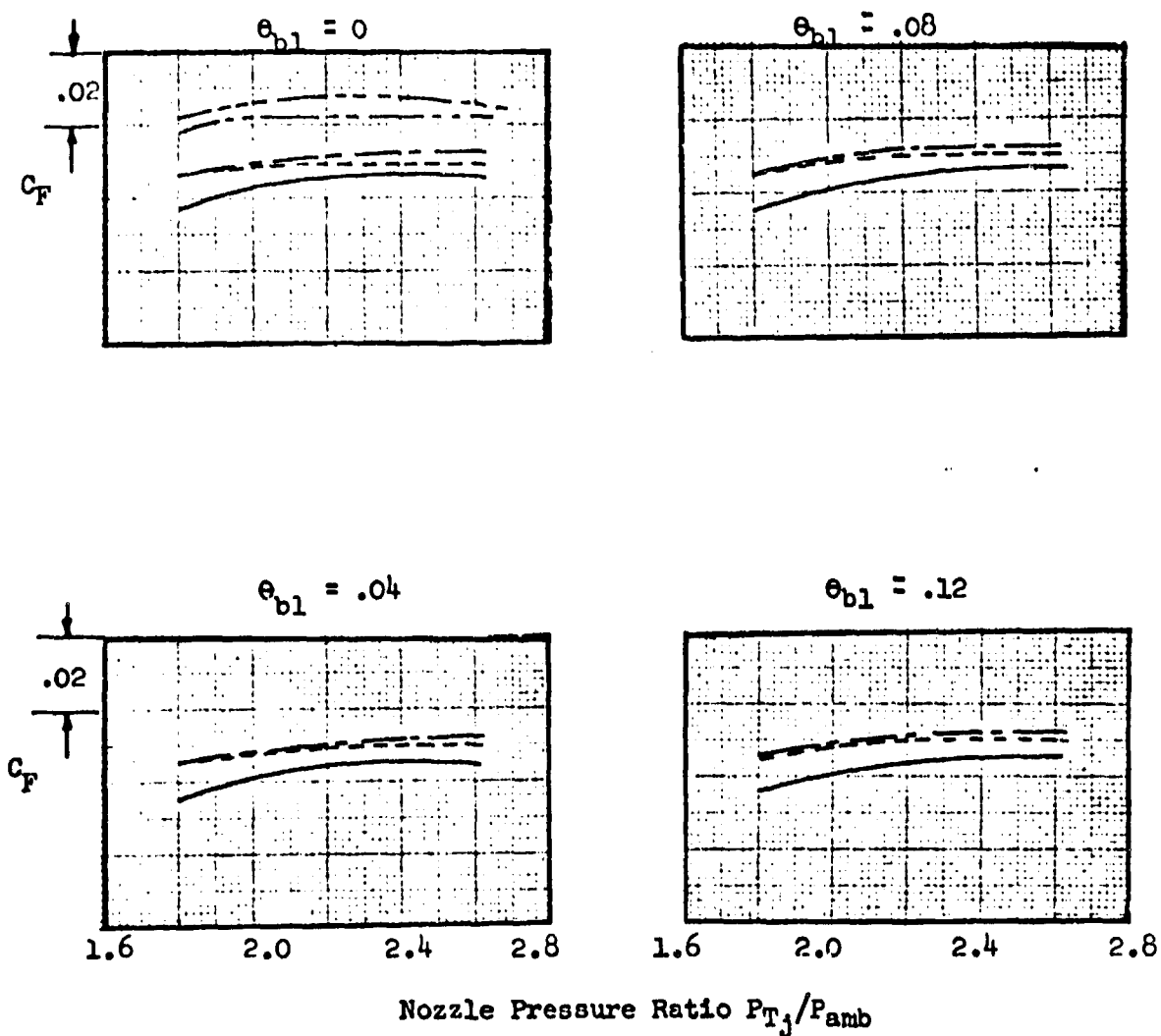


FIGURE 8-136. Variation of Nozzle Performance and External Drag Characteristics with Mach Number for a Jet Total-Pressure Ratio Schedule.



θ_{b1} ; Corrected Boundary-Layer
Bleed-Air Mass Flow Ratio
 θ_s ; Corrected Secondary-Air-
Mass-Flow Ratio

————— 0
 - - - - - .02
 ————— .04
 ————— 0 } Isolated Nozzle
 - - - - - .04 }

Figure 8-137. Variation of Average Nozzle Performance Coefficient with Primary Total-Pressure Ratio, Mach No., = .70, $\alpha = 5.5^\circ$ (angle of attack).

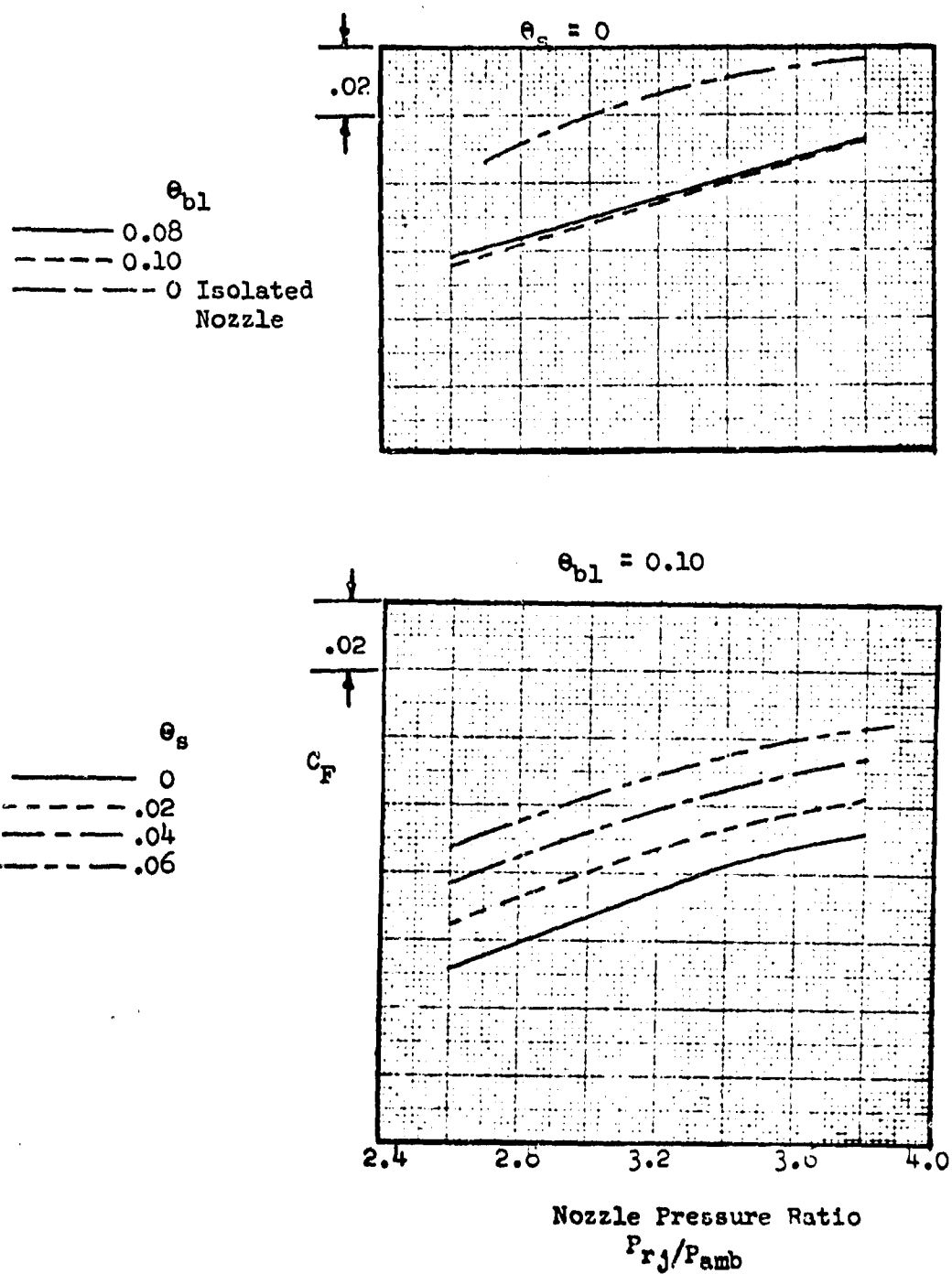


Figure 8-138.. Variation of Average Nozzle Performance Coefficient with Primary Total-Pressure Ratio; Mach No., 1.2; α , 20° .

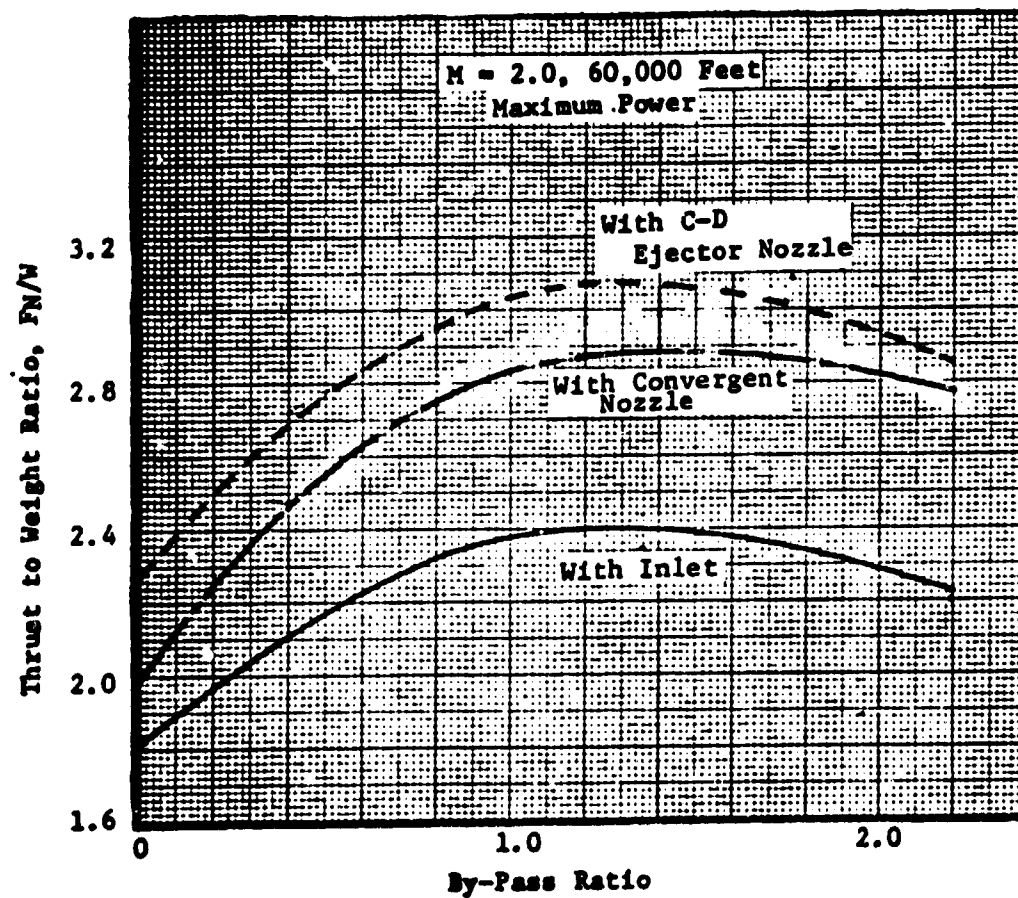


FIGURE 8-139 Propulsion System Weight

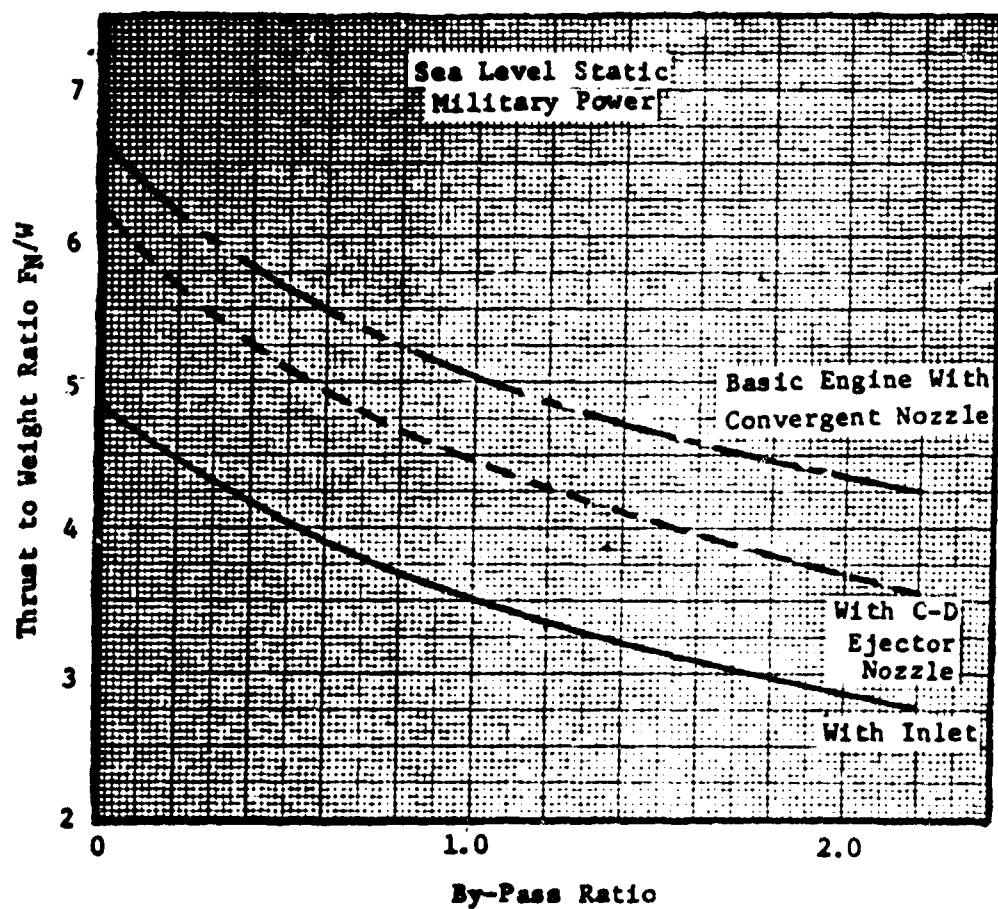


FIGURE 8-140 Propulsion System Weight

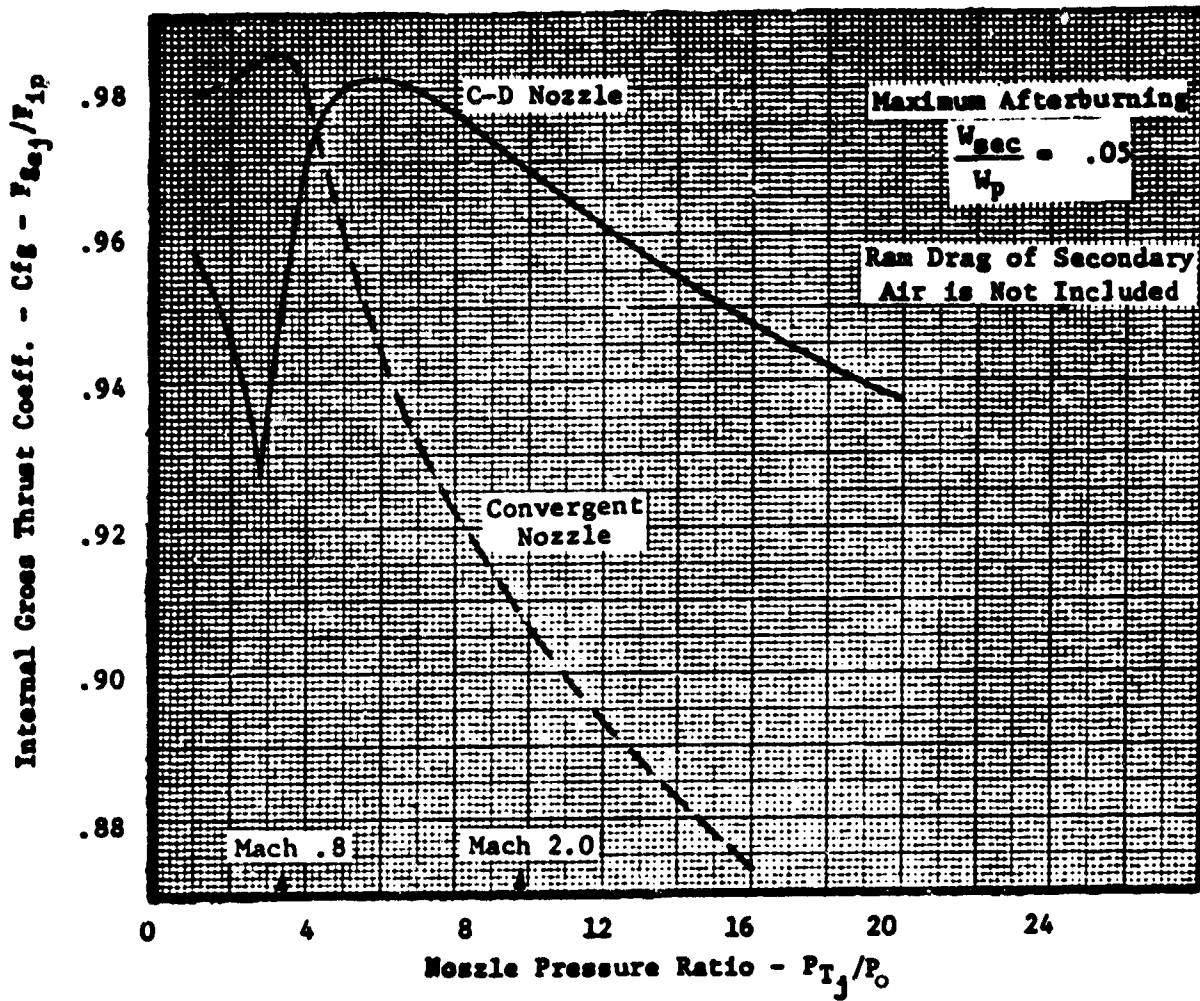


FIGURE 8-141 Nozzle Performance Comparison

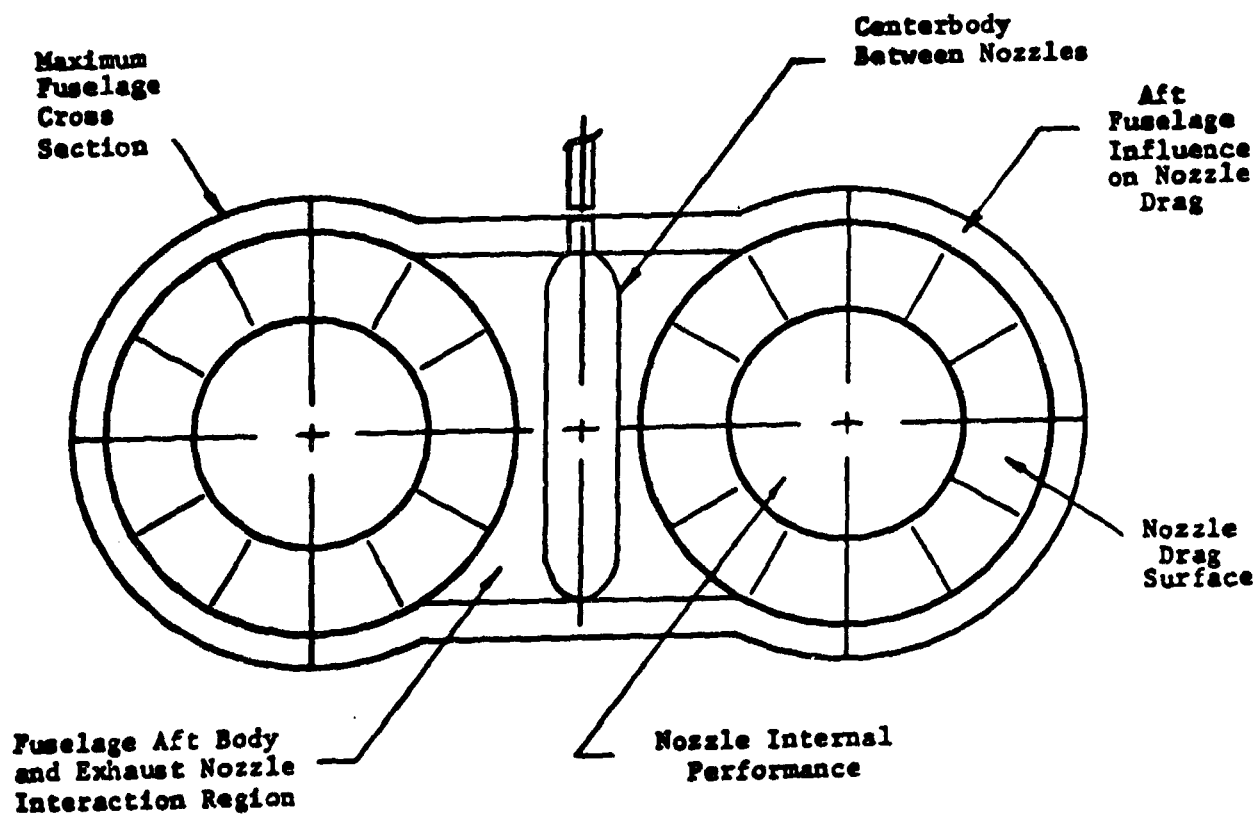


FIGURE 8-142. Nozzle and Afterbody Analysis Area

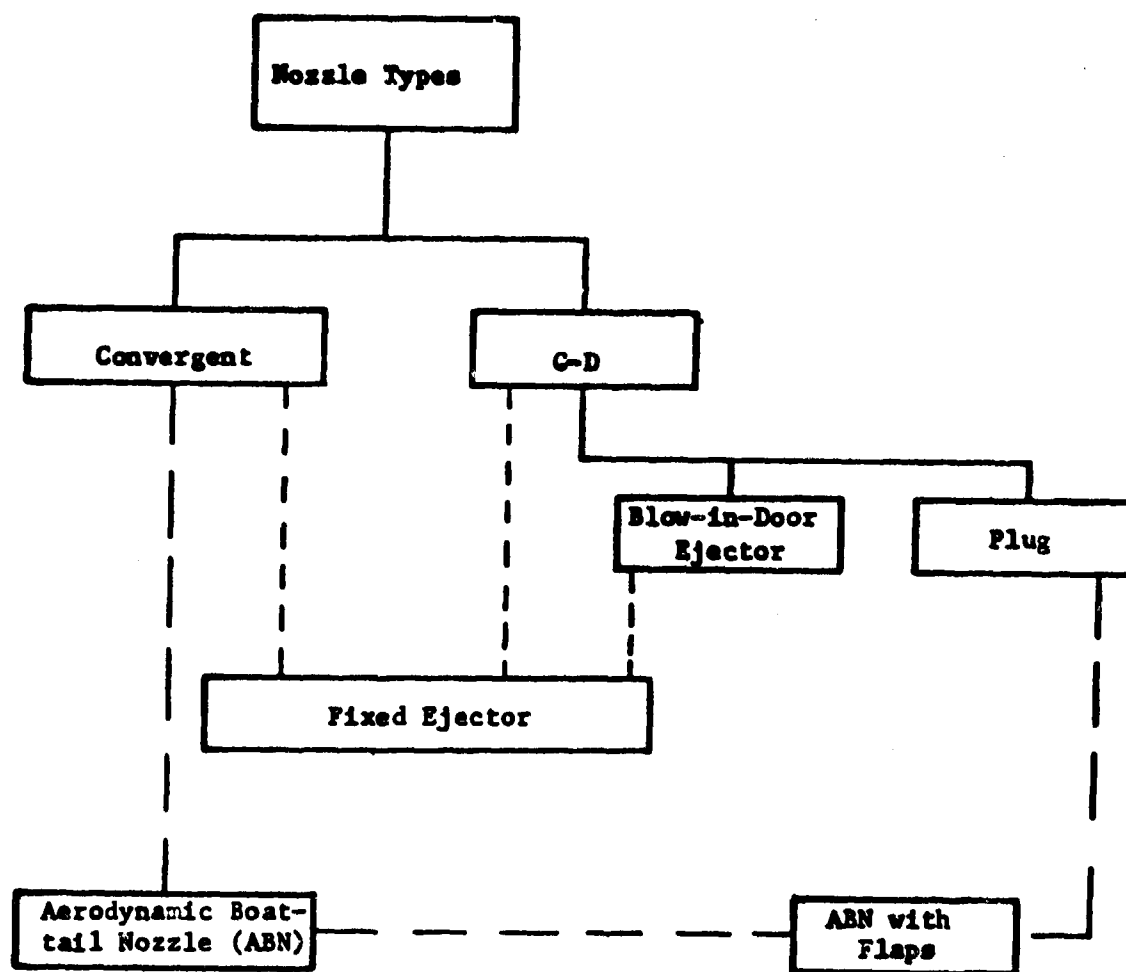


FIGURE 8-143. Nozzle Types and Relationship

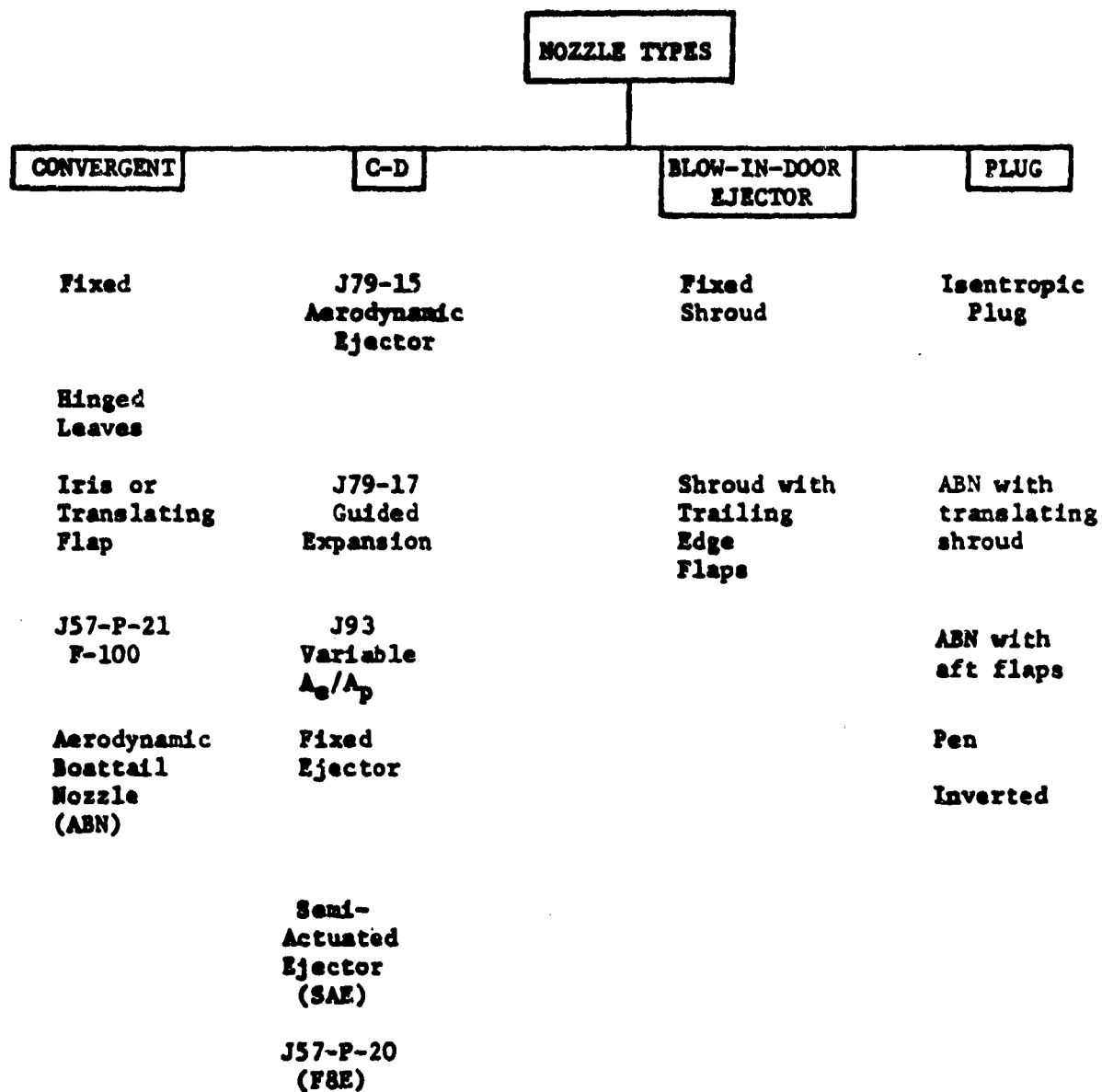


FIGURE 8-144. Nozzle Variations

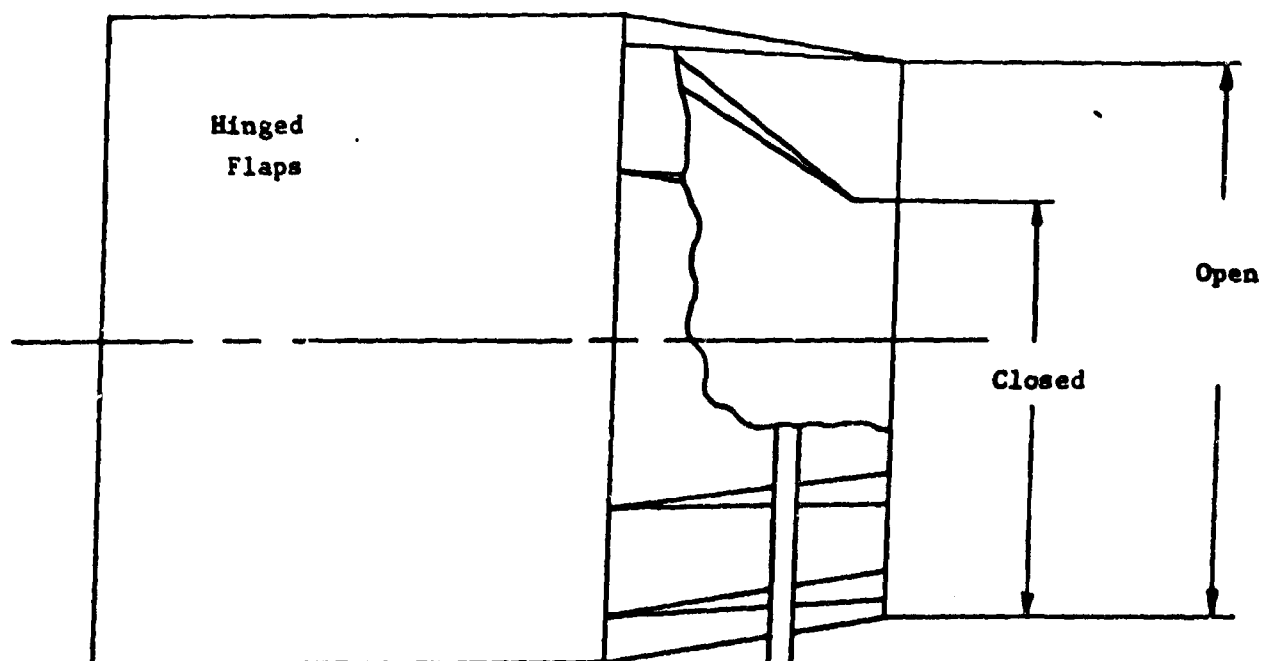
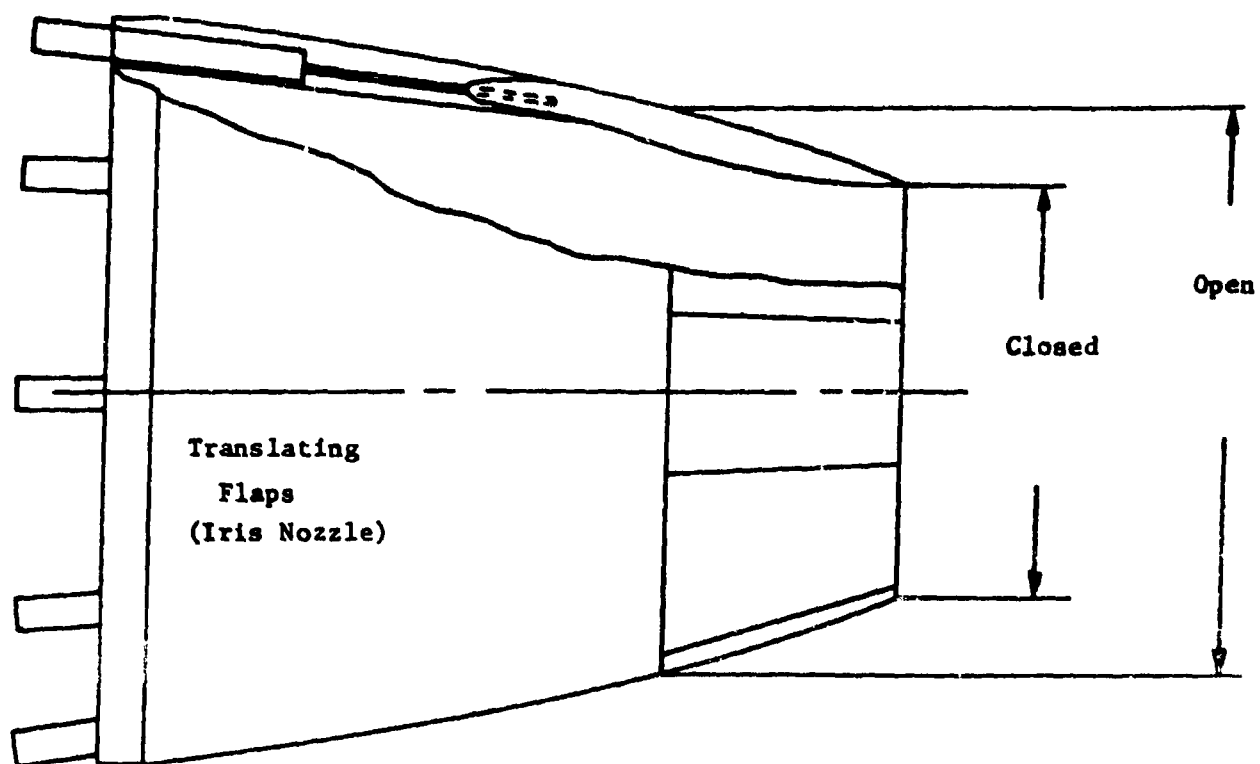


FIGURE 8-145. Convergent Nozzles

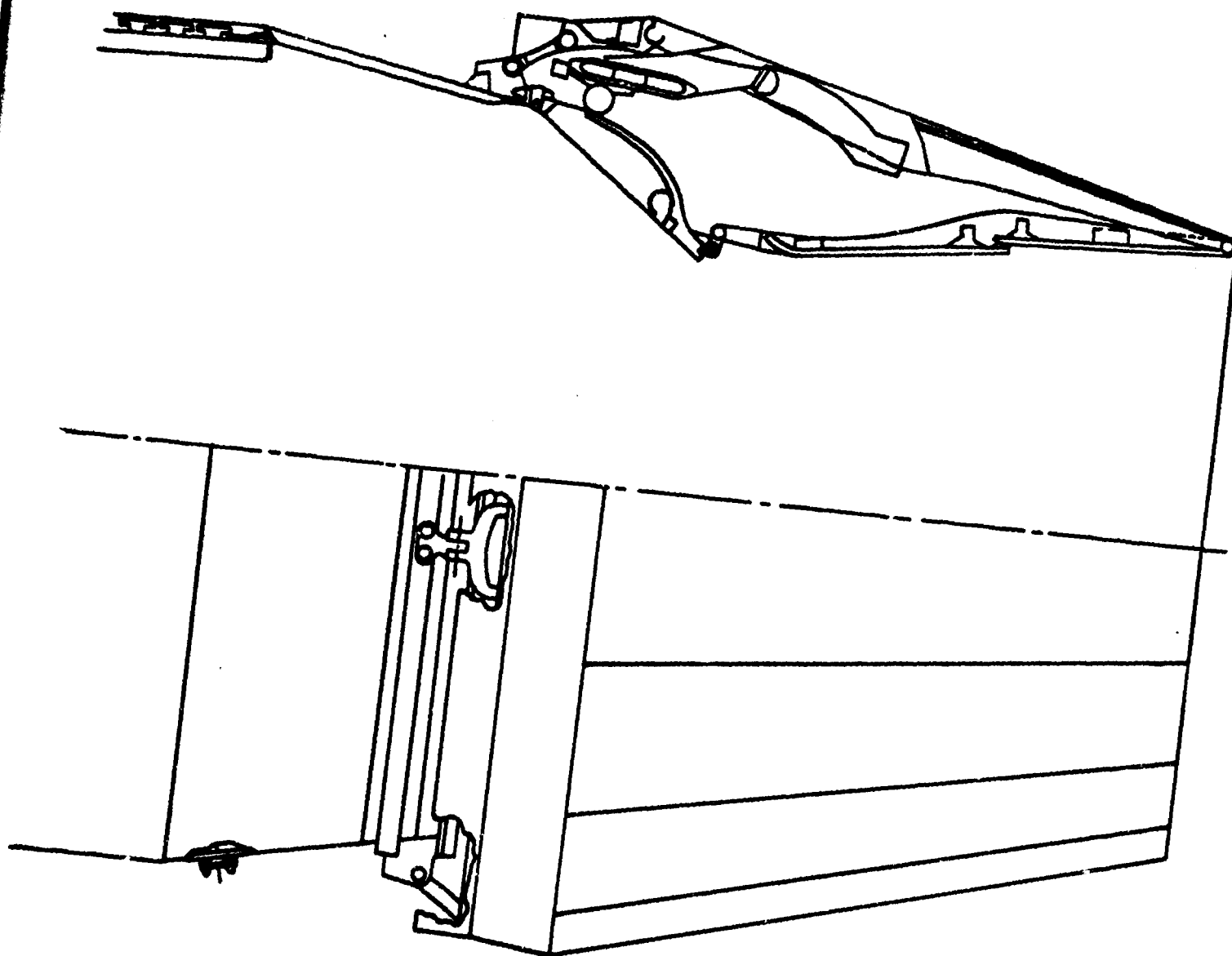


FIGURE 8-146. J79-10, 17 Convergent Divergent Nozzle,
Guided Expansion

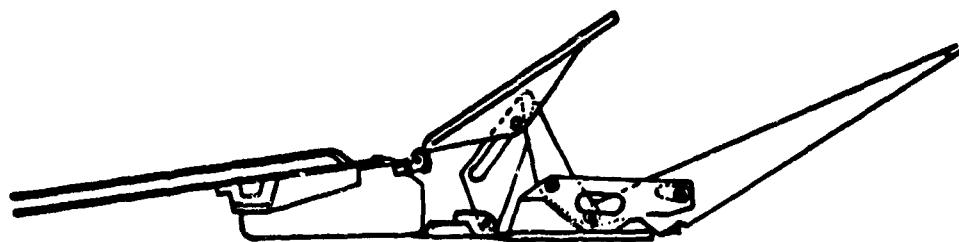
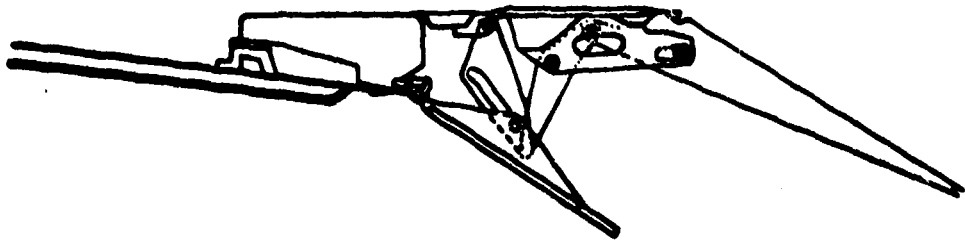


FIGURE 8-147 J79-8,15 Aerodynamic Ejector Nozzle

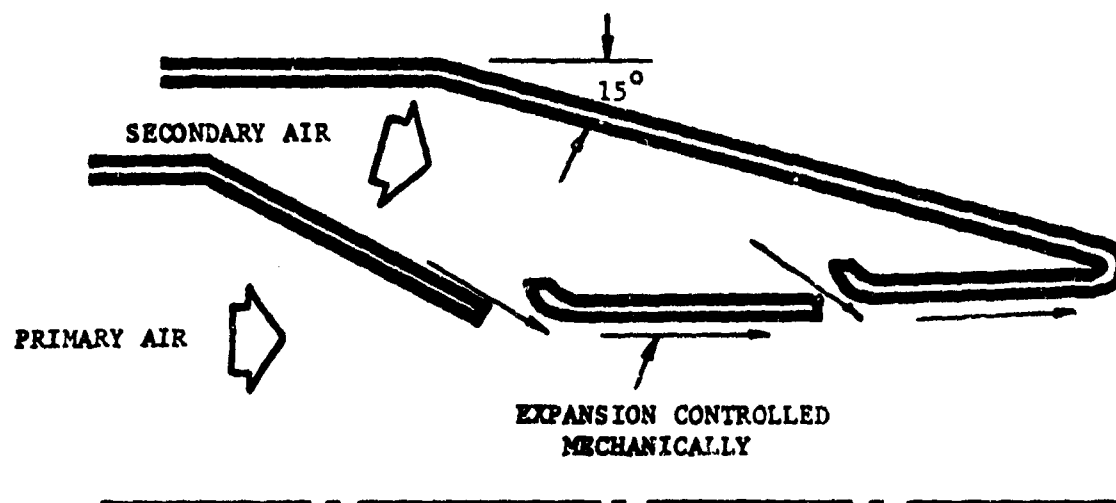
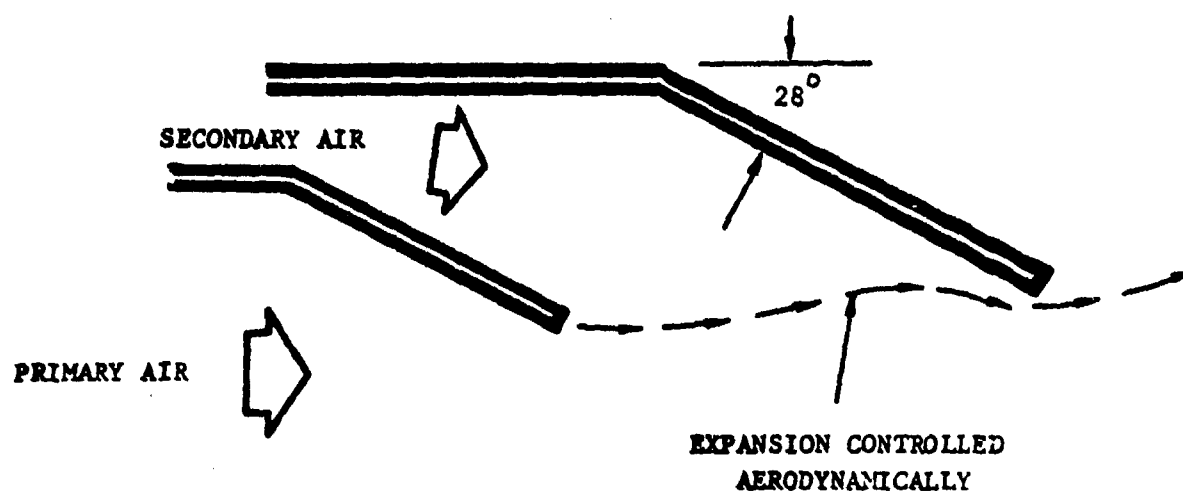


FIGURE 8-148 Flow Diagrams for J79 Exhaust Nozzles

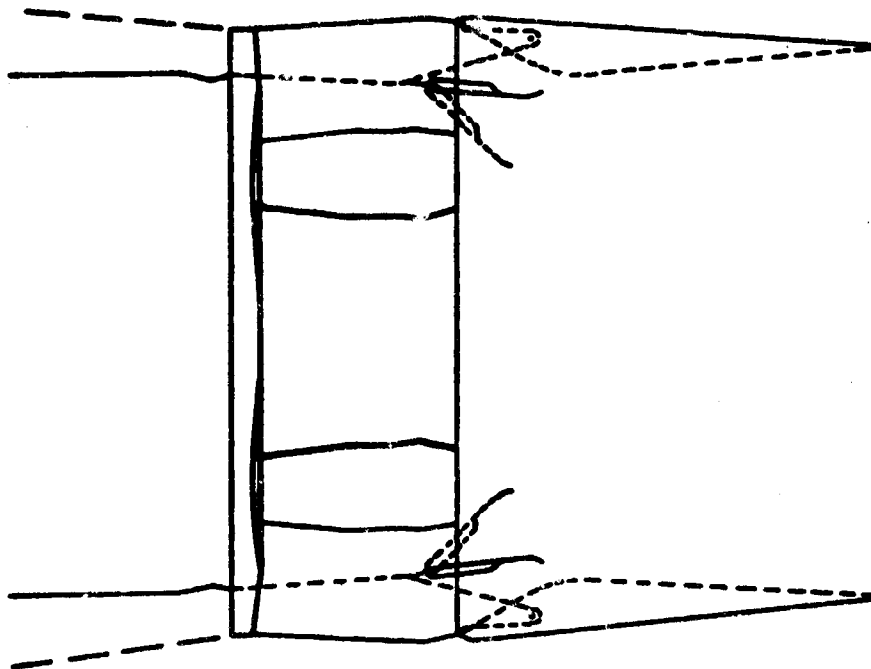


FIGURE 8-149 Blow-In-Door Ejector

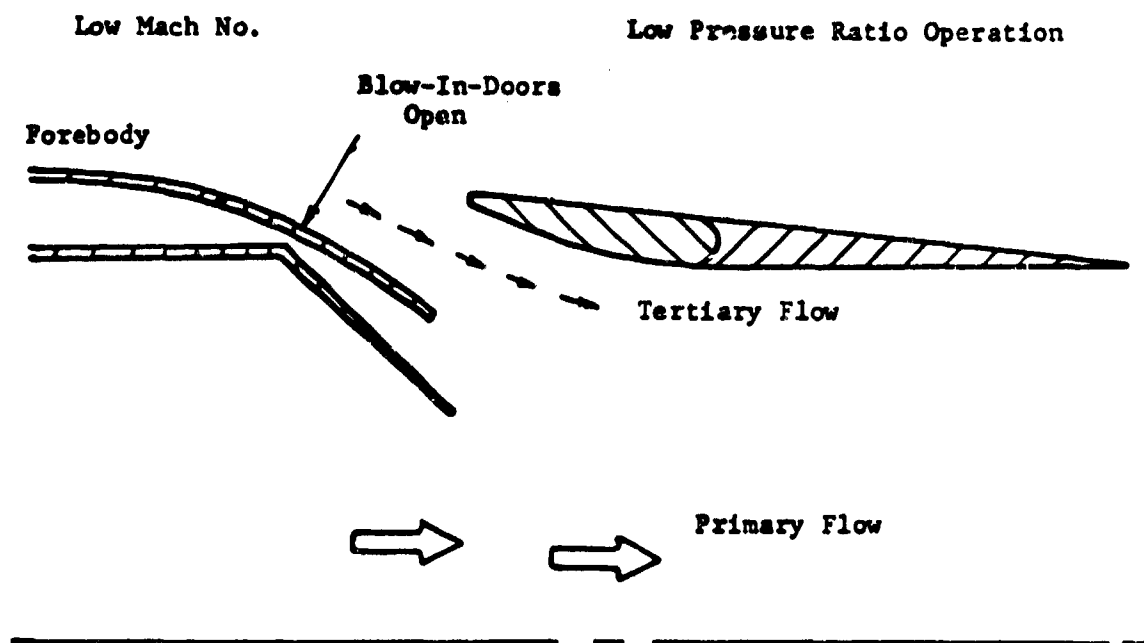
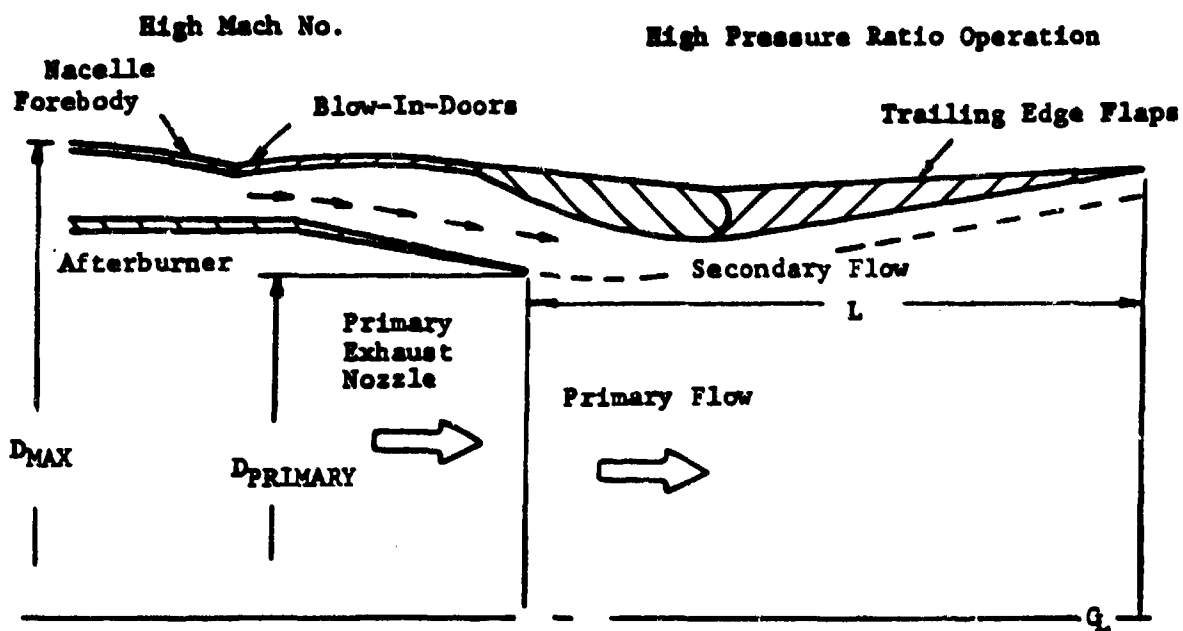


FIGURE 8-150 Blow-In-Door Ejector Flow Diagram

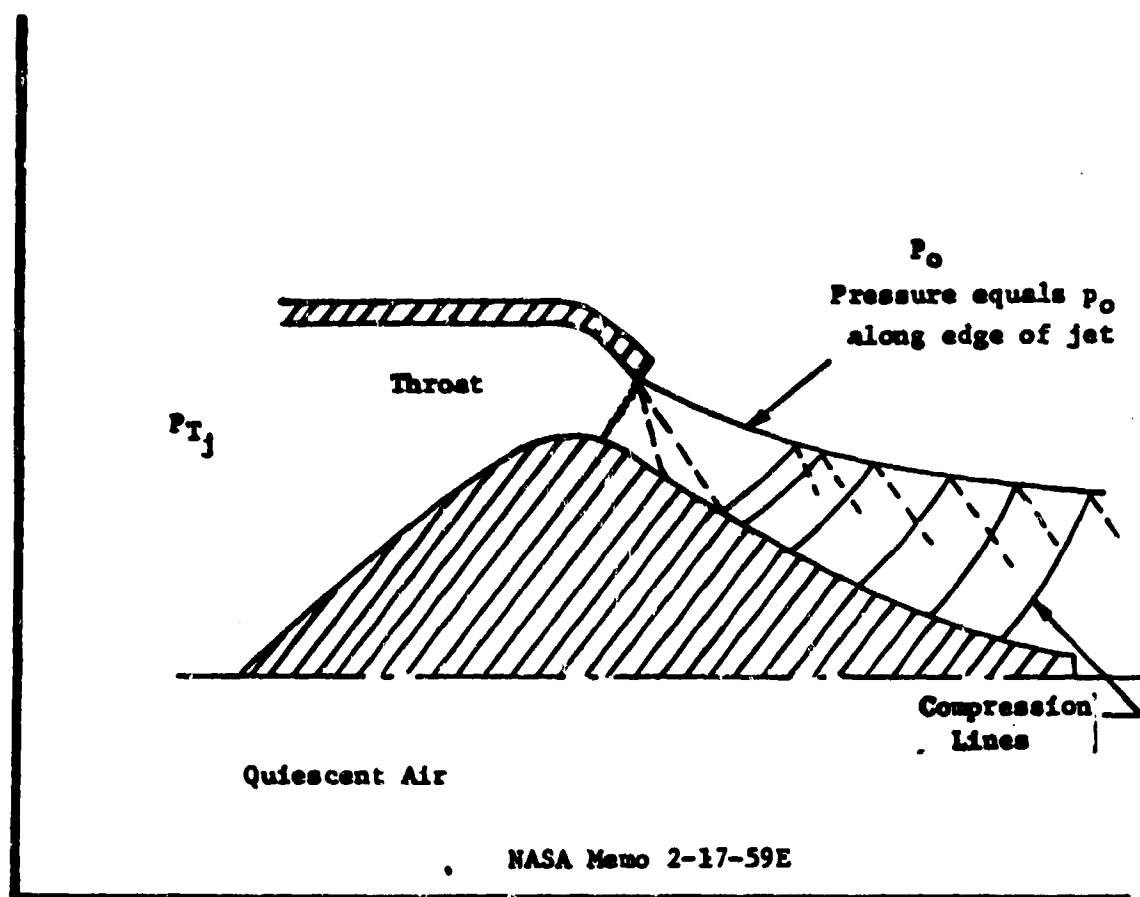


FIGURE 8-151. Isentropic Plug Nozzle

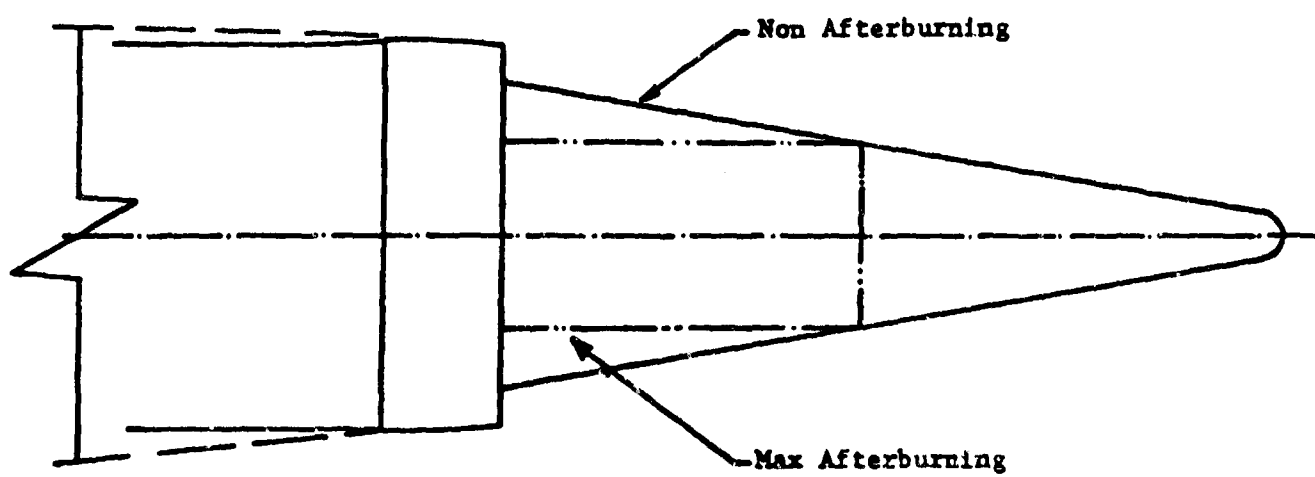


FIGURE 8-152 Aerodynamic Boattail Nozzle

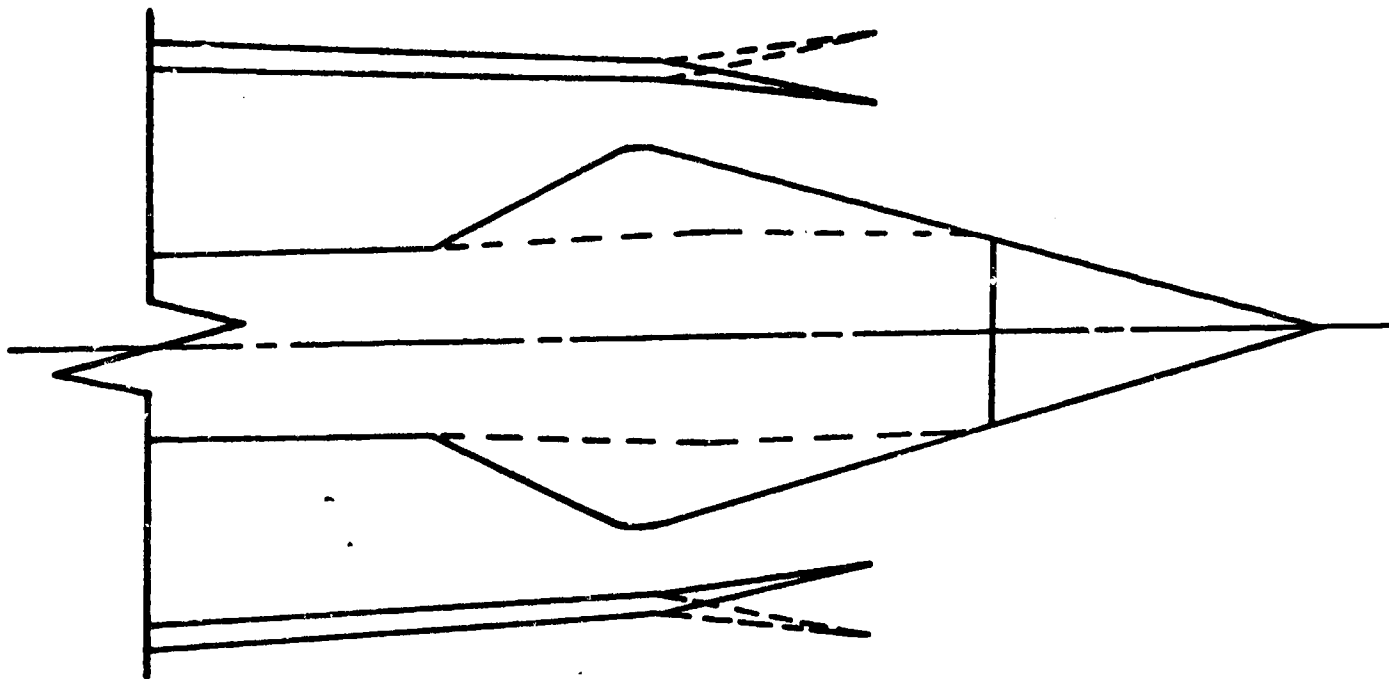


FIGURE 8-153. Aerodynamic Boattail Nozzle with Aft Flap

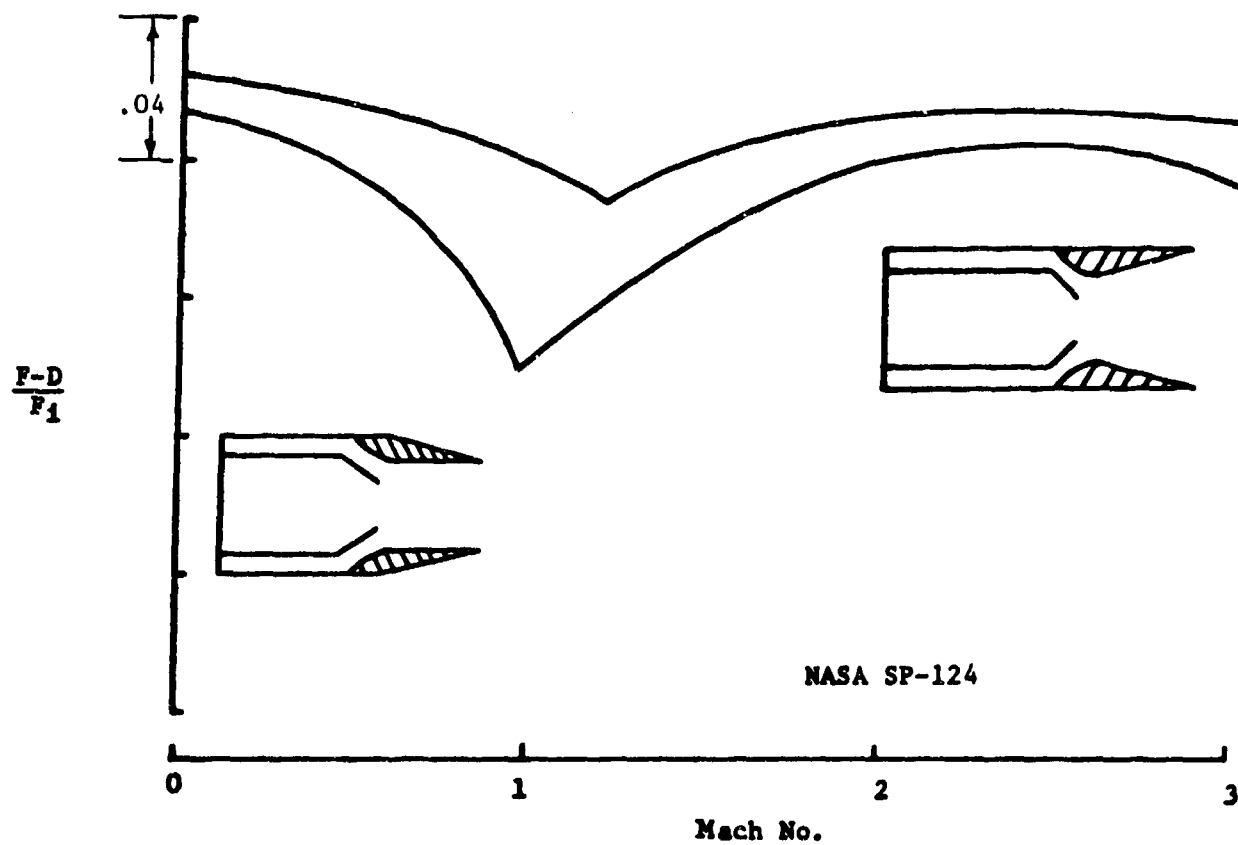


FIGURE 8-154. Performance of Convergent-Divergent Ejector Nozzles

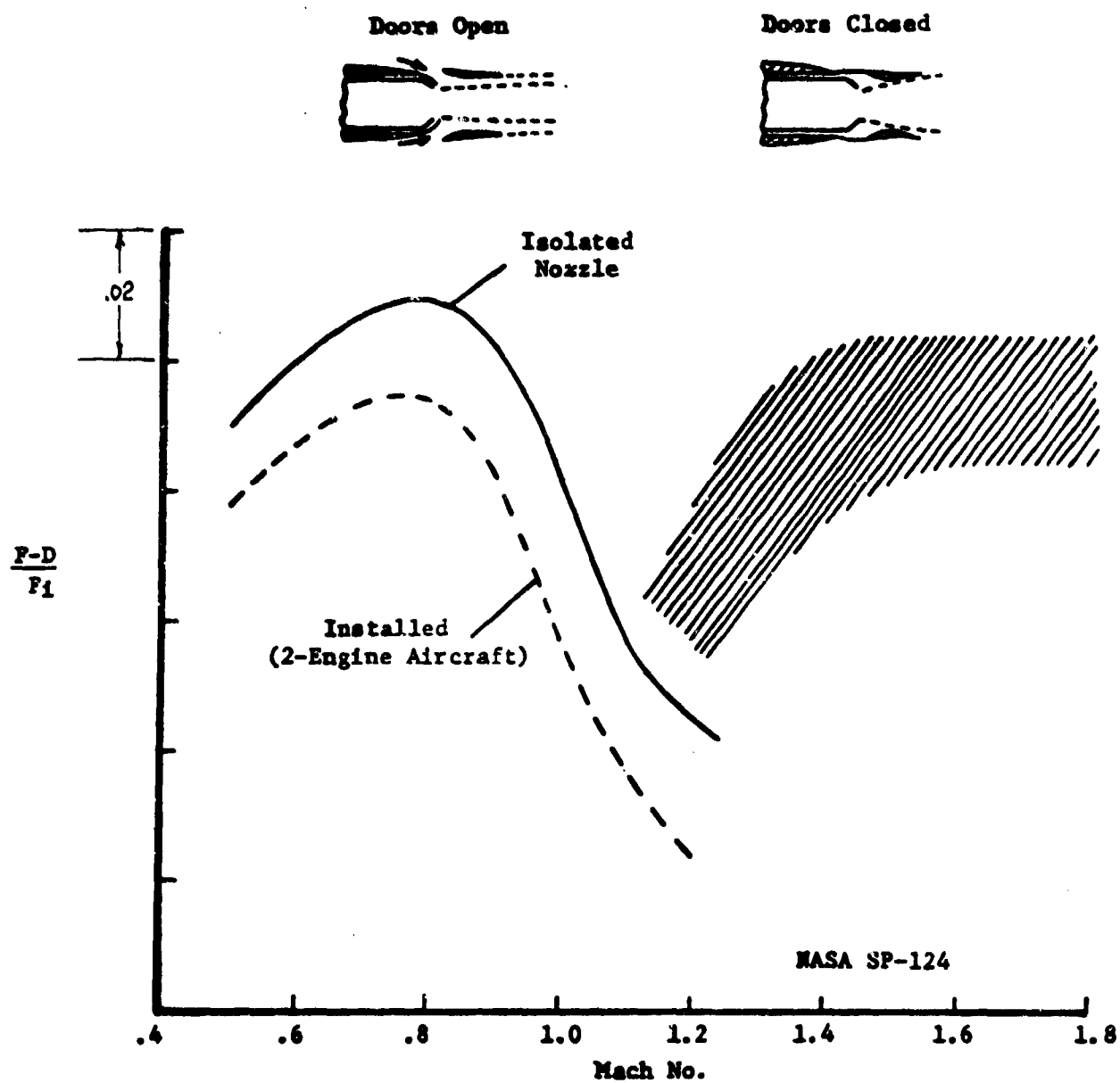


FIGURE 8-155: Blow-In-Door Ejector Nozzle

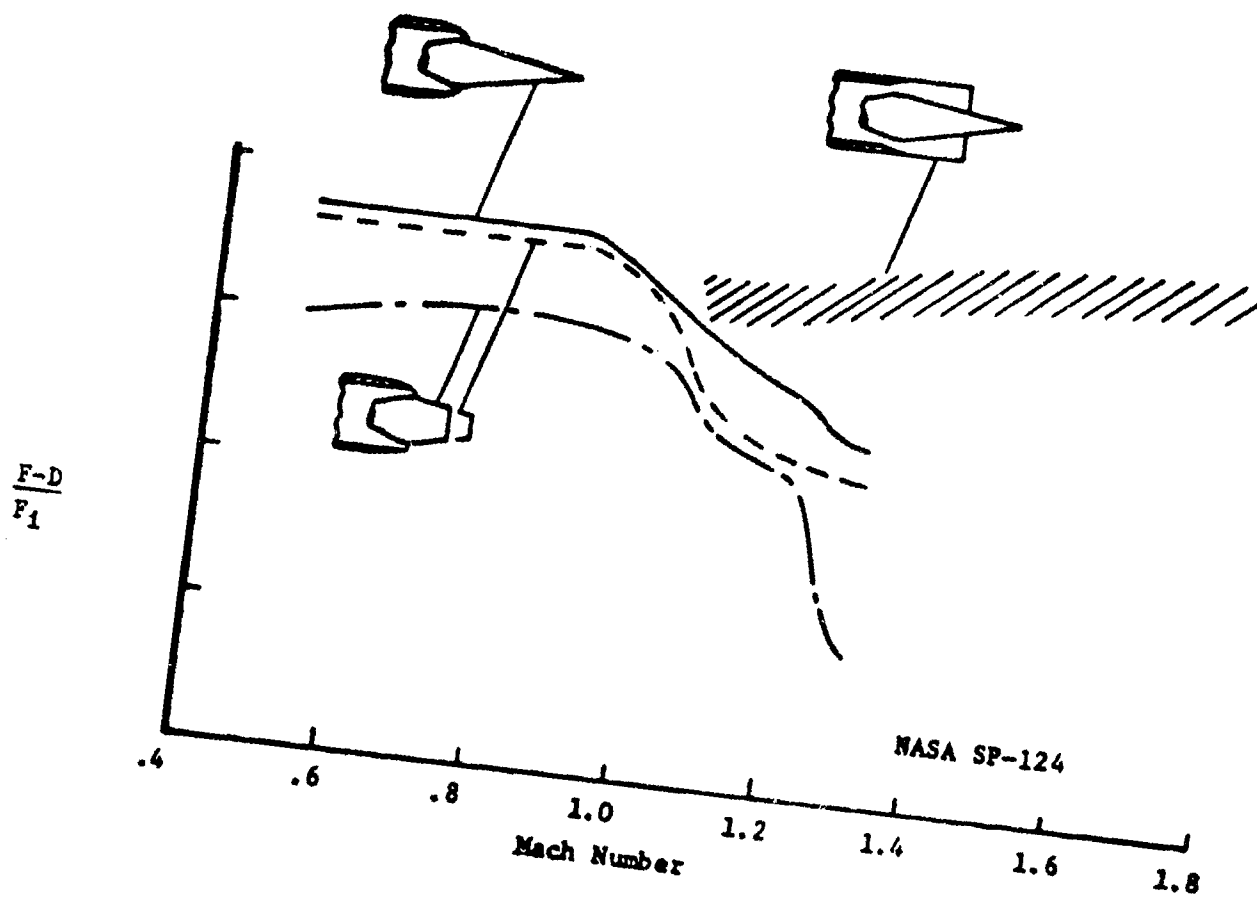
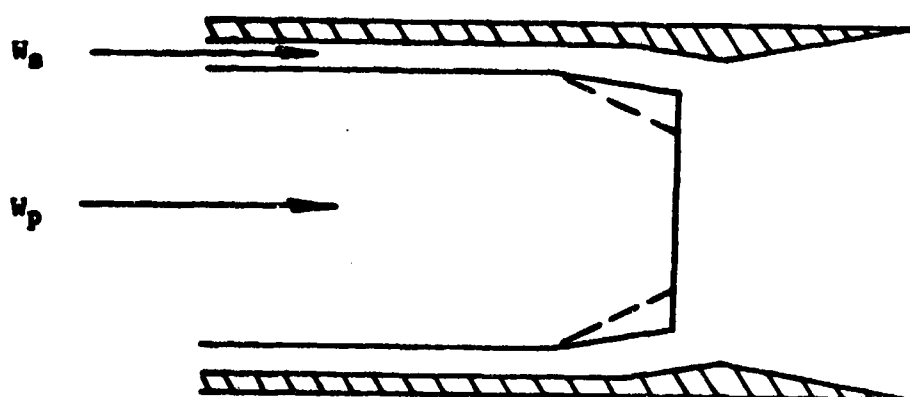


FIGURE 8-156. Long-Cone Plug Nozzle, (ABN)



$$\frac{A_{exit}}{A^*} = 2.4$$

FIGURE 8-157. Fixed Ejector Exit Configuration

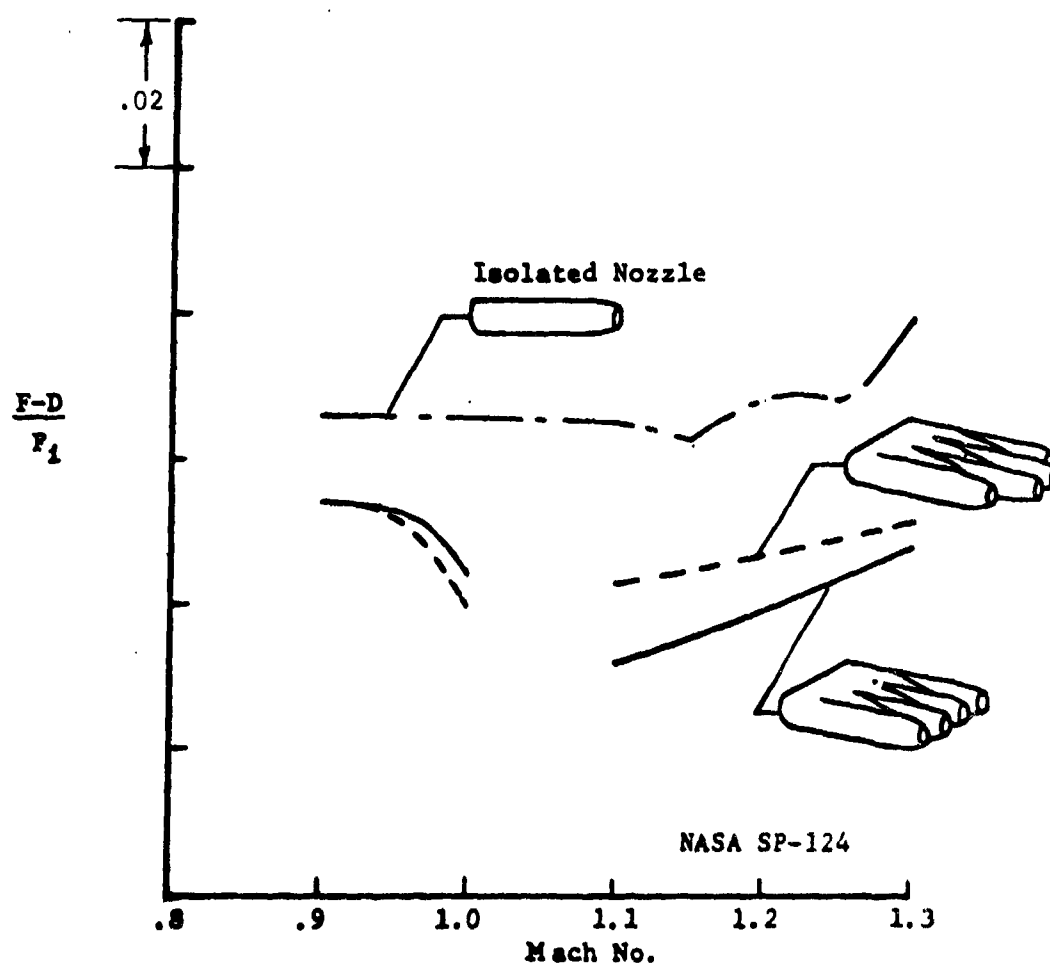


FIGURE 8-158. Clustered Jet Exits

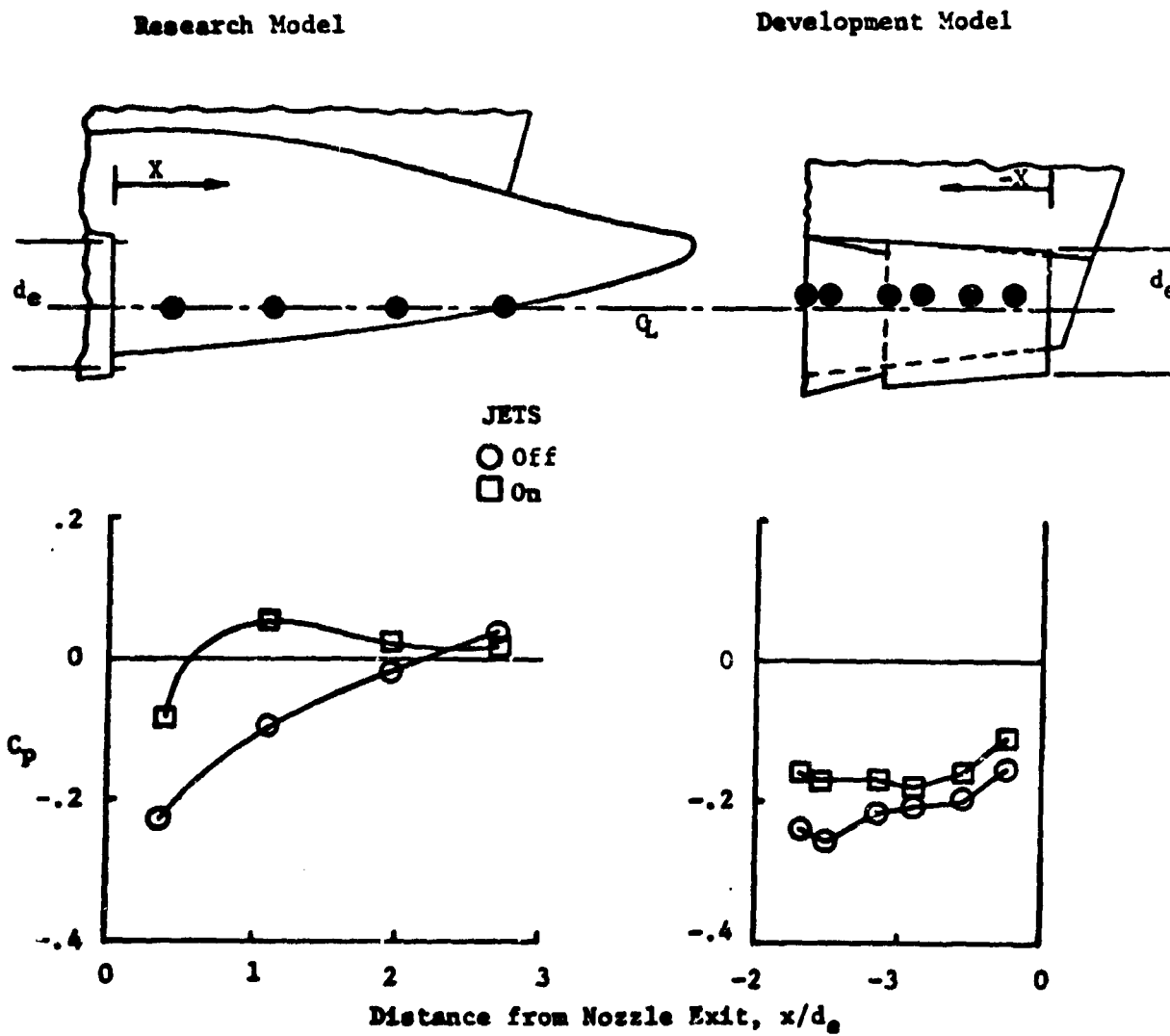


FIGURE 8-159 Engine Interfairing Pressure Distributions $M = 1.2$

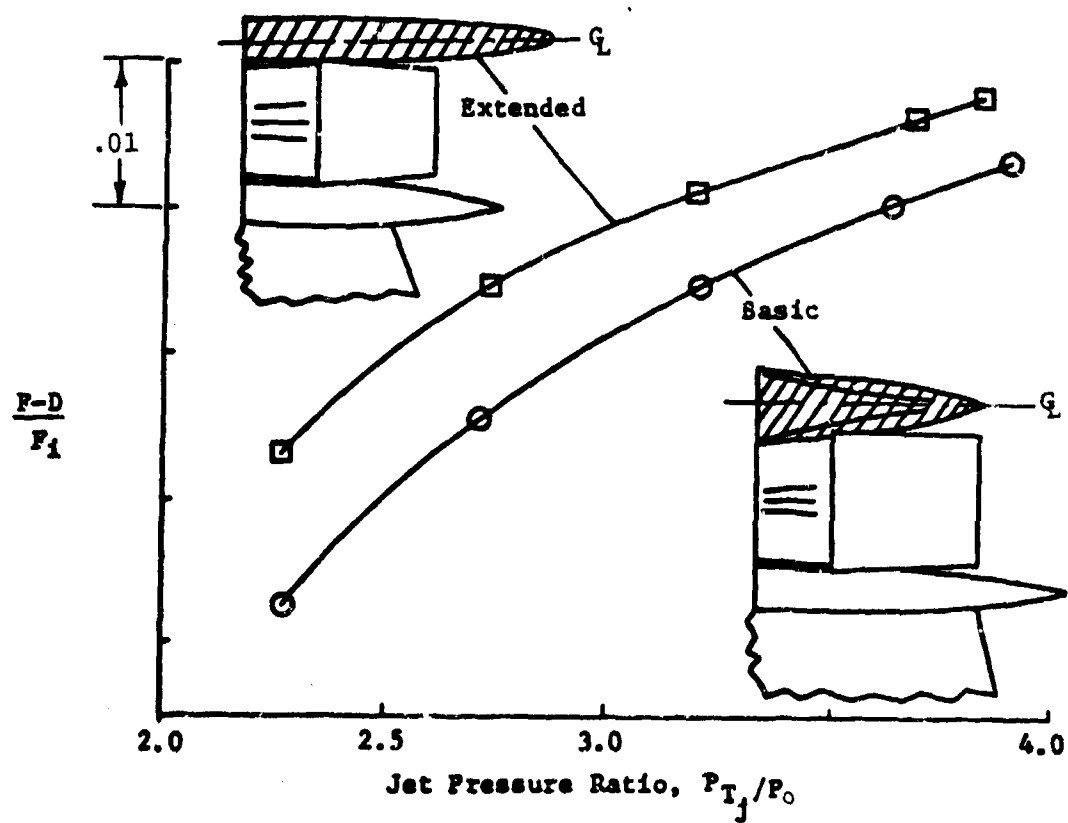


FIGURE 8-160 Performance of Basic-and Extended-Interfairing Configurations $M = 1.2$

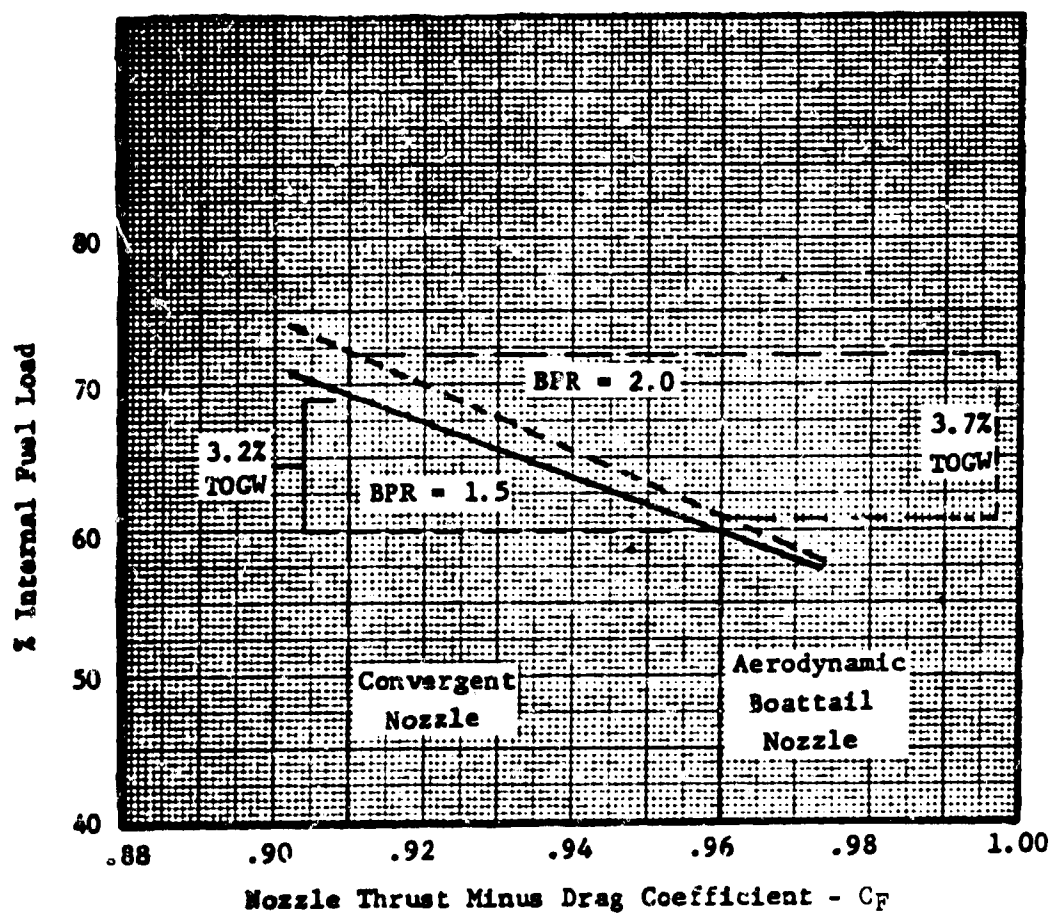


FIGURE 8-161. Effect of Nozzle Efficiency on Sea Level Dash Fuel Requirements. $M = 0.85$ Sea Level

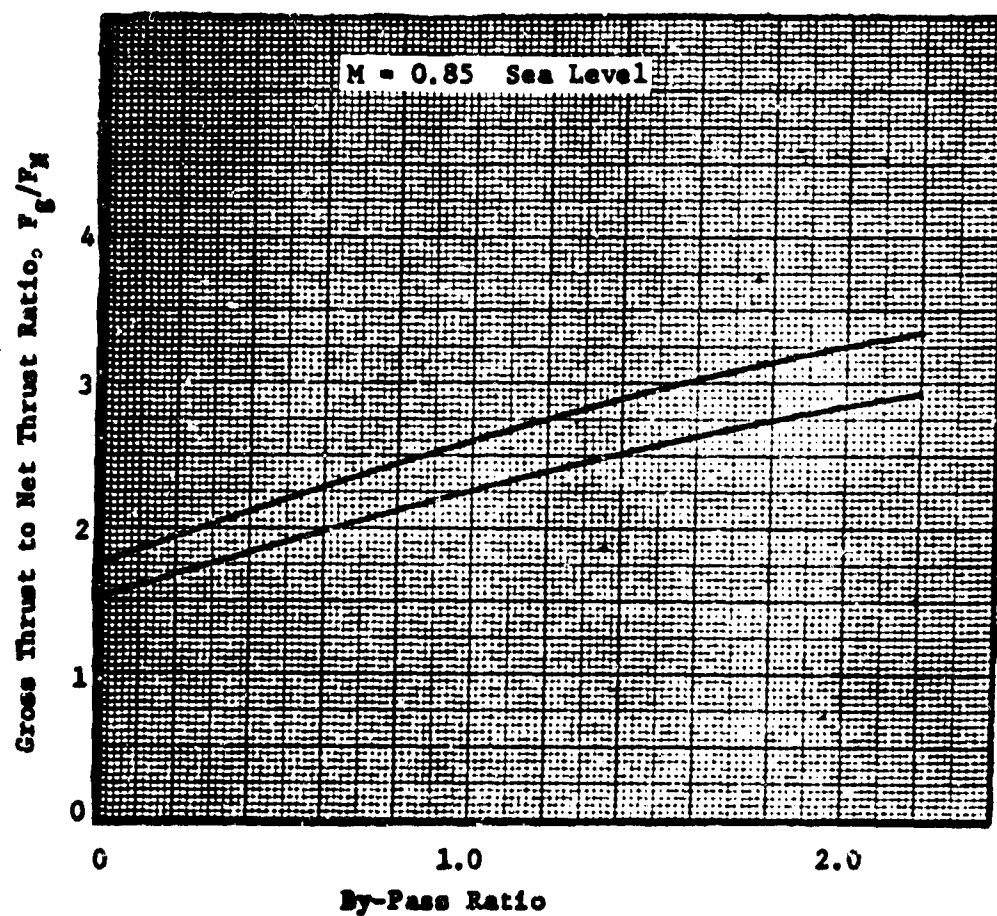


FIGURE 8-162. Ratio of Gross to Net Thrust with Bypass Ratio

Brakes and Thrust Reverser:

Aircraft Thrust Factor (F/W)
 0 (Brakes only)

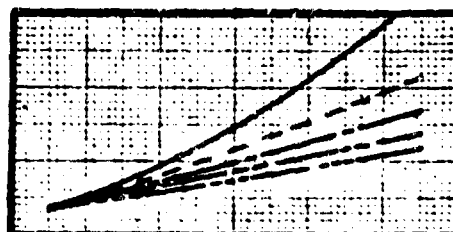
----- 0.25
 ----- 0.50
 ----- 0.75
 ----- 1.00

Brakes and Drag Parachute:

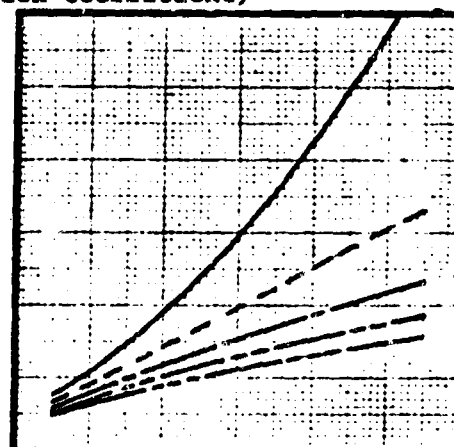
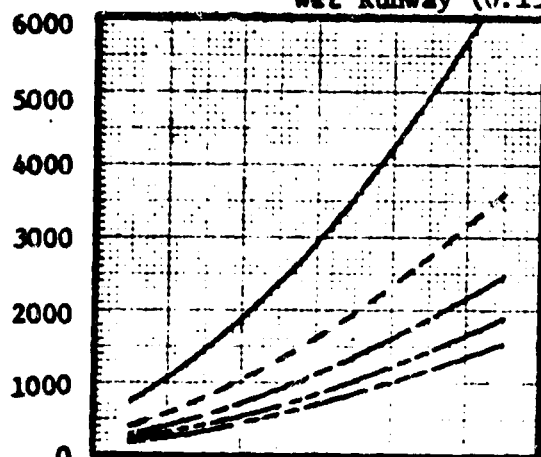
Parachute Size Factor ($C_D A_p/W$)
 0 (Brakes only)

----- 0.005
 ----- 0.010
 ----- 0.015
 ----- 0.020

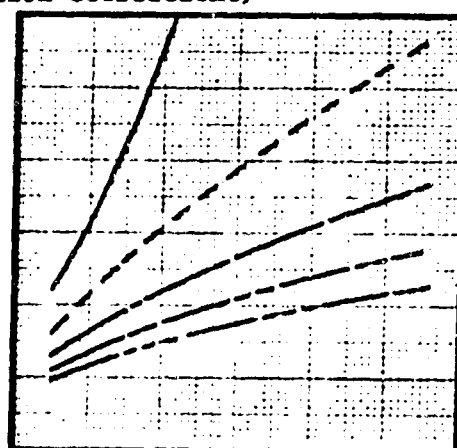
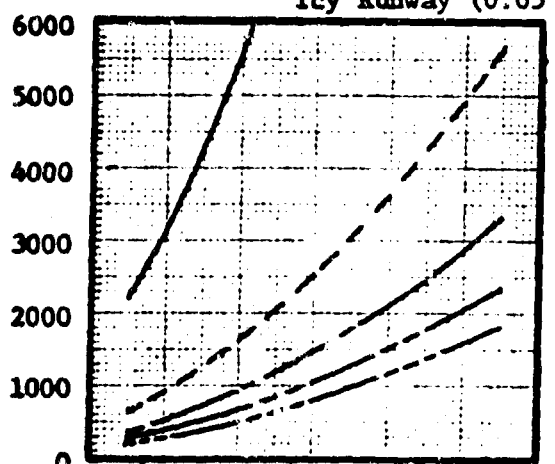
Dry Runway (0.30 Friction Coefficient)



Wet Runway (0.15 Friction Coefficient)



Icy Runway (0.05 Friction Coefficient)



Ground Roll Distance After Landing Touchdown or Take-Off Refusal - Ft.

Landing Touchdown or Take-Off Refusal Velocity - Knots

F = engine (forward) thrust - Lb
 W = aircraft weight - Lb
 (Reverser assumed 50% effective)

C_D = parachute drag coefficient
 A_p = parachute area - ft^2
 W = aircraft weight - Lb

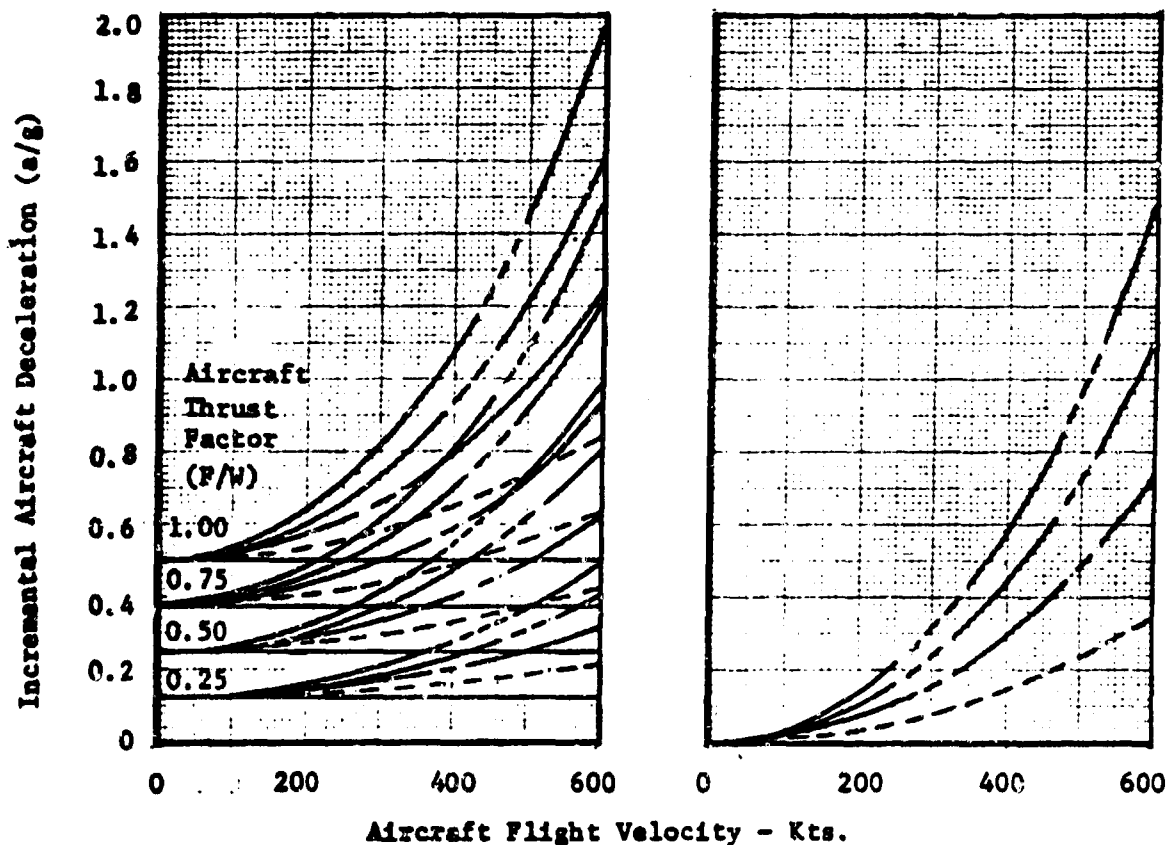
FIGURE 8-163 Comparative Effectiveness of Thrust Reversers and Drag Parachutes for Ground Roll Distance Reduction

Thrust Reverser:
Base Drag Factor ($C_D A_R / F$)

————— 0
----- 0.00025
----- 0.00050
----- 0.00075
----- 0.00100

Speed Brakes:
Brake Size Factor ($C_D A_B / W$)

----- 0.00025
----- 0.00050
----- 0.00075
----- 0.00100



C_D = engine base drag coefficient C_D = brake drag coefficient
 A_R = reverser base area - ft^2 A_B = brake area - ft^2
 F = engine (forward) thrust - Lb W = aircraft weight - Lb
 W = aircraft weight - Lb
 (Reverser assumed 50% effective)

(a/g) = aircraft deceleration "g" force at sea level flight altitude

FIGURE 8-164 Comparative Effectiveness of Thrust Reverser Speed Brakes for In-Flight Aircraft Deceleration

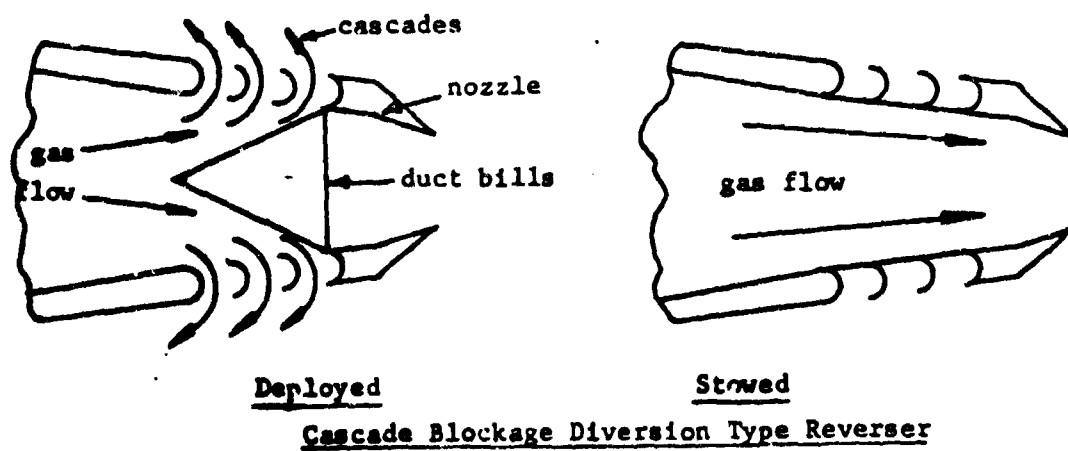
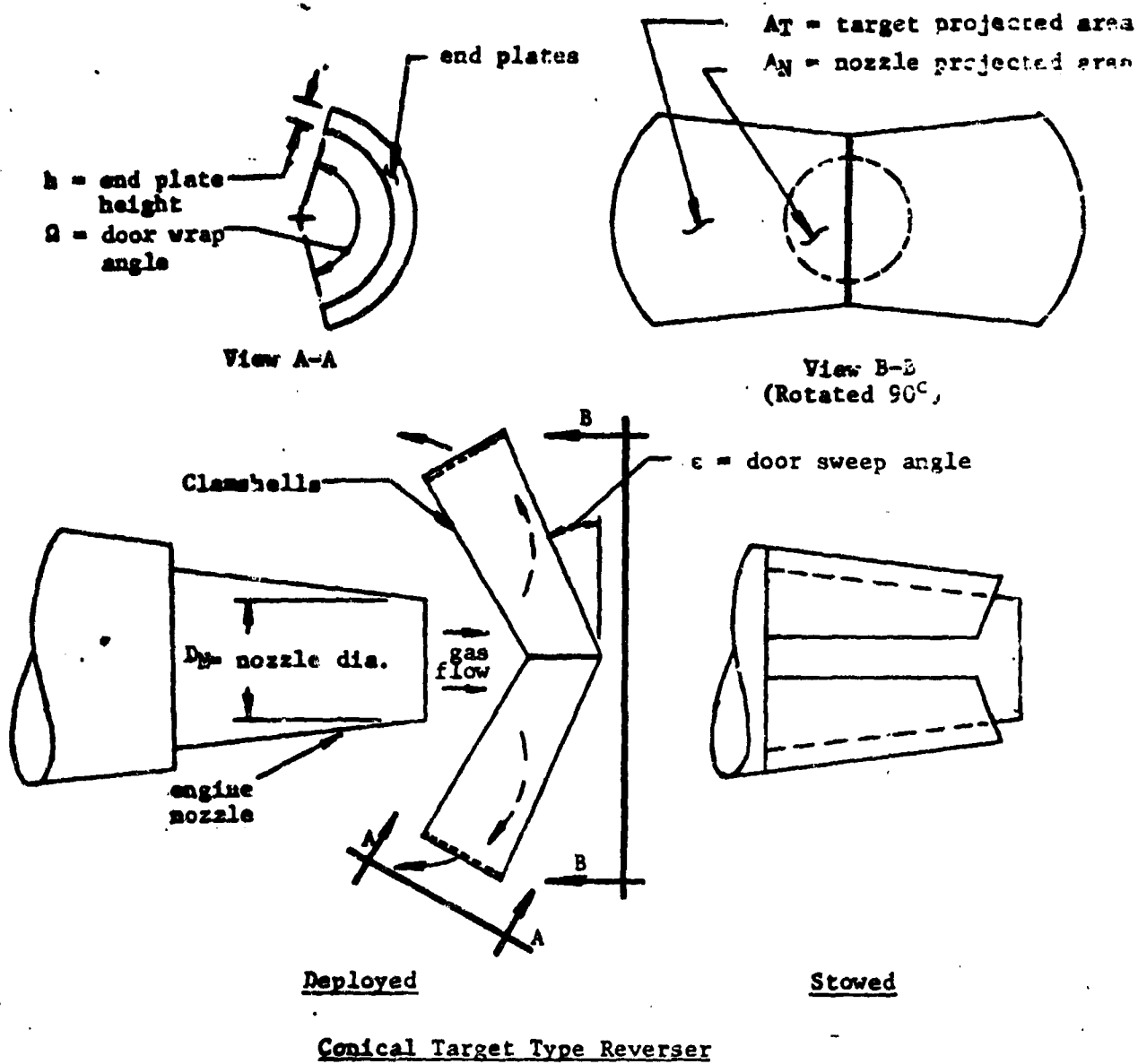


FIGURE 8-165 Typical Types of Common Reversers

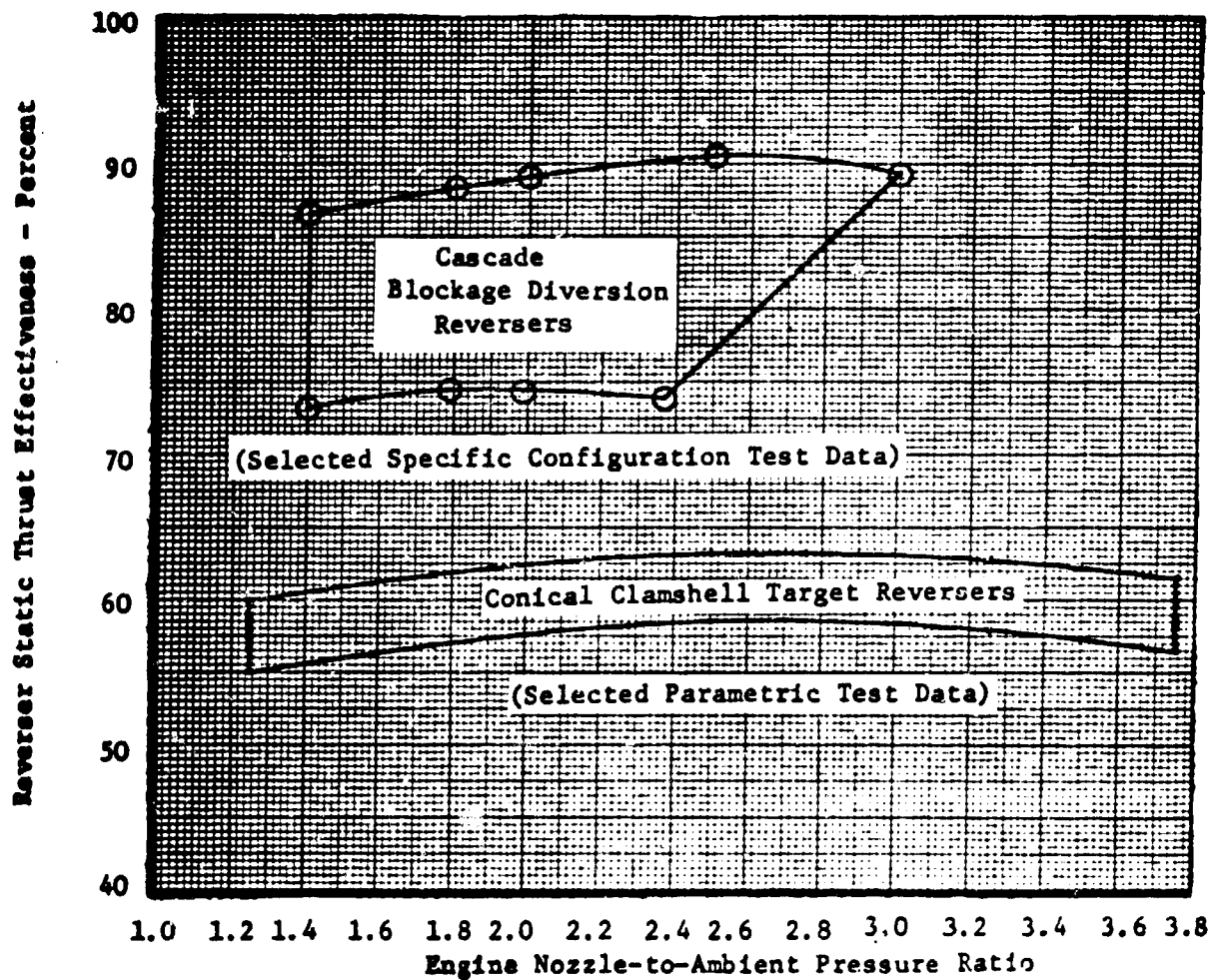


FIGURE 8-166 Typical Thrust Reverser Static Performance (Reference 3 and 4).

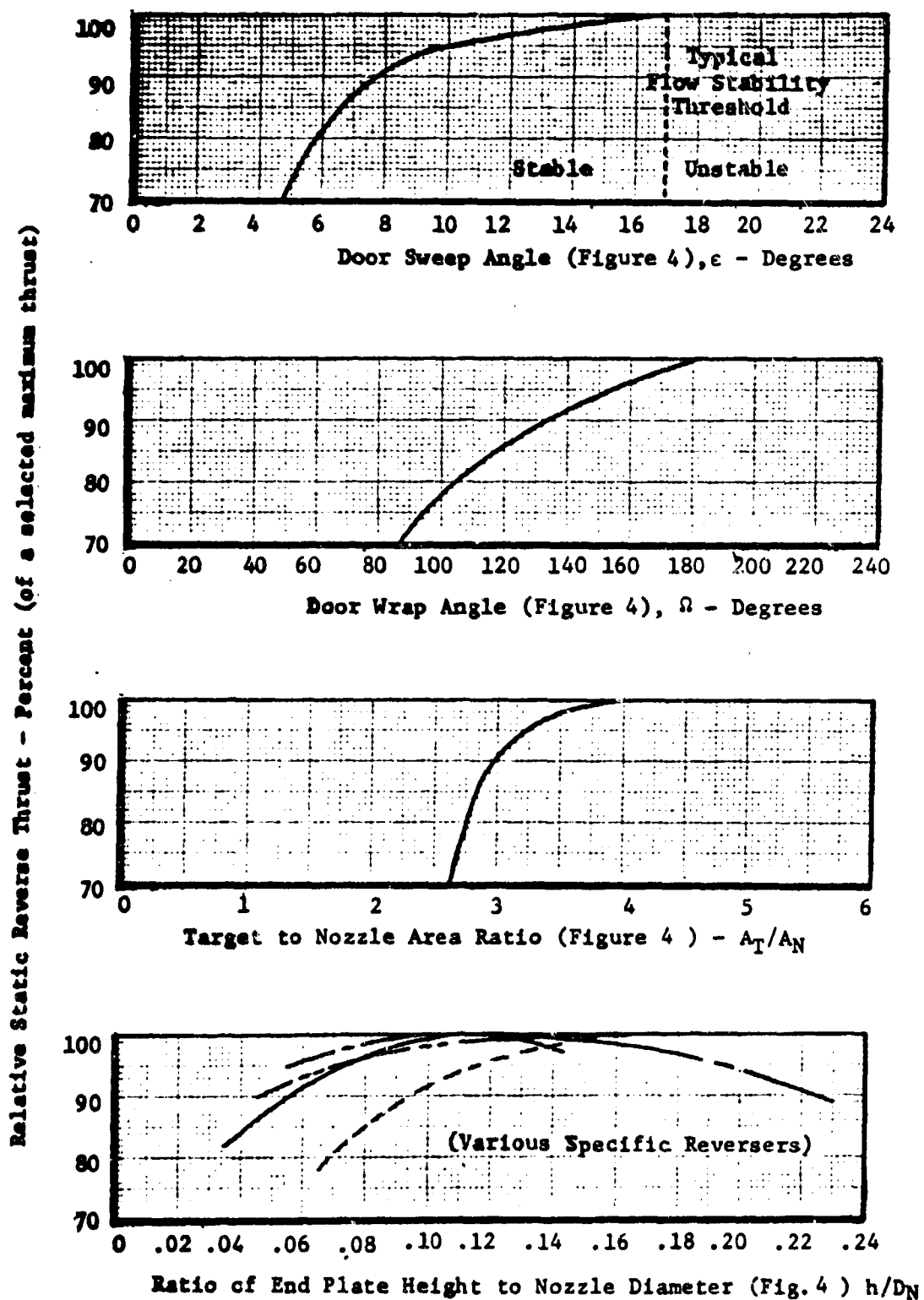


FIGURE 8-167 Conical Clamshell Target Reverser Performance Trends
(Reference 5)

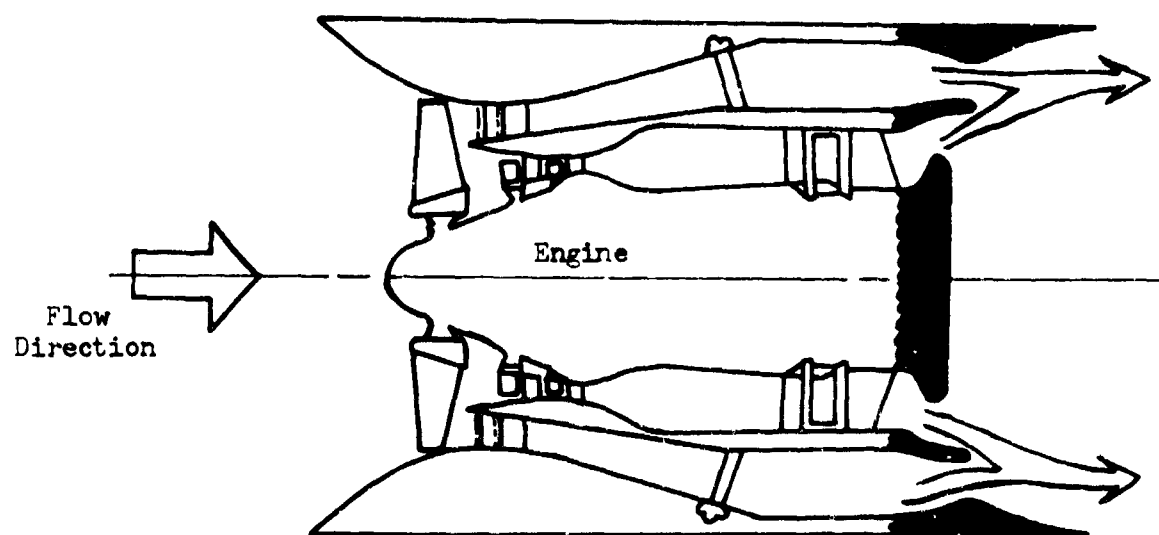


FIGURE 8-168. Coannular E-D Nozzle

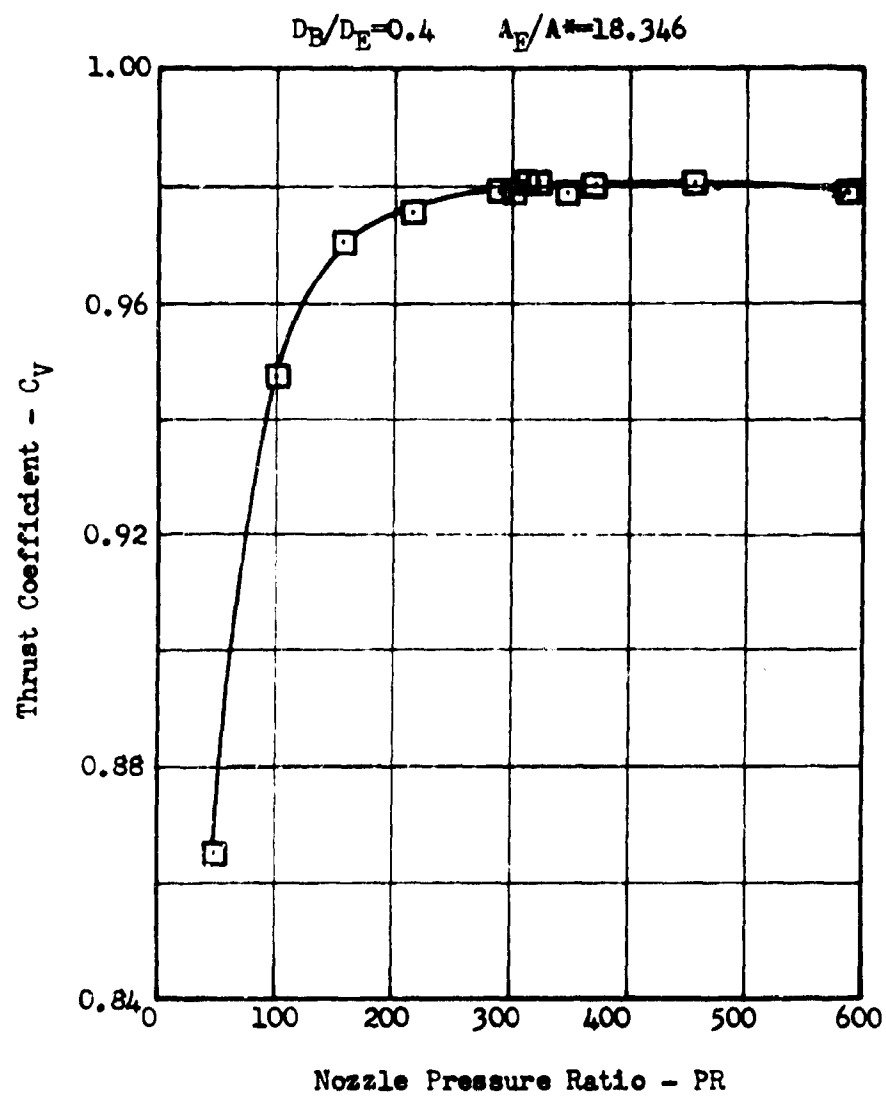


FIGURE 8-169. E-D Nozzle Performance

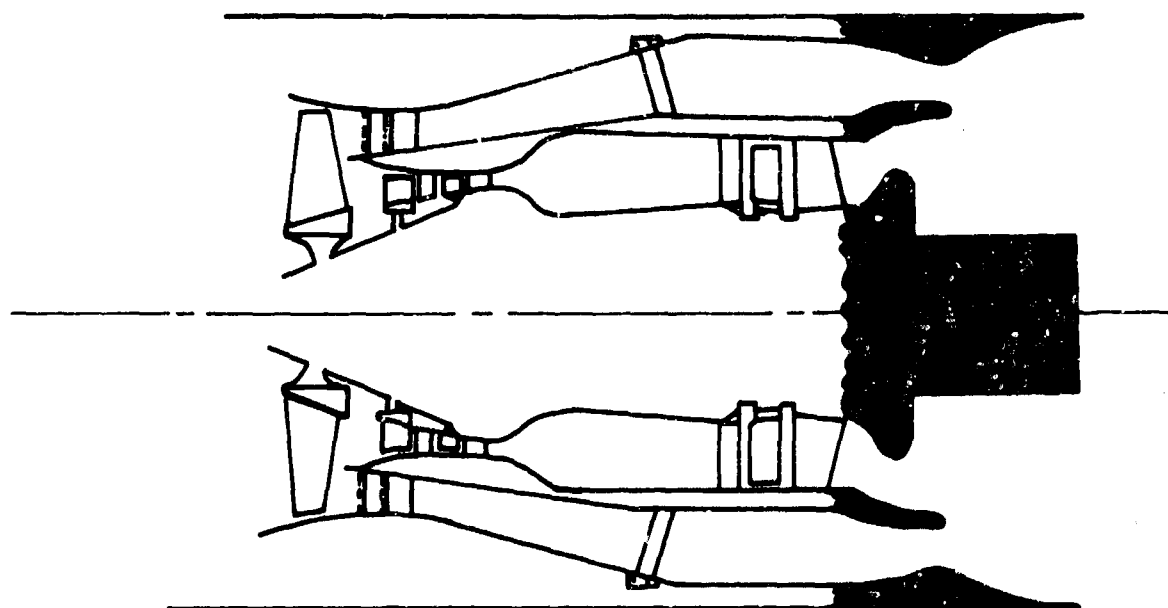


FIGURE 8-170. Sting in Base

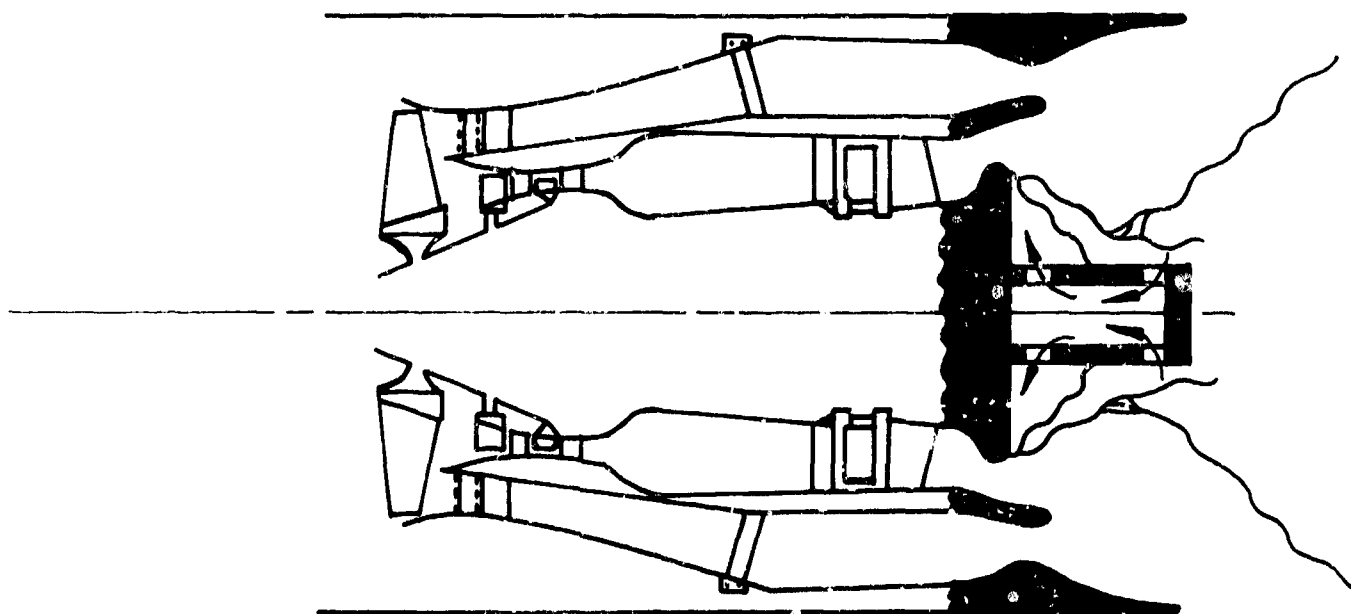


FIGURE 8-171. Base Vent Through Sting

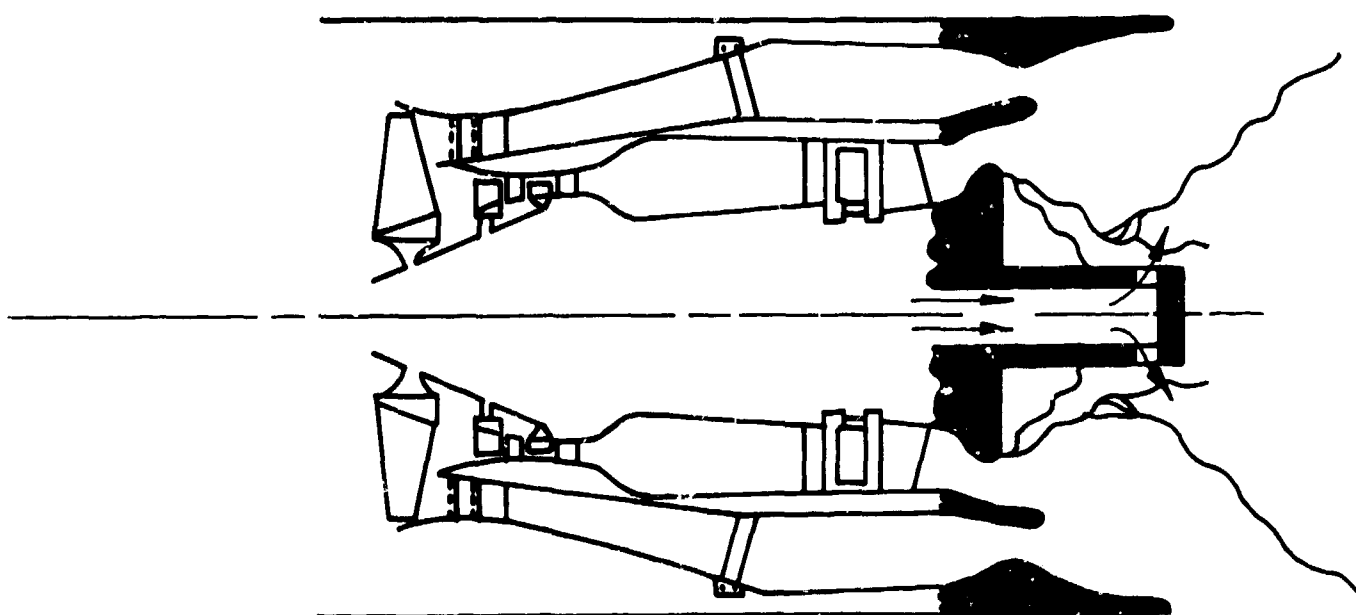


FIGURE 8-172. Base Bleed Through Sting

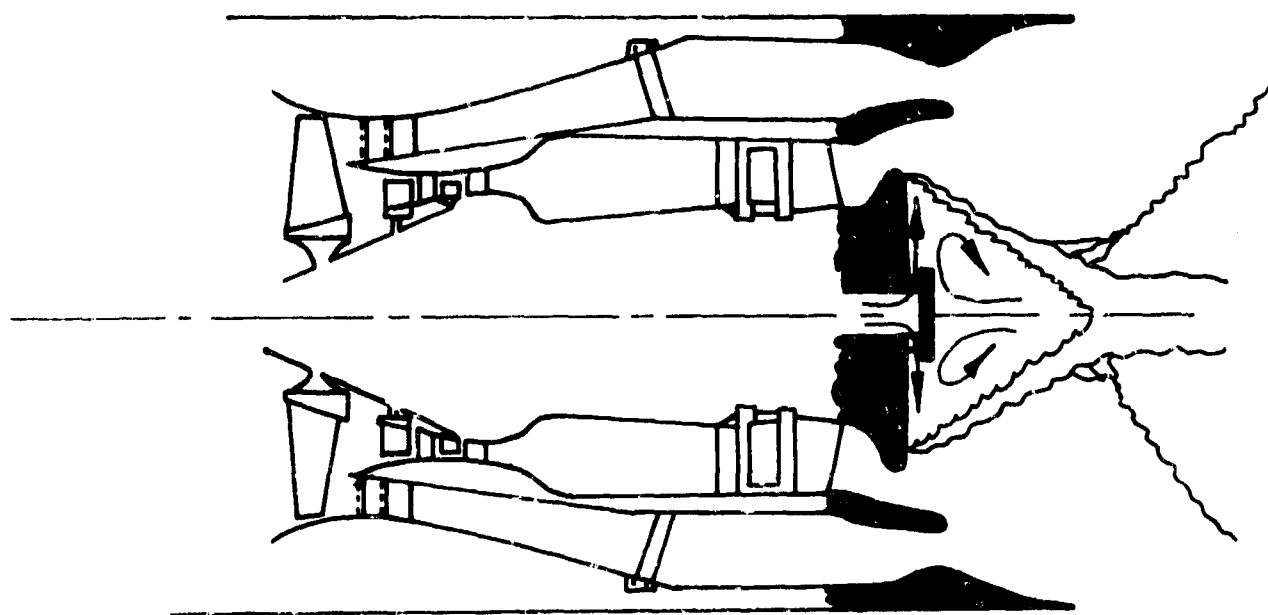


FIGURE 8-173. Radial Base Bleed

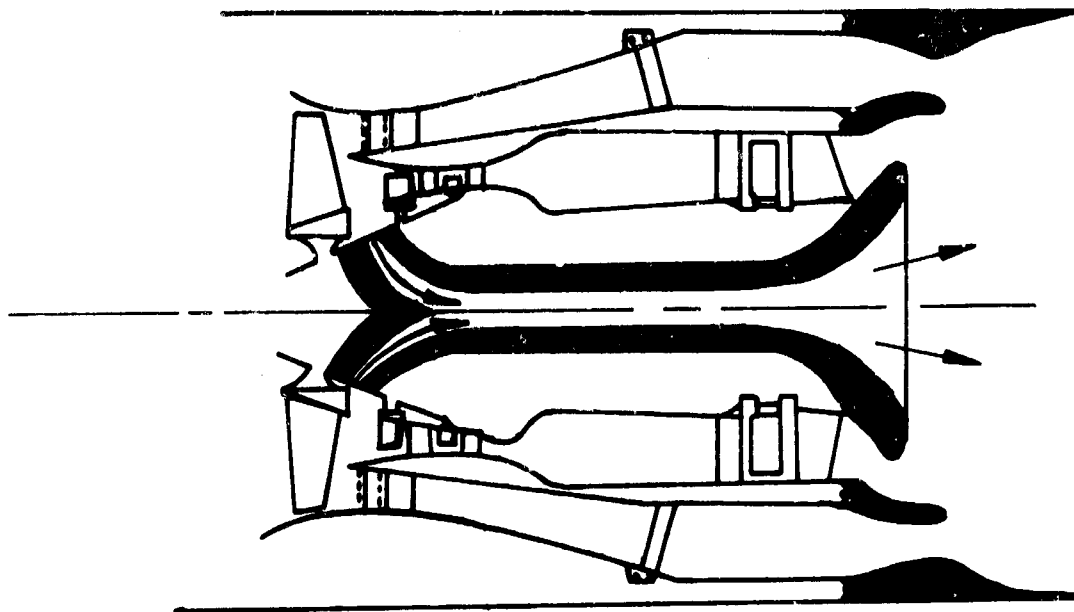
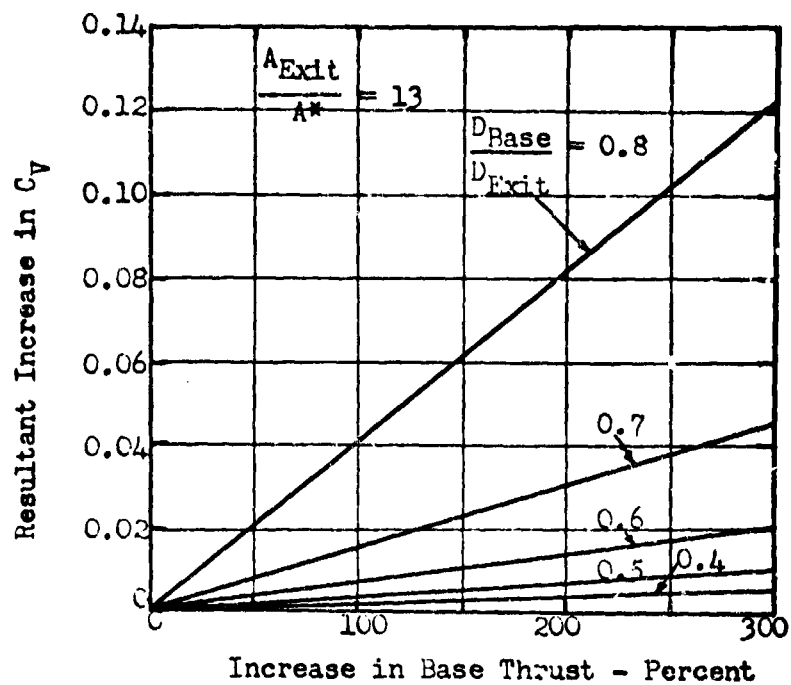


FIGURE 8-174. Axial Base Bleed



Resultant Increase in E-D Nozzle Efficiency Due to Increase in Base Thrust

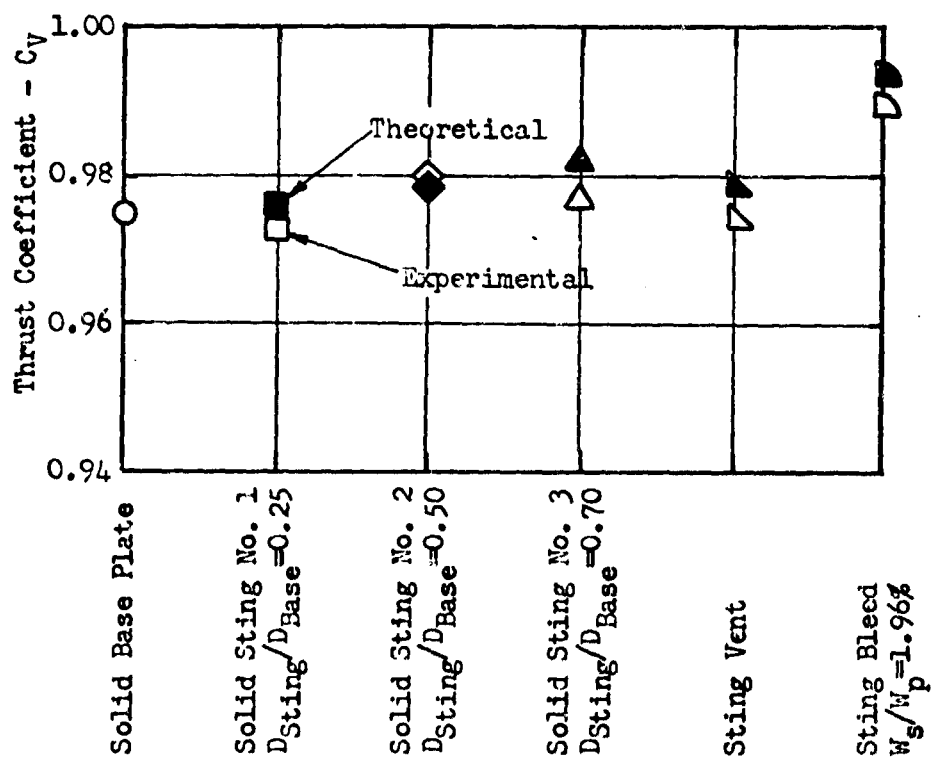


FIGURE 8-175. Effectiveness of Sting Concepts in Increasing Base Thrust

The net propulsive efficiency of an air vehicle power plant installation is governed by the difference between the nozzle thrust level and the overall afterbody and exhaust system drag. While thrust production is ideally a function of nozzle performance parameters and drag production a function of the aerodynamics of the flow over the external body surfaces, in reality, there exists a definite inter-relationship between thrust and drag of the installed system due to the interaction of the external airstream with the exhaust stream discharged from the nozzle.

For instance, optimum thrust is obtained when the static pressure ratio across the outer-most boundary of the exhaust stream at the nozzle exit is exactly equal to one (commonly called the nozzle design condition) in which case the exhaust stream undergoes no change in direction upon being discharged from the nozzle. Thrust level will decrease at all other pressure ratios although the variation of thrust production with pressure ratio will not be as great at pressure ratios greater than one as it will be at pressure ratios less than one. At these off-design conditions the exhaust stream will either expand or contract upon leaving the nozzle depending on whether the pressure ratio is greater or less than one, respectively. If the pressure ratio is appreciably lower than the design condition the thrust penalty can be quite severe except that flow separation within the nozzle will likely take place thereby allowing feed-back of the higher static pressures attributable to the external airstream over the afterbody and any base region that may exist. On the other hand, when the pressure ratio is greater than one, the exhaust stream will flare out beyond the nozzle exit diameter and directly interfere with the external airstream. If the amount of pluming is appreciable, the attendant pressure disturbance will be increasingly difficult for the external boundary layer to negotiate and flow separation will eventually take place, this time, on the surface of the afterbody itself.

In either case, the static pressure ratio at the nozzle exit is clearly a primary factor relevant to the strength of the interaction phenomena and, consequently, the inter-relationship between the thrust and drag characteristics of the overall afterbody and exhaust system installation. When the exhaust system is operated at off-design conditions, the strength of the interaction between the external airstream and the nozzle exhaust stream increases as the pressure ratio becomes increasingly different than one. This is not to infer, however, that the interaction phenomena is non-existent at the design condition but only that the interaction strength is minimized at this condition. Indeed, the exhaust

stream still exerts an effect on the afterbody and exhaust system drag through its ability to entrain some of the mass flow existing in a base region, for instance, and also by producing second-order pressure effects due to heat exchange from the usually much hotter exhaust stream. When the exhaust system is operating in the off-design condition, the influence of the thermo-chemical state of the exhaust stream becomes increasingly significant in direct proportion to the strength of the flow stream interaction. This additional effect on the interaction phenomena is introduced primarily by two means. First, by virtue of the control exerted by the temperature-dependent specific heat ratio on the rate of flow expansion and thereby, the shape of the exhaust plumes and second, by virtue of the heat exchange resulting from the mass diffusion process occurring in the reattachment region of the external airstream and the hot exhaust stream. The significance of heat exchange by mass diffusion may be particularly important in base flow regions and on afterbody surfaces lying beneath extensive areas of separated flow since the hot exhaust stream will form one of the boundaries defining such flow regions.

Clearly then, the drag of the installed afterbody and exhaust system combination is integrally dictated by both the aerodynamic efficiency of the external body geometry and by what may be considered as interference effects caused by the presence of a thrust producing exhaust stream. However, the primary sources of aerodynamic drag remain the result of the viscous and inviscid nature of the external airstream over the afterbody surfaces and on any base surfaces that may exist. The drag affecting afterbody surfaces is normally broken down into its skin friction and wave pressure drag components to account for the influence of the boundary layer and the potential flow field, respectively. The drag affecting base surfaces is most correctly classified as a pressure drag although the fluid mechanism which produce the pressure forces develop from strong viscous interaction of the total flow entering the base region from both the afterbody surfaces and the exhaust nozzle. Consequently, base drag is known to depend appreciably upon boundary layer characteristics. In order to determine the total drag of the afterbody and exhaust system herein defined in coefficient form as,

$$C_{DT} = C_{Df} + C_{D\pi} + C_{Db} \quad (9.1)$$

it is therefore often necessary to determine not only the Mach number and static pressure distributions along the entire length of both the external body surfaces and the nozzle wall but also to have knowledge of the manner in which the boundary layer develops along each of these surfaces as well. Because of these

requirements, the design engineer often finds himself confronted with a formidable task in attempting to optimize a typical aircraft and/or missile configuration on the basis of minimum total drag. Even though the importance of such analyses has been recognized for a good many years the evaluation of total afterbody and exhaust system drag remains a fundamental problem. Increased attention is currently being directed in this area in light of the larger degree of aerodynamic efficiency required of the upcoming generation of high performance aircraft capable of sustained supersonic flight. The fluid dynamic mechanisms that govern base drag, in particular, are as yet largely not well understood and are the subject of much recent large-scale research being conducted both in this country as well as in England.

The methods that are available for predicting the total drag characteristics of afterbodies and exhaust systems are primarily of a semi-empirical nature where theoretical treatment of single isolated body configurations with a cold air jet are employed in conjunction with available test data to simulate the compound body configurations in the presence of an exhaust stream(s) of hot combustion products which are more generally encountered in the flight operation of typical aircraft and/or missile configurations. The degree to which such semi-empirical techniques have been developed varies significantly with flight regime being more highly successful at supersonic speeds where many analytical tools are readily available for aerodynamic investigation. At subsonic and, more importantly, at transonic speeds where afterbody and base drag levels are generally most critical, the development of prediction techniques is hampered by the absence of analytical tools so that limited test data from experimental programs are more often the only source of information available at these speeds. The consequence, of course, of this almost total reliance on test data for arbitrary aircraft and/or missile configurations is that subsonic and transonic methods of drag prediction are currently ill-defined except in the presence of rather ideal flow situations. Definitely, more work is needed to further develop methods of drag analysis in these speed ranges. However, to the degree to which they have been formulated, semi-empirical prediction techniques have been demonstrated to provide the design engineer with a satisfactory method of estimating afterbody and base drag levels.

While not being altogether theoretically rigorous even when the state-of-the-art permits, the methods described in this chapter have been formulated with the design engineer in mind whose interest is in the application of a unified approach to afterbody and exhaust system drag prediction without being encumbered with formidable analytical tasks in order to achieve reasonably accurate results. The ensuing presentation of methods of drag analysis follows a three-section format whereby each component of the total

drag, i.e., afterbody skin friction drag, afterbody wave pressure drag and base pressure drag, is discussed separately in the first two sections while completely disregarding the existence of an exhaust stream being discharged from a nozzle. Methods of analysis to include the effects of nozzle flow on afterbody and base drag will be covered in the third and last section of this presentation. Unless otherwise noted, the techniques outlined herein apply to cases where the boundary layer is completely turbulent over the afterbody surfaces and ahead of the base region which is a realistic condition on full-scale aircraft and/or missile configurations. The semi-empirical methods of predicting the wave pressure drag of afterbodies are based primarily on wedge, conical and parabolic configurations although it will be shown that these methods can be applied to any arbitrary shape. Likewise, the base drag analysis is based on pressure measurements on zero-boattailed two-dimensional and axially symmetric bodies but employ a flow analogy model to account for the effects of boattailing, angle of attack and afterbody flow separation. Whereas each drag component is determined by integration of the source of disturbance over the surface area on which it acts, each component is herein referenced to the maximum cross-sectional area of the afterbody so that the total drag of the system may be evaluated from equation (9.1) by straight-forward addition.

9.1 Afterbody Drag

9.1.1 Skin Friction Drag Component

Skin friction drag is a direct consequence of the molecular resistance exerted by the individual particles making up any fluid medium to the imposition of relative translational motion brought about by only a local application of forces in an otherwise stress-free medium. The necessary force is supplied by any solid surface moving at a velocity that is different than that of the adjacent fluid medium. The fluid particles in immediate contact with the solid surface possess the same velocity as the boundary, thereby establishing a no-slip condition at the surface, whereas the fluid particles a sufficient distance away from the solid surface remain at the velocity of the initial uniform medium. Thus, the relative motion of the solid surface causes a local velocity deformation of the fluid medium. By virtue of the viscous nature of all real fluids, this velocity deformation is converted into a shear stress acting tangentially to the solid surface. This is represented mathematically by the relation,

$$\tau = \mu \frac{\partial u}{\partial y} \quad (9.2)$$

where τ is the magnitude of the resulting shear stress, μ is the coefficient of viscosity of the fluid medium and $\partial u / \partial y$ is the rate of the velocity deformation in the direction normal to the solid surface. That region of the fluid medium in which the velocity deformation takes place is referred to as the boundary or friction layer the thickness of which defines the extent of the fluid domain where mechanical work in the form of shearing stress is generated as a result of the viscous characteristics of the medium.

Within the boundary layer, the deficit of fluid velocity and the resulting shear stress varies continuously from its outer edge to the wall of the solid surface where the rate of velocity deformation, $\partial u / \partial y$, usually achieves its greatest magnitude. The amount of work imparted to the solid surface due to the action of viscous shearing stress is, therefore, primarily governed by the fluid properties immediately adjacent to the wall. Since the shearing stress acts tangentially to the wall in the direction opposite to that of its line of motion, the work imparted to the surface is exerted as an aerodynamic drag; called specifically, the skin friction drag. In coefficient form, the local skin friction of the solid surface is related to the viscous shearing stress by the following equation:

$$C_f = \frac{\tau_w}{\frac{1}{2} \rho_\infty V_\infty^2} = \frac{\mu_w \left(\frac{\partial u}{\partial y} \right)_w}{\frac{1}{2} \rho_\infty V_\infty^2} \quad (9.3)$$

The overall skin friction drag of a body in relative motion with a fluid medium is described by the viscous shearing stress acting on the entire wetted surface area of the body. If the fluid medium is essentially uniform, the skin friction drag of the body relative to its maximum cross-sectional area is,

$$C_{D_f} = \frac{\int \tau_w d(A_{wet})}{\frac{1}{2} \rho_\infty V_\infty^2 A_{wet}} \left(\frac{A_{wet}}{A_{max}} \right) = \frac{\int C_f d(A_{wet})}{A_{max}} \quad (9.4)$$

It will be recalled that referencing the skin friction drag to the maximum cross-sectional area of the body simplifies the determination of the total drag coefficient previously defined by equation (9.1).

For the realm of flight by aircraft and tactical missiles within the continuum atmosphere, the viscosity of air in equation (9.3) would depend solely upon the temperature of the wall of the vehicle. While the rate of velocity deformation (i.e., the velocity gradient normal to the surface) is also evaluated at the wall, it is governed primarily by the rate of momentum exchange between fluid particles. Hence, this term is not simply dependent on wall conditions but is also affected by any parameter that in some way controls the rate at which the boundary layer develops along the surface and also its dynamic stability. Boundary layers normally originate in the laminar state in which viscous fluid motion follows in neatly ordered paths. As the boundary layer moves downstream from its point of origin, the accumulative action of viscous shear stress tends to retard the fluid motion thereby causing the thickness of the boundary layer to increase with distance along the surface of the body. However, the effectiveness of stress retardation of fluid motion is highly dependent on the amount of momentum energy that is available within the viscous layer. The rate at which the boundary layer develops, therefore, is closely governed by the magnitude of the local fluid properties, and their gradients, at the two extreme boundaries of the viscous layer (i.e., the inviscid flow field and the wall of the surface). Most generally, as the thickness of the laminar boundary layer grows it eventually induces the characteristic steady motion of fluid particles to destabilize into random ordered motion indicative of transition to the turbulent viscous state. This change to the turbulent boundary layer state is accompanied by a significant increase in the viscous efficiency of momentum exchange and in the rate at which the boundary layer develops along the surface. This results in a greater rate of velocity deformation, $\partial u / \partial y$, at the wall and, consequently, an increase of surface skin friction than would normally be possible with a laminar boundary layer under identical fluid properties at the boundaries of the viscous region.

The determination of vehicle drag due to friction therefore requires knowledge of the free-stream flight conditions, profile shape and geometry of the vehicle, its surface temperature, location of boundary layer transition and the length of viscous development. It is also known that the surface finish (smoothness) of the vehicle walls can definitely alter the structure of the boundary layer thereby affecting the frictional drag as well. In the following presentation of methods of prediction, the skin friction characteristics of two- and three-dimensional body geometries are cited along with the effects of wall temperature and surface roughness. Since the present interest is directed to the afterbody surfaces, it is assumed that the boundary layer over these surfaces is completely turbulent by virtue of the large surface distances over which viscous development occurs before reaching these body regions on full-scale configurations.

9.1.1.1 Two-Dimensional Bodies

Based upon the extension of Von Karman's incompressible mixing-length hypothesis of viscous motion to include the effects of compressibility, the turbulent skin friction acting on a plane surface is,

$$C_f = \frac{0.472 \left(1 - \frac{1.12}{\log_{10} Re_x} \right)}{(\log_{10} Re_x)^{2.58} \left(1 + .88 \frac{\gamma - 1}{2} M^2 \right)^{0.44}} \quad (9.5)$$

where M is the Mach number, γ is the ratio of specific heats and Re_x is the Reynolds number based on the surface length of boundary layer development. All fluid properties in the above equation are those of the inviscid free-stream. It is also important to point out that equation (9.5) describes the skin friction of a plane surface whose wall is both thermally insulated (i.e., no heat transfer into or out of the boundary layer) and aerodynamically smooth. However, even from the geometric standpoint, the case of the plane surface represents the most basic form of boundary layer development on two-dimensional bodies where skin friction varies solely with distance along the surface.

For afterbodies of arbitrary profile, skin friction will be influenced by the variations of the inviscid fluid properties along the body section. Of particular significance is the existence of pressure gradients along the more general afterbody shapes which do not exist on plane surfaces and is therefore not accounted for in equation (9.5). Pressure gradient plays an important role in controlling the viscous flow characteristics and may therefore be expected to have a direct influence on the skin friction drag of the afterbody. Generally, the thickness of the boundary layer will decrease in a negative pressure gradient. Assuming that the fluid conditions (i.e., pressure, temperature, velocity) at both the inner and outer edges of the viscous layer remain unchanged, a reduced boundary layer thickness will increase the rate of velocity deformation at the wall. It can thus be readily seen that the influence of the negative pressure gradient will be to increase the local skin friction above that which would result in a zero pressure gradient field such as exists in the case of plane surfaces. Likewise, skin friction can be expected to decrease in a positive pressure gradient.

While it may be desirable to account for the presence of a pressure gradient for skin friction prediction on afterbody surfaces, this effect is not included herein due to the complexity of the required

computational procedures. The consequence of omitting this influence on skin friction drag will result in only very small error once the afterbody shape is additionally optimized on the basis of pressure drag (see Section 9.1.2). The major first-order effects on the local friction coefficient along the surface of arbitrary afterbody profiles can be readily handled by employing equation (9.5) for plane surfaces but making sure that the flow conditions appearing in this relation are evaluated at outer edge of the local boundary layer. This is analogous to rewriting equation (9.3) to read:

$$C_f = \frac{\tau_w}{\frac{1}{2} \rho_L V_L^2} = \frac{\mu_w \left(\frac{\partial u}{\partial y} \right)_w}{\frac{1}{2} \rho_L V_L^2} \quad (9.6)$$

where the subscript L refers to the local inviscid flow properties outside the boundary layer. Because of the geometric simplicity of two-dimensional bodies, the actual drag coefficient due to friction previously defined by equation (9.4) reduces to,

$$C_{D_f} = \frac{1}{D} \int C_f ds \quad (9.7)$$

where s is the surface length and D is the maximum diameter of the afterbody. In order to carry out the above integration of local friction, however, it is required that the surface location of transition to the turbulent boundary layer state be known since all afterbody surface distances are referenced to this location.

9.1.1.2 Three-Dimensional Bodies

The manner in which skin friction on three-dimensional bodies differs from that just described on two-dimensional bodies is attributable to both the inviscid and viscous characteristics of the flow field. Although emphasized in greater detail in Section 9.2, the most obvious difference of the flow field due to body geometry, for instance, is that the boundary layer thickness on axisymmetric boat-tailed afterbodies will be significantly greater than that on identically profiled two-dimensional afterbodies. The reason for this is that the cross-sectional area of the axisymmetric afterbody decreases at a faster rate and, in order to preserve the necessary

fluid law of continuity (i.e., constant mass flow rate), the boundary layer thickness must consequently grow at an accelerated rate. Due to the increased boundary layer thickness, the magnitude of both the local skin friction and the pressure gradients along the axisymmetric afterbody will be less than that on an identically profiled two-dimensional body. This effect on skin friction can be accounted for by applying, in reverse, the results of observations concerning the skin friction characteristics of forward-facing cones. In the case of supersonic flow past cones with an attached shock wave, experimental data have shown that, for the same values of local Mach number, Reynolds number, wall and local stream temperatures, etc., the local skin friction on cones in turbulent flow is approximately 15% higher than that on a flat plate. Since the pressure gradients of the two bodies are both zero, this difference must be attributable to the rate of change of body radius. Whereas the rate of change of body radius is in the opposite direction on afterbodies, the local skin friction on these three-dimensional geometries with a turbulent boundary layer should be approximated from the relation,

$$C_{f3-D} = \frac{C_{f2-D}}{1.15} \quad (9.8)$$

where C_{f2-D} has been defined by equation (9.5) for thermally insulated and aerodynamically smooth walls.

However, somewhat off-setting this beneficial trend, geometric effects may also serve to increase local friction as well. These adverse tendencies are due to the presence of what are called transverse curvature effects on boundary layer development where the viscous layer not only grows in the axial direction but, on three-dimensional bodies, is also spread out around the circumference of the body. Both the actual solution of the boundary layer equations and test data show that the rate of growth of the boundary layer on axial cylinders is always less than that on a flat plate. The difference in the growth rate in the two cases is a function of the ratio of boundary layer thickness to body radius, δ/r , becoming more significant as $\delta/r \rightarrow 1$ as shown in Figure 9-1. The tendency of increasing the local skin friction due to transverse curvature of the boundary layer is depicted in Figure 9-1. It is of interest to note that the local skin friction is not affected to as large a degree as the boundary layer thickness.

9.1.1.3 Effects of Wall Temperature

Up to this point of the discussion on skin friction drag, the effects of heat addition or removal across the wall have not been treated as the wall has so far been assumed to be insulated. This latter condition is representative of the thermal state of the

external body surfaces in sustained flight in the absence of transient heat sources or sinks. In this case, the temperature of the wall is referred to as the adiabatic wall temperature and, in the presence of a turbulent boundary layer, can be determined from the relation,

$$T_{aw} = T_L \left(1 + .88 \frac{\gamma_L - 1}{2} M_L^2 \right) \quad (9.9)$$

where the subscript L refers to flow properties evaluated outside the local boundary layer.

However, for afterbodies enclosing - or otherwise in proximity to - a hot exhaust stream, the insulated wall condition will not adequately describe the true thermal state of the surfaces beneath the boundary layer. With the exhaust stream acting as a significant heat source, the afterbody surface temperature will undoubtedly be greater than that defined by equation (9.9) thereby reducing the air density at the wall and, consequently, resulting in a lower surface skin friction coefficient than would be predicted for the insulated wall condition. The variation of local skin friction with wall temperature has been reported by Van Driest in Reference 2 for an isothermal surface (i.e., no wall temperature gradients) as follows:

$$C_f = \frac{\frac{0.558}{A} (\sin^{-1} \alpha + \sin^{-1} \beta) K}{\frac{0.558}{A} (\sin^{-1} \alpha + \sin^{-1} \beta) + 2 K \left(\frac{T_w}{T_L} \right)}$$

where $A^2 = \frac{T_L}{T_w} \left(\frac{\gamma_L - 1}{2} M_L^2 \right)$

$$B = \frac{T_L}{T_w} \left(1 + \frac{\gamma_L - 1}{2} M_L^2 \right) - 1$$

$$\alpha = \frac{2 A^2 - B}{\sqrt{B^2 + 4 A^2}} \quad (9.10)$$

$$\beta = \frac{B}{\sqrt{B^2 + 4 A^2}}$$

and $\frac{0.242}{A K \left(\frac{T_w}{T_L} \right)} (\sin^{-1} \alpha + \sin^{-1} \beta)$

$$= \log_{10} (K \cdot Re_x) - 1.26 \log_{10} \left(\frac{T_w}{T_L} \right)$$

The physical finish of any surface that is scrubbed by a boundary layer very definitely will affect the magnitude of the friction drag that will result. Up to the present point of the discussion of skin friction characteristics appropriate to afterbody surfaces, the wall has, of necessity, always been defined as being aerodynamically smooth. Such a wall condition is usually adequate to describe the external surfaces of test models for which extreme care is taken in their construction and preparation preliminary to the conductance of experimental flow tests. However, the surfaces of full-scale, operational flight vehicles are not nearly so ideal as those of test models due to the more typical existence of protruding rivets, mis-matched structural joints, pitting, oxidation and corrosion of the surface, etc., etc..... all of which act to pre-empt any similarity to an aerodynamically smooth surface. Accounting for the effects of surface roughness is, therefore, of practical significance in order to describe the frictional drag characteristics of vehicle surfaces; in this case, afterbody surfaces.

The most complete investigation of the frictional characteristics of roughened surfaces was that carried out by Nikuradse who conducted low speed experiments of water flow inside cylindrical pipes whose walls were artificially roughened by means of uniformly distributed sand grains. These incompressible data, which are published in Reference 3, have been singularly instrumental in discovering three basic ingredients inherent in any qualitative description of roughness effects. The most general observation made from these data is that, for constant fluid properties at the outer edge of the boundary layer (denoted by a constant local Reynolds number in the incompressible tests), the friction at the surface tends to increase in proportion to the effective height of the roughness element. Surprisingly, though, the dependency of surface friction on local Reynolds number has been found, for a constant roughness size, to vary widely over the Reynolds number range which was always sufficient to describe a completely turbulent boundary layer. At the low end of this range, the skin friction data showed their greatest dependency on Reynolds number; the same dependency as represented by equation (9.5) for aerodynamically smooth surfaces scrubbed by a turbulent boundary layer. However, at high Reynolds numbers, the data indicated that skin friction would eventually become essentially independent of Reynolds number. The departure from the aerodynamically smooth condition and the establishment of Reynolds number independence occurred at distinct values of Reynolds number that

depend on the relative size of the roughness element. This trend was consistent and followed the rule that as the relative roughness size increased both these unique Reynolds number values steadily decreased. Of course, in the extreme case of zero roughness these Reynolds numbers became infinite as there was no departure from the aerodynamically smooth condition.

The significance of this odd behavior observed from the incompressible pipe data is that it has identified that, although a surface may be physically rough, it can display a very different "effective" roughness ranging from being "hydraulically smooth" to being "completely rough" as far as the effect on the structure of the boundary layer and, consequently, the friction drag of the surface is concerned. The "hydraulically smooth" surface condition is represented in the incompressible data at low Reynolds numbers where the skin friction of a surface with finite roughness has the same Reynolds number dependency as if the surface were aerodynamically smooth (i.e., zero roughness). The "completely rough" surface condition is represented at the higher Reynolds numbers where skin friction increases solely as a function of roughness size. The concept of the "effective roughness" of a surface is, therefore, highly important to the definition of roughness effects in that it correctly draws attention to the idea that the physical surface condition acts as a source of disturbance to the viscous processes within the boundary layer and it is the efficiency by which these disturbances are transmitted within the subsonic regions of the boundary layer that will determine the skin friction drag of the roughened surfaces.

A number of investigators have, over the years, conducted skin friction tests of high speed airflow over rough surfaces with the purpose of determining both the usefulness of the Nikuradse incompressible data which were obtained from water flow tests inside of pipes and also to determine whether any new phenomena are introduced in the compressible flow case. About the most comprehensive of these investigations was that carried out by Goddard at Mach numbers from 0.70 to 4.54 which is reported in Reference 4. While for the moment tentatively accepting the validity of the incompressible water data, Goddard has shown, by referencing his test results to the Nikuradse data, that the effect of compressibility on the skin friction of a "completely rough" surface is that depicted in Figure 9-2. Also shown in this figure for comparison is the compressibility effect on smooth surfaces as determined from the data of Reference 5 and represented analytically in equation (9.5). Apparently, the entire compressibility effect is due to the continual reduction of fluid density at the surface as Mach number increases. Whereas this density effect is partially offset by viscosity effects

when the surface is smooth, the role of density must be the dominant one when the surface has roughness. This would explain the larger decrease of skin friction with increasing Mach number on the rough surface shown in Figure 9-2. It is also important to note that the compressibility effect on the rough surface is independent of the roughness size as the multiple symbols at each Mach number represents test data obtained on surfaces with different degrees of roughness. However, the uniqueness of the compressibility effect depicted in Figure 9-2 and its independence of roughness size is contingent upon the surface being defined as "completely rough". If the Reynolds number remains the same, the effect of increasing Mach number tends to alter the "effective roughness" of a surface even though the physical size of the surface roughness does not change. Thus, a surface that is classified as being "completely rough" at a low Mach number will tend to show "hydraulically smooth" characteristics at higher Mach numbers. This change in the "effective roughness" of a surface will be displayed by compressibility effects which are intermediate between the two curves in Figure 9-2. Conversely, if the Mach number remains constant, the "completely rough" nature of a surface will be enhanced as Reynolds number increases. As a result, the compressibility effect depicted in Figure 9-2 for this latter state of "effective roughness" can be employed with confidence to predict skin friction at all Reynolds numbers greater than the value indicated. In this instance, the local friction coefficient of a "completely rough" surface can be calculated from the relation,

$$C_{f(k,M)} = \frac{C_{f(k,M)}}{C_{f(k,o)}} C_{f(k,o)} \quad (9.11)$$

where the subscripts k and M refer to the roughness size (height) and local Mach number, respectively. As shown in Figure 9-2, the bracketed term, depicting the compressibility effect on the rough surface, can be represented by a rather simple analytical expression so that equation (9.11) reduces to,

$$C_{f(k,M)} = \frac{C_{f(k,o)}}{(1 + .88 \frac{\gamma - 1}{2} M_L^2)} \quad (9.12)$$

where $C_{f(k,o)}$ refers to Nikuradse's incompressible water data. Values of the incompressible skin friction on roughened surfaces are not presented herein but may be obtained directly from Reference 3 or from the resistance charts prepared by Prandtl-Schlichting, Moody, etc. that are available in most textbooks

on low speed fluid dynamics. Equation (9.12) can not be used to predict the skin friction of anything other than "completely rough" surfaces and, of course, depends on the validity of the incompressible water data to represent the skin friction characteristics in incompressible airflow.

In Reference 4, the validity of these data has been demonstrated by two different means. Initial confirmation was first obtained on the basis of direct comparison between the test data generated by Goddard at Mach 0.70 and those of Nikuradse which should ideally correspond to the skin friction characteristics at zero Mach number. On surfaces of identically finite roughness, this comparison has shown that the magnitudes of the Mach 0.70 data were generally the lower of the two and the agreement was always within 11 percent for the range of roughness considered. While these results are, by themselves, inconclusive they do represent a reasonable compressibility effect of air from Mach zero to Mach 0.70 and consequently tends to lend credence to the validity of the Nikuradse water data. More meaningful correlation was obtained, however, which emphasizes that the increase in skin friction due to surface roughness is essentially a disturbance phenomena where the source of disturbance originates at the surface and propagates within the immediate viscous regions of the boundary layer. The nature of the correlation that was obtained is shown in Figure 9-3 where the ratio of skin friction of a rough surface to that of an "aerodynamically smooth" surface is plotted as a function of a parameter known as the roughness Reynolds number. This parameter is denoted as,

$$Re_k = \left(\frac{v^* k}{\nu} \right)_W \quad (9.13)$$

where k is the roughness size (height) and v^* and ν are the friction velocity and kinematic viscosity, respectively, of the fluid medium evaluated at the wall condition. The friction velocity in the above relation is related to the viscous stress by the expression,

$$v_W^* = \sqrt{\frac{\tau_W}{\rho_W}} \quad (9.14)$$

For air with a 0.76 power law dependency of viscosity with temperature, the roughness Reynolds number denoted by equation (9.13) can ultimately be written in terms of the local fluid properties at the outer edge of the boundary layer to become,

$$Re_k = \left(\frac{v_k}{\nu} \right)_L \sqrt{\frac{C_f}{2}} \left(1 + \frac{\gamma_L - 1}{2} M_L^2 \right)^{-1.26} \quad (9.15)$$

where C_f in this expression refers to the friction coefficient of an "aerodynamically smooth" surface which has previously been defined by equation (9.5) for a thermally insulated wall. Equation (9.15) provided the means of reducing the test data obtained in Reference 4 for air in the form of roughness Reynolds number which may be considered as a general boundary layer disturbance parameter.

The skin friction correlation thus obtained, and shown in Figure 9-3, is unique for two reasons. First, at the local stream Reynolds number indicated, all the skin friction data in air for Mach numbers inclusive from 0.70 to 4.54 correlate in the same manner with the disturbance parameter regardless of explicit identification of the nature of the inviscid fluid medium or further reference to roughness size. It is therefore not by coincidence that this same relationship between skin friction rise due to roughness and the disturbance parameter was also observed by Nikuradse from his incompressible water data (see Reference 3). In Figure 9-3, the relationship found in the incompressible tests is represented approximately by the solid lines. From the agreement thus shown, it can be concluded that any difference in the roughness effects in air and in water is completely taken into account in the specification of Reynolds number thereby establishing the validity of employing the Nikuradse data to form the basis of the compressibility effect depicted in Figure 9-2, and of course, the correctness of equation (9.12).

The correlation of skin friction with the disturbance parameter is also unique in that it clearly discerns that the previously described "effective roughness" of a surface is dictated by the existence of a critical roughness Reynolds number. Below this critical Reynolds number, which is shown in Figure 9-3 to be numerically equal to $Re_k \approx 10$, a rough surface displays the same frictional characteristics as that of an aerodynamically smooth surface. Alternately, it can be said that there exists a critical roughness size to the boundary layer and below this size the viscous processes of shear stress production remain unaffected by the absolute finish of the surface. From the results of the data correlation shown in Figure 9-3 and by employing equation (9.13), the critical roughness size can be identified as,

$$k \approx 10 \left(\frac{v}{v_*} \right)_w \quad (9.16)$$

It was noted with great interest in Reference 4 that this critical size is approximately equal to the thickness of the laminar sublayer portion of the turbulent boundary layer that was found experimentally by Von Karman on smooth surfaces in incompressible flow. This equivalence is not expected to change in the presence of finite compressibility effects since the extent of the laminar sublayer is always confined to a narrow low-speed region near the surface and, of course, the pertinent fluid properties are evaluated at the wall temperature. In addition, Figure 9-3 shows no significant change in the critical roughness Reynolds number occurs between Mach numbers 0.70 and 4.54.

From this instructive observation, then, it is apparent that the frictional characteristics of a surface remain "hydraulically smooth" whenever the disturbance caused by surface roughness originates within the laminar sublayer of the viscous fluid environment. When the surface roughness extends beyond this portion of the turbulent boundary layer, local skin friction increases in direct proportion to the roughness size in the manner depicted in Figure 9-3. For the purpose of predicting the skin friction drag of a surface it is therefore first necessary to determine its "effective roughness" as seen by the local boundary layer. This may be accomplished by calculating the critical roughness size from equations (9.5) and (9.15) with $Re_k = 10$. Second-order effects due to three-dimensional surface geometry, transverse curvature of the boundary layer and the existence of heat transfer across the wall can be included using the procedures given in Sections 9.1.1.2 and 9.1.1.3. If the actual surface roughness size is less than the critical values thus calculated, skin friction remains unchanged from that determined for the aerodynamically smooth surface in accordance with the above discussion. If, however, the actual surface roughness size is larger than the critical value, skin friction must be corrected for roughness effects such that

$$C_{f(k)} = \frac{C_{f(k)}}{C_{f(o)}} \cdot C_{f(o)} \quad (9.17)$$

where $C_{f(o)}$ refers to the skin friction coefficient of aerodynamically smooth surfaces. The effect of surface roughness, represented by the bracketed term in the above equation, is a function of the local stream Reynolds number as the transition from the "hydraulically smooth" to the "completely rough" state of surface condition is not instantaneous but instead occurs over a finite Reynolds number range as discussed earlier in this

section. At the stream Reynolds number depicted in Figure 9-3, however, the surface may be classified as "completely rough" for Mach numbers up to $M_L \approx 5$ and for all roughness sizes exceeding the critical value. For this state of surface condition, then, the skin friction rise due to surface roughness can be represented analytically so that equation (9.17) reduces to,

$$C_{f(k)} = \left[0.11 + 0.89 \log_{10} (Re_k) \right] \cdot C_{f(o)} \quad (9.18)$$

where Re_k is given by equation (9.15). It may be noted that the skin friction of a "completely rough" surface may be determined from either the above equation or from equation (9.12). Equation (9.18) is to be preferred since it does not rely directly on the Nikuradse water data as does the earlier equation.

9.1.2 Pressure Drag Component

9.1.2.1 Subsonic-Transonic Speeds

In general, afterbody pressure drag can be broken down into two components: that due to the principal afterbody pressure distribution which exists on an afterbody preceded by an infinite cylinder, and that due to the interference pressures imposed on the afterbody caused by the presence of a forebody. At subsonic and transonic speeds, forebody interference drag can be very large. For a general aerodynamic shape consisting of a forebody, a cylindrical center section and an afterbody, the flow over the forebody does not have enough energy to negotiate the abrupt change in body contour occurring at the junction of the forebody and the cylindrical section without greatly over-expanding in the vicinity of the body junction and finally recompressing as it travels downstream over the cylinder. As a result, the primary pressure distribution over the afterbody following the cylindrical section is usually affected in varying degrees depending on the fineness ratio of the forebody and the distance separating the forebody and afterbody. At low speeds, the distance required for full pressure recovery is generally quite large so that on many practical aircraft and/or missile configurations, analysis of the pressure drag of afterbodies would, of necessity, have to take into account the interference effects of body surfaces upstream of the afterbody. In practice, afterbody pressure drag is determined by considering the interference effects to be linearly superimposed on the principal afterbody pressure distributions as permitted by linear theory cited in Reference 7. The process of superimposing the pressure distributions on a simplified configuration consisting of a cone-cylinder and conical afterbody is illustrated in Figure 9-4. It can be seen that for this type of configuration body regions of rapid flow expansion exist at the junction of both the forebody and cylinders and the cylinder and afterbody and that downstream of each junction the flow recompresses over a finite body length until the pressure coefficients would eventually become zero if the corresponding body section was of sufficient length. If full pressure recovery has not been attained immediately upstream of the afterbody, the absolute level of pressures acting on the principal afterbody would change although, in the case of the cylindrical center section, the distribution of pressures would remain the same. Where, on other configurations, the body surfaces upstream of the afterbody do not have zero surface slope, the distribution of afterbody pressures would also change.

The principal wave drag of conical and circular-arc afterbodies following transverse cylinders at subsonic-transonic speeds

are shown in Figures 9-5 and 9-6, respectively. The curves in these figures have been derived in Reference 6 on the basis of experimental data from References 9 and 10 for the conical afterbody and from Reference 10 for the circular-arc afterbody. The drag curves for the circular-arc afterbody are, in addition, based on method of characteristics solutions in the presence of boundary layer development obtained in Reference 11 for parabolic afterbodies in the higher transonic speed range where the free stream Mach number is greater than one. Because of the close similarity between the circular-arc and parabolic afterbodies, there should be only small differences between their respective drag levels. The comparison between these data shown in Reference 6 has demonstrated that the parabolic and circular-arc afterbody drags are in excellent agreement so that reference to these bodies may be made interchangeably. It should be emphasized, however, that the afterbody drag represented in Figures 9-5 and 9-6 is applicable only to the appropriate afterbody shapes preceded by a transverse cylinder for the reasons previously cited. Methods for determining the effect on subsonic-transonic afterbody drag due to forebody interference do not appear to be available at present.

In Reference 8 an analytical hypothesis is offered which would permit the drag of arbitrary afterbody shapes to be determined if the pressure distribution on a conical afterbody is known. According to this hypothesis, the pressure at a point on an afterbody is independent of the flow path to that point as long as the surface slope (boattail angle) and local-to-maximum area ratio are preserved. This boattail analogy is illustrated in Figure 9-7 where a conical boattail body is circumscribed at a point on an afterbody of arbitrary shape. As a consequence of this hypothesis, the pressure at the point of tangency is the same for both the circumscribed conical boattail and afterbody shape for a given Mach number immediately upstream of the afterbody. Although this analogy has not been tested at subsonic-transonic speeds, it was tested by the authors of Reference 8 at supersonic speeds with good results. Assuming this hypothesis can be applied regardless of the speed range, then, given the pressure distribution on conical afterbodies, the drag of any convex afterbody shape can be determined by integration of the local pressures obtained by employing the conical boattail analogy at each point on the arbitrary afterbody.

9.1.2.2 Supersonic Speeds

In contrast to the state-of-the-art of drag prediction at subsonic-transonic speeds, methods for predicting the pressure

distribution and, consequently, the wave drag of afterbodies at supersonic speeds are well facilitated by the availability of theories offering almost any degree of accuracy desired. Of course, it is most generally the rule that the level of accuracy desired in an analysis is a direct function of the complexity of the theory required for application. About the most consistently accurate theory that exists for flow field prediction work is that theory commonly referred to as the method of characteristics. The complexity of this analytical method, however, makes it unwieldy to use in design studies even with the aid of a digital computer. As a result, its use is usually restricted to the final design stage. Occasionally it is used to evaluate the accuracy of other theoretical prediction methods which are more easily employed in design analysis but at the expense of being tailored in application to a specific aerodynamic regime.

In this section, methods of predicting supersonic wave drag of afterbodies are accomplished by the presentation of correlation charts of drag in terms of the similarity parameter $\sqrt{M^2 - 1} \sin \beta$. These charts were originally presented in Reference 11 and, for three-dimensional afterbodies, were determined by fairing the solutions of a number of theories each of which has application over only a finite range of the similarity parameter. Although each of the theories employed in developing these drag charts is identified along with its range of application, specific details of these theories is not discussed herein but should instead be obtained from the references that are cited. The applicability of each of these theories and the fairing procedure employed between them was substantiated both by comparison with test data and "spot checks" provided by method of characteristics solutions. Details of this latter method can be obtained from a standard textbook.

9.1.2.2.1 Two-Dimensional Afterbodies

In Figure 9-8, the principal wave drag of wedge afterbodies is presented on the basis of a best fit curve through calculations using Prandtl-Meyer expansion theory (Reference 12). This theory simply assumes that a uniform two-dimensional supersonic airstream, in the absence of external disturbances in the flow field, expands isentropically over a convex surface. Also shown in this figure is the range of accuracy established with the single fitted drag curve. This curve was chosen so as to maintain an arbitrarily set 5 percent error limit on drag for the largest possible range of wedge boattail angle. As is indicated, the accuracy of this curve decreases at low supersonic Mach numbers and high boattail angles.

Also, at any given Mach number, a maximum boattail angle exists beyond which the flow can not remain attached to the afterbody surface. In this range of flow expansions, the local airstream separates from the surface and permeates into a wake such as exists in base regions. Although methods for predicting drag on body surfaces under the influence of wake-type flows will be discussed later on in Section 9.2, it can be said at this time that the general effect on such body surfaces would be realized in an increase in the drag level than if the flow remained attached. The maximum level to which the drag can increase is depicted in Figure 9-9 as

$$C_{D\pi \max} = \frac{1}{.7 M^2} \quad (9.19)$$

to represent the condition where the local surface pressures decrease to vacuum. Of course, this condition would never actually exist although at very high Mach numbers the difference between the true pressure level and the vacuum condition is quite small.

The boattail analogy discussed in Section 9.1.2.1 may also be applied for two-dimensional bodies to predict the pressure distribution and therefore, the drag, of arbitrary two-dimensional afterbody shapes if the wedge pressures are known. Figure 9-8 can be used to obtain these pressures since, for a two-dimensional wedge, $C_D \pi = -C_p$. By applying the boattail analogy on two-dimensional bodies, the pressure at any point on an arbitrary afterbody will be the same as that on a wedge whose boattail angle is equal to the local surface slope at a given Mach number. No methods appear to be available at present for determining the interference drag due to a forebody. For blunt forebodies producing a curved two-dimensional shock wave, the interference drag can be quite severe, particularly at high Mach numbers.

9.1.2.2.2 Three-Dimensional Afterbodies

The principal wave drag of conical and parabolic afterbodies is presented in Figures 9-9 and 9-10, respectively. As previously pointed out, the drag curves for each of these bodies were determined from an assortment of theories depending on the range of the similarity parameter. The region of application for each theory is shown on the figures. Slender body theory (Reference 13) is used rather extensively on both afterbodies for high fineness ratio and at moderate supersonic speeds. It should be noted, however, that slender body theory was employed throughout the full similarity range on the conical afterbody with $d/D = 0$. The drag indicated for the $d/D = 1$ curve is appropriate to wedge

drag in the limit and is identical with the curve presented in Figure 9-8. The consequence of this curve implies that the initial expansion of flow at the immediate shoulder of the conical afterbody takes place two-dimensionally. Second order theory (Reference 14) is employed for the less fine conical afterbody at high supersonic speeds. The drag of parabolic afterbodies at high speeds is predicted with the use of shock expansion theory. This theory is fully described in Reference 15, however, specific application of this theory was obtained from Reference 16. In the intermediate range of the similarity parameter, parabolic afterbody drag was calculated from quasi-cylinder theory as presented in Reference 17. It is important to note that the wave drags presented in Figures 9-9 & 9-10 are based on the annular area of each afterbody. It is advantageous in afterbody drag analysis to add the wave drag directly to the base drag in order to evaluate the total drag of the afterbody system. The wave drags will first have to be based on the maximum cross-sectional area of the body which can be accomplished by dividing by $(1-d^2/D^2)$.

The conical boattail analogy discussed in Section 9.1.2.1 can be employed to determine the principal wave drag of arbitrary afterbody shapes by assuming the local pressure to be found by knowing the pressure at a similar point on a conical afterbody. For this purpose, the pressure distribution on conical afterbodies is presented in Figure 9-11. These pressures have been calculated from second order theory (Reference 14).

Methods for determining the interference drag due to a forebody do not appear to be widely available as yet. However, Reference 18 was found to present solutions for the inviscid, steady, axisymmetric supersonic flow about cone-cylinders as determined by the method of characteristics. Pressure coefficients have been calculated from these data and curve fitted on the basis of a 5% error limit over the maximum range of applicability.

The resulting curve fits are presented in similarity form in Figure 9-12, as a function of the distance from the cone-cylinder junction. It should be pointed out that the pressures from this figure can not be extrapolated to greater distances along the cylinder since the original characteristic solution was limited to a point on the cylinder at which the Mach wave extending from the cone-cylinder junction reflected from the nose shock wave and impinged on the surface. These cylinder pressure curves should nevertheless be useful for determining the interference drag of conical forebodies on short configurations such as munition stores, canisters, etc. The need for more data on interference pressures due to arbitrary forebody shapes is obvious.

9.1.2.3 Bodies of Arbitrary Cross-Section

In a great many cases, aircraft configurations (particularly, aircraft employing multiple power plants buried within the fuselage) are encountered with cross-sections that are highly asymmetric. Determination of the wave drag on such configurations can sometimes be facilitated by dividing the total cross-sectional area into a finite number of smaller regions using the radius of curvature in the cross-sectional plane as a criterion. Once this is accomplished, it is then possible to identify regions of large curvature as being segments of axisymmetric bodies and regions of small curvature as being essentially flat. The methods outlined in the previous sections for two- or three-dimensional bodies can then be applied to each appropriate body region and the resulting wave drags carefully weighed according to the percentage of the total cross-sectional area represented by each region to estimate the total wave drag. Of course, it is also possible that, within each selected region of the cross-sectional area, the boattail angle may vary along the periphery in which case the axial pressure distribution at many points of the periphery would have to be determined using the boattail analogy previously discussed and integrated to obtain the wave drag.

9.2

Base Drag

9.2.1

Two-Dimensional Base Drag

9.2.1.1

Base Flow Characteristics and Flow Analogy

The flow characteristics in the base region of bodies is principally of two basic types depending on the Mach number of the airstream immediately upstream of the base. At subsonic speeds the base flow consists of the large vortical eddies that are typical of the so-called "open wakes". When the airstream immediately upstream of the base is transonic, the flow leaving the body surface undergoes an isentropic expansion toward the body centerline thereby establishing a supersonic shock wave just downstream of the base shoulder. The vortical eddies present at subsonic speeds thereby become displaced further downstream from the base of the body and replaced by a region of supersonic viscous mixing between the base and the shock wave that follows. This change in the base flow characteristics is demonstrated in the schlieren photographs presented in Figure 9-13. These photographs were obtained from Reference 19 and represent the flow in the base of a 8.6° total angle wedge-flat plate model. As pointed out in the original report, the seemingly odd body shape shown in these photographs is caused by a hardware fitting on the viewing window to which the model was mounted. At higher Mach numbers, the "closed wake" character of the base flow would remain essentially unchanged from that depicted at the high transonic speeds. The main effect of Mach number in the supersonic speed regime would be to increase the efficiency of the viscous mixing process in the base region.

The differences between the two base flow characteristics is largely responsible for the success to which analytical techniques have been devised for the prediction of base pressure, or drag, throughout the speed range. At Mach numbers greater than one, the base pressures result from the viscous mixing process that takes place within a region extending from the base of bodies and terminating at the position of the shock wave in the wake. The geometry of the mixing region is therefore well defined if the location of the shock wave can be determined. By taking advantage of the "closed wake" characteristic, semi-empirical methods have subsequently been developed to predict the effect on base pressure due to afterbody boattailing and angle of attack at supersonic speeds. The most successful of these methods will form the basis for the discussion on base pressure prediction in this lecture. Unfortunately, the "open wake" characteristic existing at subsonic speeds has, so far, defied analogical procedures so that methods for predicting base pressures at these

speeds do not exist. As a result, base pressure estimation behind boattailed afterbodies, and the effect of angle of attack, remains a matter of experimentation at subsonic speeds. The discussion to follow will include methods of prediction applicable at these speeds only to the extent that test data is available.

The method of predicting base pressure at supersonic speeds, is based on a flow analogy model reported in Reference 20 and later expanded in application by the authors of Reference 8. The flow analogy essentially stipulates that the characteristics of the flow behind a two-dimensional base is not much different than the phenomena of boundary layer separation ahead of forward-facing steps. As the Mach number of the flow ahead of the forward-facing step is increased, the local flow is more highly deflected ahead of the step with an attendant increase in the strength of the shock wave required to support the higher pressures resulting from this deflection. Eventually, as the Mach number is increased, the pressure rise across the shock wave will reach a particular value at which point a turbulent boundary layer will separate from the surface ahead of the step. The basic concept of the flow analogy employed for supersonic base pressure prediction is therefore, that the critical pressure-rise coefficient at which the boundary layer ahead of the forward-facing step will separate is essentially the same as the pressure coefficient existing across the shock wave behind a rearward-facing step or base. This analogy is illustrated in Figure 9-14. It must be remembered that this analogy requires that the boundary layer immediately upstream of the afterbody is completely turbulent. In addition, it is required that the boundary layer be relatively thick compared to the step height of the base (or, for a truly free wake region, the local body radius at the base). Experimental investigations have shown that under these two conditions the effect of Reynolds number on the base drag level is small and, in the analysis which follows, this influence is not initially considered.

The pressure-rise coefficient across the trailing shock wave behind the base is therefore a direct function of only the Mach number (M_1) in the wake which, for two-dimensional bases, is constant along the wake. Experimental values of the variation of the turbulent pressure-rise coefficient with Mach number in the wake have been determined in Reference 20 and are shown in Figure 9-15. At supersonic speeds, the flow upstream of the base enters the wake through an isentropic expansion process at the base shoulder. Working backwards from the wake, then, the critical pressure-rise coefficient can be related directly to the Mach number of the flow upstream of the base by the turning angle of the expansion process. Since, due to the wake mixing process, the wake pressure and the base pressure are one and the same, it should therefore be possible to determine the base pressure simply by knowing the flow condition upstream of the base and the turning angle into the wake.

If this base flow analogy is unique, then the base pressure should be able to be predicted, for any given Mach number upstream of the base, using the experimentally determined pressure rise coefficients in Figure 9-15, and the Prandtl-Meyer expansion tables given in Reference 12. For the purpose of evaluating this analogy, the base pressures determined in this manner should correlate with available experimental data. In Reference 8, data on zero-boattailed two-dimensional bodies at zero angle of attack and with no jet flow were compiled and curve fitted to show the experimental base pressure variation with Mach number shown in Figure 9-16. On the basis of these data, it has been found that the analogy is not quite unique in that the wake turning angle required to correlate with experimental base pressures is not the Prandtl-Meyer angle. The required angle, instead, was found to be that shown in Figure 9-17.

The Mach number, M_R , is introduced as the abscissa in this figure as this variable will be a necessary working parameter in the next section where the base pressure behind boattailed afterbodies will be discussed. This Mach number, however, is a fictitious parameter and not an actual flow condition. M_R is defined as the "effective" Mach number immediately upstream of the wake flow region having a direction parallel to the trailing flow behind the shock wave in the wake. M_0 is the actual Mach number on a cylindrical mid-section immediately upstream of an afterbody. For a zero-boattailed body (no afterbody) at zero angle of attack and with no jet flow, M_R equals M_0 . It should be recalled that if significant interference effects are present due to the existence of a forebody, then the Mach number, M_0 , will be different than the free-stream Mach number, M_∞ . This notation is illustrated in Figure 9-18.

In summation, then, if the pressure data curve in Figure 9-16 is valid, the supersonic base pressure on a two-dimensional, zero-boattailed body at zero angle of attack and in the absence of jet flow can be predicted if the Mach number immediately upstream of the base is known by using the wake turning angle given in Figure 9-17. The step-by-step calculation procedure is as follows:

A. Given: M_0

B. Procedure:

1. Determine $\frac{P_0}{P_{T_0}}$ corresponding to M_0 using the equation:

$$\frac{P_o}{P_{T_o}} = (1 + .2 M_o^2)^{-3.5} \quad (9.20)$$

2. Find Prandtl-Meyer expansion angle δ_{P-M} , corresponding to M_o either from the tables provided in Reference 12 or from the equation:

$$\delta_{P-M} = 2.45 \tan^{-1} \left(\sqrt{\frac{1}{6} [M_o^2 - 1]} \right) - \tan^{-1} \left(\sqrt{M_o^2 - 1} \right) \quad (9.21)$$

3. Find two-dimensional wake turning angle, δ , for $M_o = M_R$ from Figure 9-17.

4. From tables provided in Reference 12, find Mach number, M_1 , corresponding to $\delta_{P-M} + \delta$.

5. Determine $\frac{P_b}{P_{T_o}} = (1 + .2 M_1^2)^{-3.5} \quad (9.22)$

6. Calculate base pressure coefficient, C_{P_b} , from the equation:

$$C_{P_b} = \frac{\left(\frac{P_b}{P_{T_o}} - \frac{P_o}{P_{T_o}} \right)}{0.7 \left(\frac{P_o}{P_{T_o}} \right) M_o^2} \quad (9.23)$$

NOTE: It should be pointed out that, throughout this discussion, the base pressure is considered constant across the base area so that the base drag can be determined from:

$$C_{D_b} = -C_{P_b} \frac{d_b}{D} \quad (9.24)$$

9.2.1.2 Effects of Afterbody Boattailing

9.2.1.2.1 Subsonic Speeds

As pointed out in Section 9.2.1.1, analogical procedures for subsonic base pressure prediction on two-dimensional bodies have not as yet been devised. As a result, this is an area definitely in need of more research and experimentation. On zero-boattailed two-dimensional bodies, the subsonic base pressures denoted by the fitted curve in Figure 9-16 appear to be in good agreement with most sources of data for the case where the boundary layer at the base shoulder is completely turbulent and the boundary layer is relatively thick relative to the body diameter at the base. These pressures may at least be useful for preliminary design estimates until reliable test data on boattailed bodies become available.

9.2.1.2.2 Supersonic Speeds

The range of base flow situations that can occur on two-dimensional boattailed afterbodies is depicted in Figure 9-19. It has been previously shown in Figure 9-13 that, when the afterbody boattail angle β is zero, the wake is well contained behind the base of the body and converges at an angle equal to the wake turning angle, δ , whose variation with flow conditions immediately upstream of the base has been shown in Figure 9-17.

For wedge afterbodies whose boattail angle, β , is finite but less than the wake turning angle, the local body flow at the base shoulder still undergoes an expansion process upon entering the wake as it does when the boattail angle is zero. Although the Mach numbers, M_0 and M_R , have previously been defined so that they are now separately displaced on the boattailed afterbody surface (see Figure 9-19a), they still have identical values. This can be visualized by noting that M_R is calculated by assuming the local flow along the afterbody surface is compressed isentropically in the direction of the trailing flow behind the shock wave in the wake. This direction is parallel to that of M_0 , immediately upstream of the afterbody for the case of zero angle of attack and no jet flow. For two-dimensional bodies, the local Mach number on the afterbody surface, itself, results through an isentropic expansion from M_0 immediately upstream of the afterbody. Since isentropic processes are additive (no change in total pressure), M_R and M_0 have identical values. If it is recalled that the wake turning angle, δ , is dependent on M_R , then it can be seen that; for a given M_0 , the base pressure will not vary on wedge afterbodies whose boattail angle is less than or equal to the wake turning angle. This conclusion is substantiated by available test data.

For boattail angles greater than the wake turning angle, the local body flow now enters the wake through a compression process and, as a result, an additional shock wave is initially formed at the base shoulder as depicted in Figure 9-19b. The pressure rise across this shock wave will steadily increase with larger boattailing until, at any given M_0 , this pressure rise will exceed the critical pressure-rise coefficient and the turbulent boundary layer will separate. On wedge afterbodies, it can be assumed that the onset of flow separation permits the wake to immediately jump upstream to the afterbody shoulder due to the absence of surface pressure gradients on such two-dimensional bodies. This situation is depicted in Figure 9-19c. Actually, this may not be a true representation of flow separation on wedge afterbodies since there is usually an associated pressure feed-back through the boundary layer upstream of the point of separation. This would have the

effect of reducing the effective pressure rise of the compression process thereby retarding the forward progression of flow separation. However, a local adverse pressure gradient would also be induced ahead of the point of flow separation and these two effects would be counter-balancing. Overall, the significance of this pressure feed-back is expected to be small on the wedge afterbody so that only nominal error is incurred by assuming the influence of the wake to immediately jump to the afterbody shoulder. Of course, in this event, the wedge boattail problem reduces simply to the zero boattail case where the flow upstream of the afterbody again enters the wake through an expansion process. If the two-dimensional afterbody is curved, then the wake advances upstream only to the point where the local surface Mach number and the local compressive deflection into the wake, $(\beta_1 - \delta)$, produce a pressure rise across the boattail shock wave equal to the critical pressure-rise coefficient of incipient separation. This situation is depicted in Figure 9-19d.

Both Figures 9-19c and 9-19d clearly show that the presence of flow separation adversely affects the aerodynamic performance of the afterbody for the case when there is no jet flow due to a propulsion system (cases in which jet flow are present will be treated in the succeeding section). If it is recalled that the pressure along the wake is equal to the base pressure* then it can be seen that the effect of flow separation is two-fold. First, the effective cross-sectional area over which base pressure acts is increased and second, both the afterbody wave drag coefficient (which is the integrated pressure distribution over the effective wetter afterbody surface) and the cross-sectional annulus over which it acts is decreased. Therefore, since base drag is almost always much greater than afterbody wave drag, the effect of the presence of flow separation is to increase the overall drag of the afterbody "system".

In a design analysis of afterbody performance, it is necessary to be able to predict the occurrence and extent of flow separation on the afterbody surfaces. For this purpose the boattail angle at which turbulent flow separation will occur for a given Mach number upstream of the afterbody has been calculated in Reference 8 and is presented here as Figure 9-20. These angles

*Footnote - Again, this is an over-simplification of the facts when the wake advances onto the afterbody surfaces in that the wake pressures acting on the afterbody will generally not be as low as the wake pressure on the base surface. However, this wake pressure gradient will not be large and can thus be neglected in design analyses.

were determined from a cross plot of the variation of the compressive deflection angle ($\beta - \delta$) with local afterbody Mach number, for a given M_0 and β , and the variation with local afterbody Mach number of the compressive deflection angle required to produce the critical pressure-rise coefficient of incipient separation. The wake turning angle, δ , and the critical pressure-rise coefficient denoted in Figures 9-17 and 9-15, respectively, were employed in these calculations. As noted in Reference 8, the boattail angle at incipient separation, β_{sep} , in Figure 9-20 has not been completely experimentally verified at present due to a lack of available test data on two-dimensional afterbodies with large boattail angles.

The base drag of two-dimensional boattailed afterbodies can be determined using a step-by-step procedure as follows:

A. Given:

1. M_0
2. Afterbody shape

B. Procedure:

1. From afterbody shape, determine boattail angle, β_b , at base shoulder.
2. Since $M_0 = M_R$, determine wake turning angle, δ , from Figure 9-17.
3. If $\beta_b \leq \delta$, follow the procedures given in Section 9.2.1.1 since base pressure will equal zero boattail base pressure. Upon cross-sectional area at base shoulder to calculate base drag,

$$C_{D_b} = - C_{P_b} \frac{d_b}{D} \quad (9.25)$$

4. If $\beta_b > \delta$, find β_{sep} from Figure 9-20 at given M_0 . Also determine local Mach number, M_L , of afterbody air-stream at base shoulder. This can be found by adding β_b to the Prandtl-Meyer expansion angle corresponding to M_0 and reading the Mach number corresponding to this sum using the tables provided in Reference 12.
5. If $\beta_b \leq \delta_{sep}$, no boundary layer separation takes place so that:

$$C_{P_b} = \frac{\frac{P_b}{P_0} - 1}{.7 M_0^2} = \frac{\frac{P_2}{P_1} \left(\frac{P_1}{P_0} \right) - 1}{.7 M_0^2} \quad (9.26)$$

$$\text{where, } \frac{P_2}{P_1} = \frac{7 M_L^2 \sin^2 \theta - 1}{6} \quad (9.27)$$

(θ) is obtained from Reference 12 for given M_L and ($\beta_b - \delta$)

$$\frac{P_1}{P_o} = \left[\frac{1 + 2M_o^2}{1 + 2M_L^2} \right]^{3.5} \quad (9.28)$$

$$\text{and } C_{D_b} = -C_{P_b} \frac{d_b}{D}$$

6. If $\beta_b > \beta_{sep}$, boundary layer separation takes place somewhere on afterbody surface. If the afterbody surface is curved, continue with next step. If afterbody is a wedge, base pressure will be same as zero boattailed base pressure and therefore will be determined using the procedures given in Section 9.2.1.1. Base drag, however, is now

$$C_{D_b} = -C_{P_b} \quad (9.29)$$

Remember, for this case wave drag of afterbody is non-existent.

7. If flow separation takes place on curved afterbody, determine location of incipient separation, d_{sep} , by interpolation between the local boattail angle at three stations on the afterbody. Also, determine local Mach number, M_{sep} , of afterbody airstream at station of incipient separation using procedure described in step 4 above with β_{sep} .

8. Finally, determine base drag as follows:

$$C_{P_b} = \frac{\frac{P_b}{P_o} - 1}{.7 M_o^2} = \frac{\frac{P_2}{P_1} \left(\frac{P_1}{P_o} \right) - 1}{.7 M_o^2} \quad (9.30)$$

$$\text{where, } \frac{P_2}{P_1} = \frac{7 M_{sep}^2 \sin^2 \theta - 1}{6} \quad (9.31)$$

(θ) is obtained from Reference 12 for M_{sep} and ($\beta_{sep} - \delta$)

$$\frac{P_1}{P_0} = \left[\frac{1 + 0.2 M_0^2}{1 + 0.2 M_{sep}^2} \right]^{3.5} \quad (9.32)$$

$$\text{and } C_{D_0} = - C_{P_b} \frac{d_{sep}}{D} \quad (9.33)$$

9.2.1.3 Effect of Angle of Attack

In order to account for the effects of finite angle of attack in design analyses of boattailed afterbodies, a slightly different analytical flow model from what has been employed up to this point of the discussion must be introduced. The flow model to be used on two-dimensional afterbodies at angle of attack is shown in Figure 9-21.

The primary differences in the flow model can be seen to be that the direction of flow behind the trailing shock waves in the wake is no longer parallel to the direction of the flow immediately upstream of the afterbody and, as a result, the Mach number, M_T , is different in value and direction from M_0 . The newly introduced parameter, ϵ , is the downwash angle of the trailing flow and θ is the angle between the direction of the trailing flow and the body centerline. In addition to the asymmetry of the Mach numbers, M_0 , M_T , between the upper and lower surfaces of the inclined body, there is also an asymmetry of the wake turning angle, δ , between the upper and lower surfaces as well. It is important to note that, again because of the different directions of M_0 and M_T the boattail angle, β , and the wake turning angle, δ , no longer share the same reference plane.

The calculation procedure for handling cases of finite angle of attack is an iterative process since the downwash angle, ϵ , is generally not initially known for a given angle of attack, α , and free-stream Mach number, M_0 . Therefore, the first step in the calculation procedure is to assume a value for the downwash angle (one-half the angle of attack might be a good starting point) and then proceed separately along each of the upper and lower surfaces of the body in much the same fashion as in the zero angle of attack case. The criterion of this iterative procedure is to equalize the static pressures on both sides of the trailing flow line behind the shockwave in the wake. Assuming this criterion has not been satisfied on the first try, a new value of the downwash angle is used and the procedure is again repeated separately on the upper and lower body surfaces until pressures of the trailing flow equalize. Normally a maximum of three iterations are necessary after which, if convergence has not occurred, the correct value of the downwash angle can be interpolated from a plot of ϵ versus pressure

difference across the trailing flow line. When the solution is achieved, a value of base pressure for each the upper and lower body surfaces will have been determined. The average of these base pressures is employed in design analyses, however a pressure gradient across the base can be determined by assuming the pressure resulting from calculations at zero angle of attack to act at the mid-point of the base.

Handling of the case of finite angle of attack can be very complicated in that it requires knowledge of the Mach numbers, M_{OU} and M_{OL} , immediately upstream of the afterbody. To determine their respective values usually requires calculation of the entire flow process from the forebody on downstream. On the windward or lower body surfaces, the possibility of interference effects, due to the forebody, affecting the flow over the afterbody surfaces is increased over what would be present at zero angle of attack. At even less than moderate angles of attack, the leeward body surfaces upstream of the afterbody may be completely immersed in separated flow.

9.2.2 Axisymmetric Base Drag

9.2.2.1 Three-Dimensional Wake Characteristics

The "closed-wake" characteristics of three-dimensional bodies of revolution are very much different than those of two-dimensional bodies. In contrast to these latter-type bodies, the supersonic axisymmetric wake is a strong recompression region where the flow properties vary between the base and the trailing shock wave located downstream. As a consequence of the pressure variation, the Mach number accordingly decreases along the wake as the trailing shock wave is approached. The effect of the adverse pressure gradient in the axisymmetric wake induces a pressure feed-back to the base region by increased flow recirculation causing the base pressures to be higher than those on the two-dimensional bases. This can be seen by comparing Figure 9-22 with Figure 9-16 which are applicable to the bases of circular cylinders and two-dimensional wedge-flat plate models, respectively. As in the case of the two-dimensional bodies, Figure 9-22 represents a best curve fit of the test data compiled from a number of sources. The original data on cylinders may be obtained from Reference 21.

Although the wake characteristics of the two types of bodies are very much different from one another, it is desirable to retain the simplicity afforded by the two-dimensional flow analogy for the purpose of calculating the supersonic base pressures on three-dimensional bodies. As previously described in Section 9.2.1.1, the uniqueness of the two-dimensional flow analogy is attributed to the use of an effective wake turning angle to relate the base pressure directly to the Mach number at the base shoulder. For the purpose of applying this type of flow analogy to axisymmetric bodies, the wake convergence angle, ϕ , corresponding to cylindrical bodies was determined in Reference 20 from Schlieren photographs and shadowgraphs. This turning angle is

presented in Figure 9-23. In similar fashion to the two-dimensional bodies, however, it was found in Reference 8 that an effective turning angle, different from ϕ , is required in order to match the axisymmetric base pressures in Figure 9-22. This angle, δ_e , is also shown in Figure 9-23 for comparison with the experimentally determined wake convergence angle, ϕ . It will later be seen that, due to the recompression of the supersonic axisymmetric wake, the angles δ_e and ϕ will be used to represent the limits of the wake turning angle at the base of the cylindrical body and at the trailing shock wave in the wake, respectively.

At subsonic speeds, the wake of axisymmetric bodies is of the "open wake" type as found for the two-dimensional bodies. Consequently, for the same reasons cited in Section 9.2.1.1 for two-dimensional bodies, the analogical procedure employed for the prediction of supersonic base pressures can not be applied at low speeds. An entirely different procedure must therefore be used for subsonic base pressure prediction. Fortunately, in contrast to the situation faced with two-dimensional bodies, enough experimental data on axisymmetric bodies are available to permit the development of a strictly empirical method of predicting subsonic base pressures. While not having as strong theoretical basis as the supersonic analogy, the subsonic method of prediction is still effective. This empirical method will be employed herein. Oddly, it was found that the supersonic analogy can not be used down to Mach numbers close to one as could the analogical method developed for two-dimensional bodies. For axisymmetric bodies, therefore, both the subsonic and transonic speed ranges are handled by the same empirical technique.

9.2.2.2 Effects of Afterbody Boattailing

9.2.2.2.1 Subsonic-Transonic Speeds

For all Mach numbers less than approximately $M_0 \approx 1.2$, the base pressure on axisymmetric boattailed afterbodies, at zero angle of attack and with no jet flow, can be estimated using the empirical procedure formulated in Reference 6. This method is based on a compilation of test data obtained on conical, parabolic and circular-arc afterbodies under conditions in which the boundary layer is completely turbulent. It must also be mentioned that the maximum boattail angle of each of the afterbodies included in this data compilation was low enough to preclude the presence of flow separation on the afterbody surfaces. From the data that was compiled, the rate of change of base pressure with boattail angle at the base of each model was determined as a function of the Mach number, M_0 , upstream of the afterbody and base-to-maximum cross-sectional area ratio, A_b/A_M .

The curve fitted data are presented in Figure 9-24. Using the curves from this figure along with the cylinder base pressure data represented in Figure 9-22, the base pressure of any three-dimensional boattailed afterbody may be reasonably estimated by using the following rather simple relation:

$$C_{p_b} = C_{p_b(\text{cylinder})} + \left(\frac{\Delta C_{p_b}}{\Delta \beta} \right)_0 \cdot \beta_b \quad (9.34)$$

where β_b is in degrees.

Estimates of the occurrence of boundary separation can be obtained from Figure 9-25. The subsonic estimates of the boattail angle at which separation will occur were determined as a result of the conference denoted by Reference 22. The transonic estimates at Mach numbers less than one were made on the basis of a limited amount of experimental data. These data are presented in Reference 6. The transonic estimates at Mach numbers greater than one are primarily extensions of the supersonic curves which have been calculated.

At subsonic-transonic speeds, the base drag of axisymmetric afterbodies may be estimated using the following step-by-step procedure:

A. Given:

1. M_0
2. Afterbody shape

B. Procedure:

1. For given M_0 , determine base pressure on cylindrical afterbody from Figure 9-22, and boattail angle at which separation is likely to occur, β_{sep} , from Figure 9-25.
2. For given afterbody shape, determine boattail angle at base of afterbody, β_b , and base-to-maximum cross-sectional area ratio, A_b/A_M .
3. If $\beta_b \leq \beta_{sep}$, determine the rate of change of base pressure with boattail angle at base,

$$\left(\frac{\Delta C_{p_b}}{\Delta \beta} \right)_0$$

from Figure 9-24 for known M_0 and A_b/A_M . Then calculate base drag as follows:

$$C_{p_b} = C_{p_b(\text{cylinder})} + \left(\frac{\Delta C_{p_b}}{\Delta \beta} \right)_0 \cdot \beta_b \quad (9.34)$$

4. If $\beta_b > \beta_{sep}$, determine local area ratio at point of separation, A_{sep}/A_M , by interpolation of β versus A/A_M at two additional stations on afterbody. Determine rate of change of base pressure with boattail angle at point of separation,

$$\left(\frac{\Delta C_{P_b}}{\Delta \beta^\circ} \right)_{sep}$$

from Figure 9-24 for known M_0 and A_{sep}/A_M . Then calculate base drag as follows:

$$C_{P_b} = C_{P_b}(\text{cylinder}) + \left(\frac{\Delta C_{P_b}}{\Delta \beta^\circ} \right)_{sep} \cdot \beta_{sep} \quad (9.35)$$

$$C_{D_b} = -C_{P_b} \frac{A_{sep}}{A_M} \quad (9.36)$$

9.2.2.2.2 Supersonic Speeds

The primary base flow situations that occur on axisymmetric boat-tailed afterbodies are shown in Figure 9-26. Figure 9-26(a) represent the simplest relationship between the afterbody flow and the wake flow and is a useful flow model for calling attention to certain aspects of the axisymmetric wake which differentiate it from the two-dimensional wake. It will be recalled from Section 9.2.2.1, for example, that the pressure varies along the wake due to a flow recompression process. Therefore, the pressure differential between the base and the trailing shock wave would become smaller as the position of the base goes from 1 to 2 to 3 and finally to 4. It is apparent, then, that in order to predict the base pressures, the pressure variation along the wake must be taken into account. If the two-dimensional flow analogy discussed in Section 9.2.1.1 is employed to relate base pressure directly to the flow conditions upstream of the afterbody, then the change in pressure along the wake can be accounted for simply by assuming the effective wake turning angle varies along the wake. It has already been seen that the experimentally determined wake convergence angle, ϕ , does not produce the proper base pressures at the base of a cylinder so that it is likely that this angle is more correctly applicable at the downstream end of the wake region. On the other hand, the proper turning angle required to match available test data at the cylinder base was found to be the angle, δ_e . In Reference 8, comparison with test data had shown that δ_e and ϕ apply at opposite extremes of the wake and the wake turning angle varied linearly between them so that $\delta = \delta_e + \left[\frac{1 - d_b}{D_M} \right] (\phi - \delta_e)$. It can be seen that in using this relation the base pressure will vary with local-to-maximum diameter ratio, for a given M_0 .

A similar difference between the axisymmetric and the two-dimensional cases exists through the Mach number parameter, M_p . For axisymmetric bodies, M_p will not be the same as M_0 (as in the two-dimensional case) due to the aforementioned recompression process along the afterbody length except when $\phi = \delta_e$ is depicted in Figure 9-26(a). In carrying out axisymmetric base pressure calculations, it can be seen that additional dependency on the diameter ratio enters into the shock wave-separation criterion due to the definition of the axisymmetric turning angle, δ .

The over-all effect of conical flow recompression on the development of shock waves and separation over axisymmetric bodies is illustrated in Figure 9-26(c). Although the boattail is represented as conical, the wake does not jump to the afterbody shoulder as it did in the two-dimensional case. Similarly, the shock wave would tend to advance along the wake slowly with increasing boattail angle on axisymmetric bodies and not move immediately to the base shoulder as it does on two-dimensional bodies. The reason for both of these effects, of course, is attributable to the favorable Mach number gradient along the wake induced by the recompression process.

The pressure-rise coefficient required for flow separation on axisymmetric boattails has been calculated from experimental data in Reference 6 and is presented here as Figure 9-27. These coefficients were used to determine the boattail angles for incipient separation shown in Figure 9-25.

The calculation of base drag on axisymmetric boattails is carried out using the same step-by-step procedure outlined in Section 9.2.1.2.2 for two-dimensional boattails. The only differences in this procedure may be noted as follows:

1. Use Figure 9-27 to predict point of incipient separation.
2. Use $\delta = \delta_e + \left[1 - \frac{d_b}{r_M} \right] (\phi - \delta_e)$ as the effective wake turning angle; where ϕ and δ_e are given in Figure 9-23.
3. Account for effect of flow recompression attendant on axisymmetric bodies in calculating local pressures and Mach numbers. These calculations can be facilitated with the use of the local pressure coefficients on conical afterbodies given in Figure 9-21 and then by employing the conical boattail analogy described in Section 9.1.2.1 to determine the recompression effects on any afterbody shape.

In order to simplify the process of determining base drag, calculations have been carried out in Reference 6 and are presented here in Figures 9-28 & 9-29. The base drags represented in these figures do not include the effects of separation. However, the point of separation is noted, beyond the range of which these drag calculations are no longer valid. In this case the drags will have to be hand calculated following step-by-step procedure given in Section 9.2.1.2.2 except to employ the comments given above.

9.2.2.3 Effect of Angle of Attack

Conducting a valid analysis of base drag on axisymmetric boattails at finite angle of attack is an extremely comprehensive task requiring a knowledge of the downwash angle and the flow conditions around the cross-sectional plane of all stations on the afterbody. Such a detailed map of flow conditions is generally not available unless a test program is conducted specifically for this purpose on a particular configuration. To date, no acceptable analytical method of calculating the flow conditions on arbitrary three-dimensional bodies at angle of attack is known to exist.

Reference 8 reports some degree of success with base pressure prediction at small angles of attack by considering only the angle of attack effects on the afterbody surfaces mid-way between the most windward and leeward meridians. These effects were approximated using the equation,

$$C_p = C_{p_{\alpha=0}} - 3\alpha^2 \quad (9.37)$$

Handling the angle of attack effects in this manner is a fairly simple procedure since the side pressures are not affected by the accompanying change in downwash angle. However, such a procedure implies that the most windward pressures are cancelled by the most leeward pressures which is only a reasonable assumption at very low angles of attack. In this range of angles, then, the base pressures are determined in the same manner as for the zero angle of attack case (Section 9.2.2.2.2) since there would be no change in the downwash angle in the side plane of the body. The effects of angle of attack are accounted for by applying the above equation at the side meridian immediately upstream of the afterbody.

9.3 Jet Interference Effects on Afterbody and Base Drag

Jet interference effects present themselves whenever aircraft and/or missiles are operated at altitudes other than the design altitude to which the propulsion system has been optimized for efficiency. At greater than design altitudes, the jet-to-ambient static pressure ratio is large thereby causing the exhaust gases to billow out and extend beyond the base area of the flight vehicle. This pluming of the exhaust gases interferes with the primary aerodynamic flow over the afterbody and base surfaces by creating a pressure disturbance which feeds back upstream from the nozzle exit. If the strength of the pressure disturbance is sufficiently large, then the primary airstream will separate from the aft body surfaces. In the case where either aerodynamic control or stabilizing surfaces are positioned close to the afterbody region, the presence of flow separation can have serious adverse effects on vehicle performance.

Were it not for concern of these surfaces, however, then the presence of flow separation due to exhaust pluming could very well be advantageous to vehicle performance. The reason for this is that the larger pressures within the plume itself reduce or eliminate the scavenging action of flow normally acting on any base areas and the attendant pressure feedback within the upstream separated region reduces the rate of flow expansion over the afterbody surfaces. The result is that both the afterbody and base drag is significantly reduced from the levels existing at the nozzle design altitude. It is altogether possible to even realize some aerodynamic thrust due to the jet interference phenomenon under favorable conditions. This is in contrast to the undesirable effect of flow separation on boattailed afterbodies without jet flow discussed previously. In the absence of jet flow, it will be recalled, flow separation increases the effective cross-sectional area on which the low base pressures act while decreasing the wetted afterbody surface area on which the higher wave pressures act.

When aircraft and/or missiles are operated at lower than design altitude of the propulsion system, the jet-to-ambient static pressure ratio is less than one and the exhaust gas stream contracts toward the nozzle centerline. At a sufficiently low pressure ratio, flow separation will take place this time within the nozzle itself. When this occurs, the thrust level of the propulsion system will decrease in proportion to the extent of nozzle flow separation. At the same time aerodynamic drag of the vehicle will also increase due to an increase of the effective base area of relatively low pressure.

The jet interference phenomenon is basically, then, a problem of boundary layer separation from both the external aerodynamic surfaces and also within the exhaust nozzle. The present discussion will, therefore, review the characteristics of separated flow and, together with the analytical methods presented in Sections 9.1 and

9.2, provide a means of predicting the influence of jet interference effects on afterbody and base drag. Because the mechanism of flow separation is highly dependent on the state of the boundary layer, the methods to be discussed are applicable only to the turbulent state which is the most prevalent condition existing on realistic aircraft and/or missile configurations. In addition, only the case of supersonic aerodynamic flow will be treated since subsonic methods of prediction presently remain largely a matter of experimentation.

9.3.1 Description of Jet Interference Flow Phenomena

For the purpose of presenting a method of handling the influence of jet interference in a drag analysis, the discussion to follow will be directed to the special case in which the exhaust gases plume out beyond the base diameter and interact with the primary airstream over the afterbody surfaces. The aerodynamic criterion that will be employed to investigate this type of flow interaction problem, however, may also be applied to investigate the below nozzle design condition which may lead to flow separation from the nozzle wall if the differences between the thermodynamic and chemical properties of air and the exhaust gases are taken into account. Since the present interest is devoted to vehicle drag evaluation, methods will be discussed to determine the pressure disturbance resulting from the interaction of the primary afterbody airstream with the exhaust gas stream, the conditions at which the turbulent boundary layer will separate from the afterbody surfaces and both the extent of the separated flow region and the attendant pressure levels within this region.

It should be noted that the criterion for incipient separation at supersonic speeds that will subsequently be presented is different than that used in Section 9.2. In addition, the present discussion shall also introduce the fact that the pressure rise within the separated flow region and the associated angle at which the flow separates from the body surface is dependent on both Mach number and Reynolds number. This separation angle, it will be recalled, is analogous to the wake turning angle, δ , employed in the supersonic drag prediction methods of Section 9.2. Both the incipient separation criterion and the separation angle as will be defined in the present section reflect a more rigorous description of this special class of flow and should therefore replace their respective "first order" counterparts previously introduced.

9.3.1.1 Analytical Flow Model

Under conditions of mild exhaust gas pluming, the turbulent boundary layer over the vehicle afterbody surfaces can remain in the

attached state as represented schematically in Figure 9-30. As can be seen from this figure, exhaust pluming results whenever the jet static pressure at the nozzle exit, P_j , is greater than the pressure in the interaction region of the external and jet flow streams, P_w . It should be noted that, with supersonic flow on the afterbody, $P_j/P_o > 1$ does not necessarily represent a condition of exhaust pluming since the local static pressure on the afterbody, P_o , is always less than P_w due to the oblique shock wave ahead of the interaction region. Reference should more correctly be made to the expansion process at the jet exit in which case $P_j/P_w > 1$ would always represent a condition of exhaust gas pluming.

Immediately at the nozzle exit, the expansion of the jet flow may be thought of as a two-dimensional process so that the initial deflection of the jet, ψ , can be calculated from two-dimensional theory. The accuracy of this hypothesis has been verified in Reference 26 by comparison with experimental data obtained on axisymmetric nozzles for a wide range of jet and supersonic external flow conditions. This initial jet deflection angle is also the initial turning angle through which the external flow close to the afterbody surface is deflected by the exhaust plume. If the jet pressure ratio, P_j/P_o , becomes sufficiently large, the deflection of the external flow creates a pressure rise too great for the oncoming boundary layer to sustain in an attached condition. The boundary layer over the afterbody surface therefore separates and the flow resolves itself to the condition shown in Figure 9-31 at supersonic speeds. A bifurcated shock system is formed much like the Mach reflection system which forms in strong interactions with a solid surface. The flow on the afterbody surface separates upon reaching the first lambda-compression shock and eventually reattaches with the jet boundary layer flow of the plumed exhaust by means of a jet mixing process.

The full sequence of jet interference events, ranging from the condition of no jet expansion from the nozzle exit and proceeding through to the extreme condition of extensive flow separation, is depicted in Figure 9-32 as the jet pressure ratio becomes progressively larger. In the figure, the juncture angle between the boat-tailed afterbody and the nozzle wall at the jet exit, Γ , is introduced so that the initial event represents a condition where the jet pressure ratio, P_j/P_o , is greater than one although no jet expansion process takes place at the nozzle exit. Consequently, for condition (a), the pressure rise P_w/P_o that the attached boundary layer on the afterbody surface must negotiate is identical to the jet pressure ratio, P_j/P_o . At larger values of jet pressure ratio, the jet expands to the wake pressure, P_w , as in condition (b). Because of the outward deflection of the jet flow, the shock wave on the afterbody becomes stronger so that the pressure rise,

P_w/P_o , that the boundary layer of the external flow must negotiate is now larger than that of condition (a). In condition (b), the pressure rises to a value just under that required to separate the external boundary layer. A further increase in the jet pressure ratio, P_j/P_o will be enough to cause incipient separation as denoted in condition (c). Beyond this point, extensive separation takes place on the afterbody surfaces (conditions (d) and (e)) in proportion to additional increases of the jet pressure ratio above that required to cause incipient separation.

Up to the condition at which a finite separated flow region is formed (conditions (a) through (c)), the pressure rise resulting from the deflection of the external air stream can be determined the same as if the source of disturbance was a solid-boundary, two-dimensional compression corner. This analogy can be applied to evaluate the initial stages of the jet interference problem, with accurate results, for two reasons. First, since the initial deflection of the jet flow, ψ , in the immediate neighborhood of the nozzle exit is essentially two-dimensional, the shock wave that is generated on the upstream afterbody surface is also two-dimensional at least close to the surface. It must be remembered, however, that since the afterbody is axisymmetric, the flow conditions upstream of the interaction region vary along the afterbody surface. The second reason for the applicability of the compression-corner analogy is realized on the basis that the onset of flow separation is known to be dependent only on the local Mach number and Reynolds number ahead of the interaction region and not on the mode of disturbance causing the pressure rise. Therefore, it makes no difference to the oncoming flow as to whether the pressure rise is created by the interaction with a solid surface or with a jet boundary. The solid-boundary compression corner analogy has been employed to investigate jet interference effects in Reference 27 and found to provide good agreement with test data. Thus, when the flow interference caused by the plugging of the exhaust gases is not severe so that the boundary layer on the afterbody remains in the attached state, the angle, ϕ , by which the external air stream is deflected and the resulting pressure rise, P_w/P_o , can be determined from two-dimensional supersonic flow theory given only the Mach number, M_o , immediately upstream of the jet interaction region. The actual calculation procedures are given in Section 9.3.2 of this presentation.

When turbulent boundary layer separation occurs on a solid-boundary compression corner, the attendant pressure rise within the separated region is primarily a constant value, P_{PL}/P_o , and is related to the pressure at the point of separation, P_s/P_o , by the relation,

$$\frac{P_{PL}}{P_o} = \sqrt{2} \cdot \frac{P_s}{P_o} \quad (9.38)$$

Test data have been correlated by numerous investigators to show that both P_{PL}/P_0 (commonly called the plateau pressure rise) and P_s/P_0 are functions of the Mach number, M_0 , and Reynolds number, Re_{x_0} , of the undisturbed flow. Typical values of P_{PL}/P_0 have been determined in Reference 23 and are presented here in Figure 9-33. It has also been found (as in Reference 28) that the turbulent boundary layer separates from the surface at an angle, ϕ , whose magnitude is determined by the plateau pressure rise, P_{PL}/P_0 , so that it is also a function of Mach number and Reynolds number. Values of ϕ appropriate to the separated flow on two-dimensional compression corners have been calculated in Reference 25 and are presented in Figure 9-34 :

However, several important differences exist between the characteristics of flow separation from compression corner test models and the flow separation which takes place on afterbodies due to jet interference effects (conditions (d) and (e) in Figure 9-32). The flow analogy provided by the solid-boundary, compression corner must be extensively modified to take into consideration the strong interaction processes that take place in the reattachment region of the external and jet flow streams. Instead of being forced to follow the direction of the wall as it would along a solid surface, each flow stream should be free to deflect, upon reattachment, into a wake region so as to produce a static pressure, P_w , common to both streams. The flow analogy to be adopted for the separated boundary layer condition also requires that the mass exchange resulting from the mixing of the air stream with the exhaust stream in the reattachment region be taken into account. Because of this mixing process, the difference between the thermodynamic states of the external air stream and the exhaust gases will affect both the extent of boundary layer separation and the pressure rise within the separated region. Therefore, in addition to being dependent on the Mach number, M_0 , and Reynolds number, Re_{x_0} , immediately upstream of the interaction region, both ϕ and P_e/P_0 (see Figure 9-31) are also dependent on the conditions along the jet boundary. In Reference 25, calculations have been performed to indicate that the pressure rise in the separated region of the jet interference problem, P_e/P_0 , is virtually the same as the plateau pressure rise, P_{PL}/P_0 , associated with the separated flow region of the solid-boundary compression corner during the initial stages of separation. This is the stage denoted by condition (d) in Figure 9-32. However, in cases of extensive flow separation, P_e/P_0 is usually greater than the plateau pressure rise, P_{PL}/P_0 , of the compression corner as denoted by condition (e) in Figure 9-32. The amount by which P_e/P_0 will exceed P_{PL}/P_0 depends on the increment by which the jet pressure ratio, P_j/P_0 , exceeds that required for incipient separation.

9.3.1.2 Criterion for Incipient Separation

As is illustrated by condition (a) in Figure 9-32 it is possible for the turbulent supersonic boundary layer to tolerate a pressure rise that is in excess of the plateau pressure rise, P_{PL}/P_0 , and still remain in the attached state. This demonstration of superior supersonic boundary layer stability has been noticed by a number of investigators (Reference 29, for example) to occur at low Reynolds numbers which is an opposite effect to that observed for subsonic flow separation. In an attempt to explain this curious phenomenon, Reference 23 applied Huygen's¹ principle of wave propagation to show that pressure disturbances can be transmitted upstream through the supersonic as well as the subsonic portions of the boundary layer, as long as the origin of the disturbance is in the subsonic portion of the stream.

For a turbulent boundary layer having a laminar sublayer close to the wall, the relative height within the boundary layer, (y/δ) , through which pressure disturbances are transmitted depends on the fullness of the boundary layer as well as the intensity of the disturbance. On the basis of providing the best correlation of experimental pressure data on compression corners, it was concluded in Reference 23 that all portions of the boundary layer from the wall up to the $M = 1.4$ line are the regions most sensitive to pressure disturbances. The relative height of the $M = 1.4$ line can be obtained from Figure 9-35 as a function of the Mach number, M_0 , and Reynolds number, Re_{x_0} , immediately upstream of the flow interaction region. To use this figure, enter from the right-hand side for a given Mach number and traverse to the left until either the proper Reynolds number line and the turbulent boundary layer line is reached. It should be noted that the turbulent portion of the boundary layer represented in this figure is assumed to possess a $1/7$ -power velocity profile and is invariant with Reynolds number. At high Mach numbers, the pressure disturbances will be transmitted primarily through the laminar sublayer.

The amount by which the pressure rise required to separate the turbulent boundary layer, P_W/P_0 , can exceed the plateau pressure rise, P_{PL}/P_0 , is given in Figure 9-36 in terms of the relative boundary layer height. Therefore, the pressure rise at incipient separation,

$$\frac{P_W}{P_0} = K \cdot \frac{P_{PL}}{P_0} \quad (9.39)$$

¹Huygen's principle states that every point on a wave front acts as though it were itself a center of disturbance, sending out little wavelets of its own always away from the source, the collective effect of which constitutes a new wave front.

can be determined as a function of M_o and Re_{x_o} from Figures 9-35 and 9-36. It will be more convenient, however, to define the point of incipient separation in terms of the jet pressure ratio, P_j/P_o , since this parameter is more readily known. Using the schematic shown in Figure 9-37 as a guide, $(P_j/P_o)_{sep}$ can be calculated as follows:

A. Given:

1. Mach number, M_o , Reynolds number, Re_{x_o} , and specific heat ratio, γ_o , of flow immediately upstream of interaction region.
2. Mach number, M_j , and specific heat ratio, γ_j , of jet flow at the nozzle exit.
3. Juncture angle, Γ , between nozzle wall and afterbody surface, at nozzle exit.

B. Procedure:

1. Calculate the plateau pressure ratio, P_{PL}/P_o , using the more generalized version of the semi-empirical relationship given in Figure 9-33.

$$\frac{P_{PL}}{P_o} = 1 + \left[\frac{0.885 \gamma_o M_o^2}{Re_{x_o}^{1/10} \sqrt{M_o^2 - 1}} \right] \quad (9.40)$$

2. Calculate the pressure rise, P_w/P_o , at incipient separation from,

$$\frac{P_w}{P_o} = K \cdot \frac{P_{PL}}{P_o} \quad (9.39)$$

where K is obtained from Figures 9-35 and 9-36.

3. Determine the Mach number, M_{on} , normal to the shock wave,

$$M_{on} = \sqrt{\left[\left(\frac{P_w}{P_o} - 1 \right) \frac{\gamma_o + 1}{2 \gamma_o} \right] + 1} \quad (9.41)$$

4. Calculate the shock wave angle, θ , from,

$$\theta = \sin^{-1} \left(\frac{M_{on}}{M_o} \right) \quad (9.42)$$

5. Determine the two-dimensional surface deflection angle, ξ , that will generate the shock wave angle at M_o from,

$$\xi = \tan^{-1} \left[(2 \cot \theta) \frac{(M_o^2 \sin^2 \theta - 1)}{M_o^2 (\gamma_o + \cos 2 \theta) + 2} \right] \quad (9.43)$$

6. Determine the jet deflection angle, ψ , corresponding to the deflection angle of the external stream, ξ , by,
 $\psi = \xi - \Gamma$

7. Determine the two-dimensional Prandtl-Meyer angle, ν_j , corresponding to the jet Mach number, M_j , from the tables in Reference 12.

8. Determine the Mach number, M_j , to which the jet will expand at the nozzle exit using the tables in Reference 8 for the total turning angle, $(\nu_j + \psi)$.

9. Calculate the total-to-static pressure ratio, $\frac{P_{Tj}}{P_w}$, of the isentropically expanded jet flow from,

$$\frac{P_{Tj}}{P_w} = \left(1 + \frac{\gamma_j - 1}{2} M_j^2 \right)^{\gamma_j / (\gamma_j - 1)} \quad (9.44)$$

10. Calculate the total-to-static pressure ratio, $\frac{P_{Tj}}{P_j}$, of the jet flow at the nozzle exit from,

$$\frac{P_{Tj}}{P_j} = \left(1 + \frac{\gamma_j - 1}{2} M_j^2 \right)^{\gamma_j / (\gamma_j - 1)} \quad (9.45)$$

11. Finally, the jet pressure ratio required for incipient separation, $\left(\frac{P_j}{P_o} \right)_{SEP}$ is determined from,

$$\left(\frac{P_j}{P_o} \right)_{SEP} = \left(\frac{P_j}{P_{Tj}} \right) \cdot \left(\frac{P_{Tj}}{P_w} \right) \cdot \left(\frac{P_w}{P_o} \right) \quad (9.46)$$

For illustrative purposes, typical results of this calculation procedure are presented in Figure 9-38. Each constant Reynolds number line represents the limiting values of jet pressure ratio, for increasing values of Mach number, that the afterbody boundary layer is able to negotiate without separating. At a given Mach number, jet pressure ratios to the right of a constant Reynolds number line indicate a separated flow, while jet pressure ratios to the left indicate an attached flow. The $\psi = 0^\circ$ line represents the limiting case of no jet deflection at the nozzle exit. The "SHOCK Detach" line is the upper limit to the calculation procedures and represents the maximum flow deflection angle at each Mach number in order to retain an attached external shock wave at the nozzle exit. Each Reynolds number line has been cut off at the maximum Mach number to retain turbulent flow. These values can be obtained from Figure 9-34. The peculiar reversal of the Reynolds number lines is actually a consequence of employing Huygen's principle to define the transmission of pressure disturbances through the boundary layer. The Reynolds number reversals therefore represent the dominating influence of the laminar sublayer at high Mach numbers.

In Reference 25, by carrying out a sufficiently large number of such calculations, certain basic trends have been identified relative to the onset of separation. These trends may be summarized as follows: other quantities remaining constant, the possibility of turbulent flow separation occurring on the afterbody was found to be enhanced by (1) increasing the jet pressure ratio, P_j/P_0 , (2) decreasing the specific heat ratio of the jet, γ_j , and (3) increasing the juncture angle, Γ , between the air and jet flow streams at the nozzle exit. Figure 9-38c clearly shows that, in general, decreasing Reynolds number and/or increasing Mach number lessens the chance for separation.

9.3.1.3 Pressure Rise Across Reattachment Region

The pressure rise, P_w , across the reattachment region of the external air stream and the jet flow is the result of a complex mixing process between the two streams. Reference 30 treats the reattachment region by employing a two-dimensional jet-mixing theory modified for application to annular-based bodies of revolution. A flow model is used in which there exists a particular pressure rise associated with the interaction of two streams, and that this rise is a function of the Mach number, specific heat ratio and the total temperature of the two adjoining streams. Also, to account for the state of the mixing process in the region of reattachment, a mixing length ratio, X , must be specified. Unfortunately, the methods that have been developed to calculate the wake pressure rise involves a tedious double-

iteration procedure. For this reason, values of P_w/P_e from the digital computer program developed in Reference 30 are presented in graphical form in Figures 9-39 through 9-41. To use these figures requires knowledge of six parameters. The Mach number and specific heat ratio of each stream immediately upstream of reattachment, the ratio of their respective total temperatures and the mixing length ratio, X' . Methods to calculate each of these parameters will be described in the next section.

9.3.2 Calculation Procedures

The forthcoming discussion presents the methods for calculating the afterbody pressures resulting from the influence of jet flow interference at supersonic speeds. For conditions in which the boundary layer remains attached to the surface, straight-forward two-dimensional flow theory is employed. The procedure for handling cases of flow separation basically involves matching a wake pressure rise ratio, $(P_w/P_e)_{2-D}$, obtained from two-dimensional flow theory with a theoretical wake pressure rise ratio, $(P_w/P_e)_{theo}$, computed by methods developed for axisymmetric flow in Reference 30. This procedure asserts that when the ratios determined by the two different methods are equal, the flow solution has converged, whereupon relevant flow parameters can then be calculated by processing the data generated while leading to this equality.

A. Given:

1. Conditions M_0 and Re_{x_0} on the afterbody surface immediately upstream of the nozzle exit, and the static pressure, P_0 , along the entire afterbody surface. ($\gamma_0 = 1.4$).
2. Jet pressure ratio, P_j/P_0 .
3. Exhaust properties, M_j and γ_j , at the nozzle exit.
4. Juncture angle, Γ , between the afterbody surface and the nozzle at the nozzle exit.
5. Ratio of jet-to-air stream total temperature, $\frac{T_{Tj}}{T_{T0}}$

B. Assumptions:

1. Total temperatures T_{T0} and T_{Tj} are uniform in both streams.

2. Specific heat ratios γ_0 and γ_j of both streams are assumed to be in frozen equilibrium at all stations downstream of their respective separation points. Thus effects of recombination are neglected.
3. Mass transfer to or from the afterbody is non-existent.
4. Heat transfer to or from the afterbody is negligible. (By neglecting heat transfer into the afterbody, conservative (low) values of P_w/P_e will result).
5. Fully developed turbulent boundary layers exist on the afterbody and within the nozzle.

C. Procedure:

1. For the given initial conditions, determine whether the boundary layer on the afterbody is attached or separated. This can be accomplished by comparing $(P_j/P_0)_{SEP}$ calculated by the methods cited in Section 9.3.1.2 with the (P_j/P_0) given as initial data. If the given (P_j/P_0) is less than or equal to $(P_j/P_0)_{SEP}$, the boundary layer is attached and the procedures in Step 2 are used. If (P_j/P_0) is greater than $(P_j/P_0)_{SEP}$, the boundary layer is separated and the procedures starting with Step 3 are used.

2. Attached Flow.

Referring to Figure 9-37, assume an initial value for ξ . Using the tables provided in Reference 12 for the given Mach number, M_0 , determine the two-dimensional shock wave angle, θ , necessary to turn the external flow at the angle ξ . Calculate the Mach number, M_{0n} , normal to the shock wave. With this Mach number, calculate the pressure rise across the shock wave by,

$$\left(\frac{P_w}{P_0}\right)_1 = \frac{2 \gamma_0 M_{0n}^2 - (\gamma_0 - 1)}{\gamma_0 + 1} \quad (9.47)$$

Determine the angle, $\psi = \xi - \Gamma$, the jet must turn to enter the wake. Then determine the total Prandtl-Meyer expansion angle, $\nu_1 = \nu_j + \psi$, into the wake. Use the tables in Reference 12 to read the Mach number, M_1 , corresponding to ν_1 . Calculate the static-to-total pressure

ratios, $\frac{P_1}{P_{T1}}$ and $\frac{P_j}{P_{Tj}}$ for the respective Mach numbers,

M_1 and M_j , using the generalized equation,

$$\frac{P_n}{P_{Tn}} = \left(1 + \frac{\gamma_j - 1}{2} M_n^2\right)^{-\frac{\gamma_j}{\gamma_j - 1}} \quad (9.48)$$

Finally, for the given jet pressure ratio, $\frac{P_j}{P_o}$, calculate a second estimate (this time based on the jet expansion into the wake) of the pressure rise across the external shock wave from,

$$\left(\frac{P_w}{P_o}\right)_2 = \frac{P_j}{P_o} \cdot \left(\frac{P_1/P_{T1}}{P_j/P_{Tj}}\right) \quad (9.49)$$

$(P_w/P_o)_1$ is compared to $(P_w/P_o)_2$. Unless the two values are equal, a new value for ξ is chosen and the procedure repeated until the two pressure rises agree.

3. Separated Flow

First, determine an initial value of ϕ from Figure 9-34. Calculate the pressure rise P_e/P_o in going through a two-dimensional shock wave whose strength is that required to deflect M_o by ϕ amount.

4. The resulting value of the trailing shock pressure rise ratio, $(P_w/P_e)_{2-D}$, is then determined.

Prandtl-Meyer and oblique shock theories are sufficient to analyze the flow phenomena for this case. Jet and external stream curvature is considered negligible so that the flow directions of the internal and external streams are essentially constant from their respective points of separation to their common point of reattachment. It is further assumed that the static pressure along the free jet boundaries is constant and equal to P_e , and as a consequence the Mach numbers along the two jet boundaries, M_e and M_1 , are likewise constant although not necessarily equal to each other. Thus by expanding the flow at the jet exit and compressing the flow on the afterbody to the

assumed ratio P_e/P_o from Step 3, the resulting directions, ϕ and ψ , and Mach numbers, M_e and M_i , of the internal and external free jet boundary streamlines immediately upstream of their intersection point become known.

The trailing shock pressure rise ratio $(P_w/P_e)_{2-D}$ is then that required to produce parallel flow (at angle ϕ), with uniform static pressure, P_w , downstream of the shock intersection point.

5. The theoretical wake-pressure rise ratio $(P_w/P_e)_{theo}$ able to be sustained by the two adjoining streams is calculated. This is done by use of the charts provided in Figures 9-39 through 9-41. The following parameters must be specified: M_e , M_i , T_{T_i}/T_{T_e} , γ_e , γ_i , and X . The Mach numbers, M_e and M_i , to be used are those previously calculated in Step 4. Stagnation temperatures T_{T_i} and T_{T_e} are the stagnation temperatures of the jet (T_{T_j}) and afterbody stream upstream of the interaction region, respectively. By means of assumption (1), T_{T_i} = combustion chamber temperature. Similarly, the ratio of the specific heats remains unchanged by the expansion or compression so that $\gamma_e = \gamma_o = 1.4$ and $\gamma_i = \gamma_j$. The mixing length parameter X (see Figure 9-40) can be calculated from the data generated in Step 4.:

$$X = \frac{x_i}{x_e} \cdot \left(\frac{\sigma_e}{\sigma_i} \right) \quad (9.50)$$

where $\sigma = 12 + 2.758 (M)$

X = length from point of separation to point of reattachment.

By constructing the geometry of the flow model of Step 4, the ratio x_i/x_e can be obtained; σ is to be calculated using M_i and M_e of Step 4.

After the six parameters have been calculated, enter the charts in Figure 9-39 to first obtain a value of $\frac{P_w}{P_e} \text{ theo}$ for M_e , M_i and T_{T_i}/T_{T_e} . Specify this ratio as $(P_w/P_e)_{theo}^A$.

This quantity must now be corrected for X , should X be other than 1.00, and for γ_i , should γ_i be other than 1.24. A correction factor for X other than 1.00 is

arrived at in the following manner. Enter Figure 9-40 along the relevant $(M_e + M_i)$ line. Record a P_w/P_e corresponding to $X = 1.00$ similarly, a P_w/P_e corresponding to the actual X as determined from the preceding paragraph. Form the ratio of these two values, and multiply $(P_w/P_e)_A^{theo}$ by this ratio. The new values of P_w/P_e , which shall be designated as $(P_w/P_e)_B^{theo}$, is the wake pressure ratio corrected for X . Thus,

$$\left(\frac{P_w}{P_e}\right)_B^{theo} = \left(\frac{P_w}{P_e}\right)_A^{theo} \times \frac{\left(\frac{P_w}{P_e}\right)_X}{\left(\frac{P_w}{P_e}\right)_{X=1.00}} \quad (9.51)$$

The correction factor for γ_i is derived in the same manner. Figure 9-41 provides the necessary data. Form the ratio of $(P_w/P_e)_{\gamma_i}$ and $(P_w/P_e)_{\gamma_i=1.24}$, and multiply $(P_w/P_e)_B^{theo}$ by the ratio. Doing so,

$$\left(\frac{P_w}{P_e}\right)_C^{theo} = \left(\frac{P_w}{P_e}\right)_B^{theo} \times \frac{\left(\frac{P_w}{P_e}\right)_{\gamma_i}}{\left(\frac{P_w}{P_e}\right)_{\gamma_i=1.24}} \quad (9.52)$$

the ratio $(P_w/P_e)_C^{theo}$ is the desired ratio of $(P_w/P_e)_{theo}$ for Step 5 of the calculation procedure.

6. $(P_w/P_e)_{2-D}$ of Step 4 is compared with $(P_w/P_e)_{theo}$ from Step 5. Unless the two values are equal, a new value for ϕ must be chosen for Step 3, and the procedure repeated for the new ϕ . Sufficient ϕ 's are assumed until a graphical representation of (P_w/P_e) versus ϕ is possible. The intersection point of $(P_w/P_e)_{theo}$ versus ϕ and $(P_w/P_e)_{2-D}$ versus ϕ correspond to the theoretical value of ϕ .

Corresponding to the theoretical value of ϕ , calculate P_0/P_∞ , the pressure rise in going through the plane shock of strength enough to M_0 through the angle ϕ .

$$\frac{P_0}{P_\infty} = 1 + \frac{2}{\gamma_0 + 1} (M_0^2 \sin^2 \phi - 1) \quad (9.53)$$

The angle, θ , may be found in various shock tables such as Reference 12. The pressure P_e acting in the separated region can then be calculated by:

$$P_e = \left(\frac{P_e}{P_o} \right) \cdot P_o \quad (9.54)$$

Finally, the maximum pressure rise P_w/P_o can be found by,

$$\frac{P_w}{P_o} = (P_w/P_e) \left(\frac{P_e}{P_o} \right) \quad (9.55)$$

The maximum pressure rise, P_w/P_o , will now be used in Step 7 to determine the extent of separation.

7. Determine the extent of separation, D , upstream of the point of disturbance.

First compute $C_{p \text{ MAX}}$:

$$C_{p \text{ MAX}} = \frac{2}{\gamma M_o^2} \left(\frac{P_{\text{MAX}}}{P_o} - 1 \right) = \frac{2}{\gamma M_o^2} \left(\frac{P_w}{P_o} - 1 \right) \quad (9.56)$$

Enter Figure 9-42 with $C_{p \text{ MAX}}$ and M_o and determine the parameter D/δ_o^* is the undisturbed displacement thickness of the boundary layer at x_o , immediately upstream of the interaction region. The turbulent displacement thickness, δ_o^* can be calculated by:

$$\delta_o^* = (0.0475) \left[\frac{1+0.35 M_o^2}{1+0.88 \left(\frac{\gamma_o-1}{2} \right) M_o^2} \right]^{0.44} \left(\frac{x_t}{Re_{xt}^{1/5}} \right) \text{ ft.} \quad (9.57)$$

as suggested in Reference 1. x_t is the equivalent length of growth for the turbulent boundary layer, i.e., the distance from the apparent origin of flow transition to the beginning of the interaction region, and $Re_{xt} = \frac{(aM)_o}{\nu_o} \cdot x_t$

where a = speed of sound

ν = kinematic viscosity

It should be noted that it is required that the point at which flow transition takes place be known. This can only be determined when the entire vehicle configuration is specified. If the extent of separation determined in the last calculation step is significant it will be necessary to repeat the calculation procedure for a new set of M_o and Re_{x_o} until an equilibrium size of the separated region is established.

9.3.3 Test Results

The Columbus Division of North American Rockwell Corporation and Langley Research Center cooperated during CFY 1969 to accomplish tests on fighter type twin jet afterbodies. North American Rockwell designed and structured the test as a parametric study developed about a theme of extremely close spaced nozzles so that the NASA Langley general afterbody twin jet spaced nozzle investigation would be complemented by NR's afterbodies. Reference (31) was employed to propose this afterbody shaping program to NASA and the Navy. This program was approved by the Propulsion Division of the Naval Air Systems Command, who then requested NASA Langley participation. NASA Langley's 16 foot transonic and 4 foot supersonic wind tunnels were utilized for the test program.

The test objectives were to define the effects of afterbody boat-tail, interengine fairing shape, nozzle shape, and jet pressure ratio on the afterbody drag and nozzle efficiency. These objectives were accomplished by utilizing NASA Langley's tandem balance installation and by measuring nozzle, afterbody and boundary layer pressures. A complete description of the model and the test data and results are presented in Reference (32). Grumman Aircraft has also conducted airframe/nozzle tests and the data and results are included in Reference (33).

9.3.3.1 Afterbody Shaping

In order to aid the evaluation of the test data, the overall continuity and slope of the basic bodies cross-sectional area distribution and the slope of the local body contours must be considered. From potential flow studies and evaluation of experimental data, the following hypothesis was adopted:

Hypothesis I

The body causing the least disturbance to the free stream flow field (i.e., the best closure body) will have the lowest drag.

It should be noted that exceptions to this statement are known to exist because of jet effects and flow conditions where separation increases the pressure on the body. The data obtained during this test will be discussed in light of this hypothesis.

To establish the best closure body, the cross-sectional area distribution must be evaluated. The cross-sectional area as a function of body station for a best closure body should be uniformly continuous, the derivative of this function should change evenly with no

discontinuities and no points of inflection should exist other than at the maximum cross-sectional area. However, the local surface contours cannot be sacrificed to obtain the uniform cross-sectional area distribution. The local surface contours of a best closure body should have a constant radius of curvature with no discontinuities and no areas in which exist steep contour angles to the centerline of the body.

The surface area of the body is also important in establishing the lowest drag shape. The afterbody closure rate must be chosen so that the total of the pressure drag and skin friction drag is a minimum. The body best attaining these criteria is the best closure body. These criteria follow the Area Rule developed by Whitcomb.

9.3.3.2 Test Model Design

To obtain information about the close spaced nozzle concept, and to illustrate the hypothesis, the test model was designed with afterbody closure changes in the form of interengine fairing and boattail contour variations. With this in mind, the test model was built with the following geometric parameters held constant:

- 1) Model forebody
- 2) Afterbody maximum cross-sectional area
- 3) Spacing of nozzles
- 4) Nozzle-afterbody interface position

(These parameters are illustrated in Figure 9-43)

The following geometric parameters are variables:

- 1) Afterbody boattail angle
- 2) Interengine fairing contour
- 3) Type of nozzle
- 4) Tail (On or Off)
- 5) Booms

These parameters are illustrated in Figure 9-44.

9.3.3.3 Analysis of Results

Because the test is primarily a parametric study of surface contours and cross-sectional area distribution, the bodies are analyzed from a drag standpoint. The total drag of the afterbody and nozzles is discussed, then the afterbody drags, nozzle drags and pressures are utilized to explain the analysis of the total drag. All results will be discussed with reference to the hypothesis.

9.3.3.3.1 Consider drag at subsonic Mach numbers for configuration with non-augmented nozzles.

- 1) The 3° boattail body and the 9° boattail body represent two distinct methods of afterbody closure. The rate of closure for the 9° boattail body is more rapid toward the afterbody-nozzle interface.
- 2) Since the nozzle closure should conform to and continue the closure contour started by the afterbody, the conical convergent nozzle completes the 9° boattail body and the 3° boattail body is completed by the iris nozzle.
- 3) Because the blunt interengine was designed with a flat base, this blunt body has the largest discontinuity at the nozzle-afterbody interface.
- 4) All bodies have a discontinuity at the afterbody-nozzle interface. The discontinuity is due to the tandem balance installation. In order to measure the afterbody drag independent of gross thrust minus drag, the afterbody shell has to move independently of the nozzles so that a gap was required to keep the nozzles and afterbody shell from interfering with each other.

The study of the cross-sectional area distributions gives an insight to the relative drags of the bodies since the bodies with the largest discontinuities and high rates of closure have higher total drag than the bodies with lower rates of closure and no discontinuities. Referring to point (2), an informative example of the hypothesis is noted. When comparing the total drag of the bodies with the iris nozzle, the 3° boattail body should have the lowest drag. Also when comparing the total drag of the bodies with the conical nozzle, the 9° boattail body should have the lowest drag.

Consider now the local contouring of the afterbodies and nozzles. The best closure boattail is the 3° boattail because both the 6° and 9° boattails have a break point in the contour (See Figure 9-44). The interengine fairing contouring is analyzed similar to the afterbody boattail angle; however, because the fairing forms a trough between the nozzles, the contouring at the end of the trough in the neighborhood of the nozzles can have higher rates of closure. When a deep trough exists, surface friction slows the flow causing drag so that an initially shallow trough with high final closure rate is often acceptable. A good comparison of interengine fairing closure is that of the circular arc fairing to the elliptical fairing. Consideration must be given to the size and shape of the nozzle

plume. For non-augmented conditions, the plume is usually small so that the base of the afterbody is not in a high pressure field. The data are discussed first for jet off conditions, then with jet on. The schedule of nozzle pressure ratios is shown in Figure 9-45.

- a) For the jet-off condition, the hypothesis holds. The body-nozzle combination with the best closure contour has the lowest total drag (i.e., the 3° boattail body with circular arc interengine fairing and iris nozzle has the lowest total drag, (see Figure 9-46). However, the increase in total drag with increasing boattail angle is small (compare configurations in Figure 9-46.) The significant increase in total drag is shown to be due to nozzle contour and blunting of the interengine fairing (see Figures 9-47 and 9-48). The increase in total drag of the blunt fairing is due to separation of base flow. The increase in total drag with the change of nozzle contour (i.e., contour change from circular to conical nozzle profile), is due to the abrupt change in surface contour of the conical nozzle, and the increased total drag is seen in the increased afterbody drag (compare nozzle, afterbody and total drag in Figures 9-46, 9-47 and 9-48). Also note the drag of the 9° boattail body with elliptical fairing and conical nozzle is lower than the 3° and 6° boattail as previously discussed (see Figure 9-46).
- b) For the jet-on condition, the body-nozzle combinations with slightly blunter aft ends have the lowest total drag (i.e., the 3° boattail body with elliptical interengine fairing and iris nozzle. (See Figure 9-47). However, the jet interaction effect is not large enough to compress the blunt fairings so that these fairings have significantly higher total drag. The hypothesis when considered with jet effects is again demonstrated to be correct because the nozzle contour changes (compare Figures 9-48 and 9-50), and fairing changes (compare Figures 9-47 and 9-51) have the same general effect upon model drag as in the no-jet case.

In summary, for subsonic Mach numbers and non-augmented nozzles two general conclusions can be made:

- 1) The effect of the jet on all configurations is to lower the total drag (compare Figures 9-46 and 9-49).
- 2) The total drag is lower for configurations that allow flow between the nozzles than for configurations with blunt base or extended fairing between nozzles.

9.3.3.3.2 Consider drag at subsonic Mach numbers for configurations with augmented setting nozzles

The change of nozzle type changes the relative closure rates of the bodies. The cross-sectional area distribution and local contours are analyzed as in previous section; however, more emphasis must be on the jet plume.

- 1) For the no-jet condition, the best closure body changes to the 3° elliptical body with the C-D nozzle. This fact is confirmed by the total drag data (See Figures 9-52 and 9-53). The body-nozzle combination with the base end extension has considerably less total drag than it did when combined with the non-augmented nozzle (compare Figures 9-46 and 9-52). The nozzle contour has a very substantial effect on afterbody drag and is therefore very important in determining the total drag. This fact is noted in the nozzle and afterbody drag comparison between the conical nozzle (i.e., C-D augmented), the circular arc nozzle (iris augmented), and the nozzle with a straight section followed by a radius (i.e., shrouded iris nozzle) (compare Figures 9-54, 9-55, 9-56 and 9-57). The interengine fairing change affects the drag in the same manner as for non-augmented nozzles (see Figures 9-54 and 9-55). The 3° elliptical body with the conical nozzle has lowest drag because it has the best closure contour; hence, the hypothesis is again confirmed.
- 2) The jet effect for the augmented nozzles is again beneficial and significantly reduces the total drag (compare Figures 9-52 to 9-58 and 9-53 to 9-59). The blunter fairings and nozzles are most affected by the larger plumes of the augmented nozzles (see Figures 9-58 and 9-59). The nozzles are most affected by the jet plume (compare Figures 9-62 and 9-63 to 9-56 and 9-57) while the pressure ratio is still too low to significantly improve the blunt fairing (compare Figures 9-60 and 9-61 to 9-54 and 9-55). Because the iris augmented nozzle has a greater external surface slope and a large exhaust plume, the jet effects are very beneficial (compare Figures 9-57 and 9-63), and for large jet pressure ratios the iris augmented nozzle is superior to the other nozzles tested (compare Figures 9-58 and 9-59).

In summary, for subsonic Mach numbers and augmented nozzles, the general conclusions made for the non-augmented nozzle still hold.

- 1) The effect of the jet on all configurations is to lower the total drag.
- 2) The total drag is lower for configurations that allow flow between the nozzles than for the blunt base configurations.

9.3.3.3.3 Consider drag for low supersonic Mach numbers and configurations with augmented nozzles

The range of low supersonic Mach numbers considered is small (i.e., Mach number = 1.2 to 1.3). For supersonic flow, separation becomes beneficial, and the jet plume is larger than in subsonic flow so that the blunt base configuration should have an advantage.

- a) For the no-jet case, the bodies with the blunt and extended blunt interengine fairings have the lowest total drag (see Figures 9-52 and 9-53). These configurations have the lowest total drag because of base separation. The bodies with high boattail angles have significantly higher total drag because the afterbody contours are not continuous (see Figures 9-54 and 9-55). Although the blunt base bodies have the lowest drag, the total drag of the 3° boattail body with the elliptical interengine fairing is almost as low (see Figure 9-52).
- b) The jet effects are very pronounced lowering the total drag significantly (see Figures 9-58 and 9-59). Since the pressure ratios are higher than in subsonic flow, the exhaust plume is larger so that the jet interaction effects are greater than in subsonic flow. The greater amount of jet interaction affects the blunt base interengine fairings most (see Figures 9-60 and 9-61). The body with the extended fairing has the lowest drag, because its fineness ratio is better and the extended fairing is in the exhaust plume; however, the elliptical fairing with the low boattail angle has nearly the same total drag. The bodies with high boattail angles again have high total drag as expected (see Figures 9-58 and 9-59).

In summary, for supersonic flow and augmented nozzles, the following statements can be made.

- 1) The nozzle plume is large; however, only the part of the afterbody close to the nozzle is affected by the plume.
- 2) The blunt fairings have a slight drag advantage.

9.3.3.4 Conclusions

The test demonstrated a method of drag evaluation for twin jet afterbodies (i.e., the hypothesis). It also demonstrated that the surface closure rate and total cross-sectional area distribution are the most important factors in determining the relative drag of the configurations. The following specific effects were noted and confirm the hypothesis stated in the text of this report:

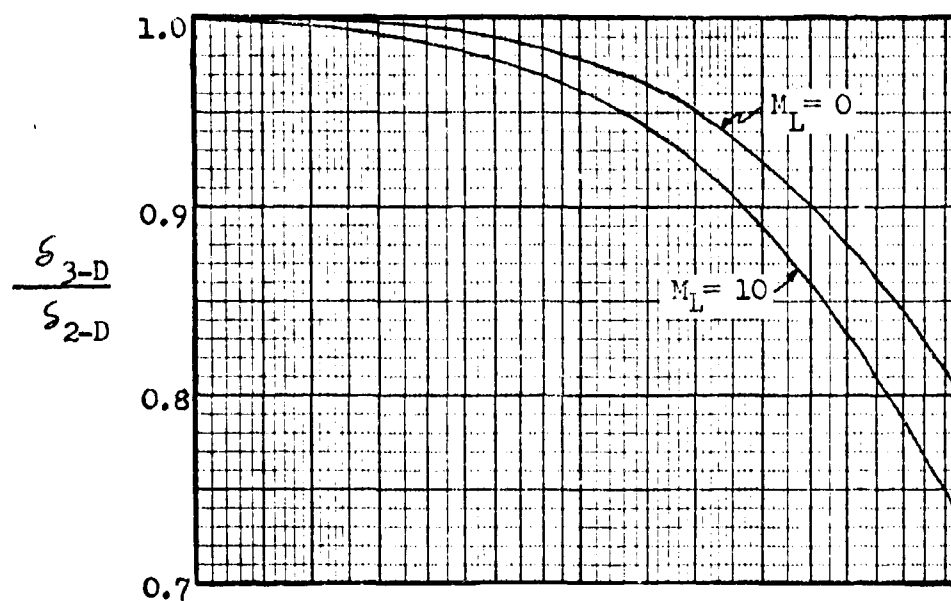
- 1) The effect of the jet is beneficial to all configurations.
- 2) The jet exhaust increases the nozzle boattail pressures, but has a much smaller effect upon the afterbody.
- 3) For subsonic Mach numbers, flow between the nozzle permits high nozzle inboard surface pressures and therefore lowers drag.
- 4) For supersonic Mach numbers the blunt fairings exhibit an advantage, but the low boattail bodies with elliptical fairings have nearly the same drag level.
- 5) The tail surfaces depress the pressures on the whole afterbody/nozzle surfaces.

REFERENCES

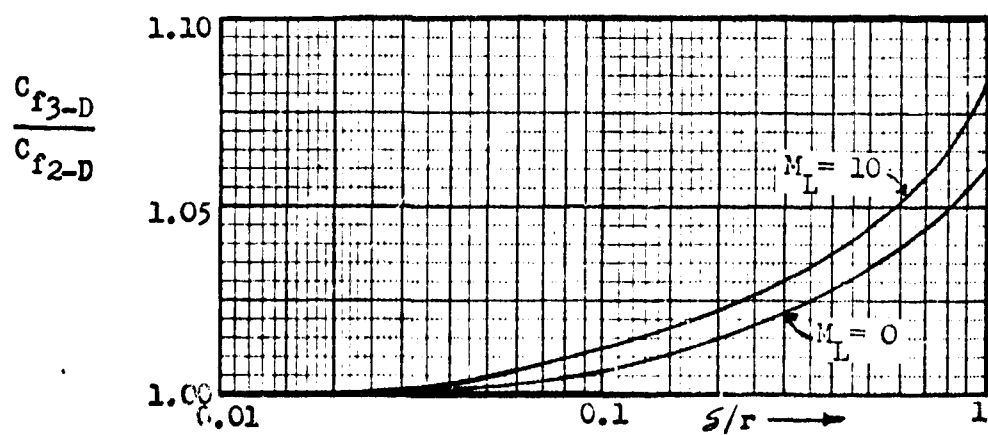
1. Shapiro, A.H., "The Dynamics and Thermodynamics of Compressible Fluid Flow, Volume II," The Ronald Press Company, 1954.
2. Van Driest, E.R., "Turbulent Boundary Layer in Compressible Fluids," Journal of the Aeronautical Sciences, Vol. 18, No. 3, p. 145, 1951.
3. Nikuradse, J., "Strömungsgesetze in rauhen Rohren," Verein deutscher Ingenieure Forschungsheft, Vol. 40, No. 361, pp. 1-22, July-August, 1933. (English translation, "Laws of Flow in Rough Pipes," NACA TM 1292, November, 1950).
4. Goddard, F.E., Jr., "Effect of Uniformly Distributed Roughness on Turbulent Skin-Friction Drag at Supersonic Speeds," Journal of the Aero/Space Sciences, Vol. 26, No. 1, pp 1-15, January 1959.
5. Coles, D., "Measurements in the Boundary Layer on a Smooth Flat Plate in Supersonic Flow, III. Measurements in a Flat Plate Boundary Layer at the Jet Propulsion Laboratory," Jet Propulsion Laboratory Report No. 20-71, June 1953. (Also, "Measurements of Turbulent Friction on a Smooth Flat Plate in Supersonic Flow," Journal of the Aeronautical Sciences, Vol. 21, No. 7, pp 443-448, July 1954).
6. Hessman, F.W., "Drag Analysis for Boattailed Afterbodies in the Mach Number Range 0.6 to 2.5 with Emphasis Placed on Boundary Layer Separation," North American Aviation, Inc. Report No. NA64H-891, 30 October 1964.
7. Fraenkel, L.E., "The Theoretical Wave Drag of Some Bodies of Revolution," Aero Report 2420, British RAE, 1951.
8. Hargis, C.B., Jr., Davison, P.H. and Savage, S.B., "Methods for Estimating Base Pressures on Aircraft Configurations." WADC TN 58-27, July 1957.
9. Silhan, F.V. and Cabbage, J.M., Jr., "Drag of Conical and Circular - Arc Boattail Afterbodies at Mach Numbers from 0.6 to 1.3," NACA RM L56K22, 1957.
10. Patterson, R.T., "A Wind Tunnel Investigation of the Drag of Conical Missile Afterbodies at Mach Numbers from 0.40 to 2.47," David Taylor Model Basin, TMB Aero Report 857, 1954.
11. Aero-Thermodynamics Unit, "External Drag Manual," North American Missile Division Report, MD 59-453, 1960.
12. Ames Research Staff, "Equations, Tables and Charts for Compressible Flow," NACA Report 1135, 1953.
13. Fraenkel, L.E., "The Theoretical Wave Drag of Some Bodies of Revolution," British Ministry of Supply, R&M 2842, September 1955.

14. Jack, J.R., "Theoretical Pressure Distributions and Wave Drags for Conical Boat-Tails," NACA TN 2972, July 1953.
15. Savin, R.C., "Application of the Generalized Shock-Expansion Method to Inclined Bodies of Revolution Traveling at High Supersonic Airspeeds," NACA TN 3349, April 1955.
16. Eggers, A.J., Jr., "On the Calculation of Flow About Objects Traveling at High Supersonic Speeds," NACA TN 2811, October 1952.
17. Lighthill, M.J., "Supersonic Flow Past Bodies of Revolution," British Ministry of Supply, R&M 2003, January 1945.
18. Clippinger, R. F., Giese, J.H. and Carter, W.C., "Tables of Supersonic Flows About Cone Cylinders, Part I; Surface Data," Ballistic Research Laboratories, Report 729.
19. Nash, J.F., Quincey, V.G. and Calliman, J., "Experiments on Two-Dimensional Base Flow at Subsonic and Transonic Speeds," ARC, R&M 3427, January 1963.
20. Love, E.S., "The Base Pressure at Supersonic Speeds on Two-Dimensional Airfoils and Bodies of Revolution (With and Without Fins) Having Turbulent Boundary Layers," NACA TN 3819, 1957.
21. Steele, P.E. and Bonner, E., "Preliminary Analysis of Jet Interference Effects on Base Pressures and Afterbody Drag for the Turbulent Boundary Layer Condition," North American Report NA-57-1059, 1957.
22. NASA Conference on Aircraft Aerodynamics, January 18-20, 1967.
23. LeBlanc, L.P. and Webb, H.G., Jr., "Boundary Layer Separation in a Supersonic Stream," North American Space and Information Systems Division Report, SID 61-72, March 1961.
24. Gadd, G.E., "Interactions Between Wholly Laminar or Wholly Turbulent Boundary Layers and Shock Waves Strong Enough to Cause Separation," Journal of Aeronautical Sciences, Vol. 20, No. 11, November 1953, pp. 729-739.
25. Hessman, F.W., "Methods for Predicting the Occurrence and Extent of Boundary Layer Separation Induced by a Jet Exhaust Plume," North American Columbus Division Report, NA63H-1071, January 1964.
26. Love, E.S., Grigsby, C.D., Lee, L.P. and Woodling, M.J., "Experimental and Theoretical Studies of Axisymmetric Free Jets," NASA TR R-6, 1959.
27. Fetterman, D.E., Jr., "Effects of Simulated Rocket-Jet Exhaust on Stability and Control of a Research-Type Airplane Configuration at a Mach Number of 6.86, NASA TMX-127, October 1959.

28. Erdos, J. and Pallone, A., "Shock Boundary Layer Interaction and Flow Separation," Proceedings of the 1962 Heat Transfer and Fluid Mechanics Institute, June 1962.
29. Kuehn, D.M., "Experimental Investigation of the Pressure Rise Required for the Incipient Separation of Turbulent Boundary Layers in Two-Dimensional Supersonic Flow," NACA Memo 1-21-59A, February 1959.
30. Beheim, M.A., Klann, J.L. and Yeager, R.A., "Jet Effects on Annular Base Pressure and Temperature in a Supersonic Stream," NASA TR R-125, December 1961.
31. "An Experimental Wind Tunnel Program to Study Afterbody and Interengine Fairing Effects on a Close Spaced Twin Jet Afterbody Configuration," NR68H-232, North American Rockwell Corporation, March 15, 1968.
32. "Close Spaced Twin Jet Afterbody/Nozzle Tests, TPA 107, Task 0002, Final Report," NR69H-614, North American Rockwell Corporation.
33. "Twin Jet Airframe/Nozzle Tests for VFAX Applications," Grumman Aircraft Engineering Corporation; AD502313, March 1969, Confidential Report.



a.) Boundary Layer Thickness



b.) Skin Friction Coefficient

FIGURE 9-1. Transverse Curvature Effects of Turbulent Boundary Layer (Reference 1)

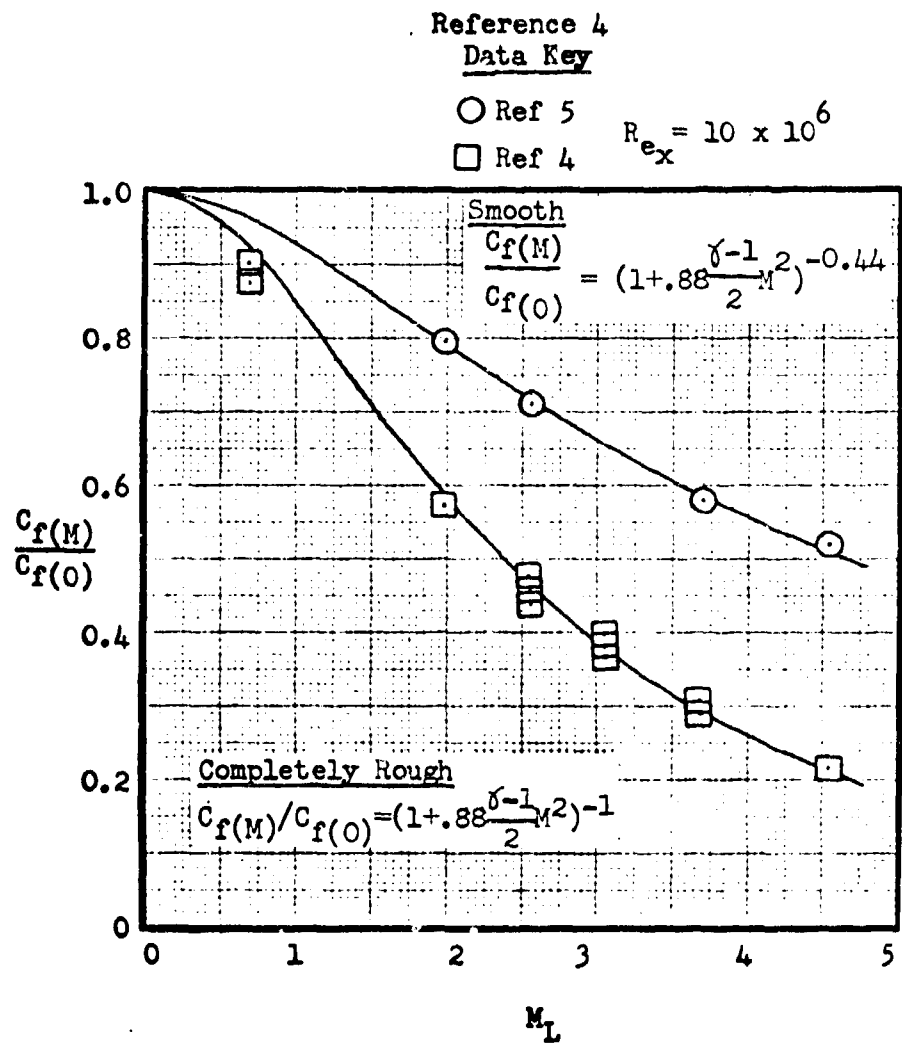


FIGURE 9-2. Effect of Compressibility on Skin Friction to Smooth and "Completely Rough" Surfaces

Reference 4
 $0.70 \leq M_L \leq 4.54$

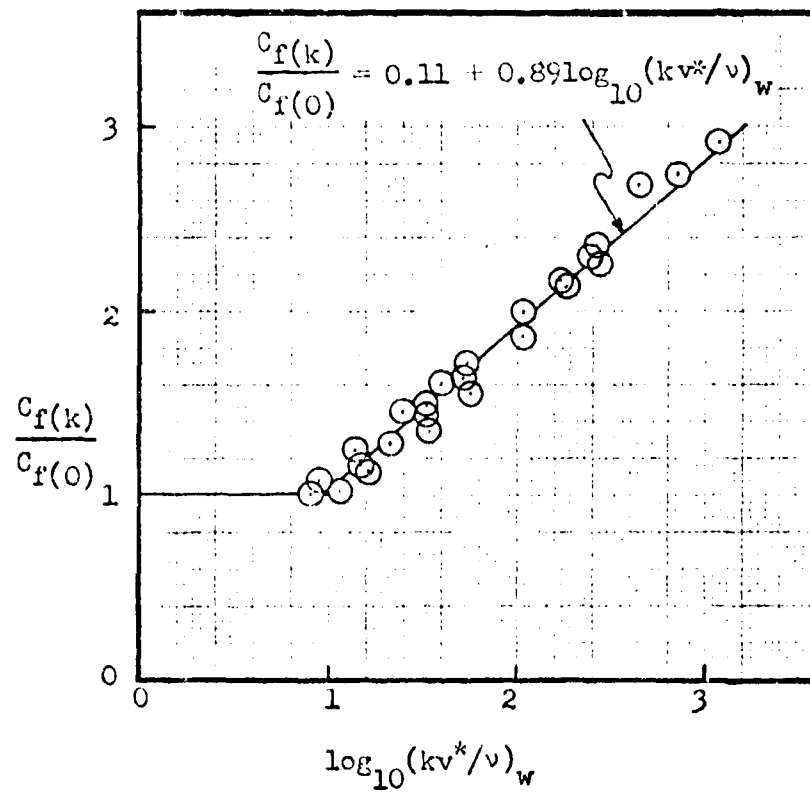


FIGURE 9-3. Increase of Skin Friction Due to Surface Roughness.

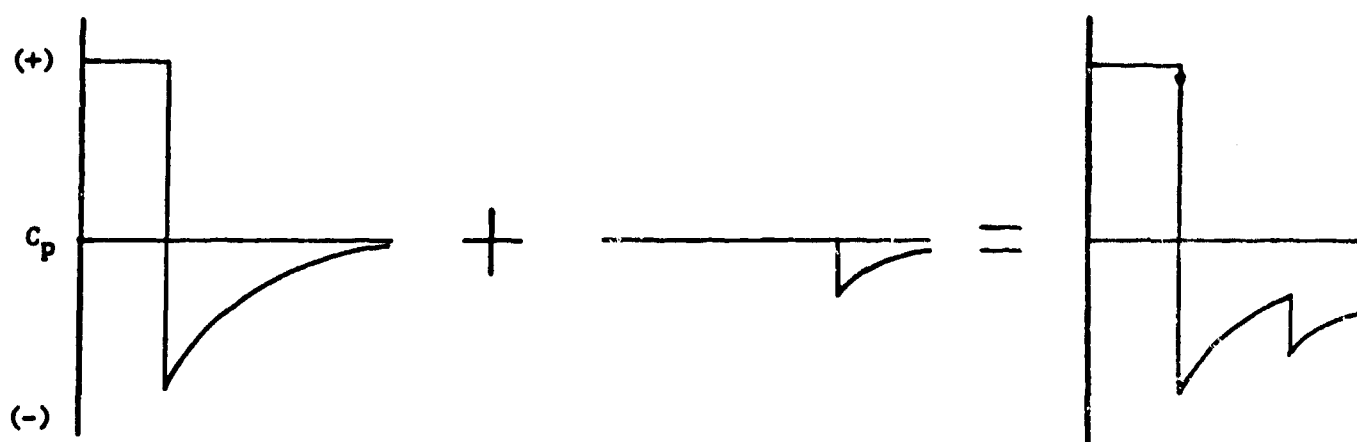
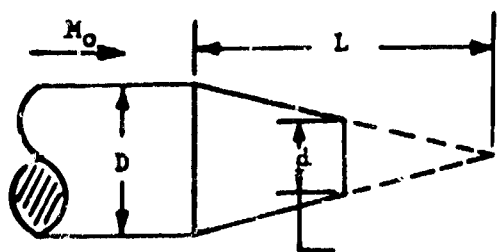
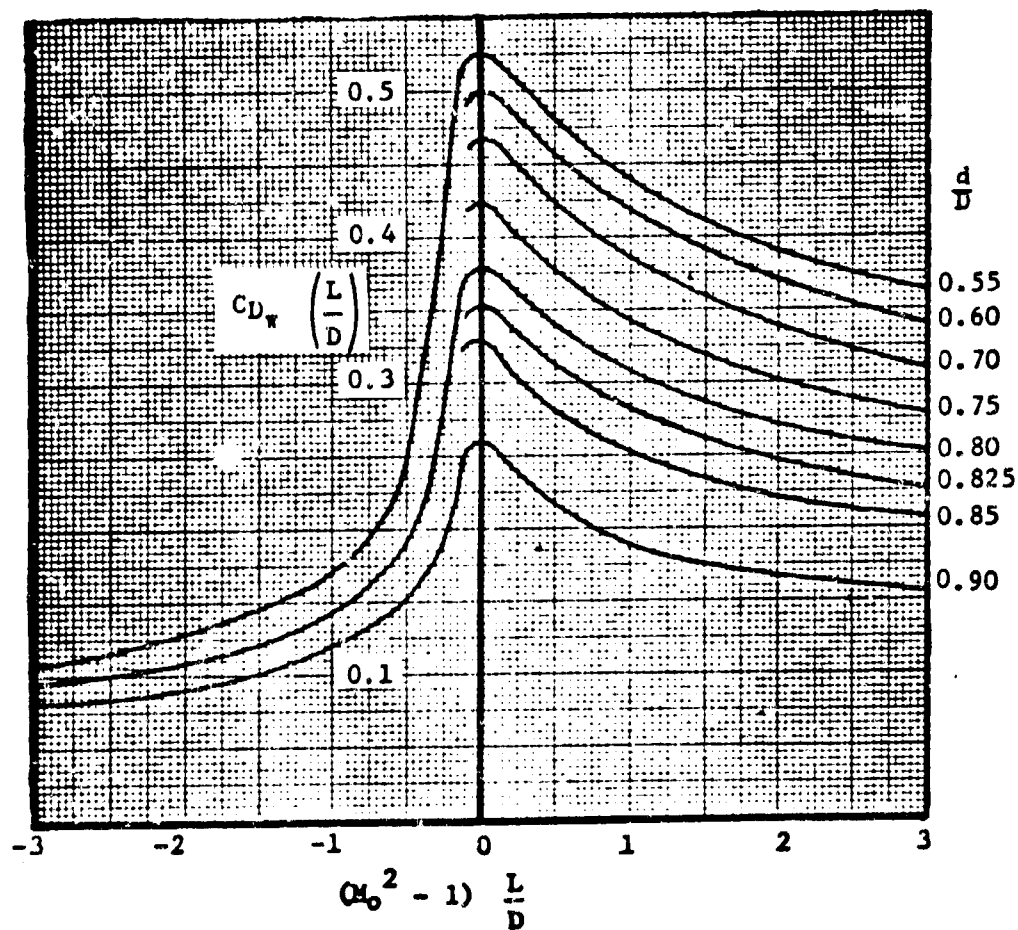
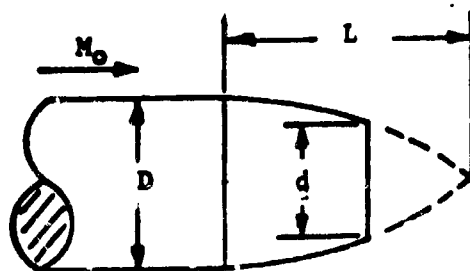
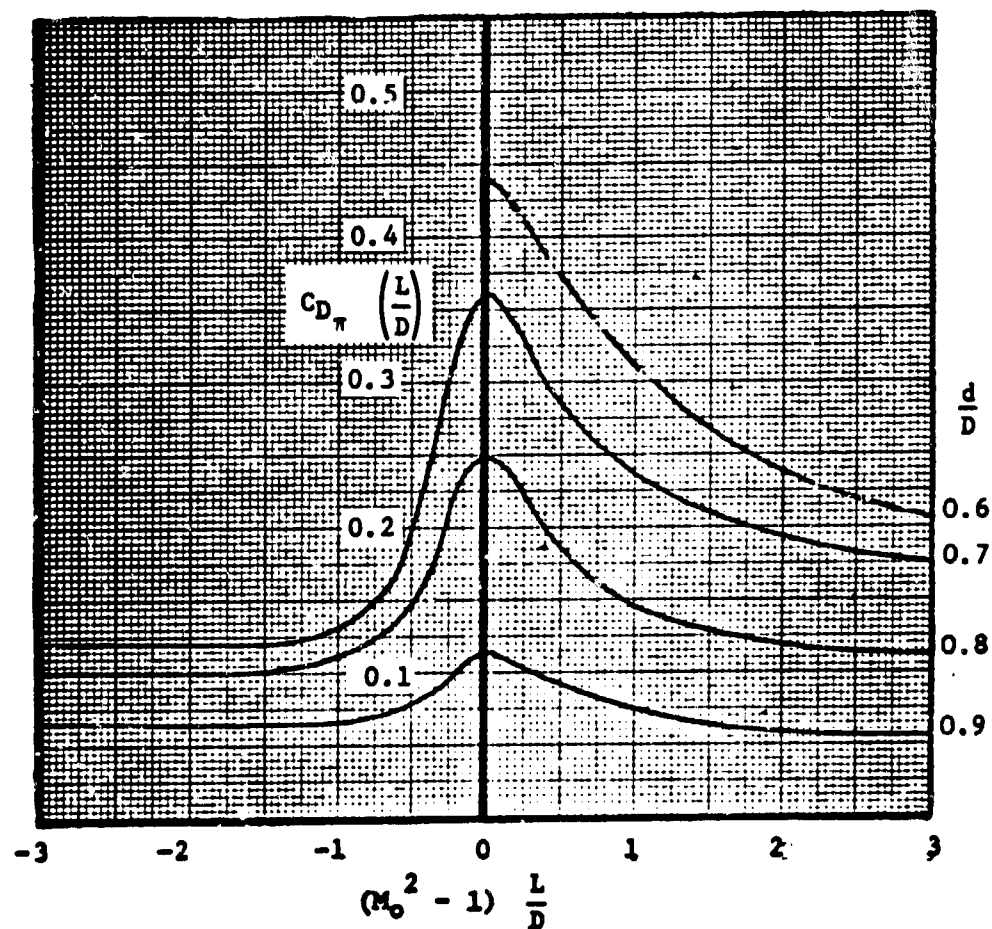


FIGURE 9-4 Superposition of Pressure Distribution
(Reference 8)



Note: C_{D_w} based on maximum cross-sectional area $\frac{\pi D^2}{4}$

FIGURE 9-5. Subsonic Wave Drag of Conical Afterbodies



Note: C_{D_w} based on maximum cross-sectional area $\frac{\pi D^2}{4}$

FIGURE 9-6. Subsonic-Transonic Wave Drag of Circular Arc Afterbodies

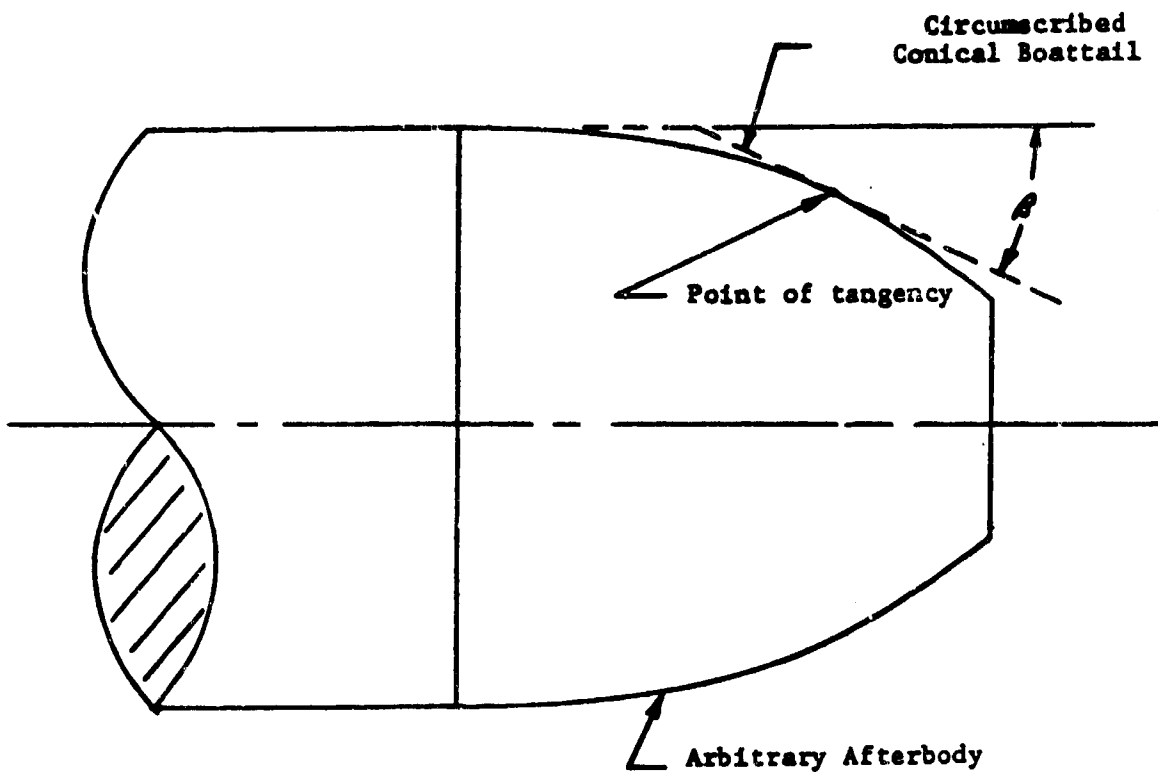


FIGURE 9-7. Conical Boattail Analogy (Reference 8)

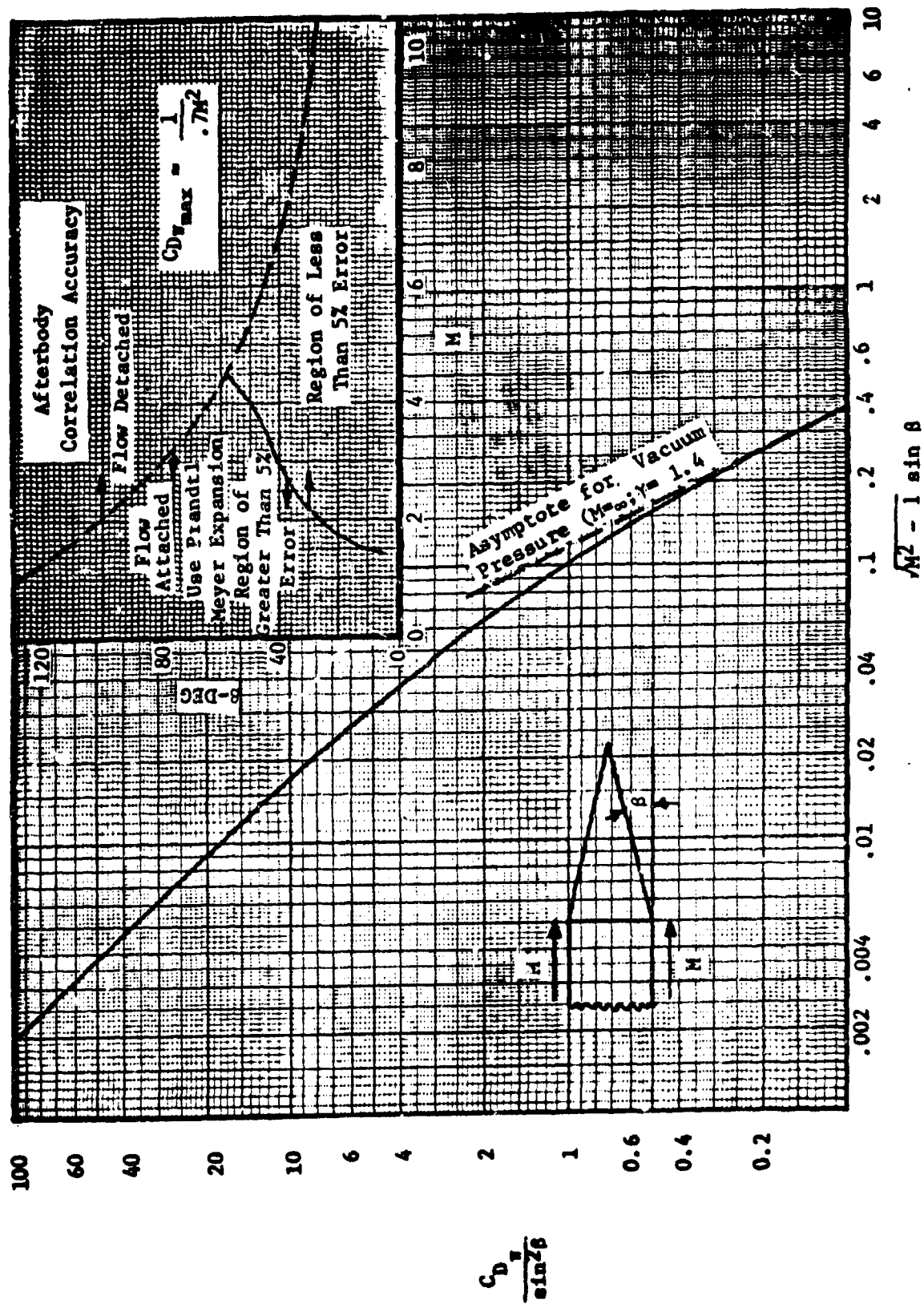


FIGURE 9-8. Supersonic Wave Drag of Wedge Afterbodies (Reference 11)

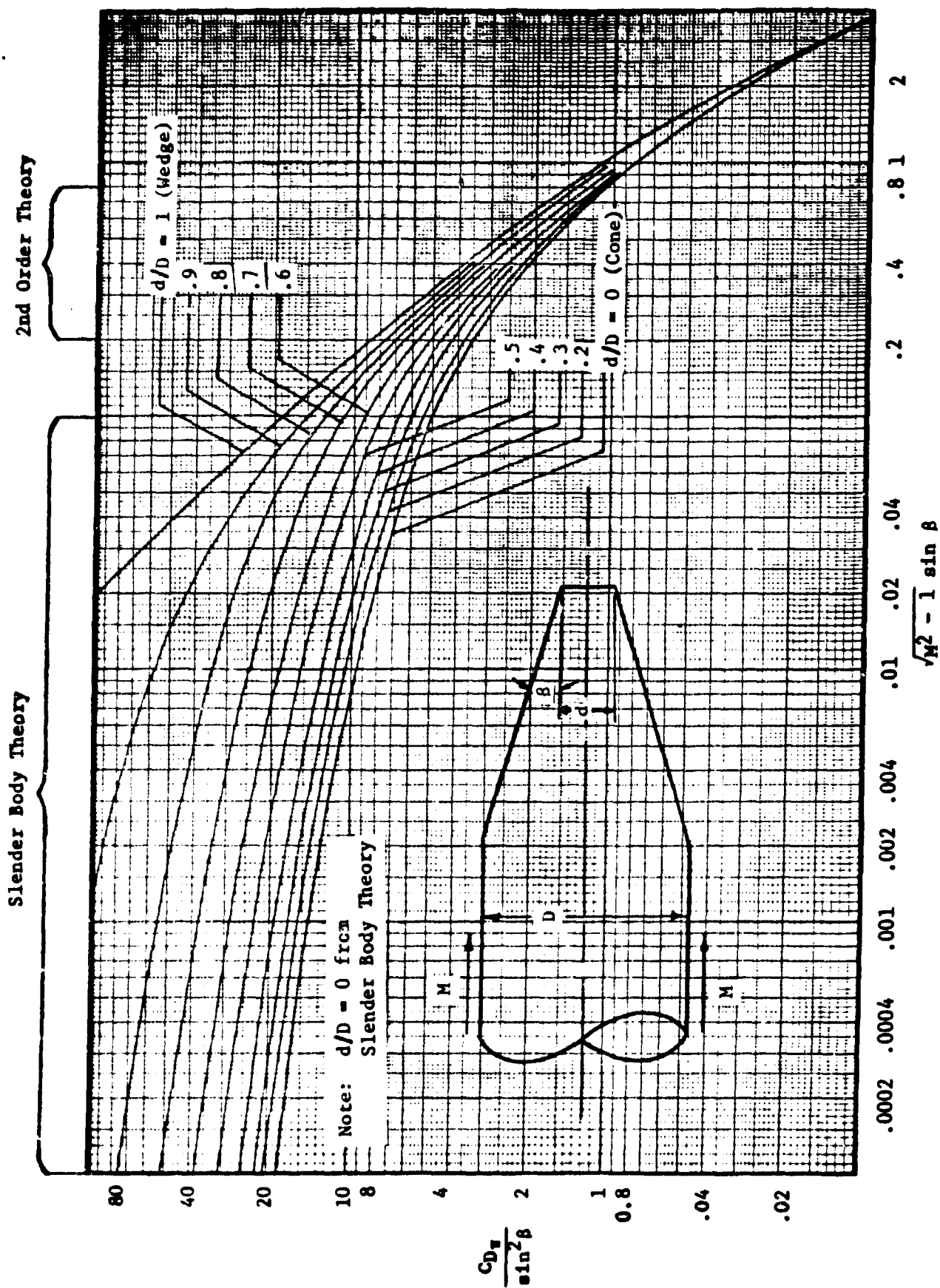


FIGURE 9-9. Supersonic Wave Drag of Conical Afterbodies (Reference (41))

Slender Body Theory

Quasi-Cylinder Shock Expansion Theory

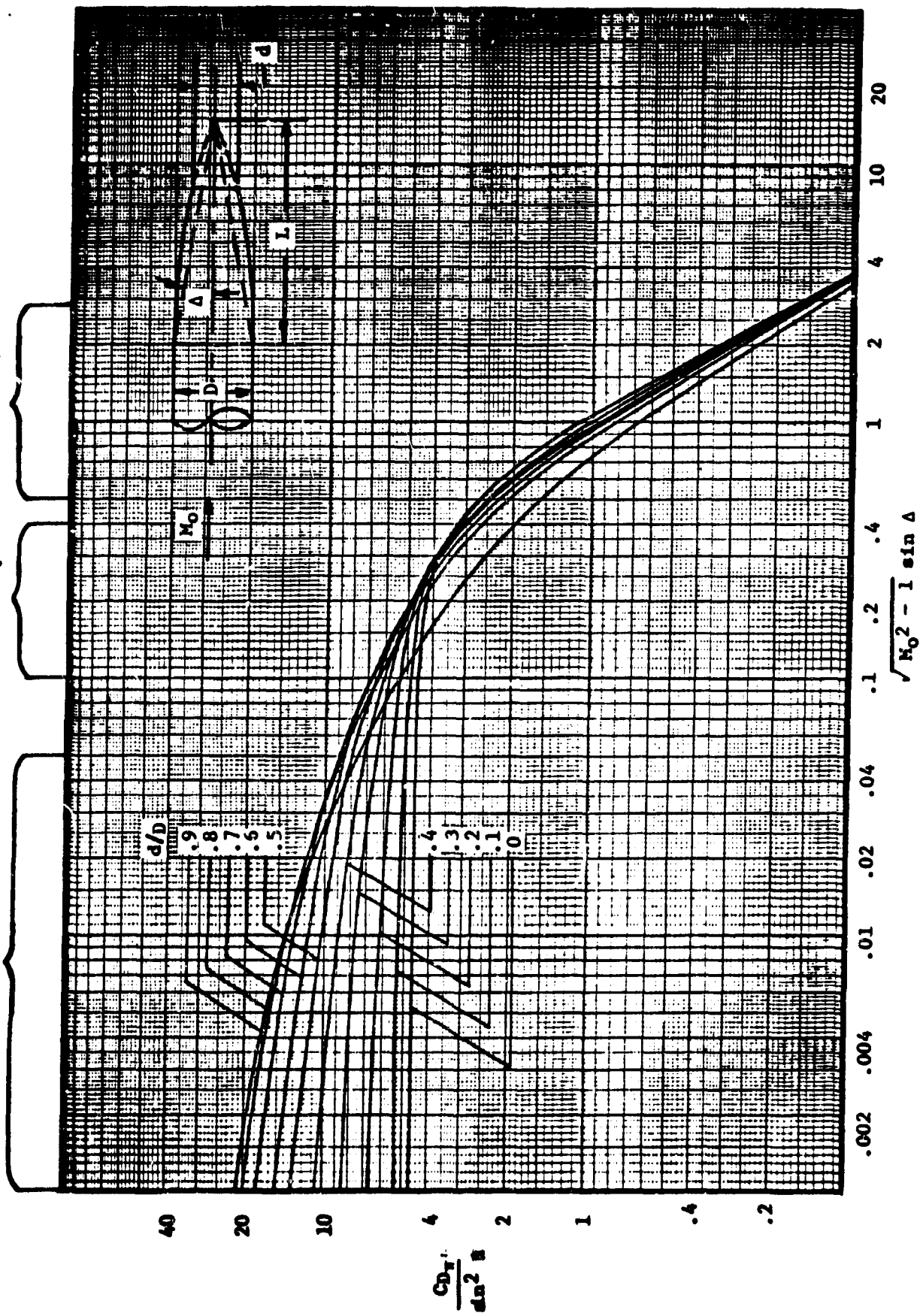


FIGURE 9-10. Supersonic Wave Drag of Parabolic Afterbodies (Reference 11)

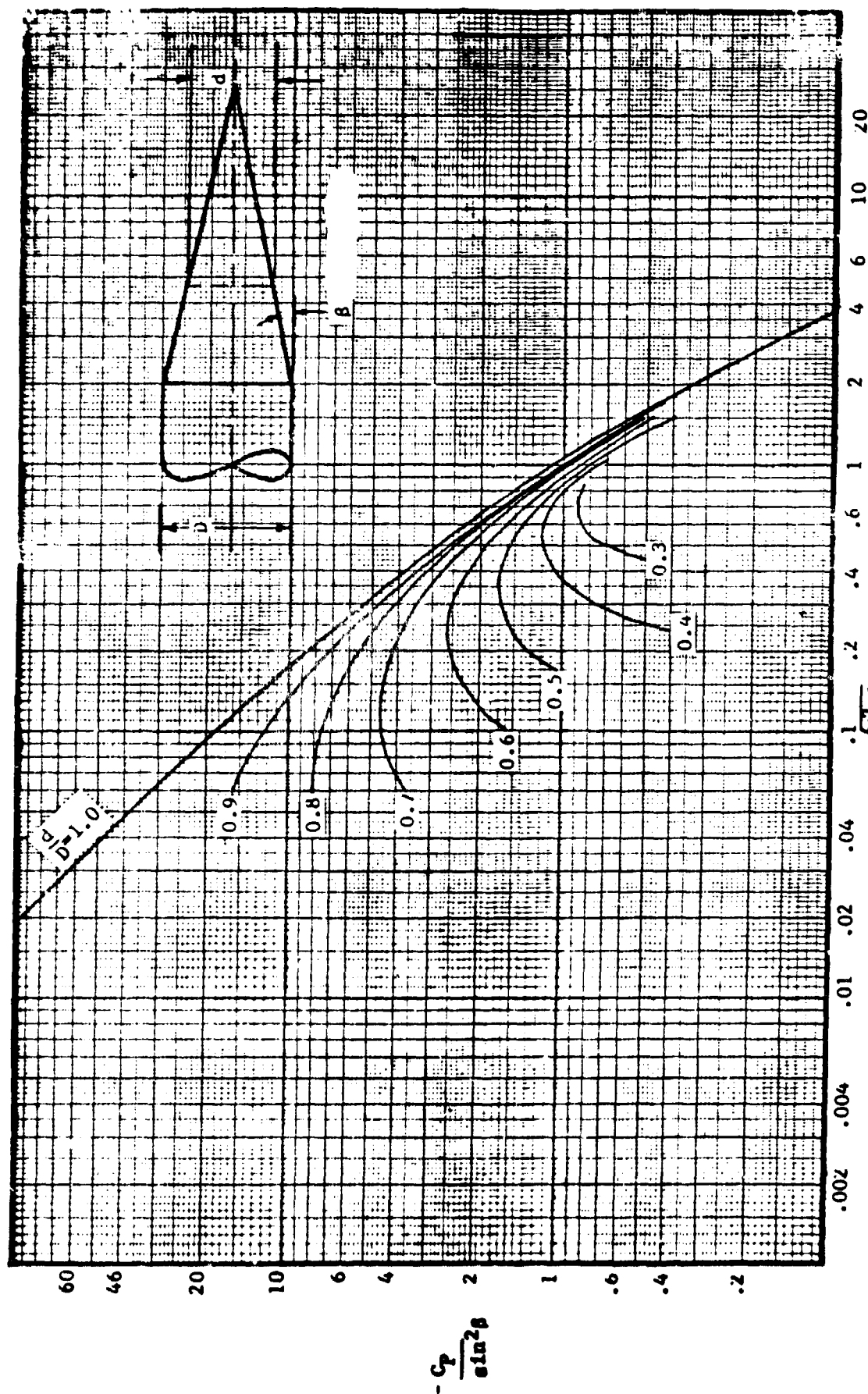


FIGURE 9-11. Pressure Coefficients on Conical Afterbodies at Supersonic Speeds (Reference 11)

$$-C_p \sin^2 \beta$$

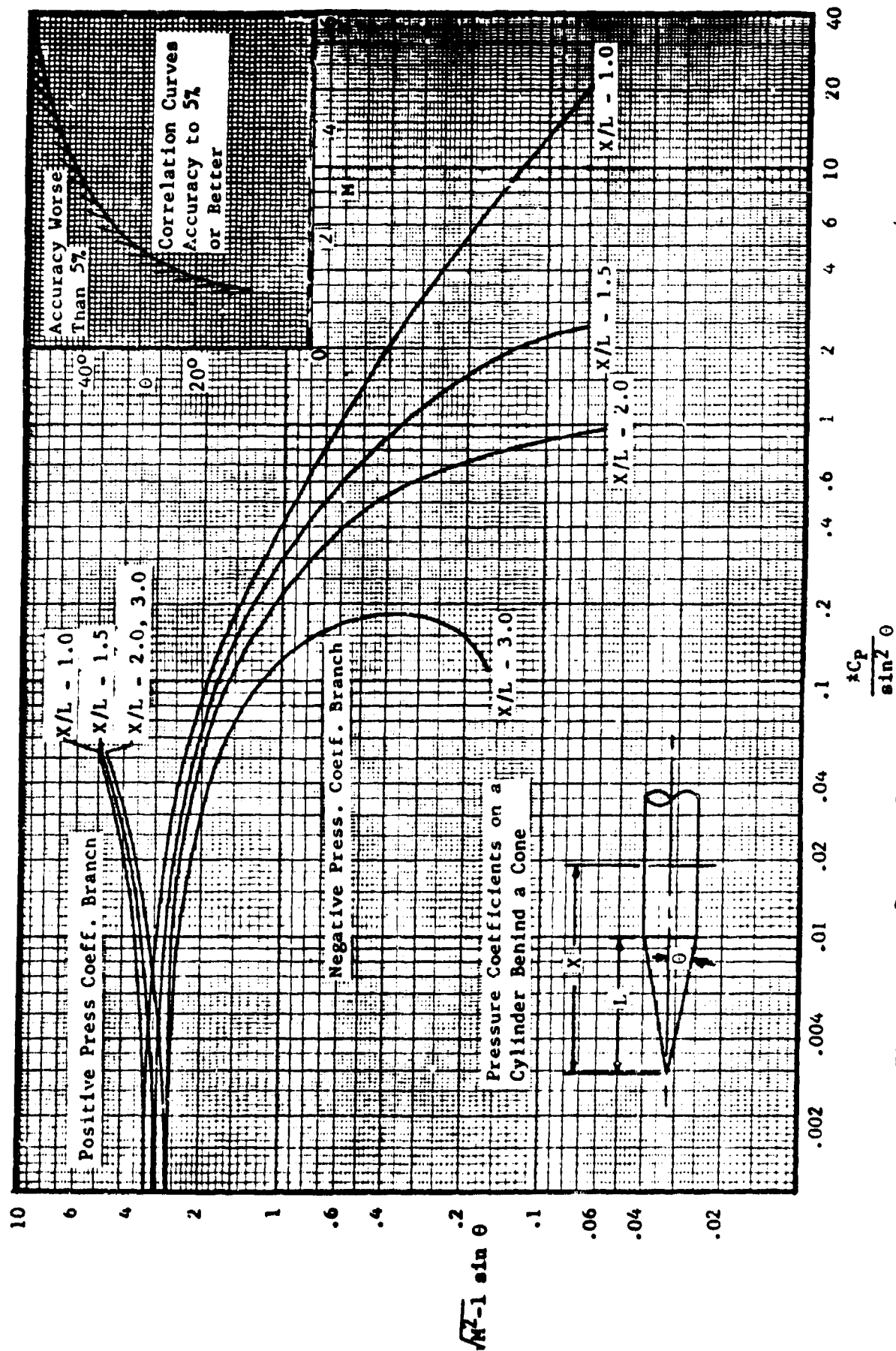


FIGURE 9-12. Pressure Coefficients on Cylinder Behind Cone (Reference 11)



(a) $M_x = 0.4$.



(b) $M_x = 0.8$.



(c) $M_x = 0.9$

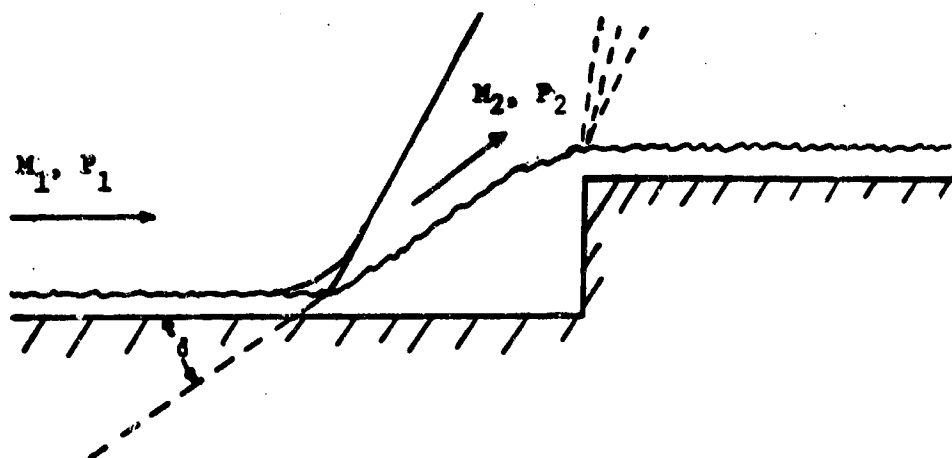


(d) $M_x = 1.0$.

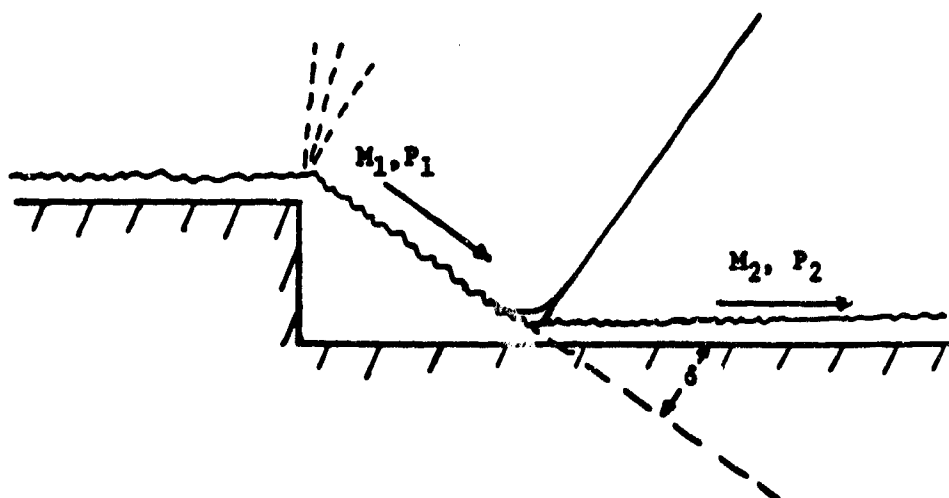


(e) $M_x = 1.12$.

FIGURE 9-13. Subsonic and Transonic Flow Past a Blunt-Trailing-Edge Section (Reference 19)



a) Forward-Facing Step



b) Rearward-Facing Step or Base

FIGURE 9-14. Supersonic Flow Analogy

FORM 351-F REV 10/87

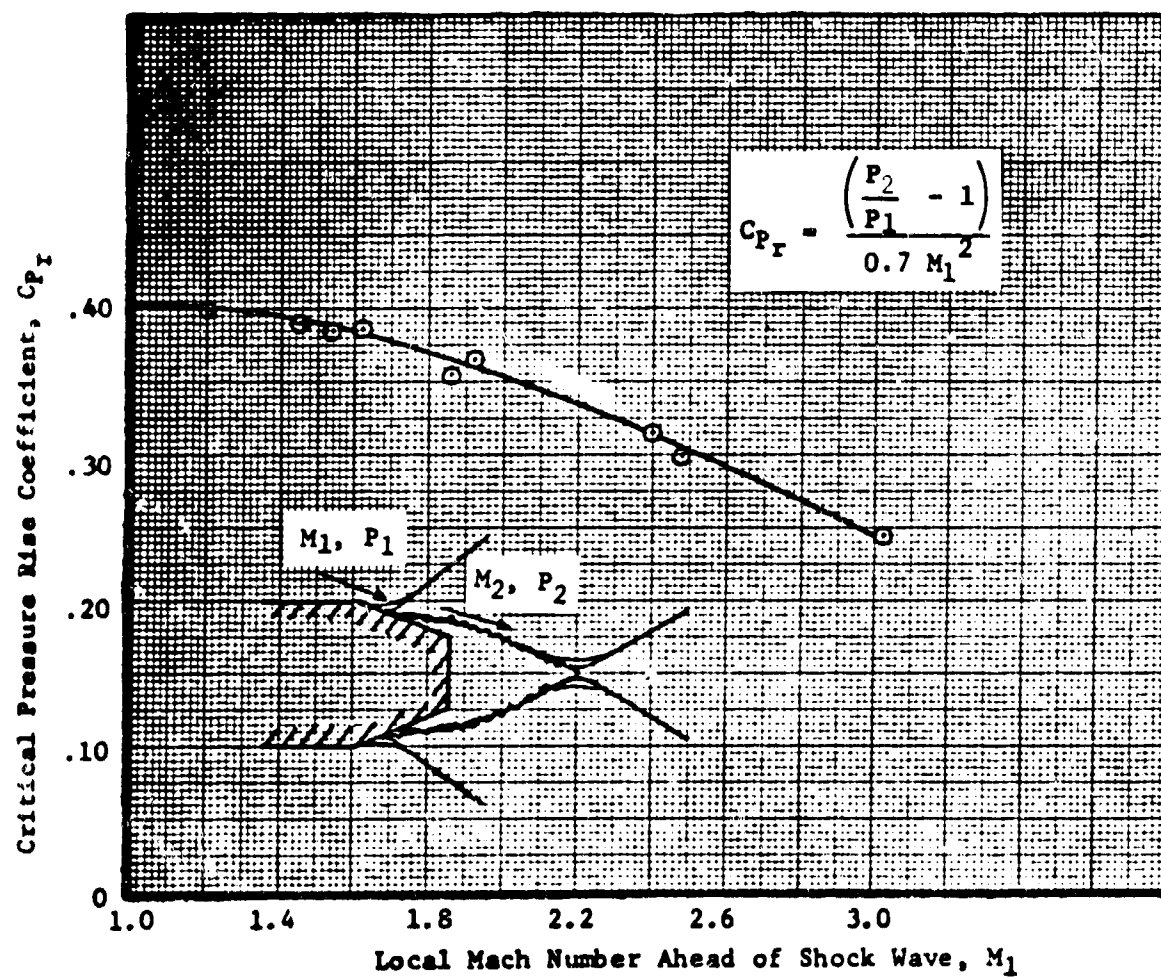


FIGURE 9-15. Critical Pressure-Rise Coefficient for Turbulent Boundary Layer on Two-Dimensional Afterbodies

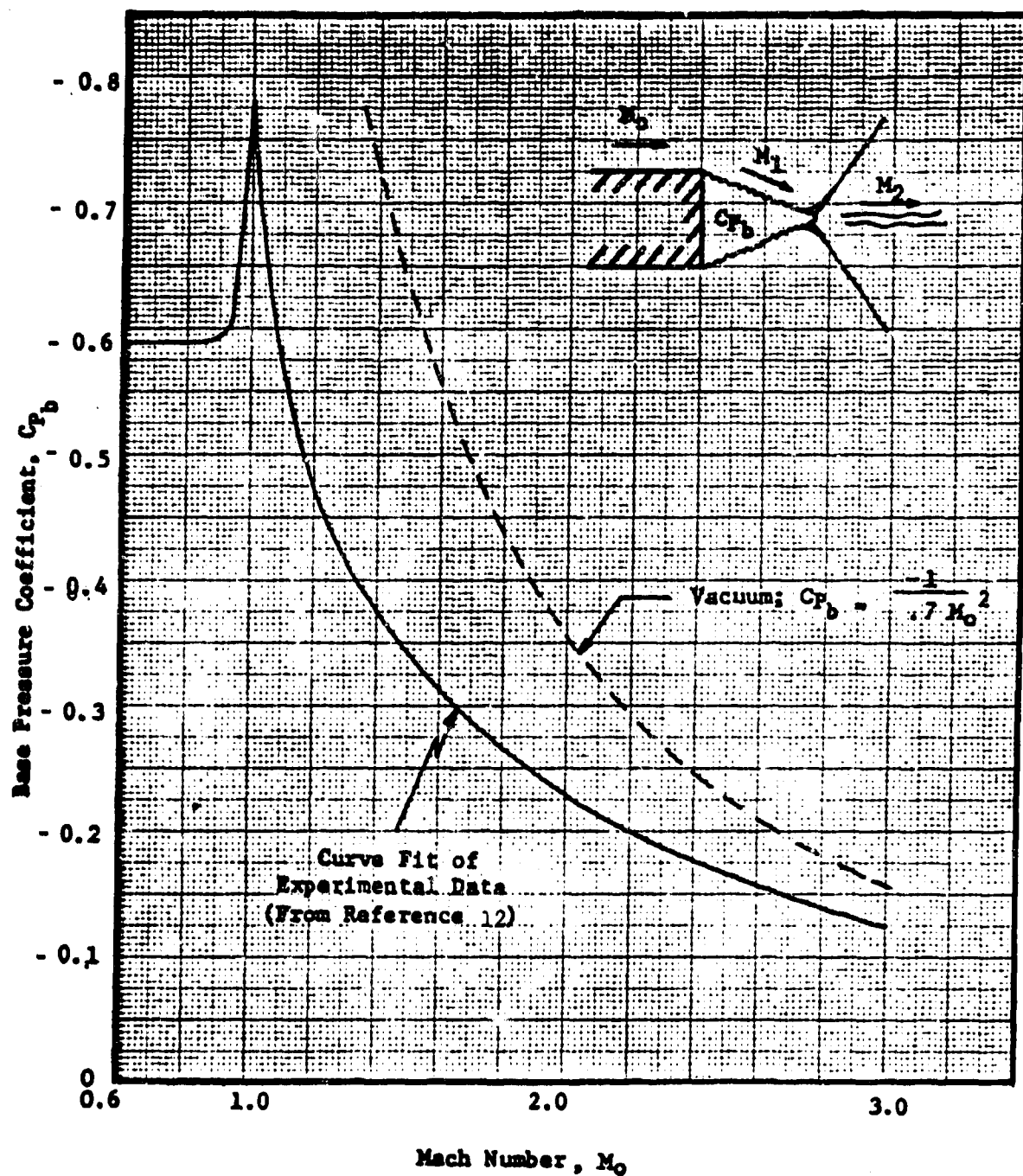


FIGURE 9-16. Two-Dimensional Base Pressures ($\alpha = \beta = 0^\circ$, No Jet)

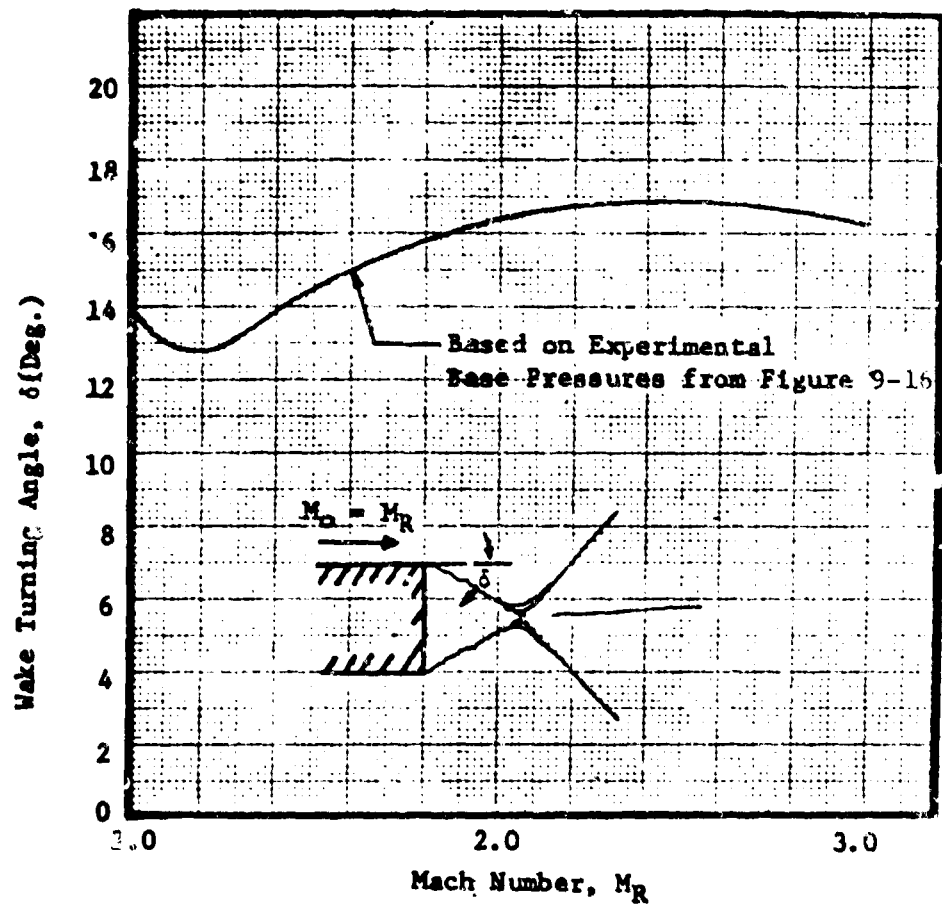


FIGURE 9-17. Two-Dimensional Wake Turning Angle

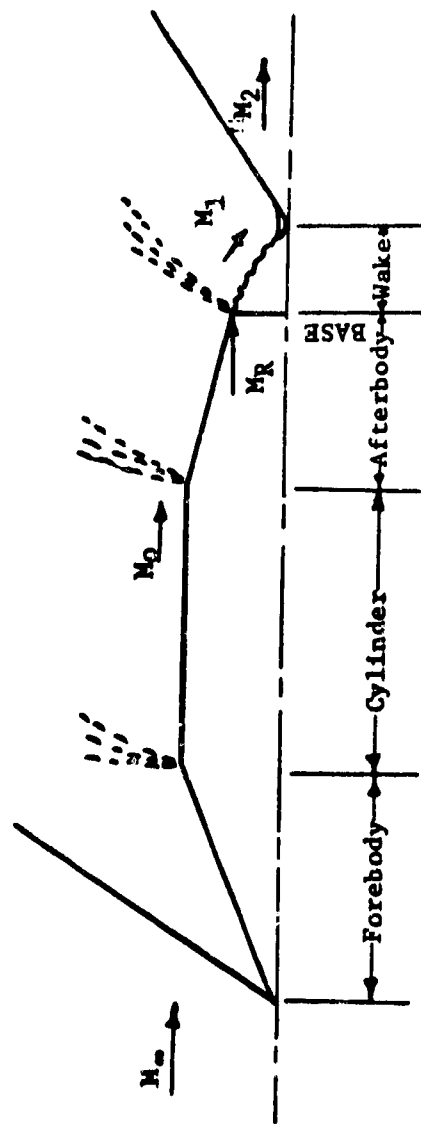


FIGURE 9-18. Mach Number Notation

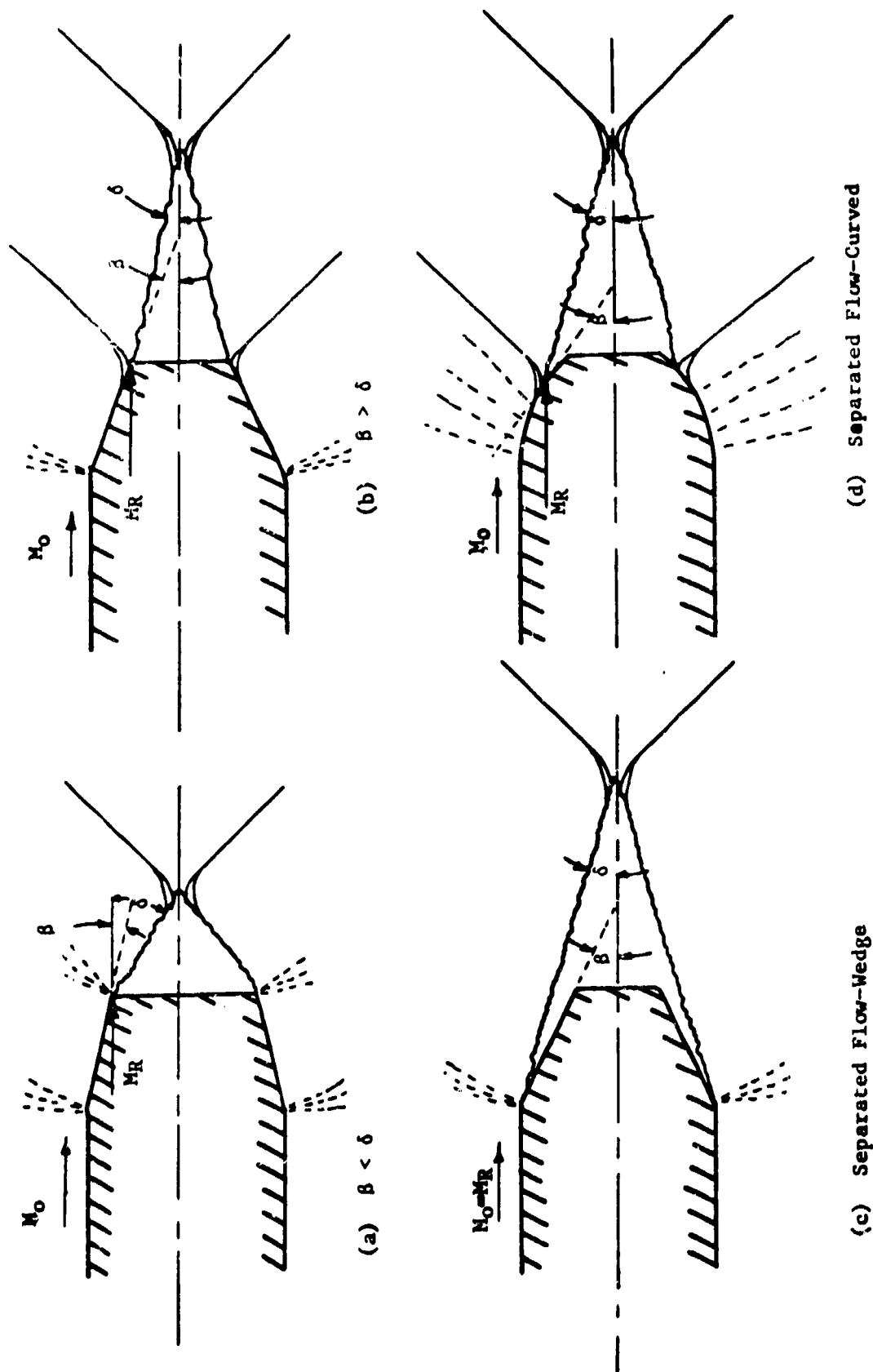


FIGURE 9-19. Two-Dimensional Boattail Flow Conditions

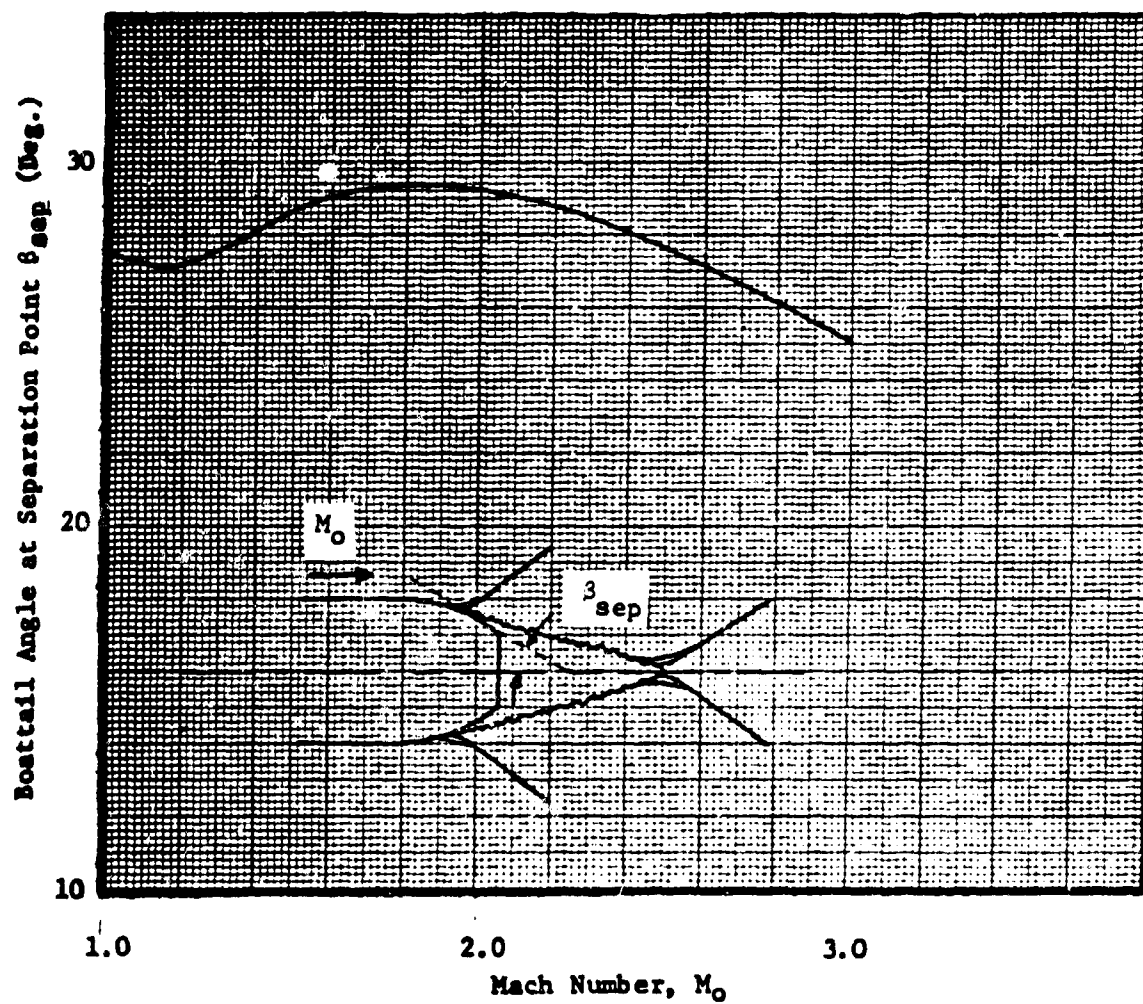


FIGURE 9-20, Two-Dimensional Boattail Separation Angle

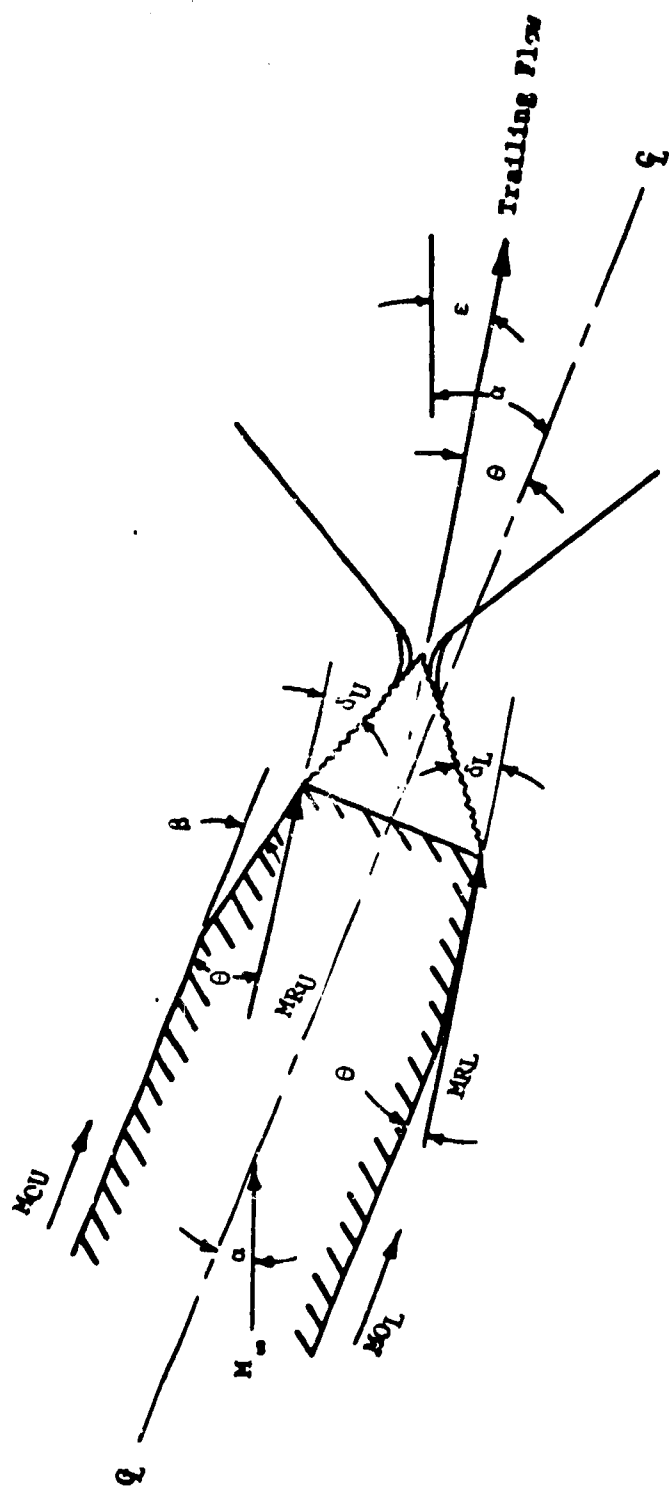


FIGURE 9-21. Two-Dimensional Afterbody at Angle of Attack

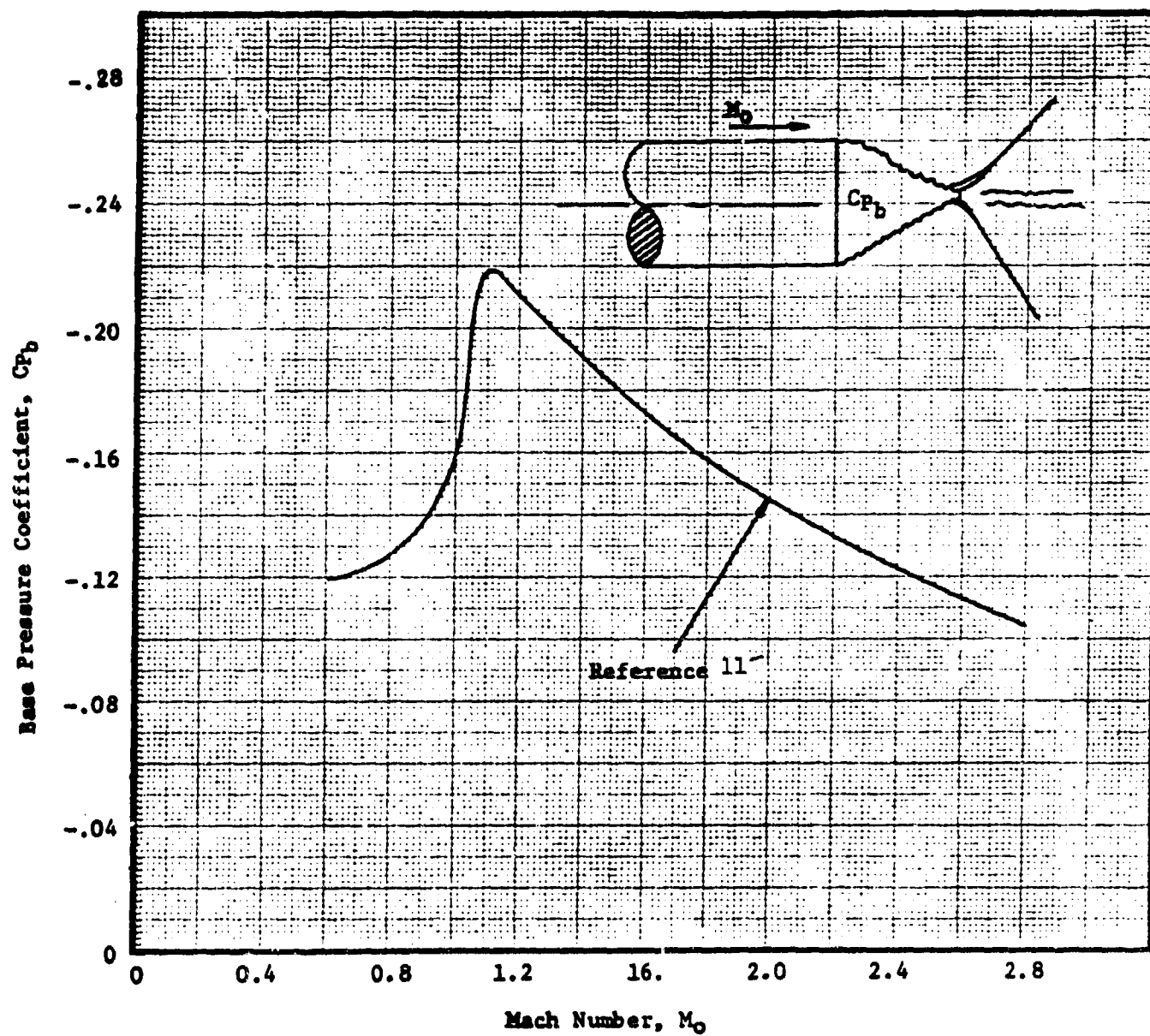


FIGURE 9-22. Base Pressure Coefficient for Cylindrical Afterbodies

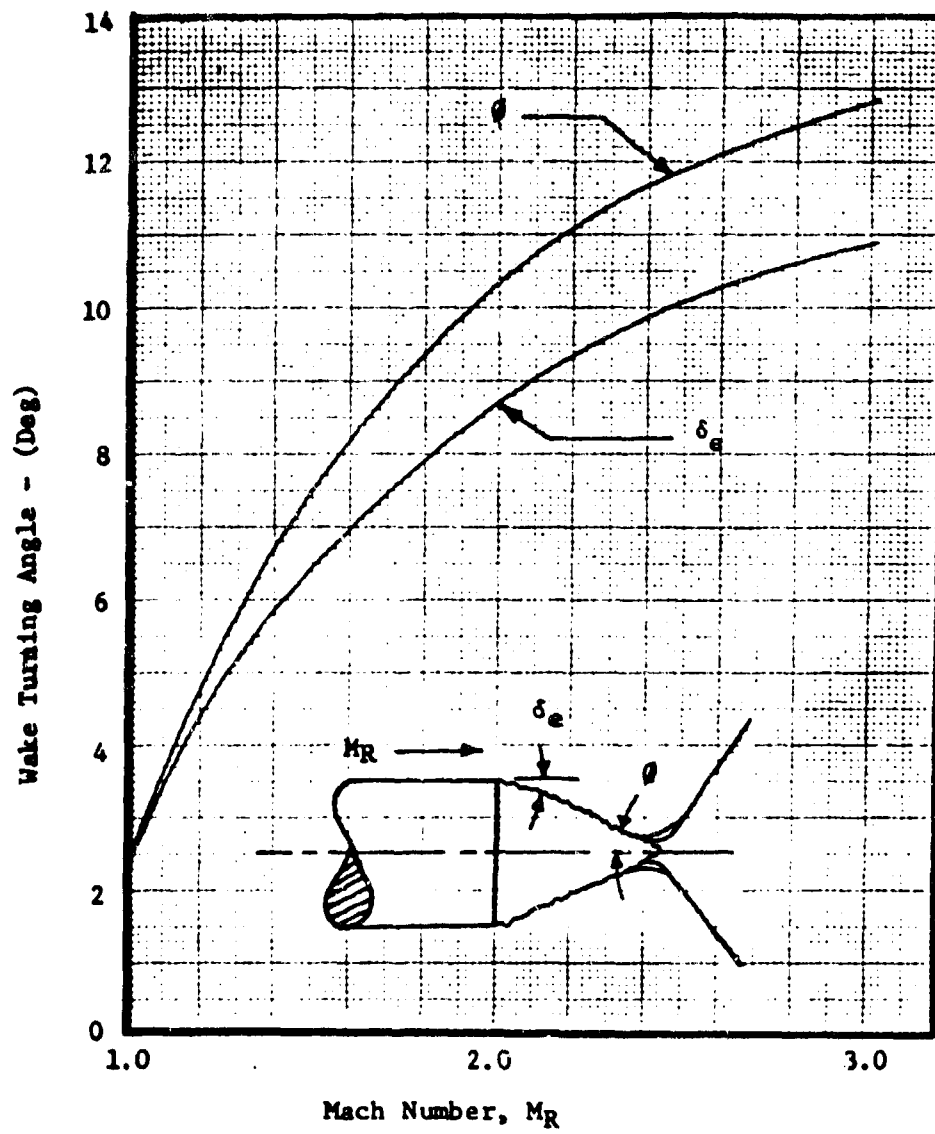


FIGURE 9-23. Axisymmetric Wake Turning Angle (Reference 8)

Rate-of-Change of Base Press. Coeff. with Boat-Tail Angle, $\frac{\Delta C_{p_b}}{\Delta \theta} - (\text{Degree})^{-1}$

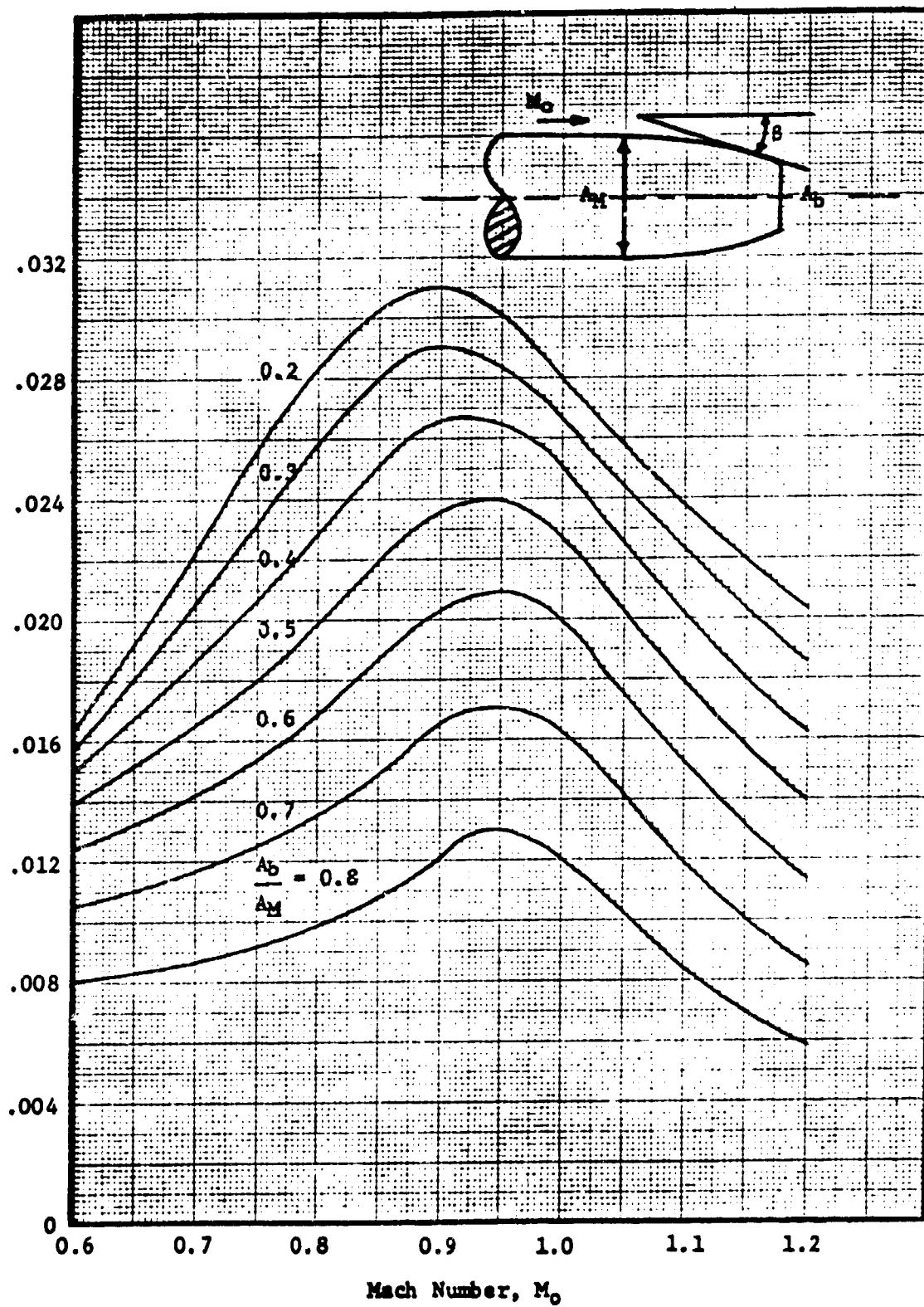


FIGURE 9-24. Subsonic-Transonic Base Pressures on Axisymmetric Boattails

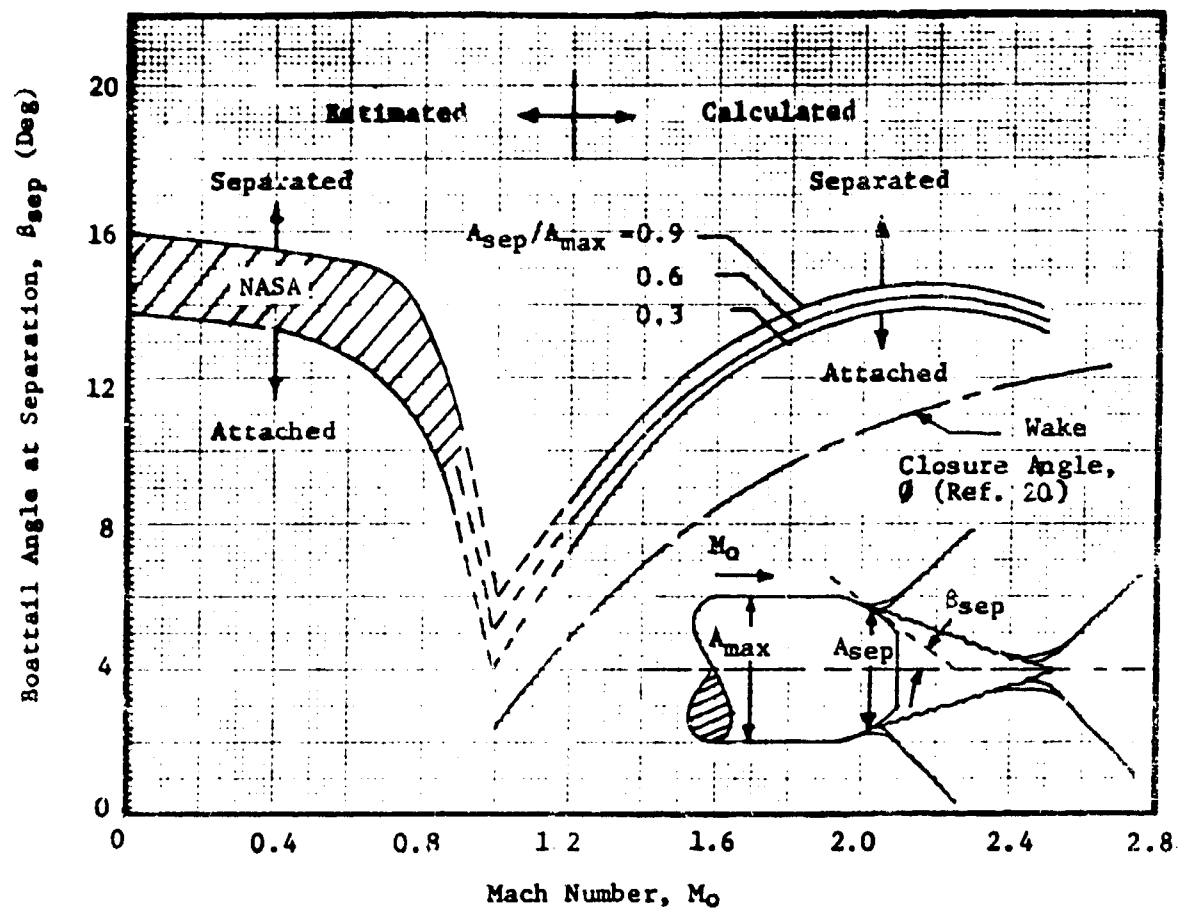


FIGURE 9-25. Axisymmetric Boattail Angle at Separation

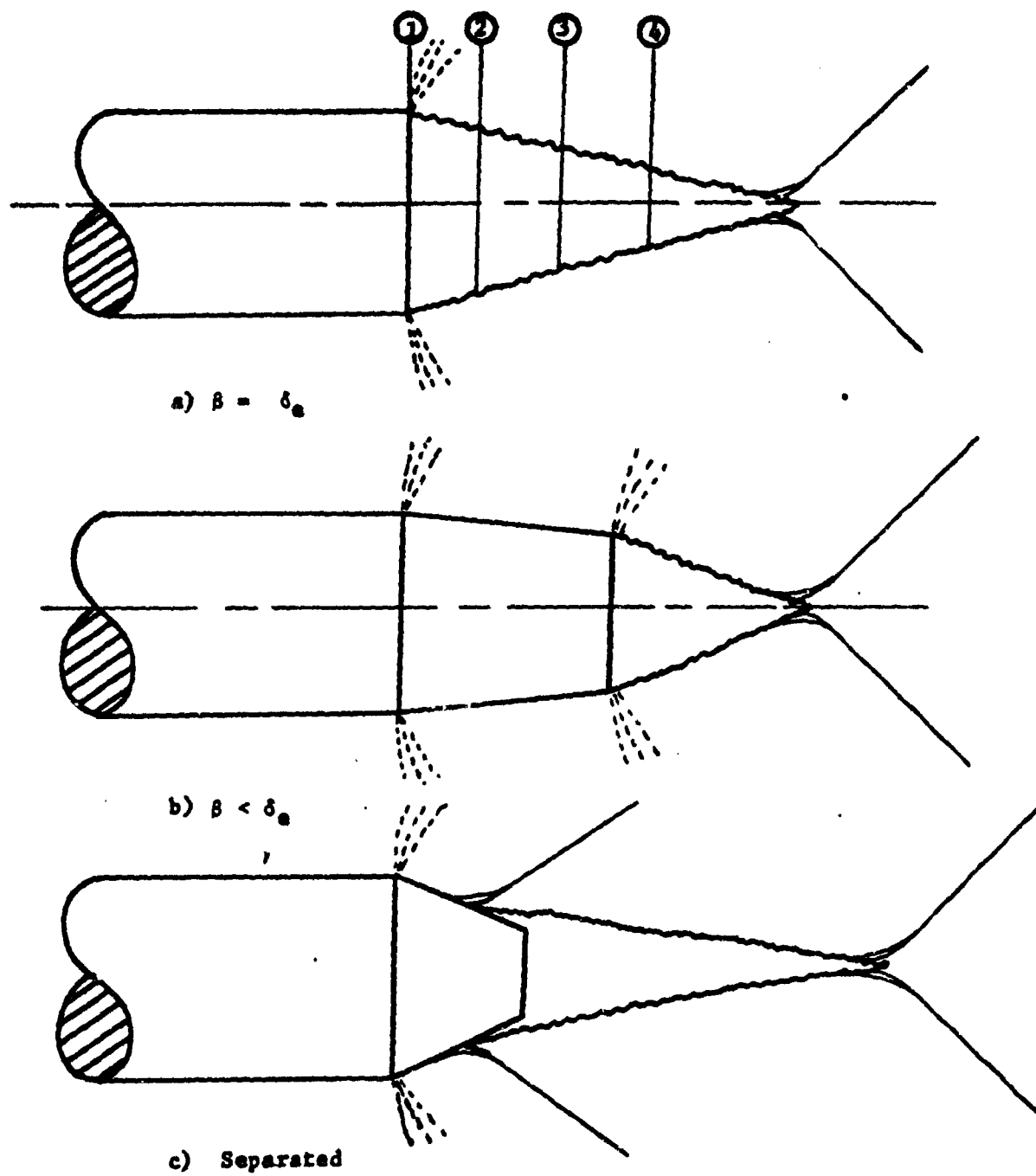


FIGURE 9-26. Axisymmetric Boattail Flow Conditions

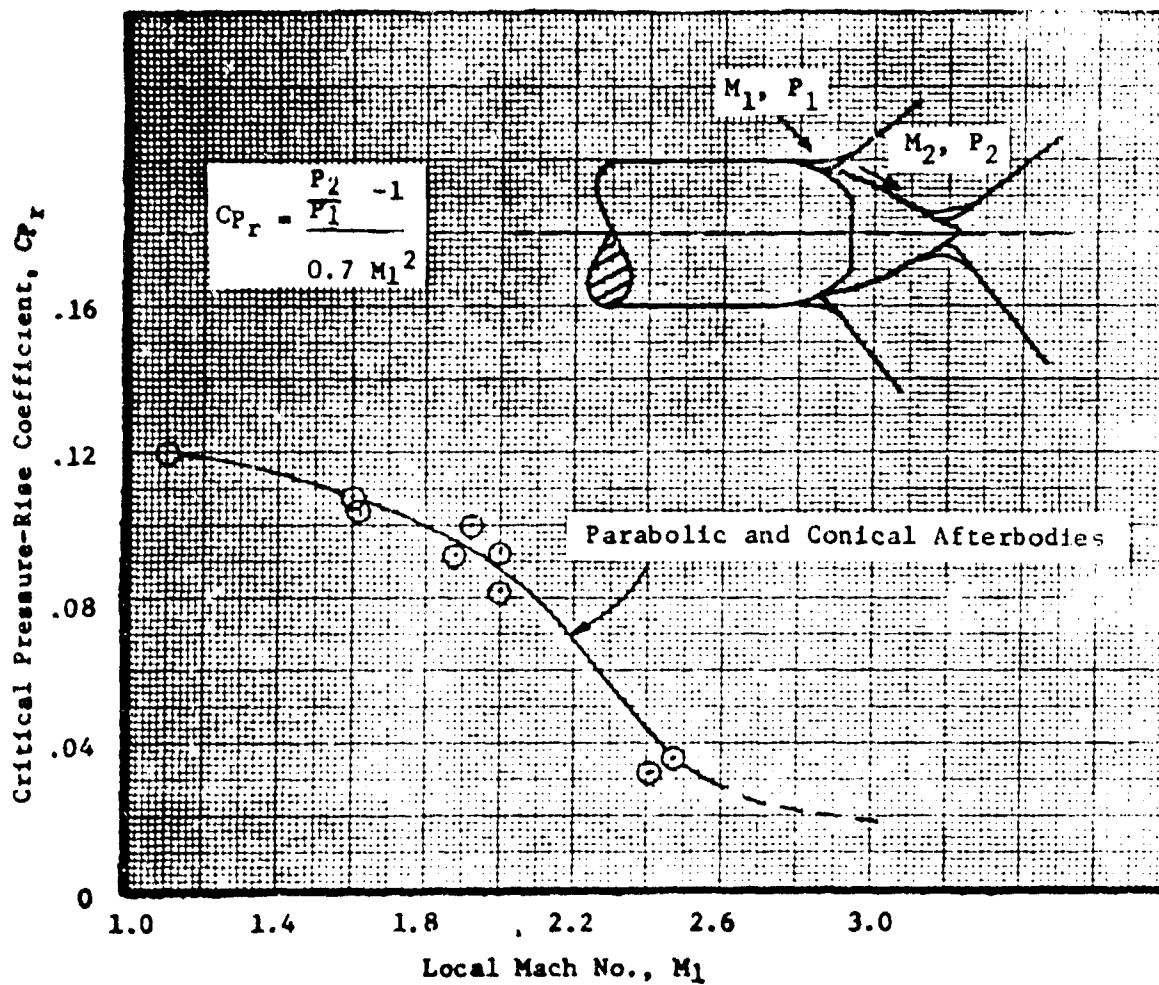


FIGURE 9- 27 Pressure Rise Required for Separation of a Turbulent Boundary Layer on Afterbodies of Revolution (Reference 6)

Note: C_{D_b} based on maximum area, $\frac{\pi D^2}{4}$

Estimated onset of separation

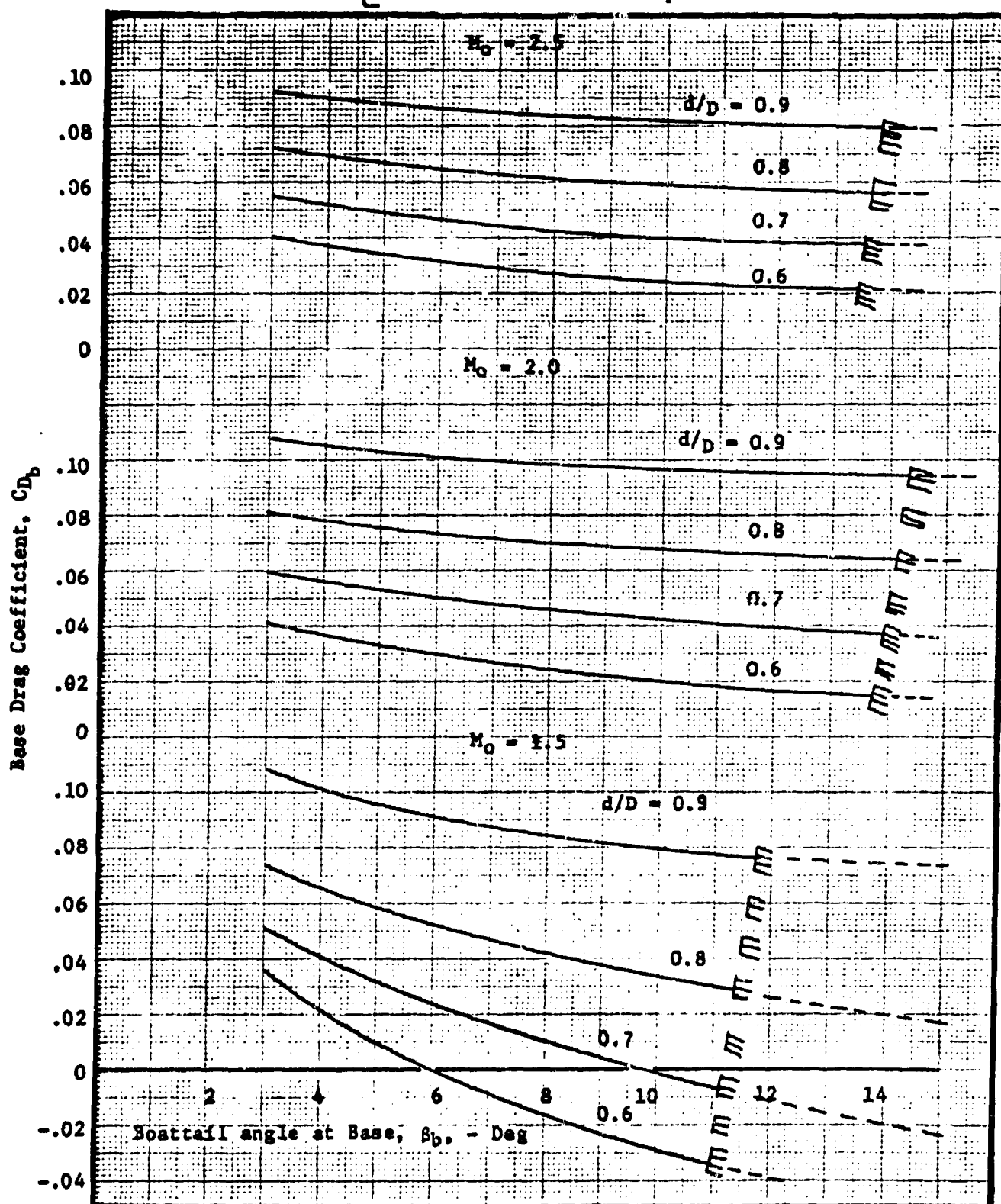


FIGURE 9-28. Supersonic Base Drag Coefficients on Axisymmetric Boattails (Reference 6)

Note: C_{D_b} based on maximum area, $\frac{\pi D^2}{4}$

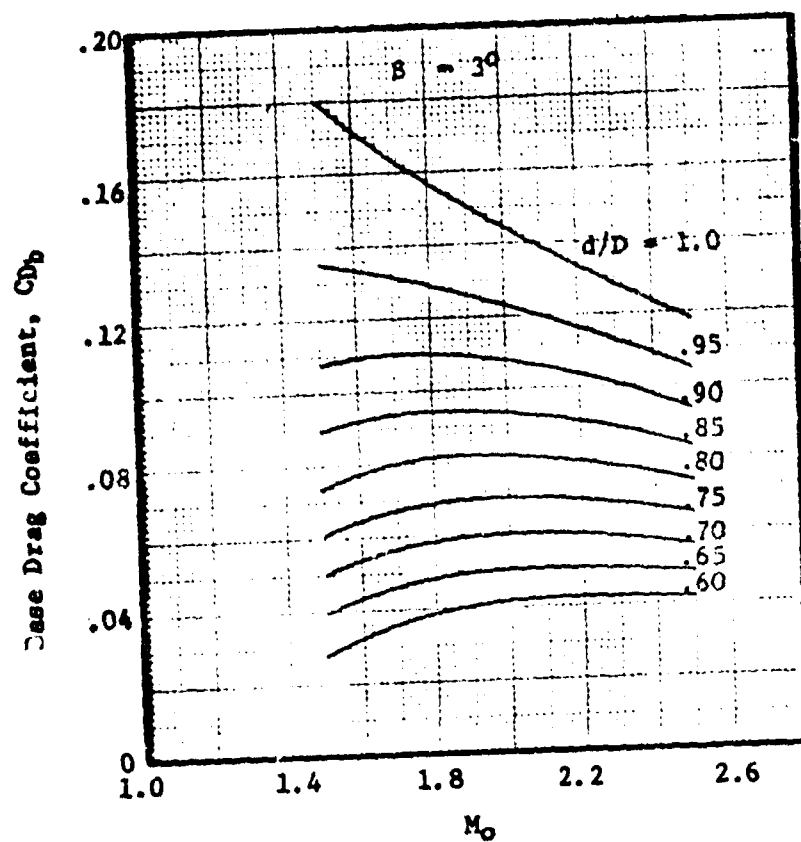


FIGURE 9-29a. Supersonic Base Drag Coefficients on Axisymmetric Boattails (Reference 6)

Note: C_{D_b} based on maximum area, $\frac{\pi D^2}{4}$

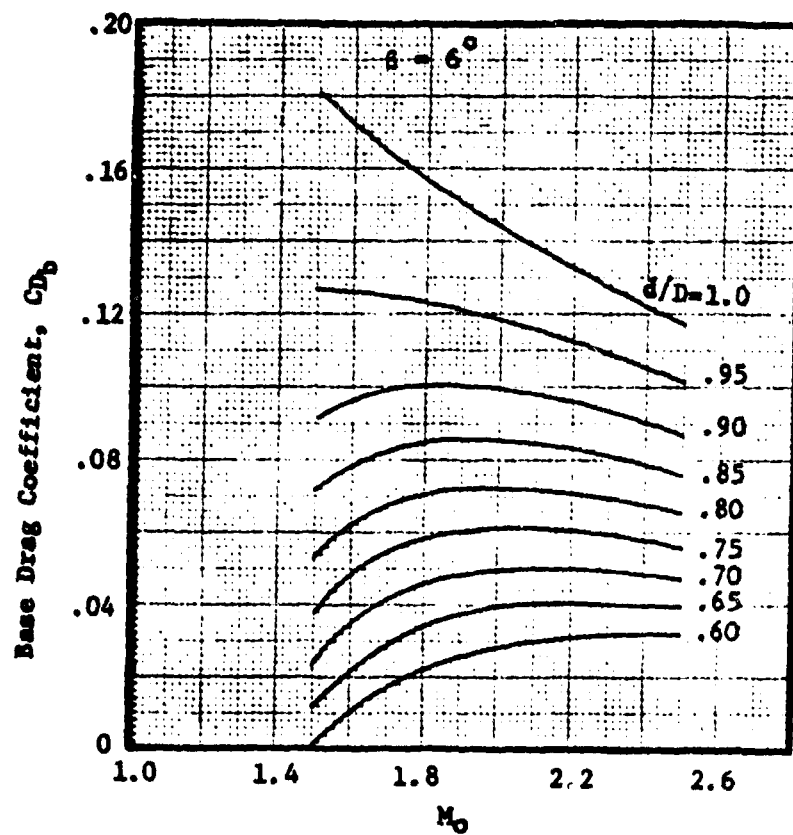


FIGURE 9-29b. Supersonic Base Drag Coefficients on Axisymmetric Boattails (Reference 6)

C_{D_b} based on maximum area, $\frac{\pi D^2}{4}$

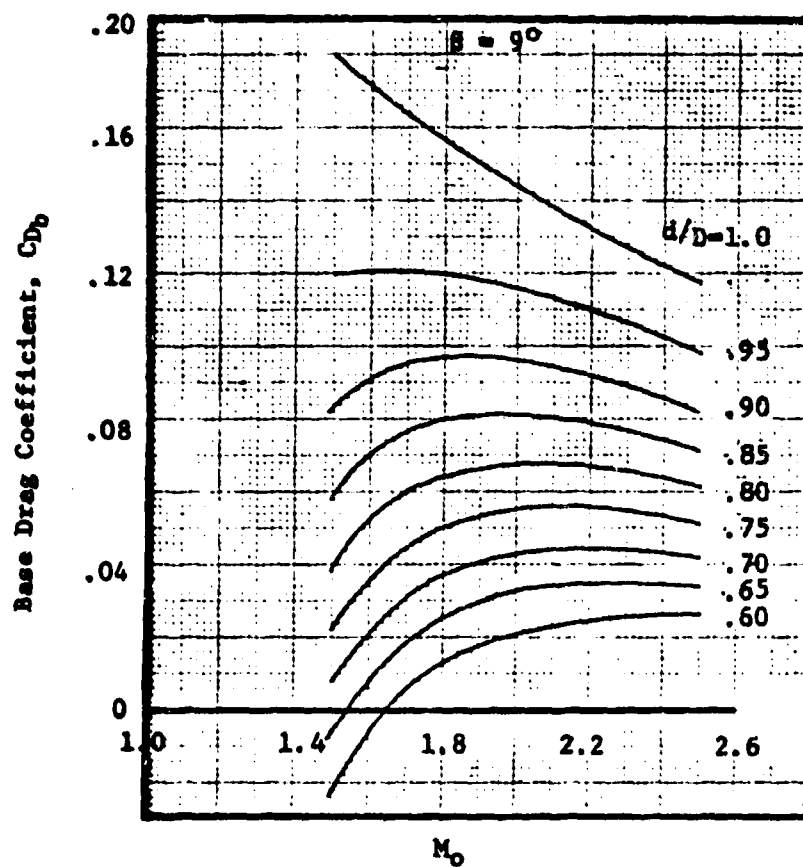


FIGURE 9-29c. Supersonic Base Drag Coefficients on Axisymmetric Boattails (Continued) (Reference 6)

Note: C_{D_b} based on maximum area, $\frac{\pi D^2}{4}$

Estimated Onset of Separation

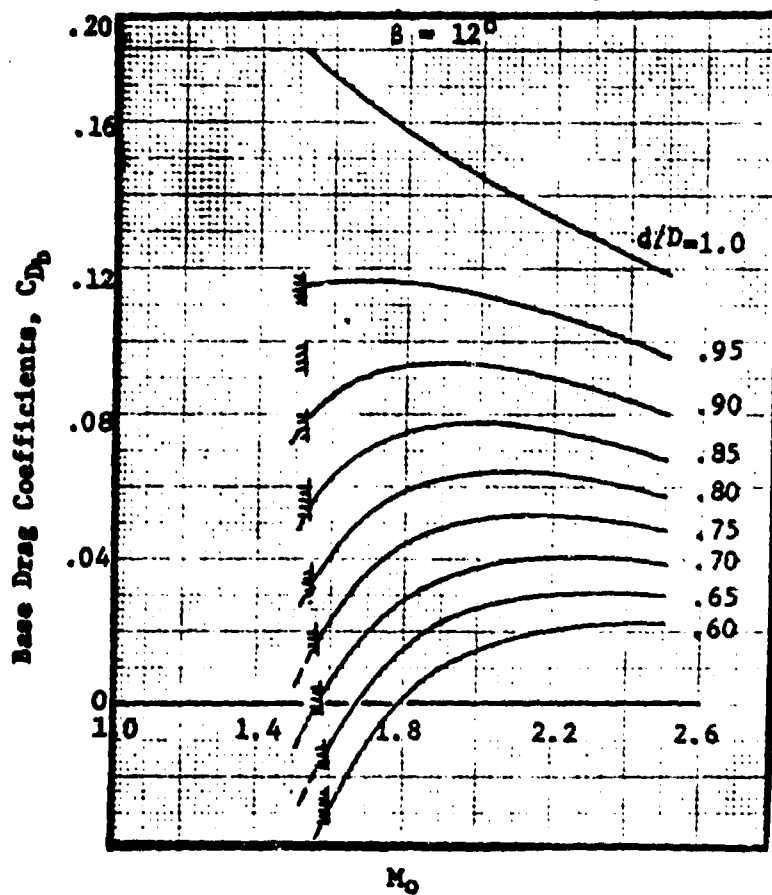


FIGURE 9-29d. Supersonic Base Drag Coefficients on Axisymmetric Boattails (Continued) (Reference 6)

Note: $\frac{1}{4}$ on maximum area, $\frac{vD^2}{4}$

region of separated flow

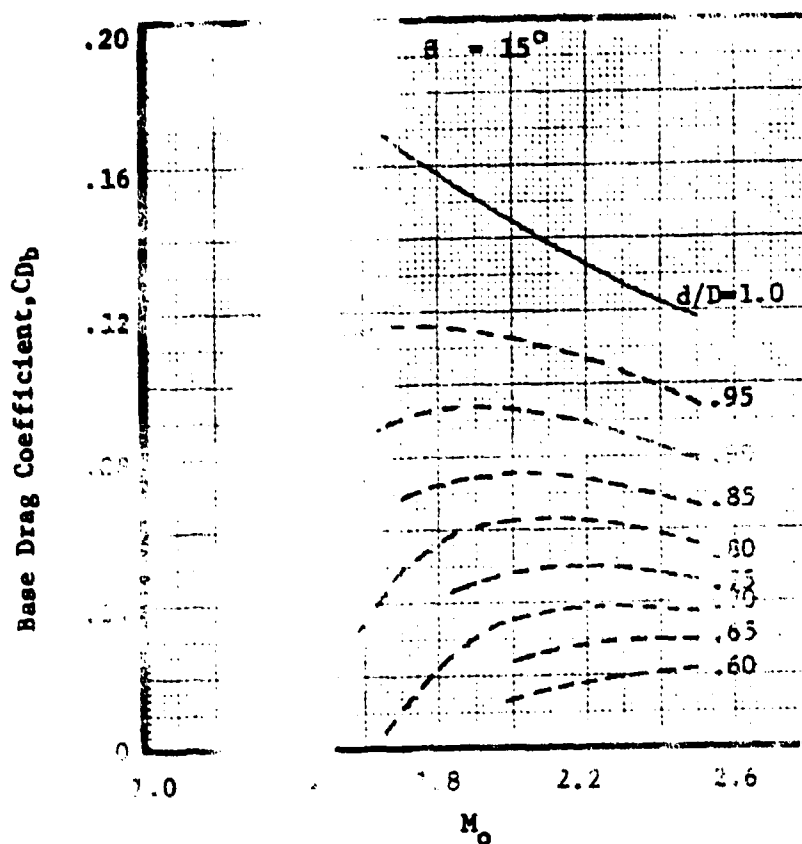


FIGURE 9-29a. Supersonic Base Drag Coefficients on Axisymmetric Boattails (Concluded) (Reference 6)



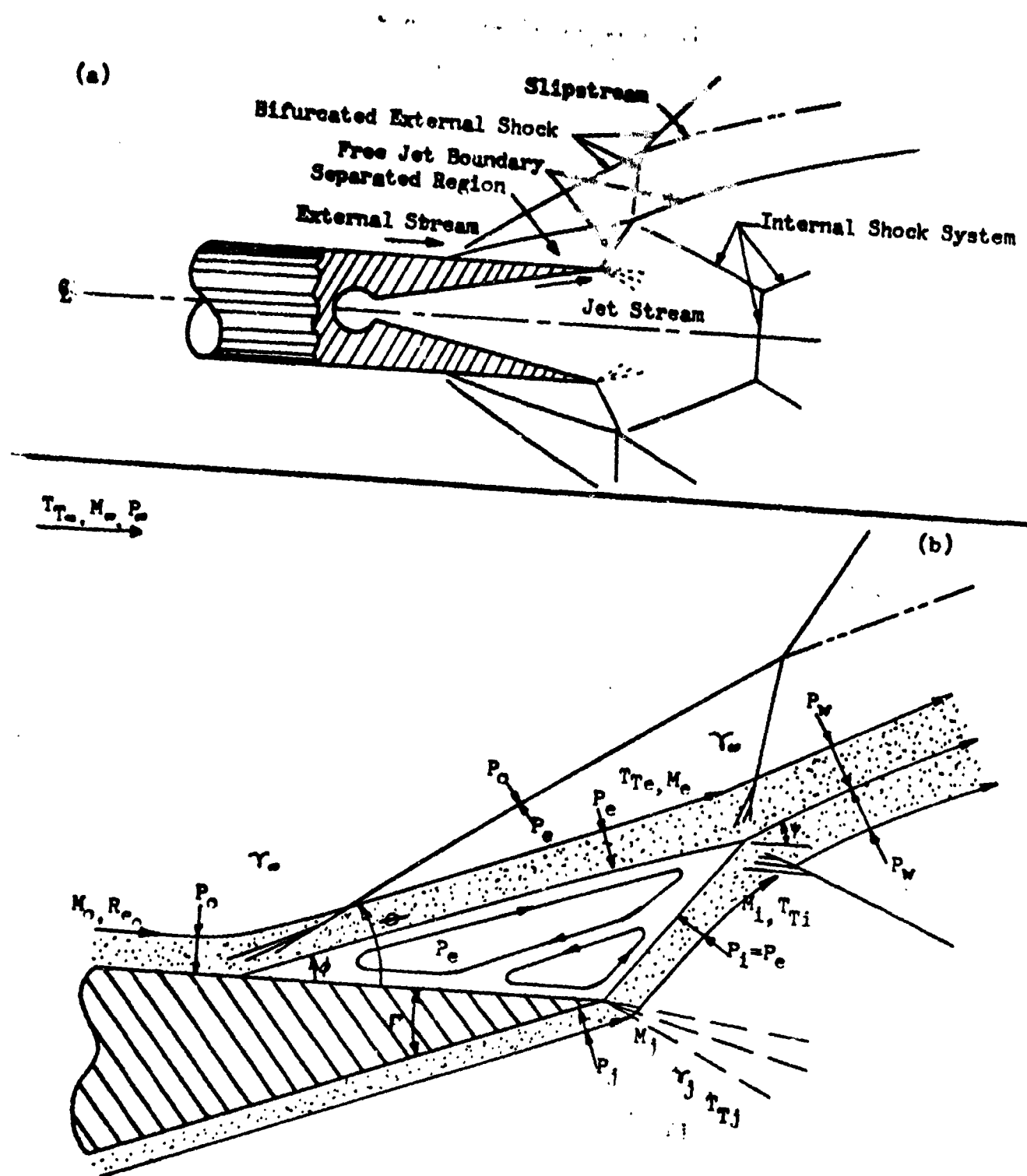


FIGURE 9-31. Schematic Diagram of Separated External Flow

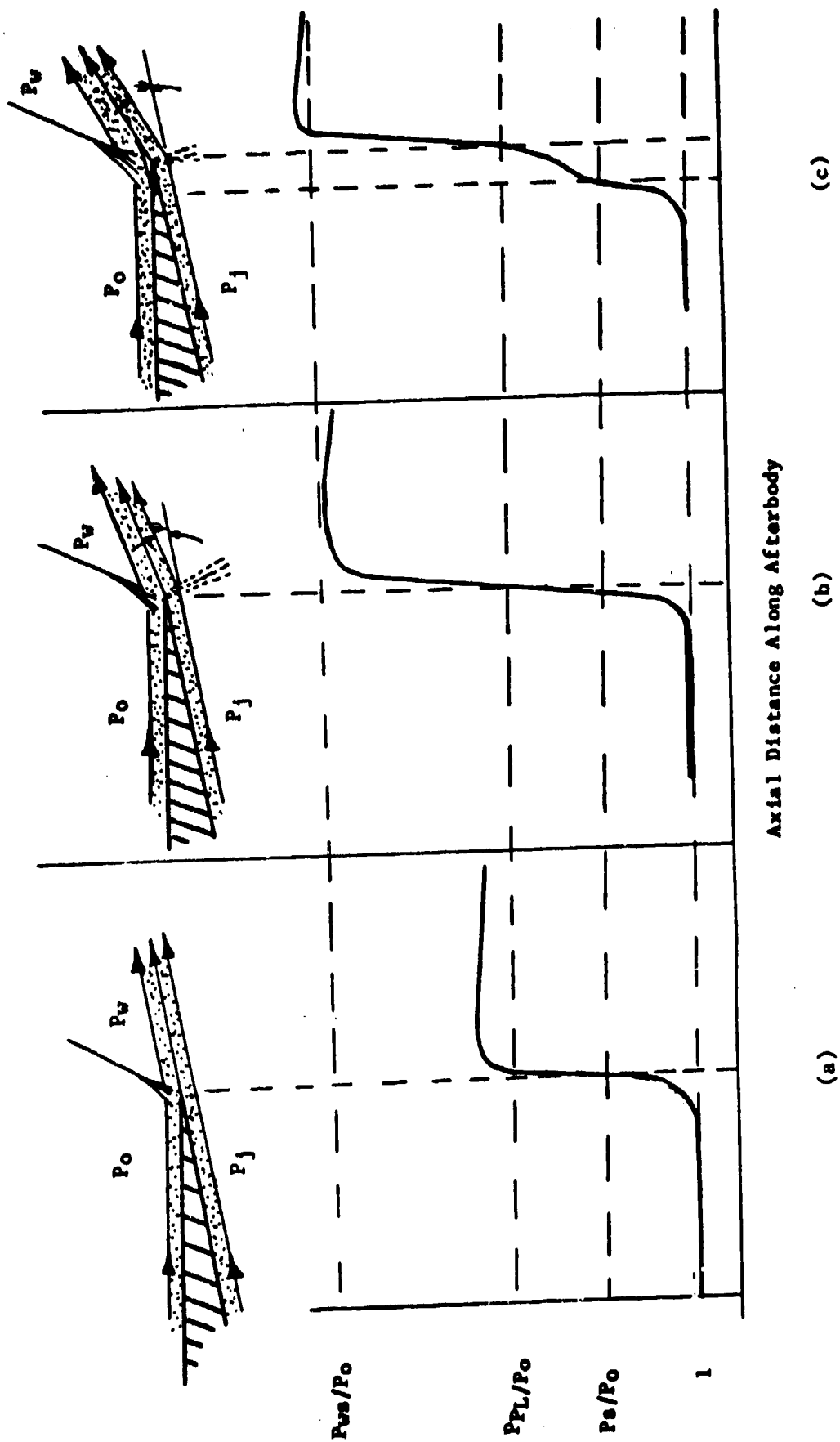
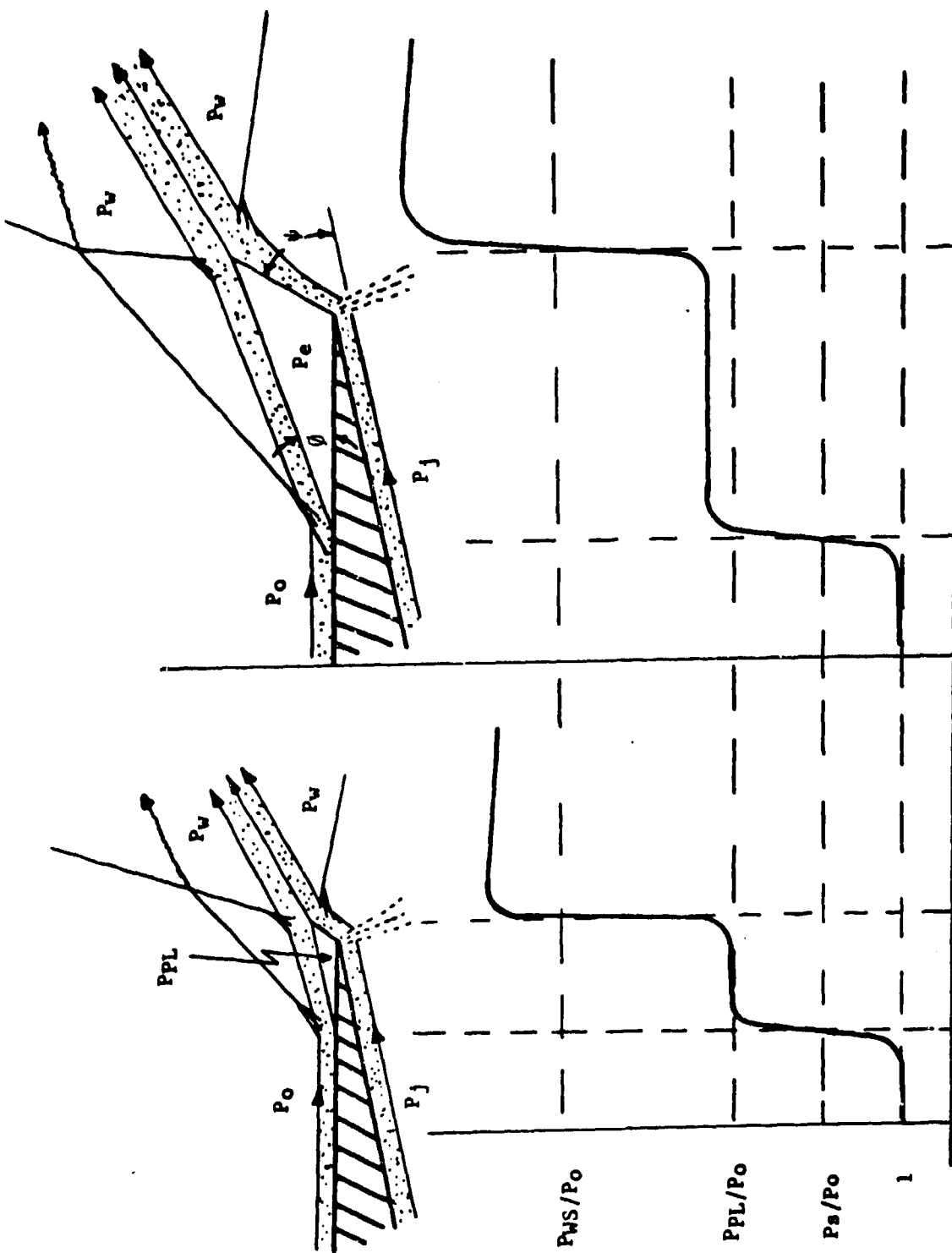


FIGURE 9-32 a. Sequence of Events Denoting Jet Interference Effects on Afterbody (Reference 25).



Sequence of Events Denoting Jet Interference Effects on Afterbody (Reference 29) - Concluded

(d)

(e)

FIGURE 9-32b Sequence of Events Denoting Jet Interference Effects on Afterbody (Reference 29) - Concluded

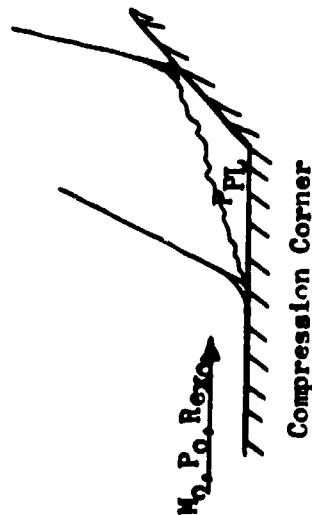
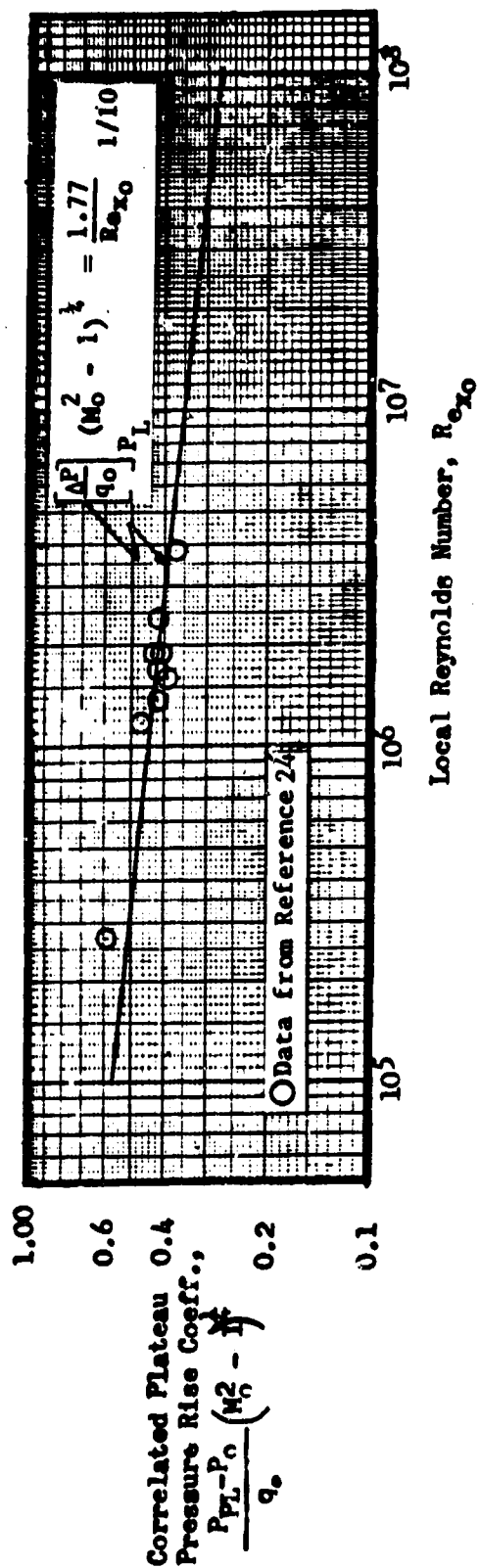


FIGURE 9-33. Plateau Pressure Rise Coefficient in Turbulent Separated Flow (Reference 42)

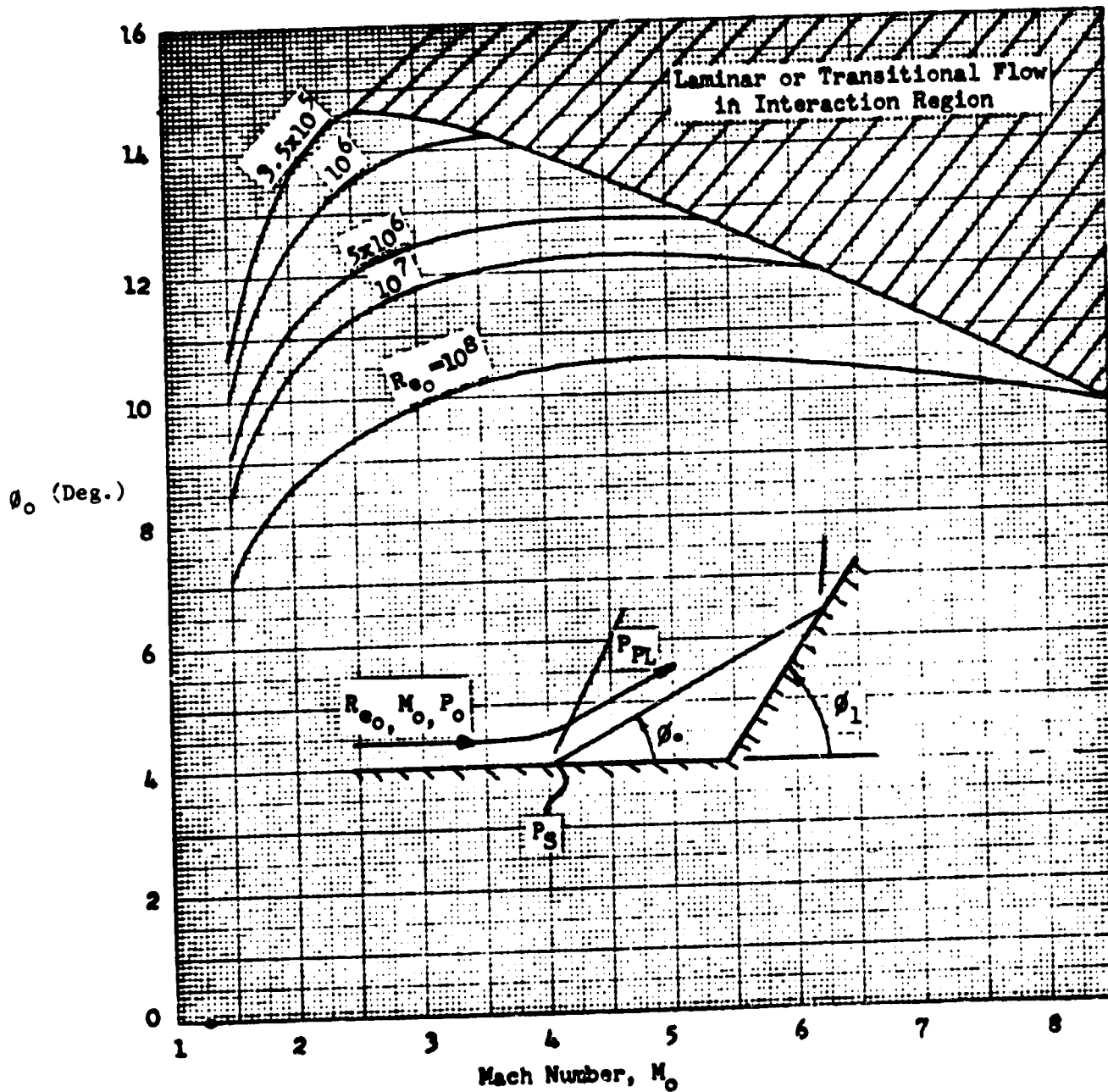


FIGURE 9-34. Turning Angle Required to Compress Flow to Plateau Pressure Level (Reference 25)

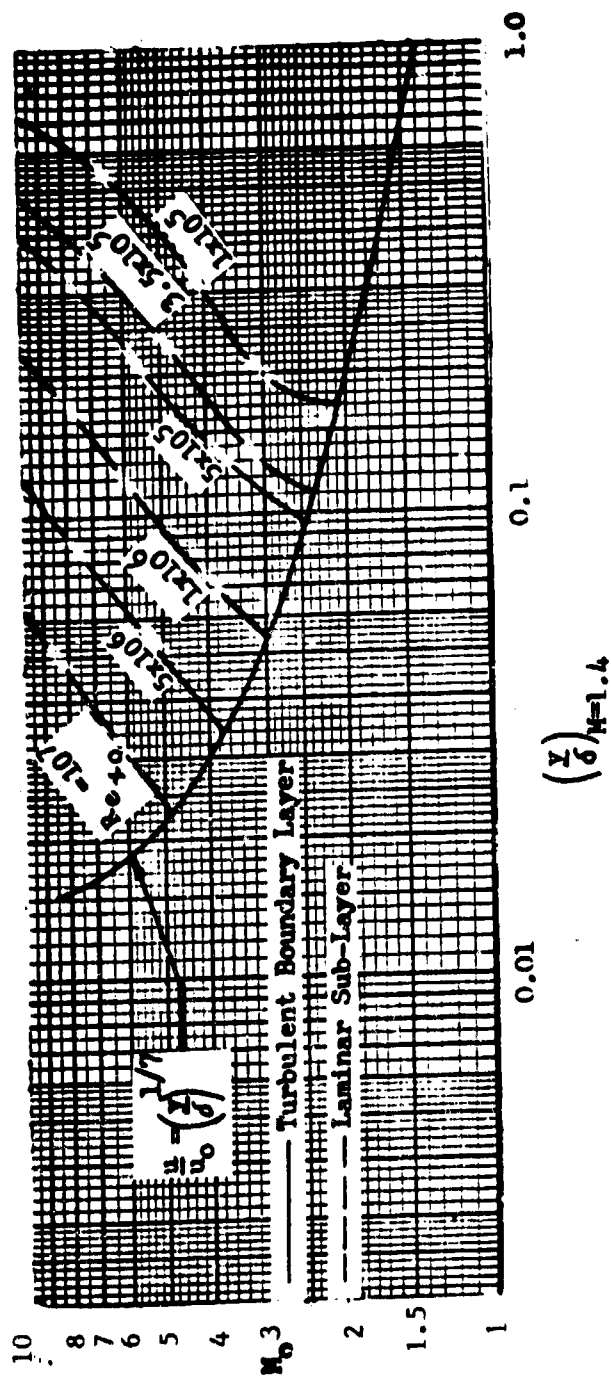


FIGURE 9-35. Height of Mach 1.4 Line in Turbulent Boundary Layer

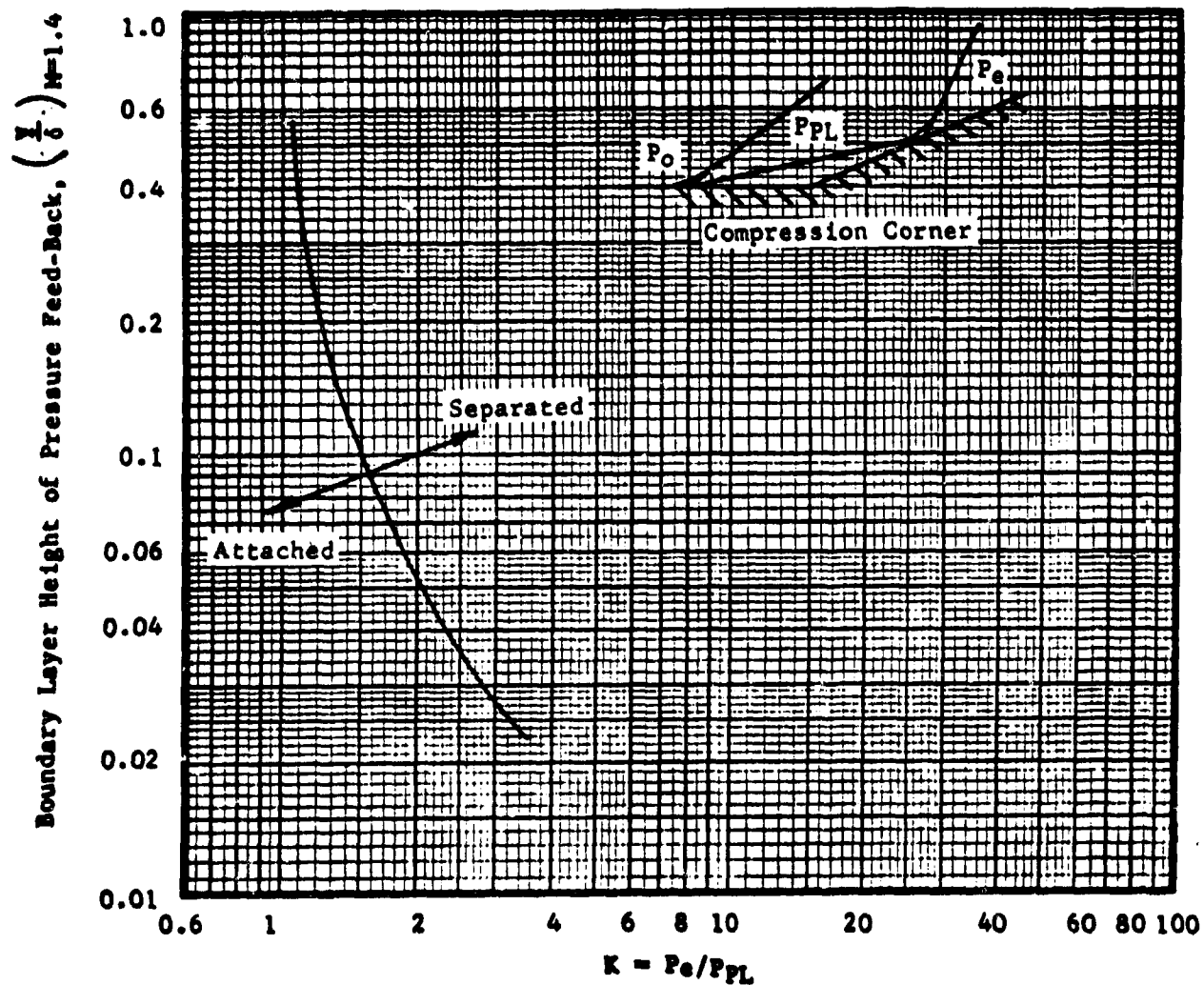


FIGURE 9-36. Effect of Pressure Feed-Back on Incipient Separation of Turbulent Boundary Layer (Reference 32)

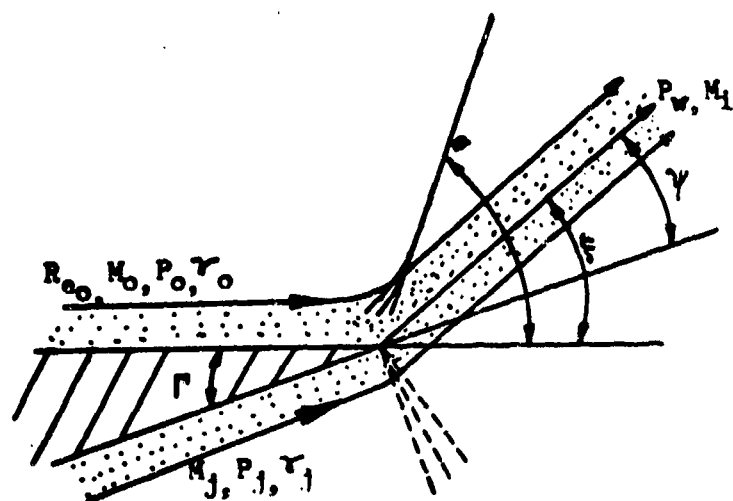


FIGURE 9-37. Flow Schematic of Jet Interference Problem with Attached Boundary Layer

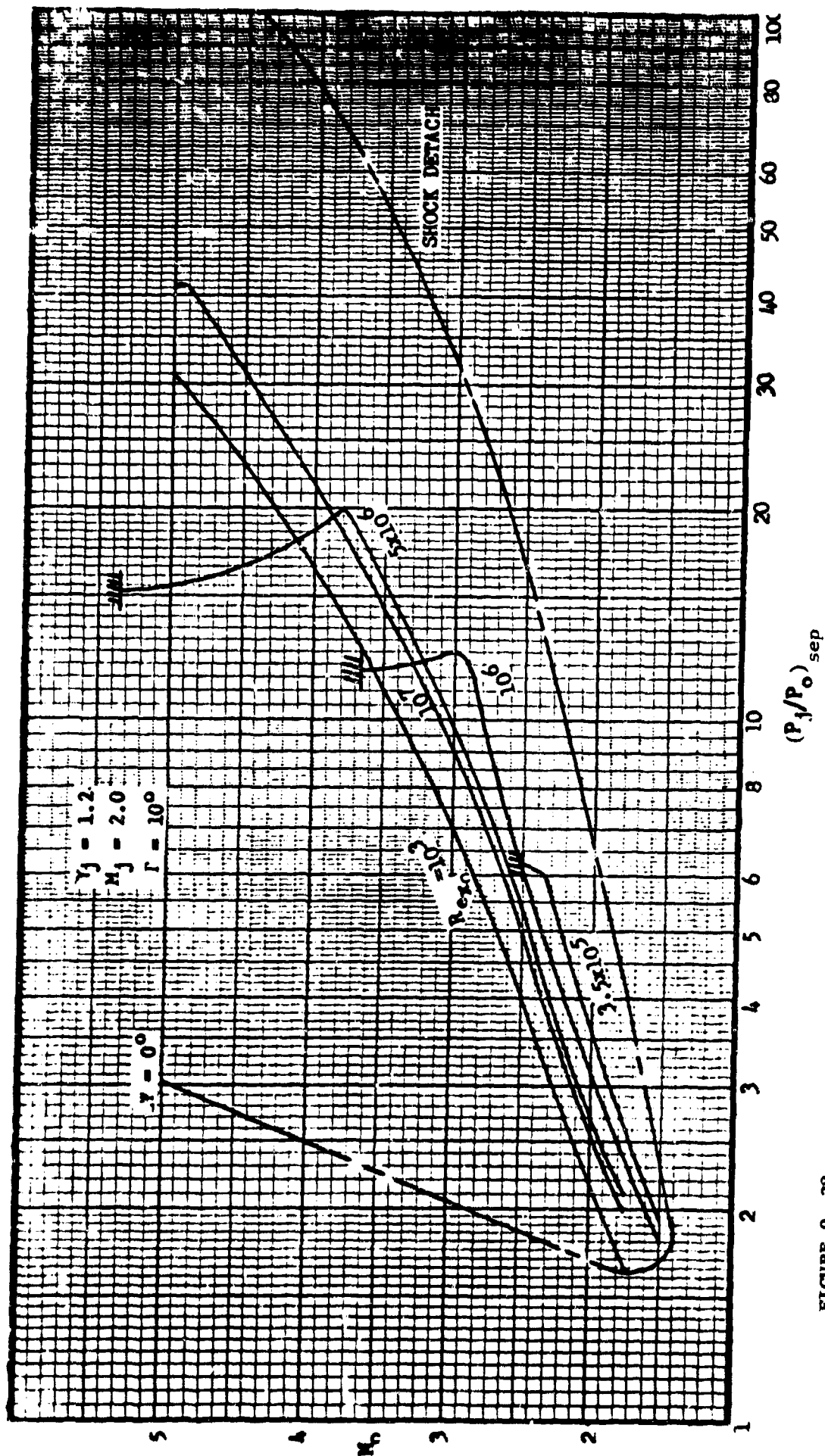


FIGURE 9-38. Calculated Requirements for Incipient Separation

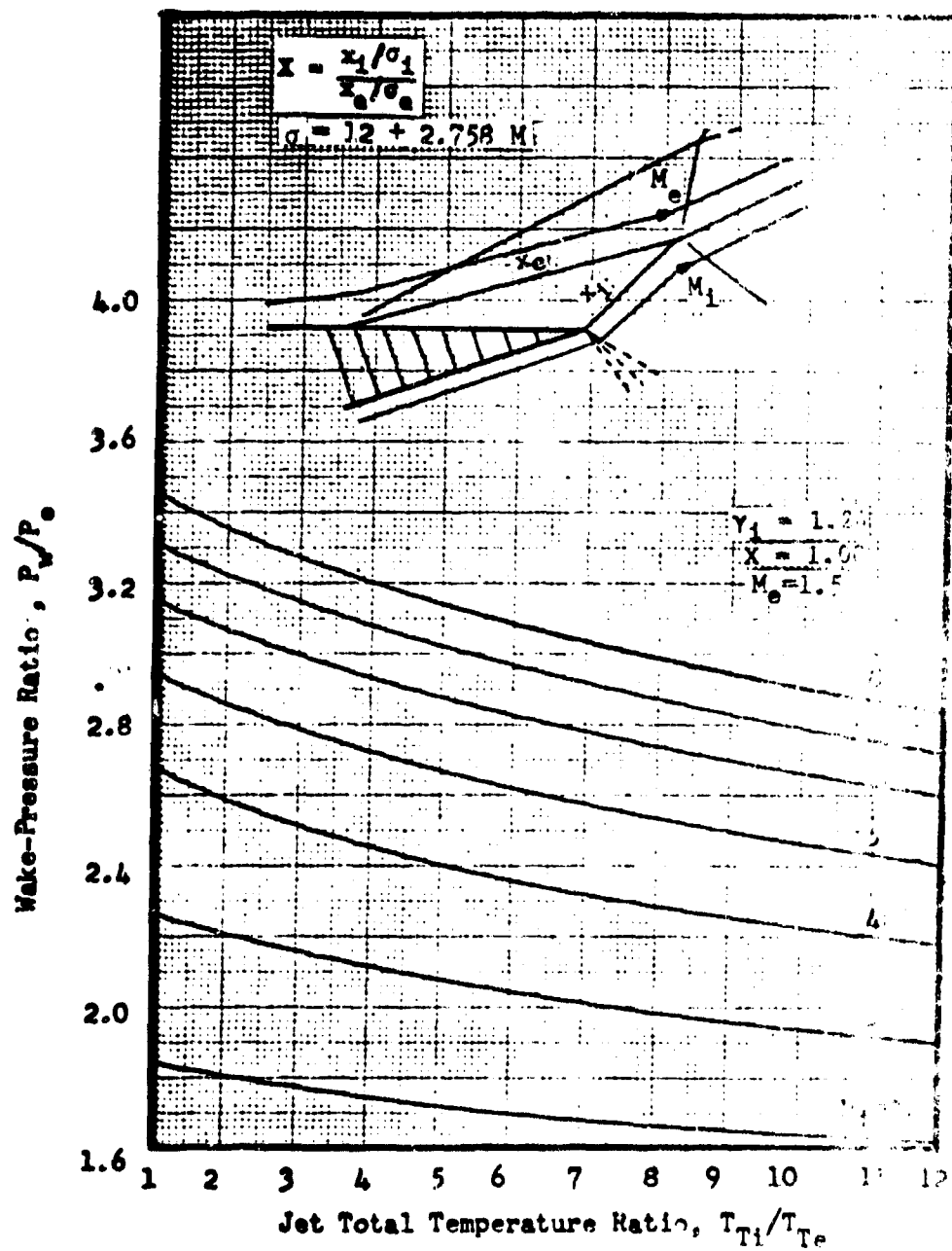


FIGURE 9-39a. Effect of Jet Temperature Ratio on Wake Pressure Ratio - Continued (Reference 25)

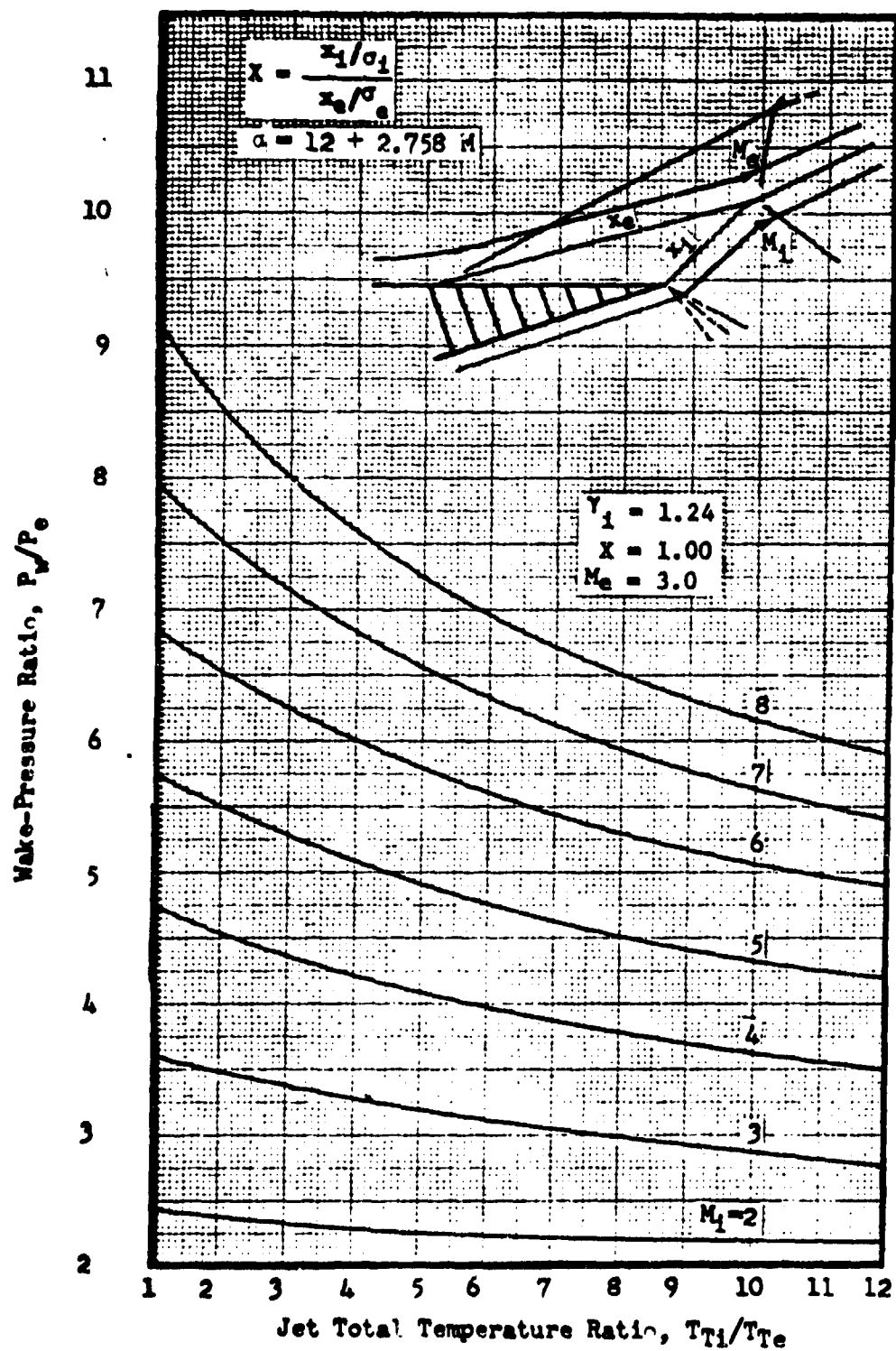


FIGURE 9-39b. Effect of Jet Temperature Ratio on Wake Pressure Ratio - Continued (Reference 25)

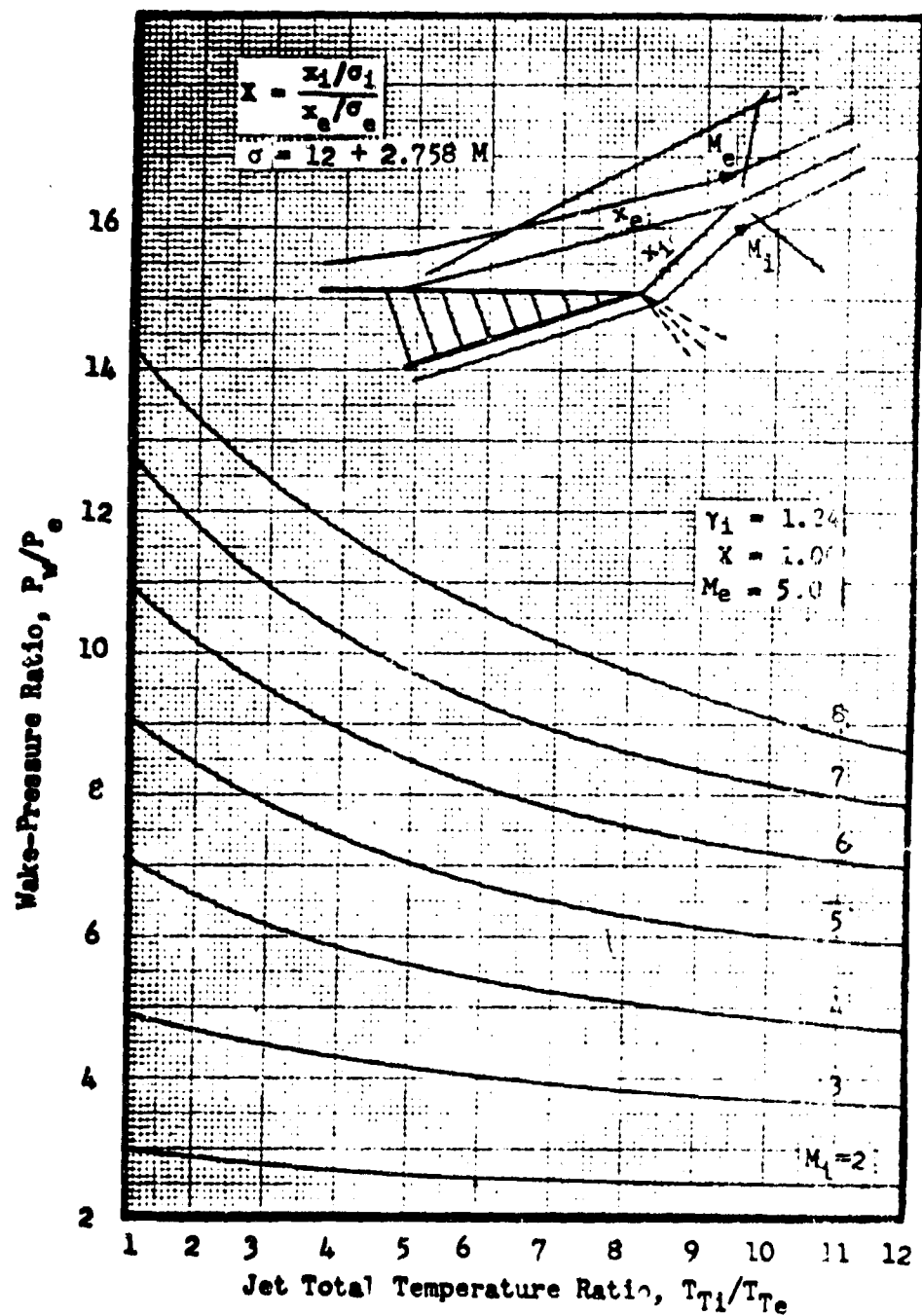


FIGURE 9-39c. Effect of Jet Temperature Ratio on Wake Pressure Ratio - Concluded (Reference 25)

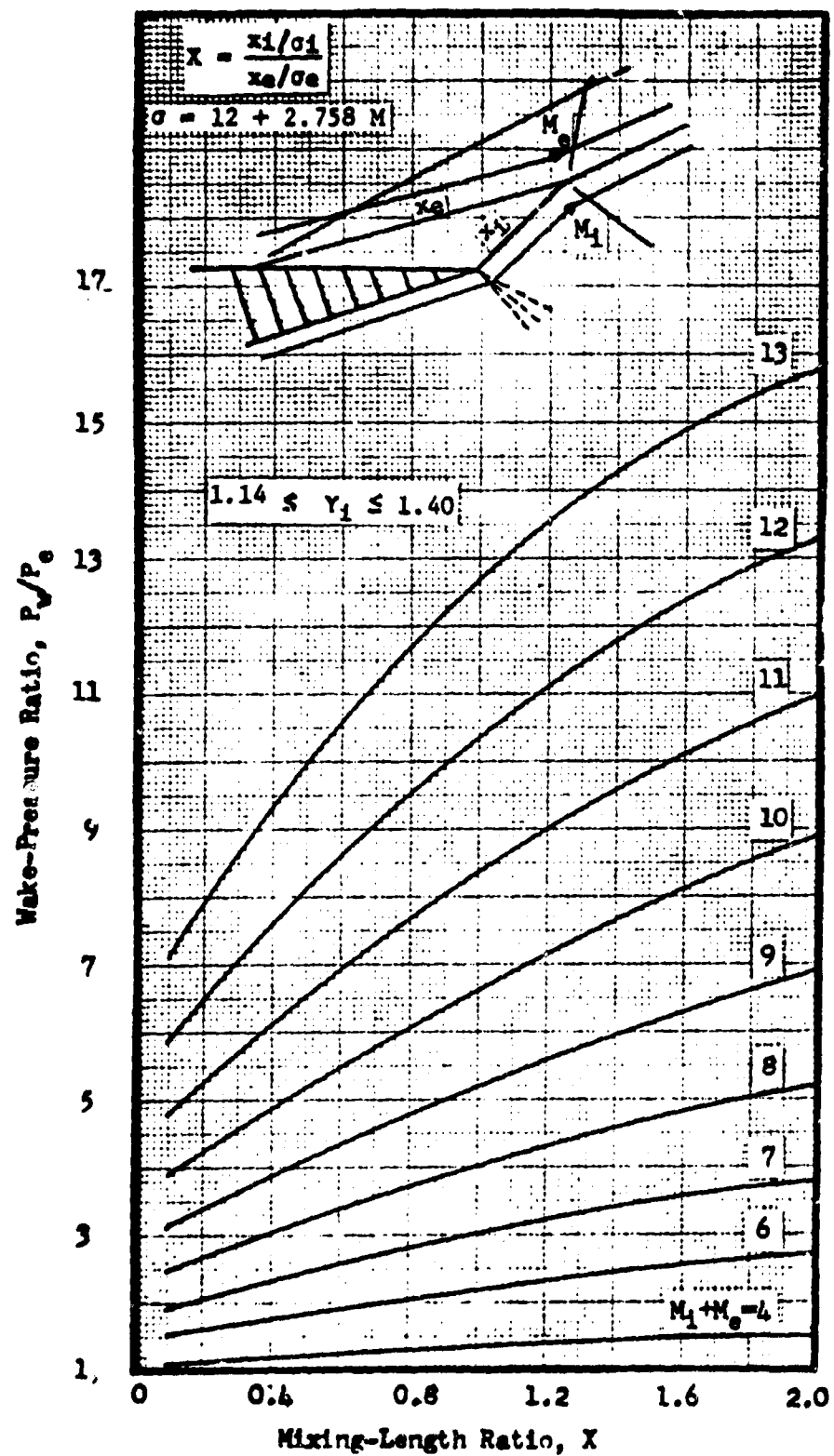


FIGURE 9-40. Effect of Mixing Length Ratio on Wake-Pressure Ratio (Reference 25)

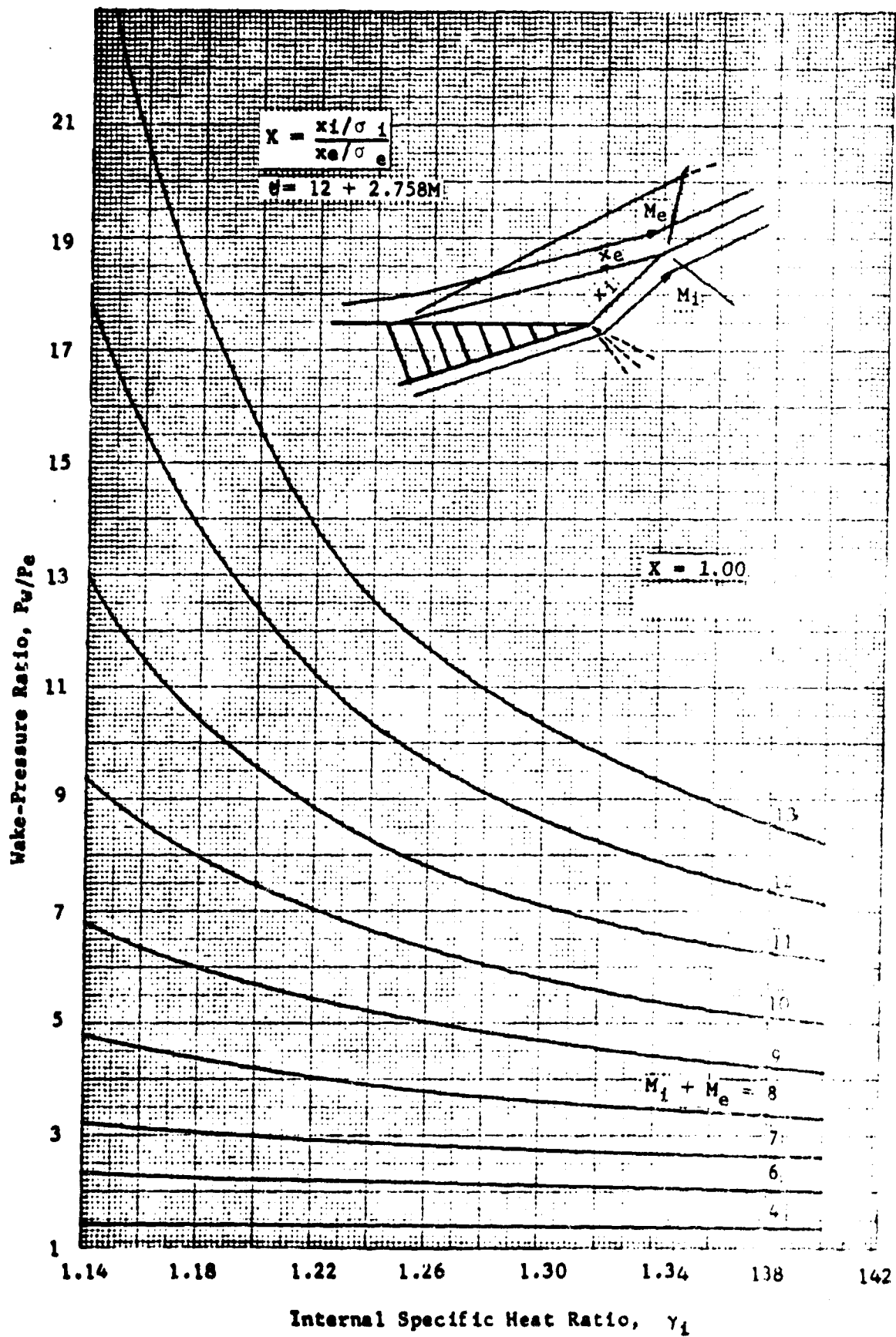


FIGURE 9-41. Effect of Internal Specific Heat Ratio on Wake-Pressure Ratio

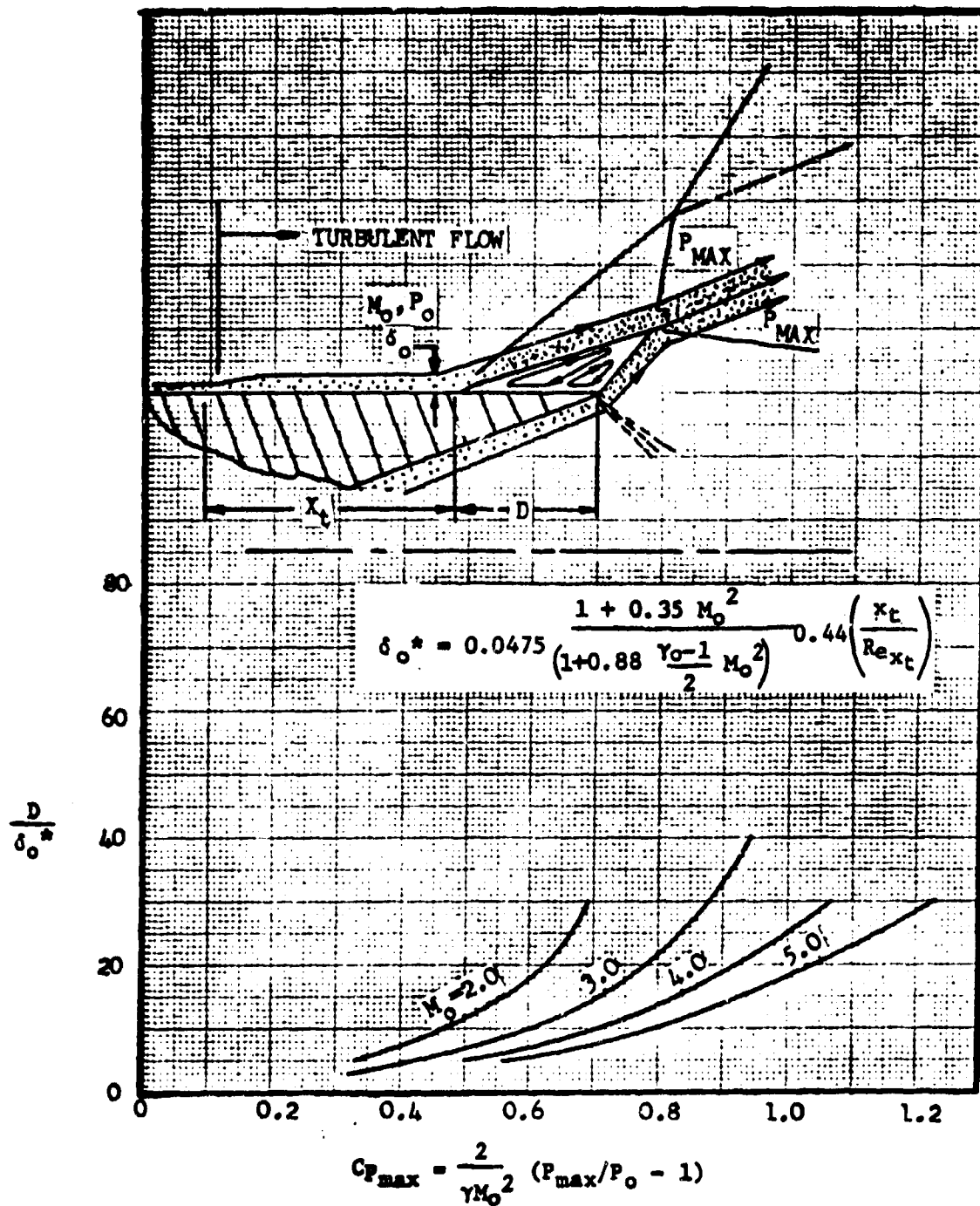


FIGURE 9-42. Extent of Separation Upstream of Disturbance for Turbulent Flow

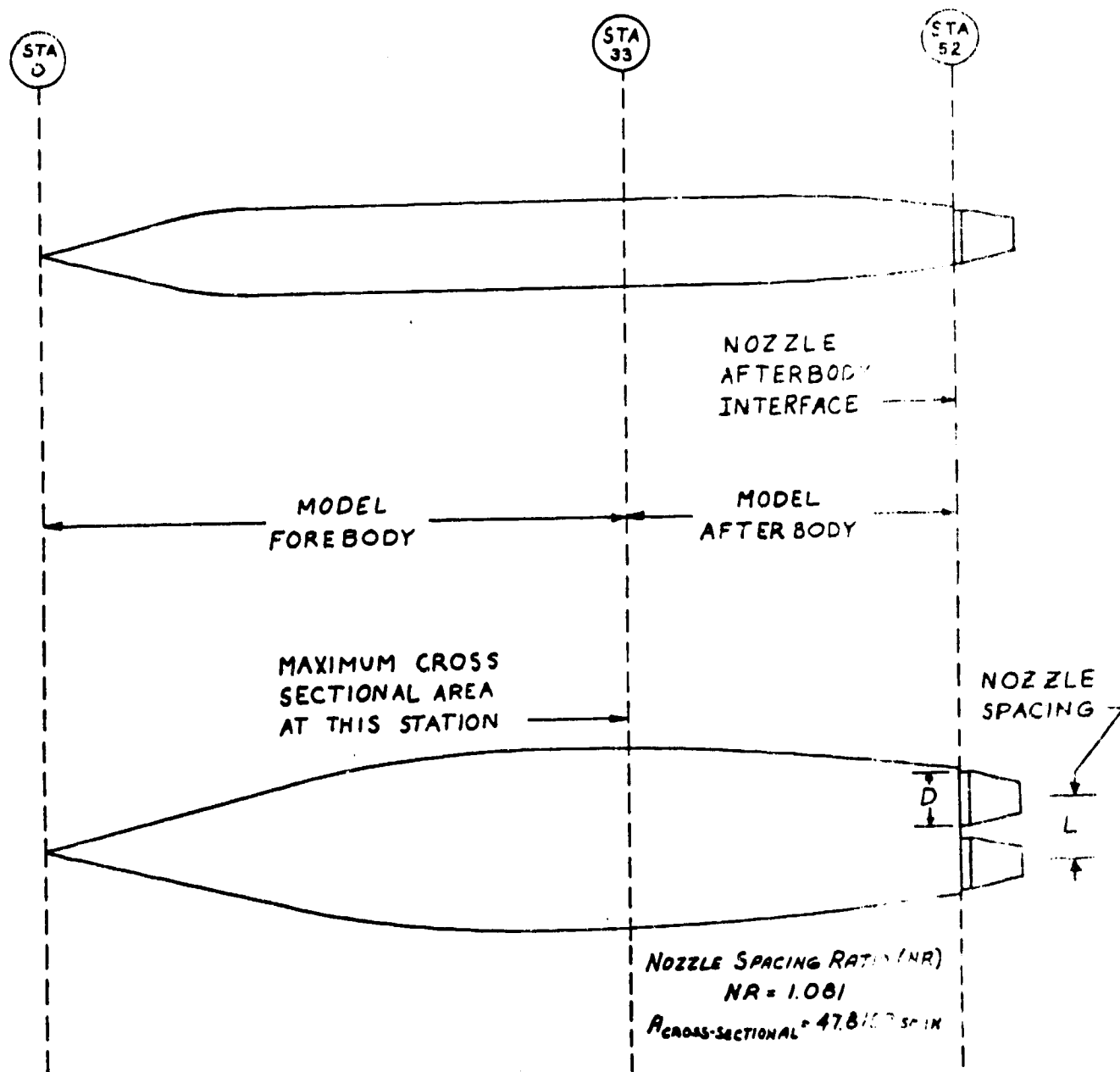
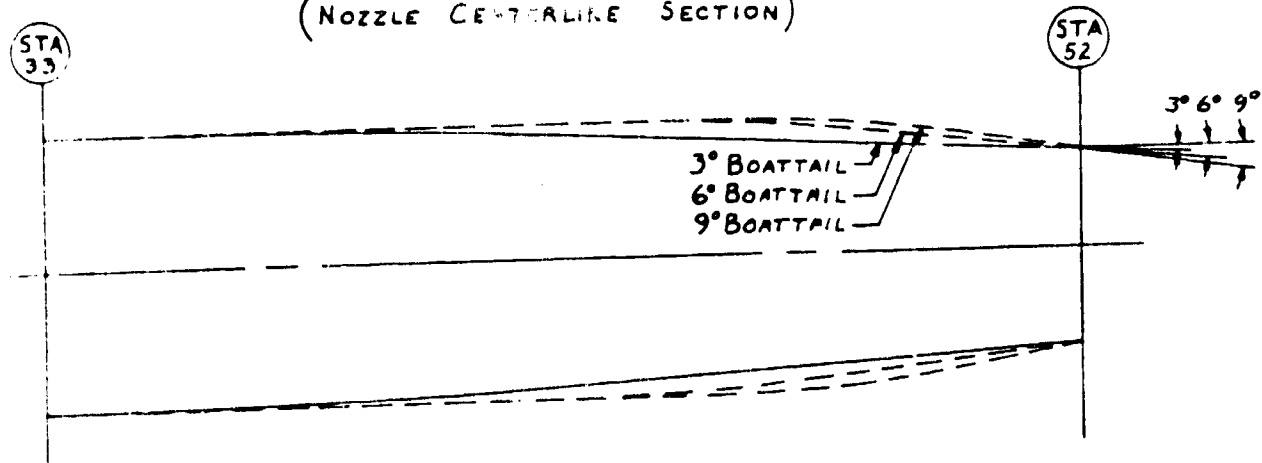


FIGURE 9-43: The Geometric Parameters Held Constant during the NR-Langley Tests are Illustrated

AFTERBODY BOATTAIL ANGLE
(NOZZLE CENTERLINE SECTION)



INTERENGINE FAIRING CONTOUR
(MODEL CENTERLINE SECTION)

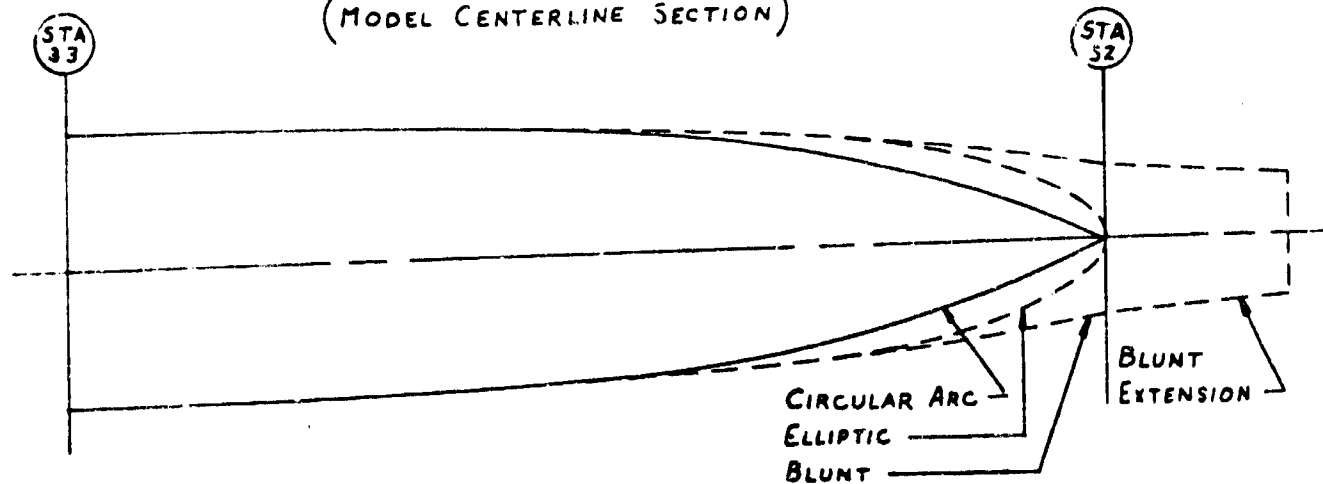
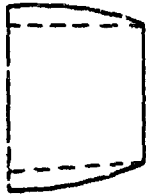


FIGURE 9-44a: The Geometric Parameters Varied during the NR-Langley Tests are Illustrated

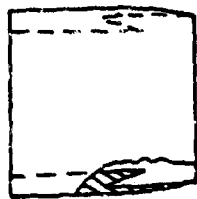
NOZZLE TYPE

(ALL NOZZLES ARE AXISYMMETRIC)

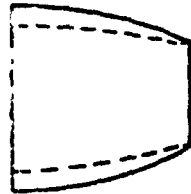
ST
J2



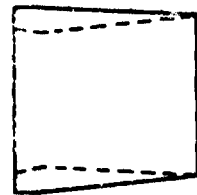
IRIS NOZZLE - AUGMENTED



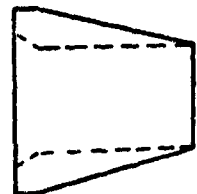
SHROUDED IRIS NOZZLE - AUGMENTED



IRIS NOZZLE - NON-AUGMENTED



CONVERGENT-DIVERGENT NOZZLE - AUGMENTED



CONICAL NOZZLE - NON-AUGMENTED

FIGURE 9-44b: The Geometric Parameters Varied during the NR-Langley Tests are Illustrated

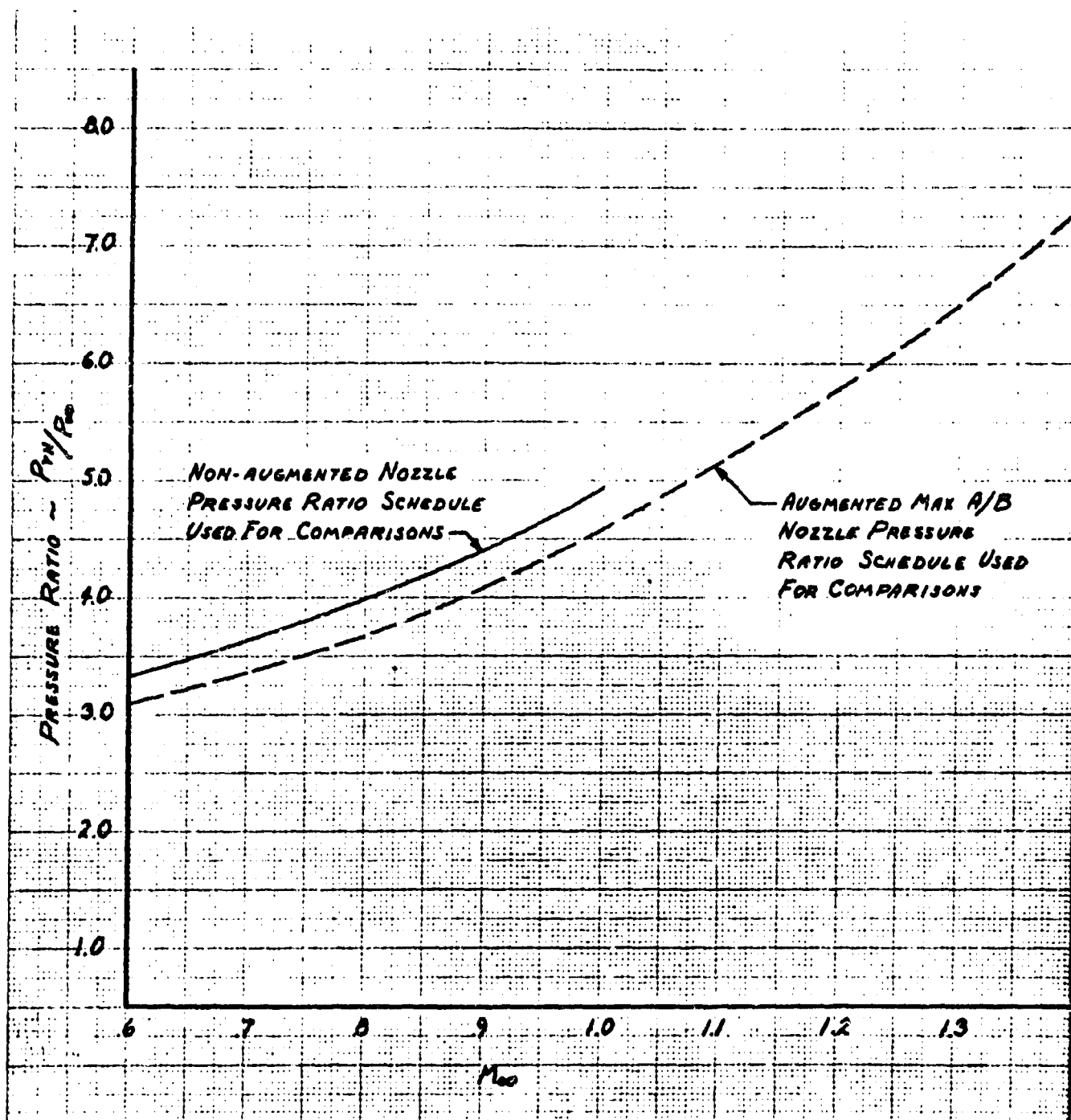


FIGURE 9-45: Nozzle Pressure Ratio Schedule

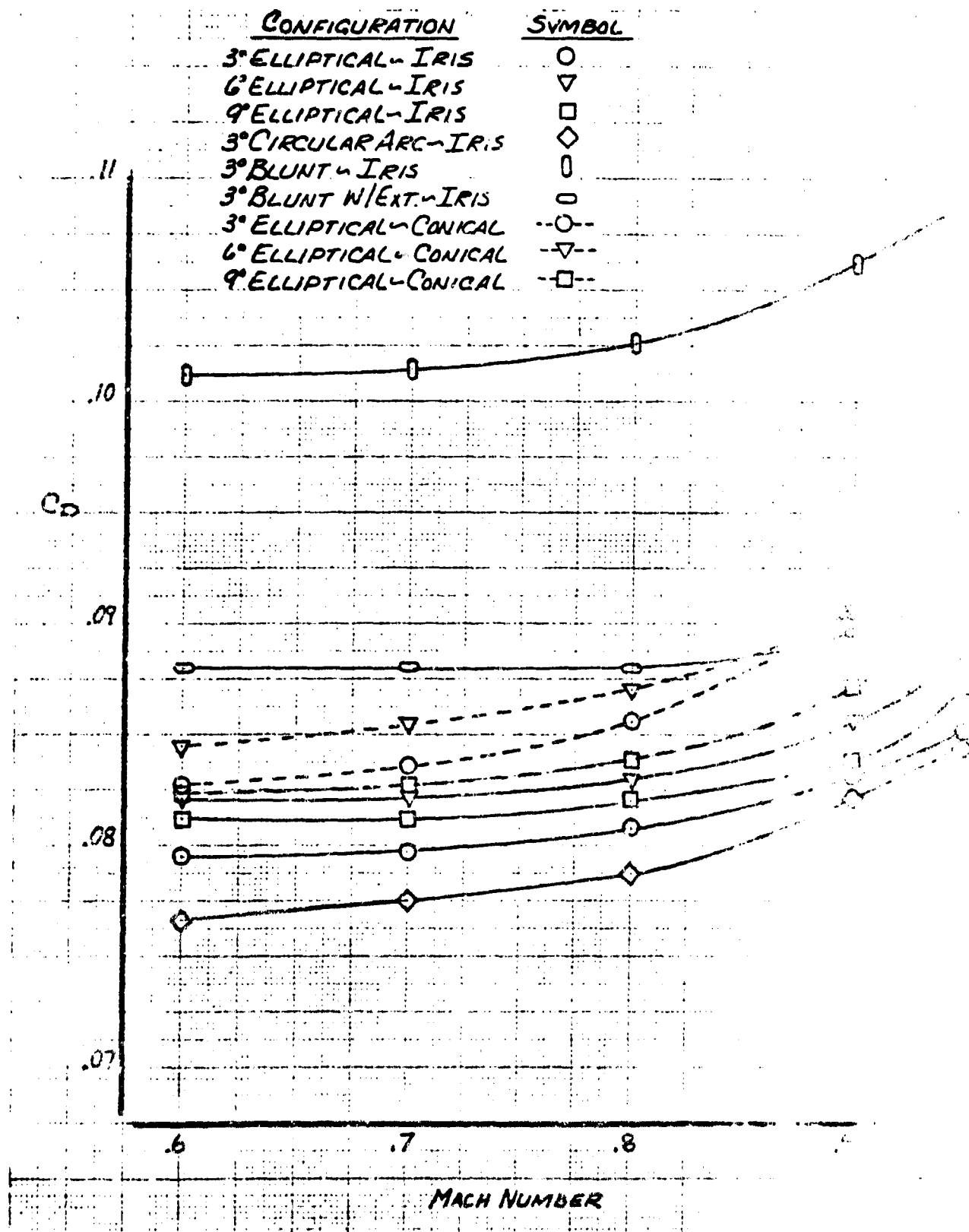


FIGURE 9-46: Total Drag vs Mach Number

$$P_{T_j}/P_{AMB} = 1$$

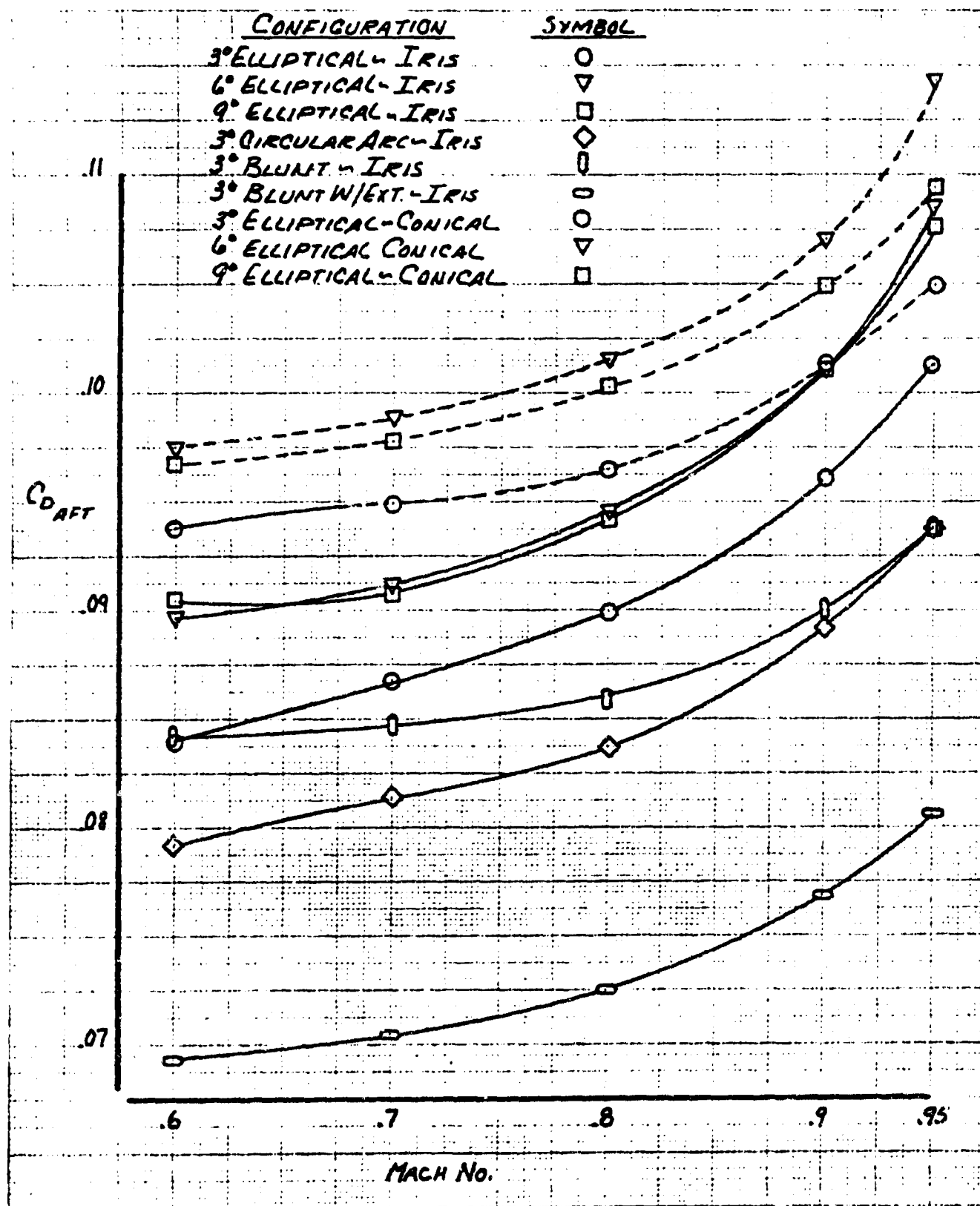


FIGURE 9-47: Afterbody Drag vs Mach Number

$$P_{T_j} / P_{AMB} = 1$$

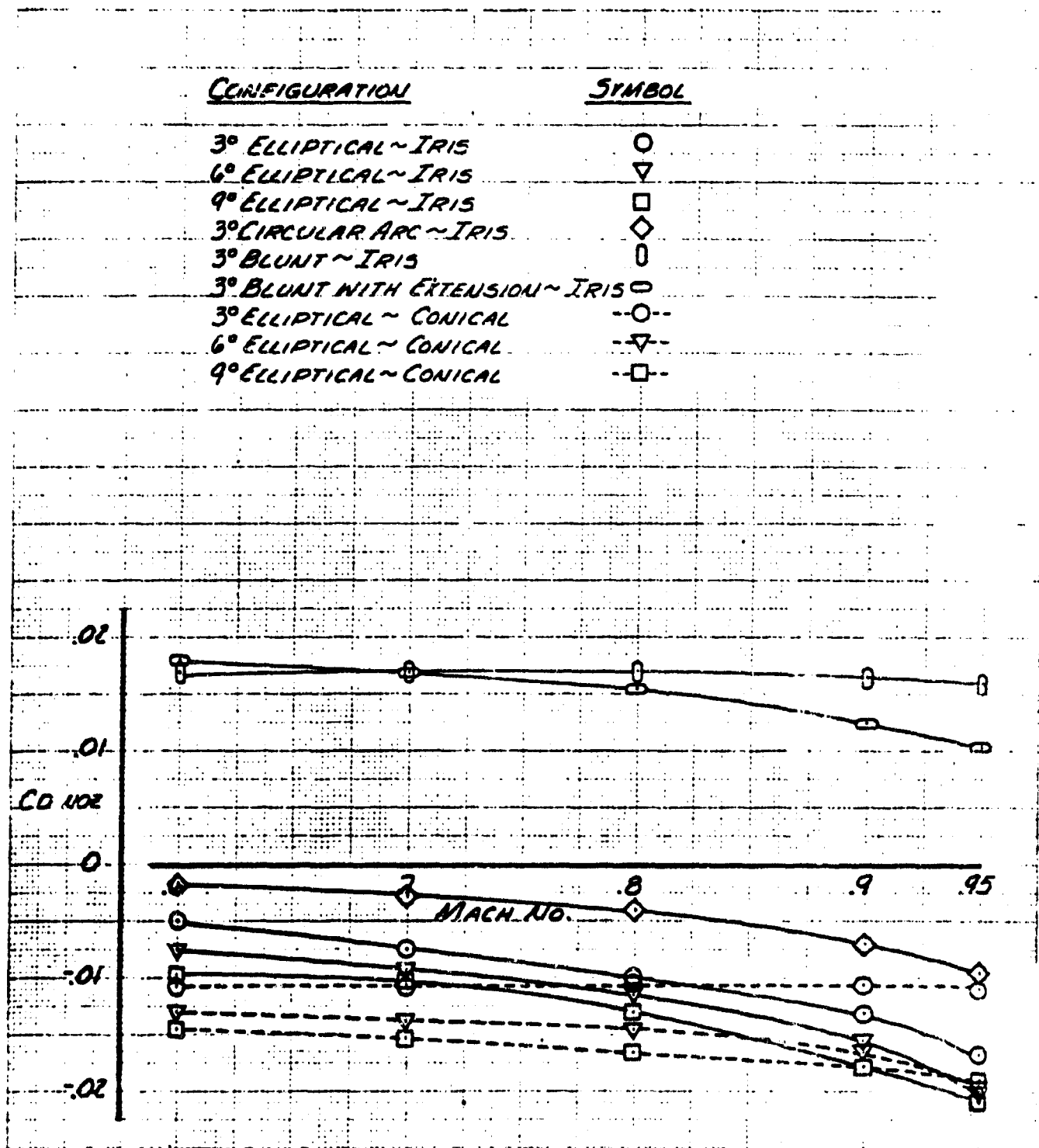


FIGURE 9-48: Nozzle Pressure Drag vs Mach Number

$$P_{T_j} / P_{AMB} = 1$$

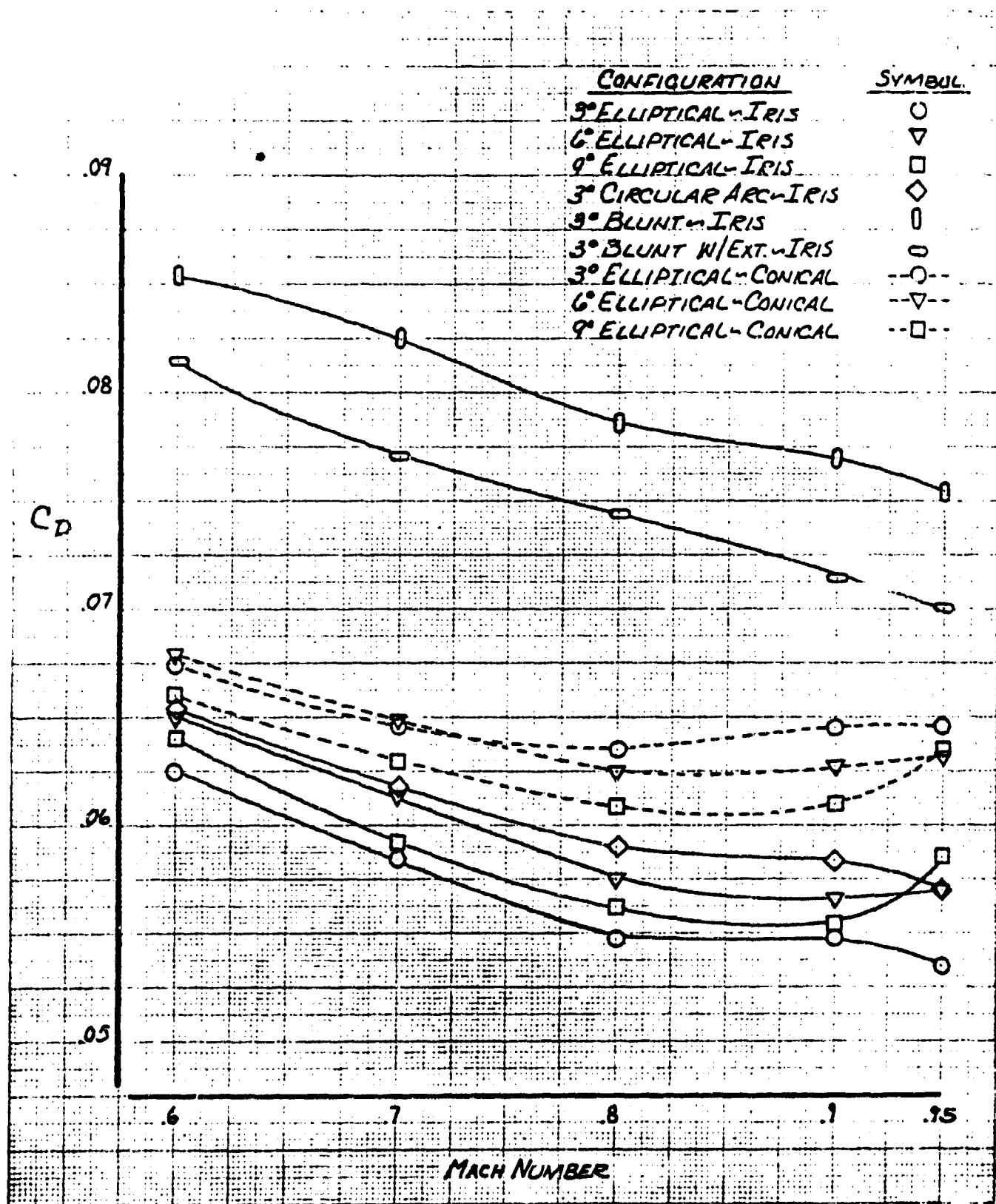


FIGURE 9-49: Total Drag vs Mach Number

P_{T_j} / P_{AMB} Set to Schedule

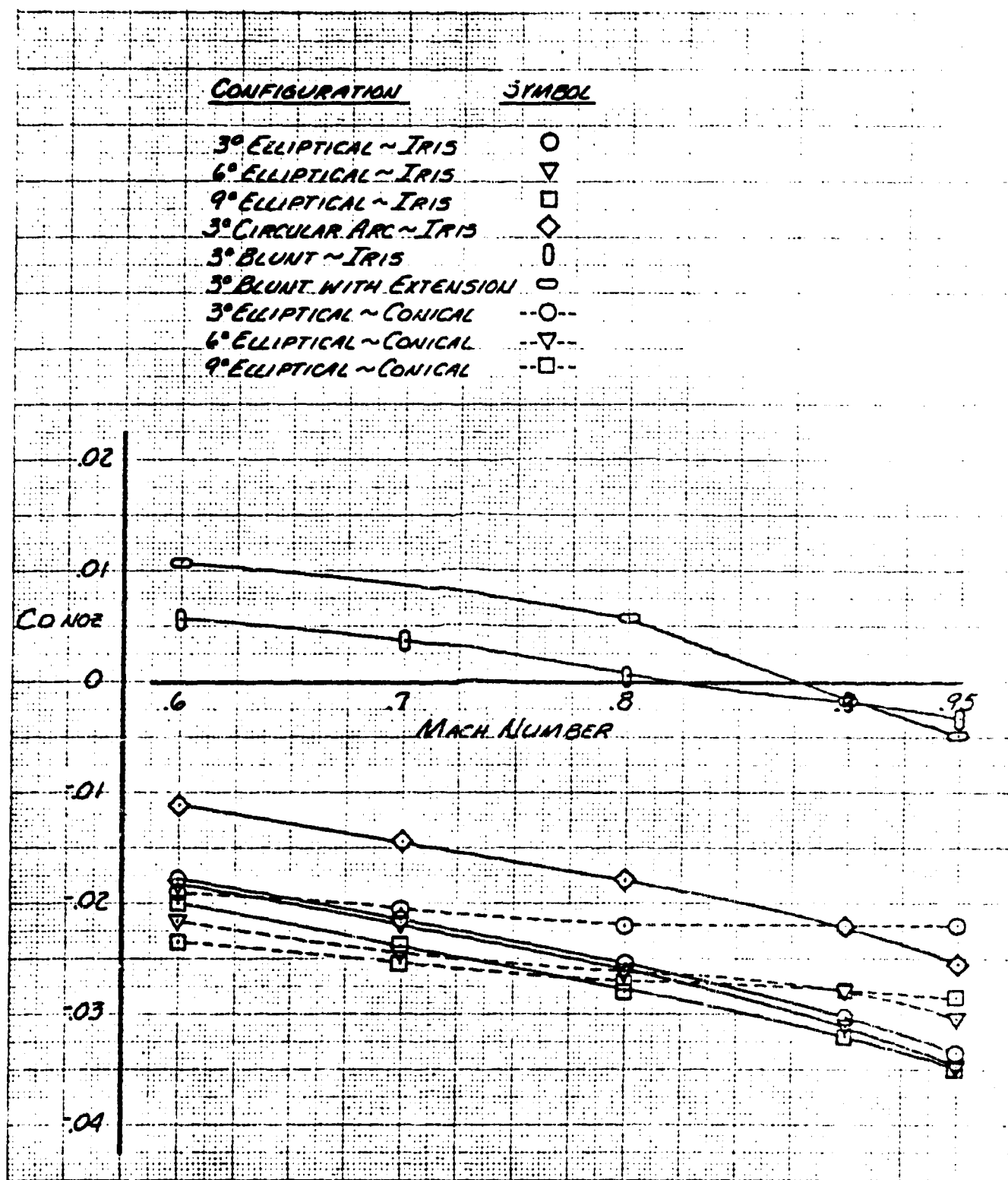


FIGURE 9-50: Nozzle Pressure Drag vs Mach Number

P_T / P_{AMB} Set to Schedule
J

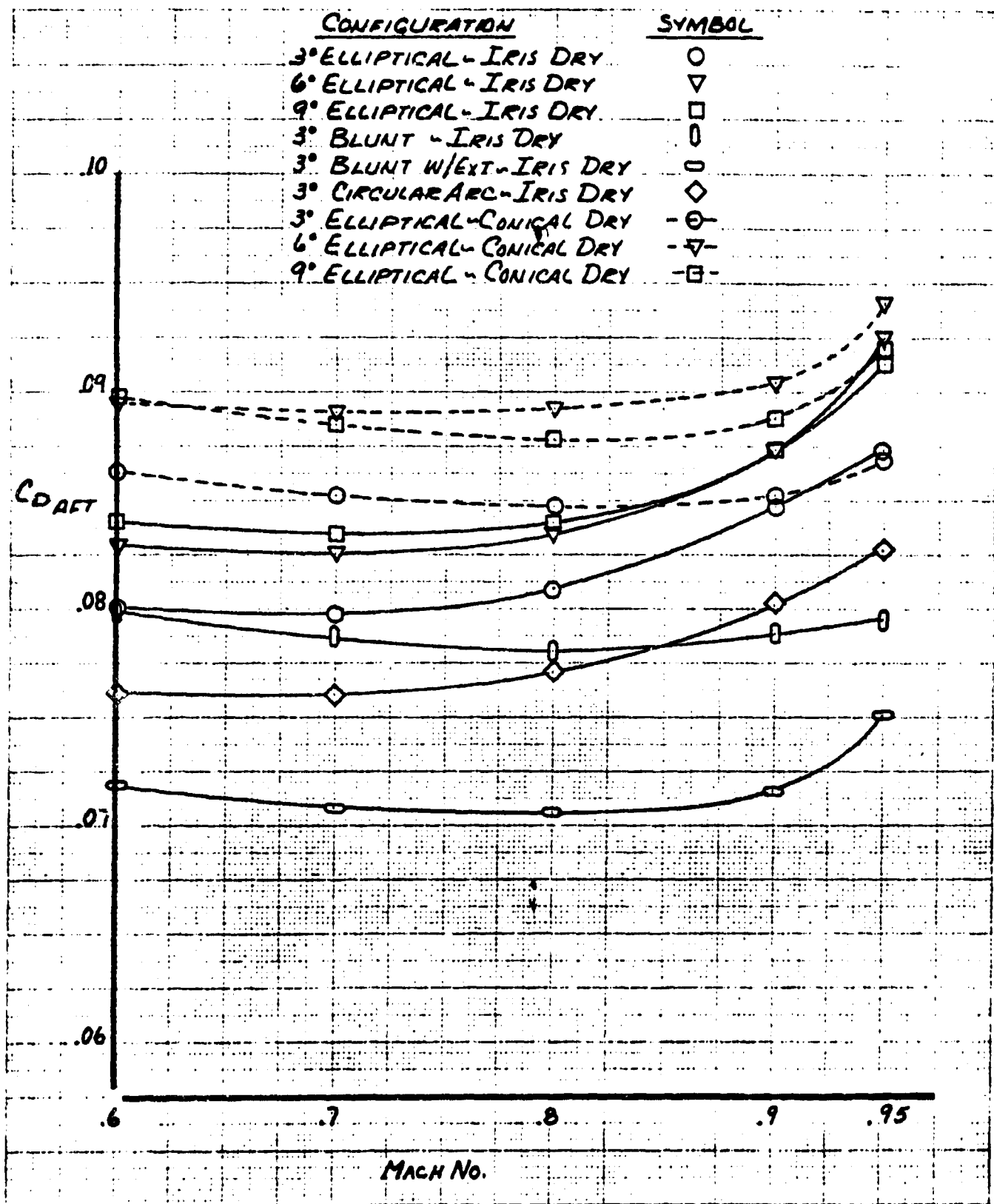


FIGURE 9-51: Afterbody Drag vs Mach Number

P_{T_j}/P_{AMB} Set to Schedule

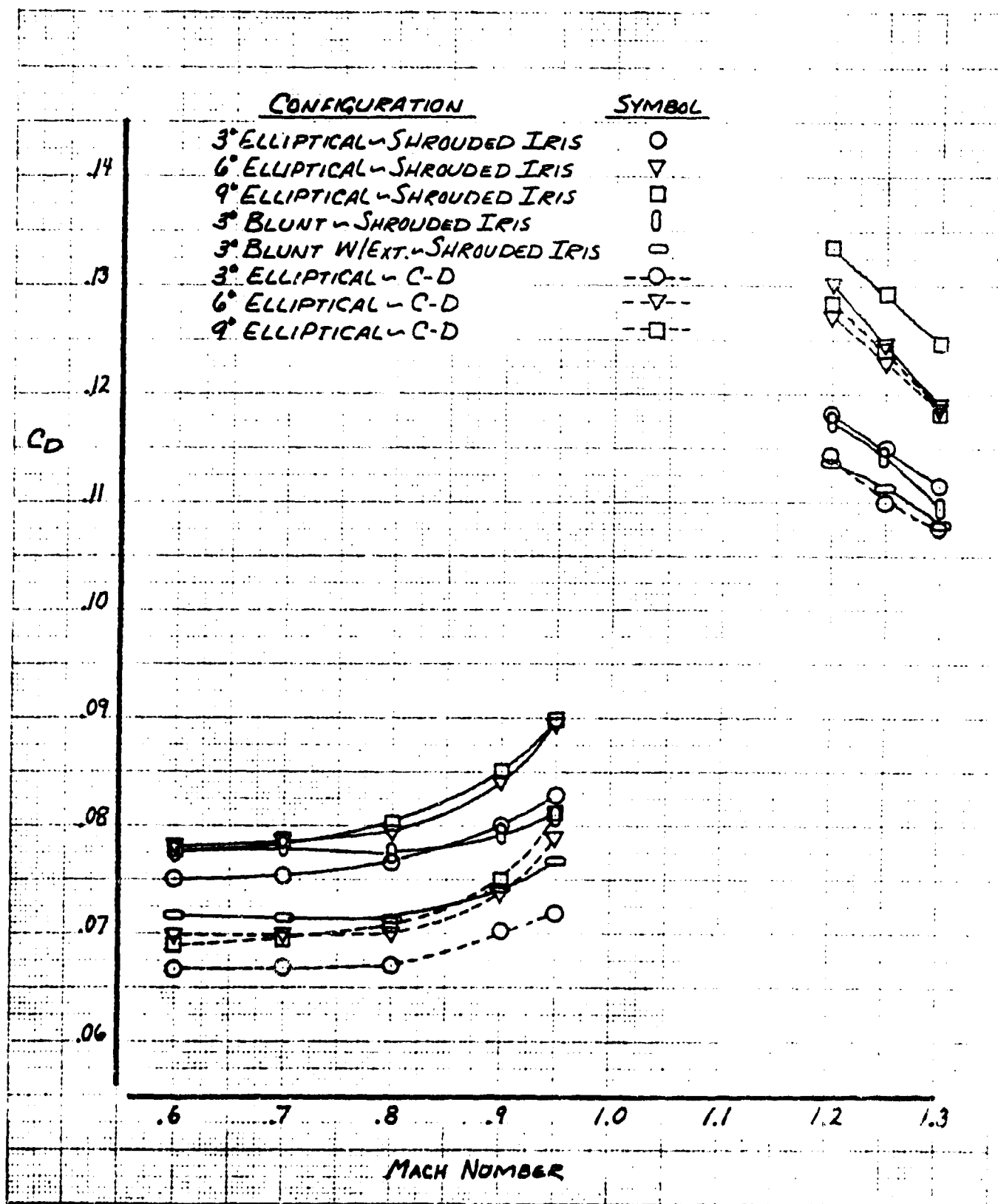


FIGURE 9-52: Total Drag vs Mach Number

$$P_{T_j} / P_{AMB} = 1$$

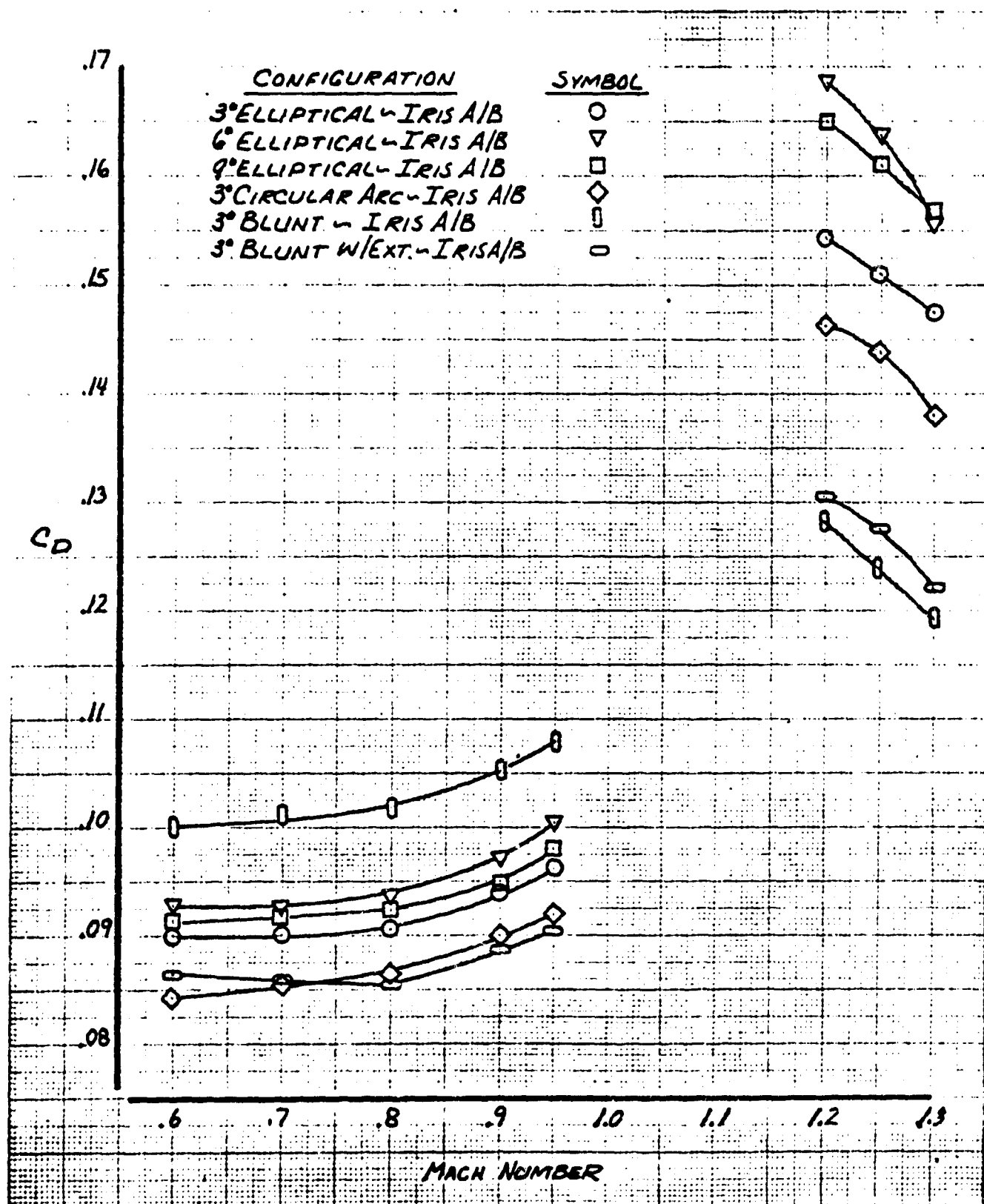


FIGURE 9-53: Total Drag vs Mach Number

$$P_{T_j}/P_{AMB} = 1$$

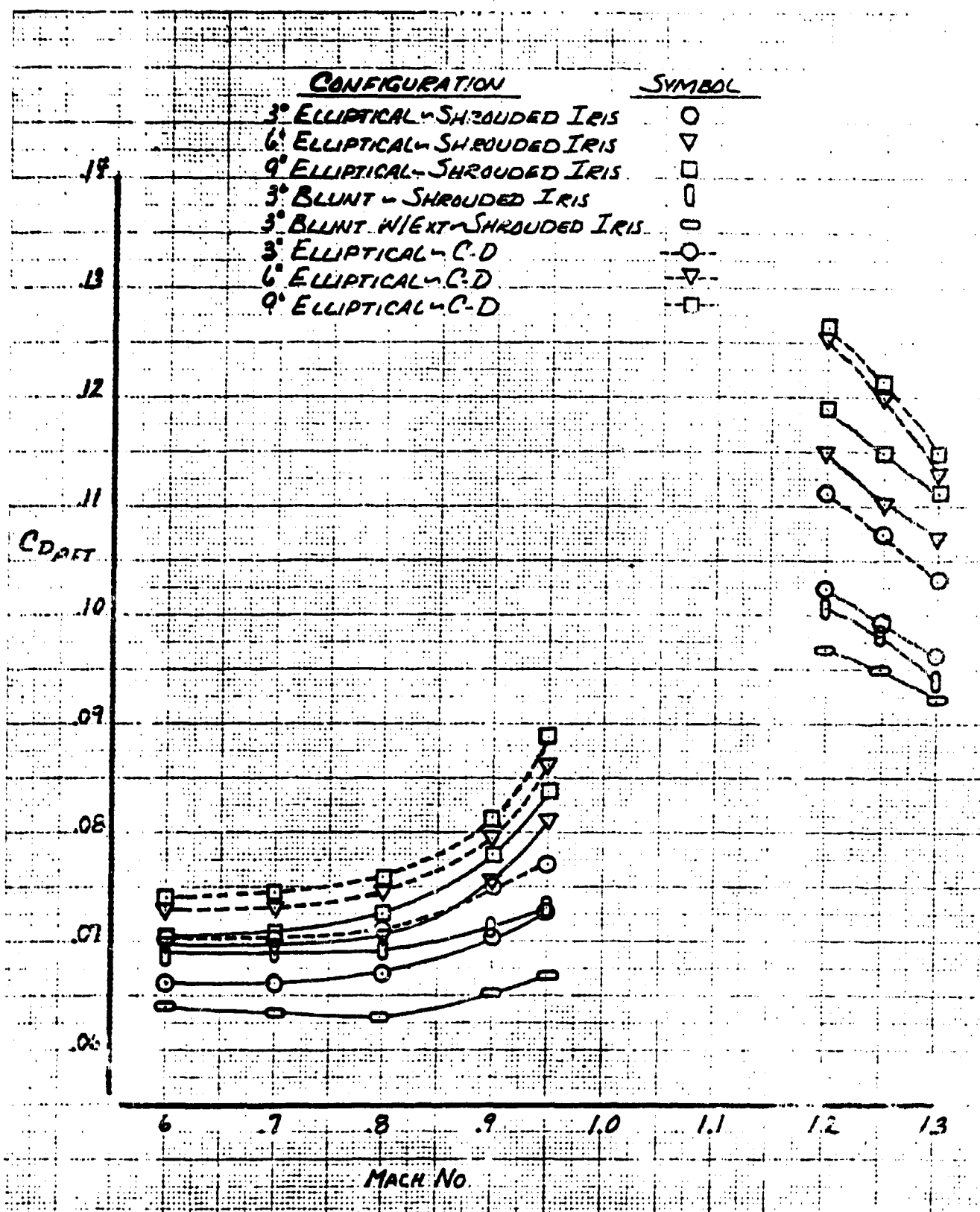


FIGURE 9-54: Afterbody Drag vs Mach Number

$$P_{T_j} / F_{AMB} = 1$$

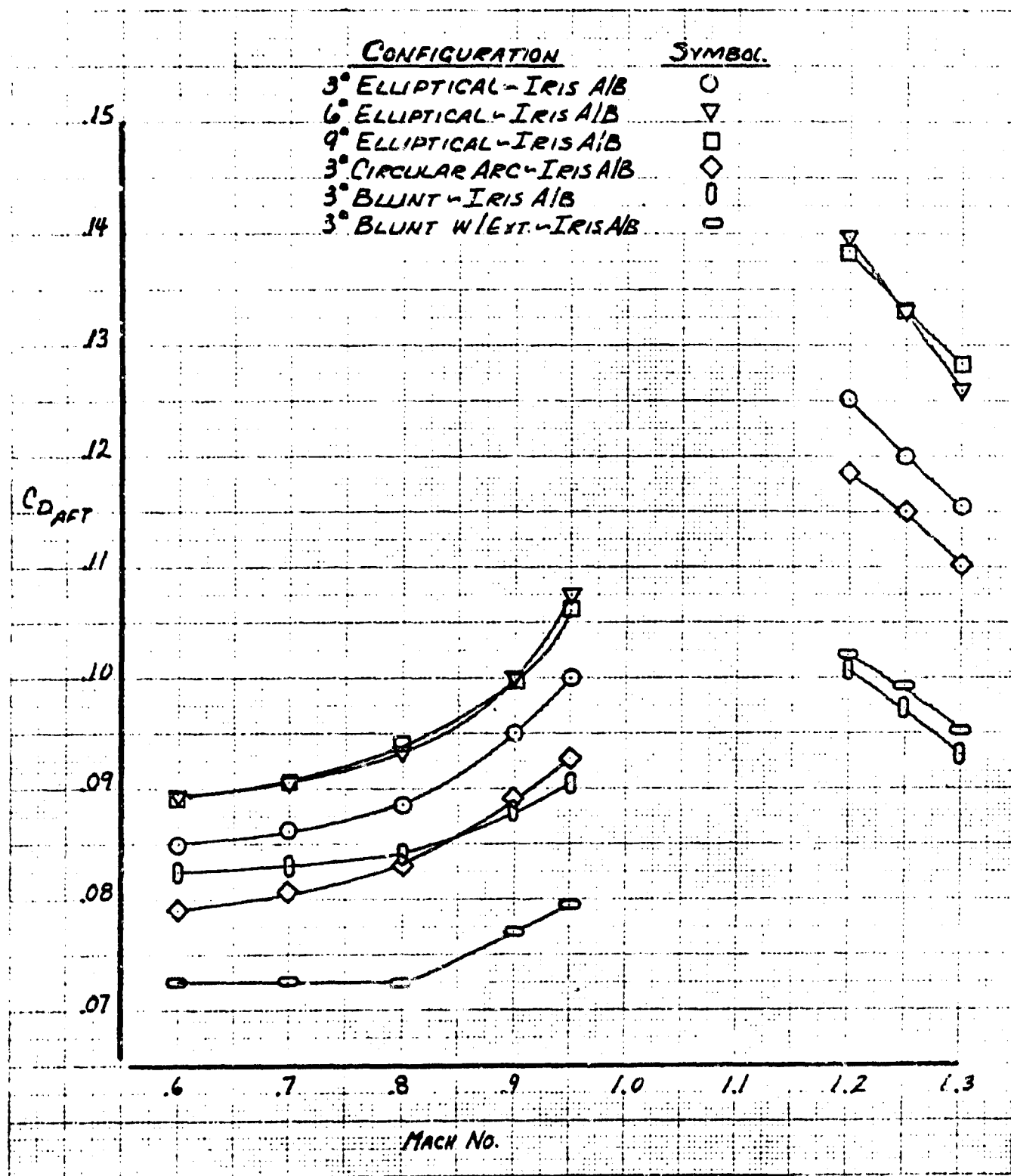


FIGURE 9-55: Afterbody Drag vs Mach Number

$$P_{T_j} / P_{AMB} = 1$$

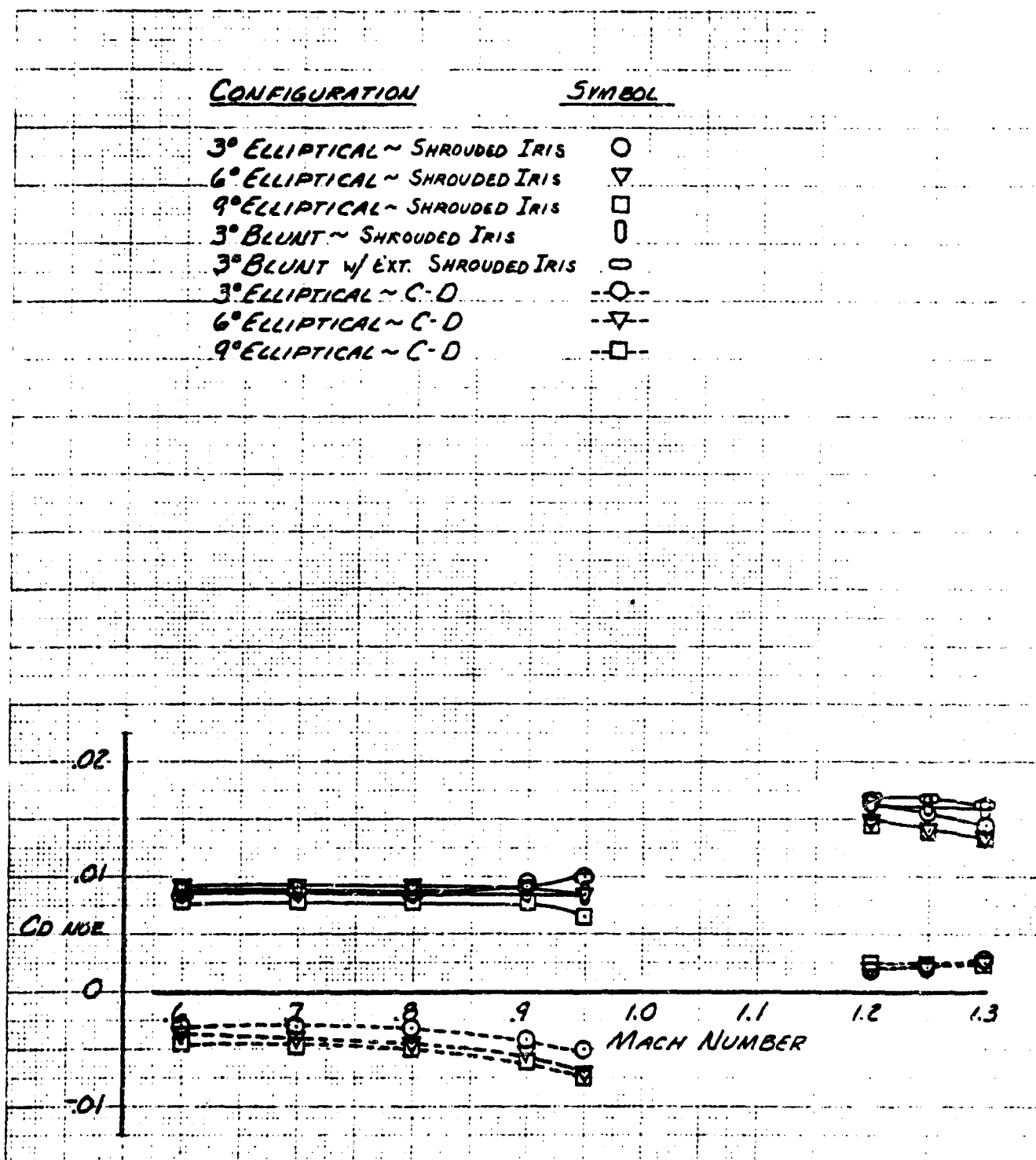


FIGURE 9-56: Nozzle Pressure Drag vs Mach Number

$$P_{T_j} / P_{AMB} = 1$$

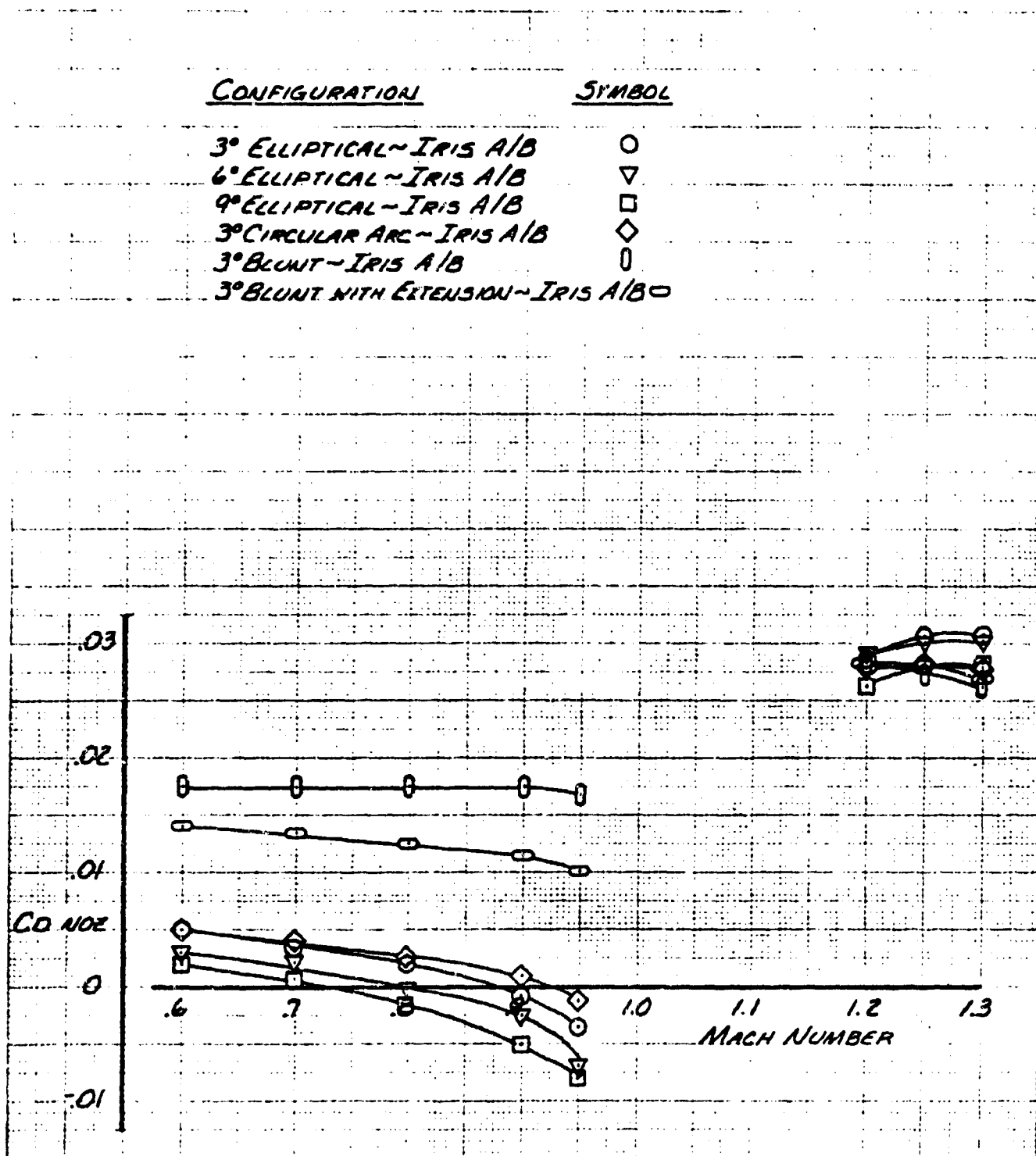


FIGURE 9-57: Nozzle Pressure Drag vs Mach Number

$$P_{T_j} / P_{AMB} = 1$$

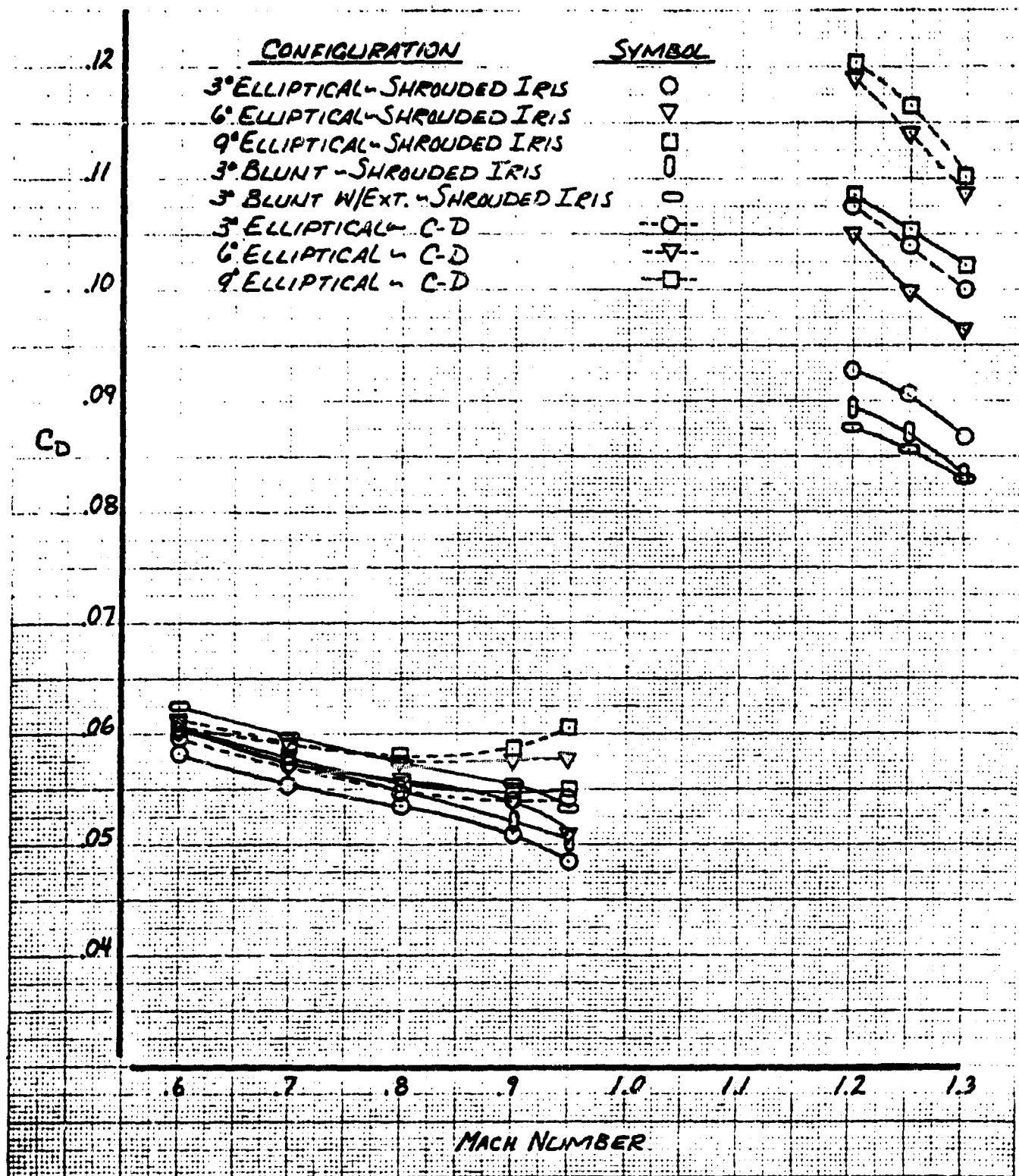


FIGURE 9-58: Total Drag vs Mach Number

P_{T_j}/P_{AMB} Set to Augmented Schedule

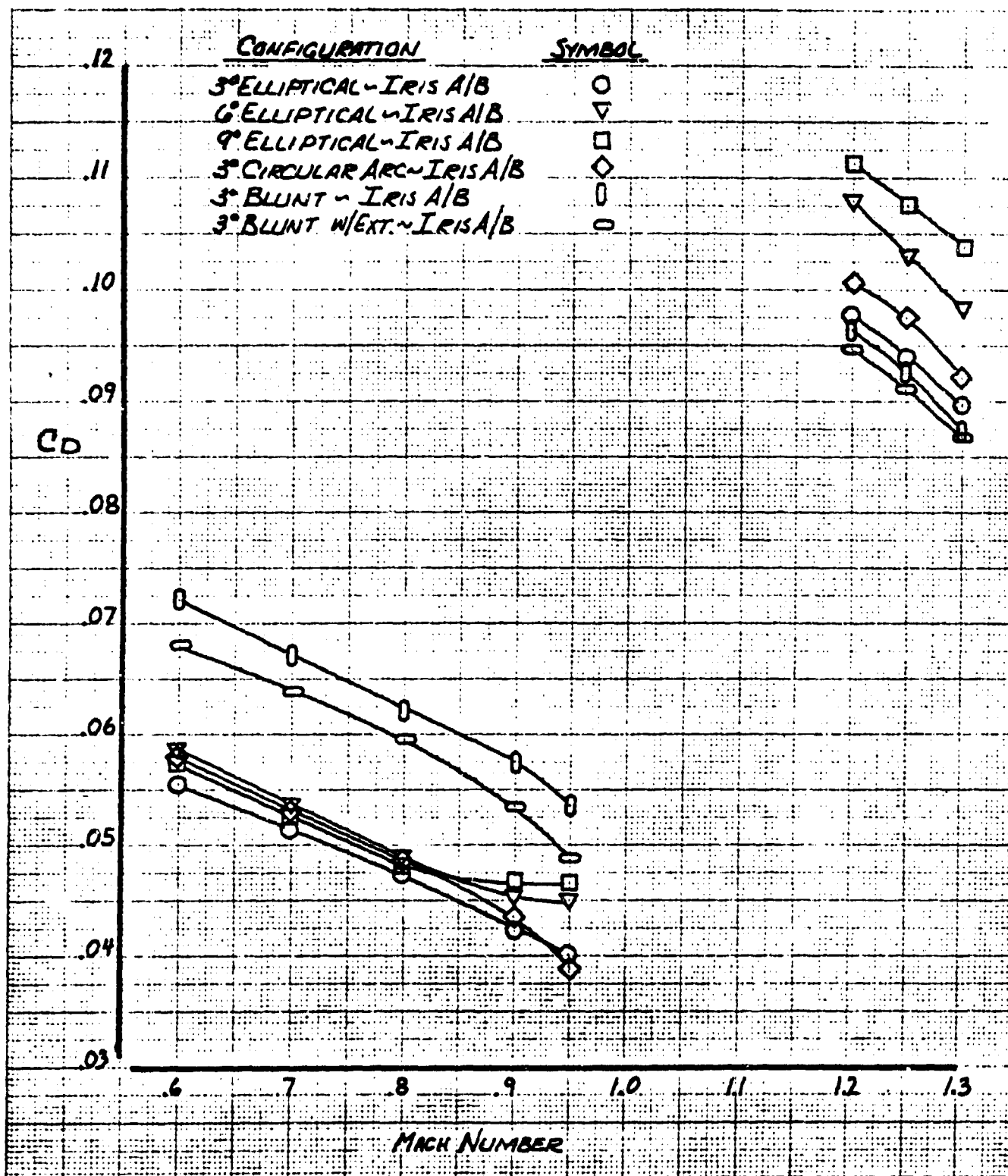


FIGURE 9-59: Total Drag vs Mach Number

P_{T_j} / P_{AMB} Set to Augmented Schedule

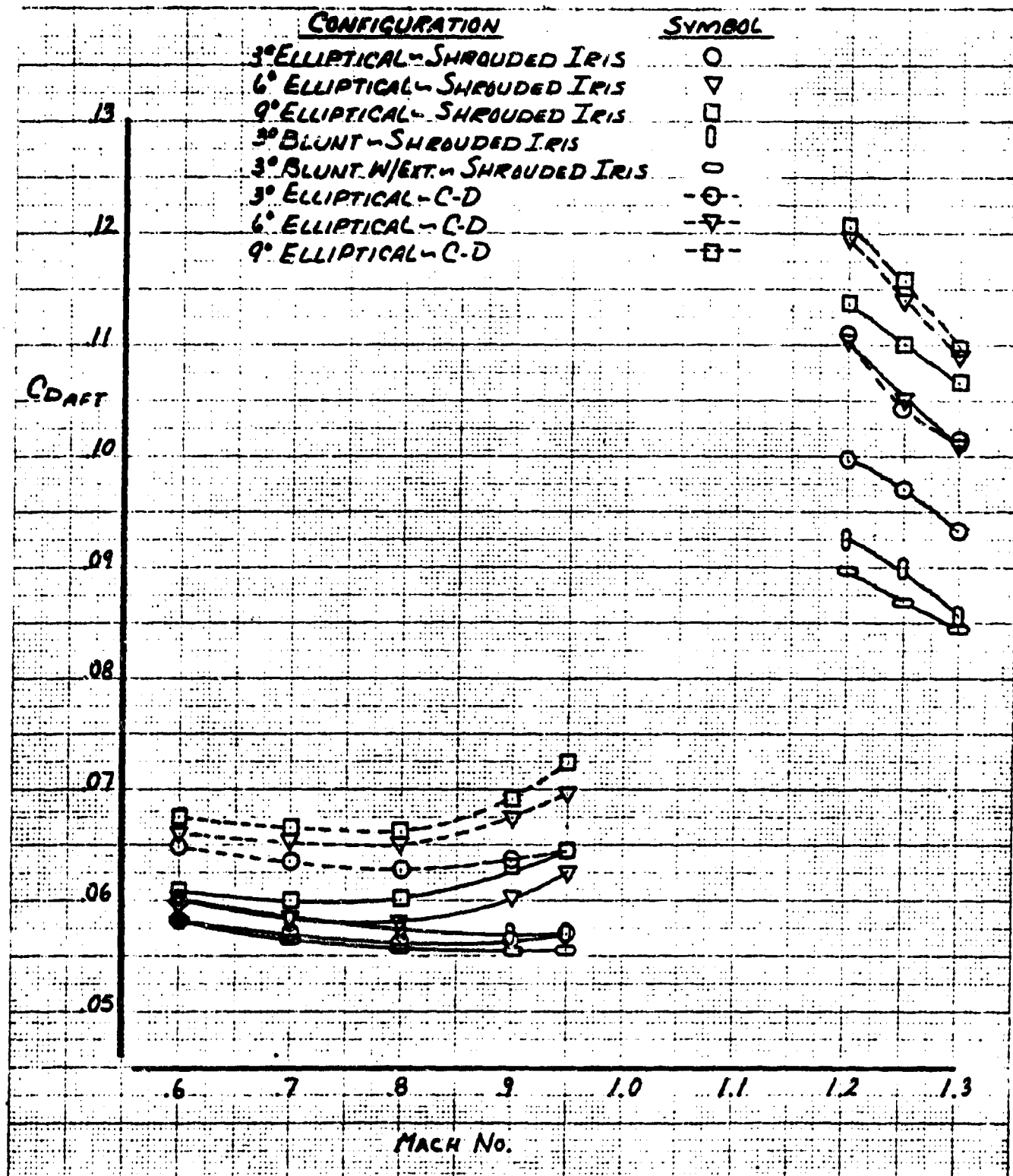


FIGURE 9-60: Afterbody Drag vs Mach Number

P_T / P_{AMB} Set to Augmented Schedule
J

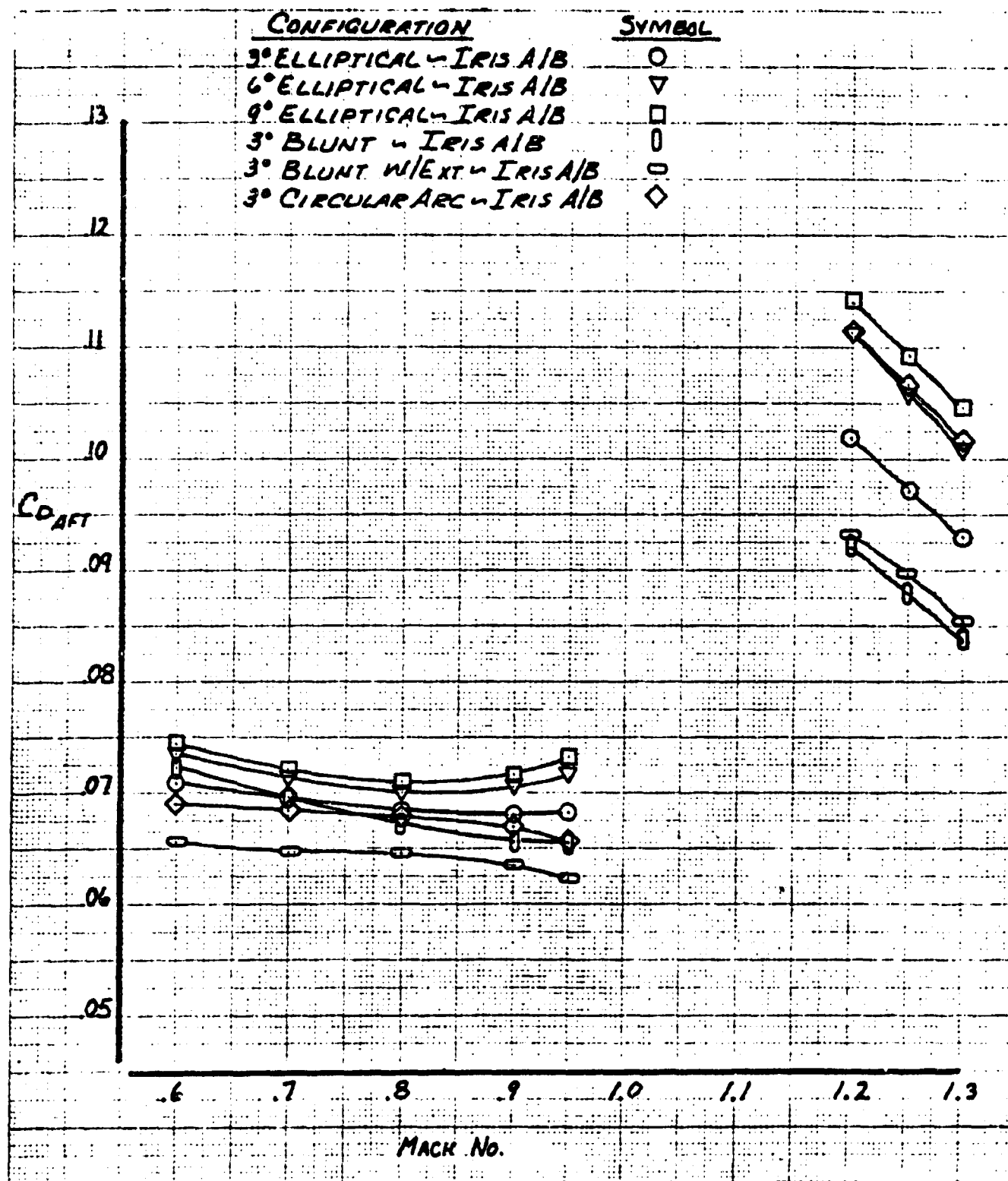


FIGURE 9-61: Afterbody Drag Vs Mach Number

P_{T_j}/P_{AMB} Set to Augmented Schedule

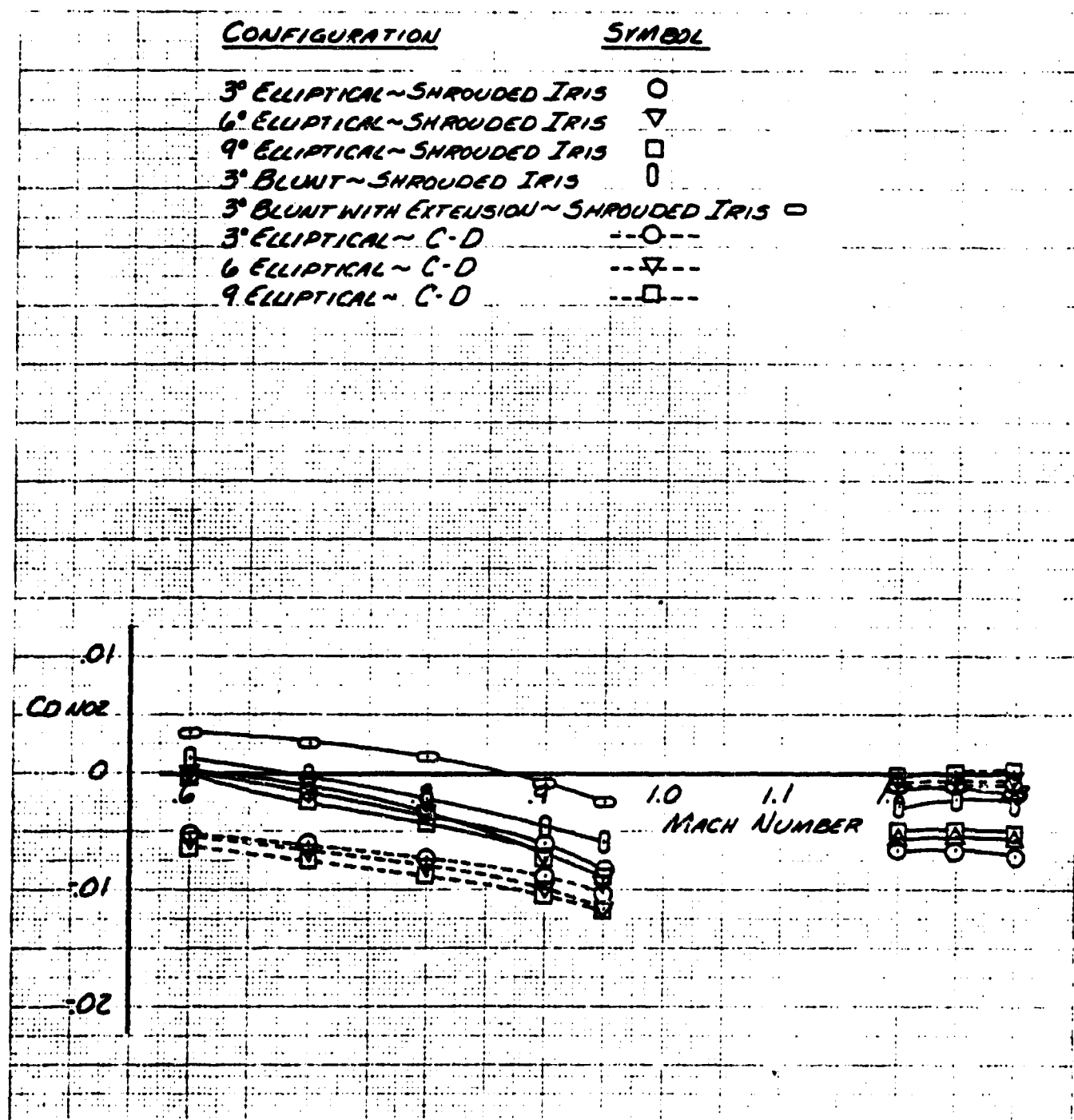


FIGURE 9-62: Nozzle Pressure Drag vs Mach Number

P_T / P_{AMB} Set to Augmented Schedule
j

CONFIGURATION	SYMBOL
---------------	--------

3° ELLIPTICAL ~ IRIS $\frac{A}{B}$	○
6° ELLIPTICAL ~ IRIS $\frac{A}{B}$	▽
9° ELLIPTICAL ~ IRIS $\frac{A}{B}$	□
3° CIRCULAR ARC ~ IRIS $\frac{A}{B}$	◇
3° BLUNT ~ IRIS $\frac{A}{B}$	◻
3° BLUNT WITH EXTENSION IRIS $\frac{A}{B}$	◻

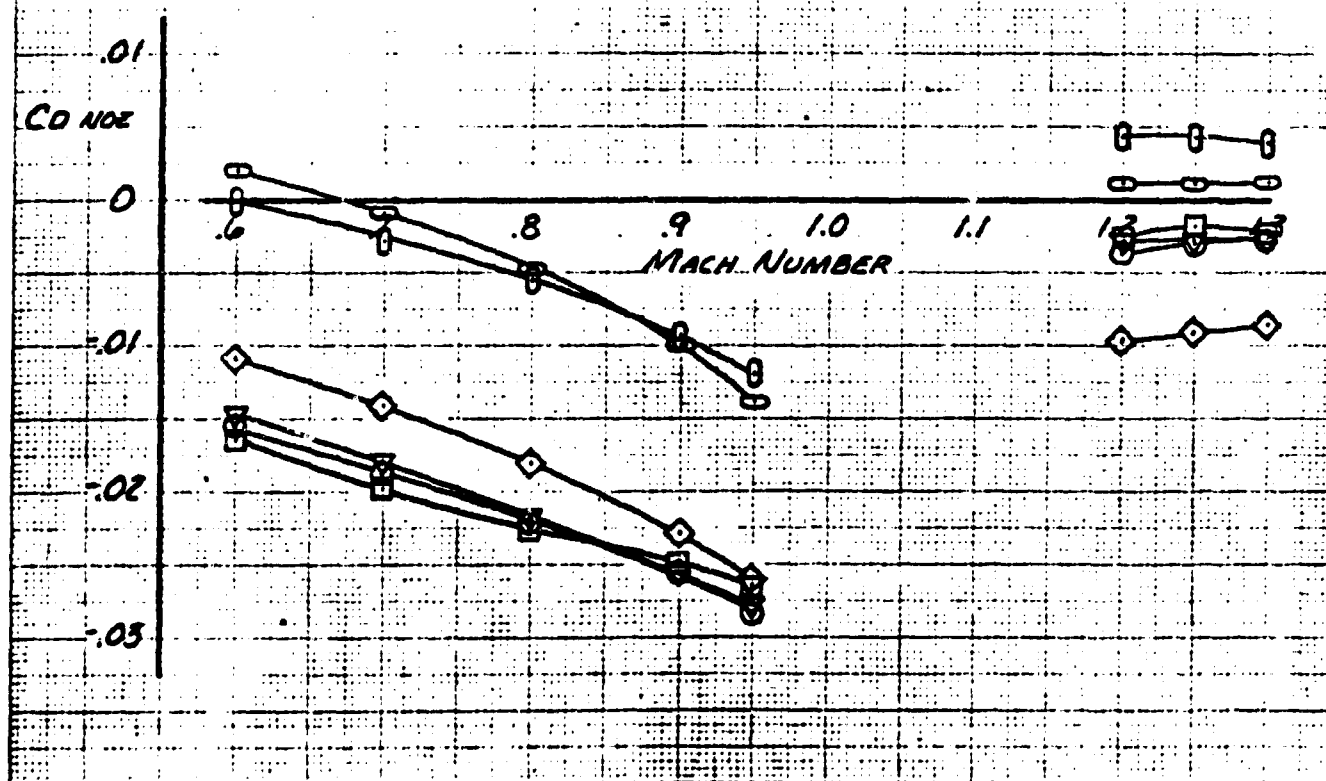


FIGURE 9-63: Nozzle Pressure Drag vs Mach Number

P_{T_j} / P_{AMB} Set to Augmented Schedule

10.0 High Bypass Ratio Turbofan Installation

10.1 Introduction

Installation items requiring particular attention in airframe/high bypass ratio turbofan engine integration are outlined in this section. Representative design techniques and test methods are presented. The reader is referred to preceding chapters for detailed inlet, nozzle and afterbody design criteria and empirical data. A generalized method for determining the incremental propulsion system losses is presented which can be tailored for a particular installation.

High bypass ratio turbofan engines are perhaps the leading engine development of the mid-1960's. The TF39-GE-1 engine, currently in production for the USAF/Lockheed C-5A, is the arch-prototype of the class of engines designed specifically for long range cruise vehicles such as transport, cargo and patrol aircraft. Some of the high bypass engines under development or in production and their applications are: JT9D, Boeing 747; RB 211, Lockheed L-1011; CF-6, McDonnell Douglas DC-10; and TF34-GE-2, Navy/Lockheed S-3A. A partial listing of these engines and their characteristics is presented in Table I. The large variation in the size of these engines is indicative of their wide potential application. All of these engines are front-fan engines. Aft fan engines, such as the TF37, are currently produced only as low bypass engines.

Bypass ratio is defined as:

$$BPR = \frac{W_a \text{ FAN}}{W_a \text{ GAS GENERATOR}}$$

The bypass ratio at which an engine is designated a high bypass ratio engine varies somewhat in existing literature. In order to be consistent with a large body of the literature, it is recommended that high bypass be defined as greater than 2.5 with low bypass equal to or less than 2.5.

The turbofan, or bypass engine, converts some of the work of the turbines downstream of the combustor into driving a large fan stage or stages. The fan does work upon the entering air and provides thrust upon exhausting the air overboard without going through the combustor. The gas flow paths are shown in Figure 10-1. The basic turbofan cycle was developed to obtain lower specific fuel consumption at subsonic aircraft speeds.

TABLE 1

HIGH BYPASS TURBOFANS

ENGINE DESIGNATION	MFR.	BPR	TAKE-OFF THRUST LBS.	CRUISE SFC 36,000 FT.	OVERALL PRESSURE RATIO	TOTAL AIRFLOW LBS/SEC	DIAMETER INCHES	LENGTH INCHES	WEIGHT POUNDS
1F39	GE	8.0	41,100		25.0	1549	100.0	324.0	7026
JT9D-3	P&W	5.0	43,500		22.0	1484	95.6	128.2	8430
JT18D	P&W	5.0	35,000	.64	24.0	1181	85.1	116.0	6520
CF6-6	GE	6.3	40,000	.64	26.7	1465	93.7	190.0	7350
CF6-50	GE	4.5	50,000	.65	29.9	1448	93.7	188.0	8100
RB 211	RR	5.0	40,600		27.0		88.2	128.7	7189
RB 203	RR	3.0	9,730		16.0	300	38.7	82.0	1776
JT15D	P&W	3.2	2,200	.8	10.0	73	27.21	50.0	480
PLF1C	Lycoming	6.0	5,220			201	41.1	66.3	1010
ATF-3	Garrett	3.0	4,050		25.0	140	31.95	92.0	874
TFE731	Garrett	2.67	3,500		15.0	113	28.2	54.4	625
M45H	RR/SNECMA	2.85	7,760		18.8	233	42.9	116.0	1483

NOTE: These data were obtained from a variety of unclassified sources, including the references at the end of this section, and are subject to revision, particularly through engine development.

The specific fuel consumption (fuel flow rate per unit thrust) of a jet engine is inversely proportional to the overall efficiency, η_o .

$$\text{SFC} \propto \frac{V}{\eta_o}$$

The overall efficiency in turn is the product of the thermal efficiency, η_{th} , where, for the gas generator,

$$\eta_{th} = \frac{\Delta H - 1/2 V^2}{f Q_n}$$

f - fuel air ratio
 Q_n - heating value of fuel

and the propulsive efficiency, η_p , where

$$\eta_p = \frac{V(V_j - V)}{\Delta H - 1/2 V^2}$$

or the more familiar,

$$\eta_p = \frac{2V_o}{V_o + V_j}$$

i.e. overall efficiency is the product of the two

$$\eta_o = \eta_p \eta_{th}$$

Equations for a non-mixed flow turbofan, such as the typical high bypass turbofan, are more complex, but the principle is the same.

The TF30, TF33, JT8D and TF41 turbofans are low bypass turbofan engines. To obtain even lower specific fuel consumption, increased amounts of air are bypassed around the core engine. This logical development of the basic turbofan cycle results in the high bypass turbofan engine.

A typical curve of propulsion efficiency is shown in Figure 10-2. This points up the basic inefficiency of the straight turbojet engine for subsonic applications in that the comparatively low value of the ratio of free stream to jet velocity, V/V_j , results in correspondingly low values of propulsive efficiency. To improve propulsive efficiency, and in turn overall efficiency, it is required that the jet velocity more nearly approximate the aircraft's flight velocity. If this is accomplished by lowering the temperature of the gas at the turbine inlet, the gas generator thermal efficiency is lowered. The turbofan, or bypass engine, while maintaining the basic thermal efficiency level of the gas generator, by running at higher temperatures consistent with advanced technology, converts more work at the turbine stage or stages into driving a fan which compresses and expands a stream of air in addition to that required for the gas generator compressor. The desired result, improved efficiency, is obtained -- a greater mass of air accelerated in the thrust direction at a lower speed. The improvement in specific fuel consumption increases with increased bypass ratio; that is with increased amounts of air passed through the fan relative to that going through the gas generator, resulting in lower net jet velocity. This effect is shown in some data obtained by Rolls Royce (Reference 1) in Figure 10-3. Note that a specific fuel consumption reduction on the order of 25 percent is achieved by engines in the 6 to 8 bypass ratio range compared to low bypass (1 to 2) engines currently in service such as the JT3D/TF33. Corresponding to the improvement in SFC is a decrease in specific thrust, defined as thrust divided by the airflow, as shown in Figure 10-4. This is from the same Rolls Royce data. The specific thrust relationship is important in engine/airframe sizing/matching.

The high bypass turbofan is designed specifically for cruise vehicles. The high thrust lapse rate with speed makes the high bypass engine poorly suited to vehicles with high subsonic speed or maneuvering requirements. Thrust lapse with speed is shown in Figure 10-5. The effect is a combination of a number of engine characteristics but results mainly from the lowering of thrust to airflow ratio as bypass ratio is increased. Owing to this high thrust lapse rate, sea level static thrust is of much less significance in aircraft/engine sizing than it is with turbojets. Of primary importance is the determination of proper engine sizing, chiefly through bypass ratio selection, to match aircraft take-off and cruise/loiter requirements. The ratio of cruise to static thrust, as a function of bypass ratio, is shown in Figure 10-6.

Cutaways of the JT9D, typical of a two-shaft high bypass turbofan, and of the RB203, a three-spool turbofan, indicating basic design features, are presented in Figures 10-7 and 10-8. From these, we can see basic features of the typical high bypass turbofan -- the large air passage outside of the core engine, the absence of inlet guide vanes, and the separate turbines driving the fan and the compressor.

10.2 High Bypass Ratio Turbofan Installation Considerations

10.2.1 Windmilling Performance

The large quantities of air passing through the fan require careful consideration, particularly with respect to one engine-out stability. A representative plot of windmilling drag versus bypass ratio is presented in Figure 10-9, based on data from Reference (2).

10.2.2 Exhaust Path Design

Turbofans have two distinct jet wakes which must be considered, the typical high temperature exhaust from the core engine and the relatively low temperature fan exhaust. In contrast with the typical turbojet engine, the core engine exhaust is at a relatively low energy level, since most of the energy is extracted in the fan and core engine turbines. The fan exhaust, after passing typically through only one stage, operates unchoked through a portion of the flight regime. The nozzle pressure ratio is changed by external flow effects. Thus the unchoked portion is different for installed and isolated engines. This imposes an important installation constraint. Everything located downstream of the fan must be designed so as not to impose unacceptable distortion upon the fan, which is more susceptible when operating unchoked. Excitation of the fan, a dynamic mechanical problem, occurs when the fan is loaded unequally. To maintain fan loading within an acceptable range, the engine manufacturer establishes distortion limits in terms of a downstream pressure profile variation in the same manner as inlet distortion limits are specified. The minimization of fan distortion is important not only from a structural integrity standpoint, but also because the fan in the larger engines contributes on the order of 3/4 of the total thrust.

Among the items which must receive careful consideration in design to maintain high fan performance and integrity are that portion of the pylon located in the fan wake, which imposes a one-per-rev disturbance on the fan, accessories orientation, core engine cowl protuberances, thrust reverser, and proximity of external stores, wing and variable geometry lift devices, tail surfaces and the fuselage. A typical plot of the static pressure distribution downstream of the fan showing the influence of the pylon is shown in Figure 10-10. Preliminary test data indicate that the pylon effect

can be minimized by contouring the nozzle, as opposed to the typical symmetrical nozzle, such that additional flow channel relief is provided adjacent to the pylon. The allowable pylon width within the fan stream has to date been specified on an individual engine basis. The major typical criteria governing pylon width appear to be fan diameter and fan duct length; the latter tends to attenuate distortion. Pylon width to fan diameter ratios for contemporary high bypass turbofans are typically around 0.2. Cowl protuberances generally have considerably less effect on fan performance. To eliminate the possibility of other surfaces affecting the fan, and to avoid the drag penalty imposed by the higher dynamic pressure of the fan stream, it is recommended that such surfaces be located outside the boundary traced by a constant annular area of fan air.

One design consideration which has evoked considerable discussion and studies is the fan cowl length. Long fan cowls, which result in nacelles with coplanar fan and primary exhausts, frequently called long duct nacelles, are to be found on JT8D engine installations and on the TF33 as installed on the C-141. Short fan cowls, in which the exhaust from the annular fan nozzle washes or scrubs the cowl over the gas generator, are found on the TF39 on the C-5A, the JT9D on the 747, and the TF34 on the S-3A. The CF-6 engine, as installed on the DC-10, has a fan cowl of intermediate length. See sketches, Figure 10-11.

Many of the studies of fan cowl length conducted to date, including those reported in References (3), (13), and (21), have been conducted for specific installations. The fact that as a result of such studies, different conclusions have been reached, emphasizes the importance of the intended installation on the long duct/short duct decision. In general, the long duct nacelles have higher tailpipe losses and higher weight; the short duct nacelles have higher drag owing to the higher velocity air from the annular fan exhaust scrubbing the gas generator cowl. A pod drag + internal duct loss trade-off for three different length cowls, based on some data from Rolls Royce for large engines, is presented in Figure 10-12.

Primary considerations in the determination of the nacelle configuration are engine bypass ratio, thrust reverser effectiveness desired, aircraft performance requirements and the costing method of evaluation. Long fan ducts are recommended for the lower bypass ratio engine installations as the weight and pressure loss disadvantages are outweighed by other installation factors. Thrust reverser effectiveness requirements have had a major influence on nacelle configuration. Whether a device which blocks the fan air alone suffices, or whether both exhaust streams must be blocked with separate or combined devices, and the effect of such devices on adjacent lifting surfaces, affects the location and directional orientation and hence the total nacelle configuration. Aircraft performance considerations include range versus short field performance trade-offs; cost methods include life cycle costing with its maintainability and reliability considerations. Other considerations include accessory arrangement and engine mounting.

10.2.3 Cooling

Cooling of the high bypass turbofan is somewhat simplified in that the large quantity of relatively cool air passing through the fan provides a positive cooling source whenever the engine is running. Thus the core engine compartment, the generator, engine mounted accessories and the CSD (Constant Speed Drive) or VSCF (Variable Speed Constant Frequency) drive are cooled with uniflow cooling systems, with higher pressure/velocity air provided at high power settings. In long fan duct installations, accessories are located outside the fan duct and are cooled even more easily. One item that does require particular attention is the pylon, which interrupts the cooling symmetry. Special cooling provisions must be made for pylon cooling so as to preclude elevated structure stress levels and circumferential temperature gradients in the turbine. One scheme for handling this is detailed in Reference (3). Typical compartment temperature zones for a high bypass-short fan duct installation are shown in Figure 10-13.

10.2.4 Miscellaneous

Initial experience with high bypass turbofan engines does not indicate any FOD (Foreign Object Damage) susceptibility. The large fan tends to centrifuge the air it takes aboard, presenting the cleanest air to the more susceptible high pressure compressor.

Typical static and low speed inlet velocity profiles ahead of a high bypass turbofan engine, obtained through the use of the Douglas Neumann computer program solution (Reference 4), are presented in Figure 10-14.

10.3 Installation Loss Breakdown

Installation losses may be conveniently divided into those internal to the engine nacelle such as inlet recovery and shaft power extraction, and those external to the nacelle such as additive drag and scrubbing drag.

10.3.1 External Losses

The external losses of a high bypass turbofan installation differ somewhat from those of the turbojet and low bypass turbofan. A sample breakdown is illustrated in Figure 10-15. These drag items, tabulated below, are discussed in succeeding paragraphs.

- a) Inlet additive drag
- b) Fan cowl friction
- c) Fan cowl boattail drag
- d) Gas generator cowl scrubbing
- e) Gas generator boattail drag

- f) Plug scrubbing
- g) Plug separation (pressure drag)
- h) Pylon scrubbing

Items (a) through (h) are directly chargeable to the engine/nacelle and should be included as installation losses, when applicable, in the computation of installed engine performance. Two drag items which are directly related to the installation of the nacelle on a wing or fuselage, but which are handled as components of airplane drag are:

- i) Pylon friction and form drag
- j) Interference drag

10.3.1.1 Additive Drag

Additive drag, the term used to account for the effects of the divergence or turning of the streamlines around an engine air inlet, is discussed thoroughly in Section 4.0. For high bypass engine installations, additive drag considerations in inlet design become more important owing to the emphasis on both cruise and loiter performance requirements and the high thrust lapse with speed of the high bypass turbofan engine.

10.3.1.2 Fan Cowl Friction

Fan cowl friction, that is the friction drag on that part of the nacelle which is unaffected by engine flows, can be handled conventionally by external aerodynamics methods.

10.3.1.3 Boattail Drag

Fan cowl boattail drag, afterbody boattail drag and plug flow separation drag can be minimized or eliminated by careful selection of the contours. Some test data from Reference 5, presented in Figure 10-16, shows that for taper radius to diameter ratios less than 4, a sharp increase in drag occurs due to separation. Separation and afterbody shaping criteria are detailed in Section 9.

Equations for the theoretical determination of boattail and separation drag are reasonably straightforward. As in all equations of this type, the determination of the coefficient values is of prime concern. In general, the coefficients used are empirically derived.

Fan cowl boattail pressure drag can be computed by the equation

$$D_{\beta F} = C_D \beta F q_o A_p$$

$$C_{D\beta F} = \phi(M_o, \frac{R_{FC}}{D_{max}}, A_p)$$

A_p = projected area

Nomenclature for this and the following equations is shown on a nacelle sketch in Figure 10-17.

Gas generator cowl boattail pressure drag is computed similarly

$$D_{\beta GG} = C_{D\beta GG} q_F A_p$$

$$C_{D\beta GG} = \phi\left(\frac{P_{TF}}{P_o}, R_{GGC}, D_{GG}, h\right)$$

Note that the cowling designated gas generator in Figure 10-17 includes the cowling over the fan turbine.

Pylon boattail pressure drag, including the effect of flow separation, for the portion of the pylon immersed in the fan stream, is calculated similarly:

$$D_{\beta PY} = C_{D\beta PY} q_F A_p$$

$$C_{D\beta PY} = \phi(M_{eF}, \text{pylon section characteristics}, A_p)$$

Plug boattail pressure drag including separation effects, can be expressed by the following equation:

$$D_{\beta P} = C_{D\beta P} q_F \frac{A_p}{2}$$

$$C_{D\beta P} = \phi(M_{epm}, \text{plug geometry})$$

Numerous published sources exist for aid in estimation of boattail coefficients, including data published by the NACA, etc. See references for Sections 8 and 9.

10.3.1.4 Scrubbing and Interference Drag

Scrubbing drag is the term used to differentiate between the friction drag of surfaces washed by free stream air and those surfaces exposed to fan exhaust or gas generator exhaust. Gas generator cowl scrubbing drag is determined by the cowl friction coefficient and fan exhaust flow conditions. Plug scrubbing drag, if the installation includes a plug nozzle, is based upon the gas generator exhaust flow conditions. For an engine configuration like the Garrett ATF-3, with both flows within the fan nozzle, a proportional quantity of fan and gas generator flow is assumed acting on the plug.

Gas generator cowl and pylon scrubbing drag can be expressed by

$$D_{\text{scrubGG}} = C_f A_w q_f R C_K$$

where:

C_f - skin friction coefficient

The preferred basis for C_f is test data obtained from similar configurations. In current practice, coefficients based upon flat plate theory and pipe flow theory are used as well and are considered to give satisfactory results. One engine manufacturer recommends a refinement over the use of an average coefficient whereby the growth of the boundary layer along the cowl, including the initial boundary layer growth upstream of the fan nozzle exit, is taken into account. C_f is then varied along the length of the cowl. This method is inherently more accurate. At cruise conditions, the difference in scrubbing drag for one particular installation computed by this method and that computed using an average coefficient is on the order of 3 percent. For either the average or varying coefficient method of solution, skin friction coefficients may be obtained empirically or from Prandtl-Schlichting and Frankl-Voishel equations.

For preliminary design effort, including the trade-offs inherent in configuration development, skin friction coefficients derived from Prandtl-Schlichting and Frankl-Voishel equations are considered satisfactory in the absence of empirically derived C_f values. The Prandtl-Schlichting skin friction drag coefficient based on surface wetted area is presented in Figure 10-18. Reynolds number, the abscissa of Figure 10-18, may be obtained from Figure 10-19. To correct the coefficient thus obtained to account for compressible flow, the Frankl-Voishel equation is employed, which is shown graphically in Figure 10-20. Local skin friction drag coefficients, plotted as a function of Reynolds number and showing the variation with Mach number, are presented in Figure 10-21.

A_w - area wetted by fan efflux

Fan flow relative to the pylon is shown in Figure 10-17. Although the straightback representation of the fan flow is considered satisfactory for preliminary estimation purposes, a more accurate assumption is considered to be the assumption of a constant flow area from the fan nozzle exit to the end of the gas generator cowl.

$$q_F = \frac{\gamma}{2} P_{eF} M_{eF}^2$$

R_C - skin friction roughness coefficient
 = 1.05 (Reference 6), = 1.06 (Reference 7)

K_C - compressibility correction (discussed above)

M_{eF} - average fan nozzle exit Mach number

Plug scrubbing drag can be expressed by essentially the same equation:

$$D_{scrubp} = C_f A_w q_p R_C K_C$$

$$q_p = \frac{\gamma}{2} P_{eGG} M_{eGG}^2$$

M_{eGG} - Gas generator (+ fan turbine) nozzle exit Mach number

A_w - area wetted by gas generator efflux

Typical scrubbing drag for an actual high bypass turbofan engine installation is presented in Figures 10-22 and 10-23. These data are for cruise conditions at 36,089 feet and are presented in terms of uninstalled thrust. These data show scrubbing drag increasing with Mach number and thrust although at higher thrust levels, the scrubbing drag is seen to be a smaller percentage of the thrust.

Pylon friction and form drag, for that portion of the pylon that is not scrubbed by fan exhaust air can be handled conventionally, as stated above, as components of airplane drag.

Interference drag, a function of the nacelle position relative to the wing or fuselage is best obtained empirically. Some typical data from Reference 5, using long fan cowl nacelles, which indicates the incremental airplane drag change with nacelle position, are shown in Figure 10-24. Nacelle pressure coefficients which reflect the fuselage and wing proximity effects, are shown in Figure 10-25. These data were obtained with a short fan cowl configured powered simulator. Owing to the individuality of each configuration, testing is recommended to sort out interference drag.

10.3.1.5 Testing Methods

Three basic model schemes have been used to simulate turbo-fan propulsion systems:

- a) Flow-through nacelles
- b) Blowing simulators
- c) Powered fan simulators

Flow-through nacelles are a conventional tool for evaluating the external drag of the engine nacelle as installed on the airplane. Typical flow-through nacelles are presented in Figure 10-26. Flow-through nacelles are used extensively, primarily because of their low cost owing to the simple construction, and also because of the ease with which they can be moved around on the model so as to test a large matrix of nacelle positions. A flow-through nacelle is usually designed so as to simulate cruise airflow conditions, i.e., match the cruise inlet mass flow ratio. Lower mass flow ratios can be achieved by the use of annular restrictors or screens in the exhaust passages. In designing the basic flow-through nacelle to simulate cruise inlet mass flow ratio, other nacelle criteria are compromised. Among these are nozzle area and nacelle blockage, which are larger than the actual engine, and afterbody boattailing, which is less. The latter could result in an optimistic picture of the interference drag, particularly in the testing of nacelle positions in close proximity to adjacent surfaces. In Figure 10-27, wind tunnel test data obtained from flow-through and powered fan simulator tests of geometrically similar nacelles is presented. These data, for two nacelle positions, were obtained during a series of tests in the same wind tunnel. As the nacelle is moved aft, more under the wing, the data indicate a significant difference between the unpowered and powered results.

Blowing simulators provide the capability of simulating the proper afterbody shape and the effect of fan air on the nacelle drag. A sketch of one is shown in Figure 10-28. Afterbody, i.e., gas generator cowl scrubbing drag obtained using isolated blowing nacelles, compared with predicted drag based on boundary-layer theory used with velocity decay measurements, is presented in Figure 10-29. These data, presented by Lawrence in Reference 8, show that in the lower fan exit pressure ratio region, typical of high bypass ratio single stage fans, theoretical prediction methods are verified.

Inlet mass flow conditions, and the effect of flow over the forward cowl on the aft portions of the nacelle are not simulated with the blown nacelle. In testing nacelle positions where these items are considered of minor importance, the blowing simulator provides the capability of testing a variety of afterbody geometries over a wide spectrum of fan pressure ratios and flows, for a modest model investment.

To overcome the limitations of the flow-through and blowing nacelles, and as a part of the continual striving to obtain simulation of the characteristics of an actual installed engine nacelle, powered fan simulators were developed. These simulators provide the capability to simultaneously simulate aerodynamic and geometric properties. A sketch of such a simulator is presented in Figure 10-30.

High pressure air or nitrogen is used to drive a turbine which runs the fan at the front of the simulator. The turbine and the fan are designed to provide the simulation of the desired pressure ratios. A typical full scale engine characteristic for static operation is compared with data obtained from a calibration of a powered fan simulator in Figure 10-31. Static calibration of powered simulators, important in the delineation of the pressure drag breakdown can be accomplished in facilities similar to that sketched in simplified form in Figure 10-32. In current design simulators, all of the flow which enters the inlet exhausts through the fan, therefore if the proper pressure ratios and nozzle geometries are simulated, the inlet mass flow ratio is somewhat less than desired, e.g., for a 5 to 1 bypass ratio fan the resulting mass flow would be 5/6 of that required to simulate exactly the full scale engine. This characteristic does not detract seriously from the simulator's effectiveness.

Scrubbing drag of an isolated nacelle can be obtained from a static calibration of a powered fan simulator. Net thrust including scrubbing and boattail drag, as presented in Figure 10-33, is obtained from the balance reading in testing with a setup such as that shown in Figure 10-32. Gross thrust and boattail pressure drag is computed from model nozzle and surface pressures respectively, and subtracted to obtain the isolated scrubbing drag.

Development of this type simulator was initiated for the C-5A program. A complete description and results of early tests are presented in Reference 9.

No simulator has yet been developed which would combine the aerodynamic and geometric properties of the powered fan simulator with full scale engine jet temperature simulation. This would be in effect a small scale engine. The potential advantage of easier flow simulation might well be outweighed by model design difficulties, cost and facilities limitations as well as limited flexibility. Temperature simulation in a powered simulator intended for higher speed applications is discussed in Reference 23.

Simulation of various engine nacelle characteristics is summarized in the following table from Reference 10.

ENGINE NACELLE SIMULATION SUMMARY

<u>Simulation of</u>	<u>Simulated by</u>
Inlet Geometry (Inlet mass flow ratio)	Flow-through nacelles Powered nacelles ¹
Fan aft cowl and gas generator cowl geometry (Nozzle pressure ratios)	Blowing nacelles Powered nacelles ¹
Nacelle-pylon-wing interaction Thrust Reverser Operation	Powered nacelles ² Blowing nacelles Powered nacelles
Jet wakes and scrubbing ³	Blowing nacelles Powered nacelles

¹some compromise on inlet and nozzle areas

²includes interaction between nacelle surfaces

³simulation of temperature effects possible by
heating air supply to blowing nacelle

10.3.2 Internal Losses

Inlet recovery, compressor airbleed, shaft power extraction, long fan cowl duct losses, cooling drag and nozzle efficiency variation, must be accounted for, when applicable, in the computation of installed engine performance.

Inlet recovery for subsonic cruise vehicles is maintained close to 100 percent at cruise conditions so that the only portion of the flight regime significantly affected by inlet recovery losses is the take-off mode, where inlets designed for high speed cruise operate less efficiently. This characteristic has prompted the use of auxiliary inlets on many installations. A sketch of a typical auxiliary inlet is shown in Figure 10-34. Static performance of an inlet with a highlight to throat ratio of 1.18 with and without auxiliary inlets is presented in Figure 10-35, based on Reference 11 data. Note, however, that an inlet with a ratio of 1.26 matches the performance of the 1.18 ratio inlet with auxiliary inlets. Thus, as with any subsonic aircraft inlet system, the trade-off between inlet recovery and inlet drag must be considered. Subsonic inlet design is delineated in Section 2.

Compressor airbleed has a significant effect on the high bypass engine, owing to the considerably higher cycle pressures of the high bypass turbofan compared to the conventional turbojet. Intermediate stage bleed ports alleviate this problem somewhat. In performance optimization, the use of compressor bleed in auxiliary systems must be traded against systems utilizing direct power extraction. Preliminary data

indicate that for a given incremental change in SFC, between 3 and 10 horsepower, depending on flight condition, can be extracted from the engine per 1 lb/min compressor bleed.

Long fan cowl duct losses can be computed by conventional methods such as Reference 22. These losses are usually included in the internal losses accounted for by the engine manufacturer is his determination of uninstalled engine performance, however, and thus do not show up as a separately stated loss in performance evaluation. When considering the trade-off between long and short fan cowl configurations, computation of fan duct losses is required. Pressure losses for a typical long duct configuration are on the order of 1-1/2 percent.

Nozzle efficiency is affected by length and area variation, by pylons and protuberances, and nozzle offset, i.e., flow turning to exhaust through a larger annulus. Typical data showing the effect of offset is presented in Figure 10-36. The gross thrust of each stream is computed separately, taking into account any differences in nozzle performance compared to the performance of the referee nozzles upon which the engine specification is based. Conventional nozzle performance is discussed in Section 8. The effects of pylon and local fairing blockage are best estimated from tests of similar configurations. Limited data obtained with a faired protuberance with a frontal area equal to 7 percent of fan efflux area indicated a 1-1/2 percent gross thrust penalty. As the gas generator cowl is the plug for the fan nozzle, gaps, steps and surface waviness must be minimized to maintain high nozzle efficiency.

10.4 Performance Summary

For a typical high-bypass ratio turbofan, the net propulsive effort, that is the thrust available after taking into account all propulsion system losses, is computed by correcting engine specification data for:

- a) Inlet duct losses
- b) Low pressure (interstage) compressor bleed
- c) High pressure (last stage) compressor bleed
- d) Power extraction
- e) Fan and gas generator nozzle area deviations from referee area
- f) Fan and gas generator nozzle velocity and flow coefficient deviations from referee value
- g) Fan and gas generator nozzle duct pressure loss deviations from specification nozzle levels
- h) Inlet additive drag
- i) Miscellaneous airflow drag (environmental control system heat exchangers, air-oil coolers, generator cooling systems, etc.)

- j) Nacelle drag
- k) Ambient temperature effects

In equation form

$$F_{ne} = F_n \left(\frac{F_{namb}}{F_{nstd}} \right) - \sum (\Delta F_n) - D'_{add} - D'_{misc} - D_{nac}$$

F_{ne} - net propulsive effort

F_n - specification net thrust

F_{namb}/F_{nstd} - Ratio of thrust at desired ambient temperature to thrust at standard ambient temperature

ΔF_n - Thrust corrections for duct loss, compressor air bleed and power extraction, and nozzle deviations from reference nacelle

D'_{add} - Corrected inlet additive drag (theoretical additive drag corrected for cowl lip shape variation and changes in external nacelle pressures)

D'_{misc} - Net ram drag of miscellaneous airflow (full ram drag of miscellaneous airflows adjusted for thrust of exiting momentum)

D'_{nac} - Scrubbing and form drag of nacelle and pylon, including effects of flow separation. Friction drag of the fan cowl and that part of the pylon unwashed by fan efflux are generally considered part of nacelle drag but may optionally be considered portions of aircraft drag. As noted in Figure 10-27 and Reference 12, wing interference effects must be considered in the evaluation of nacelle afterbody drag and overall installed performance.

Corrections for ambient temperature variations, inlet duct loss, compressor bleed, power extractions, and deviations from the reference nozzles are obtained from the applicable specification for a particular engine configuration. A typical nacelle drag breakdown at aircraft cruise conditions is presented in Figure 10-37, which shows that total nacelle drag represents approximately 8 percent of the engine net thrust loss due to installation. The effect of installation drag plus bleed and power extraction on cruise SFC is presented in Figure 10-38. Cruise SFC may be directly related to range, so that the curve shows the relative contribution of internal losses and external losses on range. For a typical high bypass turbofan installation, the total installation loss, as a percentage of uninstalled cruise thrust at 36,089 feet, is presented in Figure 10-39.

10.5 Thrust Reverser Installation

For high bypass installations, it is frequently necessary to reverse only the fan thrust to achieve sufficient reversal effectiveness. This is because the high bypass fan produces approximately 3/4 of the jet thrust. A comparison of reverser effectiveness is presented in Figure 10-40 for three reversing schemes:

- a) fan only
- b) fan stream reversed and primary stream spoiled
- c) fan and primary streams reversed

Complexity and weight increase must be traded against landing requirements in reverser scheme selection. Only modest reversal of the primary stream is assumed in the scheme with both flows reversed in consideration of fan flow interaction and high temperature constraints on the primary stream reverser design. A sample of the cascade type fan thrust reverser is presented in Figure 10-41. This is the system used on the C-5A.

Sketches of a target-type reverser such as currently in use on the 727, and a proposed plug spoiler type reverser are also presented in Figure 10-41. CF6 engine thrust reverser and spoiler features are detailed in Reference 24.

Important criteria in the thrust reverser design, as discussed in Section 8, are minimum drag (stowed) and minimum performance penalty, landing distance, and engine ingestion of exhaust gases. A sketch showing attached flow reingestion with a cascade reverser is shown in Figure 10-42. The effects of such reingestion are shown in the graphs following Figure 10-42. The data for Figures 10-43 through 10-45 were obtained with powered fan simulators which are discussed in paragraph 10.3.1.5. The inlet distortion shown in Figure 10-44 is defined as

$$n_D = \frac{P_{T_{\max}} - P_{T_{\min}}}{P_{T_{\text{avg}}}}$$

The deleterious effects of reingestion on reverse thrust are summarized in Figure 10-46. Note that at 60 knots, the reverse thrust achieved is only 50% of that desired. This is reflected in increased stopping distance. Recommended improvement methods include aerodynamic surfaces, vane placement so as to cancel undesirable flow vectors, and spoiler systems, e.g., mechanical and compressor air bleed driven systems.

References

1. Wilde, G.L. and Pickerell, O.J., The Rolls-Royce Three-Shaft Turbofan Engine, AIAA Paper No. 67-375, American Institute of Aeronautics and Astronautics, June 12-14, 1967.
2. Wooten, J.R., Windmill Drag of 902-C Series Engines, AK.0000-172, Allison Division, General Motors Corporation, 30 November 1965.
3. Allison, H.B. and Leslie, H.R., Installation Considerations for High Bypass Ratio Turbofan Engines, AIAA Paper No. 67-390, American Institute of Aeronautics, June 12-14, 1967.
4. Kojima, J., Instructions for Use of the Douglas-Neumann Potential Flow Program for Axisymmetric Flow, NA65-385, North American Aviation, Inc., May, 1965.
5. Swan, W.C., A Discussion of Selected Aerodynamic Problems on Integration of Propulsion Systems with the Airframe on Transport Aircraft, D6-18084, The Boeing Company, AGARD Specialists Meeting, Arnold Air Force Station Tullahoma, Tennessee, October 25-27, 1965.
6. Estimated Scrubbing Drag, Engine, Aircraft Turbofan T64/F1C, General Electric Company.
7. Frazier, G.T., Aerodynamic Considerations for Engine Exhaust Design for Subsonic High Bypass Fan Engines, 660734, Society of Automotive Engineers, Inc., October 3-7, 1966.
8. Lawrence, R.L., Afterbody Flow Fields and Skin Friction on Short Duct Fan Nacelles, J. Aircraft Vol. 2, No. 4, 318-327, July-August 1965.
9. Kutney, J.T., Wind Tunnel Simulation of Inlet and Exhaust System Effects with the Powered Nacelle for Wing-Nacelle Combinations, R66FPD207, General Electric, 20 June 1966.
10. Lawrence, R.L., Testing as an Aid to Locating Engines on Subsonic Transports, AIAA Paper No. 66-640, American Institute of Aeronautics and Astronautics, June 13-17, 1966.
11. Viall, W.S., Aerodynamic Considerations for Engine Inlet Design for Subsonic High Bypass Fan Engines, 660733, Society of Automotive Engineers, Inc., October 3-7, 1966.

12. Hower, G.K. and Nye, J.L., Aerodynamic Effects of Environment and Geometrical Variations on SST Nacelle Afterbody Drag, R63FPD141, Flight Propulsion Division, General Electric Co., April 30, 1963.
13. Douglass, W.M., Aerodynamic Installation of High Bypass Ratio Fan Engines, 660732, Society of Automotive Engineers, Inc., October 3-7, 1966.
14. Neitzel, R.E. and Hemsworth, M.C., High Bypass Turbofan Cycles for Long Range Subsonic Transports, J. Aircraft, Vol. 3, No.4, July-August 1966.
15. Kutney, J.T., High Bypass Versus Low Bypass Engine Installation Considerations, 660735, Society of Automotive Engineers, October 3-7, 1966.
16. Bagby, C.L. and Andersen, W.L., Effect of Turbofan Cycle Variables on Aircraft Cruise Performance; AIAA Paper No. 65-796, American Institute of Aeronautics and Astronautics, November 15-18, 1966.
17. L'Anson, L.R., The Application of the High Bypass Turbofan for Business and Executive Aircraft, SAE 660221, Society of Automotive Engineers, March 30-April 1, 1966.
18. JT9D, S-1261B, Pratt and Whitney Aircraft, October 1967.
19. Kester, J.D. and Slaby, T.G., Designing the JT9D Engine to Meet Low Noise Requirements for Future Transports, 670331, Society of Automotive Engineers, April 24-27, 1967.
20. Thompson, J.D., Thrust Reverser Effectiveness on High Bypass Ratio Fan Powerplant Installations, Society of Automotive Engineers, Inc., October 3-7, 1966.
21. Saylor, J.M. and Smith, R.E., Jr., Internal and External Aerodynamics of the C-141A Nacelle, AIAA Paper No. 65-604, American Institute of Aeronautics and Astronautics, June 14-18, 1965.
22. Henry, J.R., Design of Power-Plant Installations Pressure-Loss Characteristics of Duct Components, ARR L4F26, NACA, May 13, 1944.
23. Naujokas, J.A., Teasley, H.M. and DeLany, J.T., Powered Model Simulator Study, Final Report, NR69H-675.
24. Lennard, D.J., Design Features of the CF6 Engine Thrust Reverser and Spoiler, 690411, Society of Automotive Engineers, Inc., April 21-24, 1969.

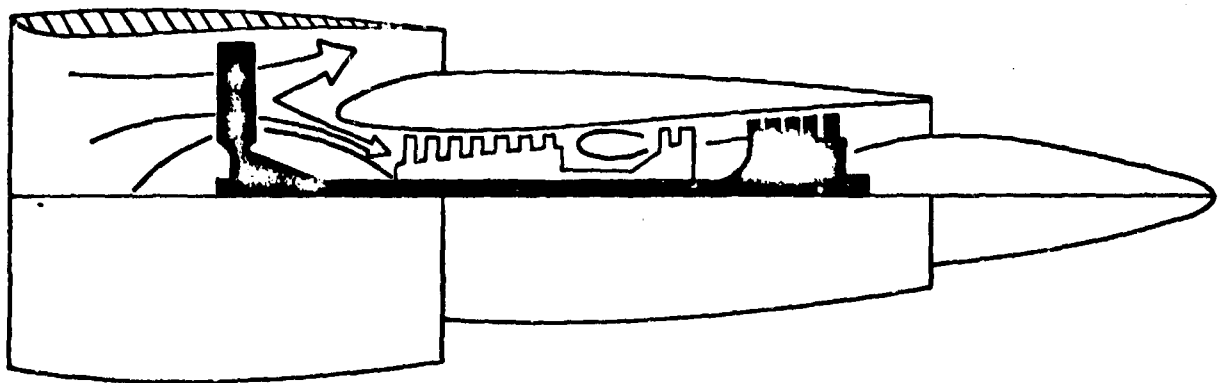


FIGURE 10-1. Turboprop Gas Flow Paths

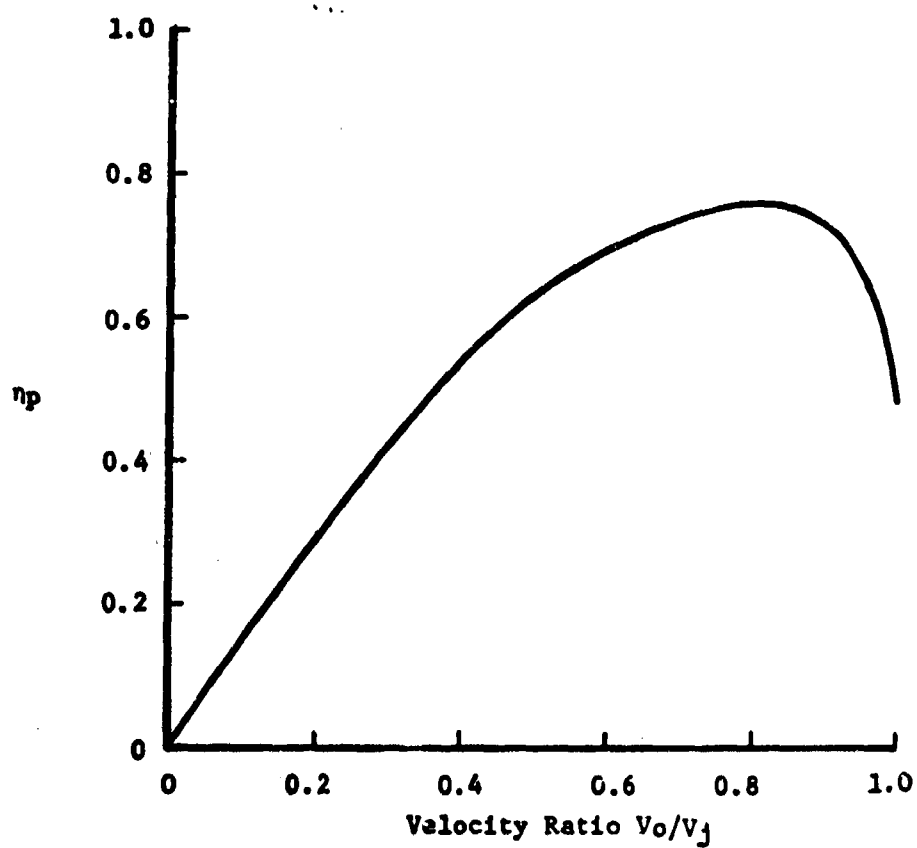


FIGURE 10-2. Propulsive Efficiency

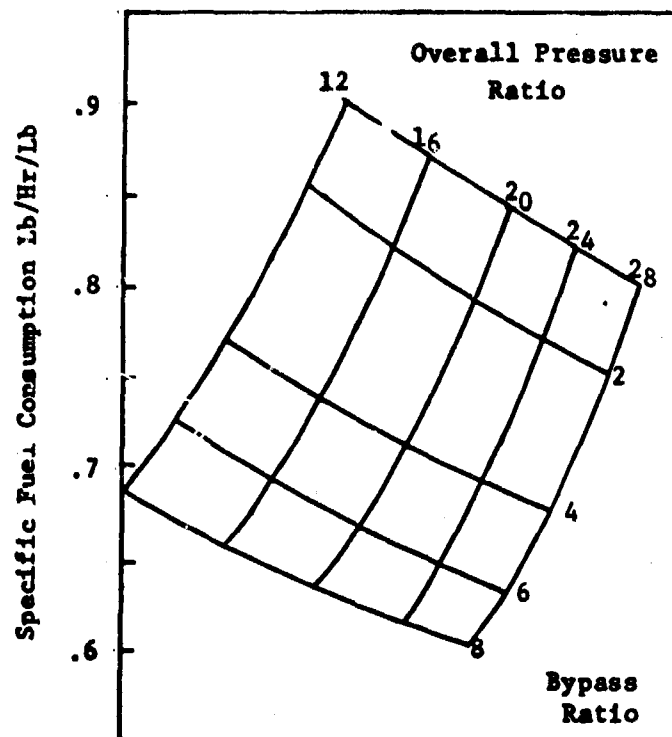


FIGURE 10-3. Specific Fuel Consumption

Mach 0.8

36,089 Ft

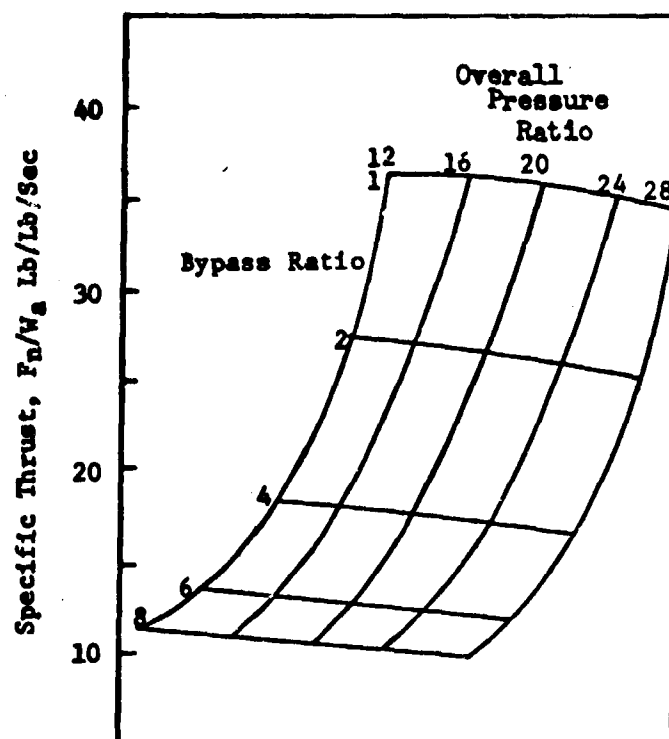


FIGURE 10-4. Specific Thrust

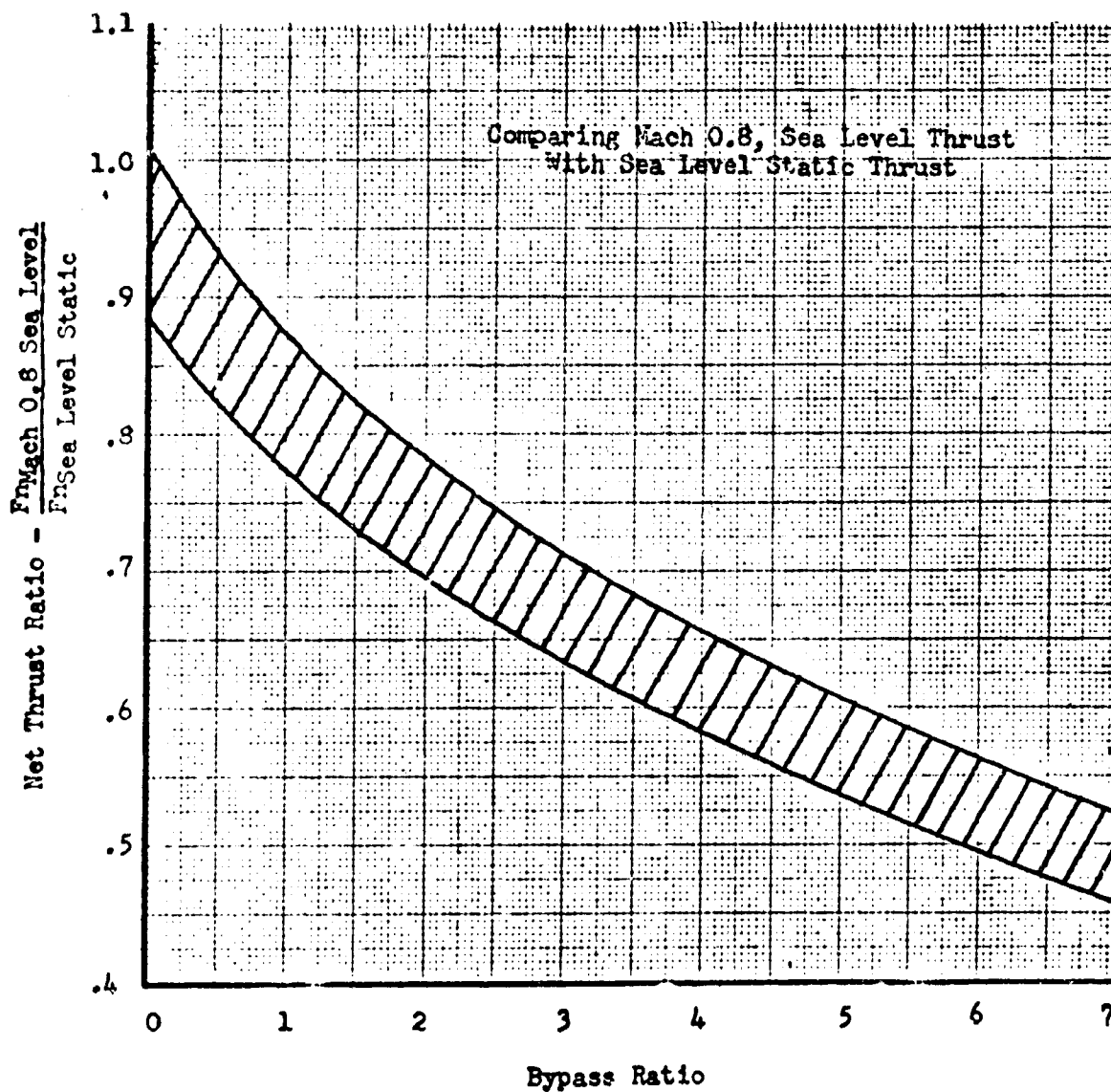


FIGURE 10-5. Thrust Lapse With Speed.

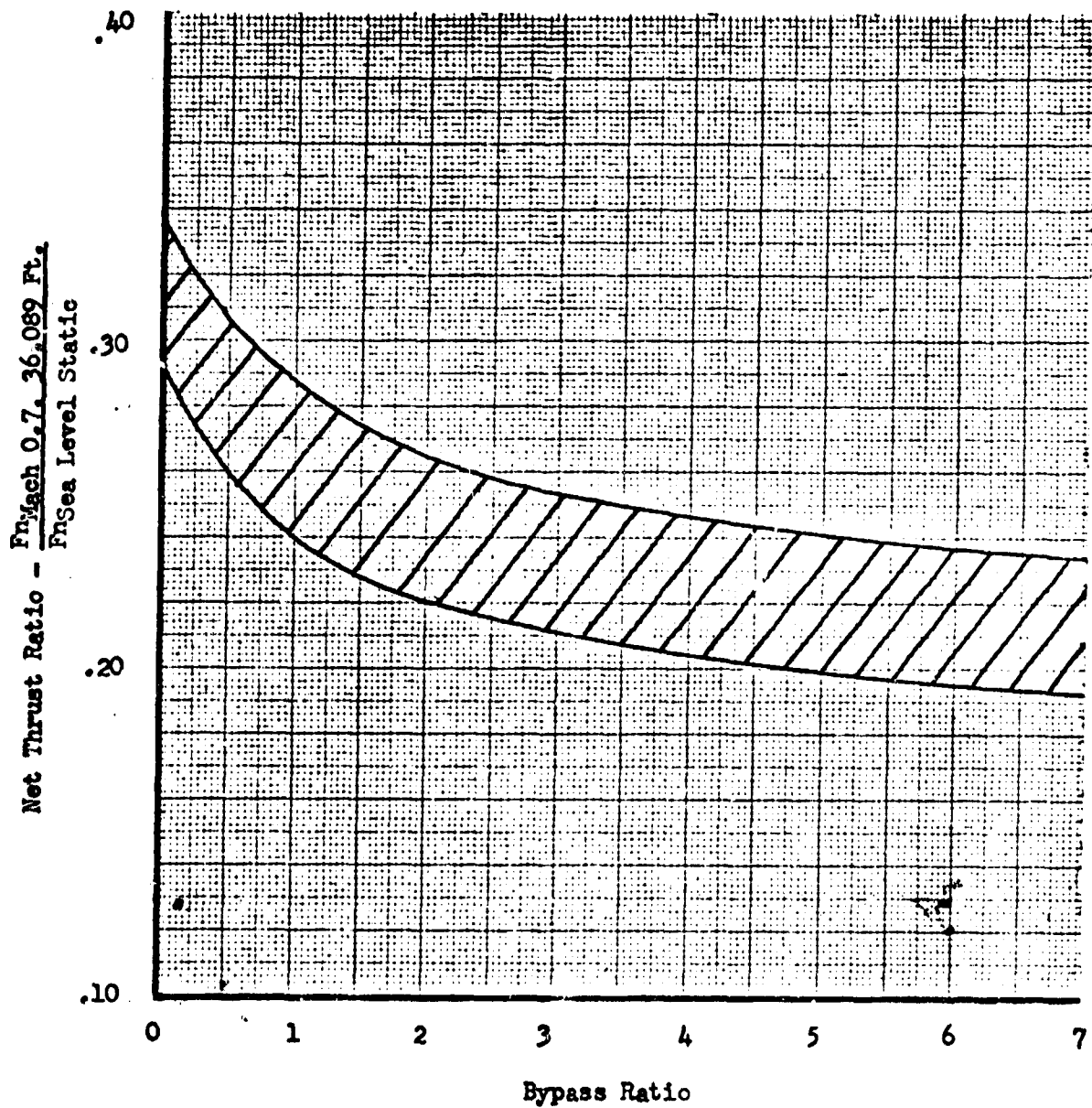


FIGURE 10-6. Cruise to Static Thrust Ratio.

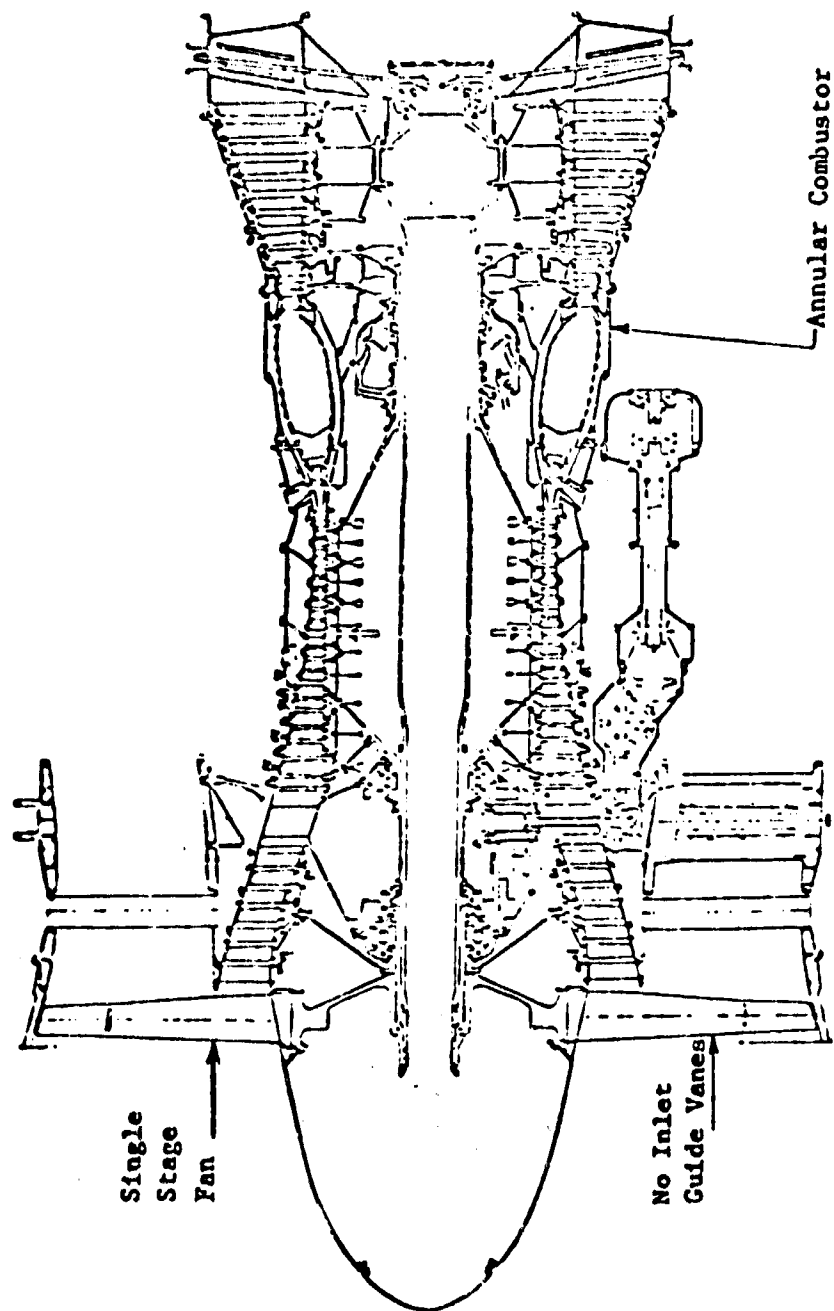


FIGURE 10-7. JT9D-1 Cutaway.

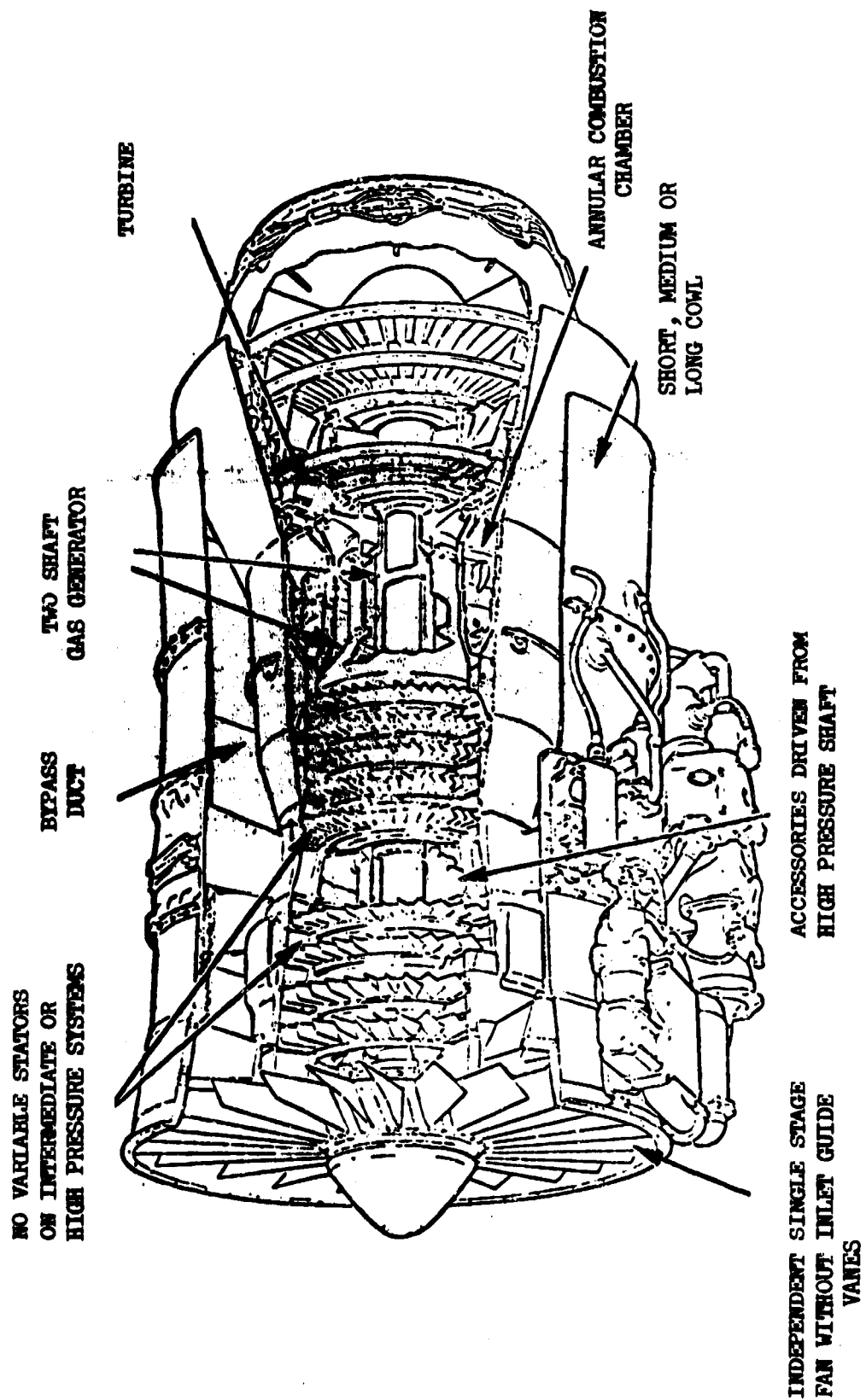


FIGURE 10-8. RB. 203 Trent Cutaway

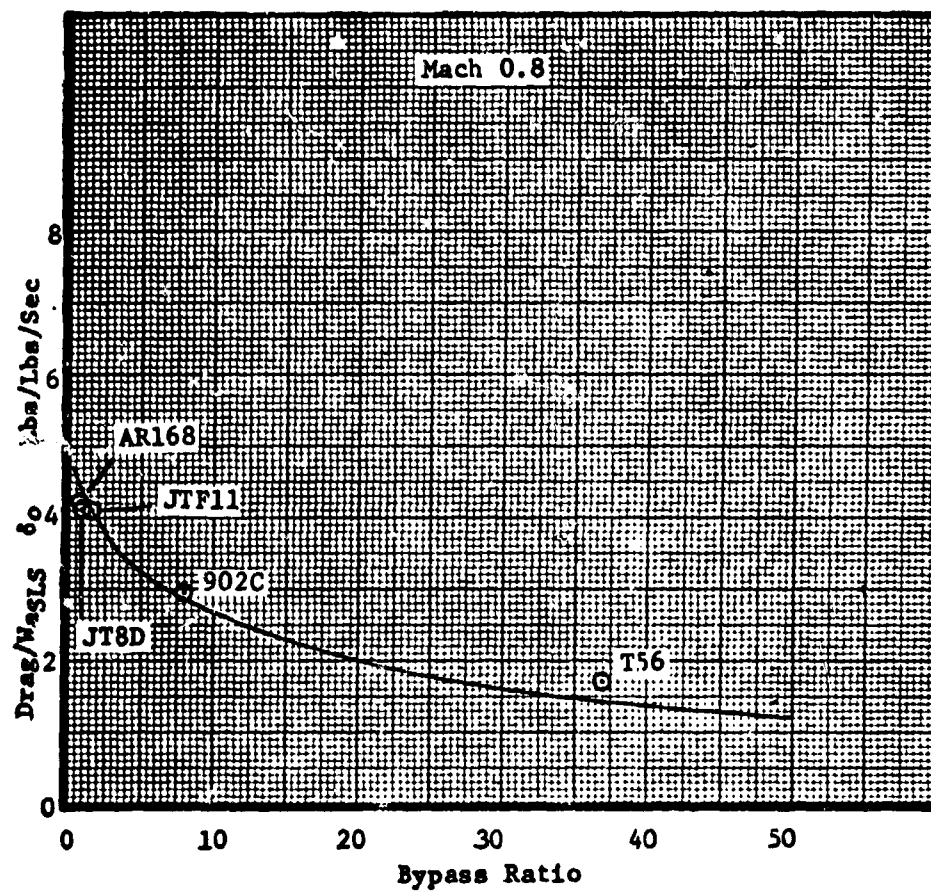


FIGURE 10-9. Estimated Windmilling Drag

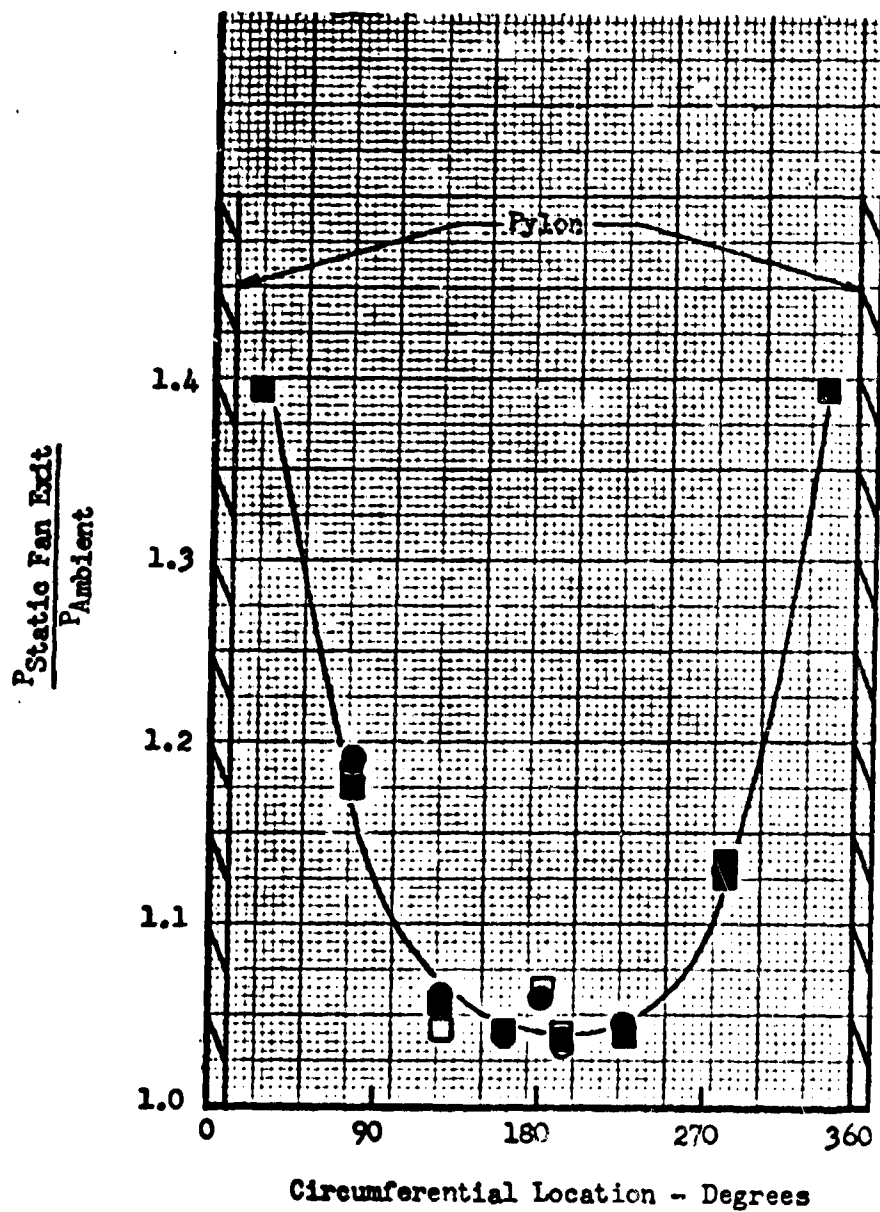
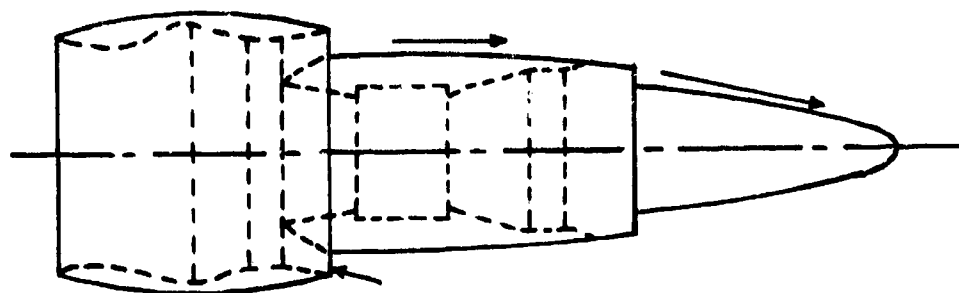
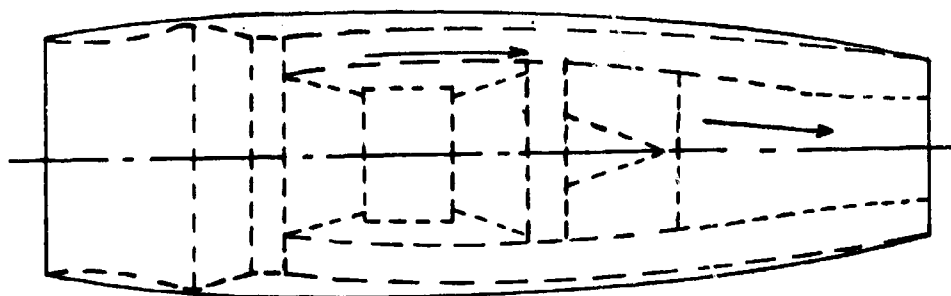


FIGURE 10-10. Typical Fan Exit Static Pressure Distortion.



Short Fan Cowl



Long Fan Cowl

FIGURE 10-11. Fan Cowl Comparison

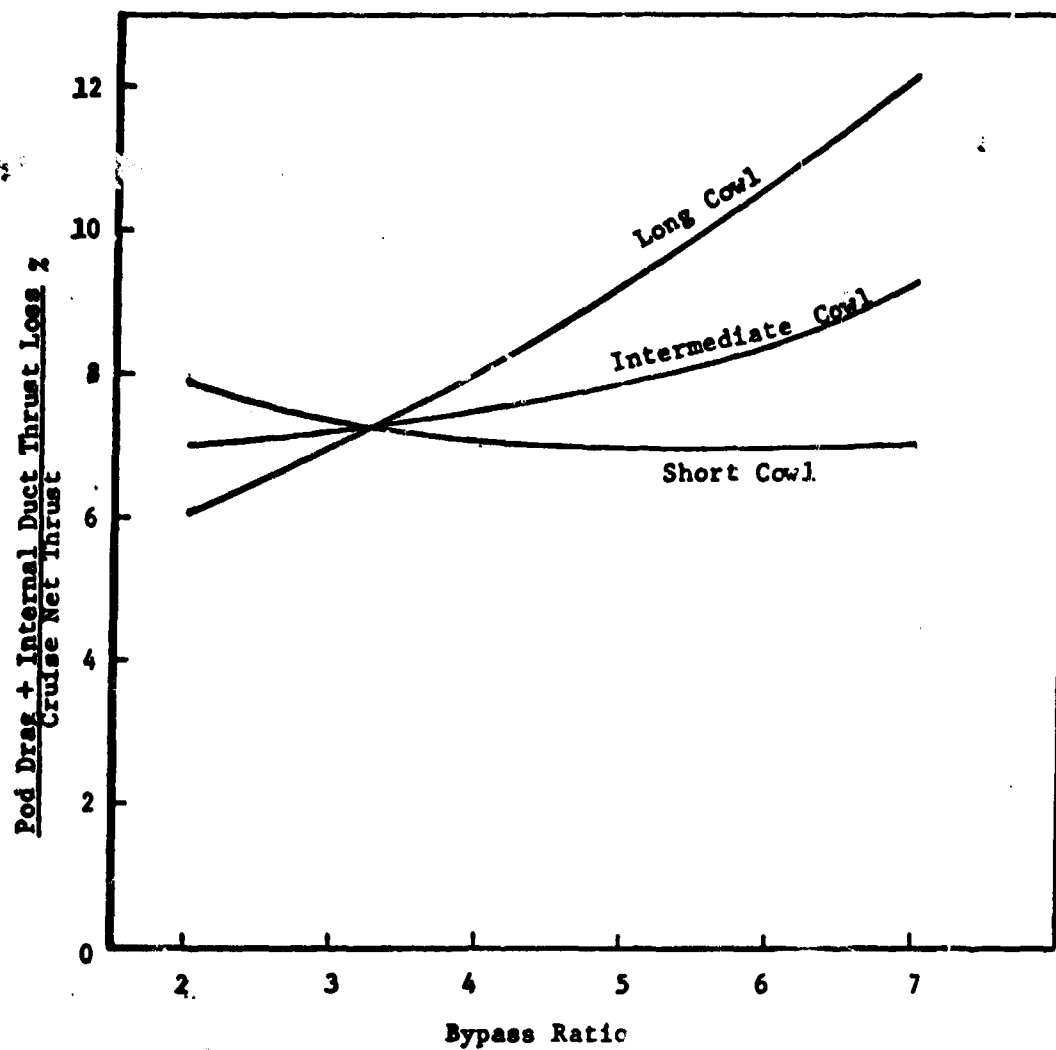


FIGURE 10-12. Cowl Length Comparison

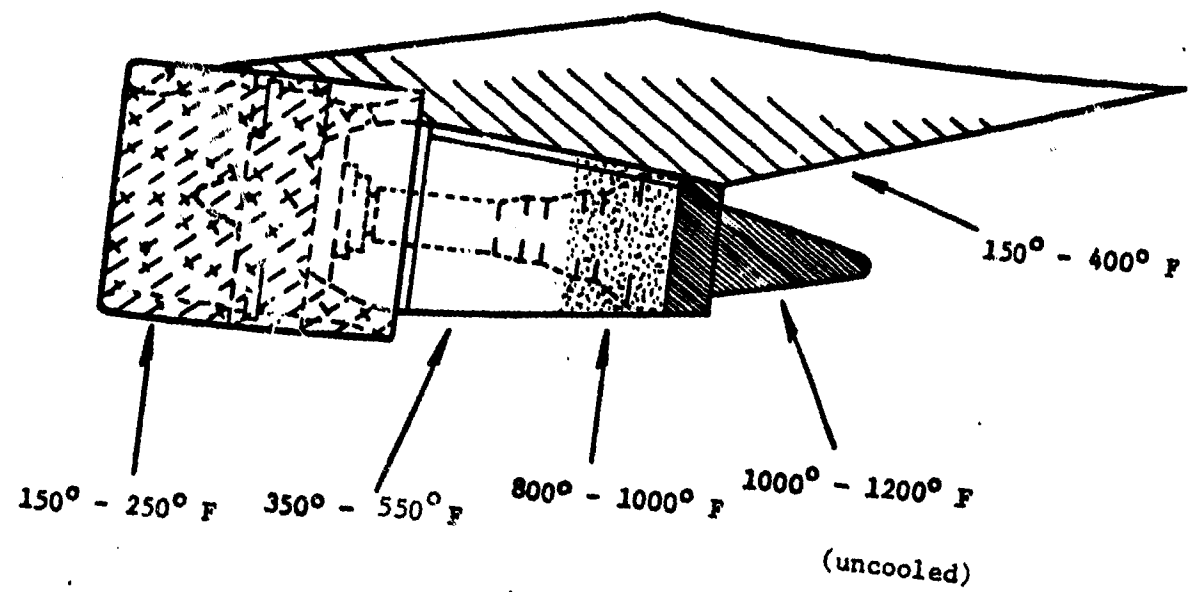


FIGURE 10-13. Typical Compartment Temperature Zones

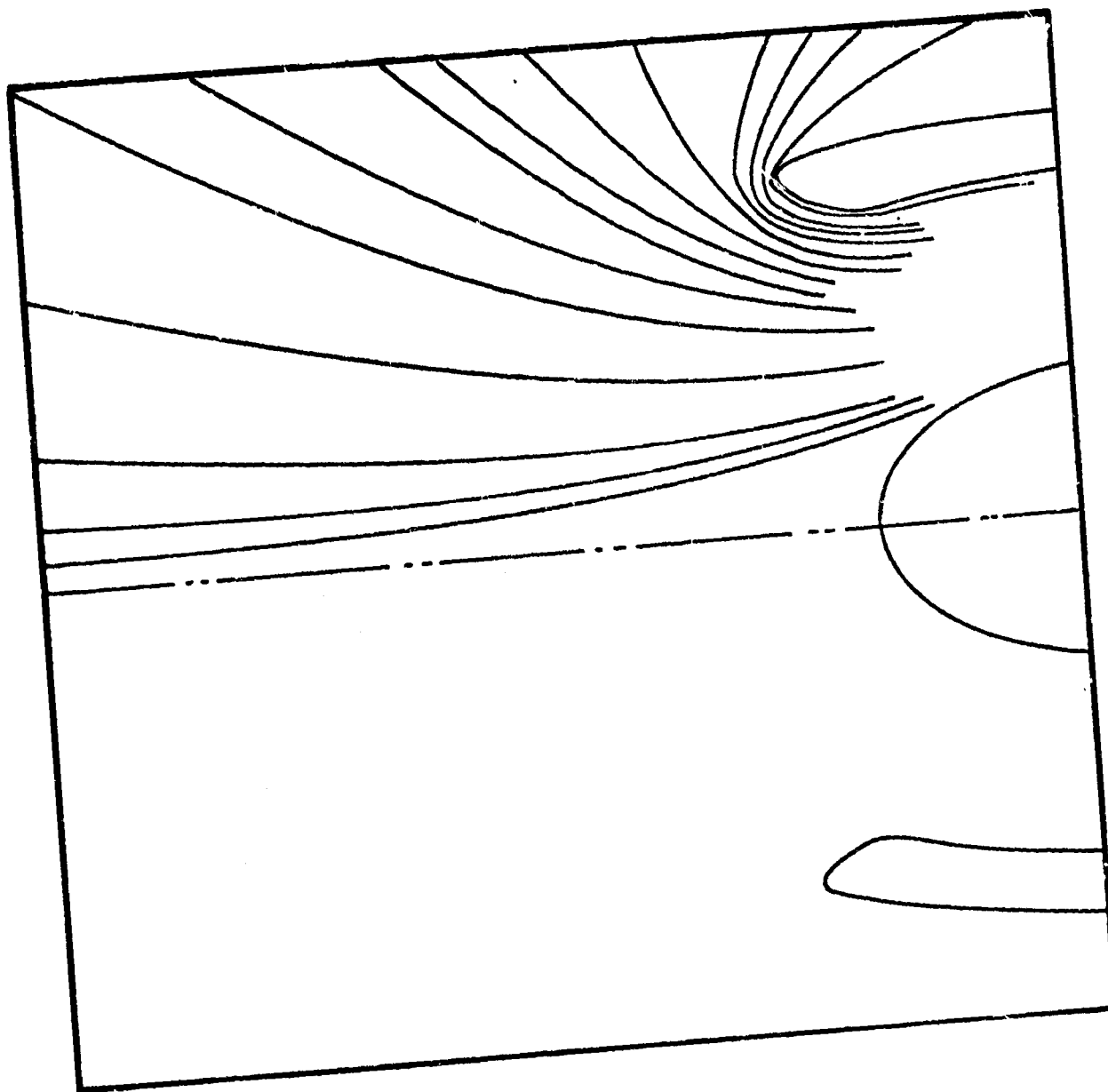


FIGURE 10-14. Typical High Bypass Turbofan Inlet Velocity Profile
Static and Low Speed

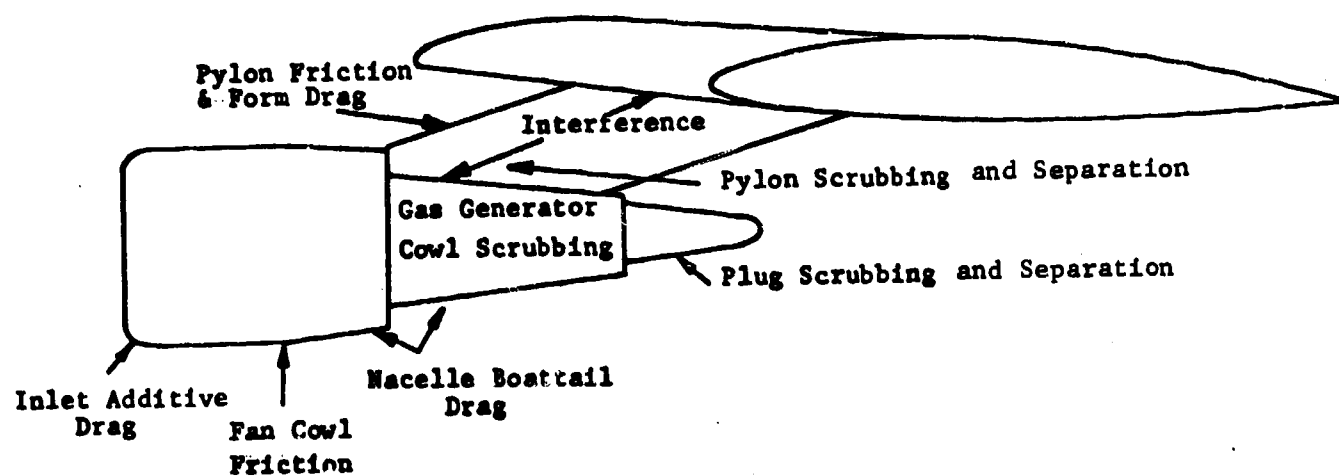


FIGURE 10-15 External Drag Breakdown

$M_0 = .8$
 $H = 0.5775 \text{ in.}$
 $D_b = 3.0 \text{ in}$
 $h/D_b = .15$

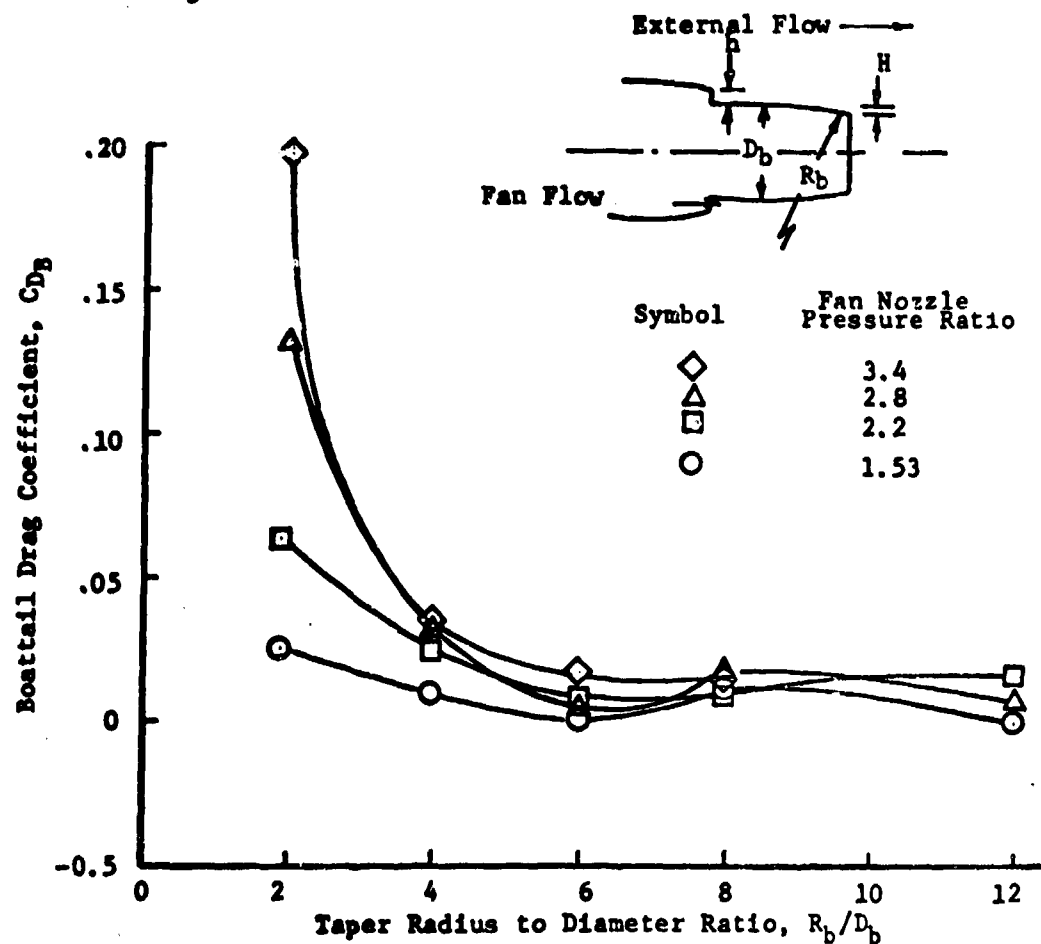


FIGURE 10-16. Afterbody Boattail Drag Test Results
From Reference 9

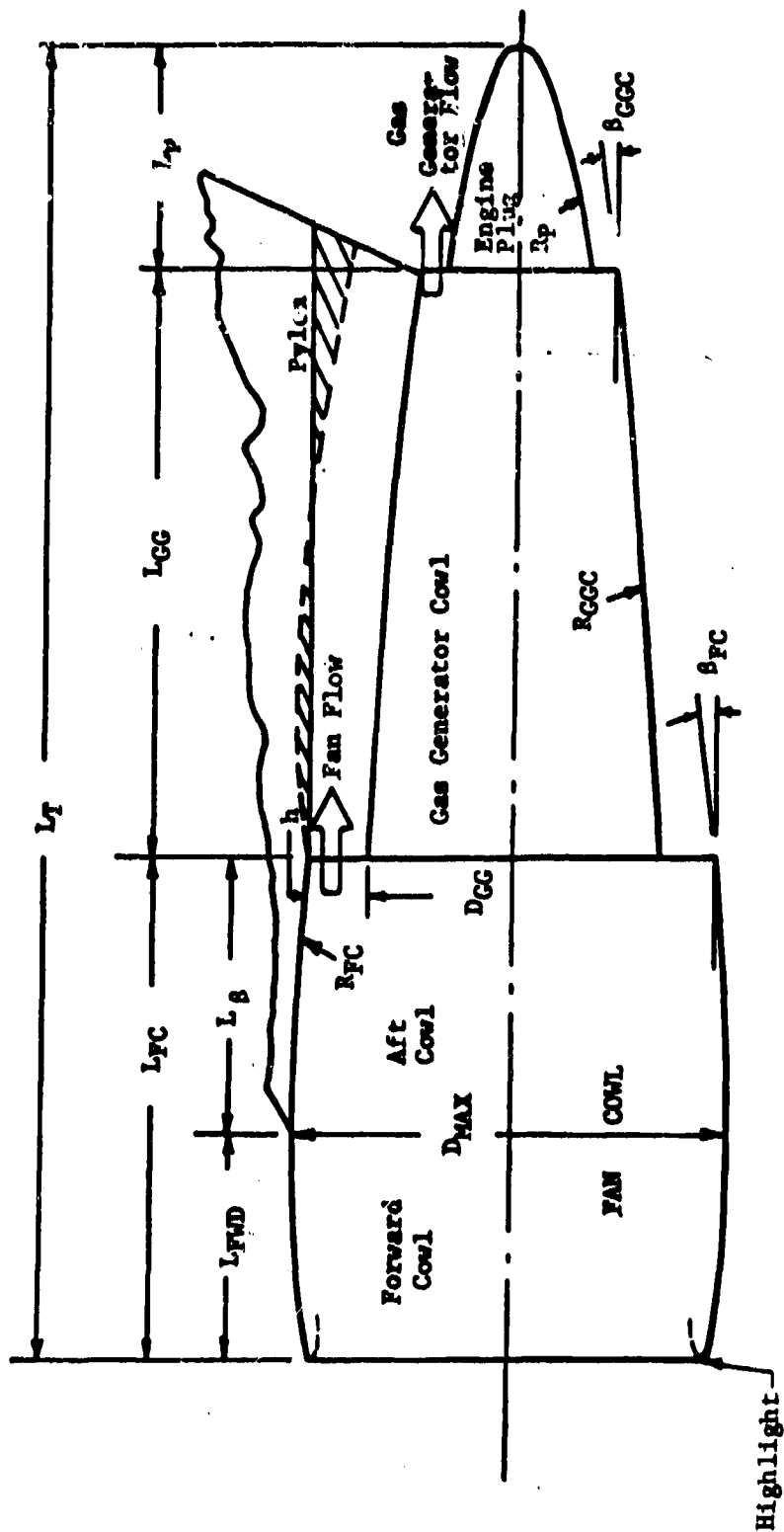


FIGURE 10-17. Front Fan Nacelle

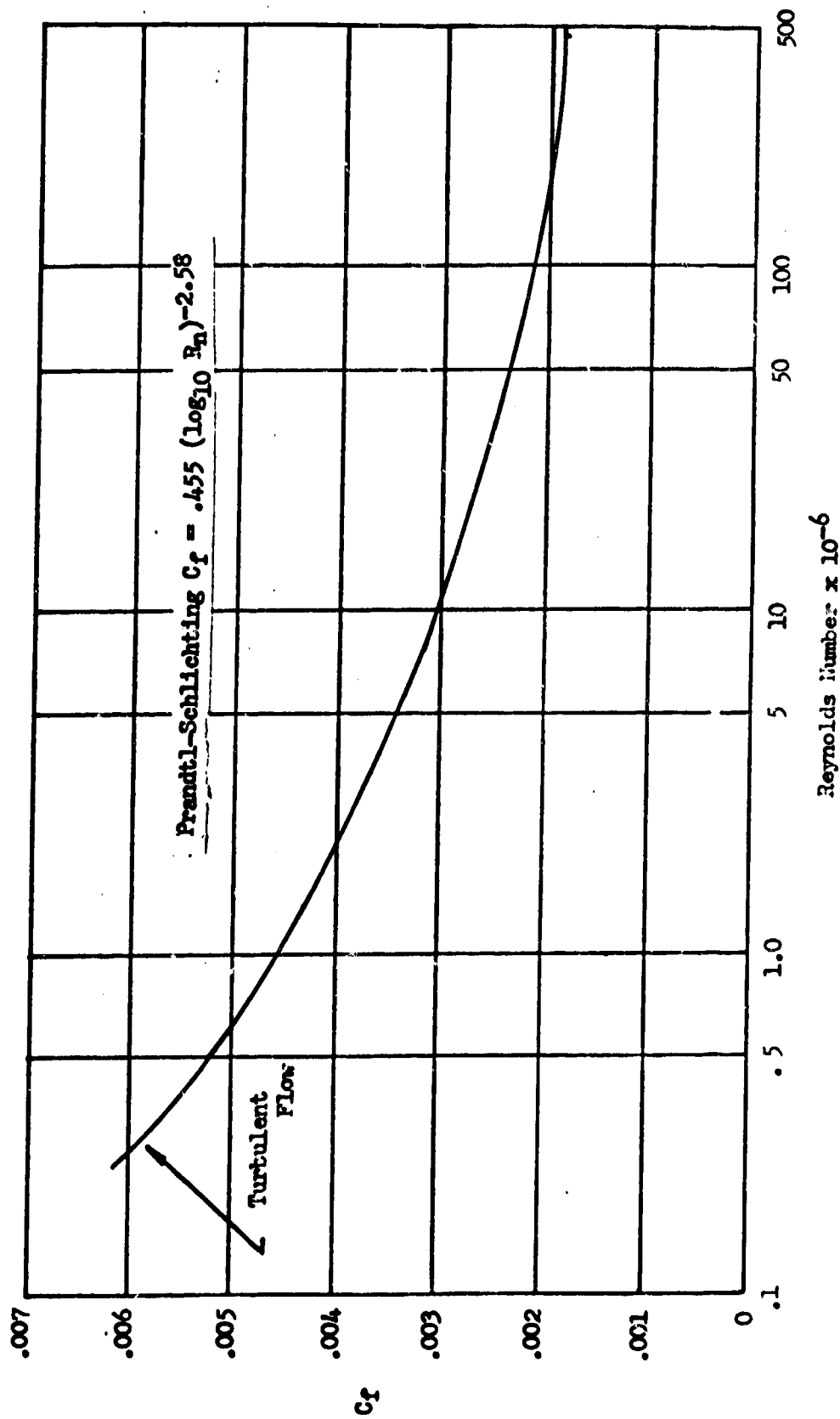


FIGURE 10-18. Skin Friction Drag Coefficient Based on Surface Wetted Area.

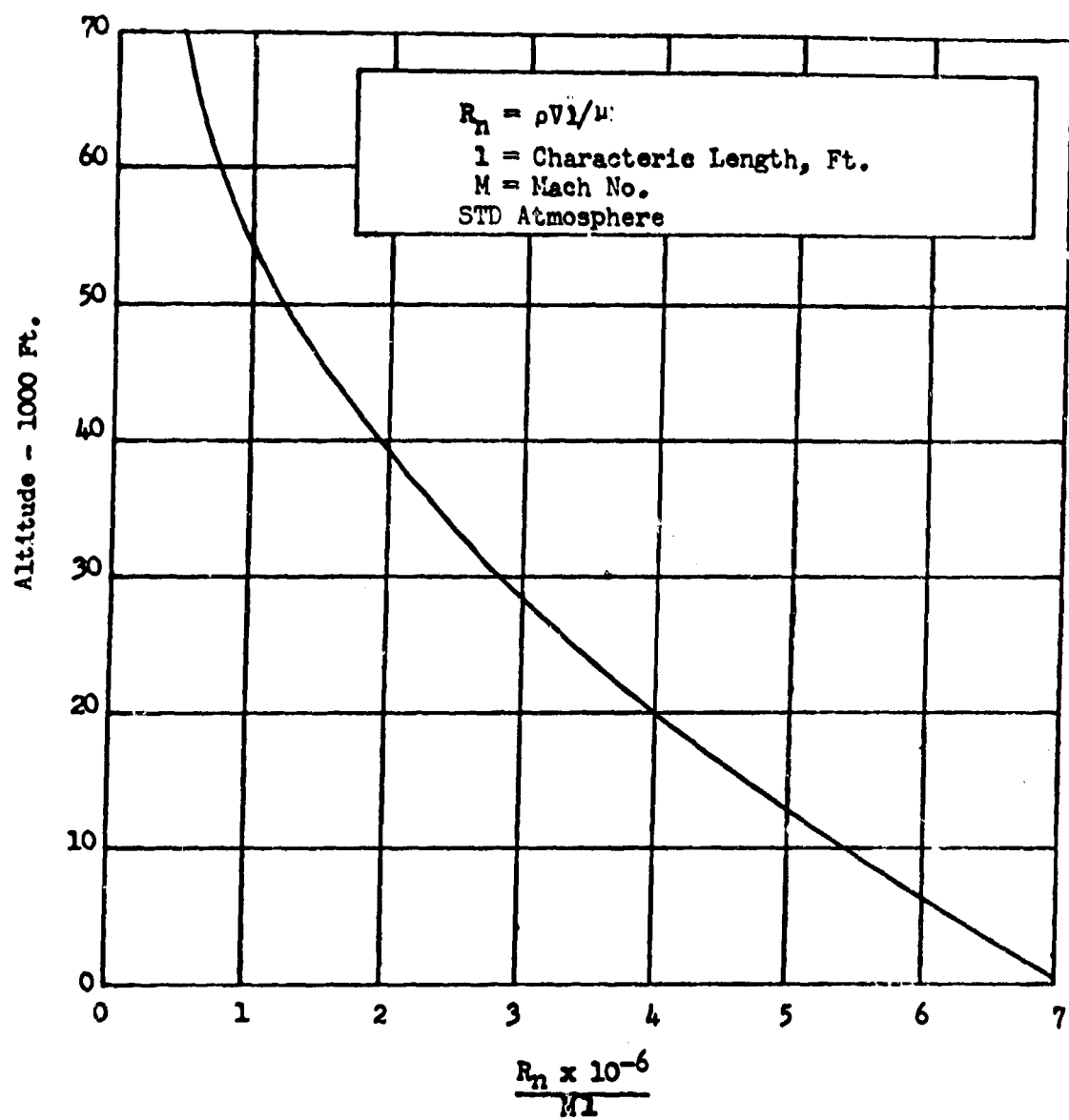


FIGURE 10-19 . Reynolds Number.

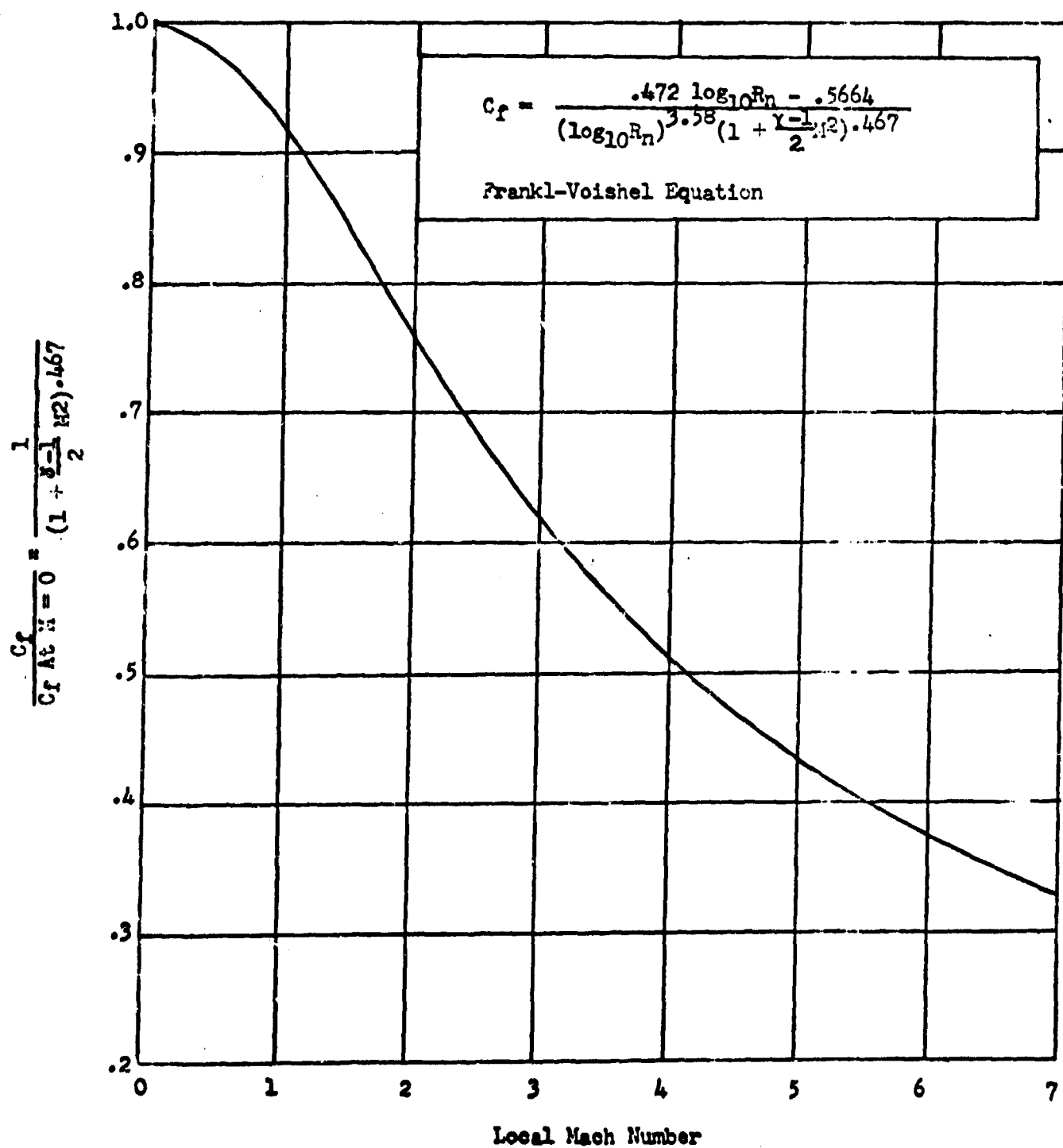


FIGURE 10-20. Effect of Mach Number on the Skin-Friction Coefficient.

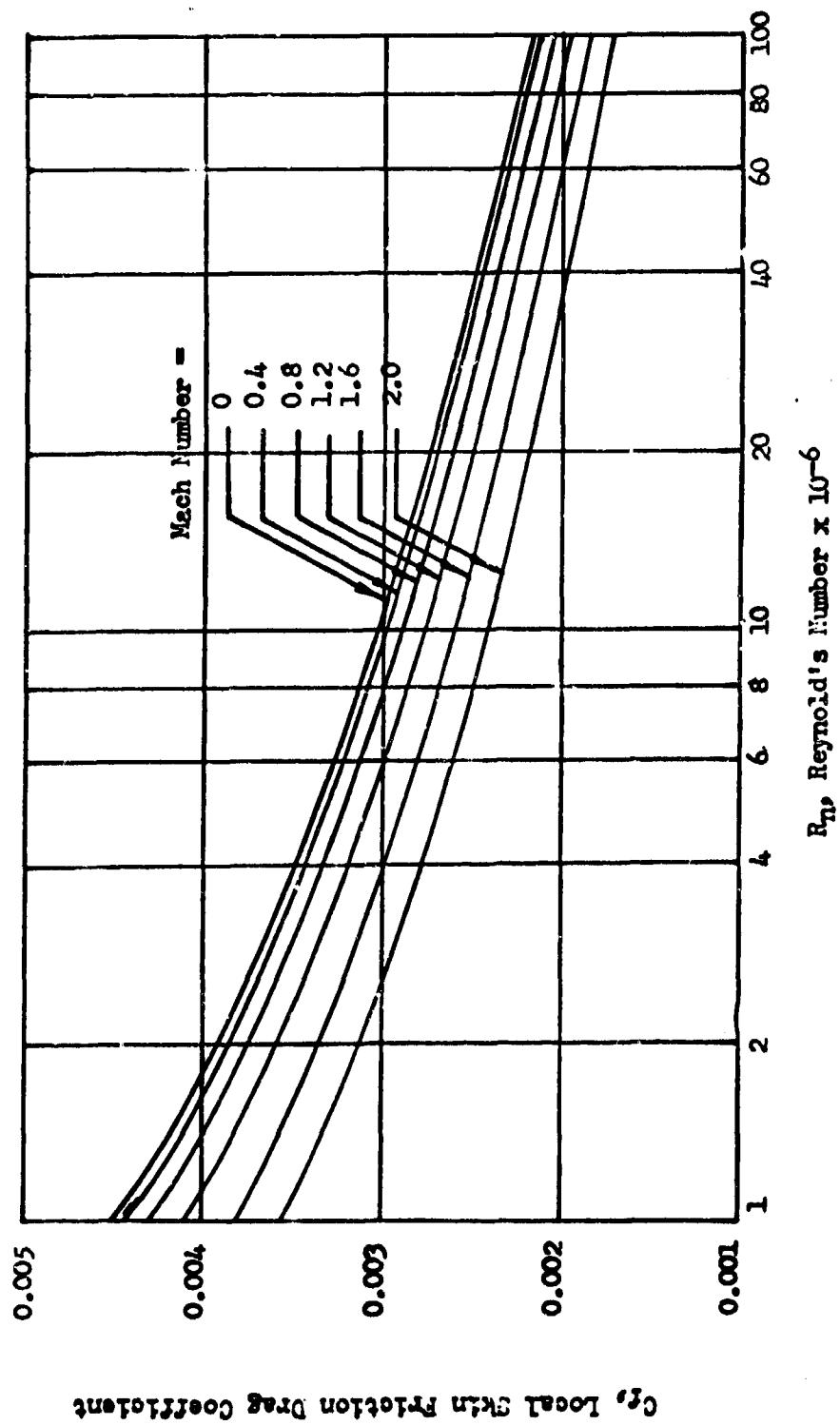


FIGURE 10-21. Skin Friction Drag Coefficient.

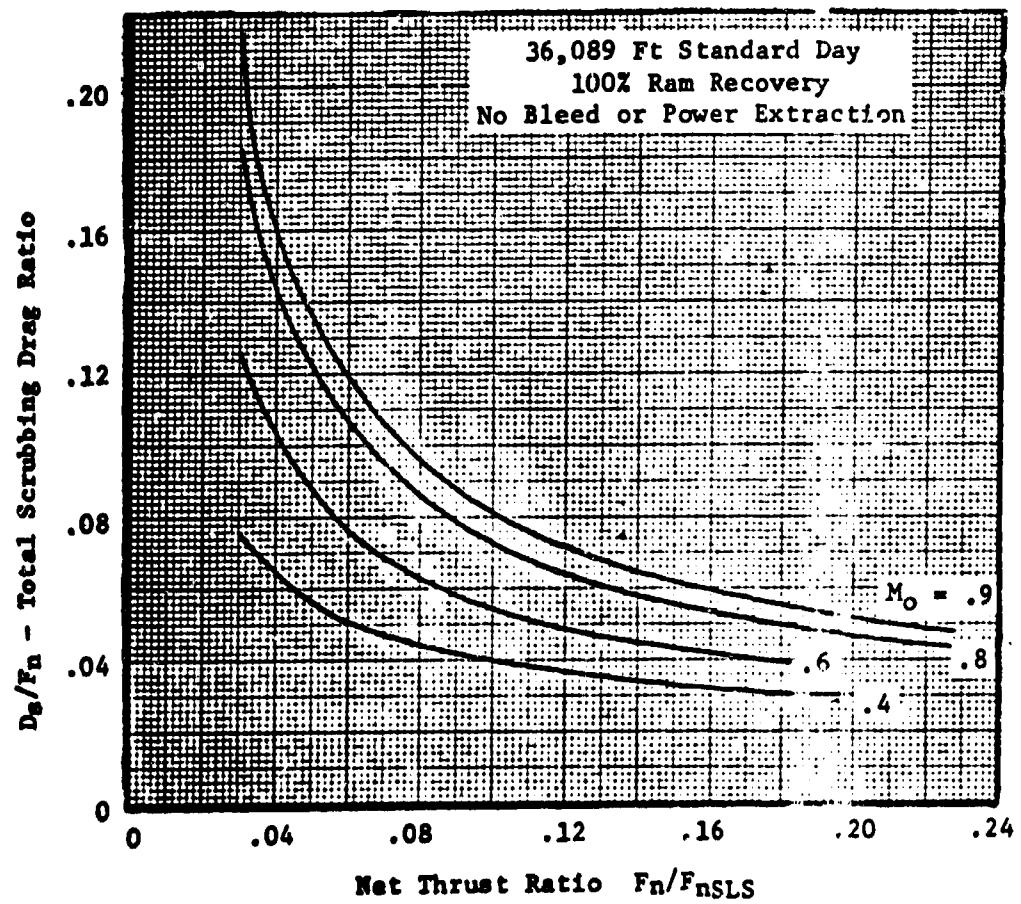


FIGURE 10-22. Total Nacelle Scrubbing Drag

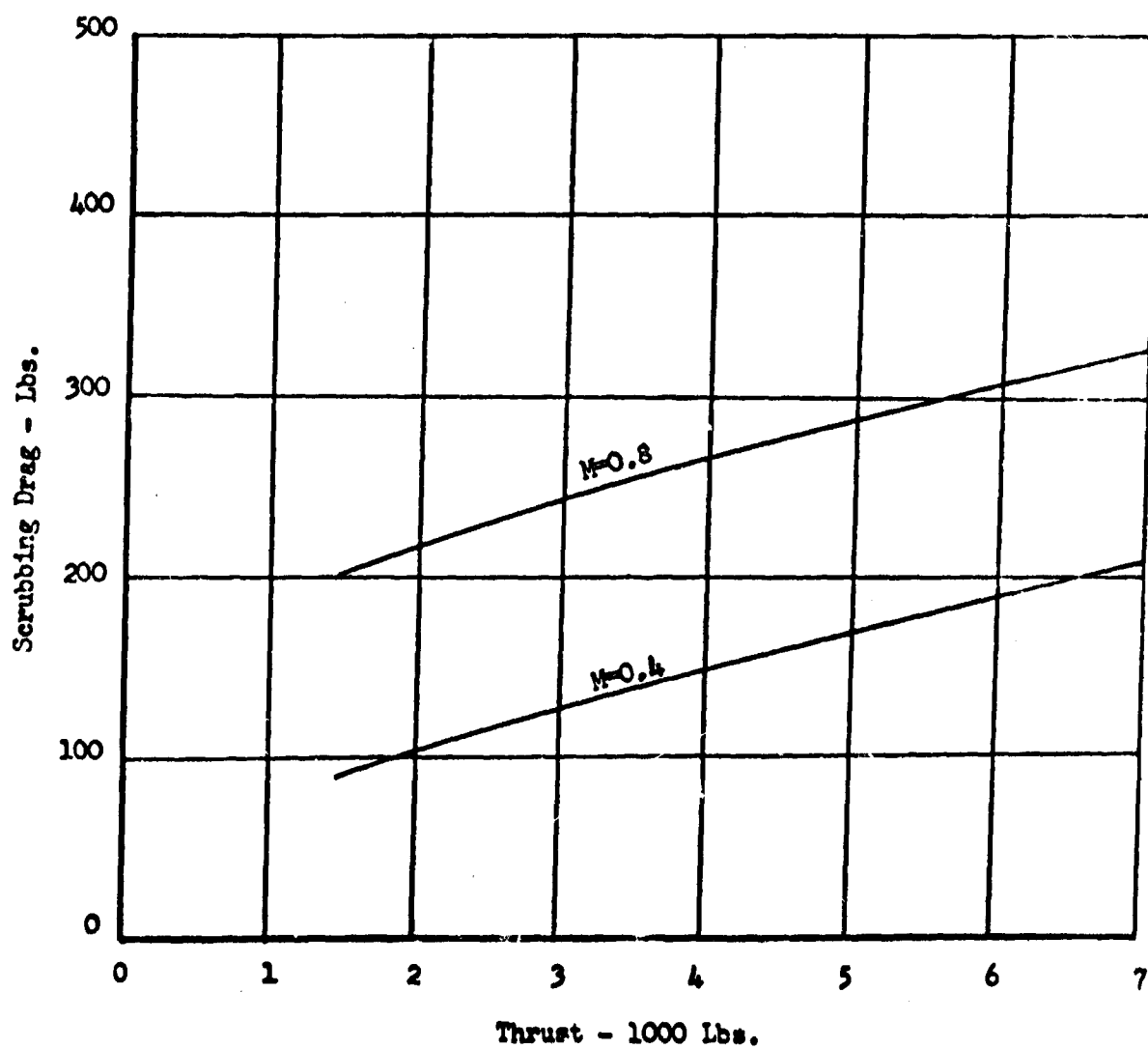


FIGURE 10-23. Scrubbing Drag.
36,089 Ft. Standard Day

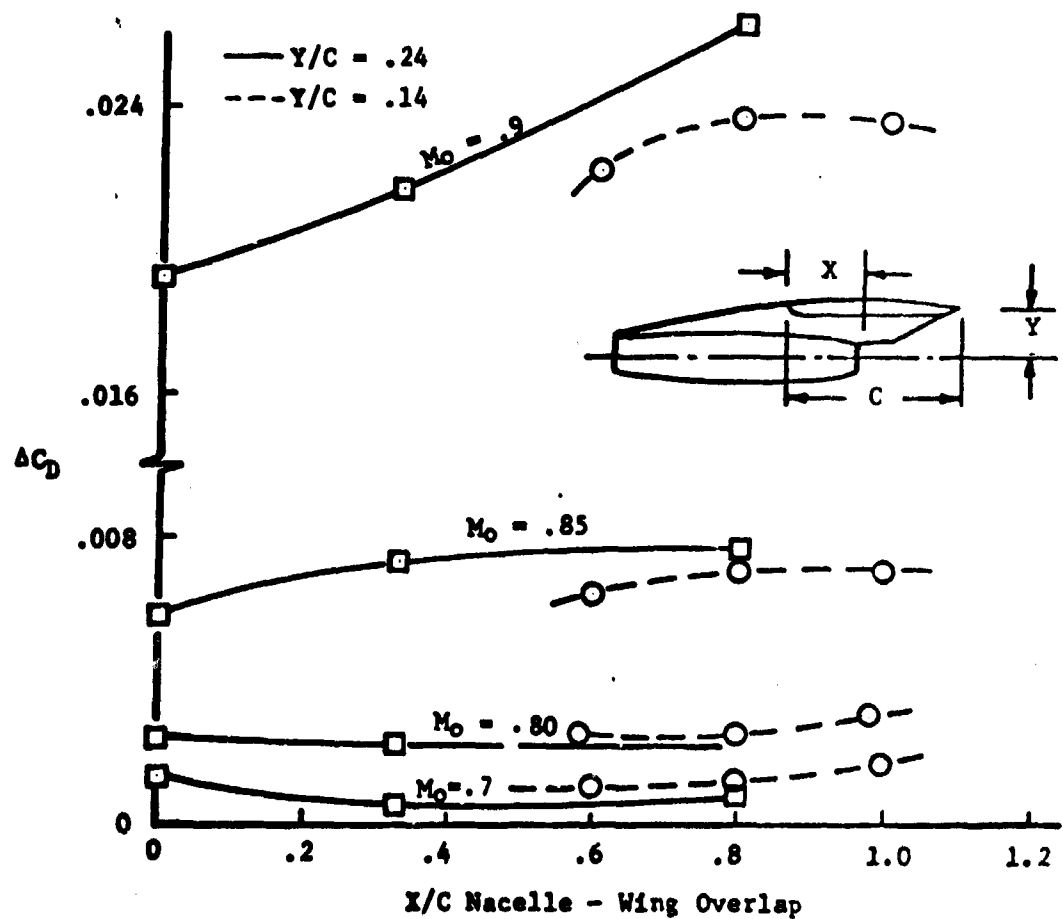


FIGURE 10-24 . Change in Airplane Drag With Nacelle Position

$$\Delta C_D = \frac{\text{Drag}}{q_0 A_w} \quad \text{Referred to a Typical Nacelle at } M_0 = 0.8, X/C = 0.25$$

From Reference 9

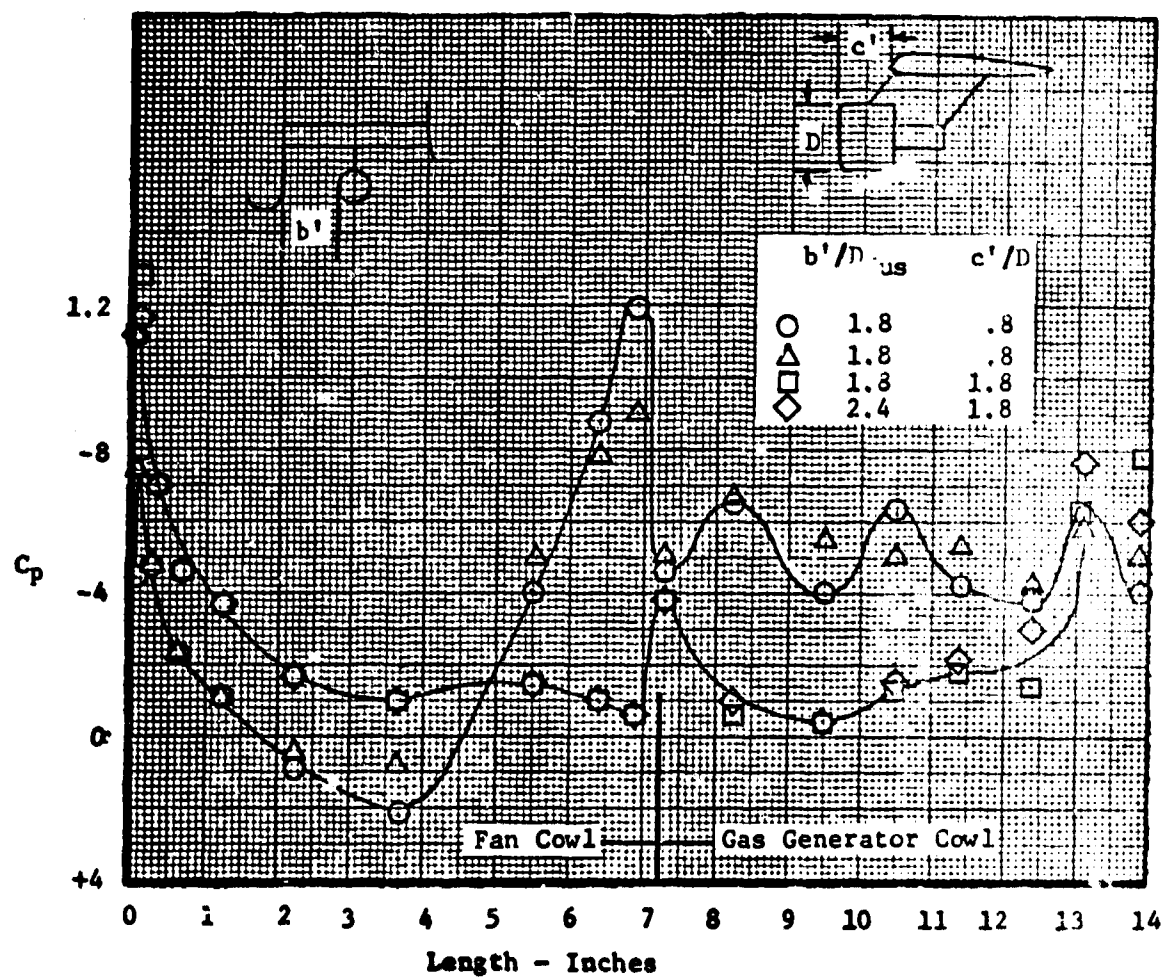


FIGURE 10-25. Nacelle Pressure Coefficients, Effect of Fuselage and Wing Proximity

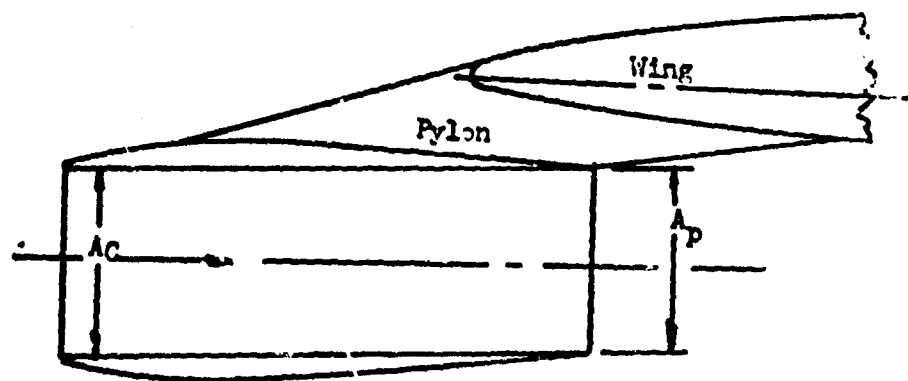
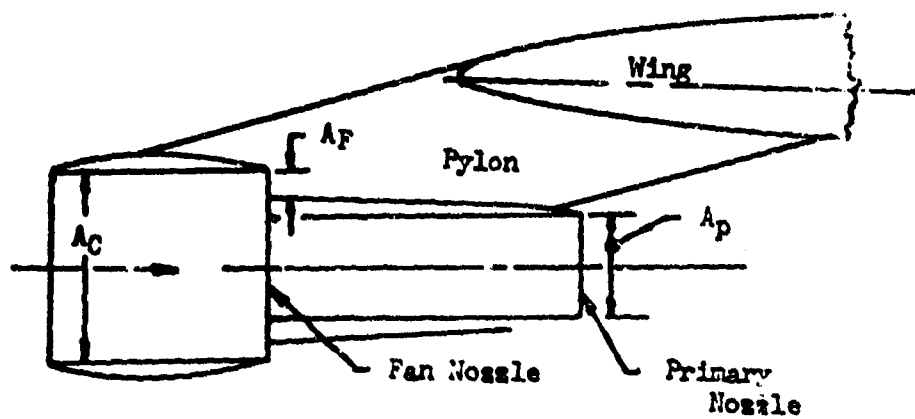


FIGURE 10-26. Flow-Through Nacelles

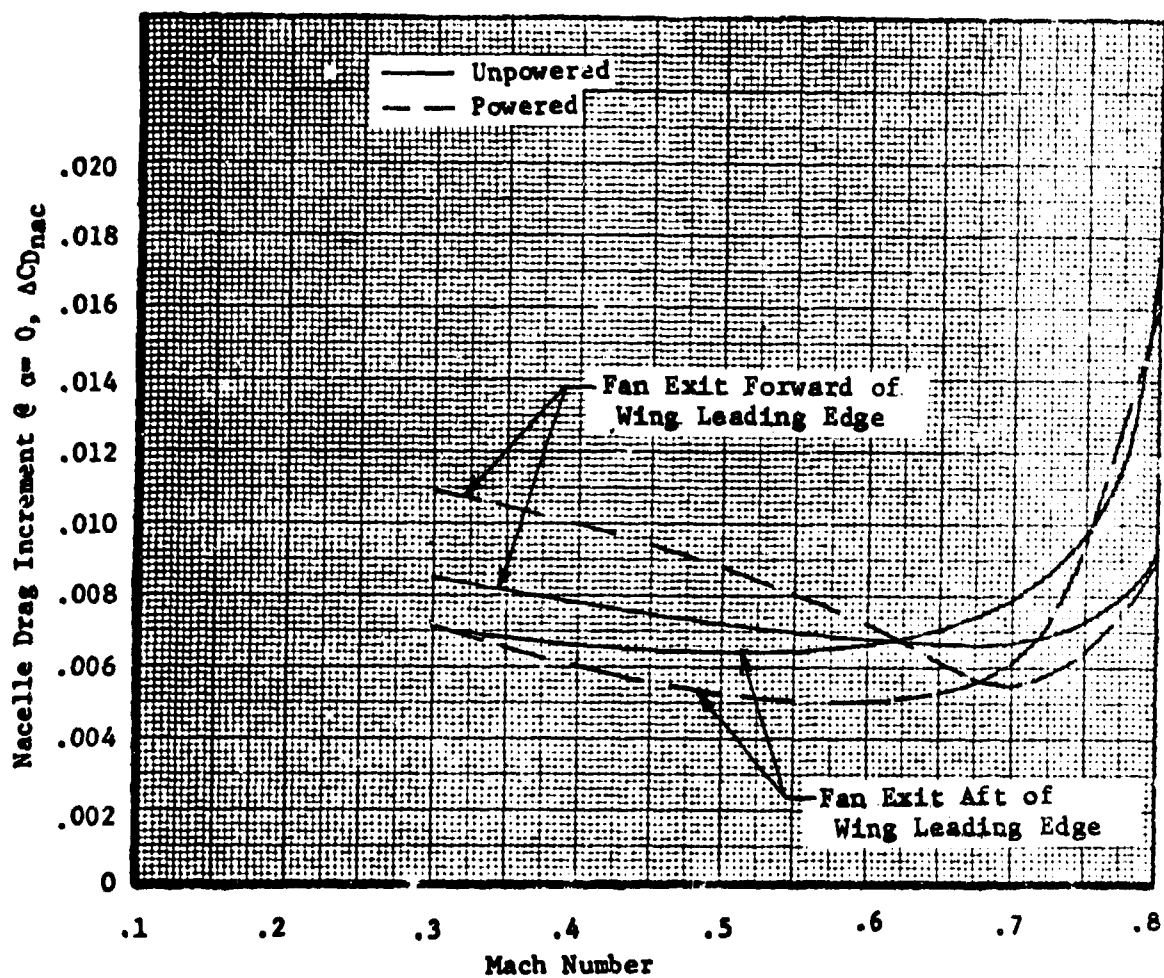


FIGURE 10-27. Incremental Nacelle Drag Comparison

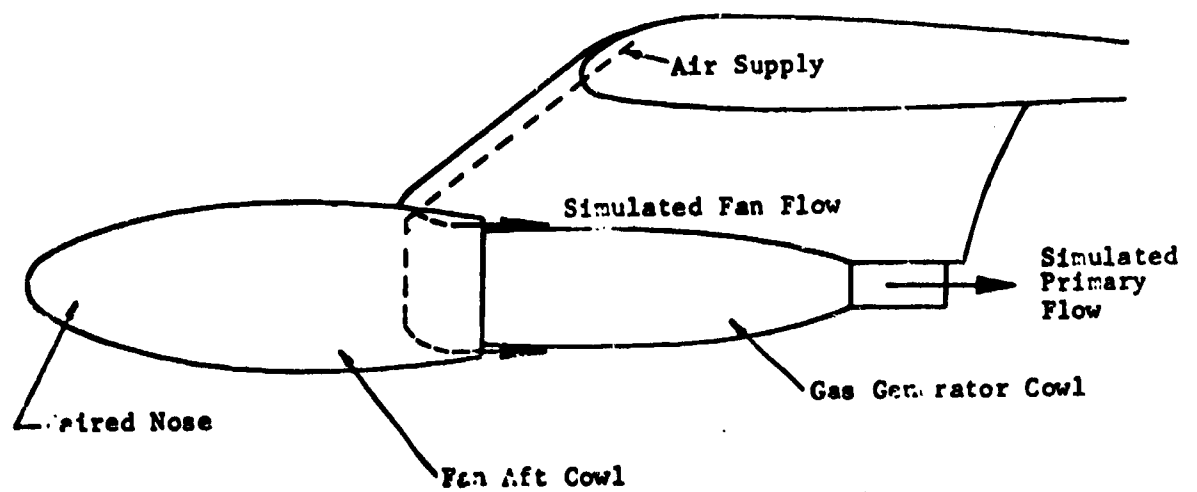


FIGURE 10-28. Blowing Nacelle

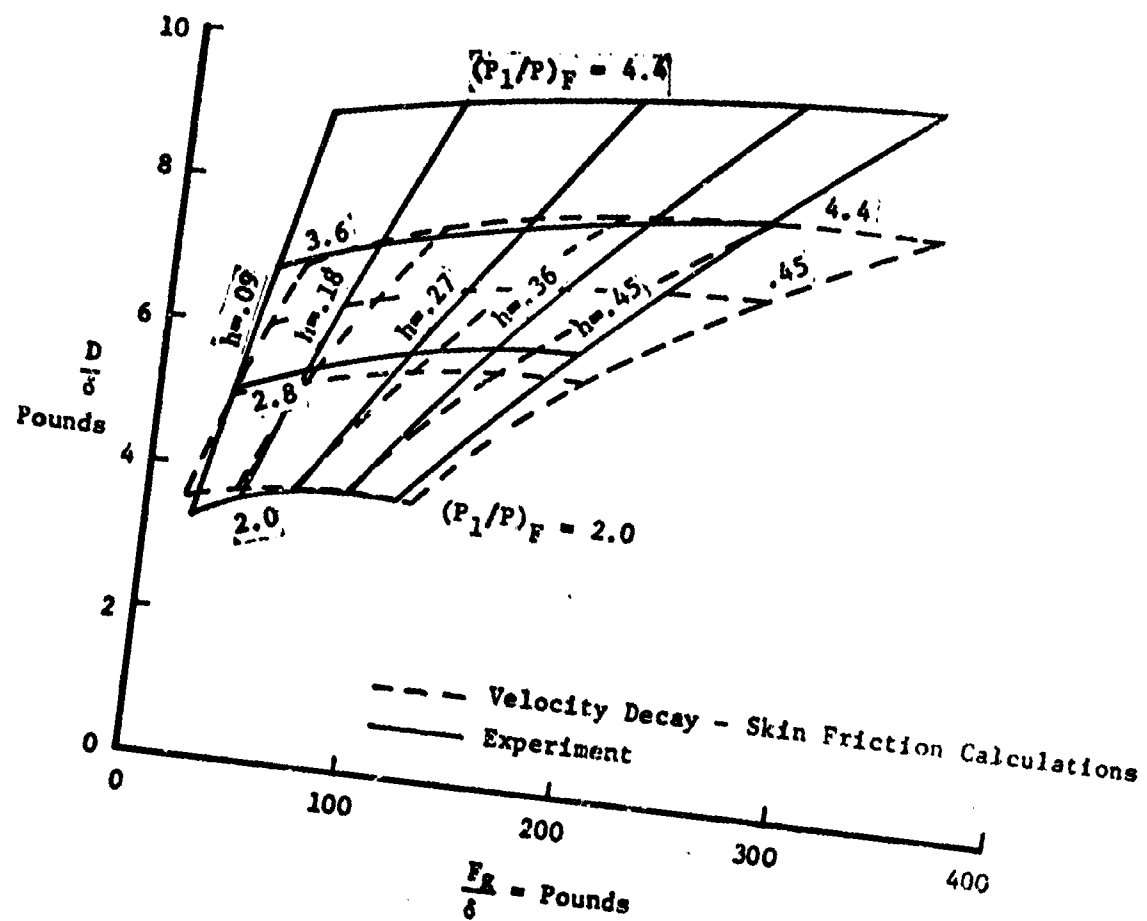


FIGURE 10-29. Afterbody Drag vs. Fan Gross Thrust:
 $M_\infty = 0.8$, $L = 12$ in.

n - fan exit height
 δ - P_∞/P_{SLS}

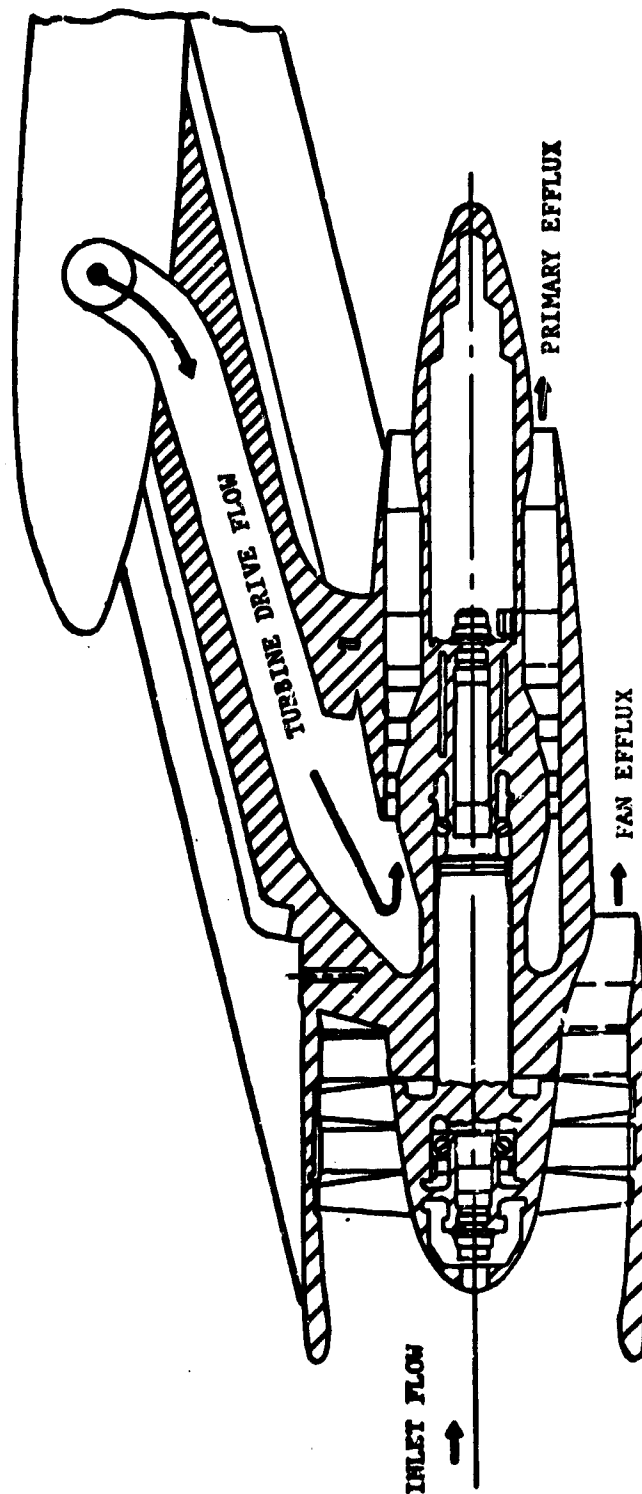


FIGURE 10-30. Powered Fan Simulator

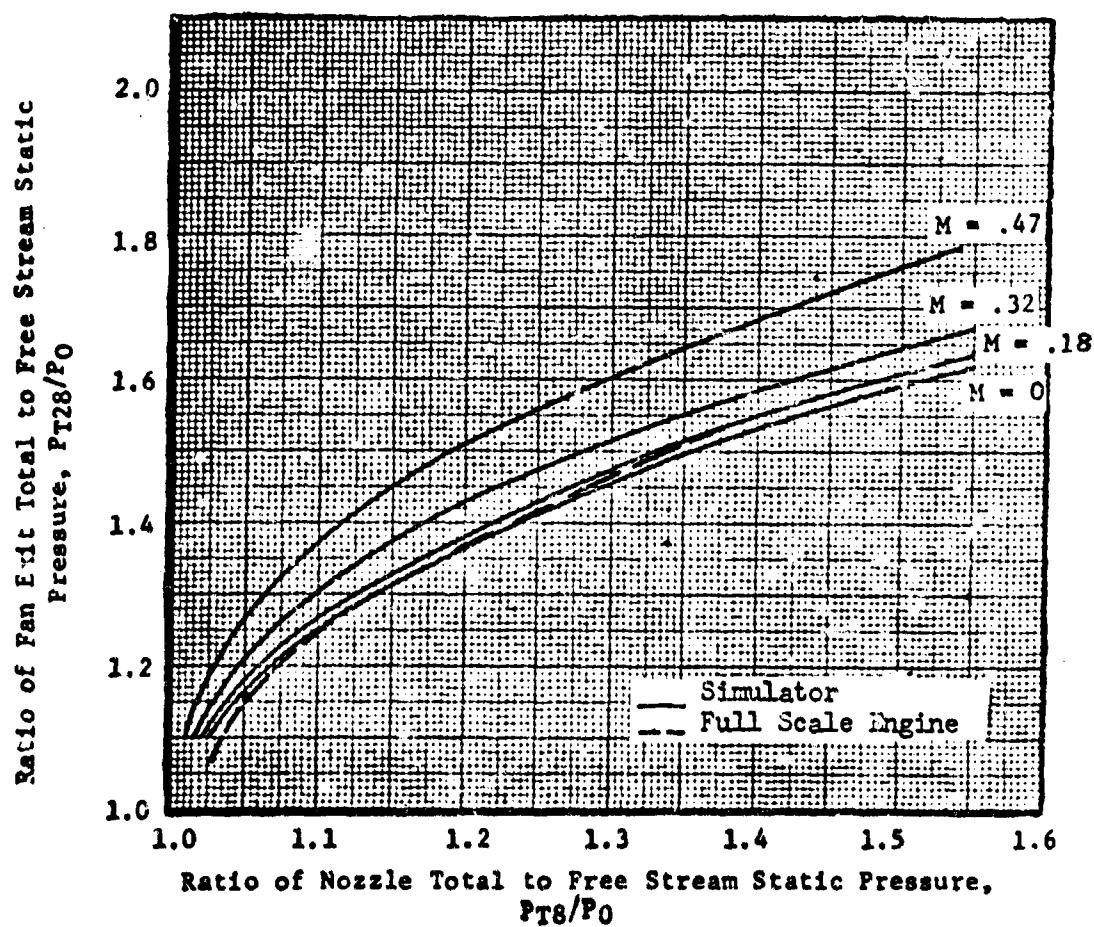


FIGURE 10-31. Powered Fan Simulator Calibration

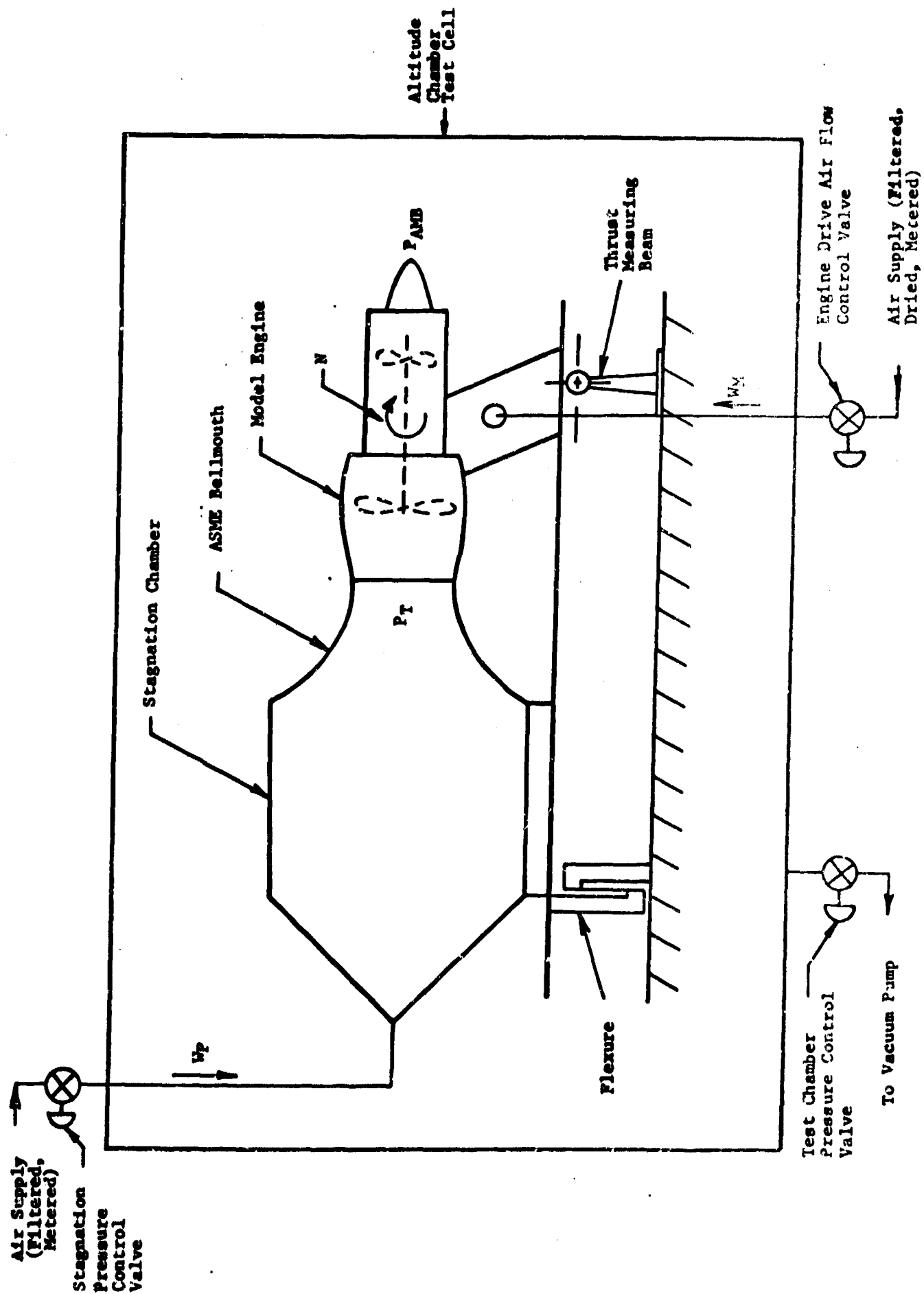


FIGURE 10-32 . Powered Fan Simulator Calibration Facility

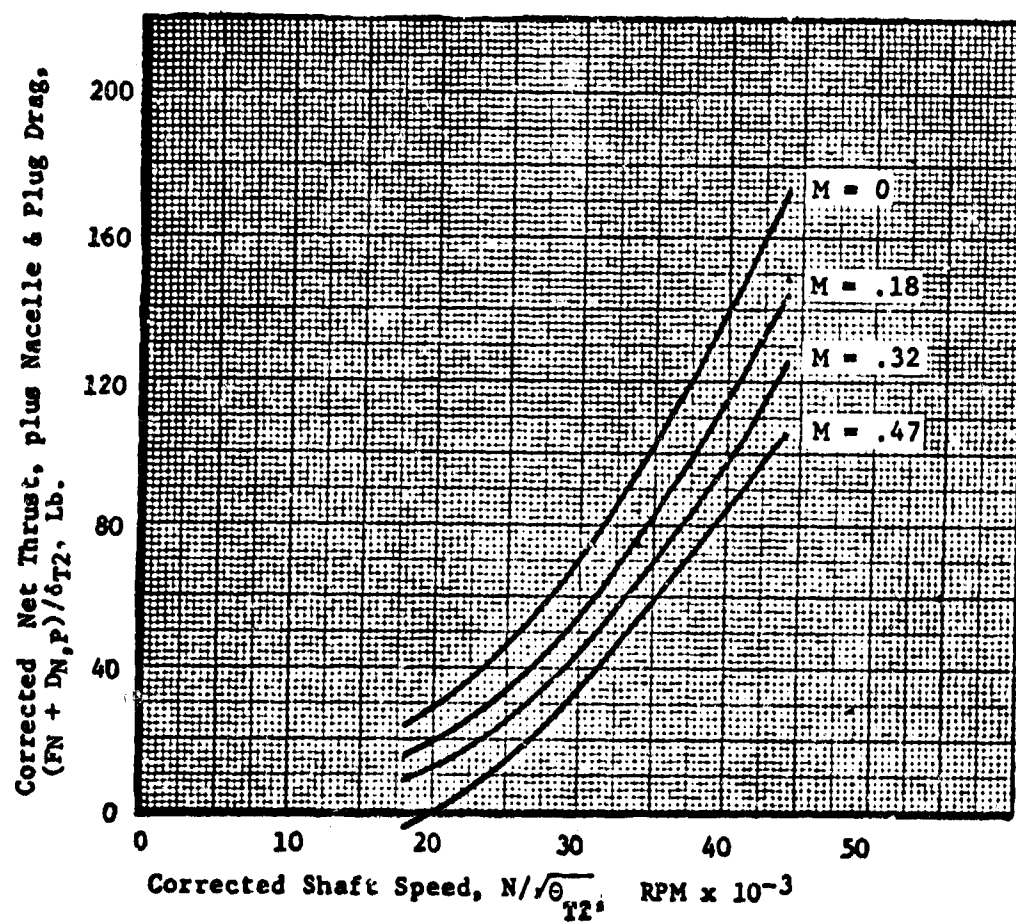


FIGURE 10-33. Powered Fan Simulator Performance

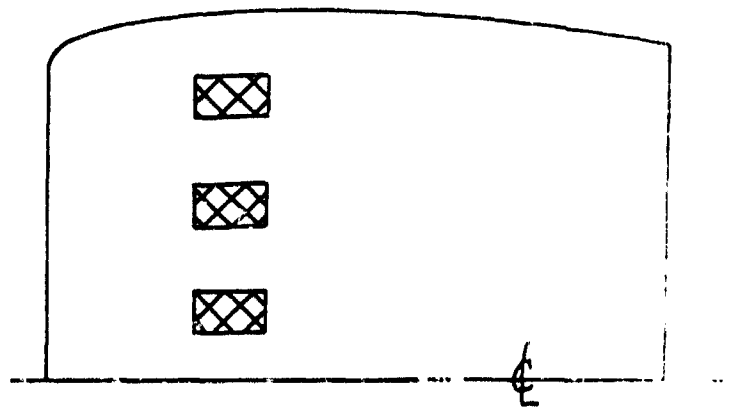
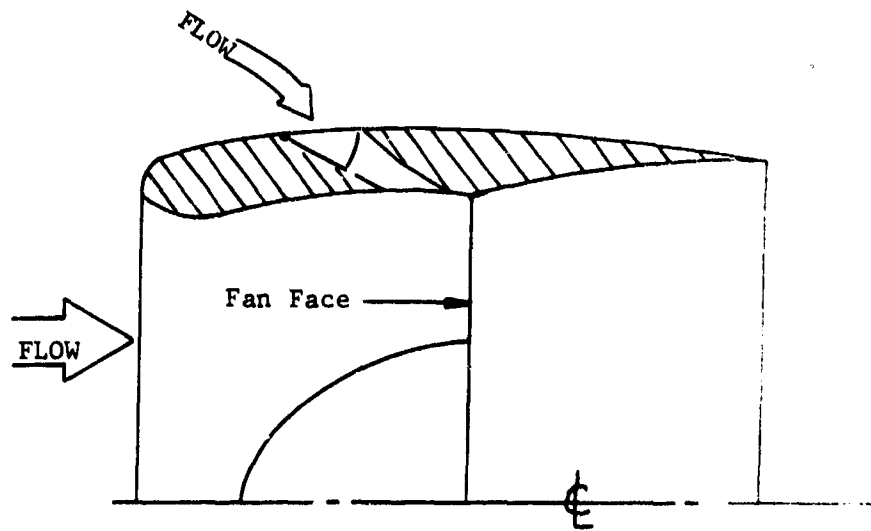


FIGURE 10-34 . Auxiliary Inlets

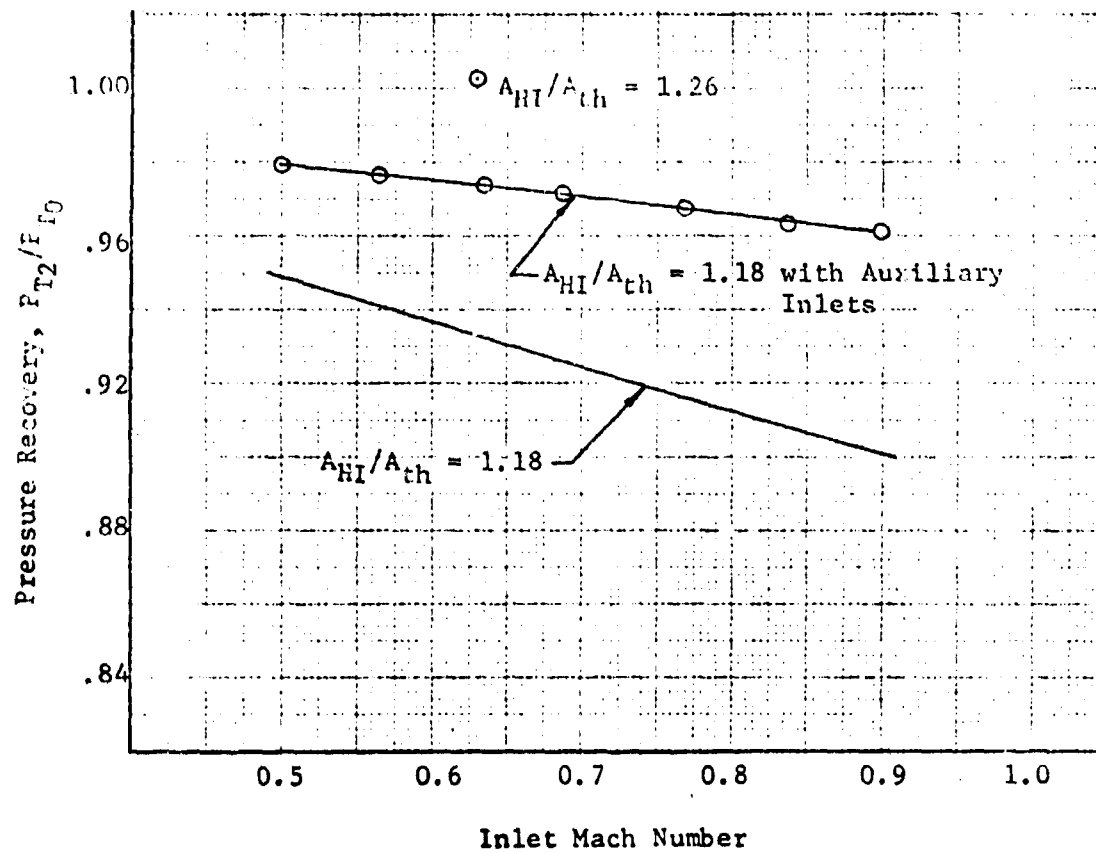


FIGURE 10- 35 Auxiliary Inlet Performance

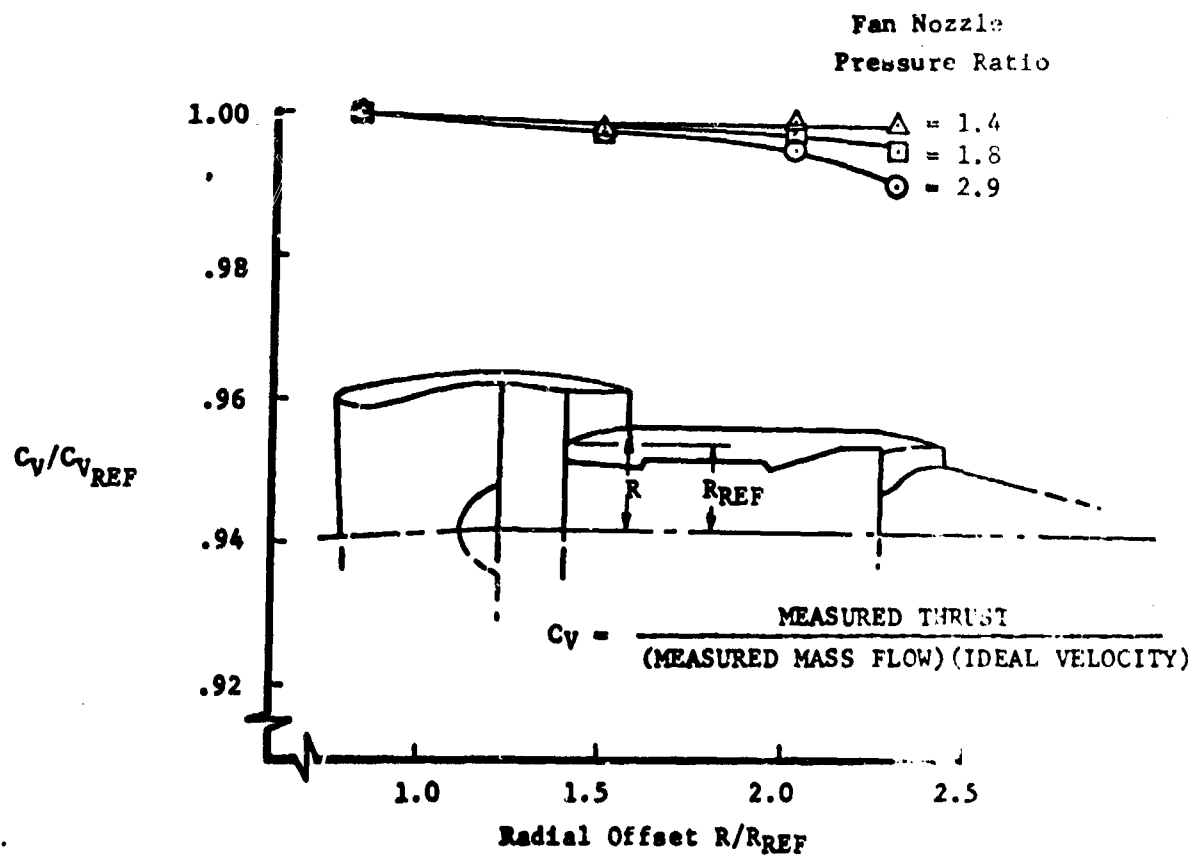


FIGURE 10-36. Offset Fan Nozzle Velocity Coefficients

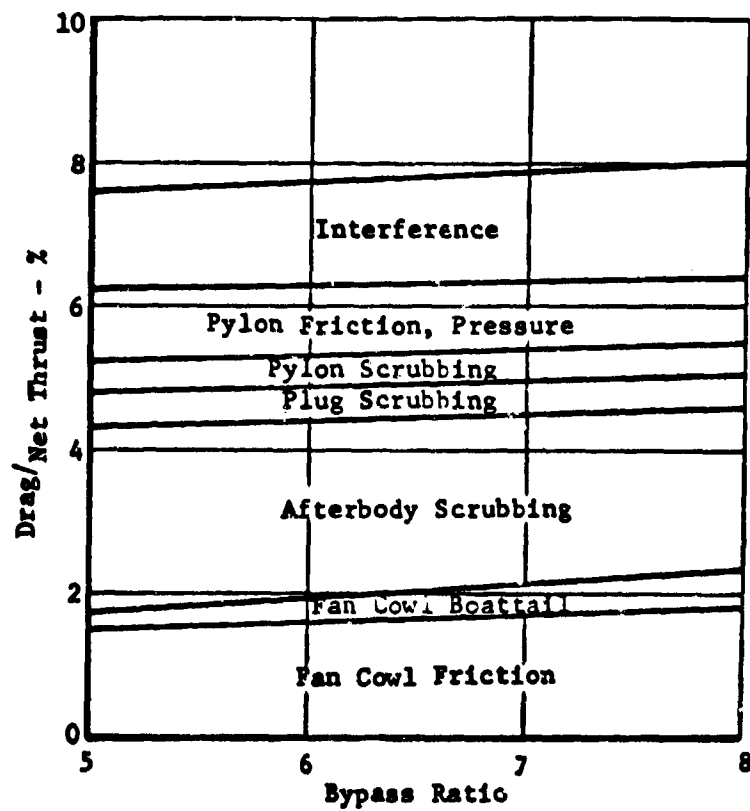


FIGURE 10-37. Typical Nacelle Drag Breakdown

Installed Performance
Engines Sized for Constant F_n at $M=0.85$

Comparative Installed

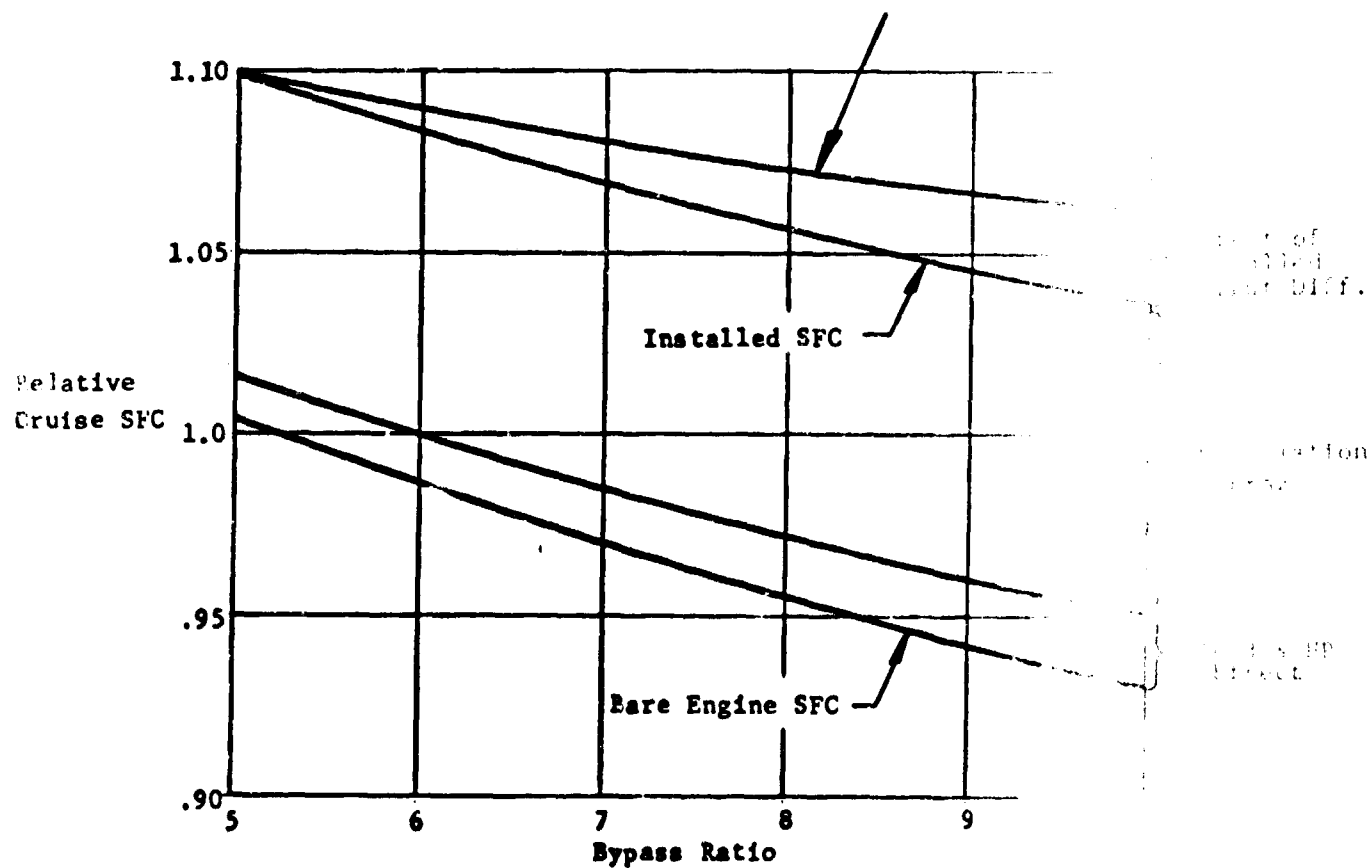


FIGURE 10-38. Effect of Installation on Cruise SFC

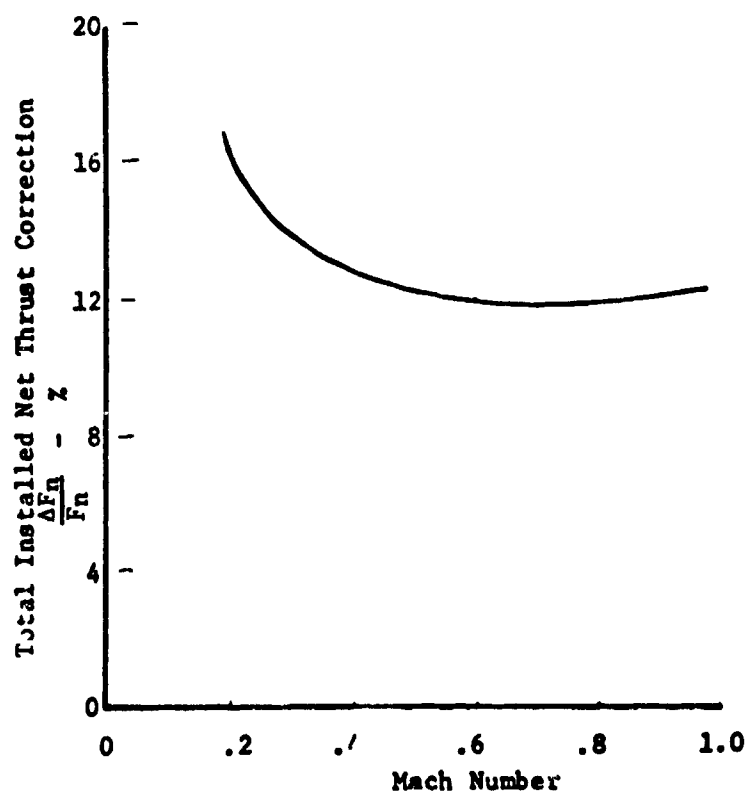


FIGURE 10-39. Total Installation Loss
Cruise at 36,089 Feet

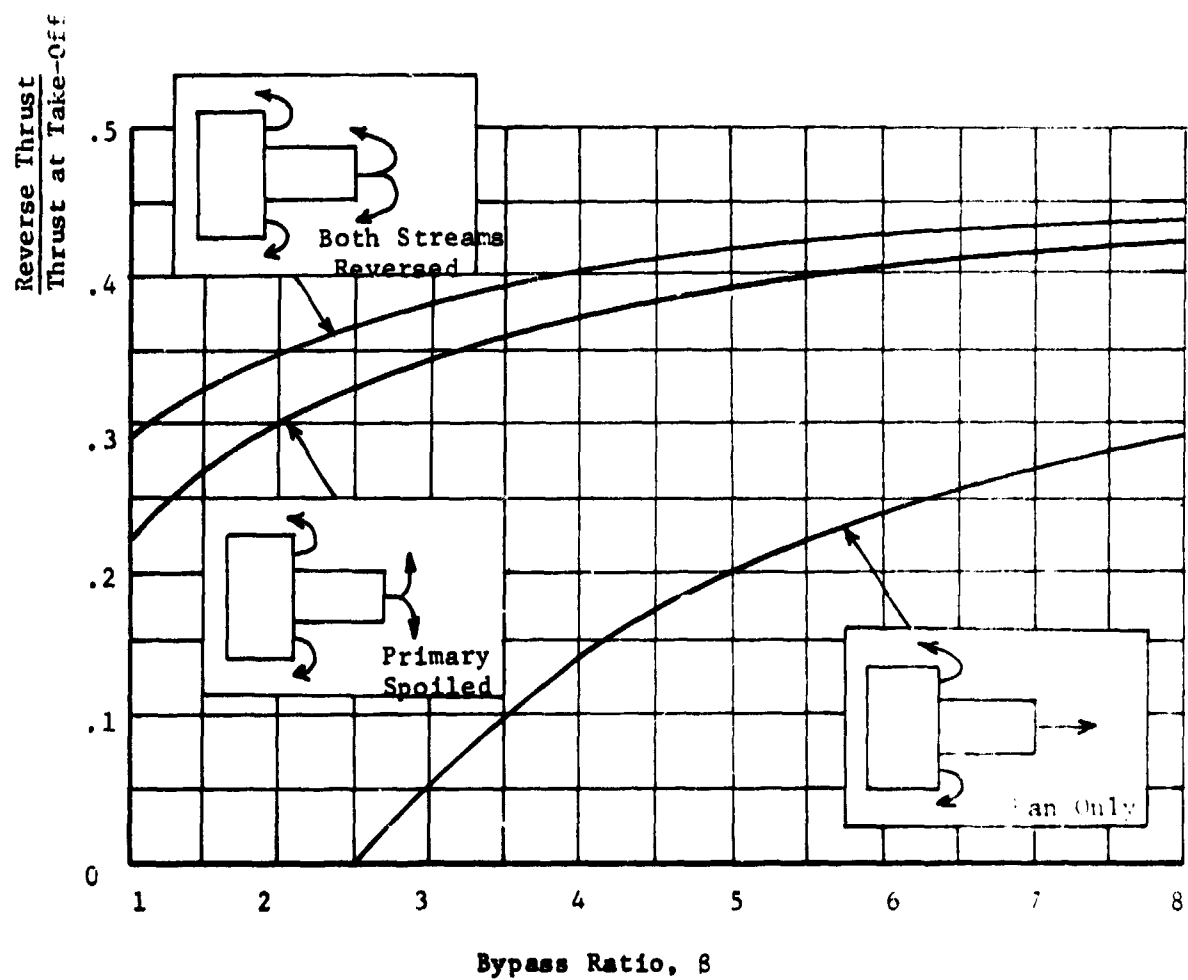
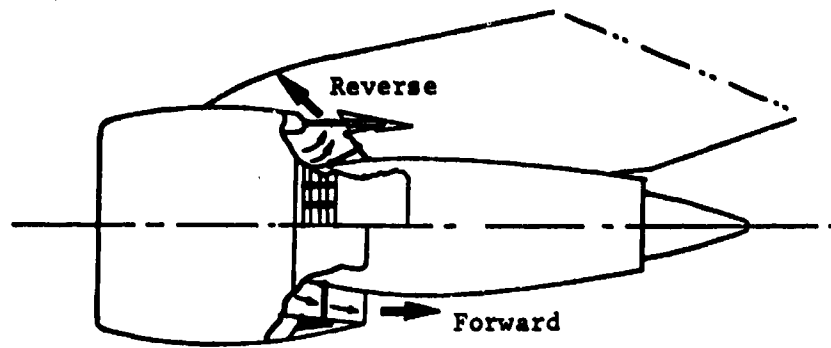
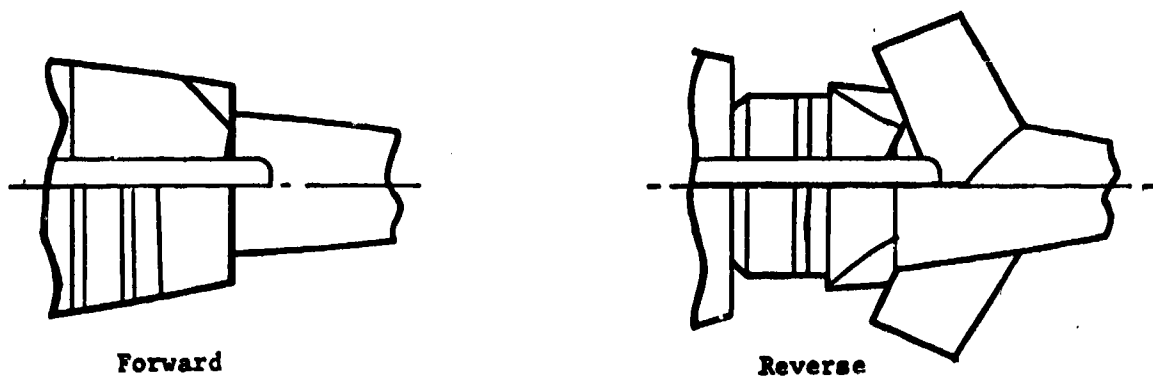


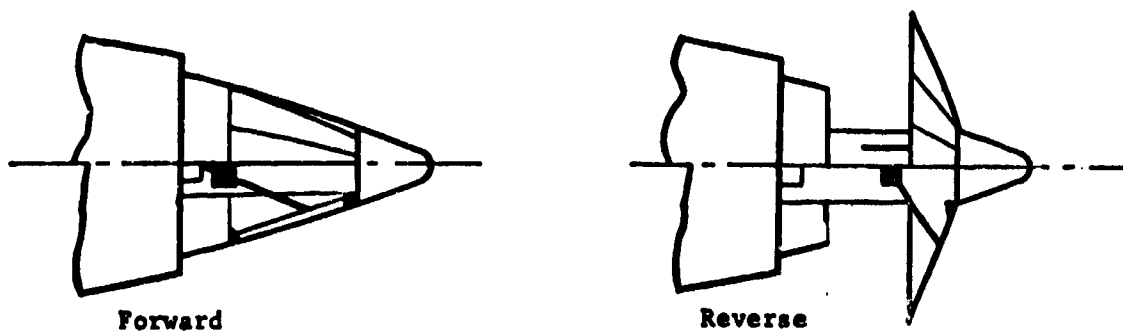
FIGURE 10-40. Typical Reverser Effectiveness



a. Cascade Type



b. Target Type



c. Plug Type

FIGURE 10-41. Thrust Reverser Comparison

ATTACHED FLOW REINGESTION

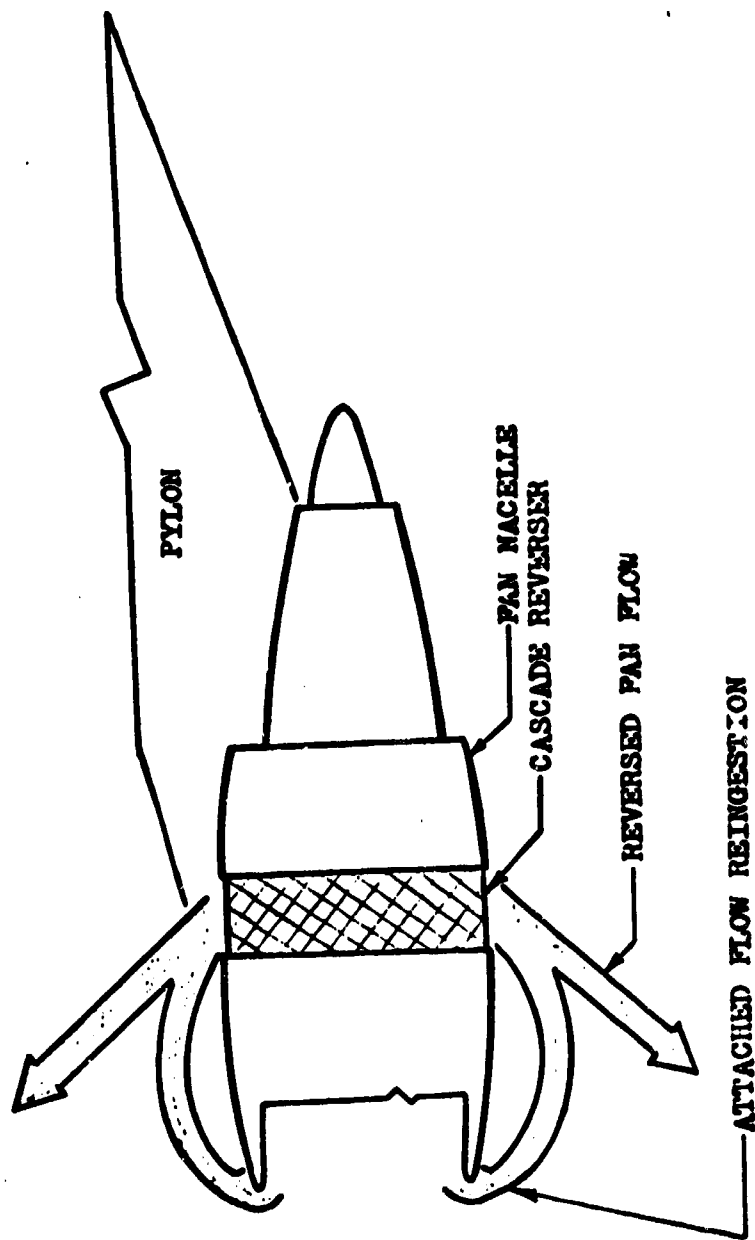


FIGURE 10-42 Attached Flow Reingestion.

INLET PRESSURE RECOVERY
OUTBOARD ENGINE
54 KNOTS

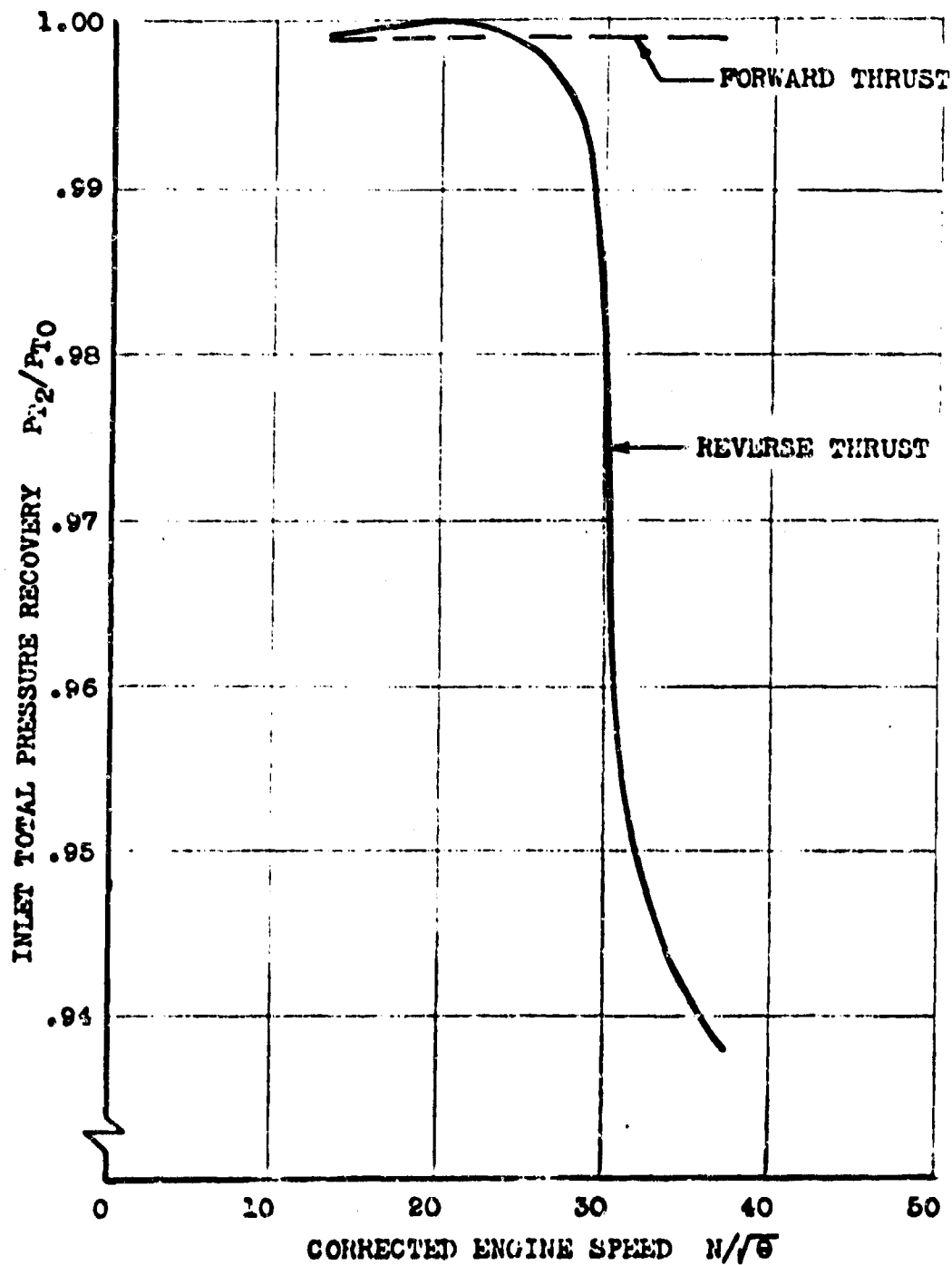


FIGURE 10-43. Inlet Pressure Recovery

INLET DISTORTION
OUTBOARD ENGINE
54 KNOTS

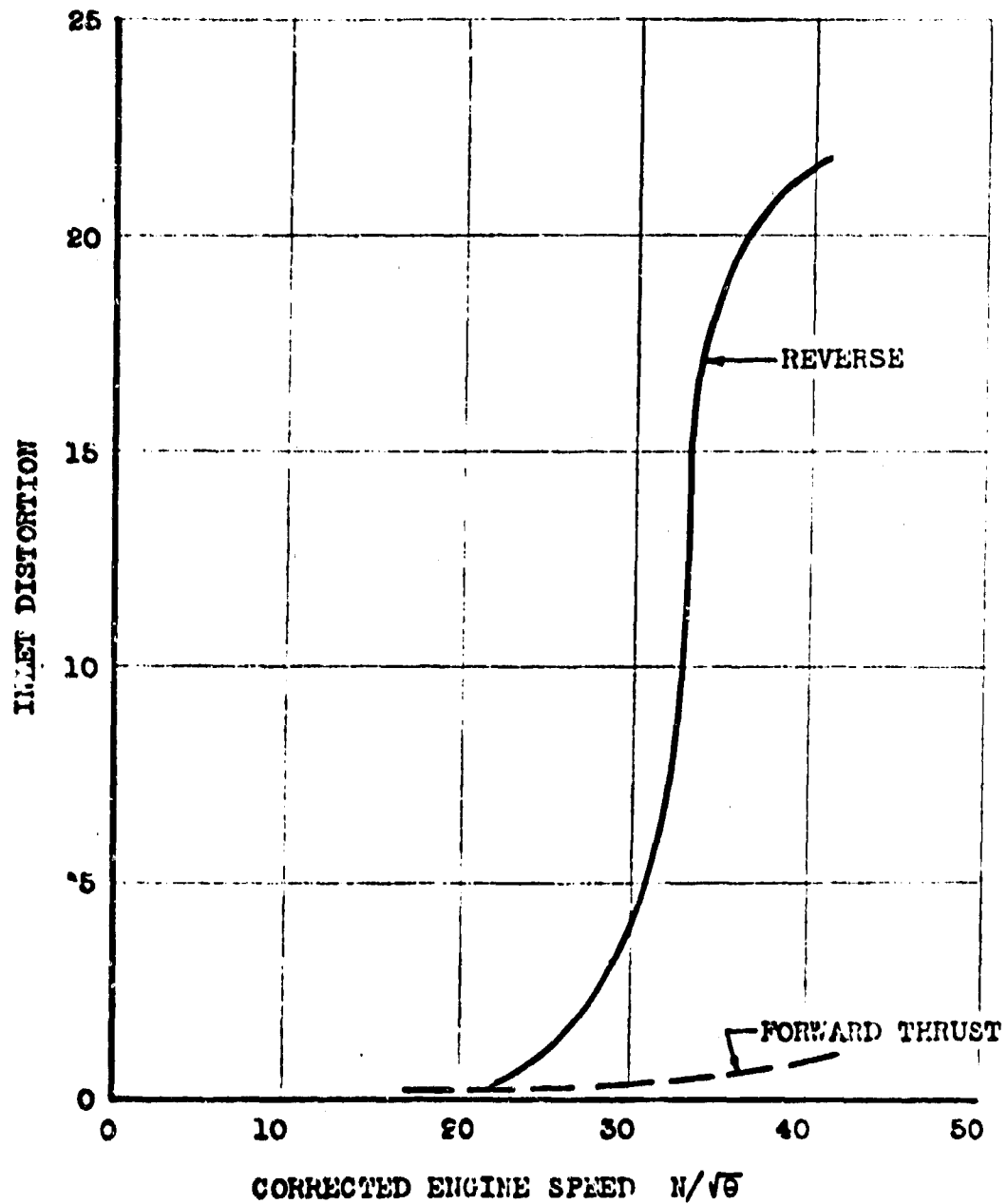


FIGURE 10-44. Inlet Distortion.

INLET DISTORTION
OUTBOARD ENGINE
54 KNOTS

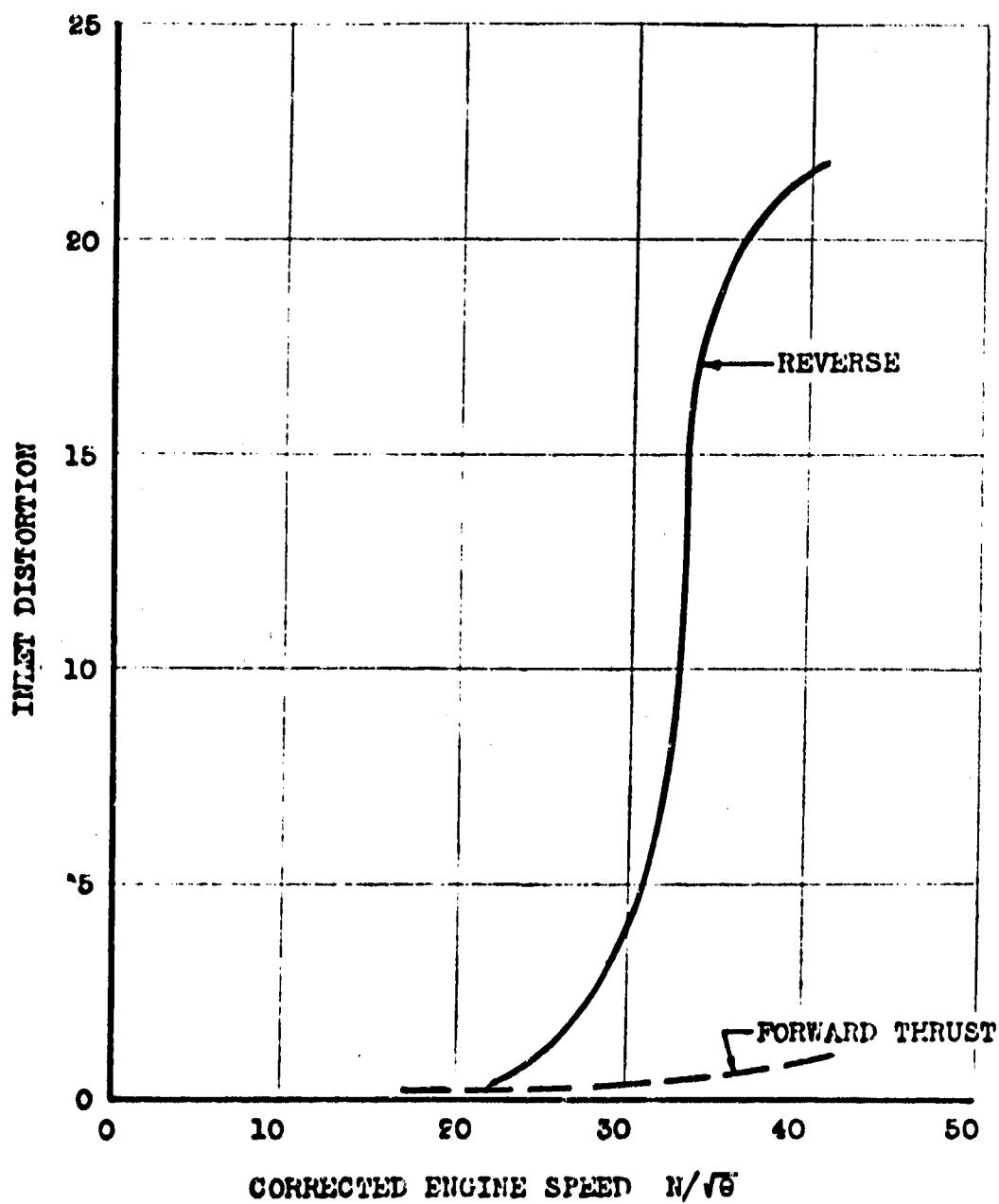


FIGURE 10- 44. Inlet Distortion.

EFFECT OF REINGESTION ON REVERSE THRUST SEA LEVEL TROPICAL DAY

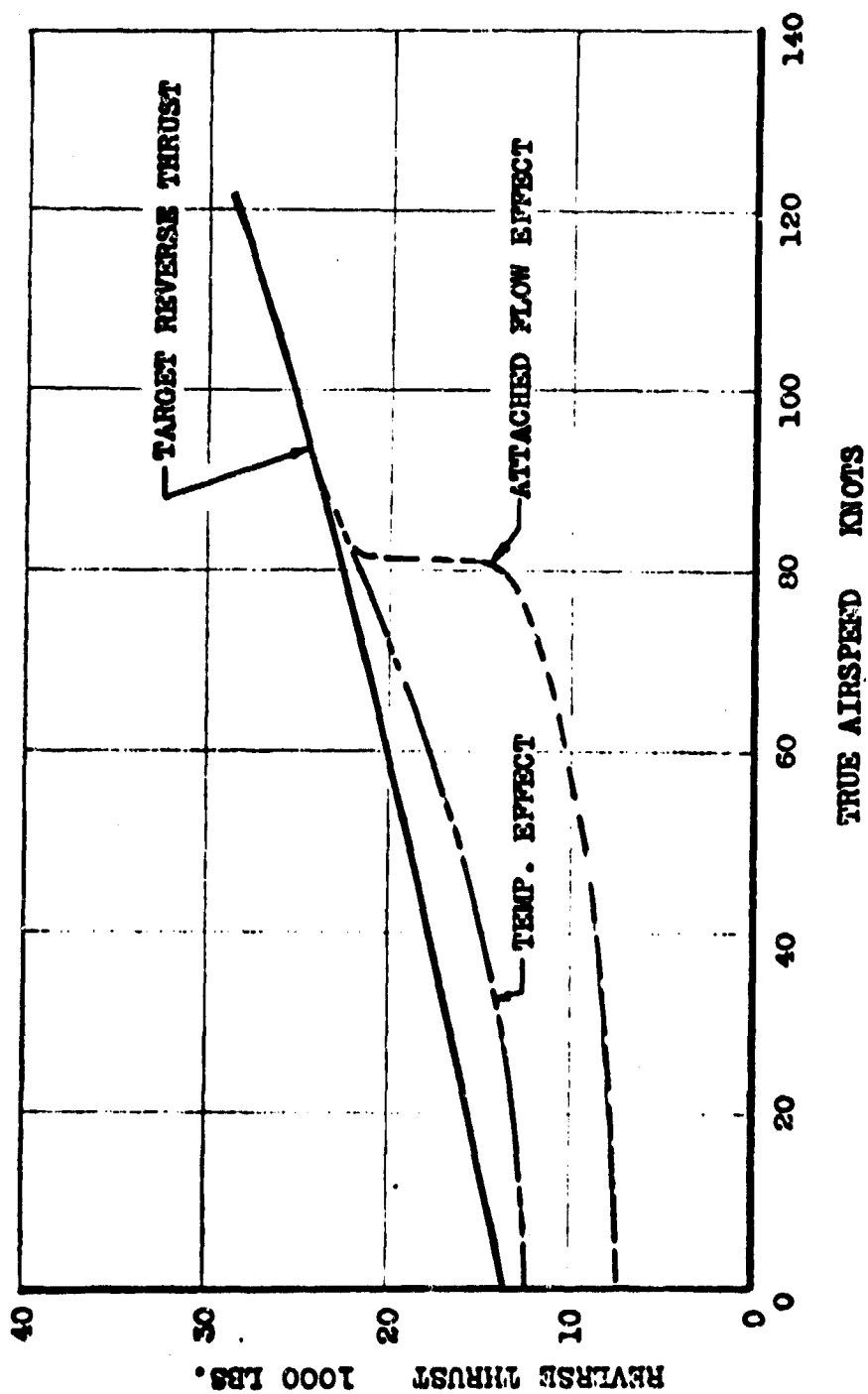


FIGURE 10-46. Effect of Reingestion on Reverse Thrust